KENS REPORT-VIII

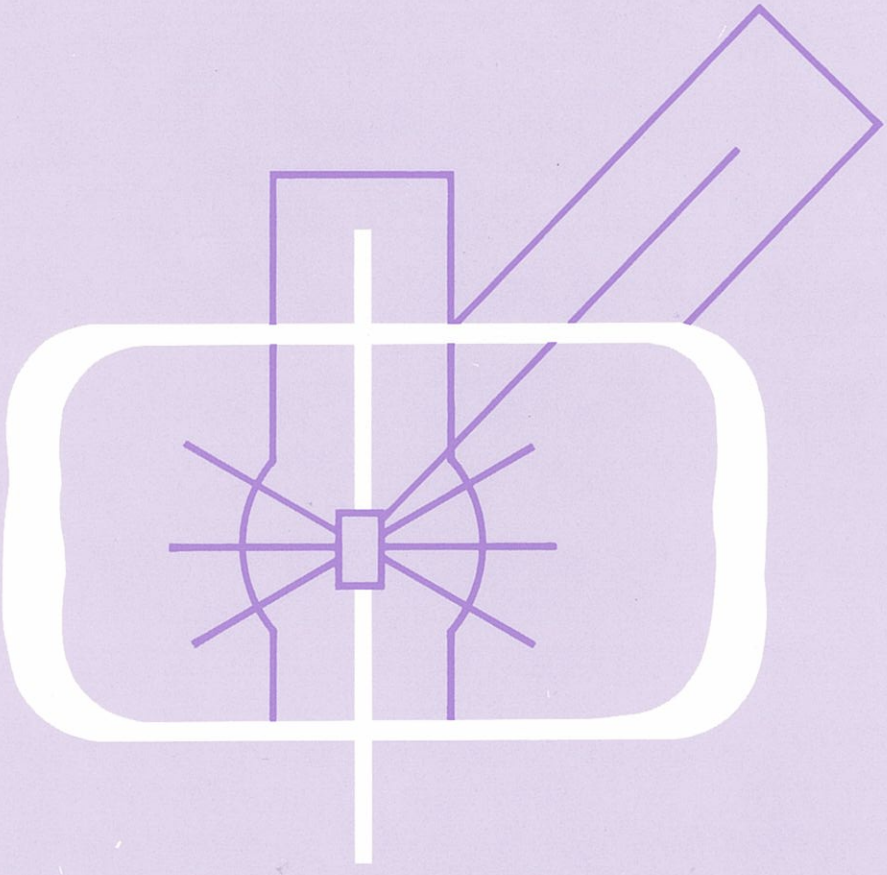

1989/90

NATIONAL LABORATORY FOR HIGH ENERGY PHYSICS, KEK

KENS REPORT-VIII
1989/90

Panel Discussion at ICANS-XI, KEK (October 22-26, 1990)

Edited by

H. Ikeda
M. Furusaka
N. Watanabe

KEK Progress Report 90-2 M

KEK Reports are available from:

Technical Information & Library
National Laboratory for High Energy Physics
1-1 Oho, Tsukuba-shi
Ibaraki-ken, 305
JAPAN

Phone: 0298-64-1171
Telex: 3652-534 (Domestic)
(0)3652-534 (International)
Fax: 0298-64-4604
Cable: KEKOHO

KENS NEUTRON SCATTERING FACILITY

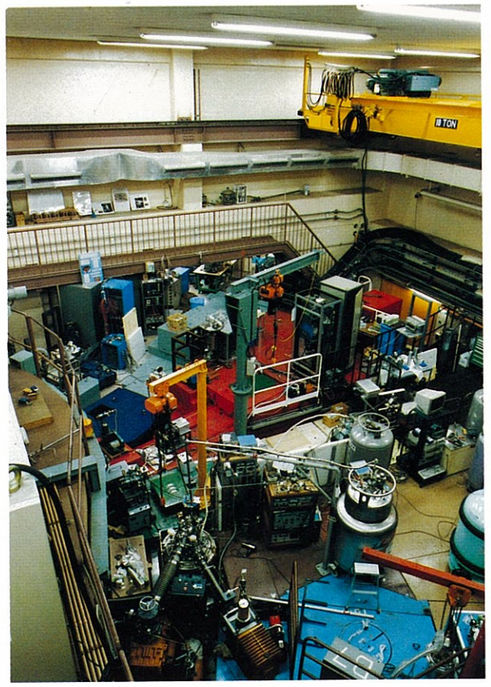

LAM-40, WINK, INC,
RAC, PEN, LAM-D

MAX	Coherent Inelastic Scattering Spectrometer
MRP	Medium Resolution Diffractometer under Extreme Conditions
HIT	Liquid and Amorphous Diffractometer
WIT	Thermal Neutron Small Angle Scattering Instrument
FOX	Single Crystal Diffractometer
LAM-D	Molecular Spectrometer
PEN	Polarized Epithermal Neutron Spectrometer
CAT	Sub-eV Spectrometer
RAT	eV Spectrometer
INC	Chopper Spectrometer
LAM-40	Quasi-elastic Spectrometer
WINK	Small and Medium Angle Scattering Instrument
HRP	High Resolution Powder Diffractometer
TOP	Polarized Cold Neutron Spectrometer
LAM-80ET	High Resolution Quasi-elastic Spectrometer
UCN	Ultra Cold Neutron Machine
SAN	Small Angle Scattering Instrument

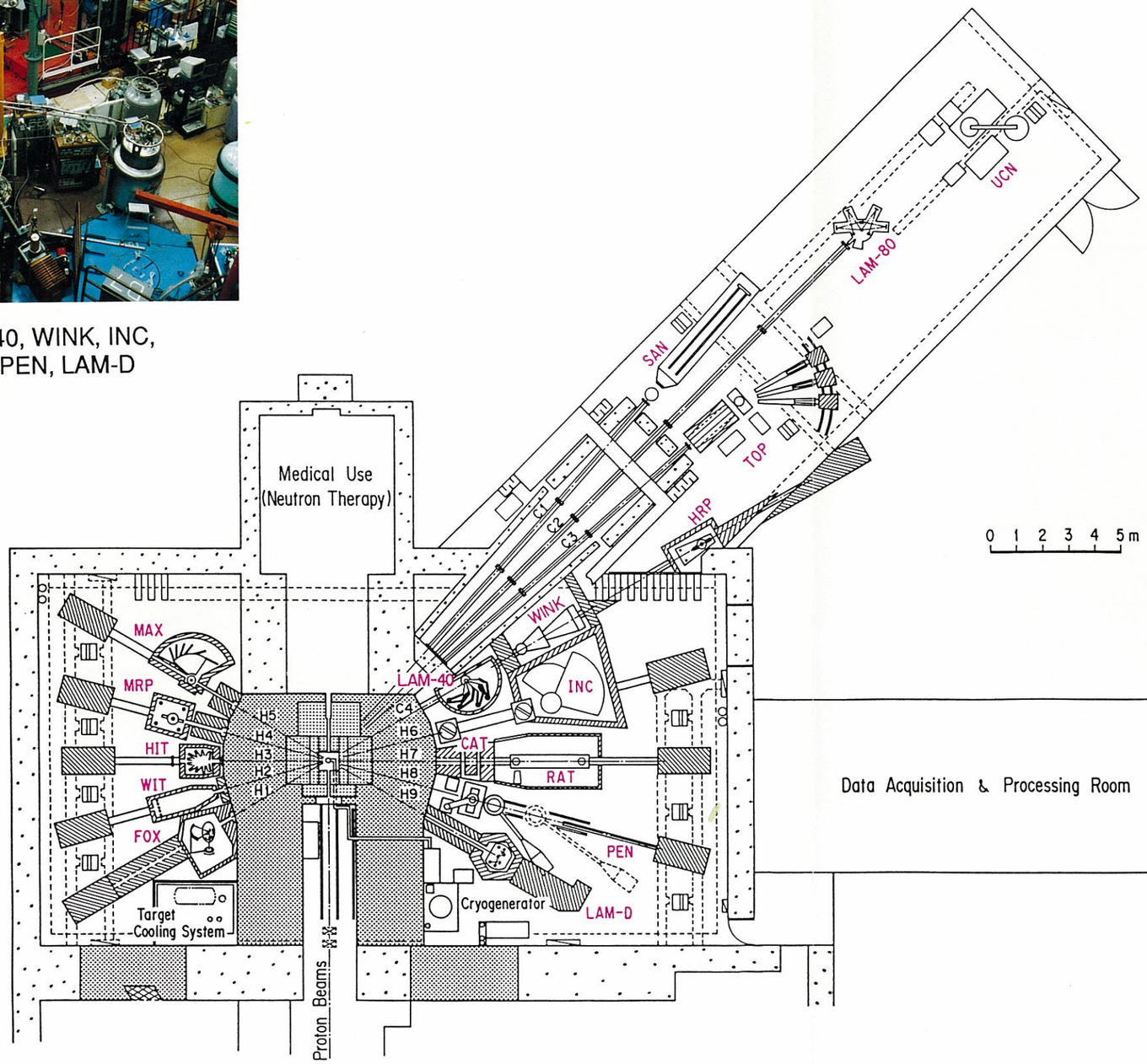

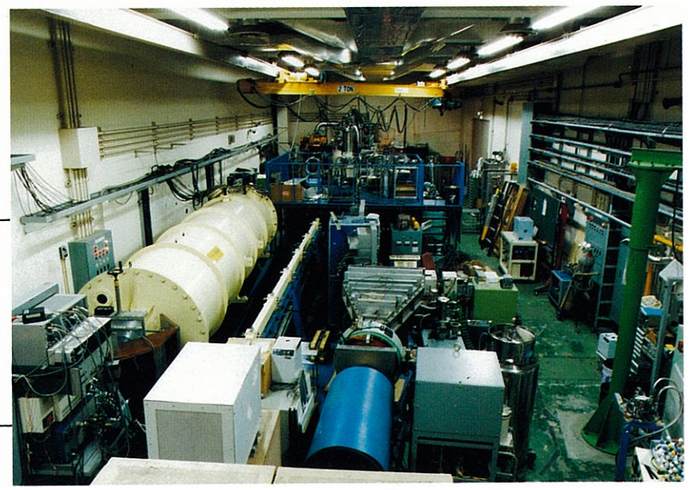

SAN, TOP, LAM-80ET

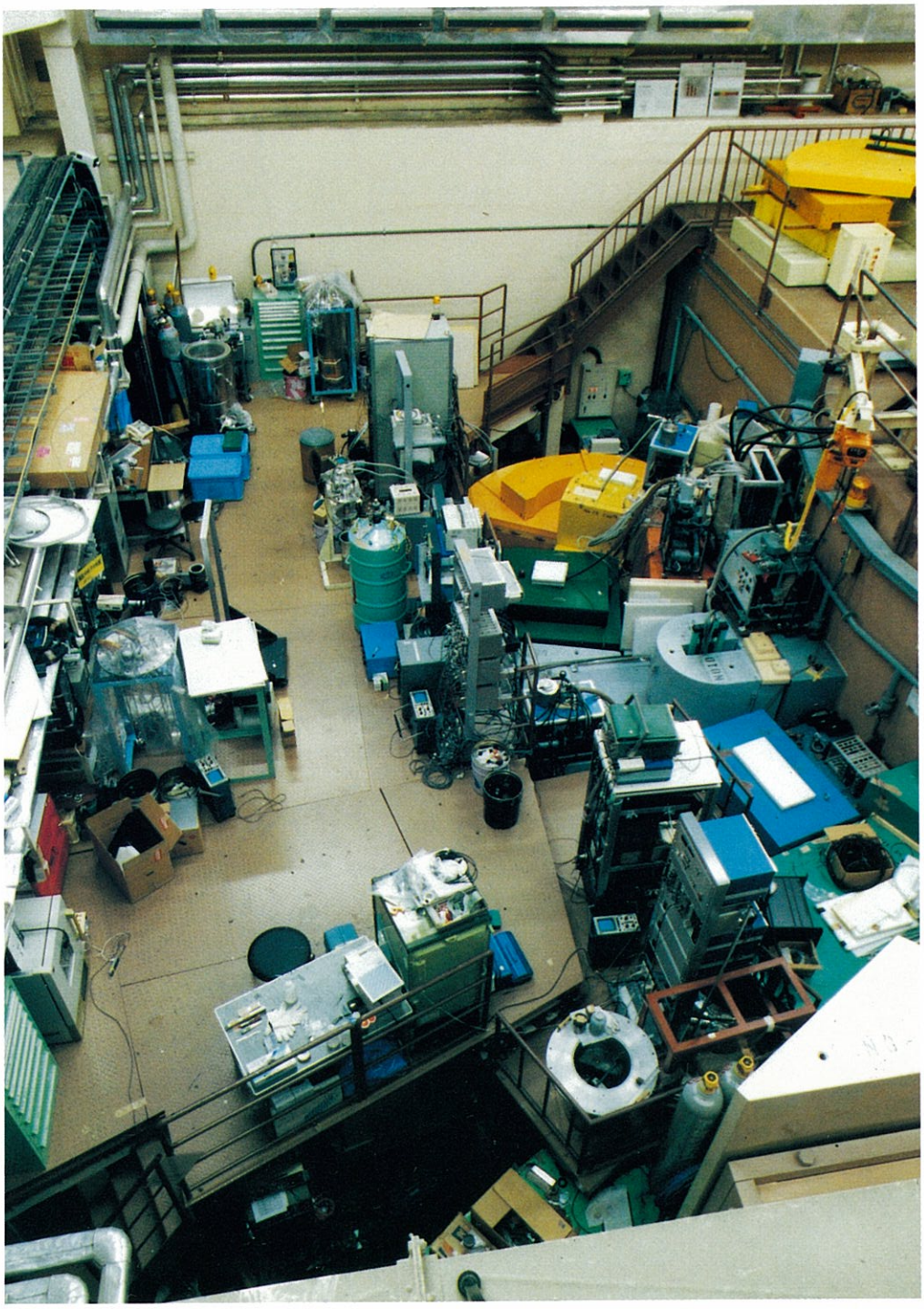

Photograph of experimental hall (A side).
From top to bottom, MAX, MRP, HIT, WIT, FOX.

PREFACE

The present issue follows a previous issue, KENS Report-VII published in Dec. 1988 and summarizes research progress at the KENS facility during the period between April 1988 and September 1990.

In this period the proton beam intensity was gradually increased and in March 1989 everyone in the KENS group shared the pleasure of successfully achieving a proton beam intensity of 2×10^{12} protons per pulse (corresponding to 6.7 μA in time-average beam current at 20 Hz) from the 500 MeV Booster synchrotron.

Professor Hiroshi Sasaki, Head of Booster Synchrotron Utilization Facility (BSF), retired from KEK under the age clause at the end of March 1989 and Professor Noboru Watanabe took office as a Head of BSF on April 1, 1989. We have welcome Professor Hironobu Ikeda to KEK/KENS from Ochanomizu University, Tokyo, on April 1, 1990. He is in charge of the neutron scattering group at KENS. I hope everything in KENS will go well with new staffs.

During this period a great deal of efforts were devoted to maintain research activities with a very modest proton-beam-intensity in KENS. How to compete with existing large scale spallation-neutron-facilities is one of the most important problem for us. First of all we started a program to improve the performance of all instruments by a factor of about ten in intensity equivalence (data rate, resolution, signal to background ratio, etc.). In some instruments the improvement has already been achieved, while in the remainder it is still in progress.

On the same time we started a program to build up and promote better science. As a first step, we organized many workshops or meetings, about ten a year, of reasonably small size, covering various fields of research using pulsed neutrons as listed in p. 12-13.

Recently Neutron Scattering Program Advisory Committee at KEK decided to adopt "referee system" for the selection of each proposal. I hope that the new system will bring about a better result in scientific yield in near future, combined with the other efforts mentioned above.

In the present issue we report the present status of some neutron instruments for user's convenience. Those instruments which are not reported here will appear in the next KENS Report.

In the past KENS Reports we used to include, in the chapter of Future Program, the research activities on the accelerator development for the next generation Japanese pulsed spallation neutron source, KENS-II. However, we decided to omit those from the present issue, because those will be published as a separate progress report on accelerator R&D for Japanese Hadron Project, in which KENS-II is involved. We therefore compiled contributions only on target/mopderator R&D.

Progress report on Japan-UK Collaboration on Neutron Scattering will be published separately. We therefore compiled here only a brief summary of the MARI commissioning.

Nov. 26, 1990

Noboru Watanabe
Head of Booster Synchrotron
Utilization Facility, KEK

Table of Contents

I. OUTLINE

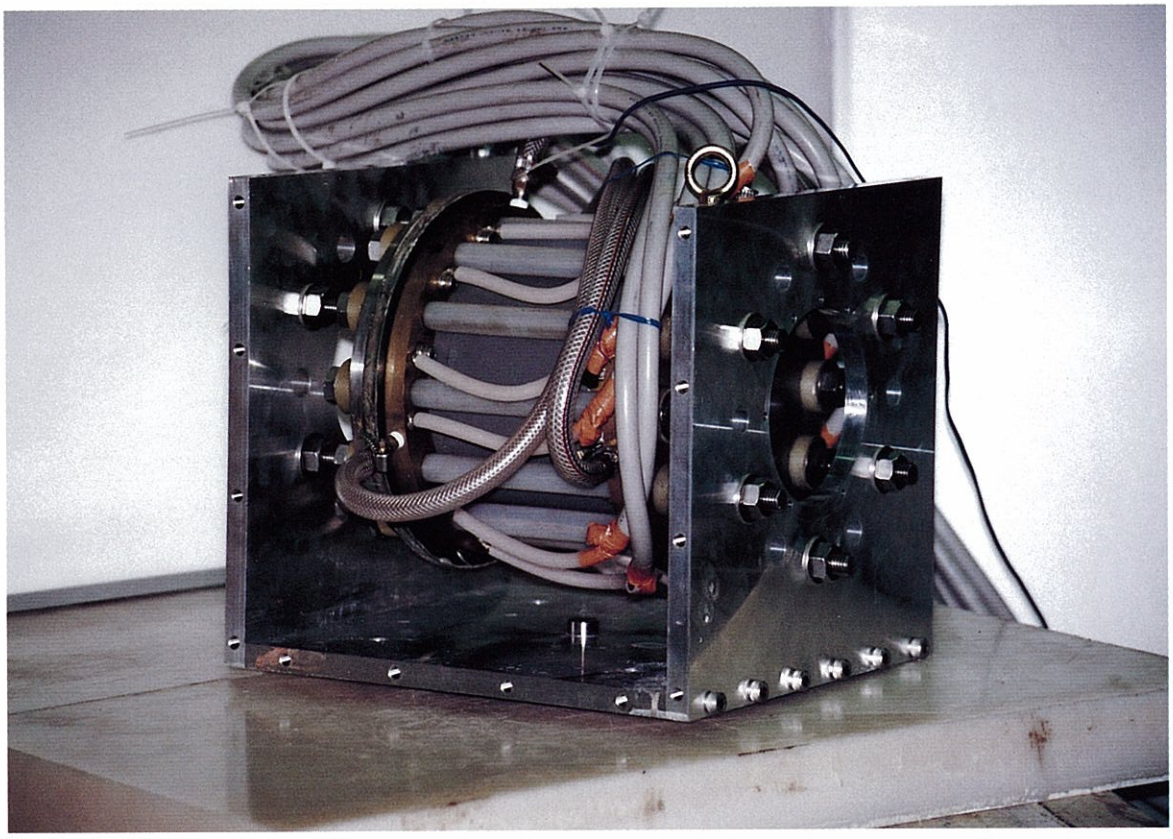

Newly developed pulsed high magnetic field instrument

Overview of the Progress in KENS

Noboru Watanabe and Hironobu Ikeda

National Laboratory for High Energy Physics, 1-1 Oho, Tsukuba-shi, Ibaraki 305

I. Outline of the KENS Facility

The present KENS Facility (KENS-I') has been successfully operated during the period since April 1988. The operation time of the 500 MeV Booster synchrotron in the past year was about 3500 hours, and the beam time allocated for neutron experiments was about 1500 hours. The average proton-beam intensity was 1.5×10^{12} protons per pulse (ppp) or less, which was lower than the maximum value of 2×10^{12} ppp already achieved in 1988. This is due to various reasons including radiation safety problems. Since about 20 % of proton-beam pulses were injected to the 12 GeV synchrotron, the average proton-beam current on the neutron target was about 4 μA. The integrated beam intensity over the one year was therefore 6000 μA or less which corresponds only to 3 days operation of ISIS. Nevertheless, we could perform various important experiments. We expect that the proton-beam intensity will reach 2×10^{12} ppp during routine operation. The beam transport line in the Booster Synchrotron Utilization Facility (BSF) has been improved to accept such intensity within a tolerable beam loss.

The depleted uranium target has been operated trouble-free since the beginning of its operation in 1985. We experienced no serious problems with the cryogenic moderator (solid methane at 20 K) in this period, because solid methane was renewed every two days before a "burp" can occur. A cold helium circulator had a problem and was repaired last year. The present cryostat which has been used for two years is still working.

During the last financial year, 76 experiments including 12 large proposals by groups responsible for the instruments were carried out. Scientists who visited the KENS facility spent about 4000 man-days.

II. Instrumental Developments

There are currently 16 instruments in the KENS facility as shown in Fig. 1. There was appreciable progress in the instrumentation. The construction of a new small/medium angle scattering instrument, WINK, started in 1989 and will be completed in 1991. The instrument was designed to realize a wider coverage in momentum transfer from 0.015 to 20 A^{-1} with a much higher data rate, hopefully more than 10 times as high as that of the existing small angle instrument, SAN. WINK will be equipped with more than 250 conventional He-3 proportional counters at a wider range of the scattering angle from forward to backward as shown in Fig. 2[1]. WINK

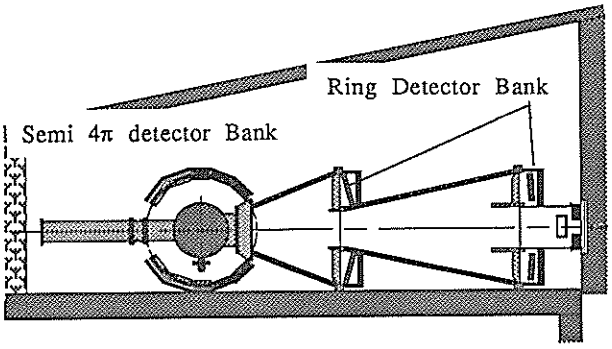

Fig. 2 Layout of WINK

was installed at the C4 beam line, sharing the beam with two existing instruments, LAM-40 (conventional-resolution low-energy spectrometer) and HRP (high-resolution powder diffractometer) on the same neutron beam line as shown in Fig. 1. We were faced with various difficulties in sharing the same neutron beam by three different instruments, but now those are almost solved. Due to the relatively shorter flight path lengths for incident and scattered neutrons (9 m and 2.5 m respectively), and to a lower repetition rate of the Booster synchrotron (20 Hz), the useful bandwidth of the incoming neutrons is quite wide, from 0.5 to 16 A, which enables the wider Q range mentioned above. In the last cycle, a preliminary measurement was performed on WINK with only one detector at each of 5 different angles. Figure 3 shows the result obtained with a measuring time of 2 hours[1]. The result proved that the coverage in Q and the data rate are quite satisfactory as expected. After the full installation of detectors, measuring time of a few minutes would be adequate for a typical sample. The momentum resolution of WINK however is relaxed a bit at the lower Q range than that of SAN, because WINK employs natural beam collimation between source and sample and the scattered neutron flight path length is limited to 2.5 m

KENS NEUTRON SCATTERING FACILITY

Fig. 1.

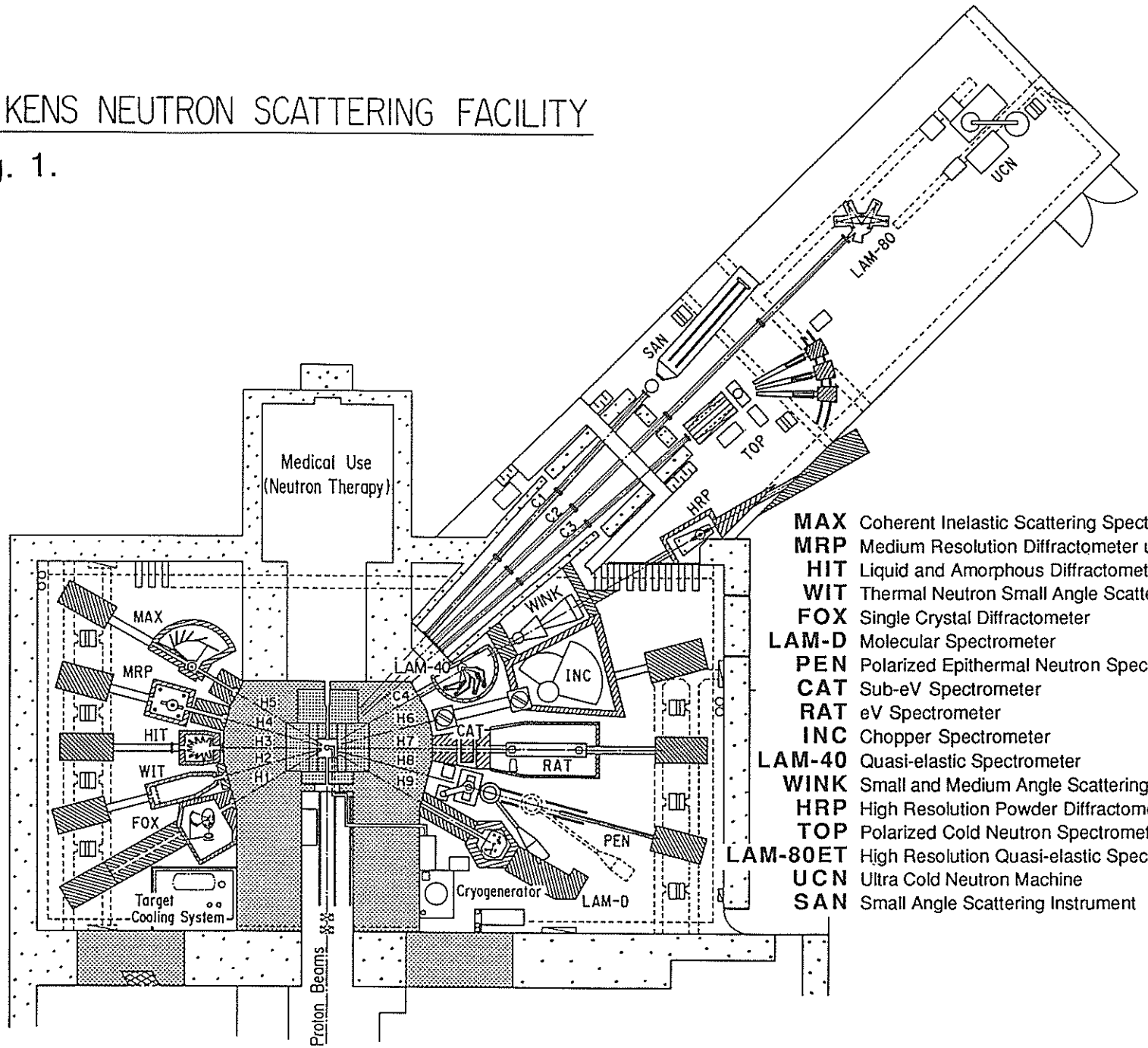

MAX	Coherent Inelastic Scattering Spectrometer
MRP	Medium Resolution Diffractometer under Extreme Conditions
HIT	Liquid and Amorphous Diffractometer
WIT	Thermal Neutron Small Angle Scattering Instrument
FOX	Single Crystal Diffractometer
LAM-D	Molecular Spectrometer
PEN	Polarized Epithermal Neutron Spectrometer
CAT	Sub-eV Spectrometer
RAT	eV Spectrometer
INC	Chopper Spectrometer
LAM-40	Quasi-elastic Spectrometer
WINK	Small and Medium Angle Scattering Instrument
HRP	High Resolution Powder Diffractometer
TOP	Polarized Cold Neutron Spectrometer
LAM-80ET	High Resolution Quasi-elastic Spectrometer
UCN	Ultra Cold Neutron Machine
SAN	Small Angle Scattering Instrument

due to limited space. Details on this instrument and its performance will be reported in chapter II.1.

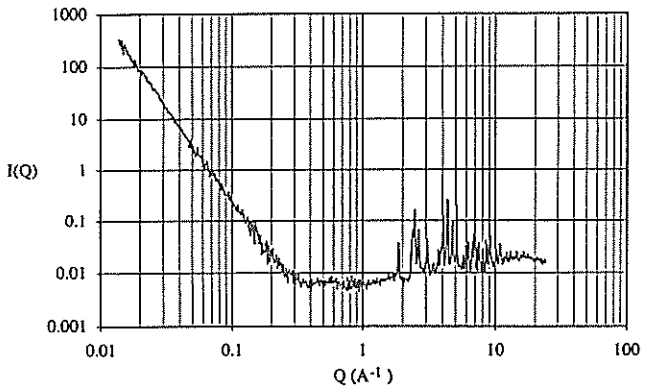

Fig. 3 Preliminary result of small angle scattering from SiC sample measured on WINK.

There was remarkable progress on the high-resolution low-energy spectrometer, LAM-80. The LAM-type spectrometer is an inverted-geometry instrument, developed by a famous Japanese neutron "Artist" Prof. Inoue, which has large analyzer mirrors composed of a large number of small analyzer crystals. LAM-80 has been improved twice. Firstly, all analyzer crystals of pyrolitic graphite were replaced by mica. This provided higher resolution but with lower data rate (about one third). Then, the hight of mirror was increased to realize a larger solid angle between sample and analyzer, and the number of mirror was also increased from four to eight. As a consequence of these improvements, a higher resolution with a higher data rate were realized. The spectrometer is now called LAM-80ET. In order to confirm the performance of this machine, we performed a measurement on reorientational tunneling. As a standard sample, N-oxy-γ-picoline was measured at 5 K. Figure 4[2] shows the result which demonstrates the superiority of LAM-80ET. In the present experiment, the 004 reflection of mica crystal was used to define the final energy (E_f) of the scattering process (E_f~0.82 meV). The energy-resolution is about 5 μeV with a very wide energy window of more than 1 meV. Signal-to-background ratio is excellent. Note that the measuring time was only 8 hours with a proton-beam current of only 3 μA. We are convinced that LAM-80ET is the best spectrometer in the world in this energy range; it is well competitive with IRIS at ISIS with 100 μA and IN5 in ILL Grenoble.

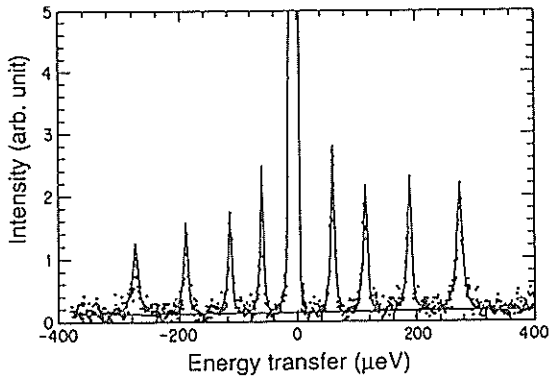

Fig. 4 Tunneling spectrum of N-Oxy γ picoline measured at 5K on LAM-80ET.

III. Neutron Scattering Experiments

One highlights of the research progress achieved in this period was neutron diffraction under high magnetic field. Scattering under extreme conditions is one of the most promising fields of research using pulsed neutrons, but we have never performed such an experiment. The maximum magnetic field so far used in neutron diffraction was below 10 T. As a first step of high field experiment, a Kobe University group developed a pulsed field instrument which can produce a high magnetic field up to 20 T every 2 sec with a pulse duration of about 1 ms. Neutron diffraction from a single crystal of metamagnetic $PrCo_2Si_2$ was measured as a first trial under various high magnetic fields on the MRP diffractometer. The pulsed magnetic field was phased to the neutron pulse. When the neutrons of a specific velocity satisfying the Bragg condition arrive at the sample, the magnet is pulsed. $PrCo_2Si_2$ shows a complicated phase transition, a so-called successive magnetic phase transitions as shown in Fig. 5[4].

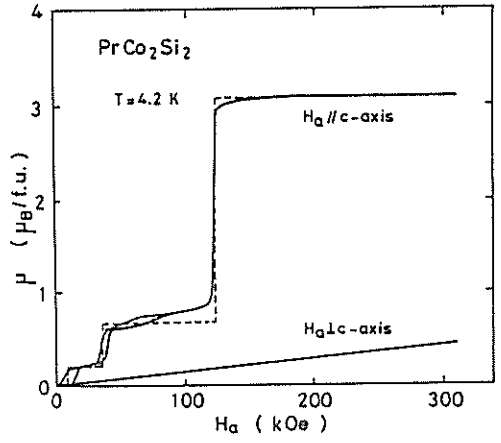

Fig.5 High field magnetization curves along the a- and c-axes at 4.2K for the $PrCo_2Si_2$ crystal [after ref. 4]

The present result proved that the proposed spin configurations shown in Fig. 6. are correct.

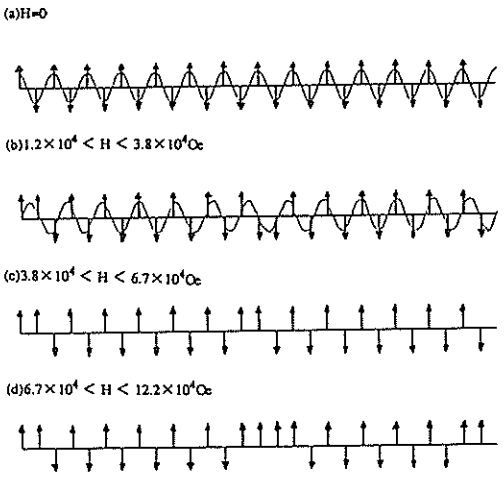

Fig. 6 A proposed spin configurations under various magnetic fields [after ref. 4]

Many other important experiments were successfully carried out in this period. Some of them are presented here.

The crystal structure of a new copper-oxide superconductor $(Ba_{0.63}Nd_{0.37})_2(Nb_{0.68}Ce_{0.32})_2Cu_3O_{8.92}$ was determined on HRP as shown in Fig. 7[5]. The structure contains two kinds of slabs: (CuO_2) (MO) (CuO_2) (MO) (CuO_2) of the $YBa_2Cu_3O_{7-y}$ (YBCO)-type slab and (CuO_2) (M') (O_2) (M') (CuO_2) of the Nd_2CuO_4 (NCO)-type slab. Ba with a larger ionic radius locates at an M site of the YBCO slab, while Ce with a smaller radius locates at an M' site of the NCO slab. Nd with an intermediate radius occupies both M and M' sites. An oxygen site on a CuO_2 plane of the YBCO slab is deficient and the occupation factor is 0.46.

The magnetic flux trapped in a high-T_c superconducting single crystal has been detected by means of depolarization experiments on the TOP spectrometer. Experiments have been done below T_c for a $La_{1.85}Sr_{0.15}CuO_4$ single crystal of T_c=34K.[6] No depolarization at zero-field cooling was confirmed and, thus, the crystal shows the true Meissner state. As shown in the Fig. 8[6], through field cooling with various fields the sinusoidal variation in the polarization with respect to the neutron wavelength appears, indicating a rotation of neutron polarization around the magnetic induction induced by the trapped magnetic fluxes in the crystal. In this way pulsed neutrons could definitely determine the lower critical field of H_{c1} for the first time.

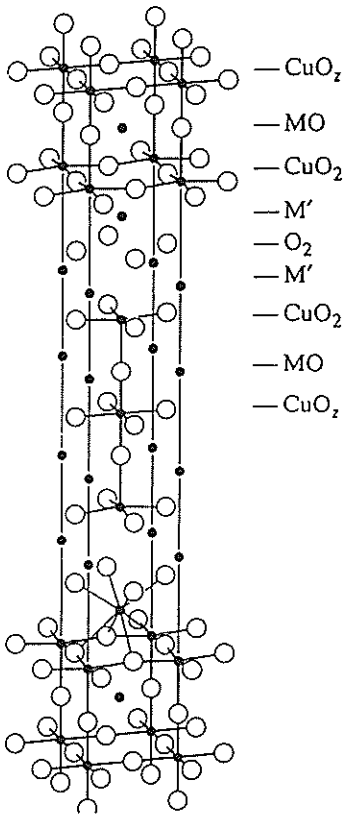

Fig. 7 Crystal structure of $(Ba_{0.63}Nd_{0.37})_2(Nd_{0.68}Ce_{0.32})_2Cu_3O_{8+z}$. M=$Ba_{0.63}Nd_{0.37}$ and M'=$Nd_{0.68}Ce_{0.32}$.

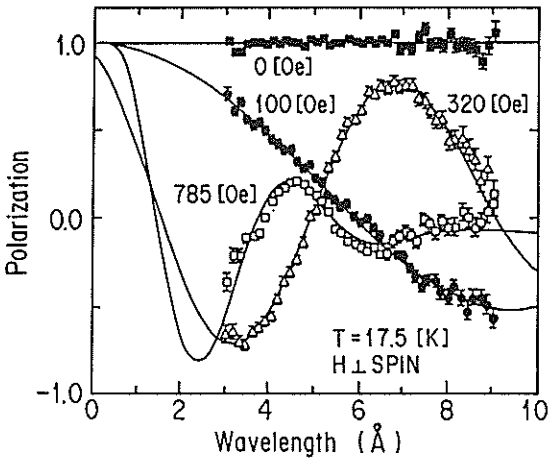

Fig. 8 Wavelength dependence of the neutron polarization in $La_{1.85}Sr_{0.15}CuO_4$ measured at 17.5K(T_c=34K) after cooling the sample in the denoted fields.

Crystal field excitations in the ferromagnetic dense Kondo system $CeSi_x$ ($1.6 < x < 2$) were studied with the chopper spectrometer INC. $CeSi_x$ is a system which shows the typical anomalies associated with competition between the single-site Kondo effect and RKKY interactions. The results are shown in Fig. 9[7]. The line widths of the excitations are anomalously large and increase with increasing x. This is direct evidence of the Kondo anomaly in the crystal field eigenstates in the $CeSi_x$ system. The increase in the line width corresponds to an increase in the Kondo temperature, which causes an ferromagnetic instability at around x = 1.85. Other anomalous rare-earth compounds, for example YbX (X = N, P, As), were also studied.

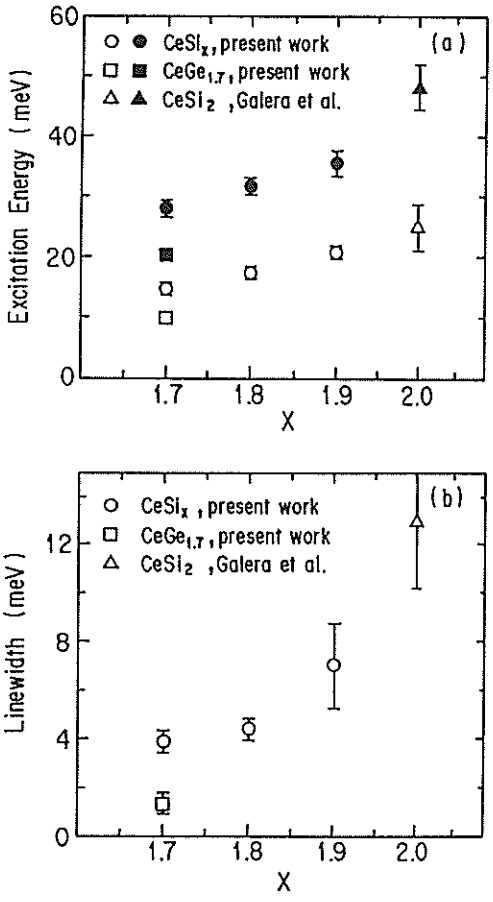

Fig. 9 The composition dependence of (a) excitation energy and (b) line width of CeSix at the lower temperature (16-20K). The line width is for the transition between the ground and first excited states. The results for $CeGe_{1.7}$ (□) and $CeSi_2$ (△ measured by Galera et al., 1989) are also plotted.

Magnetic inelastic neutron scattering from diluted two-dimensional anisotropic antiferromagnets $Rb_2Co_cMg_{1-c}F_4$ (c=0.2 and 0.3), whose magnetic concentration c is far below the percolation threshold, was studied with the chopper spectrometer INC. The results clearly show that the observed inelastic peaks (see Fig. 10) correspond to the transitions between energy levels of isolated two-spin clusters; hence, neutron scattering can even provide informations on the excited states of magnetic impurities in the host nonmagnetic substance[8].

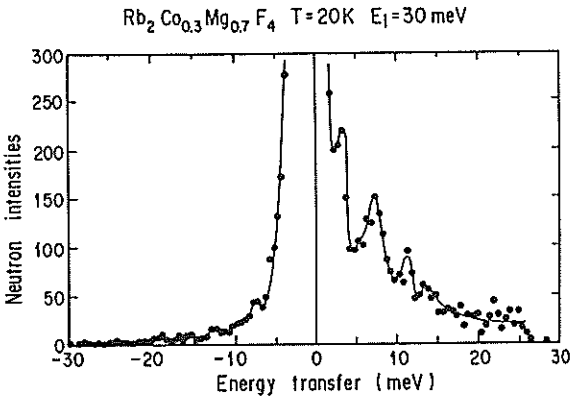

Fig. 10 Intensity distribution as a function of energy thansfer scattered from $Pb_2Co_{0.3}Mg_{0.7}F_4$ at 20K.

IV. Future program

There was considerable progress in the design study for KENS-II, a next-generation Japanese pulsed spallation neutron source. We are aiming to realize the world's best pulsed neutron source for neutron beam experiments, with a given proton beam from a proposed proton accelerator in the Japan Hadron Project, which is comparable to those in existing large-scale facilities. The design goals of the proposed source are :

(1)as many neutron beam lines as possible,
(2)the world's brightest pulsed cold neutrons,
(3)bright and narrow pulsed thermal/epithermal neutrons, at least comparable to the existing intense pulsed neutron sources,
(4)wider range of neutron spectra, and
(5)lower background.

We altered the scheme of the proton beam injection from the previous "horizontal" configuration to a "vertical" type, as shown in Fig 11, in order to provide as many neutron-beam-lines as possible[9]. The proton-beam transport-line in the experimental hall existed in the previous design was removed with its massive shielding, and a substantial number of extra beam lines can be placed in this space.

A new target-moderator coupling, the so-called "flux-trap moderator geometry", originally proposed at Los Alamos, was extensively studied by computer simulation[10]. We compared the neutron beam intensity from an optimally designed moderator in this configuration with that in the traditional wing geometry and found that the former gives a beam intensity about 1.3~1.4 times higher than the latter[10]. In order to take full advantage of this configuration, a vertical injection scheme is essential. We also found that the flux-trap moderator geometry is in principle advantageous to realize the design goal (5).

We have completed the basic design for the biological shield of the target station and the neutron beam shutter.

In order to realize design goal (2) we have proposed a new cold moderator system, which comprises of a liquid-hydrogen moderator and a hydrogenous pre-moderator at ambient temperature coupled to a reflector, and proved that the proposed moderator is very much promising[11),12]. Further optimization experiments were performed with a new cryostat which has a slim neck for minimizing the missing reflector[13-16]. We have confirmed that the conversion efficiency of the proposed moderator with the new cryostat is 16-times larger than that of the liquid-hydrogen moderator at ISIS; about 2 times larger than that of the solid methane moderator at the present KENS facility[16].

We proposed a target station which has two target-moderator-reflector assemblies, as shown in Fig. 12, with a new scheme of proton-beam delivery. For every 5 pulses (100 ms), a pair of double pulses is delivered to the target-1 (dedicated to the cold neutron source), with the other 4 pulses of single pulse being fed to the target-2 (decoupled moderators to the narrow pulses of thermal and epithermal neutrons)[9]. Both can be optimized independently. A reduction of the repetition rate on the target-1 gives no demerit, since the figure-of-merit of a pulsed cold neutron source is almost independent of the repetition rate for most experiments. Double pulses give another gain with a factor of 2. Though the number of pulses for target-2 decreases by 20 %, this can be well compensated by a gain factor of 1.3~1.4 from the "flux-trap moderator geometry". The most important advantage of the double-assembly system is that 360° coverage of neutron beam lines becomes possible using flux-trap moderators.

V. Japan-UK collaboration

The construction of the chopper spectrometer MARI, which was funded by the Ministry of Education, Science and Culture, Japan as a part of Japan-UK Collaboration in Neutron Scattering, was completed late in 1989 and detailed commissioning work was also completed September in 1990.

References

1) M. Furusaka et al. : Proc. ICANS-XI (Tsukuba, Oct. 22-26, 1990) 677.
2) S. Ikeda et al. : Tunnel 902, Proc. Japan-UK Collaboration on Neutron Scattering Research, KEK Report 90-17 (Dec. 1990) 39.
3) M. Motokawa, H. Nojiri, M. Uchi, S. Watamura, H. Kawai and Y. Endoh : Proc. ICANS-XI (Tsukuba, Oct. 22-26, 1990) 979.
4) T. Shigeoka, H. Fujii, K. Yonenobu, K. Sugiyama and M. Date : J. Phys. Soc. Jpn. **58** (1989) 394.
5) F. Izumi, H. Kito, H. Sawa, J. Akimitsu and H. Asano : Physica C160 (1989) 235.
6) T. Watanabe, Y. Endoh, S. Itoh, H. Kojima and N. Todate.: KENS Report-VIII (1990) 132.
7) M. Kohgi, T. Satoh, K. Ohoyama, M. Arai and R. Osborn : Physica **B163** (1990) 137.
8) H. Ikeda M. Kohgi, K. Ohoyama, M. Arai and T. Nakane.: KENS Report-VIII (1990) 114.
9) N. Watanabe : Design Concept for KENS-II Cold Neutron Source, to be appeared in Proc. Int. Workshop on Cold Neutron Source (Los Alamos, Mar. 5-8, 1990), in press.
10) Y. Kiyanagi and N. Watanabe : Some Optimization Studies on Flux-Trap Type Moderator, KENS Report-VIII (1990) 240.
11) N. Watanabe : A Consideration of cold Neutron Source for KENS-II, Advanced Neutron Sources 1988, Institute of Physics Conference Series Number 97, Institute of Physics, Bristol and New York, P.763.
12) N. Watanabe, Y. Kiyanagi, K. Inoue, M. Furusaka, S. Ikeda, M. Arai and H. Iwasa : Preliminary Optimization Experiments of Coupled Liquid Hydrogen Moderator for KENS-II, ibid, P.787.
13) Y. Kiyanagi, N. Watanabe, M. Furusaka, H. Iwasa and I. Fujikawa, Premoderator Optimization Studies of Coupled Liquid Hydrogen Moderator, KENS Report-VIII (1990) 229.
14) Y. Kiyanagi, N. Watanabe, M. Furusaka, H. Iwasa and I. Fujikawa, Time-Distribution of Cold Neutrons form a Coupled Liquid Hydrogen Moderator, KENS Report-VIII (1990) 235.
15) Y. Kiyanagi, N. Watanabe, M. Furusaka and H. Iwasa, Reflector Studies of Coupled Liquid Hydrogen Moderator, KENS Report-VIII (1990) 232.
16) Y. Kiyanagi, N. Watanabe, M. Furusaka and H. Iwasa, Direct Comparison of Neutronic Performance between Coupled Liquid Hydrogen Moderator and Solid Methan Moderator, KENS Report-VIII (1990) 237.

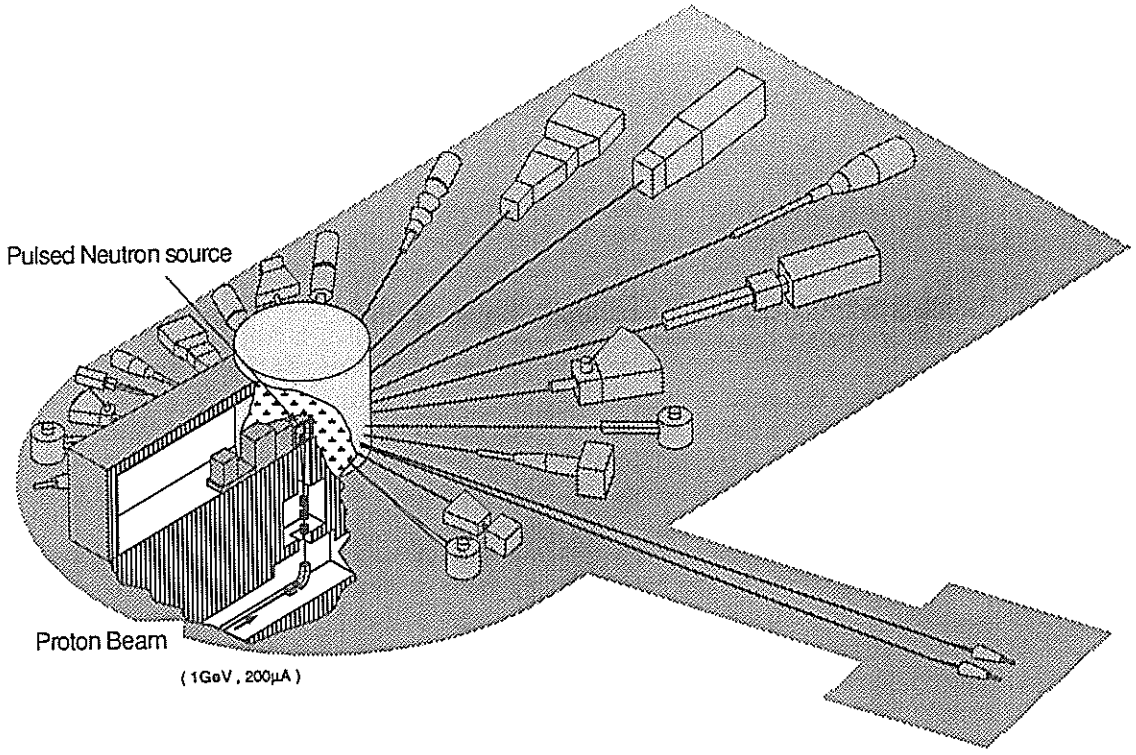

Fig. 11 Illustration of KENS-II (proton-beam injection to the target station and layout of neutron instruments)

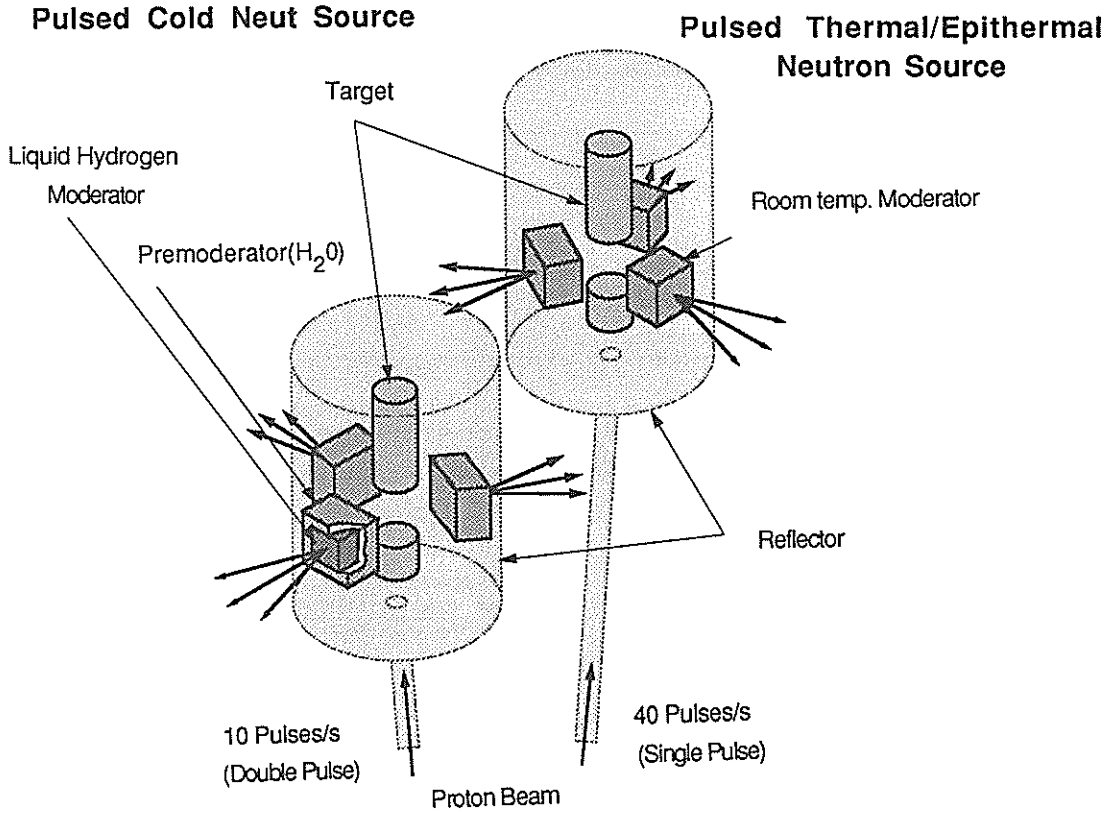

Fig. 12 Illustration of two target-moderator-reflector assemblies.

Summary of BSF Operation

Y. IRIE

National Laboratory for High Energy Physics

Table 1 shows a summary of BSF operation from May 1988 through June 1990. Total operation time is 8093.7 hours and number of protons supplied to BSF experiments and therapy is 4.6×10E20. The down-time of PS accelerator and BSF beam-line amounts to 378.2 hours during this period, which is 4.7% of the total operation time. The tedious failure of the beam-line occured in October 1988 when a power supply for a pulsed switching magnet PHB1 developed an over-voltage across the thyristor in a resonant circuit. The down-time due to this is 22 hours.

In Table 2 are shown, the average beam intensity supplied to BSF in units of 10E11 protons per pulse (ppp) or an average current during 2.6 seconds of 12 GeV PS cycle and the beam transmission. As seen in the Table, recent beam intensity has been doubled compared to that in early 1988. With an increase of beam intensity, measures have been taken for radiation protection. The shielding around a meson production target was reinforced (May 1989). A branching vacuum chamber just downstream of a pulsed switching magnet PHB1 which had a small vertical aperture and consequently showed huge residual radioactivities was replaced by a 160 mm in diameter cylindrical chamber in summer shutdown of 1989. By the replacement, an exposure rate at the duct surface was reduced from 1.5 Sv/h at most to less than 2 mSv/h after 4 days cooling time. All preamplifiers for beam-profile monitors were moved from beam-line to BSF local control room to prevent radiation damages. Degradation of S/N ratio caused by the extension of a signal cable was well cured by making a low-noise amplifier. Nine sets of beam loss monitor (4 ionization chambers per set) along the beam-line have been used in fine beam-steering and/or recognizing small apertures and eventually expected to mitigate residual radioactivities.

Table 1. Summary of BSF operation from May 1988 through June 1990

(units are "hours" unless otherwise specified)

	Neutron Experiment	Meson Experiment	Biomedical Research	Total	Ratio (%)
Beam utility					
Beam On	3384.9	3048.9	1177.2	7610.9	94.0
Reject	13.8	41.6	0.0	55.4	0.7
Beam-line trouble	15.4	27.0	9.3	51.7	0.7
Accelerator stop	178.0	112.4	36.1	326.5	4.0
Others	6.7	2.0	24.7	33.4	0.4
Beam-line study				15.8	0.2
Total	3598.8	3231.9	1247.3	8093.7	100.0
Total number of injected protons (10^{18})	240.8	207.3	11.5	459.6	

Table 2. Beam intensity and transmission

	Neutron experiment				Meson experiment				Biomedical research		
	Average intensity (10^{11}ppp)	(μA)	TR. (1)	(2)	Average intensity (10^{11}ppp)	(μA)	TR. (1)	(2)	Average intensity (10^{11}ppp)	(μA)	TR. (1)
1988 May-July	6.6	1.8	0.95	0.89	9.9	2.6	0.93	0.92	8.2	2.2	0.95
1988 September-December	9.3	2.5	0.96	0.91	9.1	2.4	0.96	0.90	9.3	2.5	0.95
1989 January-March	12.2	3.2	0.95	0.91	12.0	3.2	0.94	0.90	11.8	3.1	0.96
1989 April-July	11.1	2.9	0.96	0.88	10.7	2.8	0.96	0.91	9.1	2.4	0.97
1989 December-1990 March	9.6	2.6	0.97	0.88	8.6	2.3	0.91	0.88	9.0	2.4	0.96
1990 April-June	12.6	3.5	0.98	0.88	11.8	3.4	0.97	0.88	12.5	3.6	0.98

TR.(Transmission) (1) is defined as the ratio of beam intensity at the beam-line exit to that at the entrance.
TR. (2) is the ratio of beam intensity at the beam-line entrance to that in the booster synchrotron.

The Melcom 70 mini-computer system which has been used since beginning of beam-line operation in 1980 was completely replaced by a micro-Vax II and CAMAC system in summer shutdown of 1989 so as to increase the beam-line control functions. The end part of a beam dump-line, which goes down to an iron beam-dump, was modified in March 1990 to fit the irradiation experiment. DC magnets, profile-monitors and vacuum modules were newly installed. Irradiation experiments will start in Autumn 1990 after a new pulsed switching magnet is installed upstream which can share beam pulses between the dump experiment and other BSF experiments.

Meetings

The following workshops on technical and scientific problems on neutron scattering studies at KENS facility were organized. Scientific reports of the workshops have been published as the internal reports of KEK, and available for those who have interests.

Material Science Workshop

Workshop on material science was held on April 14-15, 1989. Some selected topics such as pattern formation in 1st order phase transition, SANS study of radiation damage, phase separation of metalic alloys, magnetic fluid etc. were discussed in relation to the future prospects of small-angle neutron scattering researches.

Japan-UK Collaboration Workshop

The second joint Workshop of Japan-UK Collaboration on Neutron Scattering Research was held on November 1, 1989. From RAL, W. G. Williams visited to make the meeting more fruitful. The results of experiments which have already been achieved under Japan-UK program and also some topics to be performed as joint research at RAL were presented and discussed. W. G. Williams gave us an invited talk on the recent status of ISIS, which was quite impressive for all participants.

Statistical Physics of Magnetism Workshop

Workshop on statistical physics of magnetic materials was held February 23, 1990. Experimental and theoretical studies related to neutron scattering such as spin glasses, dynamics of percolation, phase transitions in frustrated systems, Haldane gap etc. are reviewed and discussed.

Small-Angle Scattering Workshop

Small-angle neutron scattering (SANS) workshop was held on March 19, 1990, to do deep discussions on the technical problems on SANS instruments installed (or to be installed) at KENS (pulsed source) and JAERI (steady source). Besides technical problems, much of time was also devoted to the discussion on the organizing procedure of all SANS instruments in Japan, sample environments, analyzing software etc.

Polymer Workshop

Present status and future problems of polymer science were discussed on March 20, 1990. Two invited lectures were given from experimental and theoretical side by Takeji Hashimoto and Akira Onuki respectively. Joint discussions between polymer scientists and neutron scientists were quite successful and fruitful for the progress of researches using SANS.

Annual Meeting of KENS (1989)

On January 29, 1990, annual meeting of KENS was held and several improvements of KENS facilities and future prospects including JHP project were reported. Notable scientific activities were also reported and discussed.

Powder Diffraction Workshop

Powder diffraction workshop was held on April 23, 1990 at KEK. Two scientists from RAL, Bill David and Colin Carlile, joined us and brought valuable experience from HRPD instrument at RAL. Discussions on high-T_c superconductors, maximum-entropy analysis etc. has attracted participants' interest.

High-Resolution Spectroscopy Workshop

On April 24, 1990, technical and scientific problems on high-resolution spectroscopy were discussed at KENS in the occasion of Colin Carlile's visit to KENS. LAM-80ET spectrometer developed by a group of Kazuhiko Inoue recently achieved 1.2 μeV resolution using mica as analyser crystals. Collaborative discussions between IRIS at RAL and LAM-80ET including scientific problems such as tunneling modes in inorganic materials were of great value for all participants.

Phase Separation Workshop

Workshop on phase separation in binary metallic alloys(Al-Li etc.) was organized by Kozo Osamura and held on June 28-29, 1990. Two scientists from abroad, Hyden Chen (Univ. of Illinois) and Colin Windsor (Harwell Lab.) were invited to join us and gave excellent lectures on small angle neutron and x-ray scattering from Al-Li in early and late stages, and computer simulation on the kinetics of phase separation, respectively.

Hydrogen-bonded Materials Workshop

Workshop on hydrogen-bonded materials of KDP and its family was held on September 18, 1990. Dynamical motion and spatial distribution of hydrogen were discussed in relation to its role in the structural phase transition with special attention to the neutron scattering results on LAM, MAX and RAC at KENS.

Scattering Experiments Under Extreme Conditions Workshop

On August 11 and 12, 1990, technical and scientific problems on scattering studies under extreme conditions such as high pressure, high magnetic field and ultra-low temperature, were discussed under the joint organization of neutron scattering facility (KENS) and synchrotron facility (PF) of KEK. Joint discussions between neutron and photon scientists of more than 150 attentants were quite exciting and the future collaboration on the progress of common technical and scientific development is important and promissing.

Members of Committees

*Chairman
**Project Manager

Committee for Booster Synchrotron Utilization Facility

ENDOH, Yasuo	(Tohoku Univ.)
IMAZATO, Jun	(KEK, Physics Department)
IRIE, Yoshiro	(KEK, Booster Synchrotron Utilization Facility)
KAMIMURA, Hiroshi*	(Univ. of Tokyo)
KIHARA, Motohiro	(KEK, Director of Accelerator Department)
MASAIKE, Akira	(Kyoto Univ.)
MIYAJIMA, Mitsuhiro	(KEK, Radiation Safety Control Center)
NAGAMINE, Kanetada	(Univ. of Tokyo)
TUJII, Hirohiko	(Univ. of Tsukuba)
WATANABE, Noboru	(KEK, Booster Synchrotron Utilization Facility)
YAMANE, Isao	(KEK, Accelerator Department)

Neutron Scattering Program Advisory Committee

ENDOH, Yasuo*	(Tohoku Univ.)
FUKUYAMA, Hidetoshi	(Univ. of Tokyo)
IKEDA, Hironobu	(KEK, Booster Synchrotron Utilization Facility)
MITSUI, Toshio	(Osaka Univ.)
NODA, Ichiro	(Nagoya Univ.)
SUZUKI, Kenji	(Tohoku Univ.)
WATANABE, Noboru	(KEK, Booster Synchrotron Utilization Facility)
YAMADA, Yasusada	(Univ. of Tokyo)

Japan-UK Steering and Program Advisory Committee

ENDOH, Yasuo*	(Tohoku Univ.)
FUKUYAMA, Hidetoshi	(Univ. of Tokyo)
IKEDA, Hironobu	(KEK, Booster Synchrotron Utilization Facility)
IWASAKI, Hiroshi	(KEK, Director of P.F.Instrumentation Department)
KIKUCHI, Ken	(General Research Coordinator)
MITSUI, Toshio	(Osaka Univ.)
NODA, Ichiro	(Nagoya Univ.)
SUZUKI, Kenji	(Tohoku Univ.)
WATANABE, Noboru**	(KEK, Booster Synchrotron Utilization Facility)
YAMADA, Yasusada	(Univ. of Tokyo)

Scientific Staffs and Officers

Booster Synchrotron Utilization Facility

Head
WATANABE, Noboru

Neutron Scattering Group
ARAI, Masatoshi
IKEDA, Hironobu
IKEDA, Susumu
FUJIKAWA, Isao
FURUSAKA, Michihiro
MASUDA, Yasuhiro
MISAWA, Masakatsu
SATOH, Setsuo

Beam Line Group
ADACHI, Toshikazu
FUJIMORI, Hiroshi
IRIE, Yoshiro
KANEKO, Naokatsu
KOBAYASHI, Yasuo
TAHARA, Toshiro
YANO, Yoshiharu

Visiting Scientists
ENDOH, Yasuo (Tohoku Univ.)
YOSHIZAWA, Hideki

Leaders of Instrument-Groups

Elastic Instruments		Leader	
HRP	(High Resolution Powder Diffractometer)	ASANO, Hajime	(Univ. of Tsukuba)
MRP	(Medium Resolution Powder Diffractometer)	NOJIRI, Hiroyuki	(Kobe Univ.)
FOX	(Single Crystal Diffractometer)	OKAMURA, Fujio	(NIRIM)
SAN	(Small Angle Scattering Instrument)	FURUSAKA, Michihiro	(KEK, BSF)
WINK	(Small/Medium-Angle Diffractometer)	WATANABE, Noboru	(KEK, BSF)
WIT	(Thermal Neutron Small Angle Scattering Instrument)	NIIMURA, Nobuo	(Tohoku Univ.)
HIT	(Liquid and Amorphous Diffractometer)	FUKUNAGA, Toshiharu	(Nagoya Univ.)
TOP	(Polarized Cold Neutron Spectrometer)	ENDOH, Yasuo	(Tohoku Univ.)
PEN	(Polarized Epithermal Neutron Spectrometer)	MASUDA, Yasuhiro	(KEK, BSF)
UCN	(Ultra Cold Neutron Machine)	YOSHIKI, Hajime	(KEK)

Inelastic Instruments		Leader	
LAM-80ET	(High Resolution Quasielastic Spectrometer)	IZUMI, Yoshinobu	(Yamagata Univ.)
LAM-40	(Quasielastic Spectrometer)	IZUMI, Yoshinobu	(Yamagata Univ.)
LAM-D	(Molecular Spectrometer)	IZUMI, Yoshinobu	(Yamagata Univ.)
CAT	(Sub-eV Spectrometer)	IKEDA, Susumu	(KEK, BSF)
RAT	(eV Spectrometer)	IKEDA, Susumu	(KEK, BSF)
INC	(Chopper Spectrometer)	KOHGI, Masafumi	(Tohoku Univ.)
MAX	(Coherent Inelastic Scattering Spectrometer)	IKEDA, Hironobu	(KEK, BSF)

II. KENS INSTRUMENTS

There are currently 17 instruments in KENS; 15 are in operation, a test machine of ultra-cold neutron generator (UCN) and a new small/medium-angle scattering instrument (WINK) are under development. In the following, current status on some of these instruments is reviewed.

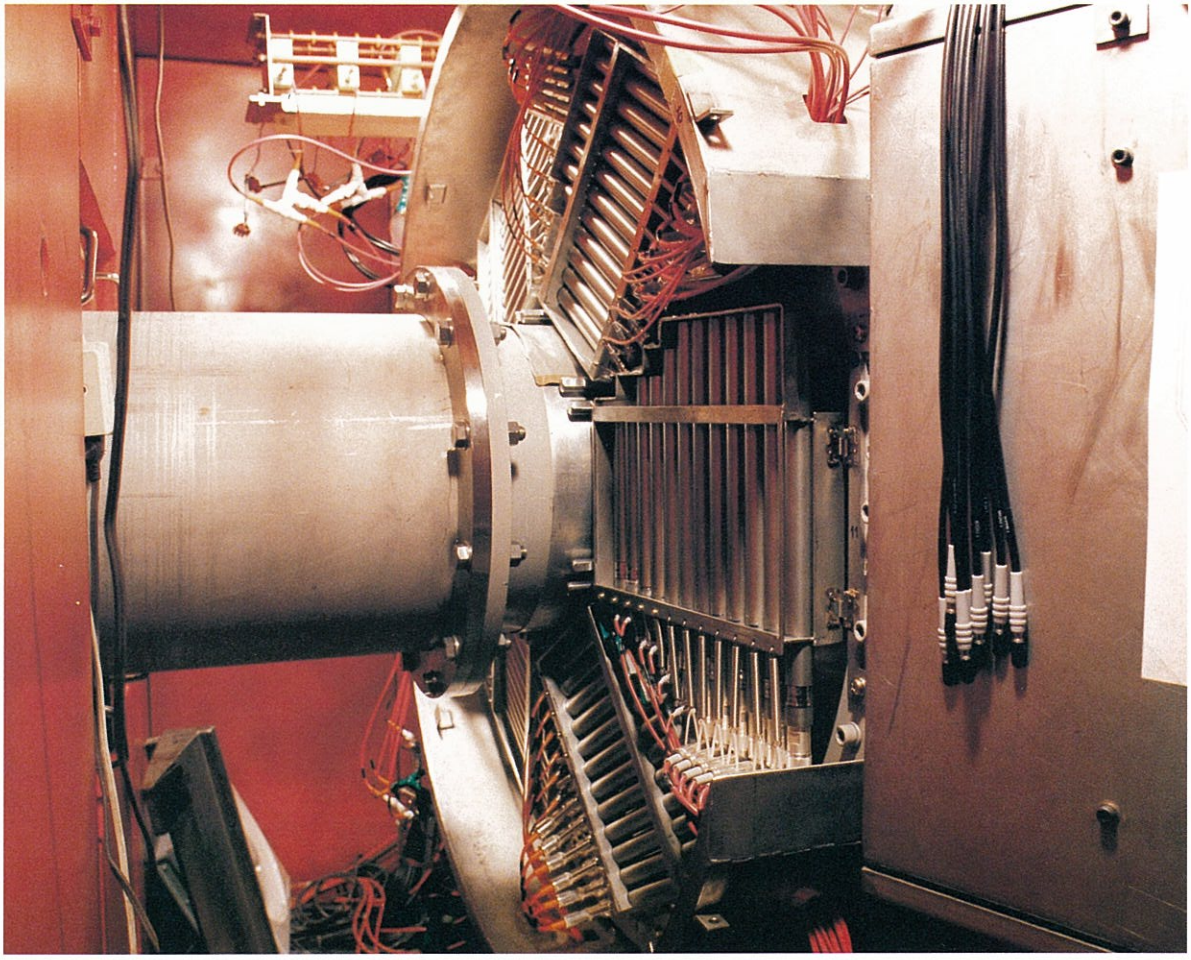

Photograph of detector bank of INC

HRP (High-Resolution Powder Diffractometer)

Instrument

HRP[1] is a time-of-flight (TOF) powder diffractometer with a resolution of $\Delta d/d \sim 3\times10^{-3}$. HRP is installed on the C4 beam line and located in a downstream position of LAM-40 and WINK spectrometers. HRP utilizes cold neutrons from the solid methane moderator at 20K.

Figure 1 shows a layout of HRP. Neutron flight paths L1 (moderator to sample) and L2 (sample to detector) are 18.9m and 0.8m, respectively. Two counter boxes in both wings of the beam line contain 12 ^{3}He counters with average 2θ of 170°. The range of d measured by HRP covers 0.5 to 5A. Figure 2 shows a resolution of HRP as a function of d. The d-range where the constant high-resolution is realized extends to d~1.3A.

A powdered sample is packed in a vanadium can and set in an aluminium vacuum chamber. The sample volume is 10mmϕ × 40mmH. The standard data-collection time for one sample is about 10h. In low temperature measurements down to 4.2K, a Cryomini or Heritran refrigerator is available.

TOF spectra from 12 detectors are stored in time analyzers and time-focussed using a VAX-Station II. Focussed data are transferred to a KEK central computer HITAC H280 and utilized in subsequent Rietveld analysis using a program RIETAN[2]. An example of the Rietveld refinement pattern is shown in Fig. 3.

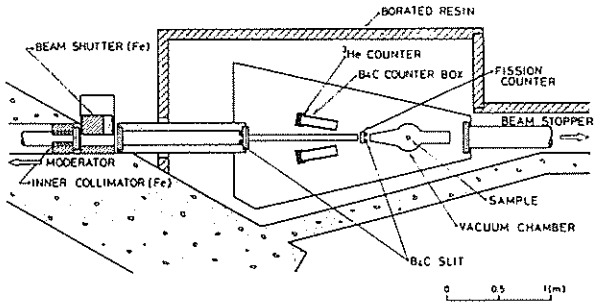

Fig. 1 Layout of HRP.

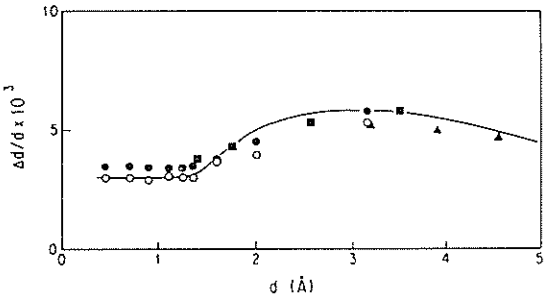

Fig. 2 Resolution of HRP.

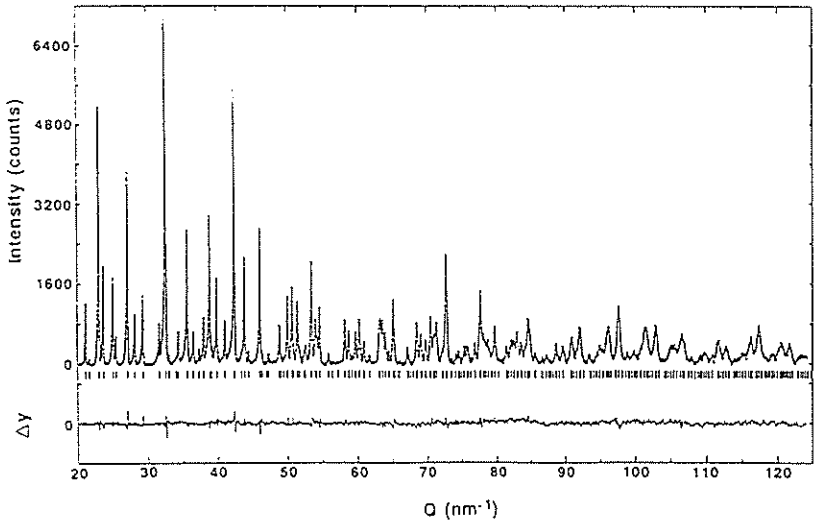

Fig. 3 Rietveld refinement pattern of $(Tl_{0.95}Cu_{0.05})_2Ba_2CuO_{6.08}$ plotted against Q (=2π/d).The background is subtracted. Dots show observed intensities, and a solid line overlying them is a calculated intensity. Markers below the diffraction pattern indicate positions of possible reflections, and Δy in the bottom is a difference between observed and calculated intensities in the same scale.

New Instrument: HRP-II

We are planning to upgrade the present HRP to HRP-II within two years. HRP-II has 200 ^3He detectors in the 2θ range from 140° to 170°. Figure 4 shows a schematic drawing of the backward counter bank. The counting rate of HRP-II will be at least 5 times higher than the present HRP without sacrificing the present resolution. The data-collection time for one sample will then be reduced to 2h.

Recent Work on Crystal Structures of High T_c Superconductors

We determined crystal structures of two new superconductors $(Nd,Sr,Ce)_2CuO_4$[3] and $(Nd,Ba)_2(Nd,Ce)_2Cu_3O_{8+z}$[4]. The former is now well-known as the T^*-phase of 2-1-4 compounds. The latter shows a hybrid structure of Nd_2CuO_4 and tetragonal $YBa_2Cu_3O_{7-z}$. We also determined an incommensurate structure of the Bi-based superconductor $Bi_2(Sr,Ca)_3Cu_2O_{8+z}$[5].

One of the recent topics is the structure analysis of a superconductor $(Tl_{0.95}Cu_{0.05})_2Ba_2CuO_{6+z}$ (Tl-2201)[6] .The crystal structure of Tl-2201 is shown in Fig. 5. The structure contains double layers of TlO, and a perovskite layer $(BaO)(CuO_2)(BaO)$ is sandwiched between two Tl_2O_2 layers. This system is known as an over-doped system; T_c increases drastically from 0K to 80K on removal of oxygen. In order to know what happens in the crystal structure of this system, we made neutron diffraction experiments on four samples with different oxygen contents. It was shown that an interstitial oxygen site within the Tl_2O_2 layer can accommodate oxygen, and the oxygen inclusion in this site distroys superconductivity in the Tl-2201 system. The Rietveld refinement pattern for $(Tl_{0.95}Cu_{0.05})_2Ba_2CuO_{6.08}$ is shown in Fig. 3.

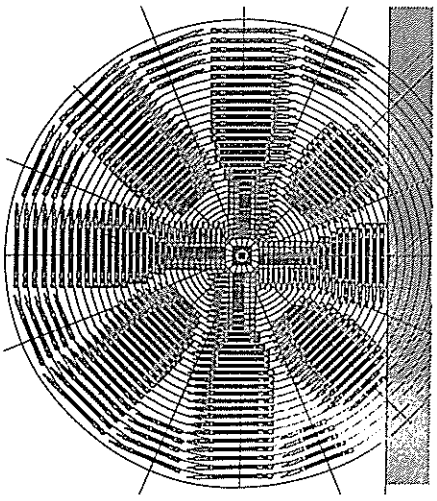

Fig. 4 Backward counter bank of HRP-II.

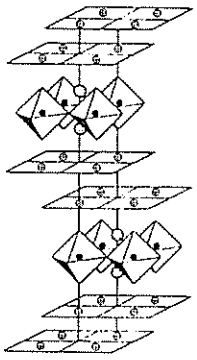

Fig. 5 Crystal structure of Tl-2201.

References

1) N. Watanabe, H. Asano, H. Iwasa, S. Satoh, H. Murata, K. Karahashi, S. Tomiyoshi, F. Izumi and K. Inoue, Jpn. J. Appl. Phys. **26**, 1164 (1987)
2) F.Izumi, H. Asano, H. Murata and N. Watanabe, J. Appl. Crystallogr. **20**, 411 (1987)
3) H. Sawa, S. Suzuki, M. Watanabe, J. Akimitsu, H. Matsubara, H. Watabe, S. Uchida, K. Kokusho, H. Asano, F. Izumi and E. Takayama-Muromachi, Nature **337**, 347 (1989)
4) F.Izumi, H. Kito, H. Sawa, J. Akimitsu and H. Asano, Physica C **160**, 235 (1989)
5) A. Yamamoto, M. Onoda, E. Takayama-Muromachi, F. Izumi, T. Ishigaki and H. Asano, Phys. Rev. B, in press
6) Y. Shimakawa, Y. Kubo, T. Manako, H. Igarashi, F. Izumi and H. Asano, submitted to Phys. Rev. B

HIT (High Intensity Total Scattering Spectrometer)

Status

HIT spectrometer was constructed in 1980 to measure strucrure factors S(Q)'s of liquids, glasses and amorphous solids over a wide Q range from 0.1 to >50 A^{-1}. For about 10 years a number of measurements on various samples have been carried out. During these years the HIT spectrometer has been improved step by step for the resolution, the data aquisition system and so on. Environmental equipments such as a high temperature furnace, low temperature refrigerator, magnet and so on have also been developed in order to cover various experimental purpose.

The present resolution in Q space, which was estimated by a Monte Carlo technique, is shown in fig. 1. The resolution ΔQ was defined as a root mean square deviation of the Q value, i.e. $\Delta Q=<(Q-\bar{Q})^2>^{1/2}$, where $\bar{Q}$ is the mean value.

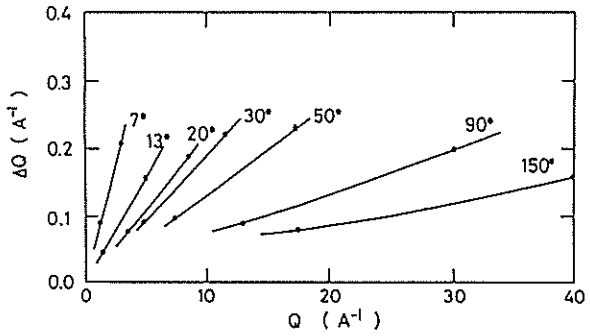

Fig. 1 Geometrical resolution of momentum transfer Q calculated for various detector banks in the present HIT. The region between two dots on each line corresponds to the wavelength between 0.3 and 0.7 A.

Future

Plans for a fundamental improvement of the HIT spectrometer is now in progress and the final design of the new spectrometer is under way. The design of the new spectrometer will be focussed to improve the counting rate of the scattered neutrons in the forward scattering direction. The counting rate will be increased by a factor of 4 or 5 in the forward scattering direction and by a factor of 2 in the backward scattering direction by employing a number of detectors. Within spacial constraints the incident flight path length from the moderator to a sample and the scattered flight path lengthes from a sample to detectors will be increased a little to improve also the resolution in Q space.

Science

Users of the HIT spectrometer are classified into two types; one is B1 group responsible for construction, operation, maintenance and improvement of the spectrometer, and the other is B2 group of pure users. The B1 group is further divided into four small groups, each of which studies in their own regions independently.

Here, we introduce topics or summaries of experimental results carried out by each B1 group, which have been reported elsewhere during a recent few years.

[1] Amorphous materials have been synthesized by many types of rapid quenching methods such as melt spinning, sputtering, evaporation and so on. Recently, it has been demonstrated that amorphous materials can be synthesized through ball-milling techniques based on solid state reactions, which are mechanical alloying(MA) and mechanical grinding(MG). The amorphization induced by MA or MG proceeds very slowly on the time scale of hours or days in comparison with the high cooling rate in the range of 10^4 to 10^{12} K/s for rapid quenching techniques. Therefore, the structural evolution during the amorphization induced by MA or MG can be easily observed.

Figure 2 shows partial distribution functions $RDF_{NiNi}(r)$'s of $Ni_{40}V_{60}$ samples after 0, 50, 100, 400 and 800 hours of MA derived as the Fourier transform of partial structure factors $S_{NiNi}(Q)$'s of the Ni-Ni correlation, together with atomic distributions of fcc-Ni crystal. It is well known that the coherent scattering length of a V atom is close to zero in comparison with that of a Ni atom for neutron scattering. Therefore, the information attributed to the Ni-Ni correlation in $Ni_{40}V_{60}$ samples can be directly observed in S(Q) or RDF(r). The $RDF_{NiNi}(r)$ of $Ni_{40}V_{60}$ sample before MA as shown in fig. 1 indicates the distribution peaks of fcc-Ni crystal. The structural evolution from a crystal to an amorphous phase can be easily realized. It is worth noting that the

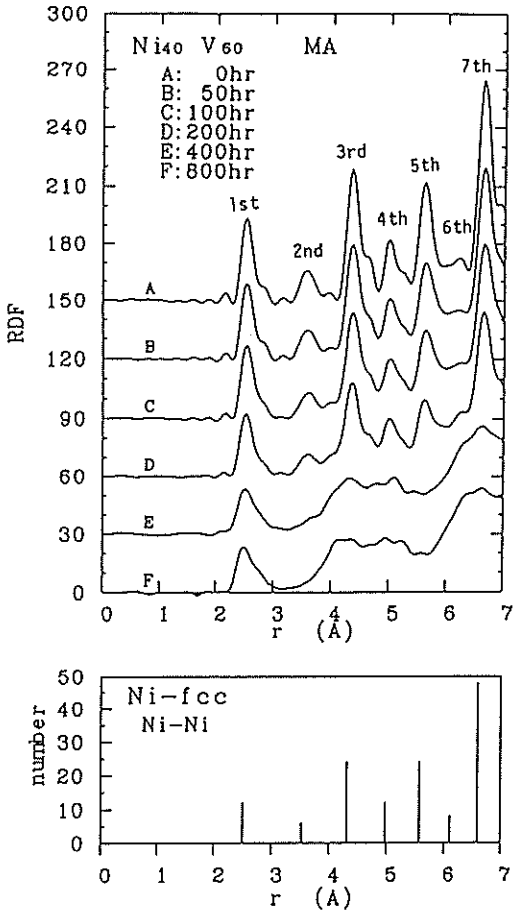

Fig. 2 Total radial distribution functions (RDF(r)'s ~$RDF_{NiNi}(r)$'s) of $Ni_{40}V_{60}$ samples after 0, 50, 100, 400 and 800 hours of MA, together with atomic distribution of fcc Ni crystal.

peaks of the 2nd and 5th Ni-Ni neighbor position observed within 7 A distance drastically decrease and eventually disappear after 400h of MA. Since the 2nd and 5th Ni-Ni neighbors contribute exclusively to the formation of the octahedral units in fcc structure, the amorphization by MA can be eventually realized to take place chemically by alloying V atoms with Ni atoms and topologically increasing the tetrahedral unit characteristic of an amorphous structure at the expense of the octahedral unit in fcc.

[2] It is generally agreed that various glasses and liquids are composed of some structural units. For instance, silica glass is built of SiO_4 tetrahedrons; liquid carbon tetrachloride is composed of CCl_4 tetrahedral molecules; liquid sulfur is composed of $(-S-)_n$ long chains or S_8 rings. Interesting points are how these structural units are distributed in the disordered states, and how we can extract this information directly from the experimental structure factors S(Q)'s. One of the simplest systems suitable to study these points is molecular liquids of small molecules. S(Q)'s of some molecular liquids with the variety of molecular shapes have been measured by using the HIT instrument from the above point of view: for example, liquids I_2, CCl_4, C_6D_6, $C_{10}D_8$, C_2Cl_4, S_2Cl_2, $SbCl_3$, S_8, etc.

It turns out that an overall feature of S(Q)'s studied here is simply characterized by both an effective dismeter of uncorrelated molecules and a packing fraction of them despite of molecular species, which are important to understand the general properties of fluids like the liquid-gas critical point. While a particular feature of each S(Q) is characterized by preferred orientations introduced between the nearest neighbors. The pattern of S(Q)'s for liquids of similar molecular shape is changed largely and systematically by the ratio of intramolecular to intermolecular atomic spacings, even if preferred orientation is fixed. Further study on more complicated systems is planned.

[3] Structural investigations on liquids and electrolyte solutions have continued. The difference technique using isotopes or isomorphous ions has been applied to aqueous electrolyte solutions.

In order to investigate the hydration of lithium and nitrate ions, 8.6 molar $LiNO_3$ solutions using ^7Li, ^0Li, ^{14}N and ^{15}N isotopes have been measured at room temperature. The interatomic distances and orientation of water molecules around the ions have been determined. The peak in G(r) ascribed to the nitrate ion - water interactions is much broader compared with that for the lithium ion - water interactions, demonstrating very weak hydration of the nitrate ion. Lanthanide(111) hydration has been investigated by measurring around 2 molar perchlorate solutions of Tb(111) and Dy(111), of Yb(111) and Tm(111), and of Pr(111) and Nd(111) ions as isomorphous pairs. The change in the hydration number from the light to heavy ions has been confirmed. The orientation of water molecules around the ions is unchanged in the series(fig. 3).

A project to study molecular liquids in a heterogeneous system has started, e.g. liquid D_2O in porous silica, Develosil 30 (the inner diameter is 30 A) at subzero temperatures from 258 down to 193 K. Difference G(r)'s as reference to that of 275 K have clearly shown the enhancement of the hydrogen bond

with decreasing temperature. Even at 193 K no Bragg peaks appeared, suggesting the formation of amorphous ice in the pores. The dynamics of water in the pores(30 and 100 A in diameter) has been further investigated by quasi-elastic neutron scattering with LAM40. The data showed slower movement of water molecules in smaller pore size and at lower temperatures. The water molecules in both pores were frozen in around 243 K, consistent with DSC and NMR data.

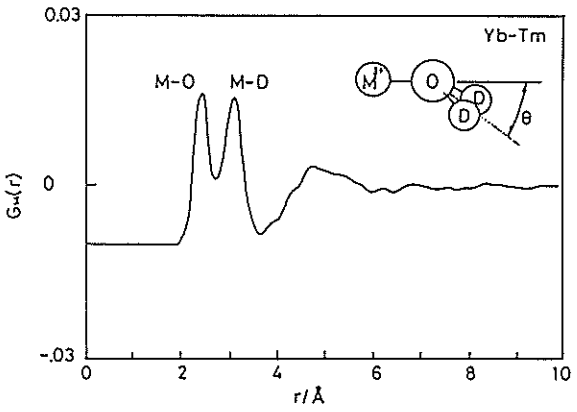

Fig. 3 Reduced pair distribution function G(r) of $Yb(ClO_4)_3$-$Tm(ClO_4)_3$-D_2O solutions.

[4] Conventional cell materials, such as Ti-Zr, quartz glass, and vanadium metal are often easily corroded by various high temperature melts. In order to avoid the corrosion by the sample melts, a nickel metal cell was developed because of its high corrosion resistance. The cell was made of 99% pure nickel metal. The part to be irradiated by the neutron beam was machined uniformly to be as thin as 0.30 mm. The bottom of the cell was sealed with a Ni rod by means of electron beam welding. The corrected and normalized intensity $I_V(Q)$ for the vanadium rod obtained at the scattering angle of 23° using the nickel metal cell is shown in fig. 4(b) in comparison with the conventional quartz glass cell(fig. 4(a)). Both $I_V(Q)$'s should be unity for all Q. The scattering intensities from the nickel metal cell are also presented in fig. 4(c) on the same scale. The diffraction from the nickel metal cell could be sufficiently subtracted from the total scattering. The quality of the resultant normalized intensities is comparable to that from the quartz glass cell, while both of them involve some noise because the accumulated counts were ca. one twentieth as small as those of usual experiments. Thus, the nickel metal cell is fully applicable to neutron diffraction measurement of highly corrosive melts inspite of the large Bragg peaks. Indeed, the structure factor S(Q) for molten alkali hydrooxides and carbonates was easily obtained by applying the nickel metal cell. This type of the cell can be extended to other corrosion resistant metals such as platinum metal.

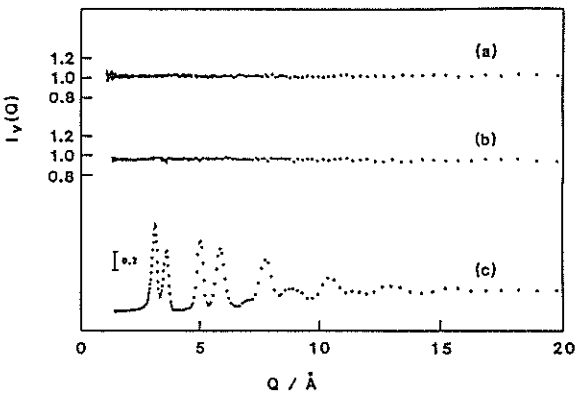

Fig. 4 Corrected and normalized intensities $I_V(Q)$ of the vanadium rod set in the quartz glass(a) and nickel metal cells(b) and the diffraction pattern(c) of the nickel metal cell at the scattering angle of 23°.

SAN (Small-Angle Neutron Scattering Instrument)

Status

SAN is a time-of-flight (TOF) type small-angle neutron scattering instrument installed at KENS. It utilizes a wide band of incident neutrons from 3 to 11 Å in wavelength to cover a very wide range of Q ($0.003 \leq Q \leq 4$ Å^{-1}) by choosing appropriate scattering path length. It is suitable for investigations in various field which have mesoscopic structure or density fluctuations of the scale from atomic size to a few thousand angstroms. It is one of the first five instruments which were built when the KENS facility began to operate in 1980. Since then, it has been one of the busiest and most productive instruments in the facility. Many scientists from various fields such as materials science, magnetism, biology, polymer, chemistry and industrial applications utilized the instrument.

The layout of SAN is shown in Fig. 1. It is installed at the exit of a neutron guide tube C1 which views a high-performance solid methane moderator at 20K. A tail cutter is used to eliminate frame overlapped long wavelength neutrons. A conversing Soller-slit is used which enables the use of larger sample. Sample position is 19 m from the moderator and the area detector can take a position of 1, 3 and 5 m from the sample in a scattering chamber. The area detector consists of 43 1D-PSDs of 1/2" in diam., 12" effective length and filled to 6atms ^{3}He gas. Spatial resolution of the detector is about $12^H \times 12^V$ mm^2. There are additional normal proportional counters at various fixed angles up to $2\Theta = 150°$. The area detector can cover a Q range of $0.003 \leq Q \leq 0.1$ Å^{-1} at 5 m position and the fixed detectors can cover Bragg- or diffuse-scattering region from 1 to 4 Å^{-1}.

The sample chamber is removable and it can be replaced by various equipments. Most experiments have been performed with a special sample container with thin windows which keeps atmosphere at the sample position. Various kinds of sample peripherals are available as listed in table 1.

Data acquisition, analysis and instrument control are carried out by a VAX station-II/GPX. Data analysis programs for isotopic and unisotopic samples are available.

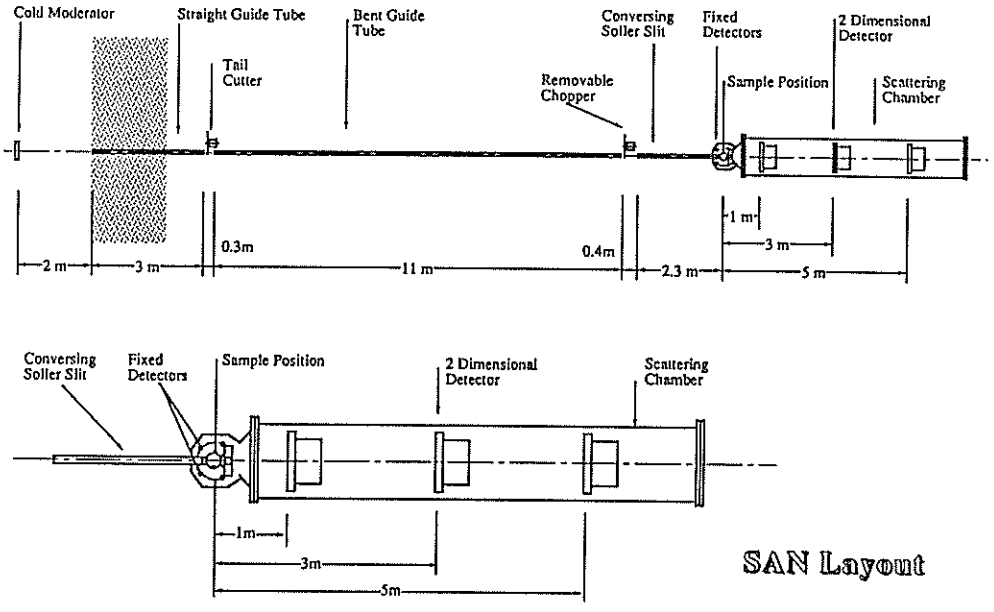

Fig. 1. Layout of the KENS-SAN instrument.

Future Plans

Shorter flight path length for incident neutrons without the guide tube will provide much higher neutron luminosity and wider wavelength band than the present. The performance of WINK, a new small/medium angle diffractometer, has proved that a bent guide as used in the present SAN is not necessary to eliminate high energy neutrons background. SAN will be upgraded after the completion of WINK.

Table 1. Specifications of the SAN instrument.

Beam-line

cold source, bent neutron guide C1.
(Cut off = 4 Å)

Incident wavelength band

$3 \leq \lambda \leq 11$ Å or $11 \leq \lambda \leq 19$ Å
(with tail cutter phase shift)

Q range

detector at	Q range area detector	Q range fixed detectors
1 m pos.	$0.02 \leq Q \leq 0.6$	$1 \leq Q \leq 4$ Å^{-1}
3 m pos.	$0.008 \leq Q \leq 0.2$	$1 \leq Q \leq 4$ Å^{-1}
5 m pos.	$0.003 \leq Q \leq 0.1$	$1 \leq Q \leq 4$ Å^{-1}

Intensity

4×10^4 n / cm^2 / sec at sample position, detector at 3 m position when accelerator operates at 2×10^{12} proton / pulse.

Ancillary equipment

Electromagnet:	1 T
Pulse electromagnet with cryostats:	0.5 T
Solenoid electromagnet with cryostats:	0.4 T
Closed circuit refrigerator:	13 K - 300 K
He flow type cryostat:	4 K - 400 K
He cryostat:	1.5 K - 200 K
Furnace:	300K - 1000 K

Typical Scientific Results

Membrane

Phosphatidylinositol diphosphate (PIP_2) is a highly hydrophilic phospholipid rich in nervous tissues, and has been considered to play an important role in the nerve excitation through the regulation by Ca^{2+} ions. Recent physicochemical studies have suggested for PIP_2 multibilayers that water molecules may penetrate into the interior region consisting of hydrocarbon chains, which are usually supposed to be very hydrophobic.

Bragg scattering from the PIP_2 multibilayers were measured on SAN. The change of neutron scattering density profiles which were calculated from the scattering data for the system are shown in Fig. 2. Since water were being replaced by D_2O, scattering length density increased with increasing volume fraction of water at specific position. From Fig. 2, it is clearly seen that with increasing relative humidity (RH), water molecules penetrate into hydrophobic interior region of PIP_2 locating at a distance of around -15 to 15 Å.

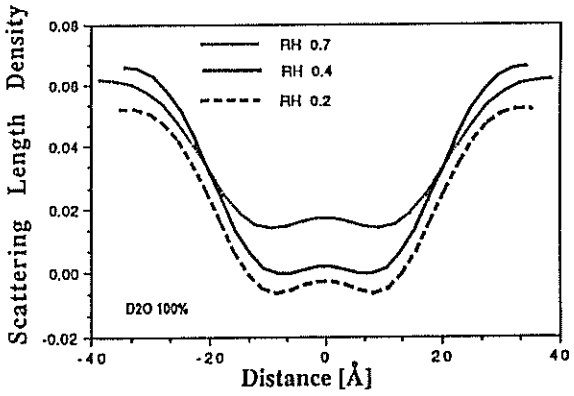

Fig. 2. Change of neutron scattering density profiles for multibilayers of PIP_2 with the change for three different relative humidity (RH) at 10°C.

Physical Gelation

The mechanism of the physical gelation has received much attention over the past several years, but it is still not well understood. We studied physical gelation of atactic polystyrene (aPS) in carbon disulfide solutions on SAN.

Scattering curves were analyzed by the assumption that the polymer has star like shape with branching points which are caused by interaction between aPS and CS_2. Temperature dependence of

Kratkey plot of the result is shown in fig. 3, together with calculated ones according to the particle scattering factor for such star molecules with monodisperse rays.

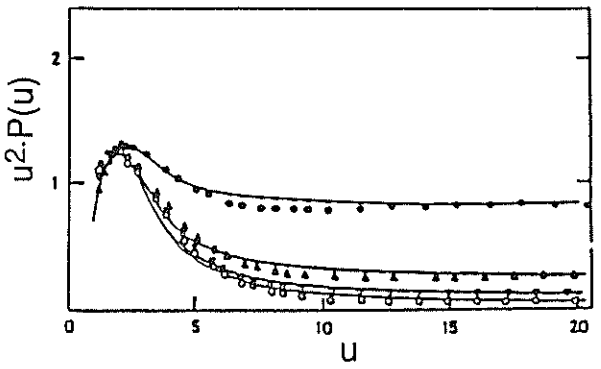

Fig. 3. Kratkey plot of small-angle neutron scattering data from atactic polystyrene (aPS) in carbon disulfide solutions. Solid curves are the calculated values.

Reentrant Spin Glass Systems

Fe_xAl_{1-x} alloy system is well known to exhibit the characteristic features of a reentrant spin glass (RSG) for the concentration range near x = 0.7. Conventional neutron scattering measurements so far being performed was limited in a narrow momentum transfer range. By extending Q range to higher Q region, which is an advantage of SAN, we found a crossover behavior in I(Q) at around Q = 0.05 $Å^{-1}$. Temperature dependences of the small-angle neutron scattering intensities are shown in Fig. 4.

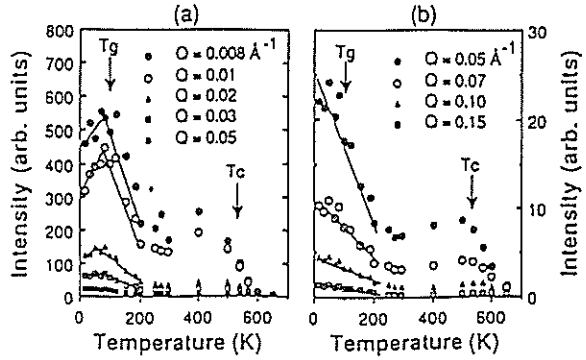

Fig. 4. Temperature dependences of the SANS intensity from $Fe_{0.715}Al_{0.285}$ alloy in the Q ranges of (a) $0.008 \leq Q \leq 0.05$ $Å^{-1}$ and (b) $0.05 \leq Q \leq 0.2$ $Å^{-1}$. The solid lines are drawn to guide to the eye.

At the smaller Q range below the crossover regime, we found a Lorentzian behavior in I(Q). For larger Q, however, I(Q) can be fitted by squared Lorentzian. The former behavior is well understood by spin fluctuation in ferromagnetic region of the system. The latter can be interpreted by the break down of the ferromagnetic region into smaller parts, magnetic domains of the order of 120Å (~2π /0.05$Å^{-1}$) with different spin directions from those in the surrounding ferromagnetic region.

Phase Separation Processes

It is well established that at the late stages of phase separation processes, scattering functions are well described by the scaling function, $F(q/q_1) = q_1^3 S(q)$, where S(q) is the scattering function, q_1 the first moment of S(q). The shape of the scaling function F(x) is, however, not well known and there is no experimental consensus about how universal the scaling law is.

Therefore, we studied phase separation in Al-Li alloy system. A typical experimental result together with a theoretical calculation by means of a mean field approach based on the interface dynamics is shown in Fig. 5. The calculated curve well reproduces the experimental result except at below x = 0.6. It is noteworthy that both have a similar small shoulder at around x = 3. The experimental result, however, shows gradual change in scaling function F(x) with annealing time; i.e. the function is not strictly a universal one. Further study of the system is underway.

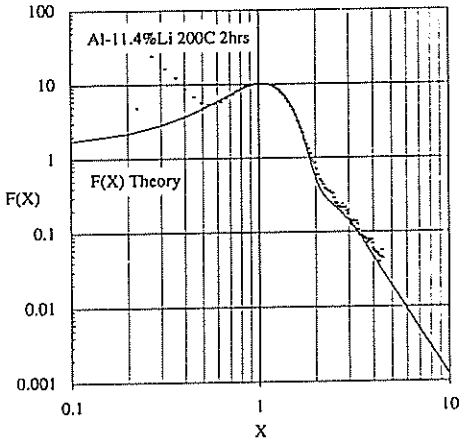

Fig. 5. Scaling function obtained from small-angle neutron scattering (dots) and theoretical result (solid curve).

WIT (Thermal Neutron Small Angle Scattering Spectrometer)

Status

We have developed a thermal neutron small-angle scattering spectrometer (WIT), and installed it at a pulsed **thermal neutron** source. The first report on general survey of the spectrometer has already been given in this report.[1] Afterwards several modifications of some parts have been carried out on WIT. The details are given in this report [2] and summaries are as follows:

1) A two dimensional converging Soller slit system has been replaced by a converging pin hole slit in order to increase transmission of incident neutrons, and the intensity at the sample position was increased about 40 times more than before by the replacement.

2) A special beam stopper which provides both scattering and transmission measurements of a sample simultaniously has been designed and installed.

3) Annular detectors equipped with glass scintillator are nearly completed, and the current Q-range covered is from 0.02 A^{-1} to 1.0 A^{-1}.

WIT is now opened to users, but most of the machine times are distributed to the persons who have developed it and should maintain it. Several scientific topics which were studied are as follows:

Biology

Lysozyme is one of the most typical biological materials as a sample to test a qualification of a small angle neutron scattering (SANS) spectrometer.

Small-angle neutron scattering measurement was made for a lysozyme sample in aqueous solution of different D_2O/H_2O ratio i.e. 100%, 90%, 66%, 12% and 0%, where a unit of the ratio is mol%. The Guinier plots are shown in Fig.1. A radius of gyration R_g of lysozyme is calculated .The mean excess scattering density ρ was determined as 2.647×10^{-10} cm^{-2} using $\sqrt{I(0)}$ vs D_2O/H_2O ratio . By carring out Stuhrmann plot, the structure parameters of lysozyme are determined, and the details are given in this report.[3]

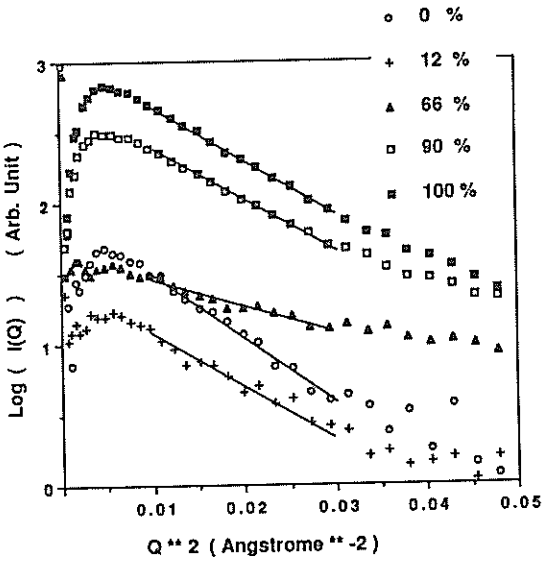

Fig. 1. Guinier plot of lysozyme in aqueous solution at different D_2O/H_2O ratio

Material

Carbon materials are considered to be candidates of materials of first walls of a nuclear fusion reactor. Carbon materials are characterized in the nature of defects produced by the irradiation of fast neutrons. Small angle neutron scattering measurement can give many informations on defects of these materials.

1) Glass-like carbon[4]

The SANS measurements of Glassy Carbon GC-10, GC-20 and GC-30 produced in Tokai Carbon Co. Ltd.were made. Glassy Carbon GC-10, GC-20 and GC-30 were produced at temperature 1300 0C, 2000 0C and 3000 0C,respectively. Radii of gyration of each material were obtained, and they are found to be linearly proportional to the production temperature as shown in Fig. 2. Micro voids produced in a glass-like carbon were found to be characterized by the radii of gyrations which depend on the production temperature linearly.

2) Glass-like carbon irradiated by fast neutrons[5]

GC-30 was irradiated by fast neutrons (fast neutron fluences of more than 1 Mev are $1.2 * 10^{20}$ n/cm^2) at temperature between 135 0C and 140 0C at JMTR. After the irradiation, the samples were annealed. SANS measurement of GC-30

was made in the following sequences. They were the measurements of 1) unirradiated ones, 2) as irradiated ones, 3)annealed ones at 573 K, and 4) annealed ones at 873 K, respectively. Guinier plots derived from the SANS measurements at each state are shown in Fig. 3. The radii of gyration among the states did not vary, but I(Q) $Q=0$ shifted as following; I(0) decreased by being irradiated and recovered to some extents by annealing, but this did not depend on temperature up to 873 K.

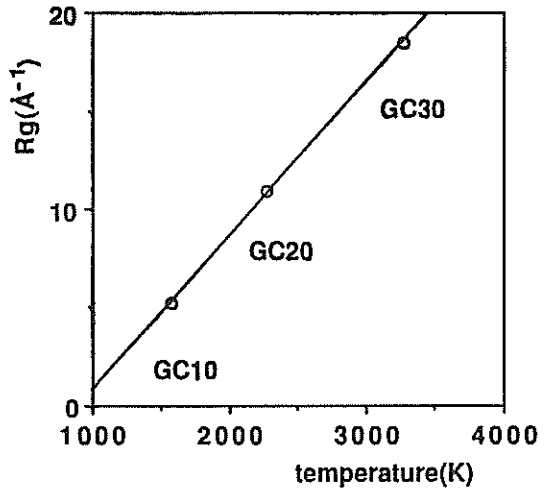

Fig. 2. Production temperature dependence of the radius of gyration

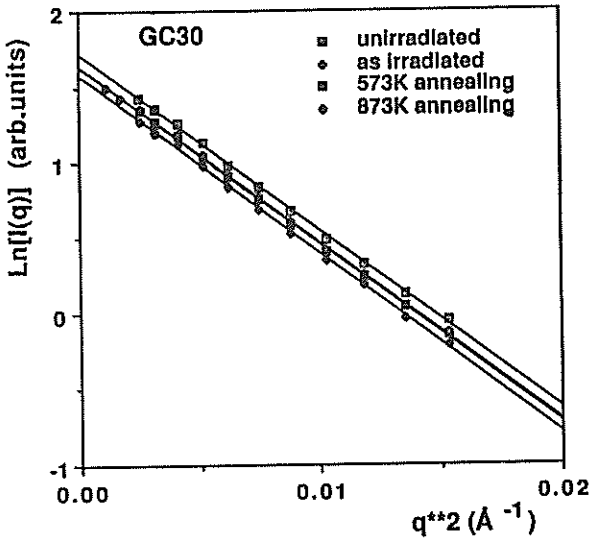

Fig. 3. Guinier plots of the irradiated GC-30 at the states after processing

3) Isotropic Graphite[6]

Isotropic Graphite samples T-6P, T-4MP and ETP-10 are produced in Ibiden Co.Ltd.

The densitis are 1.91, 1.78 and 1.75 (g/cm^3), respectively. SANS measurements were carried out and scattering functions I(Q) of three materials are shown in Fig. 4., where the graph is given by log I(Q) vs. log Q plots. Data points are on lines within wide Q-range. There are sevral models which give a non integer and nearly equal to -3 exponent, and our experimental results are explained by a model that there is one dimensional density fluctuation of graphite.

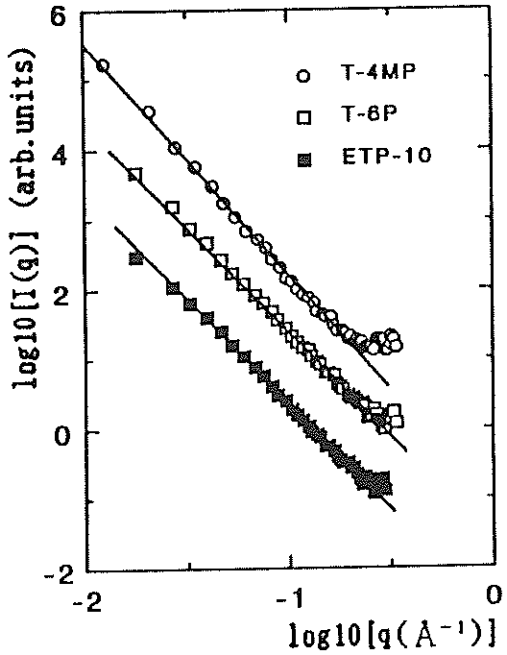

Fig. 4. Log I(Q) vs. log Q plots of T-6P, T-4MP and ETP-10

references

1) N.Niimura *et al*;KENS REPORT VI (1985/86),18-25
2) N.Niimura *et al*; KENS REPORT VIII (1989/90)
3) U.Sangawa *et al*; KENS REPORT VIII (1989/90)
4) K.Aizawa *et al*; KENS REPORT VIII (1989/90)
5) K.Aizawa *et al*; KENS REPORT VIII (1989/90)
6) K.Aizawa *et al*; KENS REPORT VIII (1989/90)

LAM (Latticed Crystal Analyser Mirror Spectrometer)

Status

LAM spectrometer was constructed to measure the quasielastic scattering and the low energy inelastic scattering process in condensed matter physics and chemistry. The LAM spectrometer is the first spectrometer that employes the KENS spallation cold neutron source and acrystal analyser mirror in the inverted geometry. This spectrometer is a very useful device to study diffusive motion or the relaxation processin molecular science and in many other fields. By measuring the quasielastic neutron scattering, one can obtain a useful information in the analysis of temporal and spatial properties of atoms and molecules which are in the random motion of characteristic time of 10^{-12} to 10^{-9} second. The LAM spectrometer was first designed and installed at the KENS spallation cold neutron source of the National Laboratory for High Energy Physics (KEK) by Prof. K. Inoue, Department of Nuclear Engineering, Hokkaido University.

We have three LAM spectrometers: the LAM-D, the LAM-40, and the LAM-80/80ET, which are installed at the H9, C4, and C2 neutron guide holes, respectively. These spectrometers are characterized by both a wide energy window and a good signal to noise ratio. For about 10 years a number of measurements on various samples have been carried out. During these years the LAM spectrometers have been improved step by step for the resolution, the data aquisition system, and so on. Environmental equipments such as a high temperature furnace, low temperature refrigirator, and so on have also been developed in order to cover various experimental purpose. The typical scattering vector Q ranges 0.2 to 3 $Å^{-1}$.

The present status of the LAM spectrometers is summarized in Table.

Table: Characteristics of the LAM spectrometers

	energy resolution	energy window
LAM-D	300-500 μeV	$0<\varepsilon<200$meV
LAM-40	100-200 μeV	$0<\varepsilon<$ 3meV
LAM-80/80ET	5- 50 μeV	$0<\varepsilon<300\mu$eV

Science

Users of the LAM spectrometers are classified into two types; one is B1 group responsible for construction, operation, maintenance and improvement of the spectrometer, the other is B2 group of pure users.

Here, we introduce topics or summaries of experimental results obtained recently by using the LAM spectrometers.

[1] The glass transition in amorphous materials is of great interest from microscopic dynamical viewpoints. Amorphous polymers are the typical amorphous materials and may be expected to reveal neutron scattering spectra due to specific dynamical motion of atoms in polymer chains which occurs above the glass transition temperature (T_g) and freezes below T_g. Incoherent neutron scattering spectra from polybutadiene (PB) and polyethylene (PE) were measured using by the LAM-80. T_g are about 173 K and 200 K for PB and PE, respectively.

Figures 1(a)-1(e) show the measured spectra at two values of Q, 1.2$Å^{-1}$and 2.0$Å^{-1}$, respectively. The

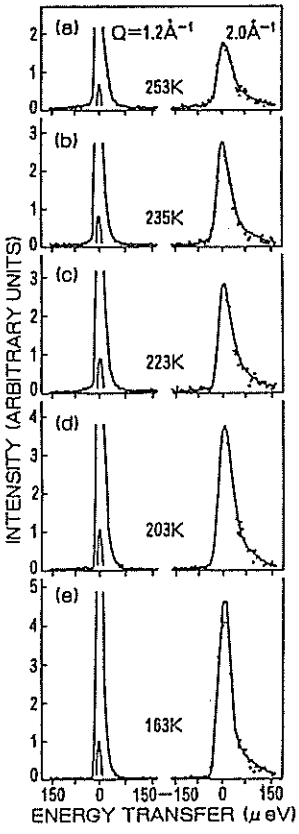

Fig. 1 Neutron scattering spectra from polybutadiene at five temperatures. The solid lines represent a fit to the data. The center peak on left column is scaled down by a factor ten.

measured spectra consist of three components. First is a strong sharp peak which relates to the very slow motion of chains and has the shape of instrumental resolution. Second is a broad and faint quasielastic peak. Third is an inelastic component which has wide energy transfer character just as continuous background. The result of PE was similar to that for PB. The scatteringcross section was assumed to be a sum of the contributions from the elastic part and a quasielastic component of single Lorenzian. Localized random motion is suggested by the fact that the observed widthdoes not change drastically in the measured Q range. Furthermore, the fact that the temperature dependence of the width is not appreciable suggests that the barriers to the random motion are small. Because the polymers employed in this study have no side-groups, the observed quasielastic spectra might be directly related to the motion of individual chain backbone. The most likely pattern of this motion is a restricted jumpwise displacement of chain segments occurring among a few different conformations which are formed by the constraint of the entangled linear chains.

[2] Below T_g, a broad low energy excitation peak is observed in many amorphous polymers. The nature of the low energy excitations was still unkonown. Neutron inelastic scattering measurements with LAM-40 were carried out on amorphous polymersin order to clarify the nature of the low energy excitations.

Figure 2 shows the densities of states $G(\omega)$s of PB calculated from the dynamic scattering laws below T_g. $G(\omega)$s of PB are almost independent of temperature below T_g. In other words, the temperature dependence of the dynamic scattering law for the excess excitation can be reduced by the Bose factor $n_B(\omega)+1$. This may indicate that the population for the excess excitation is governed by that of phonons through interactions between the asymmetric double-well systems and propagating phonons. "Phonon-assisted tunneling in asymmetric double well potential" seems to explain the experimental results, but it is a further problem which structure corresponds to the double-well potential or which unit in polymer moves in the potential.

[3] The physical gelation in atactic polystyrene solution is of great interest from microscopic dynamical viewpoints. Atactic polystyrene is one of most typical amorphous polymers and therefore the mechanism of the physical gelation of this system was still puzzling. In order to reveal the gelation mechanism from microscopic dynamical viewpoints, incoherent neutron scattering measurements were carried out by using both the LAM-40 and LAM-80.

Figures 3(a)-3(e) show the measured spectra at two values of Q, 1.2Å^{-1} and 2.1Å^{-1}, respectively. A drastic narrowing of the central peak is observed, as the gelation proceeds. This means that the observed width drastically changes in the measured q ranges. The present results are qualitatively described by a theory of the local segmental motion.

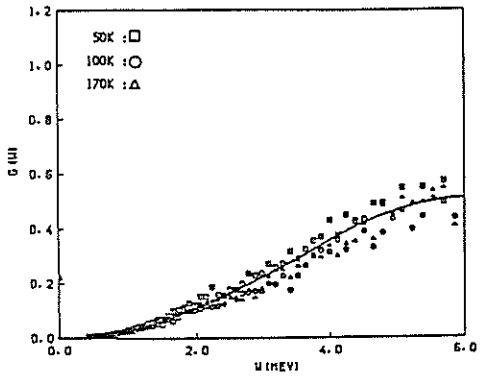

Fig. 2 Density of states of polybutadiene calculated from the data at 50, 100 and 170K (T_g=170K). All the densities of states are independent of temperature within experimental error.

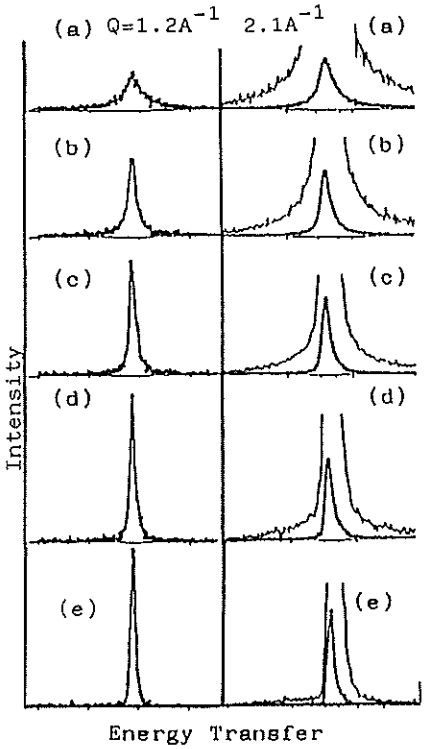

Fig. 3 Neutron scattering spectra from atactic polystyrene-carbon disulfide near the gelation point. The tails on right column is scaled up by a factor ten.

[4] The LAM-80 using mica analysers was improved in order to gain high intensity without changing the resolution. The improved LAM-80 (LAM-80ET) gave a desirable performance of energy resolution accompanying by a surprisingly sharp rise of resolution function on the energy loss scattering side and gained 8 times intensity.

The first experiment result obtained by the LAM-80ET was the observation of tunnelling of N-oxy γ picoline as shown in Fig. 4, in which the energy resolution is about 5 μeV. The counting rate and the resolution of the LAM-80ET were confirmed to IRIS at RAL.

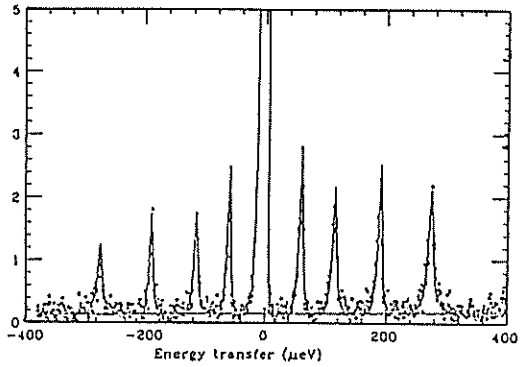

Fig. 4 Tunnelling spectrum of N-oxy γ picoline obtained by the LAM-80ET. The energy resolution is about 5 μeV.

MAX (Multi Analyser Crystal Spectrometer)

Status

Crystal analyser spectrometer MAX can observe collective excitations such as phonons and magnons in single crystals by means of TOF method. Excitation spectrum along a desired direction of the sample crystal can be measured using fifteen detectors of MAX. Because MAX takes an inverted geometry, energy of the scattered neutron is fixed by the analyser crystal (pyrolytic graphite). In practical use, the energy transfer range is 1meV to 150meV depending on the Q region to be covered. The energy resolution $\Delta E/E_f$ is about 0.1 and can be adjusted by inserting the Sollar type collimators before and/or after the analyser. MAX exhibits its ability in several tens meV energy transfer region, which energy is not so easy to observe using a triple-axis spectrometer at the steady reactor. Advantages in the application of MAX to the low-dimensional systems should be noted. All the scans made by the detectors of MAX are constant-q when the incoming neutron beam is set parallel to the direction in which the system has no correlation, i.e. the direction perpendicular to the plane (chain) of the two- (one-) dimensional material. Furthermore, better experimental condition is found in the case of low-dimensional systems because the strong restriction due to the periodicity in the (Q,ω) space is relaxed. It seems that MAX has now established the capability of observing collective excitations using the TOF method at the pulsed neutron source.

During the past few years the signal to noise ratio of the spectrometer has been improved significantly. Furthermore, new inpile collimator with sintered B_4C arrays has been inserted in order to eliminate the fast neutron background. Next, a sample chamber and shieldings which eliminates the background neutrons scattered by the sample and the surroundings will be placed. A new set of two-axis goniometer has replaced one of the previous analyser-detector systems and is now being tested. This computer controled goniometer is designed to gain more flexibility and ability of precise alignment. All pyrolytic graphite analysers have been enlarged to the size of 7cm x 10 cm from 5cm x 10cm.

Science

Most of experiments which have been carried out in these two years using MAX are on the magnetic excitations. Magnons in ferromagnetic alloy Fe_3Pt have been studied in conjunction with the effect of atomic disordering upon the excitation. It is well known that the magnetic characteristics such as the magnitude of the moment or Curie temperature of Fe_3Pt are strongly dependent on the degree of atomic order. Another interesting antiferromagnet Mn_3Pt has been studied in order to reveal the nature of its unique magnetic phase transition. At about 400K, the magnetic structure of Mn_3Pt changes from the low temperature triangular structure to the high temperature collinear phase. In both samples, magnons are observed up to the energy of about 60meV along the high symmetry directions. Magnetic excitations in three-component random antiferromagnet $K(MnCoNi)_{1/3}F_3$ has been studied extensively in order to verify the existing models and prospects on the excitations in the random magnets. The excitation spectra have been collected along three principal directions. Magnetic excitations in antiferromagnet $CoTiO_3$ have also been studied. The [110] direction of the (1,1,4.5) Brillouin zone was fully covered using thirteen detectors. Acoustic and optical magnons and higher energy magnetic excitation between orbital multiplets have been observed.

MAX can be used to observe incoherent scattering with both good energy and good Q resolutions, in other words, MAX can measure a selected excitation at a selected point Q. Using this feature, angle dependence of the hydrogen motion in single crystal KDP has been investigated. It has been found that the mode of $\hbar\omega$ = 28meV in KDP, which has attracted much attention recently, is orientation dependent: the scattering intensity of this mode varies considerably as a function of the angle between the scattering vector and the particular direction of the crystal. Within the a-c plane, the intensity become minimum when the scattering vector is parallel to the c-axis.

Most of the scientific programmes presented above are subjects to be continued. In addition to these, low-dimensional magnetic systems such as ABX_3 type trihalides and $KCu_cMn_{1-c}F_3$ flustrated system have been tested. Investigation of lattice dynamics in the system which shows the structural phase transition will be carried out.

INC (Chopper Spectrometer)

Status

After 4 years R & D, designing and constructing stages, the INC spectrometer started to work in the beginning of 1989. It is the direct geometry spectrometer using incident neutrons monochromatized by a fast Fermi type chopper system. The incident neutrons with energies from about 30 meV up to 1 eV can be obtained with the time resolution comparable to the source neutron pulse width (this is the optimum condition for the spectrometer). Scattered neutrons from sample are counted at the array of ^{3}He detectors which covers a wide range of the scattering angles (from 5 to 130 degrees; the total number of the detectors is about 190). Therefore, the INC spectrometer is suitable for the measurement of inelastic neutron scattering in a wide range of energy and associated momentum transfer. Since the observation of scattering at small momentum transfer is particularly important in many cases, the scattering angles from 5 to 12 degrees are densely covered by detectors in a hexagonal detector bank. Consequently, the INC spectrometer has especially high sensitivity for the measurement of the high energy excitations with small momentum transfer.

The spectrometer was successfully commissioned during 1989, and becomes open to outer users from the 1990/1991 fiscal year. The specification and the instrument parameters of the spectrometer are shown in Table 1. The measurable range in energy-momentum space by the spectrometer is displayed in Fig. 1.

Science

The fields of the application of the INC spectrometer spread in a wide range. Some examples of them are described below with the typical experimental results obtained during the last years:

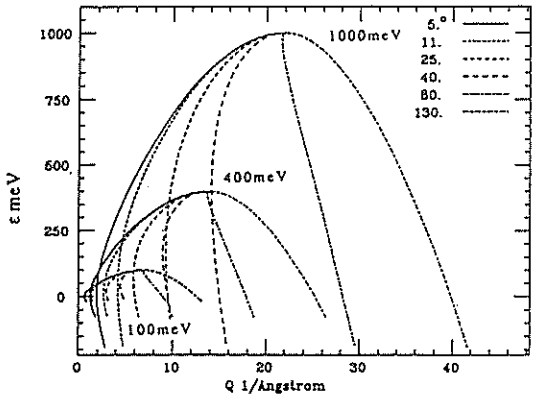

Fig. 1. (Q,ω) space accessible with scattering angles of 5°, 11°, 25°, 40°, 80° and 130° for the incident energies of 100, 400 and 1000 meV on INC.

[1] Crystalline electric field and inter-multiplet excitations

The INC spectrometer is well suited to the study of the crystalline electric field (CEF) or inter-multiplet excitations in rare-earth compounds since the nature of the scattering is in general incoherent and it allows the summation of the count rates taken at a number of detectors without loss of the important information. Recently, the observation of CEF excitations in Ce and Yb compounds is of particular interest because many of them show anomalous behaviors which come from the dense Kondo effect. Fig. 2 shows, as an example, the experimental results for polycrystalline $CeSi_x$ with x=1.7, 1.8, 1.85 and 1.9, where the compounds with x<1.85 are ferromagnetic with anomalously small saturation moment, while those with x≥1.85 are non-magnetic with heavy electron anomalies. The data are obtained by summation of the count rates at the low

Table 1. Specification and instrument parameters

Incident energy	30 - 1000 meV
Energy resolution($\Delta\varepsilon/E_i$)	1 - 3 % (2θ=5°- 40°), 1 - 5 % (41°-130°)
Momentum transfer	0.3 $Å^{-1}$ - 40 $Å^{-1}$
Momentum resolution($\Delta Q/Q$)	1 - 10 %
Chopper	7.0 m from moderator, 400 - 600 Hz phased to neutron burst within ±1/2 μs
Sample position	8.2 m from moderator
Beam size	5 cm x 5 cm
Detector position	2.5 m from sample (5°-40°) 1.3 m from sample (41°-130°)
Intensity at sample	~2 x 10^2 n cm^{-2} s^{-1} at E_i = 90 meV

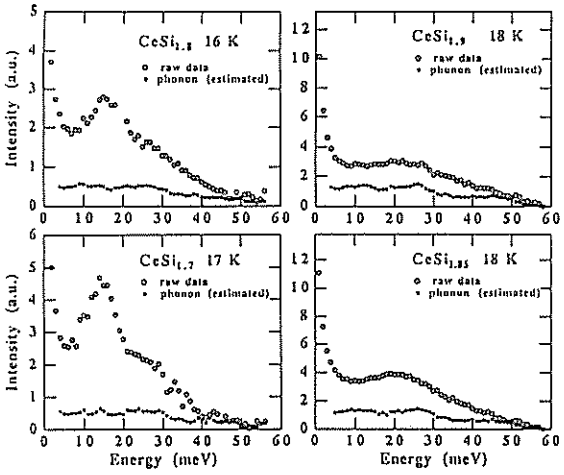

Fig. 2. Inelastic spectra of $CeSi_x$ (x=1.7, 1.8, 1.85 and 1.9) at low temperatures measured at the averaged scattering angle of 9° (summation of data at 5°-12°) on INC with incident energy of 60 meV. Open circles are the raw data and close circles are the estimated phonon contribution.

temperatures measured at the low angle detector bank (5-12 degrees) with incident energy of 60 meV. The phonon contributions estimated from the data at high angle detector bank(112.5-130.5 degrees) are shown by the solid circles. Each magnetic response, that is the difference between the raw data and the phonon contribution, consists of two inelastic peaks with rather large linewidths, and it is seen that the peak positions, linewidths and the peak intensity ratio increase gradually with increasing x. The change of the spectrum with increasing x is interpreted as the result of the increase of the strength of the hybridization between the conduction electrons and 4f electron, and this is thought to be the main origin of the cross-over transition from the ferromagnetic state to the nonmagnetic heavy electron state in $CeSi_x$ at the critical concentration around x=1.85 where the Kondo screening effect dominates the formation of the ferromagnetic order.

[2] Spin wave excitations in low dimensional spin systems

The measurement of spin wave excitations in low dimensional spin system is another example of the effective use of the INC spectrometer. This is typically demonstrated by the results of the experiments on the quasi 1-D Heisenberg antiferromagnet $CsVCl_3$. The scattering condition was chosen such that the spin chain direction is aligned parallel to the incident beam. Due to the 1-D magnetic property, the scattering events with a reduced wave vector q are detected at all directions forming a cone with the corresponding scattering angle around the incident beam. Moreover, it is possible to make the error of the reduced wave vector q small for the scattering in the forward direction. Therefore, the summation of the count rates of many detectors in the forward direction works effectively to detect the spin wave excitations in such materials. Fig. 3 is an example of the spectrum of $CsVCl_3$ thus obtained with incident energy of 305 meV at the averaged scattering angle of 7 degrees. The peaks at about 37, 57 and 82 meV correspond to the cuts of the spin wave dispersion surfaces with the TOF scan. The present result reveals that the quantum effect is also important in this S=3/2 1-D Heisenberg system.

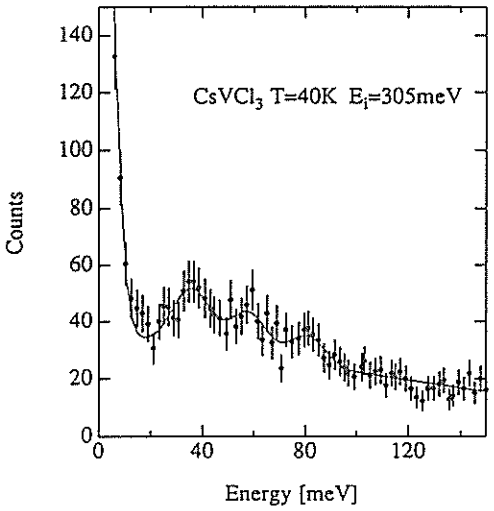

Fig. 3. Spectrum of spin wave scattering from $CsVCl_3$ at 40 K measured at the averaged scattering angle of 7° (5°-9°) on INC with incident energy of 305 meV.

[3] Dynamical structure of amorphous materials

The INC spectrometer is also suitable for the measurement of the dynamical structure of amorphous materials since a dense mapping of the dynamical scattering function $S(Q,\omega)$ in a wide (Q,ω) space can be obtained in a single measurement. Fig. 4 shows the results of the preliminary experiment on $Cu_{57}Zr_{43}$ amorphous alloy at 16 K measured with the incident energy of 60 meV. Absorption, detector efficiency and background corrections have been done. The luck of data at around Q=4 Å^{-1} comes from a gap between detector banks at the scattering angle of about 45 degrees where the second flight path is changed from 2.5 m to 1.3 m (now, the gap is filled). The energy integration of the obtained intensity $I(Q,\omega)$ is in good agreement with the static structure factor S(Q)

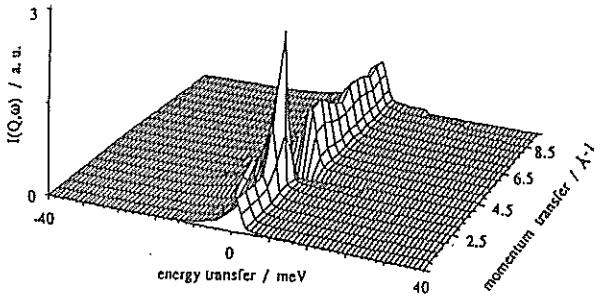

Fig. 4. Scattering intensity $I(Q,\omega)$ of $Cu_{57}Zr_{43}$ amorphous alloy at 16 K measured on INC with incident energy of 60 meV.

measured by the total scattering instrument HIT at KENS. The full analysis of the data including multiple scattering correction is under way.

[4] Hydrogen motion

Motion of hydrogen in various materials is well probed by neutrons because of its high incoherent scattering cross section. INC spectrometer is a powerful tool to study it since the scattering in a wide range of the (Q,ω) space can be observed by the spectrometer. Fig.5 shows the experimental result on

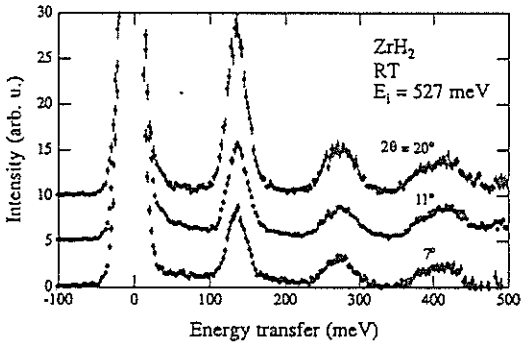

Fig. 5. Local mode spectra of ZrH_2 at room temperature measured on INC with incident energy of 527 meV.

ZrH_2 polycrystalline sample at room temperature with the incident neutron energy of 527 meV. In this case, inelastic peaks are seen at even energy intervals starting from about 140 meV. This result suggests that the local mode of hydrogen atoms in ZrH_2 is modeled well by the motion in a harmonic potential. The analysis of the Q-dependence of the intensity of each peak gives directly the information on the wave function of the hydrogen atom in the potential.

RAC (eV Neutron Scattering Spectrometer)

1. Introduction

We have developed eV and sub-eV neutron scattering spectrometers, RAT and CAT, on the H-7 neutron beam hole. The details of their spectrometers have already been reported [1][2]. Here we briefly introduce RAT and CAT.

Intense spallation neutron source, KENS can provide a useful eV neutron flux in energy range 0.1-100 eV, which is much more intense than has never been available from steady state sources, and made two fruitful techniques possible in RAT. One is an eV neutron scattering technique, which allows the impulse approximation limit to be approached. In this limit, the neutron scattering function is simply related to the momentum distribution n(p) or the effective temperature T_{eff} of the struck particle. Another one is an eV neutron absorption technique. Many heavy atoms, such as Ta, U, Sb, Ba and Ho, have large neutron resonant absorptions in the energy range 1-100 eV. Their cross section of neutron absorption is also related to T_{eff} in the weak binding approximation. Therefore, if a specific atom in a sample has a characteristic resonance, one can determine the effective temperature of the specific atom by using the width of the resonance peak, apart from the other atoms. Utilizing these unique natures in RAT, we have performed following experiments;

a) measurement of effective temperature of pyrolytic graphite[3];
b) direct observation of Bose condensation in He-II[4];
c) measurement of effective temperatures of O and Cu in high-Tc superconductor YBaCuO[5].

CAT is a sub-eV neutron scattering spectrometer with the energy resolution $\Delta E/E$ of about 2% in the energy range 0.01-1 eV. This is very useful for the investigation of the hydrogen local modes in metal hydrides etc. In CAT, we have performed following experiments;

a) local modes in metal hydrides TiH, NbH, TaH and VH [6];
b) hydrogen local modes in amorphous materials [7];
c) stretching and bending modes in KDP.

2. Instruments

Figure 1 shows the configuration of the high-resolution TOF type crystal analyzer spectrometer, CAT. It is an inverted-geometry type. White neutrons are incident on the sample, and scattered neutrons with a fixed energy Ef= 3.9 meV are selected by an analyzer crystal. Note that a time-focussing principle is adopted in the sample-analyzer-detector system in order to realize the higher counting rate and the higher energy resolution. The energy transfer ε in CAT is given by

$$\varepsilon(\text{meV}) = 5.182 \cdot 10^6 L/(t(\text{ms})-821)^2 - 3.9$$

where L is an incident flight-path length of 5.299 m and t the total tme-of-flight (TOF).

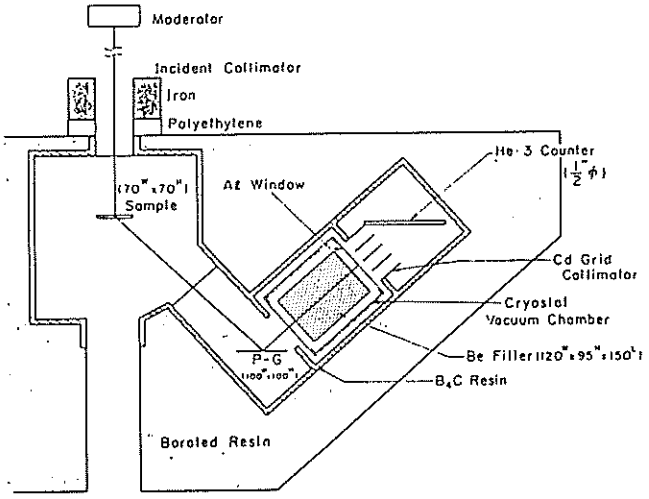

Fig. 1. Geometry of CAT spectrometer.

Figure 2 shows layouts of an eV neutron scattering spectrometer EVS (a) and a neutron absorption spectrometer NAS(b). In EVS, a γ-cascade is emitted, promptly after the neutron capture, from the resonance foil with a resonance energy E_f (for example, E_f = 4.28 eV in a case of Ta foil) and detected by a γ-ray scintillator. The incident neutron energy E_i is determined by TOF and the energy transfer ε is given by

$$\varepsilon = E_i - E_f$$

In NAS, the prompt capture g-cascade produced in a sample is just detected by a scintillator.

3. Present status

In CAT, we have continuously measured the hydrogen local modes in hydrogenous materials as KDP, CDP, RDP and so on, and their spectra have been compared with those obtained by the light scattering. The detailed discussion is just in progress.

Recently we have made a great progress in RAT. That is a successful observation of the hydrogen wave function in the condense matter. The incoherent neutron scattering function S(Q,w) is generally given by the transition probability from the initial state $\{f_0(x) \exp(iki\ x)\}$ to the final state $\{f_1(x) \exp(ikf\ x)\}$, where exp(iki x) and exp(ikf x) are the wave function of the incident and the scattered neutrons, respectively. $f_1(x)$ and $f_0(x)$ are the wave functions of the excited state and the ground state of hydrogen. Since the interaction between a neutron and the hydrogen neucleu is given by a constant value V_0, S(Q,w) is expressed as

$$S(Q,W) = |\int f_1(x)^* \exp(ik_f x)^* V_0 \exp(ik_i x) f_0(x)dx|^2 = V_0|\int f_1(x)^* \exp(iQ x) f_0(x)dx|^2,$$

where Q = ki - kf.

In the impulse approximation limit, the motion of the struck particle can be considered as that of the free particle, and $f_1(x)$ can be described by exp(ip$_f$ x).

Here $p_f = Q + p$. p_f and p are the momentums of the struck particle after and before the collision. In this assumption, we can obtain a following equation,

$$S(Q,w) = V_0|\int \exp(ipx)\ f_0(x)\ dx|^2.$$

This indicates that the eV neutron scattering spectrometer can provide a possibility of the direct observation of the wave function of the ground state. We chose a metal hydride TiH_2 as a standard sample and performed the feasibility experiment. Since the hydrogen motion in TiH_2 can be considered as harmonic oscillator, a wave function of the ground state is given by Gaussian $\exp(-a^2 x^2)$. Therefore, the scattering function S(q,w) is described as

$$S(Q,w) = MV_0 \exp(-p2/2M/E0)/Q = M\ n(p)/Q$$

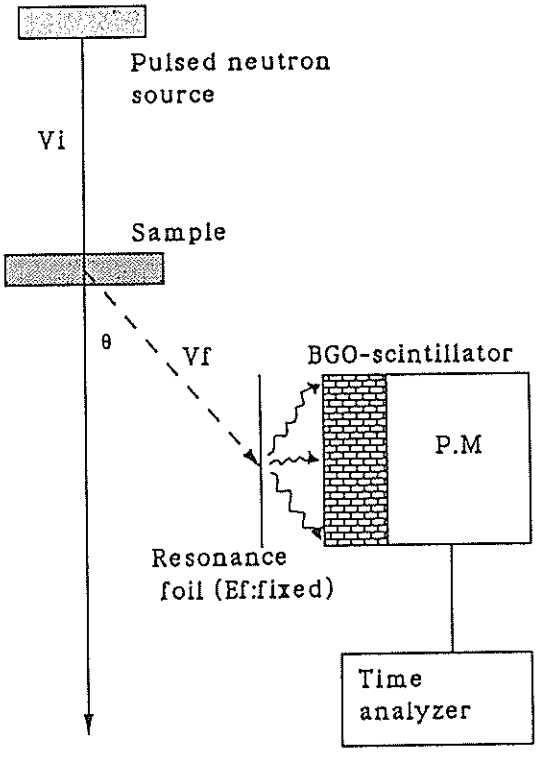

Fig. 2(a) . Layout of EVS spectrometer.

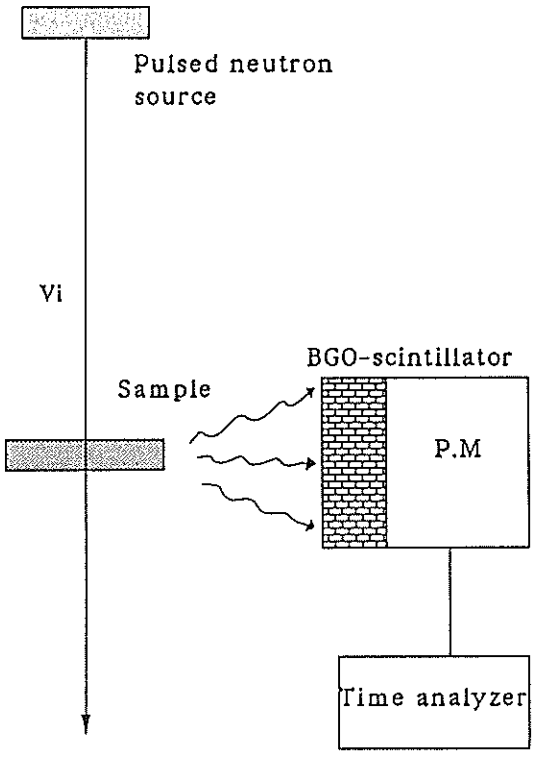

Fig. 2(b). Layout of NAS specrometer.

where p = |Q-s| and $s=\sqrt{(2M(w+E_0)}$. Figure 3 shows the observed scattering function S(Q,w). Squares and crosses in Figure 4 show the momentum distribution n(p) determined from the observed S(Q,w). A dotted line represents a calculated values when E_0 = 0.074 eV (this value is consistent to the result of the inelastic neutron scattering obtained in CAT) . The short bar represents a Q-resolution of RAT. A solid line shows calculated values including the Q-resolution. A agreement between the solid line and measured values is very good. It means that the direct observation of the wave function is possible.

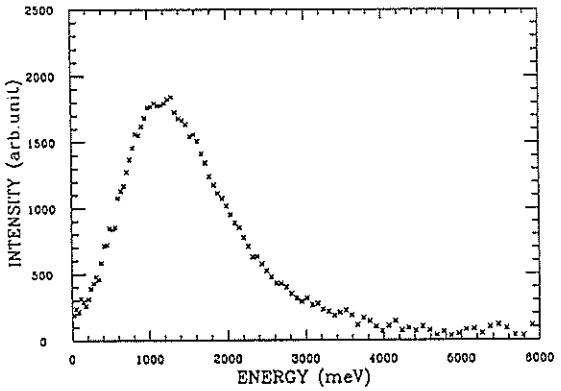

Fig. 3. Observed scattering function S(Q,w).

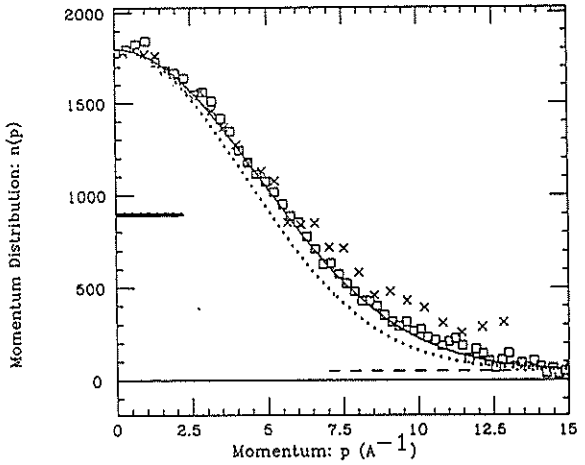

Fig. 4. Momentum distribution n(p).

On the above calculation, we used the Q-resolution simply estimated from the scattering-angle distribution $\Delta\theta$ and the final energy resolution ΔEf. However, the actual Q-resolution of RAT is much complicate. In order to accurately discuss the feasibility, we must calculate the exact TOF profile (including the multiple scattering, the sample size, the detector size, the sample angle, the detector angle, the burst time and the exact energy profile of the resonance foil), and compare it with the measured TOF spectrum. In the next papers concerning to RAT, the details of the experiments and the calculation will be discussed, and the first application of this method on PdH and PdD will be reported.

Refrence

[1]S.Ikeda and N.Watanabe, Nucl. Instr. Meth. 221(1984) 571

[2]J.M.Carpenter, N.Watanabe, S.Ikeda, Y.Masuda and S.Satoh, Physica 120 (1983) 126

[3] H.Rauh and N.Watanabe, Phys.Lett. A 100 (1984) 244

[4]S.Ikeda and N.Watanabe, Phys. Lett. A 121 (1987) 34

[5]S.Ikeda and M.Misawa, S.Tomiyoshi and M.Omori, Phys. Lett. 134(1988) 191

[6]S.Ikeda and N.Watanabe, J. Phys. Soc. Jpn. 56(1987) 565

[7]K.Kai, S.Ikeda, T.Fukunaga and N.Watanabe, Physica 120B(1983) 342

PEN (Polarized Epithermal Neutron Spectrometer)

Present performance of our polarized proton filter for polarizing epithermal neutron beam is satisfactory for polarized neutron experiments. A typical neutron polarization is 70%. The neutron transmittance of the filter is about 25% at E_n=1 eV[1]. The result gives us a polarized neutron flux of 5×10^4 n/eV·cm^2·sec at 6.6 m from the source at the present KENS intensity. By using this apparatus, following experiments were carried out in the last fiscal year.

Angular dependence in the capture γ-ray asymmetry

The experiments on P-voiolation in p-wave resonances have been carried out by several groups[2,3,4,5]. The largest observed P-violating asymmetry is for a p-wave resonance of ^{139}La at the neutron energy of E_n = 0.734 eV. We simultaneously measured capture γ-ray asymmetry and transmission asymmetry with respect to the neutron helicity at KEK[3] and obtained asymmetries in the total and radiative capture cross sections for the p-wave resonance of ^{139}La, which were denoted by $A_{L,n}$ and $A_{L,\gamma}$, respectively. The results are $A_{L,n}$ = 9.7±0.5% and $A_{L,\gamma}$ = 9.5±0.3%. The Dubna group obtained, $A_{L,n}$ = 7.3±0.5%[2]. A small difference is observed between the KEK's result and the Dubna's result. Vanhoy et al. suggested that the capture γ-ray measurement is not identical to the transmission measurement because of the effect of the a_2 term in the γ-ray angular distribution[6].

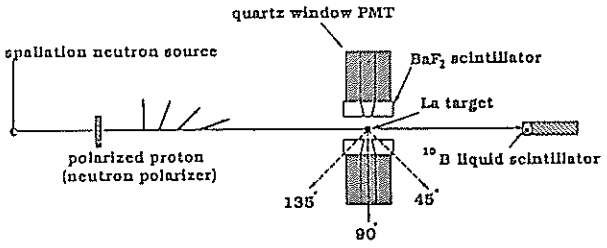

Fig. 1 Experimental arrangement for capture γ-ray measurement.

We measured the capture γ-ray asymmetry as a function of θ_γ. The experimental set-up is schematically shown in the Fig. 1. The direction of the neutron polarization is transverse to the neutron beam axis after transmission through the polarized proton filter. We rotated the neutron spin from the transverse to the longitudinal direction by means of an adiabatic passage. The direction of the neutron polarization at the target position was reversed every 2.5 sec. Neutron capture γ-rays from the target were detected by a BaF_2 scintillation counter hodoscope encircling the target. This hodoscope enabled us to detect the capture γ-rays as a function of θ_γ. γ-rays were counted as a function of neutron time of flight.

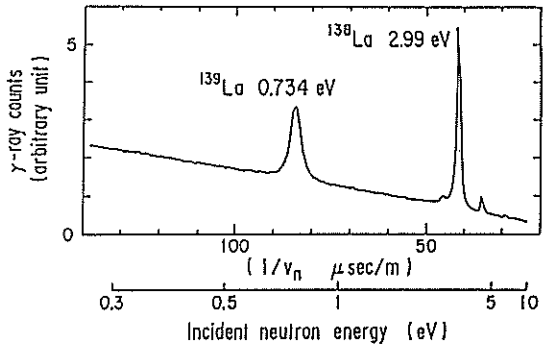

Fig. 2 Fig. 2 Capture γ-ray TOF spectrum.

A typical result of the γ-ray measurement is shown in Fig. 2. The solid and dotted lines are the results of γ-ray counts, $N_\gamma(+)$ and $N_\gamma(-)$ for positive and negative helicity states, respectively. The capture γ-ray asymmetry, which is defined as

$$\varepsilon_\gamma = 1/P_n \cdot (N_\gamma(+)-N_\gamma(-))/(N_\gamma(+)+N_\gamma(-)) \quad (1)$$

was obtained at polar angles $\theta_\gamma = 45^o$, 90^o and 135^o. The preliminary results are shown in Fig. 3. As it is shown in this figure, no significant θ_γ dependence is observed in the asymmetry. The capture γ-ray counts at the three polar angles were summed. The result of the asymmetry for summed data was consistent with the previous result at KEK. As the result, no significant effect of the a_2 term exists in the asymmetry. It is consistent with that the capture γ-ray measurement is identical to the transmission measurement for the asymmetry in the p-wave resonance.

Recently, the Los Alamos group obtained the asymmetry in the p-wave resonance by a measurement of double transmission through two targets[5]. Neutrons were polarized upon transmission through the first target by helicity dependent transmission. The second target was used as a polarization analyzer. The result of the asymmetry is $P_{L,n}$ = 9.7±0.3%. The result confirms the KEK's result.

Helicity dependent neutron scattering

We measured helicity dependence of scattered neutron intensity in order to examine a P-violating potential-resonance interference term[7]. We used the nuclear Bragg scattering for this purpose. The scattering cross section of the Bragg scattering at the scattering angle θ is expressed by the following equation.

$$\sigma_C = N \cdot (2\pi)^3/v_0 \cdot 2/k \cdot * \Sigma F_N(\tau)\, \delta(\tau^2 - 2k\tau \sin(\theta/2)) \qquad (2),$$

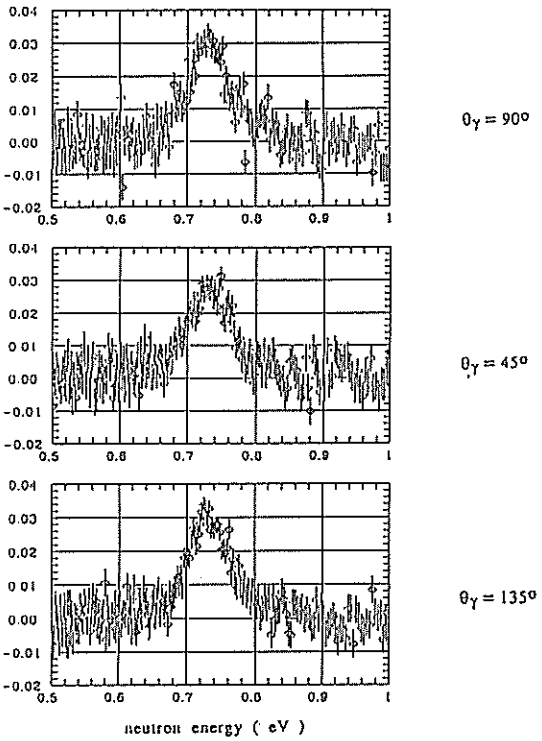

Fig. 3 Capture γ-ray asymmetry.

$$F_N(\tau) = \Sigma \exp(i\,\tau \cdot x)\, b_x \qquad (3).$$

Here,

N : number of the unit cell in a crystal

v_0 : volume of a crystal

k : neutron wave number

τ : reciprocal lattice vector

x : position vector of the nucleus in the unit cell

b_x : the neutron scattering length of the nucleus at x.

The potential-resonance interference term is included in b_x. A typical result of the Bragg scattering at θ = 33.4°, for a LaF_3 single crystal is shown in Fig. 4. The peak at the neutron wave length

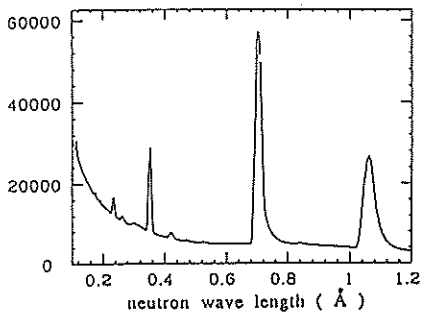

Fig. 4 The nuclear Bragg scattering of a LaF3 single crystal.

λ = 0.35 A is due to the reflection by the plane of 0.6 A spacing. The center of the Bragg peak is 0.67 eV in the neutron energy. The peak of the p-wave resonance of ^{139}La is 0.734 eV and the width is 40 meV, therefore, the Bragg peak is off the p-wave resonance at θ = 33.4°. At θ = 31.75°, the center of the Bragg peak is 0.74 eV, namely in the center of the p-wave resonance. We examined the helicity dependence of the Bragg peak. The preliminary result of the asymmetry in the Bragg peak was less than about 1% at the both scattering angles. The result suggests that the potential-resonance interference effect is small.

T-violation experiment

For the T-violation experiment, it is proposed to measure a triple correlation term, $\mathbf{I} \cdot \sigma_n \times k_n$ in the neutron transmission[8,9,10,11]. In the experiment, transmission of polarized neutrons through a polarized target is measured as it is schematically shown in Fig. 5.

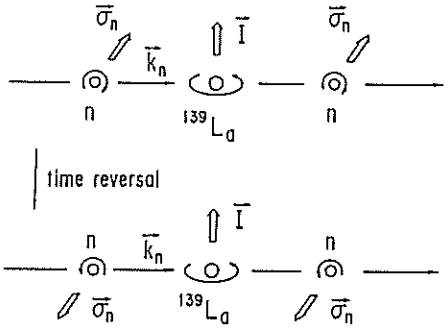

Fig. 5 T-violation test on the polarized neutron transmission through a polarized nuclear target.

The two processes in Fig. 5 transform to each other under time reversal and two rotations around the nuclear polarization axis and the beam axis. The second process is realized by inversion of the neutron

polarization in the first process. The T-odd asymmetry which is defined as,

$A_T = (T(+)-T(-))/(T(+)+T(-))$ (4),

is considered to be free from final state interactions, since initial and final states as well as motion directions are reversed in the two processes in Fig. 5. Here, T(+) and T(-) are neutron transmission for the first and second processes, respectively. The effect of final state interactions is a serious problem in the measurements of T-odd angular correlations in γ-decay and β-decay, since initial and final states can not be reversed in the decay processes.

For the T-violation experiment, we need a polarized nuclear target as well as the polarized neutron beam. We also used the dynamic nuclear polarization in order to polarize lanthanum nuclei. We replaced about 0.1% of lanthanum atoms in a LaF_3 single crystal with neodymium atoms. There are six magnetically inequivalent sites into which a paramagnetic ion may substitute. The microwave pumping was carried out at the frequency of 69.5 GHz, the magnetic field of 19.6 kG and the crystal temperature of 0.5 K. The microwave

frequency was shifted from the center of the paramagnetic resonance for one of the six sites. The shift in the frequency corresponds to the nuclear Zeeman energy. A typical result of a nuclear polarization build-up is shown in Fig. 6. In the figure, nuclear magnetic resonance (NMR) signal amplitude for fluorine nuclei is plotted against time in minute. The polarization of lanthanum nuclei can be estimated from the polarization of fluorine nuclei by means of the spin temperature theory. The precise value of the polarization was not obtained, since the NMR detector was not calibrated for the signal amplitude. The present polarization was around a few percent. However, the effect of the dynamic polarization is clear as shown in Fig. 6. The nuclear spin relaxation

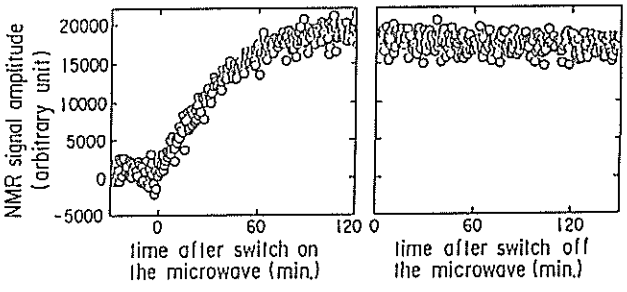

Fig. 6 Dynamic nuclear polarization of $La(Nd)F_3$.

time was more than several days, which was estimated by using the relaxation data after switching off the microwave power. We can improve the polarization by overlapping the g-factors for the six sites so that all the paramagnetic electrons contribute the dynamic polarization. It is possible by setting the crystal c axis to the direction of the magnetic field accurately, or by using some paramagnetic centers which show no anisotropy in the g-factor. We can also improve the nuclear polarization by making the nuclear relaxation time longer, if we use more strong magnetic field and a lower temperature cryostat.

Lanthanum nuclei in a $La_2Mg_3(NO_3)_{12}\cdot 24H_2O$ (LMN) crystal can be of course polarized[12]. However, other nuclei have the large neutron scattering cross section and the concentration of lanthanum nuclei is very small. In this point of view, LaF_3 is quite suitable for the transmission measurement, since the concentration of lanthanum nuclei is large and the neutron scattering cross section of the fluorine nucleus is very small. In fact, we observed clear parity violating transmission difference for this crystal. A typical example is shown in Fig. 7. The dip at E_n = 0.734 eV is due to the p-wave resonance of ^{139}La. Other small dips are due to the nuclear Bragg scattering.

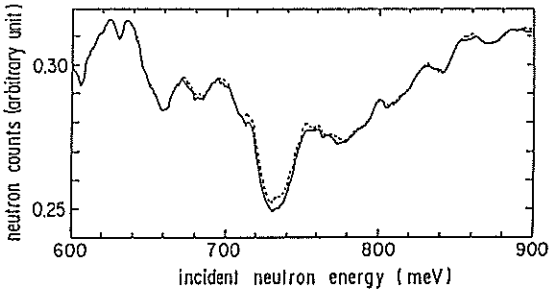

Fig. 7 P-violating transmission difference for a LaF_3 target. The solid and dotted lines are the results for positive and negative helicity states, respectively.

In the measurement of the T-violating transmission difference, we must control the neutron spin rotation. The neutron spin precesses around the magnetic field which is used for the polarization of the target nucleus spin. For example, the neutron spin precesses 60 turns during the passage through a 1-cm thick target in the magnetic field of 25 kG at E_n = 0.734 eV. The neutron spin also rotates around the nuclear polarization because of the spin dependent neutron-nucleus interaction[13]. This rotation is called pseudomagnetic rotation. This phenomena was observed by the Saclay group[14]. The pseudomagnetic rotation is obtained by the following equations,

$\omega = -\gamma_n H^*$ (5),

$$H^* = 4\pi N_0 \mu_N^* P \quad (6),$$

$$\mu_N^*/\mu_B = I/g_n \cdot ((b_+ - b_-)/(I+1/2))/r_0 \quad (7).$$

Here, γ_n is the gyromagnetic ratio of the neutron, N_0 the number of nuclei in the target, P the nuclear polarization, g_n the neutron magnetic moment expressed in nuclear magneton, r_0 the classical electron radius and μ_B the Bohr magneton. b_+ and b_- are neutron scattering amplitudes for parallel and antiparallel spin states between neutron and nuclear spins. The pseudomagnetic field H* corresponds to 25 kG for 100% polarized protons in the LMN crystal. It is possible to cancel out the two rotation in the target crystal, the Larmor precession and the pseudomagnetic rotation by adjusting the magnetic field strength. If we switch off the microwave power after the dynamic polarization, we can adjust the magnetic field strength without significant decrease in the nuclear polarization because of its long relaxation time.

In conclusion for the P-violation experiment, the present result of the angular dependence of the capture γ-ray asymmetry is consistent with that the capture γ-ray measurement is identical to the transmission measurement. The potential-resonance interference term is small. For the T-violation test, the dynamic polarization of ^{139}La is quite promising. The upper limit of the T-violating transmission asymmetry depends on the neutron counting statistics and the systematic error which comes from an uncertainty of the cancellation of the neutron spin rotation in the target. The upper limit was estimated to be less than 10^{-3}.

References

1. Y.Masuda et al., Nucl. Instr. Meth. A264 (1988) 169.
2. V.P.Alfimenkov et al., Nucl. Phys. A398 (1983) 93.
3. Y.Masuda ey al., Hyperfine Interactions 34 (1987)143, Y.M suda et al., Nucl.Phys. A 478 (1988) 737, Y.Masuda et al., Nucl.Phys. A504 (1989) 269.
4. S.A.Biryukov et al., Sov. J. Nucl.,Phys. 45 (1987) 937.
5. C.D.Bowman et al., Phys.Rev. C39 (1989) 1721.
6. J.R.Vanhoy et al., Z.Phys. A331 (1988) 1.
7. Y.Masuda, T.Adachi and H.M.Shimizu, to be published.
8. Y.Yamaguchi, J.Phys.Soc.Jpn. 57 (1988) 1518(L); ibid 1522(L); ibid 1525(L); ibid 2331; ibid 3339; ibid 3344.
9. V.E.Bunakov and V.P.Gudkov, Z.Phys. A308 (1982) 363.
10. P.K.Kabir, Phys.Rev. D25 (1982) 2013.
11. L.Stodorsky, Nucl.Phys. B197 (1982) 213, Phys.Lett. 172B (1986) 5.
12. A.Abragam and M.Chapellier, Phys.Lett. 11 (1964) 207.
13. A.Abragam and M.Goldman, "Nuclear magnetism: order and disorder" Clarendon Press, Oxford (1982).
14. H.Glattli et al., J. de Phys. 40 (1979) 629.

III. LIST OF PROPORSALS ACCEPTED

Proposals accepted (April 1989 -March 1990).

1989-A1-1 SAN-II Watanabe N KEK
Developement of Multi-Purpose Intense Small/Mediam-Angle Diffractometer (SAN-II)

1989-A2-1 UCN Yoshiki H KEK
Relevant Experiments to the Production and Storage of Urtracold Neutrons-Slow Neutron Transmission through Superfluid Liquid Helium

1989-B1-1 HIT Fukunaga T Nagoya Univ.
Structure Study of Liquids and Amorphous Solids

1989-B1-2 SAN Furusaka M KEK
Small-Angle Scattering Study of Macroscopic Structure in Condensed Matters and their Time Variations

1989-B1-3 TOP Endoh Y Tohoku Univ.
Search for Magnetic Disturbance with TOP Spectrometer

1989-B1-4 LAM Inoue K Hokkaido Univ.
Fluctuational and Low Energy Motions in Condensed Matters

1989-B1-5 PEN Masuda Y KEK
Polarized Neutron Experiment by Using Polarized Proton Filter

1989-B1-6 MAX Ikeda H Ochanomizu Univ.
Studies of Elementary Excitations by Multi-Analyzer Crystal Spectrometer

1989-B1-7 FOX Okamura F NIRIM
Study of Correlations between Atomic Fluctuations and Physical Properties in Solids

1989-B1-8 RAC Ikeda S KEK
High Energy and High Q Measurements with eV Neutron Scattering Spectrometer

1989-B1-9 HRP/MRP Asano H Univ. of Tsukuba
Crystal and Magnetic Structure Analysis by HRP and MRP

1989-B1-10 WIT Niimura N Tohoku Univ.
The Study of Semi-micro Structure of Condensed Matters Using Small-Angle Thermal Neutron Scattering Spectrometer (WIT)

1989-B1-11 INC Kohgi M Tohoku Univ.
Study of High Energy Excitations in Condensed Matter Using Chopper Spectrometer

1989-B2-1 HIT Ichikawa K Hokkaido Univ.
The Structure of Metal-Biologically Important Substances in Aqueous Solution by Using the Methods of Isotopic Substitution and Neutron Diffraction

1989-B2-2 HIT Suzuki K Tohoku Univ.
Atomic Structures in Amorphous Alloys of Immiscible Cu-Ta and Cu-V Systems Prepared by Mechanical Alloying

1989-B2-3 HIT Shibata K Tohoku Univ.
Static Structure of Superionic Conductor Glass

1989-B2-4 HIT Uemura O Yamagata Univ.
Neutron Diffraction of Inorganic Acid Aqueous Solutions and Liquid $TlAsSe_2$ Semiconductor

1989-B2-5 HIT Yasui I Univ. of Tokyo
Structural Investigation of Glasses with Heavy Metals Ion

1989-B2-6 HIT Umesaki N Osaka Univ.
Structural Analysis of Amorphous Bi-Sr-Ca-Cu-O Systems

1989-B2-7 HIT Kakinuma F Niigata Coll. of Pharmacy
Structural Analysis of Sb-Se Liquid

1989-B2-8 HIT Watanabe N KEK
Structural Investigation of Liquid Semiconductor Compounds

1989-B2-9 SAN Ichikawa K Hokkaido Univ.
Small-Angle Scattering from Carcogenite-Glass near Glass Transition

1989-B2-10 SAN Izumi Y Hokkaido Univ.
Gelation and Multi-Critical Phenomena at Low Temperature in Polymer Solutions

1989-B2-11 SAN Fukunaga T Nagoya Univ.
Chemical Frustration in Amorphous Ni-Zr-V_3 System

1989-B2-12 SAN Fujikawa S Tohoku Univ.
Study of Phase Decomposition in AlLi Alloy System by Small-Angle Neutron Scattering

1989-B2-13 SAN Yabuki S Gunma Univ.
Penetration of Water into Hydrophobic Interior Regions of Phosphatidylinositol Diphosphate (PIP_2)

1989-B2-14 SAN Okano K Univ. of Tokyo
Small-Angle Neutron Scattering from Poly (vinyl methyl ether) Solution in Alcohol/Water Solvent

1989-B2-15 SAN Ino H Univ. of Tokyo
Small-Angle Neutron Scattering Study of Cluster Formation in Rapidly-Quenched LaFe Alloy System

1989-B2-16 SAN Yoshizawa H Univ. of Tokyo
Small-Angle Neutron Scattering from Reentrant Spin Glass System $Pd_{1-x-y}Fe_xMn_y$

1989-B2-17 SAN Ochiai S Kyoto Univ.
Study of Relation between Structure of Precipitations and Flux-Line Lattice

1989-B2-18 SAN Kanaya T Kyoto Univ.
Structure of Poly (vinyl alcohol) Gels

1989-B2-19 SAN Sano H Study of Reconstitution of Tobacco Mosaic Virus

1989-B2-20 TOP Yoshiki H KEK
Reflection of Slow Neutrons on the Surface of Superconductors

1989-B2-21 TOP Shinjo T Kyoto Univ.
Magnetism of the Artificial Rare-Earth/Fe Superlattice

1989-B2-22 Nakamura Y Hokkaido Univ.
Molecular Motion of Water Molecules in Hydrate Melts

1989-B2-23 LAM Izumi Y Hokkaido Univ.
Frozen Mechanism of the Local Motion of the Gelation in Polymer Solutions

1989-B2-24 LAM Yagi T Hokkaido Univ.
Inelastic Neutron Scattering of KDP under a Uniaxial Stress

1989-B2-25 Suzuki K Tohoku Univ.
Study of Dynamic Structure on Metal Nitrates Glass $0.62KNO_3$-$0.38Ca(NO_3)_2$ near the Glass Transition

1989-B2-26 LAM Kaji K Kyoto Univ.
Dynamic Structure in Poly (vinyl alcohol) gels

1989-B2-27 LAM Ikeda S KEK
Copper Vibrators in CuO and $YBa_2Cu_3O_7$

1989-B2-28 LAM Yamaguchi T Fukuoka Univ.
Dynamics of Liquid Water in Porous Silica

1989-B2-29 PEN Morimoto K KEK
T-Violation Experiment on Neutron-Induced Reaction

1989-B2-30 FOX Ohshima K Univ. of Tsukuba
Study of Microscopic Structure in Rare-Earth Metallic Alloys with Spin-Glass Nature

1989-B2-31 FOX Era H NIRIM
Development of Light-Atom Solid Detector

1989-B2-32 RAT Suzuki K Tohoku Univ.
Hydrogen Motion in Amorphous YFe_z

1989-B2-33 HRP/MRP Kamigaki T Tohoku Univ.
Development of High-Pressure Cell and Measurement of High-pressure Phase of D_2O

1989-B2-34 HRP/MRP Fukunaga T Nagoya Univ.
Application of Radial Distribution Function Method to the Structure Analysis of Al-V and Al-Cu Quasicrystals

1989-B2-35 HRP/MRP Takita K Univ. of Tsukuba
Relation between Hole-Concentration and the Crystal Structure in the Solid-Solution System of Oxide Superconductors

1989-B2-36 HRP/MRP Uchinokura K Univ. of Tokyo
Correlation between Oxygen Arrangements and the Electronic Structure in Cu-Oxide Superconductors

1989-B2-37 HRP/MRP Kosuge K Kyoto Univ.
Cation Distribution in the $(Y_{1-x}Ca_x)$ $(Ba_{1-y}La_y)$ CuO_z System

1989-B2-38 HRP/MRP Shiozaki T Kyoto Univ.
Oxygen Location in dielectric Oxides

1989-B2-39 HRP/MRP Akimitsu J Aoyama Gakuin Univ.
Structure Analysis of New Oxide Superconductors

1989-B2-40 HRP/MRP Akiba E NCLI
Structure Analysis of Metal Hydrides and High-Tc Superconductors

1989-B2-41 INC Yamada K Tohoku Univ.
Magnetic Excitations in Two-Dimensional Antiferromagnets with Quantum Spins

1989-B2-42 LAM Tomiyoshi S Tohku Univ.
Motion of Hydrogen Atoms in Superconducting $YBa_2Cu_3O_7$

1989-B2-43 LAM Arai M KEK
Low-Energy Magnetic Excitations in Reentrant Spin Glass System FeAl

1989-B2-44 LAM Arai M KEK
Low-Energy Excitations in Glasses

1989-Urg-1 HRP/MRP Hashizume H Tokyo Inst. Tech.
High-Temperature Structure Analysis of Nonstoichiometric Oxide $BaBiO_{3-x}$

Proposals accepted (April 1990 -March 1991).

1990-A1-1 SAN-II Watanabe N KEK
Developement of Multi-Purpose Intense Small/Mediam-Angle Diffractometer (SAN-II)

1990-A2-1 UCN Yoshiki H KEK
Relevant Experiments to the Production and Storage of Urtracold Neutrons-Slow Neutron Transmission through Superfluid Liquid Helium

1990-B1-1 HIT Fukunaga T Nagoya Univ.
Structure Study of Liquids and Amorphous Solids

1990-B1-2 SAN Furusaka M KEK
Small-Angle Scattering Study of Macroscopic Structure in Condensed Matters and their Time Variations

1990-B1-3 TOP Endoh Y Tohoku Univ.
Search for Magnetic Disturbance with TOP Spectrometer

1990-B1-4 LAM Izumi Y Yamagata Univ.
Fluctuational and Low Energy Motions in Condensed Matters

1990-B1-5 PEN Masuda Y KEK
Polarized Neutron Experiment by Using Polarized Proton Filter

1990-B1-6 MAX Ikeda H KEK
Studies of Elementary Excitations by Multi-Analyzer Crystal Spectrometer

1990-B1-7 FOX Okamura F NIRIM
Study of Correlations between Atomic Fluctuations and Physical Properties in Solids

1990-B1-8 MRP Nojiri H Kobe Univ.
Neutron Diffraction Study Using Repeating Pulsed Magnetic Fields

1990-B1-9 HRP Asano H Univ. of Tsukuba
Structural Study by HRP

1990-B1-10 WIT Niimura N Tohoku Univ.
The Study of Semi-micro Structure of Condensed Matters Using Small-Angle Thermal Neutron Scattering Spectrometer (WIT)

1990-B1-11 INC Kohgi M Tohoku Univ.
Study of High Energy Excitations in Condensed Matter Using Chopper Spectrometer

1990-B1-12 RAC Ikeda S KEK
High Energy and High Q Measurements with eV Neutron Scattering Spectrometer

1990-B2-1 HIT Yasui I Univ. of Tokyo
Structural Investigation of Glasses with Heavy Metals Ion

1990-B2-2 HIT Kinugawa K GIRI, Osaka
Structural Investigation of Metal halide Glasses

1990-B2-3 HIT Mizutani U Nagoya Univ.
Amorphous Structure of YBa_2Cu_3 Alloy for Preparation of a Y-Ba-Cu-O Superconductor

1990-B2-4 HIT Suzuki K Tohoku Univ.
Structural Relaxation of Amorphous $La_{55}Al_{25}Ni_{20}$ Alloy

1990-B2-5 HIT Uemura O Yamagata Univ.
Neutron Diffraction of Liquid $Tl_x(As_2X_3)_{1-x}$(X=Se,Te) semiconductors

1990-B2-6 HIT Kakinuma F Niigata Coll. of Pharmacy
Structural Analysis of Bi-Se Liquids

1990-B2-7 HIT Suzuki K Tohoku Univ.
Amorphization of Ta-Al system by Mechanical Alloying

1990-B2-8 HIT Kita Y Osaka Univ.
Atomic Structures of Glass and Liquid of B_2O_3 System

1990-B2-9 HIT Kanaya T Kyoto Univ.
Structure of Crosslinking Points in Poly (vinyl Alcohol) Gel

1990-B2-10 HIT Umesaki N Osaka Univ.
Structural Investigation of Inorganic Glasses

1990-B2-11 SAN Sato H Keio Univ.
Magnetization Process in Reentrant Spin Glass $Ni_{77}Mn_{23}$

1990-B2-12 SAN Noda I Nagoya Univ.
Configuration of Polymer Molecules under shear Flow

1990-B2-13 SAN Kanaya T Kyoto Univ.
Gelation Processes of PVA

1990-B2-14 SAN Ochiai S Kyoto Univ.
Study of Relation between Structure of Precipitations and Flux-Line Lattice

1990-B2-15 SAN Izumi Y Yamagata Univ.
Sol-Gel-Glass Transition in Polymer-Solvent System

1990-B2-16 SAN Okabayashi H Nagoya Inst. Tech.
Study of Detergent Molecules Which Nave Asymmetric Molecular Structure in Water Solution

1990-B2-17 SAN Sano H National Food Research Institute
Study of Reconstitution of Tobacco Mosaic Virus

1990-B2-18 SAN Okano K Univ. of Tokyo
Small-Angle Neutron Scattering from Poly (vinyl methyl ether) Solution in Alcohol/Water Solution

1990-B2-19 SAN Yabuki S Gunnma Univ.
Penetration of Water into Hydrophobic Interior Regions of Phosphatidylinositol Diphosphate (PIP_2)

1990-B2-20 SAN Suzuki K Tohoku Univ.
Formation Process of Ceramics by Thermal Decomposition from Organic Metallic Compounds

1990-B2-21 TOP Yoshiki H KEK
Reflection of Slow Neutrons on the Superconducting Surface

1990-B2-22 TOP Shinjo T Kyoto Univ.
Magnetic Structure Study of Magnetic Metal Superlattices

1990-B2-23 LAM Kohgi M Tohoku Univ.
Spin Fluctuations in Systems with Competing Kondo Effect and KKY Interaction

1990-B2-24 LAM Sakuma T Ibaraki Univ.
Dynamics on the Diffusion of Proton in $Sr(Zr,Y)O_3$

1990-B2-25 LAM Yamaguchi T Fukuoka Univ.
Dynamics of Electrolyte Solutions in Undercooled and Glassy States

1990-B2-26 LAM Nakamura Y Hokkaido Univ.
Molecular Motion of Water Molecules in Hydrate Melts

1990-B2-27 LAM Kaji K Kyoto Univ.
Local Modes in PVA Gels

1990-B2-28 LAM Kobayashi M Osaka Univ.
Low-Frequency Phonon Excitation of Stearic Acid Single Crystal

1990-B2-29 LAM Suzuki K Tohoku Univ.
Dynamic Structure of Molten Metal Nitrates and It's Behavior near the Glass Transition

1990-B2-30 LAM Sakuma T Ibaraki Univ.
Low Energy Excitation in Superionic Conductors

1990-B2-31 LAM Inaba A Osaka Univ.
Rotational Tunneling of Methyl Group and Phonon Density of States in the Monolayer Film of Methyl Fluoride Absorbed on Graphite

1990-B2-32 PEN Morimoto K KEK
T-Violation Experiment on Neutron-Induced Reaction

1990-B2-33 MAX Masuyama H Yamaguchi Univ.
Phase Transition and Phonon Modes in A_2BX_4-type Incommensurate Ferroelectric Compound

1990-B2-34 MAX Takano M Kyoto Univ.
Neutron Inelastic Scattering from One-Dimensional Magnet $CsCuCl_3$ with Incommensurate Magnetic Structure

1990-B2-35 FOX Era H NIRIM
Development of Light-Atom Solid Detector

1990-B2-36 FOX Ohshima K Univ. of Tsukuba
Study of Microscopic Structure in Rare-Earth Metallic Alloys with Spin-Glass Nature

1990-B2-37 MRP Kamigaki T Toyama Univ.
Development of High-Pressure Equipment and Study of High-Pressure Phase of D_2O

1990-B2-38 MRP Kamigaki T Toyama Univ.
Neutron Diffraction Study of Amorphous High Density Phase of D_2O

1990-B2-39 MRP Akiba E NCLI
Structural Studies of Metal Hydrides and High-Tc Superconductors

1990-B2-40 MRP Uchinokura K Univ. of Tokyo
Relation between Superconducting Properties and the Structure, Especially Cu-O Bond Lengths, in High-Tc Superconductors

1990-B2-41 HRP Shibata K Tohoku Univ.
High-Resolution Powder Diffractometry on the Lattice Strain in Hydrogen-Absorbed Metals

1990-B2-42 HRP Kanno R Kobe Univ.
Mechanism of Ionic Conduction and Phase Transformation in Ionic Conductors

1990-B2-43 HRP Suga H Osaka Univ.
Phase Transition and Deuterium Location in CD_3ND_3Cl

1990-B2-44 HRP Takita K Univ. of Tsukuba
Intercorrelation among Cu-O Bond Length, Hole Concentration and Superconducting Properties in the Solid-Solution System of Oxide Superconductors

1990-B2-45 HRP Kosuge K Kyoto Univ.
Structure Analysis of Metallic Oxide $La_4BaCu_5O_y$

1990-B2-46 HRP Shiozaki T Kyoto Univ.
Oxygen Location in Dielectric Oxides

1990-B2-47 HRP Inaba A Osaka Univ.
Polymorps and Anomalous Isotope Effect in $C_6(CD_3)_6$

1990-B2-48 HRP Akimitsu J Aoyama Gakuin Univ.
Structure Analysis of High-Tc Superconductors

1990-B2-49 INC Sawada T Univ. of Tokyo
Analysis of Hydroxyl Radicals on the Surface of Silicon Fine Particles

1990-B2-50 INC Shibata K Tohoku Univ.
Atomic Structures in Metal-Metalloid Amorphous Alloys

1990-B2-51 INC Kasaya M Tohoku Univ.
Crystal Field Excitations in Dense Kondo Systems

1990-B2-52 INC Fukunaga T Nagoya Univ.
Inelastic Scattering from Ni-V and Cu-V Amorphous Alloys

1990-B2-53 INC Kanaya T Kyoto Univ.
High Energy Excitations in Polyvinylalcohol

1990-B2-54 INC Suzuki T Tohoku Univ.
Study of Kondo Systems and Rare-Earth Pnictides with Small Carriers

1990-B2-55 LAM Takeda S Osaka Univ.
An investigation of Tunneling Splitting of Hydrogen Chloride Molecule in Hydroquinone Clathrate Compounds

1990-B2-56 LAM Takeda S Osaka Univ.
Correlated Tunneling on Six Methyl Groups of Hexamethylbenzene Molecule Diluted in the Crystalline Lattice of Hexahalogenobenzenes

1990-B2-57 TOP Kanaya T Kyoto Univ.
Studies of LB Films by Means of Neutron Reflectometry

1990-B2-58 SAN Ino H Univ. of Tokyo
Magnetic Structure in Amorphous Fe-Nd Alloy

1990-B2-59 LAM Watanabe N KEK
Test Experiment on Tunneling Spectroscopy

1990-B2-61 HIT Ichikawa K Hokkaido Univ.
Structural Determination of Biological Molecules and Metal Ions in Hydrated Water by Neutron Contrast-Variation Method

1990-B2-62 HIT Ichikawa K Hokkaido Univ.
Folding of Biological Materials Caused by the Capture of Metal Ions

1990-Urg-1 HIT Endoh H Kyoto Univ.
Structure of Liquid Halide Se

1990-Urg-2 LAM Yagi T Hokkaido Univ.
Inelastic Neutron Scattering of KDP under a Uniaxial Stress

1990-Urg-3 LAM Ito Y Univ. of Tokyo
Inelastic Neutron Scattering Study of Hexokwise Dynamics

1990-Urg-4 LAM Kataoka M Tohoku Univ.
Quasielastic Neutron Scattering Study of Dynamics of Protein under Folding Process

1990-Urg-5 HRP Suematsu H Univ. of Tokyo
Magnetic Phase Transitions in O_2 Monolayer

IV. SCIENTIFIC REPORTS

1. Neutron Scattering

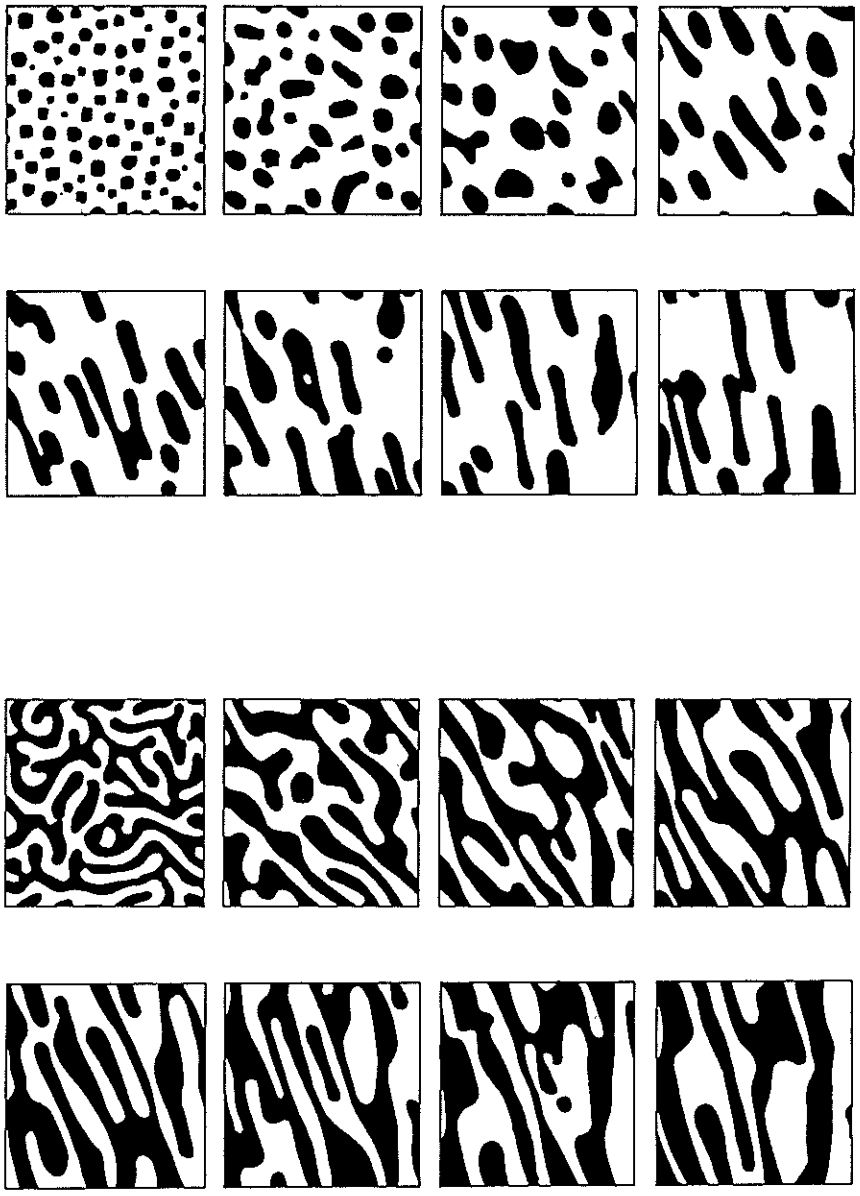

Computer simulation of phase separation process of binary mixture of polymers under shear flow (by T. Ohta)

1-1. Crystal Structures

Neutron Powder Diffraction Study of $Tl_2Ba_2CuO_{6+\delta}$

Y. SHIMAKAWA, Y. KUBO, T. MANAKO, H. IGARASHI,
F. IZUMI* and H. ASANO**

Fundamental Research Laboratories, NEC Corporation, Kawasaki 213
*National Institute for Research in Inorganic Materials, Tsukuba 305
**Institute of Materials Science, University of Tsukuba, Tsukuba 305

A Tl-containing oxide with the ideal composition of $Tl_2Ba_2CuO_6$ (Tl-2201) is one of the most tempting materials in oxide superconductors, because it shows wide T_c variation from 0 K to over 85 K without significant changes in the crystal structure[1]. In the present study[2], the crystal structures of Tl-2201 with four different T_c's were refined by Rietveld analysis of TOF neutron powder diffraction data.

Tl-2201 samples with apparent tetragonal symmetry were prepared by solid-state reactions of thoroughly mixed appropriate amounts of Tl_2O_3, BaO and CuO powders. Judging from neutron and x-ray diffraction measurements, a single-phase tetragonal sample was obtained only for a starting composition close to Tl:Ba:Cu=2:2:1.1. The neutron diffraction data were analyzed using a Rietveld refinement program RIETAN[3].

Four samples used for the neutron and x-ray diffraction measurements had different T_c's of (A) 0 K, (B) 48 K, (C) 58 K and (D) 73 K. All the samples gave diffraction patterns containing only Tl-2201 peaks in both the neutron and x-ray diffraction measurements.

The crystal structures of the four samples were analyzed based on the tetragonal space group of I4/mmm (No. 139). The neutron diffraction data were analyzed by fixing the composition at $(Tl_{0.95}Cu_{0.05})_2Ba_2CuO_y$, which was consistent with the starting composition except for the content of the evaporatable element Tl. Preliminary refinements assigned isotropic thermal parameters, B, for all the sites. A resulting large isotropic thermal parameter for O(3), which was first located at an ideal 4e position, was suggestive of static displacements of this oxygen atom. Thus the O(3) atom was split into four pieces by assigning a 16n site deviating slightly from the ideal site. Moreover, as shown in Fig. 1, the partial occupation of an interstitial O(4) site between double TlO layers was detected by neutron diffraction. The O(4) atom was then assigned at an 8g site (1, 1/2, z) close to a 4d site (0, 1/2, 1/4), and its isotropic thermal parameter was fixed at 1.0.

The final R_{wp} values for the four samples are (A) 4.23%, (B), 3.97%, (C) 4.21% and (D) 4.10%. Typical Rietveld refinement patterns are shown in Fig. 2. Important crystal data for the four samples, including lattice parameters, site occupancies and interatomic distances, are listed in Table 1.

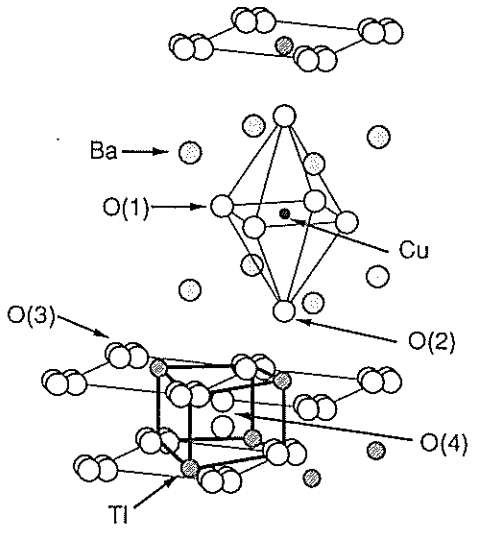

Fig. 1 Crystal structure of Tl-2201. The O(3) atom is split into four pieces by assigning a 16n site deviating slightly from the ideal site. The O(4) atom is located at the interstitial site between double TlO layers. Each O(4) atom is coordinated to four Tl atoms, and is split into two pieces by assigning an 8g site.

A systematic change in the occupancy of the O(4) site is worth noting. As the T_c value increases, the occupancy of the O(4) site decreases monotonously. In contrast, the occupancies of the O(3) site are very close to 0.25 irrespective of their T_c values. Thus, the O(3) site on the rock-salt type TlO layer is almost fully occupied, and the oxygen content in Tl-2201 is controlled by the reversible occupation of the interstitial O(4) site. The difference in oxygen content between the samples with T_c's of 0 K (A) and 73 K (D) is -0.084 per formula unit. This value agrees well with an experimental value of about -0.08 obtained by a

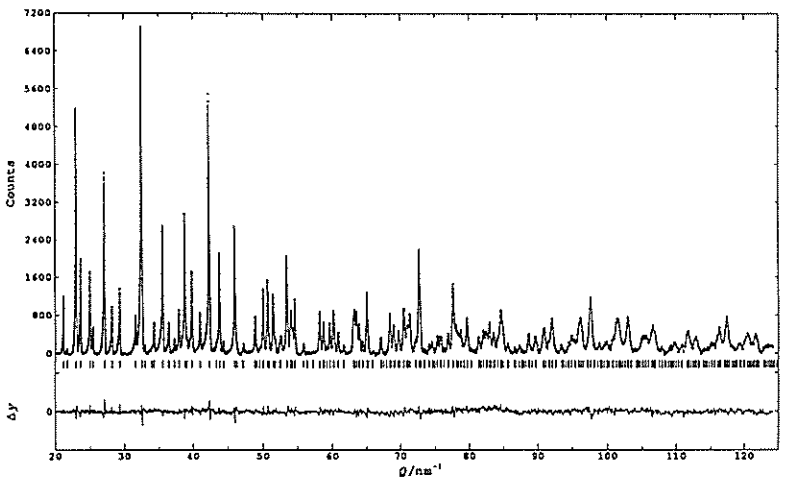

Fig. 2 Rietveld refinement patterns for Tl-2201 with T_c of 48 K (sample B) plotted against Q ($= 2\pi/d$). The background is subtracted. Plus marks are observed neutron diffraction intensities, and solid lines calculated intensities. Tick marks below the profile indicate the positions of the 484 allowed reflections. The curve in the bottom is the difference between the observed and calculated intensities in the same scale.

Table 1
Lattice parameters (Å), occupation factors, oxygen content and metal-oxygen interatomic distances (Å) in the four samples of Tl-2201.

	Samples				
	A (0 K)	B (48 K)	C (58 K)	D (73 K)	(D-A)/A×100
a	3.86298(7)	3.86276(6)	3.86273(6)	3.86248(6)	−0.013
c	23.1369(5)	23.1848(4)	23.1995(4)	23.2248(4)	0.380
g(O(3))	0.246(3)	0.250(3)	0.247(4)	0.247(2)	
g(O(4))	0.028(3)	0.020(3)	0.017(4)	0.005(2)	
$6+\delta$	6.080	6.080	6.044	5.996	(−0.084)[a]
Cu-O(1) (×4)	1.93149(4)	1.93138(3)	1.93137(3)	1.93124(3)	−0.025
O(2) (×2)	2.703(3)	2.713(3)	2.716(3)	2.721(2)	0.666
Ba-O(1) (×4)	2.743(2)	2.733(2)	2.733(2)	2.729(1)	−0.510
O(2) (×4)	2.8341(8)	2.8404(8)	2.8411(10)	2.8441(6)	0.353
O(3) (×1/4×4)[b]	2.929(5)	2.968(5)	2.972(6)	2.987(3)	1.980
Tl-O(2)	1.985(3)	1.985(3)	1.983(4)	1.984(2)	−0.050
O(3) (×1/4×8)[b]	2.490(10)	2.504(7)	2.501(6)	2.526(4)	1.446
O(3) (×1/4×8)[b]	3.009(11)	2.994(8)	2.997(7)	2.968(5)	−1.363
O(3) (×1/4×4)[b]	2.061(5)	2.044(5)	2.047(5)	2.034(3)	−1.310

[a]The difference in oxygen content between samples A and D.

[b]The O(3) atom is split into four pieces.

weight change measurement. Since sample D (T_c=73 K) scarcely has excess oxygen at the O(4) site, the highest T_c value of about 85 K must be achieved in the sample with no interstitial oxygen atoms.

We can not find any structural discontinuity in the change from a normal metal (non-superconductor) to a superconductor. As the T_c value increases, i.e., the oxygen content decreases, the a value only slightly decreases, whereas the c value considerably increases by 0.38% between samples A and D. Corresponding changes in interatomic distances along the [001] direction are specially noted. The distance between Cu and apical O(2) increases by 0.67%, which is as twice as an increase in c. In contrast, the Ba atom approaches the CuO_2 layer by as much as 1.06%, which makes the BaO layer much rougher. These structural changes are quite reasonable because the release of oxygen atoms decreases the hole carriers (positive charge) in the CuO_2 layer. Consequently, negatively charged apical O^{2-} ions are repulsed and go away from the CuO_2 layer, while positively charged Ba^{2+} ions are attracted and approach it.

Finally, we will discuss the origin of hole doping in this compound. The Tl-2201 compound should contain no carrier if it has the stoichiometric composition of $Tl_2Ba_2CuO_6$. However, substitution of Cu^+ and/or Cu^{2+} ions for Tl^{3+} ions plus incorporation of O(4) atoms must produce hole carriers. Substitution of about 5% of the Tl-site with Cu was confirmed by Rietveld analysis of x-ray diffraction data. Though it still remains open whether mixed-valency state of Tl^{3+} and Tl^+ occurs in this compound, the present study clearly reveals that a significant portion of the hole carriers in Tl-2201 is attributed to the substitution of Cu for Tl and the uptake of excess oxygen at the interstitial site between the double TlO layers.

References

1) Y. Shimakawa *et al.*, Phys. Rev. B40, 11400 (1989).
2) Y. Shimakawa *et al.*, submitted to Phys. Rev. B.
3) F. Izumi *et al.*, J. Appl. Crystallogr. 20, 411 (1987).

Structural Changes Accompanying Sr Doping in $Ba_2YCu_4O_8$

F. IZUMI[1], T. WADA[2], N. SUZUKI[2], Y. YAEGASHI[2], H. YAMAUCHI[2], H. ASANO[3], and S. TANAKA[2]

[1] National Institute for Research in Inorganic Materials, 1-1 Namiki, Tsukuba, Ibaraki 305
[2] Superconductivity Research Laboratory, ISTEC, 1-10-13 Shinonome, Koto-ku, Tokyo 135
[3] Institute of Materials Science, University of Tsukuba, Tennodai, Tsukuba, Ibaraki 305

$Ba_2YCu_4O_8$ is a high-T_c superconductor with a pressure coefficient, dT_c/dP, as high as 5.5 K/GPa.[1)] Its crystal structure under high pressure has been analyzed with angle-dispersive and TOF neutron powder diffraction data to understand the mechanism of the pressure-induced rise in T_c.[2,3)] Wada *et al.*[4)] have recently reported that the T_c of the solid solution $(Ba_{1-x}Sr_x)_2YCu_4O_8$ $(0 \le x \le 0.4)$ remains virtually constant ($T_c \approx 75$ K) regardless of its Sr content. This finding is of considerable interest because substitution of smaller Sr^{2+} ions for larger Ba^{2+} ions makes it possible to apply 'chemical pressure' to this superconductor.

We investigated the crystal structure of $(Ba_{0.7}Sr_{0.3})_2YCu_4O_8$ (BSYCO) with HRP to clarify the reason for the invariance of T_c in the $(Ba_{1-x}Sr_x)_2YCu_4O_8$ system. A sample of BSYCO was prepared by an O_2-HIP technique according to a procedure described previously[4)]. Because the sample contained a small amount of CuO, the structure parameters of BSYCO were refined with the multi-phase capability of RIETAN.

Table 1 lists the crystal data of BSYCO. $Ba_2YCu_4O_8$ has lattice constants $a_0 = 0.38454$ nm, $b_0 = 0.3876$ nm, and $c_0 = 2.7263$ nm.[5)] Then, linear compression ratios are $\Delta a/a_0 = -0.0079$, $\Delta b/b_0 = -0.0037$, and $\Delta c/c_0 = -0.0064$, which indicate the high rigidity of double chains of edge-sharing $[CuO_4]$ squares parallel to the [010] direction. All Cu–O bonds in BSYCO are shorter than corresponding ones in $Ba_2YCu_4O_8$[5)] (Table 2).

The Madelung energies, E_M, of BSYCO and $Ba_2YCu_4O_8$ were calculated to estimate the distribution of $(Cu–O)^+$ holes between CuO_2 sheets and double chains of $[CuO_4]$ squares. The valences of Ba, Y, and O were fixed at +2, +3, and –2, respectively. A simple constraint was imposed on the positive charges, p, of Cu(1) and Cu(2): $p(Cu(1)) + p(Cu(2)) = +4.5$. The lowest E_M value in BSYCO was obtained at $p(Cu(2)) = +2.24$ ($E_M = -48.107$ eV), which is very close to +2.26 ($E_M = -47.878$ eV) in $Ba_2YCu_4O_8$. Thus, the concentration of hole carriers on the CuO_2 sheet does not differ appreciably between these two, with a result that they have comparable T_c.

Table 1. Results of the Rietveld refinement for BSYCO. $R_{wp} = 4.3\%$ ($R_e = 3.0\%$), $R_p = 3.3\%$, $R_B = 3.0\%$, and $R_F = 1.6\%$.

Space group: Ammm (No. 65). $Z = 2$. $a = 0.381491(9)$ nm, $b = 0.38617(1)$ nm, and $c = 2.70875(8)$ nm.

Atom	Site	x	y	z	B_{eq}/nm^2
Ba	4j	1/2	0	0.3657(1)	0.0068
Y	2c	1/2	1/2	0	0.0050
Cu(1)	4i	0	0	0.2126(1)	0.0069
Cu(2)	4i	0	0	0.0616(1)	0.0039
O(1)	4i	0	0	0.1448(1)	0.0090
O(2)	4j	1/2	0	0.0535(1)	0.0041
O(3)	4i	0	0	0.4474(1)	0.0068
O(4)	4i	0	0	0.2817(1)	0.0128

Table 2. Cu–O bond lengths (nm) in $(Ba_{1-x}Sr_x)_2YCu_4O_8$

Bond	BSYCO	$Ba_2YCu_4O_8$
Cu(1)–O(1) (×1)	0.1836(4)	0.1841(1)
Cu(1)–O(4) (×1)	0.1873(5)	0.1881(2)
Cu(1)–O(4) (×2)	0.19371(4)	0.19430(1)
Cu(2)–O(1) (×1)	0.2253(4)	0.2288(1)
Cu(2)–O(2) (×2)	0.19202(5)	0.19392(2)
Cu(2)–O(3) (×2)	0.19462(6)	0.19543(2)

References

1) Y. Yamada *et al.*, *Jpn. J. Appl. Phys.* **29**, L250 (1990).
2) E. Kaldis *et al.*, *Physica C* **159**, 668 (1989).
3) Y. Yamada *et al.*, in preparation.
4) T. Wada *et al.*, *Phys. Rev. B* **41**, 11209 (1990).
5) P. Bordet *et al.*, *Physica C* **162–164**, 524 (1989).

The crystal structure of a new superconductor in the Nd-Ce-Sr-Cu-O system

H.SAWA, J.AKIMITSU, H.ASANO*,E.TAKAYAMA-MUROMACHI† and F.IZUMI†

Department of Physics, Aoyama-Gakuin University, 6-16-1, Chitosedai, Setagaya-ku, Tokyo 157.
*Institute of Materials Science, University of Tsukuba, Tennodai, Tsukuba-shi, Ibaraki 305.
†National Institute for Research in Inorganic Materials, 1-1 Namiki, Tsukuba-shi, Ibaraki 305.

The Nd-Ce-Sr-Cu-O system with an onset transition temperature of 28K was found[1]. The structure comprises of alternating slabs K_2NiF_4- and Nd_2CuO_4-type structures, and that there is only one Cu site in pyramidal coordination of oxygen[2]. This compound is the first case of the copper-based superconductor in which Cu ions take an only pyramidal five fold coordination.

A sample with the composition of $(Nd_{1-x-y}Sr_xCe_y)_2CuO_{4-z}$ was prepared, of which details were already published elsewhere[1].

Based on X-ray and electron diffraction experimental results, the new model consisting of stacking units K_2NiF_4- and Nd_2CuO_4-type structures was proposed[3]. We have finally determined the crystal structure of $(Nd_{1-x-y}Sr_xCe_y)_2CuO_{4-z}$ by using the TOF neutron powder diffraction technique.

A sample with the composition $(Nd_{0.66}Sr_{0.205}Ce_{0.135})_2CuO_{4-z}$ was given to be single phase. The sample used in the structure analysis experiment showed an onset of superconductivity at 22K in magnetization measurement. The Meissner signal reached about 12% at 8K.

Neutron diffraction data were taken on a high-resolution TOF neutron powder diffractometer, HRP, at the KENS pulsed spallation neutron source at the National Laboratory for High Energy Physics.

Structure parameters were refined with a RIETAN program[4] for the Rietveld analysis of TOF neutron powder diffraction data. The details of structure parameters were already published elsewhere[5]. Lattice parameters were refined to be a=3.8564(3)Å and c=12.4846(9)Å. R factors were R_{wp}=5.6%, R_P=4.3%, R_I=3.3%, R_F=2.6% and R_e=4.8%. Figure 1 illustrates final profile fit and difference patterns. The good fit between the observed and calculated patterns strongly supports the present structural model.

Figure 2 shows the crystal structure model of $(Nd_{1-x-y}Sr_xCe_y)_2CuO_{4-z}$. The unit cell consists of two parts: the upper part in Figure 2 is of the K_2NiF_4- type where the (Nd,Sr) ion is coordinated to 9 oxide ions, while the lower part is of the Nd_2CuO_4 type including (Nd,Ce) ion in 8-coordination. There is only one crystallographic site with pyramidal coordination for the Cu ion. This system has the simplest structure of superconductors that are composed of $[CuO_5]$ pyramids ever found. This material must be one of the best candidates for studying the origin of high-T_C superconductivity.

References

1) J. Akimitsu, S. Suzuki, M. Watanabe and H. Sawa: Jpn. J. Appl. Phys. 27(1988)L1859.
2) H. Sawa, S. Suzuki, M. Watanabe, J. Akimitsu, H. Matsubara, H. Watabe, S. Uchida, K. Kokusho, H. Asano, F. Izumi and E. Takayama-Muromachi: Nature 337(1989)347.
3) E. Takayama-Muromachi, Y. Matsui, Y. Uchida, F. Izumi, M. Onoda and K. Kato: Jpn. J. Appl. Phys. 27(1988)L2283.
4) F. Izumi: J. Crystallogr. Soc. Jpn. 27(1985)23.
5) F. Izumi, E. Takayama-Muromachi, A. Fujimori, T. Kamiyama, H. Asano, J. Akimitsu and H. Sawa : Physica C 158(1989)440.

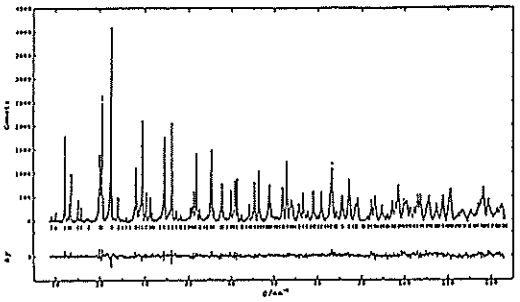

Fig. 1. Rietveld refinement pattern of $(Nd_{1-x-y}Sr_xCe_y)_2CuO_{4-z}$.

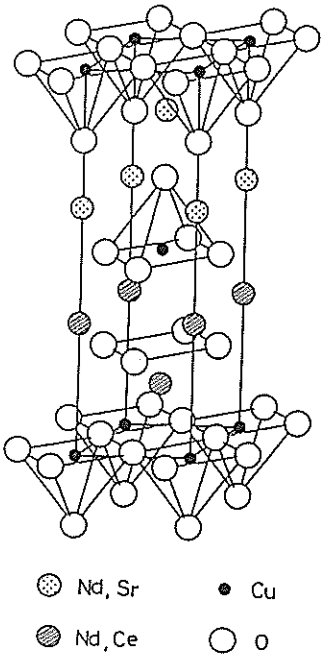

Fig. 2. Crystal structure of $(Nd_{1-x-y}Sr_x\ Ce_y)_2CuO_{4-z}$.

Effect of Annealing under High Oxygen Pressure on the Structure and Superconductivity of $(Ba_{0.85}Nd_{0.15})_2NdCu_3O_{6+z}$

T. MOCHIKU, H. ASANO, H. AKINAGA, T. OHSHIMA, K. TAKITA, F. IZUMI[a], Y. TAKEDA[b], M. TAKANO[c] and K. MIZOGUCHI[d]

Institute of Materials Science, University of Tsukuba, Tsukuba, Ibaraki 305, Japan
[a]National Institute for Research in Inorganic Materials, 1-1 Namiki, Tsukuba, Ibaraki 305, Japan
[b]Faculty of Engineering, Mie University, Tsu, Mie 514, Japan
[c]Institute for Chemical Research, Kyoto University, Uji, Kyoto 611, Japan
[d]Department of Physics, Tokyo Metropolitan University, Setagaya-ku, Tokyo 158, Japan

We have recently investigated the effect of annealing under a high oxygen pressure on the superconducting properties of $(Ba_{1-x}Nd_x)_2NdCu_3O_{6+z}$ (BNCO) within the x range of 0 to 0.25. Its T_c was considerably raised by annealing. The present work was undertaken to study the influence of annealing under a high oxygen pressure on the crystal structures of BNCO by neutron powder diffraction [1]. Two samples with x=0.15 were used: one was as-grown, and the other was annealed exhaustively.

The as-grown sample (A-BNCO) was prepared by the solid-state reaction of appropriate amounts of $BaCO_3$, Nd_2O_3 and CuO in air. An oxidized sample (O-BNCO) was obtained by annealing A-BNCO in a test-tube type pressure vessel under an oxygen pressure of 100 MPa at 350°C for 48 h. Resistivity measurements showed that the T_c (midpoint) of A-BNCO was 33.0 K and that of O-BNCO was 54.1 K. The Meissner signal reached about 19% of the total volume for A-BNCO and 36% for O-BNCO at 4.2 K, confirming the bulk nature of the superconductivity. Neutron powder diffraction data of BNCO were taken on a high-resolution time-of-flight neutron powder diffractometer, HRP, at the KENS.

The structural parameters of A- and O-BNCO were refined by the Rietveld method with RIETAN on the basis of the structure model (space group: P4/mmm) of $(Ba_{0.9}Nd_{0.1})_2NdCu_3O_{6+z}$ reported previously [2]. Preliminary refinements revealed that isotropic thermal parameters, B, for sites Cu(1), O(1) and O(2) were extraordinarily large. On anisotropic refinement, Cu(1), O(1) and O(2) atoms displayed unusually large thermal motion in a-b planes from ideal positions. Table I lists final lattice and structural parameters, their standard diviations and R factors. The 6+z values calculated from the g values listed in Table I were 6.70 for A-BNCO, and 6.98 for O-BNCO. Additional oxygen atoms, which are incorporated into the O(1) site, supply more carriers on conducting CuO_2 sheets, and improve the superconducting properties to give the higher T_c value and larger superconducting fraction. The Cu(1), O(1) and O(2) atoms are locally displaced from the ideal positions, changing their positions from cell to cell to achieve more desirable bond lengths.

References

[1] T. Mochiku, H. Asano, H. Akinaga, T. Ohshima, K. Takita, F. Izumi, Y. Takeda, M. Takano and K. Mizoguchi, Physica C 167, 560 (1990).

[2] F. Izumi, S. Takekawa, Y. Matsui, N. Iyi, H. Asano, T. Ishigaki and N. Watanabe, Jpn. J. Appl. Phys. 26, L1616 (1987).

Table I. Final results of the Rietveld refinements for A- and O-BNCO (tetragonal, P4/mmm, Z=1). a=0.38917(3) nm, c=1.17009(9) nm for A-BNCO, and a=0.38844(2) nm, c=1.16608(7) nm for O-BNCO. B values without parentheses are equivalent isotropic thermal parameters.

		as-grown			annealed		
		z	g	B(nm^2)	z	g	B(nm^2)
$Ba_{0.85}Nd_{0.15}$	in 2h	0.1862(2)	1.0	0.0097(4)	0.1808(3)	1.0	0.0091(6)
Nd	in 1d		1.0	0.0027(3)		1.0	0.0021(5)
Cu(1)	in 1a		1.0	0.0181		1.0	0.0138(8)
Cu(2)	in 2g	0.3508(1)	1.0	0.0053(2)	0.3501(2)	1.0	0.0053(4)
O(1)	in 2f		0.379(7)	0.0253		0.561(13)	0.0407
O(2)	in 2g	0.1566(2)	0.972(9)	0.0282	0.1583(4)	0.932(15)	0.0234
O(3)	in 4i	0.3701(1)	1.0	0.0065(2)	0.3699(2)	1.0	0.0061(4)
		R_{wp}=5.4%, R_I=3.1%			R_{wp}=5.0%, R_I=3.3%		

Structure Refinement of $La_{1.9}Ga_{1.1}Cu_2O_6$

H. ASANO, F. IZUMI*, E. TAKAYAMA-MUROMACHI* and Y. NAKAI

Institute of Materials Science, University of Tsukuba, Tsukuba 305
*National Institute for Research in Inorganic Materials, Tsukuba 305

A series of superconducting oxides containing Cu has two-dimensional CuO_2 planes. Cu ions on these planes are coordinated to oxide ions octahedrally, pyramidally or square-planarly. In addition, the formal charge of Cu must be within the range +2.1 - 2.3, which is required to introduce an appropriate amount of $(Cu\text{-}O)^+$ holes into the CuO_2 planes.

$La_{2-x}A_{1+x}Cu_2O_y$ compounds ($x \leqq 0.1$ for A = Ca and $0 \leqq x \leqq 0.14$ for A = Sr) do not show superconductivity, although they satisfy the structural condition. Since the structures of $La_{2-x}A_{1+x}Cu_2O_y$ were investigated only by X-ray diffraction[1], their structure parameters, particularly of oxygen, may not be accurate. More detailed knowledge of the structure is desired to understand the lack of superconductivity in these compounds. This study[2] was undertaken to reinvestigate the crystal structure of $La_{1.9}Ca_{1.1}Cu_2O_y$ with HRP. Although the concentration of $(Cu\text{-}O)^+$ holes increases with increasing Ca content, $La_{2-x}Ca_{1+x}Cu_2O_y$ has a limited homogeneity range at $x \leqq 0.1$.

A structure refinement was carried out on the basis of the refinement results of Nguyen et al.[1] with space group I4/mmm (cf. Table 1). Since occupation factors of La(1), Ca(1), La(2) and Ca(2) have relations $g_{La(1)} + g_{Ca(1)} = 1$, $g_{La(1)} + 2g_{La(2)} = 1.9$ and $g_{Ca(1)} + 2g_{Ca(2)} = 1.1$, only $g_{La(1)}$ was refined under the linear constraints. A preliminary refinement revealed that the lowest R factor was obtained at $g_{O(2)} = 1$, and this site was regarded as fully occupied in subsequent refinements. Although g of a 2b site, (0, 0, 1/2), was refined, occupation of this site proved to be neglegible. Therefore, this site was omitted in the final refinement. The resulting structure parameters are listed in Table 1, and the crystal structure is shown in Fig. 1. Tetragonal lattice parameters were refined to be a = 3.8245(2) Å and c = 19.420(1) Å. R factors were R_{wp} = 5.5%, R_e = 5.2%, R_p = 4.0%, R_I = 2.0% and R_F = 1.8%. Chemical composition of the present compound is $La_{1.9}Ca_{1.1}Cu_2O_6$, from which the formal charge of Cu is calculated to be +2.05. This value is evidently too small for the achievement of superconductivity.

Table 1. Structure parameters of $La_{1.9}Ca_{1.1}Cu_2O_6$. B_{eq} is the equivalent isotropic thermal parameter. Estimated standard deviations in parentheses refer to the last digit printed.

Atom	Site	x	y	z	g	B_{eq}/Å^2
La(1)	2a	0	0	0	0.12(1)	0.54
Ca(1)	2a	0	0	0	0.88	0.54
La(2)	4e	0	0	0.17571(7)	0.89	0.56
Ca(2)	4e	0	0	0.17571(7)	0.11	0.56
Cu	4e	0	0	0.41488(7)	1	0.47
O(1)	8g	0	1/2	0.08217(7)	1	0.77
O(2)	4e	0	0	0.2962(1)	1	1.55

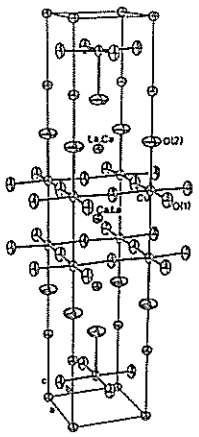

Fig. 1 ORTEP-II drawing of $La_{1.9}Ca_{1.1}Cu_2O_6$.

References

1) N. Nguyen, L. Er-Rakho, C. Michel, J. Choisnet and B. Raveau, Mater. Res. Bull. 15, 891 (1980)
2) F. Izumi, E. Takayama-Muromachi, Y. Nakai and H. Asano, Physica C 157, 89 (1989)

Neutron Powder Diffraction Studies of Microtwinning and Crystal Structure of $YBaSrCu_3O_{7-y}$

H. Hayakawa, E. Akiba, F. Izumi# and H. Asano*

National Chemical Laboratory for Industry, 1-1 Higashi, Tsukuba, Ibaraki 305 Japan
#National Institute for Research in Inorganic Materials, 1-1 Namiki, Tsukuba, Ibaraki 305 Japan
*Institute of Materials Science, University of Tsukuba, Tsukuba, Ibaraki 305 Japan

Partially Sr substituted $YBa_2Cu_3O_{7-y}$ was found to be a superconductor[1]. Superconducting transition temperature, Tc, decreased with increase of the amount of Sr substitution while at Sr/Ba=1 $YBaSrCu_3O_{7-y}$ (YBSCO), Tc discontinuously increased. The lattice parameter of b axis became shorter and occupancy of O(2) site was almost zero at Sr/Ba=1 by Rietveld analysis using powder X-ray diffraction data[1].

In Rietveld analysis of superconducting YBCO and related compounds, an orthorhombic (*Pmmm*) model was usually used. However,calculated patterns from the model did not fit to some observed peaks. Microtwinning in YBCO and related compounds was considered to be affect the powder patterns. Takeda et al. found that YBSCO showed more micro twin boundariy density than YBCO by TEM observation.[2] We, therefore, adopted a new structure model in which the effect of microtwinning was taken in to account for Rietveld analysis of YBSCO.

Structure of YBSCO was firstly described in the space group of *Pmmm* which has been reported in every literature. The structure of the microtwin boundary along (110) plane is schematically shown in Fig. 1. The structure of the twin boundary is described in large tetragonal cell. The relation of lattice parameters of this tetragonal cell to that of the bulk orthorhombic structure is as follow: $a_{tetra}=(a_{ortho}+b_{ortho})/2$, $c_{tetra}=c_{ortho}$. The structure model contains two phases, such as the usual orthorhombic phase and the tetragonal phase which expresses the structure of the twin boundary. Using the new model, R-factors were improved from R_{WP}=7.94% to 6.04% when isotropic thermal parameters were refined. Anisotropic thermal parameters were refined for all the sites and much better R-factors were obtained as shown in the Table(R_{WP}=5.32%). The thermal parameters of oxygen showed anisotropic characteristics, especially at O(1) and O(2) sites. It is due to anisotropic oxygen defect and it might related to increase of Tc at this special composition.

References
[1] H. Hayakawa, et al. *J. Ceramic Soc. Jpn.*, **90**, 174 (1990).
[2] Y. Takeda et al. *Physica C*, **157**, 358 (1989).

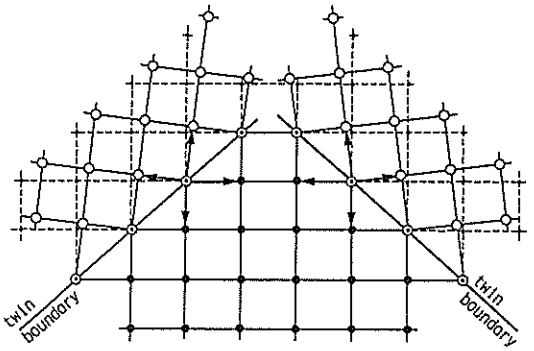

Fig.1 Schematic representation of the twin boundary

Table. Crystallographic data of $YBaSrCu_3O_{7-y}$ (orthorhombic phase)

a=3.8467(3)A, b=3.7909(3)A, c=11.527(1)A, Space group *Pmmm*

Atom	site	Occupp	x	y	z	Biso	U(11)	U(22)	U(33)
Ba	2t	0.49(1)	1/2	1/2	0.1846(1)	0.86	5(24)	149(31)	173(27)
Sr	2t	0.51(1)	1/2	1/2	0.1846(1)	0.86	5(24)	149(31)	173(27)
Y	1h	1.00	1/2	1/2	1/2	0.58	80(28)	73(27)	69(27)
Cu(i)	1a	1.01(2)	0	0	0	1.29	150(29)	331(38)	8(23)
Cu(2)	2q	0.99(2)	0	0	0.3541(1)	0.61	12(15)	74(17)	142(20)
O(1)	1b	0.85(2)	1/2	0	0	3.5	141(50)	1116(118)	60(55)
O(2)	1e	0.12(2)	0	1/2	0	3.5	1149(118)	137(50)	60(55)
O(3)	2q	0.98(2)	0	0	0.1621(2)	1.83	299(39)	409(50)	13(26)
O(4)	2r	0.99(2)	0	1/2	0.3757(6)	0.94	80(16)	38(14)	240(43)
O(5)	2s	1.00(2)	1/2	0	0.3743(7)	1.13	39(14)	77(16)	314(52)

R_{WP}=5.32, R_P=3.99, R_E=4.59, R_I=1.76, R_F=1.70, R_{INDEX}=1.16

Distribution of Zn between Two Cu sites in $YBa_2Cu_{2.8}Zn_{0.2}O_{7-y}$

H. ASANO, H. MAEDA[1], A. KOIZUMI[2], N. BAMBA[2], E. TAKAYAMA-MUROMACHI[3], F. IZUMI[3], K. SHIMIZU[2], H. MORIWAKI[1], H. MARUYAMA[2], Y. KURODA[1] and H. YAMAZAKI[2]

Institute of Materials Science, University of Tsukuba, Tsukuba 305
[1]Department of Chemistry, Faculty of Science, Okayama University, Okayama 700
[2]Department of Physics, Faculty of Science, Okayama University, Okayama 700
[3]National Institute for Research in Inorganic Materials, Tsukuba 305

Substitution of foreign elements for Cu in $YBa_2Cu_3O_{7-y}$ (YBCO) has generally unfavorable effects on superconductivity, but in different degrees for different elements. Substitution of Zn is worthy of special attention, since anomalously large T_c suppression was reported compared with other 3d elements. Therefore, a precise knowledge of the crystal structure for Zn-doped YBCO is important for understanding the mechanism of such large T_c depression.

Neutron diffraction data of $YBa_2Cu_{2.8}Zn_{0.2}O_{7-y}$ were taken on HRP. A Rietveld refinement[1] was carried out on the basis of an orthorhombic YBCO structure with space group Pmmm, where Zn was distributed between 1a and 2q sites. The resulting occupation factor, g, of Zn at the 1a site became negative. Subsequent refinements, therefore, assumed that Zn atoms share the 2q site with Cu(2) atoms in the Cu:Zn ratio of 0.9 : 0.1 and that Cu(1) atoms fully occupy the 1a site. Table 1 lists final structure parameters. Lattice parameters were refined to be a = 3.8920(2) Å, b = 3.8214(2) Å and c = 11.6829(7) Å. R factors were R_{wp} = 5.3%, R_p = 3.9%, R_I =1.4%, R_F = 1.0% and R_e = 3.6%.

EXAFS measurements[1] of the same sample show that Zn atoms are coordinated to five oxygen atoms with four short and one long Zn-O bonds. This indicates the occupation of the 2q site by Zn forming a ZnO_5 pyramid, which is consistent with the neutron diffraction results. The Zn-doped compound has a crystal structure quite similar to that of undoped YBCO; the orthorhombic distortion from the perovskite structure (a : b : c/3) are respectively 1.018 : 1 : 1.019 and 1.017 : 1 : 1.020 for doped and undoped crystals. Moreover, occupation factors for the oxygen sites O(1) and O(2) are 0.91 and 0.03, respectively, which agree well with those of the undoped crystal. In spite of the marked similarity of the crystal structures, T_c of the doped sample was as low as 40 K. This large T_c suppression must be due to the partial occupation by Zn of the 2q site on a CuO_2 plane which plays a crucial role in high-T_c superconductivity.

Table 1. Structure parameters for $YBa_2Cu_{2.8}Zn_{0.2}O_{6.94}$. B_{eq} is the equivalent isotropic thermal parameter. Numbers in parentheses are statistical uncertainties of the last significant digit.

Atom	Site	x	y	z	g	B_{eq}/Å^2
Y	1h	1/2	1/2	1/2	1	0.43
Ba	2t	1/2	1/2	0.1840(3)	1	0.57
Cu(1)	1a	0	0	0	1	0.54
Cu(2)	2q	0	0	0.3543(2)	0.9	0.39
Zn	2q	0	0	0.3543(2)	0.1	0.39
O(1)	1b	1/2	0	0	0.91(1)	0.86
O(2)	1e	0	1/2	0	0.03(1)	0.86
O(3)	2q	0	0	0.1591(2)	1	0.65
O(4)	2r	0	1/2	0.3787(3)	1	0.56
O(5)	2s	1/2	0	0.3784(3)	1	0.44

Reference
1) H. Maeda, A. Koizumi, N. Bamba, E. Takayama-Muromachi, F. Izumi, H. Asano, K. Shimizu, H. Moriwaki, H. Maruyama, Y. Kuroda and H. Yamazaki, Physica C 157, 483 (1989)

Metal Ordering in $YbInCu_4$

Y. NAKAI, K. KOJIMA*, T. SUZUKI**, T. FUJITA** , T. HIHARA*,
F. IZUMI*** and H. ASANO

Institute of Materials Science, University of Tsukuba, Tsukuba 305
*Faculty of Integrated Arts & Sciences, Hiroshima University, Hiroshima 730
**Faculty of Science, Hiroshima University, Hiroshima 730
***National Institute for Research in Inorganic Materials, Tsukuba 305

$Yb_xIn_{1-x}Cu_2$ ($0.3<x<0.65$) is known as a valence fluctuating compound with T_v=40-80K. $Yb_xIn_{1-x}Cu_2$ has been reported to have a C15 Laves phase structure[1]. Recently, Kojima et al.[2] have shown that the phase exhibiting the valence transition is $YbInCu_4$ (x=0.5) and that samples with other compositions contain primarily two phases, $YbInCu_4$ and $InCu_2$. They also suggested from X-ray powder diffraction that $YbInCu_4$ has not the C15-type structure but a C15b($AuBe_5$)-type one.

Figure 1 shows the C15b-type structure with space group $F\bar{4}3m$. There are two kinds of Be sites (4c and 16e), and Au atoms occupy a 4a site. In $YbInCu_4$, In and Yb atoms may be ordered at the 4a and 4c sites, respectively, because their random occpation of these two sites results in the C15-type structure. However, the possibility of partial disordering of In and Yb cannot be excluded completely.

In this work[3], the crystal structure of $YbInCu_4$ was refined by Rietveld analysis of TOF neutron powder diffraction data in order to distinguish three models: perfect C15b, partially disordered C15b and C15. The diffraction data were analyzed by a Rietveld refinement program RIETAN. Resulting structure parameters are listed in Table 1. R factors were R_{wp} = 5.3% , R_e=4.0%, R_p=4.0%, R_I=4.0% and R_F=3.5%. Occupation factors of In and Yb atoms were refined,but they deviated little from 1. This fact suggests that In and Yb atoms are completely ordered at the 4a and 4c sites, respectivly.

References
1)I. Felner and I. Nowik, Phys. Rev. B33, 617 (1986)
2)K. Kojima, H. Hayashi, A. Minami, Y. Kasamatsu and T. Hihara, J. Magn. & Magn. Mater. 81, 267 (1989)
3)K. Kojima , Y. Nakai , T. Suzuki , H. Asano, F. Izumi, T. Fujita and T. Hihara , J. Phys. Soc. Jpn. 59, 792 (1990)

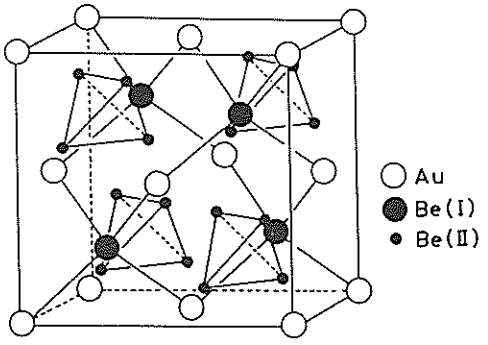

Fig.1 $AuBe_5$(C15b)-type structure

Table 1. Structural parameters of $YbInCu_4$. Lattice parameter : a=7.1575(6) Å.B_{eq} is the equivalent isotropic thermal parameter, and g is the occupation factor. Numbers in parentheses are estimated standard deviations of the last significant digit.

Atoms	Site	x	y	z	B_{eq}(Å^2)	g
In	4a	0	0	0	0.23	1
Yb	4c	1/4	1/4	1/4	0.30	1
Cu	16e	0.6254(5)	=x	=x	0.36	1

Comparison of Two Rietveld Programs, RIETAN and TF12LS, for HRP Data

T. KAMIYAMA, T. ISHIGAKI and H. ASANO

Institute of Materials Science, University of Tsukuba, Tsukuba 305

The profile function in RIETAN[1], the currently used Rietveld program for the HRP data, has not been fully optimized yet. However, the agreement between the calculated and observed profiles is considerably good. The reason for this agreement is the flexibility of the profile function, which is defined in 3 different regions:

$\Delta t<0$ $\quad h(\Delta t)=A\exp(-\Delta t^2/2\sigma_1^2)$,

$0<\Delta t<\Delta t_1$ $\quad h(\Delta t)=A\exp(-\Delta t^2/2\sigma_2^2)$,

$\Delta t_1<\Delta t$ $\quad h(\Delta t)=B\exp(-\gamma\Delta t)$,

$\Delta t=t-t_B$,

where A and B are the normalization factors, σ_1 and σ_2 the width parameters for Gaussian, γ the decay constant of exponential function and t_B the time of flight (TOF) at the Bragg position. Δt_1 and B is determined by the condition that the function of the each region is connected smoothly. Since HRP utilizes wide energy range of neutrons coming from cold moderator, the profile function also includes switching parameter R between slowing-down region and Maxwellian region with different decay constants γ_1 and γ_2. These profile parameters depend on TOF. Then, the number of total refinable profile parameters is 10.

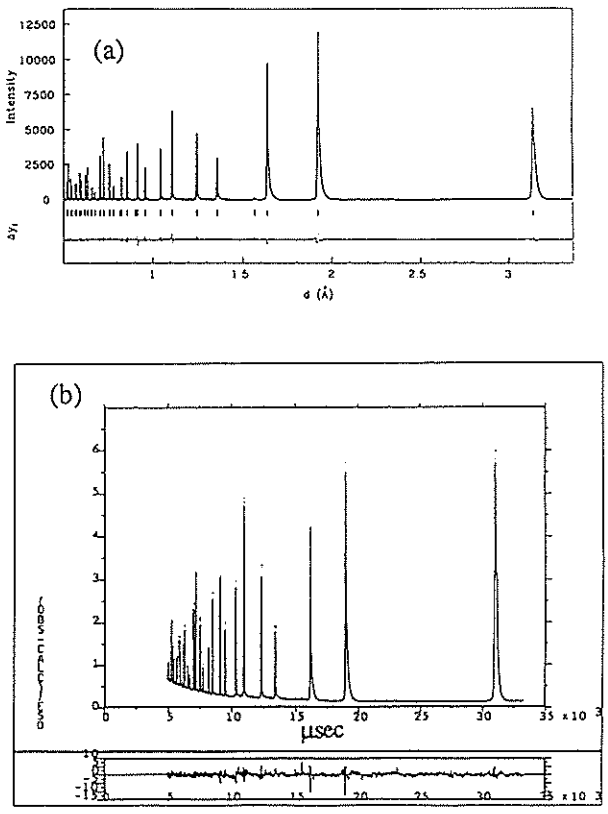

Fig. 1 Rietveld refinement pattern of NBS silicon. Background is subtracted in (a).

The function used in RIETAN has advantage in convergency in the least-squares procedures, because the profile of each region is described by a simple Gaussian or exponential. However, this function is not based on the physical reality such as the size effect and the strain effect; it is impossible to obtain any information contained in the observed profile. Moreover, the profile function used in the program has no flexibility in the case that the anisotropic broadening occurs when the sample contains imperfections. In order to include the anisotropic broadening, at least another 10 parameters, then totally 20 parameters, are necessary in the present RIETAN.

In general, the pulse shape of the burst function and the geometrical contribution to the profile are almost the same in every experiment, and the factor contributing to the profile in each experiment is the sample effect such as size and strain. Therefore, the number of parameters necessary for the refinement can be reduced. Before optimizing profile function of RIETAN for HRP, we tested another Rietveld program, TF12LS[2], developed at ISIS, in which the profile function is different from RIETAN. The profile function in TF12LS consists of exponential burst pulse from moderator, Gaussian instrumental resolution and Voigtian (convolution of Gaussian and Lorentzian) sample broadening. They are convoluted each other in the same way as reported in ref. 3). Figures 1-3 show results of fitting for the NBS silicon data. In each figure, (a) is fitting by RIETAN and (b) by TF12LS. Both results give satisfactory fit. However, fitting around tops of peaks is better in RIETAN, while tails of peaks fit better in TF12LS. The former is ascribed to the flexibility of the profile

of RIETAN and the latter to Lorentzian component of sample broadening. Table 1 shows the R factors and χ^2. These values indicate that RIETAN gives better fitting.

Table 1. Comparison of RIETAN and TF12LS.

	RIETAN	TF12LS
Rwp	4.54	4.71
Re	3.95	3.74
χ^2	1.32	1.58

We also applied TF12LS to another sample, $La_{1.85}Sr_{0.15}CuO_{4-\delta}$. We confined the number of profile parameters to be only 2. Nevertheless, χ^2 gave very low value of 1.21. It is worth noting that χ^2 by RIETAN, which uses 10 profile parameters, is almost the same value (χ^2=1.26).

We wish to thank Dr. W.I.F.David for giving us TF12LS.

References

1) F.Izumi, H.Asano, H.Murata and N.Watanabe, J.Appl.Cryst. 20(1987)411.
2) W.I.F.David, D.E.Akporiaye, R.M.Ibberson and C.C.Wilson, RAL-88-103(1988).
3) T. Kamiyama, S.Tomiyoshi, T.Shinohara, H.Asano, H.Yamamoto and N.Watanabe, KENS Report VI, (1986)113.

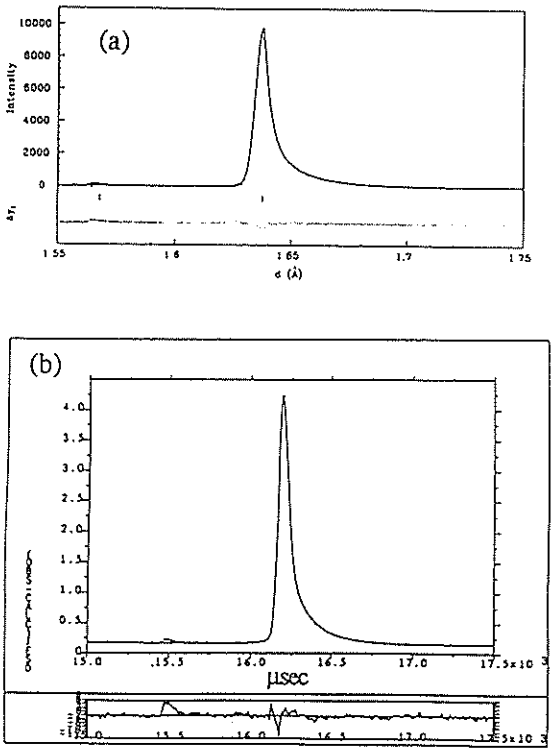

Fig. 2 A part of the Rietveld refinement pattern of NBS silicon. Background is subtracted in (a).

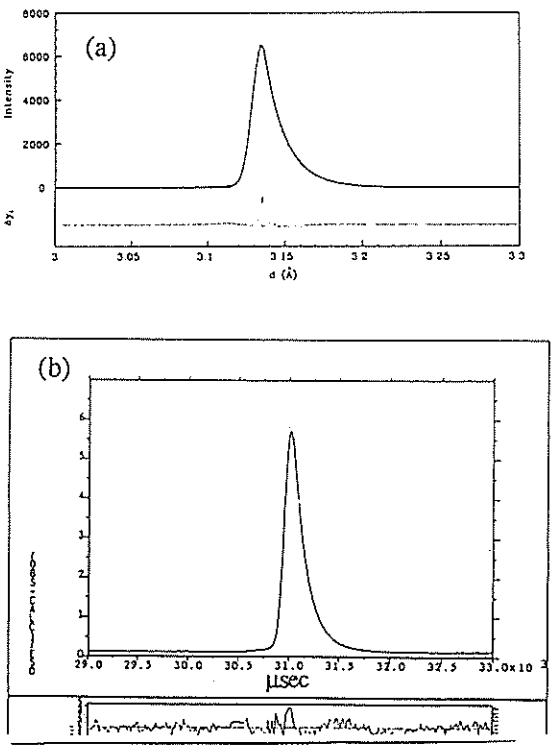

Fig. 3 A part of the Rietveld refinement pattern of NBS silicon. Background is subtracted in (a).

1-2. Structures of Liquids and Glasses

Structure of Liquid CCl_4 at Elevated Temperature

M. MISAWA

National Laboratory for High Energy Physics, 1-1 Oho, Tsukuba 305

Structure factor $S_m(Q)$ of liquid carbon tetrachloride CCl_4 has been measured along the liquid-vapor coexisting curve by using the HIT instrument. The experimental $S_m(Q)$'s measured at -20, 20, 60, 110 and 160°C are shown in Fig. 1. The melting point of liquid CCl_4 is -22.6°C and the critical temperature and pressure are T_c=283.1°C and P_c=45atm, so that the highest temperature studied in this work is 0.78 of T_c, at which pressure is 7.3atm.

Two characteristic features of the temperature dependence of the $S_m(Q)$'s are observed: (i) the first peak of the $S_m(Q)$ becomes broader and its position shifts toward the lower Q region as temperature is raised; and (ii) a small peak located at about 2.2Å^{-1} and a valley following this peak also become broad as temperature is increased.

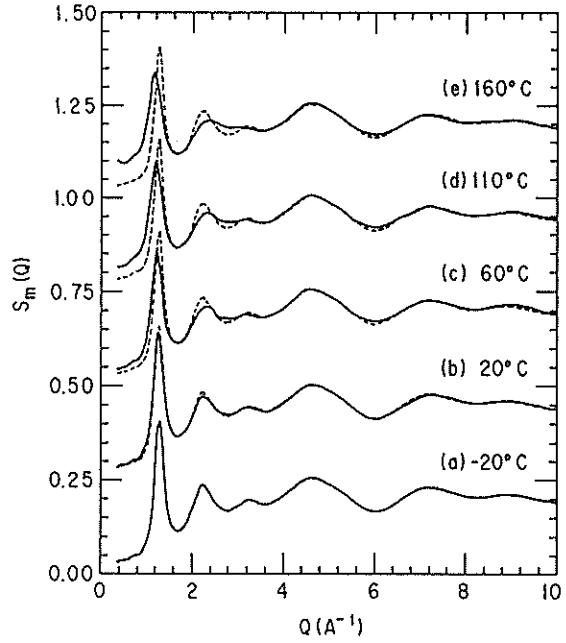

Fig. 1 Experimental structure factor $S_m(Q)$'s measured at -20, 20, 60, 110 and 160°C along the liquid-vapor coexisting curve. A dashed curve drawn on each $S_m(Q)$ curve is the $S_m(Q)$ at -20°C.

The characteristic changes of the $S_m(Q)$'s are discussed in terms of a packing of uncorrelated molecules and a preferred orientation introduced between the nearest neighbors. The first characteristic (i) described above is simply explained by the decrease of the packing fraction η of the uncorrelated molecules due to the decrease of the density. Figure 2 plots how the value of η decreases with increasing temperature. The packing fraction extrapolated to the critical point is estimated to be 0.134 which is close to the theoretical prediction of 0.13044 for the van der Waals fluid[1].

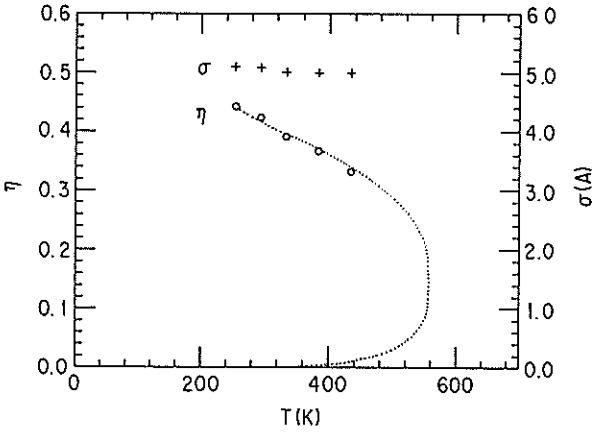

Fig. 2 Packing fraction η and effective diameter of uncorrelated CCl_4 molecules σ as a function of temperature, which are determine so as to reproduce the experimental $S_m(Q)$'s. Dotted curve denotes the packing fraction calculated from a definition of $\eta=\pi\rho\sigma^3/6$ with an experimental molecular number density ρ and an average value of σ.

While, the second characteristic (ii) is explained by both the decrease of the number of correlated molecules and the broadening of the orientational correlation. However, orientational correlation still exists even at 160°C, the highest temperature studied in this work.

Details on the present experiment and data analysis have been reported elsewhere[2].

References

1)D. A. Young and B. J. Alder, Phys. Rev. A3(1971) 364.
2)M. Misawa, J. Chem. Phys. 91(1989) 5648.

Orientational Correlation in Liquid S_2Cl_2

M. MISAWA and T. FUKUNAGA*

National Laboratory for High Energy Physics, 1-1 Oho, Tsukuba 305
*Department of Crystalline Materials Science, Nagoya University, Nagoya 464

Structure of molecules of sulfur monochloride S_2Cl_2 in the gaseous state is a twisted short chain[1] being similar to that of hydrogen peroxide. The molecule has a dipole moment of 1.6D in benzene solution. Accordingly, the interaction between the molecules is expected to be highly anisotropic, and the orientational correlation between the molecules in the liquid state is also expected to be more anisotropic compared with those of more isotropic molecules like Br_2[2], CCl_4[3], or C_6D_6[4].

Furthermore, the structure of S_2Cl_2 molecules seems to be rather similar to that of segments of consecutive any four S atoms in a long chain of sulfur molecules. If one can assume that the packing of the molecules in both of the liquids is determined primarily by the anisotropic shape of the molecules, a knowledge of the orientational correlations between the S_2Cl_2 molecules may help to understand the local packing of sulfur chains in the liquid state.

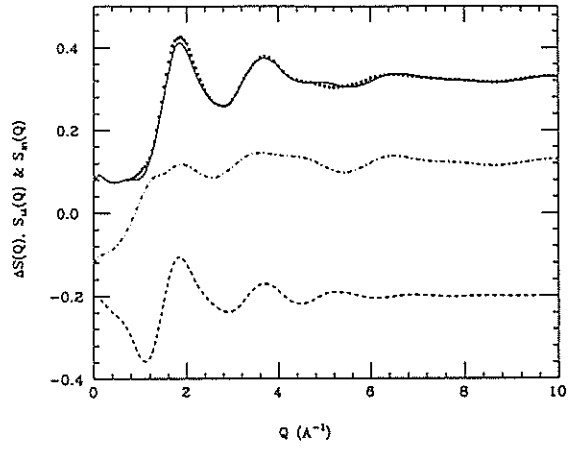

Fig. 1 Experimental structure factor $S_m(Q)$ (open squares) and fitted one (solid curve) for liquid S_2Cl_2. Lower two curves are structure factor of uncorrelated orientation $S_u(Q)$ (dotted-dashed curve) and a correction term for preferred orientation $\Delta S(Q)$ (dashed curve).

Figure 1 shows the experimental result of the structure factor $S_m(Q)$ of liquid S_2Cl_2 at room temperature, which was measured by using the HIT instrument. The $S_m(Q)$ is defined as a coherent scattering intensity per molecule so that it tends to $\Sigma b^2/(\Sigma b)^2$, i.e. 0.3234, as $Q \to \infty$.

The $S_m(Q)$ is analyzed by means of the same method as used in the structural analysis of liquid halogens[2] and carbon tetrachloride[3]: the method assumes that (i) distribution of S_2Cl_2 molecules in the liquid state is determined primarily by the packing of uncorrelated molecules having an effective hard sphere diameter σ with a packing fraction η except for very short-range, and that (ii) molecular distribution is modified due to the orientational correlations only at very short-range. Then, the $S_m(Q)$ can be written as,

$$S_m(Q) = S_u(Q) + \Delta S(Q), \qquad (1)$$

where $S_u(Q)$ is a structure factor for uncorrelated molecules [assumption (i)] and $\Delta S(Q)$ is a correction for orientational correlation [assumption (ii)]. The $S_m(Q)$ given by eq.(1) is fitted to the observed one by means of a least-squares method, of which details have been given in Ref. 2-4. The fitted $S_m(Q)$ is shown by a solid curved in Fig. 1 together with the curves of $S_u(Q)$ and $\Delta S(Q)$. The fitted values of σ and η are 4.22 A and 0.295 respectively and are consistent with the observed density of S_2Cl_2 molecules of 0.0075 A^{-3}.

The estimated intramolecular structure of S_2Cl_2 molecules in the liquid state is as follows: S-S=1.97A, S-Cl=2.06A, $\angle$S-S-Cl=107° and $\angle$Cl-S-S-Cl=85°, which are rather similar to those of gas molecules[1].

The orientation of maximum occurrence probability in liquid S_2Cl_2 estimated in this analysis is drawn schematically in Fig. 2. Average number of molecules correlated in this orientation is estimated to be about three.

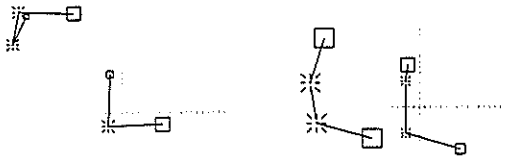

(X-Z) plan (X-Y) plan

Fig. 2 Schematic drawing of the orientational correlation between the two S_2Cl_2 molecules estimated in the present analysis. Squares denote Cl atoms, and stars S atoms.

In Fig. 3 the calculated radial distribution function is compared with the experimental one. The intramolecular atomic distribution, and intermolecular atomic distributions for both correlated and uncorrelated molecules are also shown in Fig. 3.

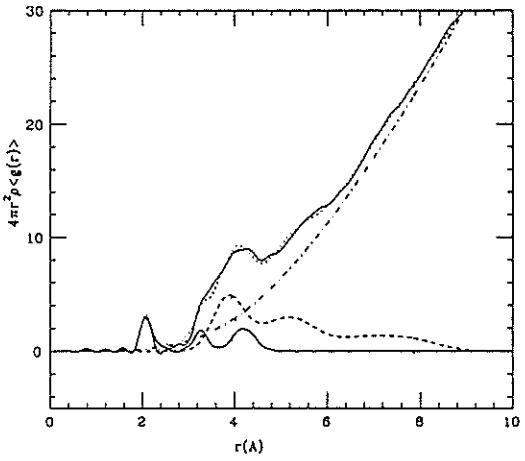

Fig. 3 Experimental radial distribution function (solid curve) and calculated one (dotted curve) for liquid S_2Cl_2. Intramolecular atomic distribution (thin solid curve), intermolecular atomic distributions for uncorrelated molecules (dotted-dashed curve) and that for molecules correlated in orientation (dashed curve) are also shown.

Figure 4 shows a comparison of the experimental S(Q)[5] of liquid sulfur at 250°C with a calculated one which is obtained simply by substituting the scattering length of sulfur nuclei for that of chlorine nuclei in the $S_m(Q)$ estimated for liquid S_2Cl_2. Despite of the crudeness of the treatment, an overall feature of the S(Q) of liquid S seems to be reproduced reasonably good, suggesting that local structure of the packing of S-chains in liquid sulfur resembles that of S_2Cl_2 molecules in the liquid state. Further discussion with respect to this aspect is given in a separate paper[5].

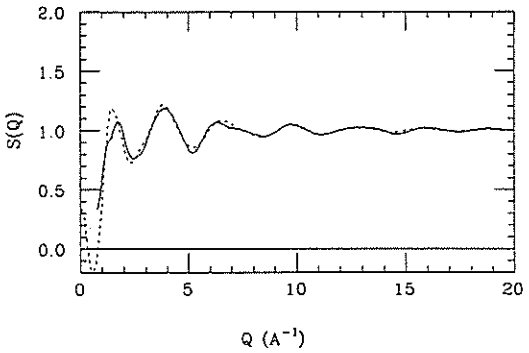

Fig. 4 Comparison of the experimental S(Q) (solid curve) of liquid sulfur at 250°C with calculated one (dashed curve) which obtained simply by substituting the scattering length of sulfur nuclei for that of chlorine nuclei in the $S_m(Q)$ estimated for liquid S_2Cl_2.

References

1) E. Hirota, Bull. Chem. Soc. Jpn 31(1958) 130.
2) M. Misawa, J. Chem. Phys. 90(1989) 6563; 91(1989) 2575.
3)M. Misawa, J. Chem. Phys. 91(1989) 5648.
4)M. Misawa and T. Fukunaga, J. Chem. Phys. (in press).
5)M. Misawa and T. Fukunaga, in this volume.

Structure of Liquid Sulfur

M. MISAWA and T. FUKUNAGA*

National Laboratory for High Energy Physics, 1-1 Oho, Tsukuba 305
*Department of Crystalline Materials Science, Nagoya University, Nagoya 464

Structure factor of liquid sulfur has been measured by using the HIT instrument in order to study the ring-chain transition of sulfur molecules in the liquid state. It is widely accepted that at the transition temperature T_{tr} of about 160°C polymerization of sulfur occurs and the sulfur molecules transform S_8 ring structure into $(-S-)_n$ long chain structure[1]. Below T_{tr} the ring molecule is dominant, while above T_{tr} both of the ring and chain molecules coexist. Weight fraction of the polymeric sulfur increases with increasing temperature, which is reported to be about 20% at 175°C and about 50% at 250°C[1-3].

Figure 1 shows the structure factors S(Q) of liquid sulfur measured at 130°C (below T_{tr}), 175°C (above T_{tr}) and 250°C (far above T_{tr}). The sulfur sample was sealed into a fused quartz cell of 8mm inner diameter and 0.3mm wall thickness in vacua, and was melted by using an infrared radiation furnace specially designed for the HIT instrument. As shown in Fig.1, characteristic temperature dependence of a prepeak and the main peak of the S(Q)'s, which has been reported by several authors[4,5], is reconfirmed in this experiment.

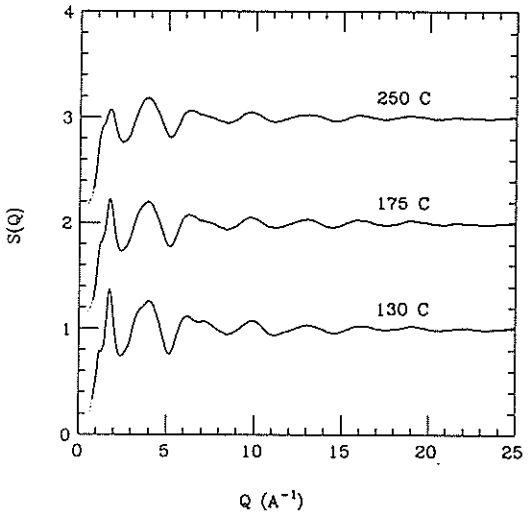

Fig. 1 Experimental structure factors S(Q) of liquid sulfur: (a) 130, (b) 175 and (c) 250°C.

The S(Q)'s are analyzed by means of the same method as used in the structural analysis of molecular liquids[6] in order to examine the intermolecular structure of liquid sulfur both above and below the transition temperature. The method assumes that (1) except for very short-range, distribution of structural units in liquid state is determined primarily by the packing of uncorrelated units having an effective diameter σ with a packing fraction η, and that (2) only at very short-range, distribution of the units is modified due to the orientational correlations between the units. The S(Q) can be written as,

$$S(Q) = S_u(Q) + \Delta S(Q), \qquad (1)$$

where $S_u(Q)$ is a structure factor for uncorrelated units [assumption (1)] and $\Delta S(Q)$ is a correction for orientational correlation [assumption (2)]. The S(Q) given by eq.(1) is fitted to the observed one by means of a least-squares method, of which details have been given in Ref. 6.

A. liquid sulfur at 135°C

The structural unit of liquid sulfur at this temperature is certainly S_8 ring molecules. The

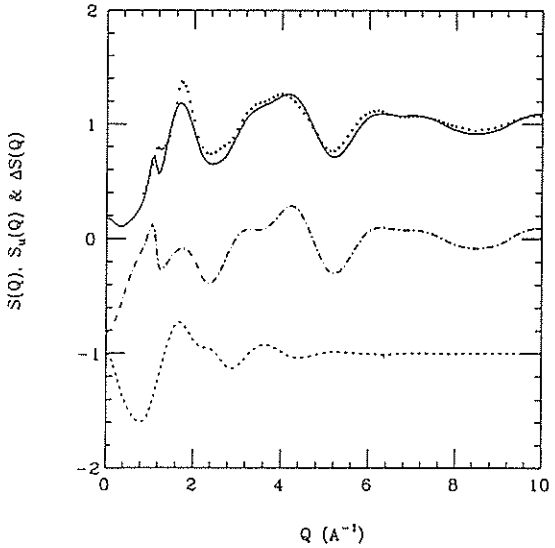

Fig. 2 Experimental structure factors S(Q) (open squares) and fitted one (solid curve) for liquid sulfur at 130°C. Lower two curves are structure factor of uncorrelated orientation $S_u(Q)$ (dotted-dashed curve) and a correction term for preferred orientation $\Delta S(Q)$ (dashed curve).

structure of S_8 units used in the analysis is S-S=2.06A, ∠S-S-S=108° and ∠S-S-S-S=99°. The fitted $S_m(Q)$ is shown by a solid curved in Fig. 2 together with the curves of $S_u(Q)$ and $\Delta S(Q)$. The characteristic feature of the experimental S(Q) is reproduced fairly well, although the agreement is not perfect, especially on the heights of the prepeak and the main peak. The fitted values of σ and η are 6.01 A and 0.461 respectively. The value of η is close to the value of 0.479 calculated from the observed density[7] of S_8 molecules of 0.0042 A^{-3} and the fitted value of σ.

A calculated radial distribution function is compared with the experimental one in Fig. 3. The intramolecular atomic distribution, and intermolecular atomic distributions for both correlated and uncorrelated molecules are also shown in Fig. 3.

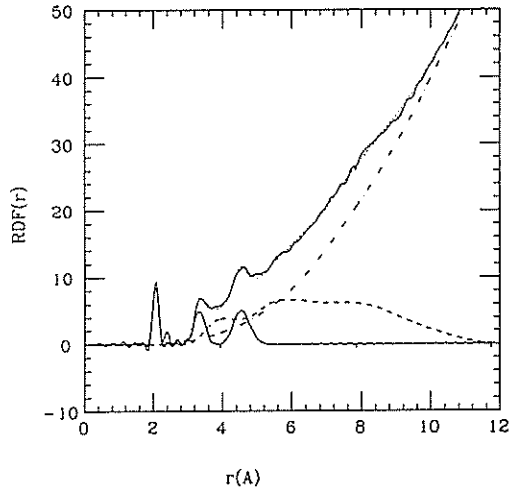

Fig. 3 Experimental radial distribution function (solid curve) and calculated one (dotted curve) for liquid S at 130°C. Intramolecular atomic distribution (thin solid curve), intermolecular atomic distributions for uncorrelated molecules (dotted-dashed curve) and that for molecules correlated in orientation (dashed curve) are also shown.

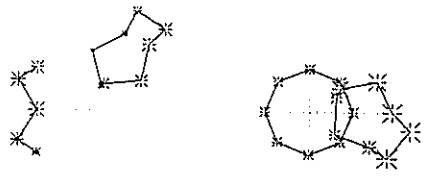

Fig. 4 Schematic drawing of the orientational correlation between the two S_8 molecules estimated in the present analysis.

The orientational configuration estimated between the two S_8 molecules is shown schematically in Fig.4. Average number of molecules correlated in such orientation is estimated to be about four.

B. liquid sulfur at 250°C

The structural unit of liquid sulfur at this temperature is not simple, because both ring and chain molecules coexist and, furthermore, structure of chain molecules is not clear. However, local structures of segments of consecutive any four S atoms in both ring and chain molecules are considered to be quite similar, independent of molecular species[8]. Ring and chain conformations are distinguished from each other only by the position of the fifth atom and the following atoms[8]. Therefore, $(-S-)_4$ segment may be a good candidate for the structural units of liquid sulfur at the high temperature. A possibility of this idea has been examine with respect to the structural analysis of liquid S_2Cl_2[9].

The structure of $(-S-)_4$ units used in the analysis is S-S=2.07A, ∠S-S-S=108° and ∠S-S-S-S=93°. The fitted $S_m(Q)$ is shown by a solid curved in Fig. 5 together with the curves of $S_u(Q)$ and $\Delta S(Q)$. The characteristic feature of the experimental S(Q) is reproduced fairly well. The fitted values of σ and η are

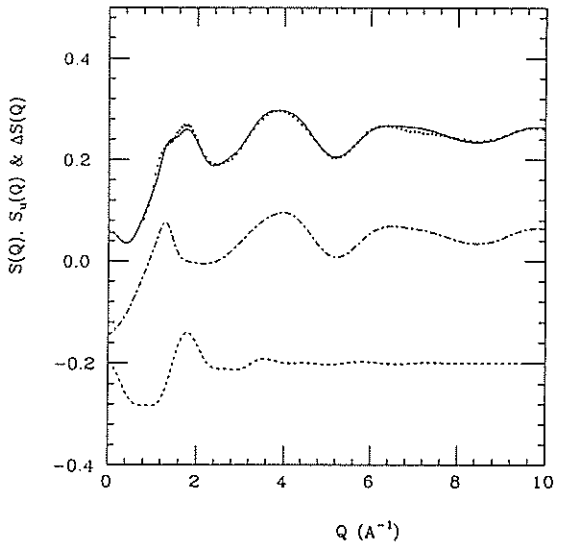

Fig. 5 Experimental structure factors S(Q) (open squares) and fitted one (solid curve) for liquid sulfur at 250°C. Lower two curves are structure factor of uncorrelated orientation $S_u(Q)$ (dotted-dashed curve) and a correction term for preferred orientation $\Delta S(Q)$ (dashed curve).

4.53 A and 0.353 respectively. The value of η does not differ much from the value of 0.394 calculated from the observed density[7] of $(-S-)_4$ units of 0.0081 A^{-3} and the fitted value of σ.

In Fig. 6 the calculated radial distribution function is compared with the experimental one. The intramolecular atomic distribution, and intermolecular atomic distributions for both correlated and uncorrelated molecules are also shown in this figure.

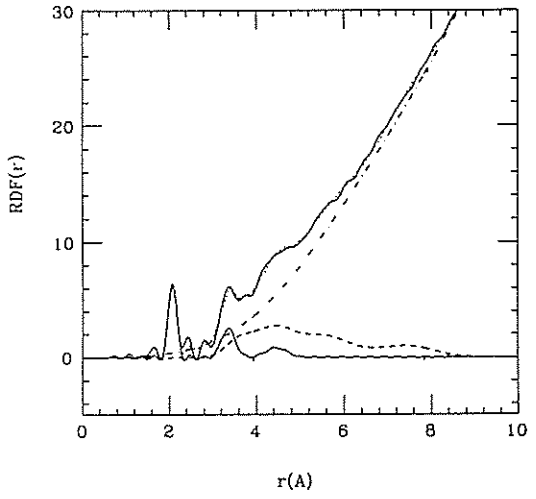

Fig. 6 Experimental radial distribution function (solid curve) and calculated one (dotted curve) for liquid S at 250°C. Intramolecular atomic distribution (thin solid curve), intermolecular atomic distributions for uncorrelated molecules (dotted-dashed curve) and that for molecules correlated in orientation (dashed curve) are also shown.

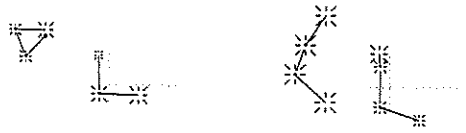

Fig. 7 Schematic drawing of the orientational correlation between the two $(-S-)_4$ units estimated in the present analysis.

The local packing of the $(-S-)_4$ units estimated in this analysis is shown in Fig.7 schematically. Average number of units correlated in this orientation is estimated to be about two.

Above results are preliminary, and further analysis is under way.

References

1) A. V. Tobolsky and W. J. MacKnight, *Polymeric Sulfur and Related Polymers* (Interscience, New York, 1965).
2) J. C. Koh and W. Klement, J. Phys. Chem. 74(1970) 4280.
3) J. C. Wheeler, S. J. Kennedy and P. Pfeuty, Phys. Rev. Lett. 45(1980) 1748.
4)C. W. Tompson and N. S. Gingrich, J. Chem. Phys. 31(1959) 1598.
5)R. Winter, T. Bodensteiner, C. Szornel and P. A. Egelstaff, J. Non-cryst. Solids 106(1988) 100.
6) M. Misawa, J. Chem. Phys. 90(1989) 6563; 91(1989) 2575, 5648.
7) Von F. Feher and E. Hellwig, Z. Anorg. Allg. Chem. 294(1958) 63.
8) M. Misawa and K. Suzuki, J. Phys. Soc. Jpn. 44(1978) 1612; K. Suzuki and M. Misawa, Proc. 3rd Int. Conf. on Liquid Metals, ed. by R. Evans and D.A.Greenwood (Bristol, 1976) p.531.
9)M. Misawa and Fukunaga, in this volume.

Structure of Molten Alkali Deuteroxides

N. OHTORI, S. OKAZAKI, O. ODAWARA, I. OKADA, T. FUKUNAGA* and M. MISAWA**

Department of Electronic Chemistry, Tokyo Institute of Technology, Nagatsuta, Midori-ku, Yokohama 227
*Department of Crystalline Materials Science, Nagoya Univ. Nagoya 464
**National Laboratory for High Energy Physics, Tsukuba 305

Alkali metal hydroxides consist of spherical alkali metal ion and the simplest polyatomic ion, OH^-. The size of hydroxide ion is as small as that of F^- ion and the center of its negative charge is polarized to the oxygen side, so that it interacts anisotropically with cation through the strong coulombic attraction[1]. The purpose of the present study was to elucidate the structure of molten alkali hydroxides by means of neutron diffraction. In a previous study,[2] neutron diffraction measurement was successfully carried out for highly corrosive NaOD melt using a nickel metal cell.

In this work, the KOD sample was prepared from the commercially available aqueous solution(CEA; 98.5 mol% D) and heavy water of high purity(Wako Pure Chem. Ind., Ltd., Osaka; 99.5 mol% D) in a similar procedure to that for NaOD.[2] The purity of the prepared sample was about 99.5 mol% D. Lithium-7 deuteroxide (^{7}LiOD) was prepared from $^7LiOH{\cdot}H_2O$ (Tomiyama Chemical Co., Ltd., Tokyo; 99.95 mol% ^{7}Li) and the heavy water. The ^{7}LiOH melt was decomposed to $^7Li_2O$ by heating it to 950 K in an alumina crucible under vacuum(ca. 1600 Pa). The obtained $^7Li_2O$ was dissolved into D_2O in a stainless steel dry box filled with dried nitrogen gas.

Figure 1 shows the obtained total structure functions for molten MOD(M=^{7}Li, Na, and K) at 773 K. The first peak for ^{7}LiOD was single and intense, while the first peaks for NaOD and KOD split into doublet. It was shown by MD calculation for molten LiOH[3] that the first peak of ^{7}LiOD is mainly based on long ranged O-O correlation.

The $Q{\cdot}i(Q)$'s oscillate nearly sinusoidally at $Q > 0.13$ pm^{-1} in all the cases. At large Q, the intraionic O-D correlation is predominant in the $Q{\cdot}i(Q)$'s. The $Q{\cdot}i_{intra}(Q)$ of the Debye equation for the intraionic O-D correlation was optimized to the experimental data in the Q range from 0.13 pm^{-1} to the Q_{max} using a least squares method. Table 1 shows the optimized parameters of r_{OD}, n_{OD} and l_{OD}. This result shows that the difference in the intraionic O-D distances among these melts was within the experimental error. The intraionic Debye structure functions obtained are also shown in Fig. 1. The values of n_{OD}'s obtained from the Debye equation are reasonable and consistent with the values calculated from the integration of the intraionic O-D correlation in the $G^n(r)$'s.

The $G^n(r)$'s of ^{7}LiOD, NaOD, and KOD calculated with a Riemann window function are shown in Figs. 2(a), (b), and (c), respectively. Each maximum peak at about 100 pm can clearly be assigned to the intraionic O-D correlation. The peaks at smaller r should be caused by the truncation of the Fourier transformation at a finite value.

The most probable Li-O distance was 194 pm, which could reasonably be assigned by taking account of the Li-O distance being 198 pm in the crystal. This is also supported from the result of MD calculation.[3] According to analogous consideration, the peaks observed at 242 and 279 pm for NaOD and KOD are assigned mainly to the Na-O and K-O correlation, respectively. The coordination number could not definitely be determined because there exists some overlap with other atom-atom correlations. The r_{MO}'s are plotted in Fig. 3 against the ionic radii of cations

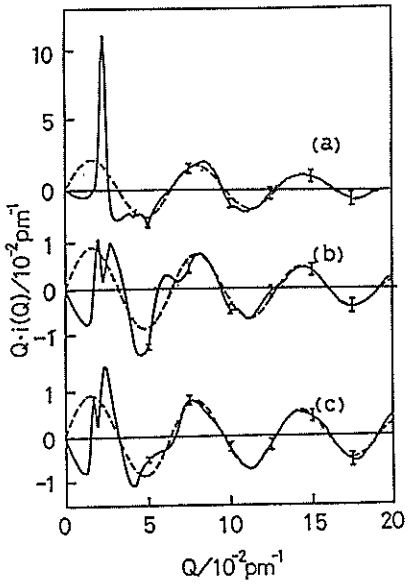

Fig. 1 Structure function $Q{\cdot}i(Q)$ for molten hydroxides at 773K. (a), (b) and (c) refer to ^{7}LiOD, NaOD and KOD, respectively. ——— ; experimental, – – – – ; $Q{\cdot}i_{intra}(Q)$ derived from the Debye equation.

Table 1. Comparison of parameters from real space for the intraionic O-D correlation and from reciprocal space for the M-O correlations in molten alkali hydroxides at 773 K.

system	r_{OD}/pm	n_{OD}	l_{OD}/pm	r_{MO}/pm	r_M/pm
^{7}LiOD	97±1	0.95±0.10	8.2±0.5	194±10	59(IV)
NaOD	98±1	0.99±0.10	7.7±0.5	242±5	102(VI)
KOD	98±1	1.02±0.10	6.7±0.5	279±5	138(VI)

The values in parentheses denote the coordination number in the crystals.

r_M[4], which are presented in Table 1. This plot shows a straight line with a slope of unity. This suggests that the OD^- ion has an effective ionic radius of 139 pm(the intersection of the ordinate in Fig. 3) in these melts.

The interionic distances of nearest-neighobour ions of an unlike sign can be determined by the cation size and the effective oxygen size in the melts. In this respect, it is interesting to investigate other oxyanion systems such as nitrates and carbonates. From the finding that the OD^- ion has an effective ionic radius in these melts, it may be inferred that the cation coordinate to OD^- ion on the O atom side also in NaOD and KOD melts. On the other hand, no distinct M-D correlation

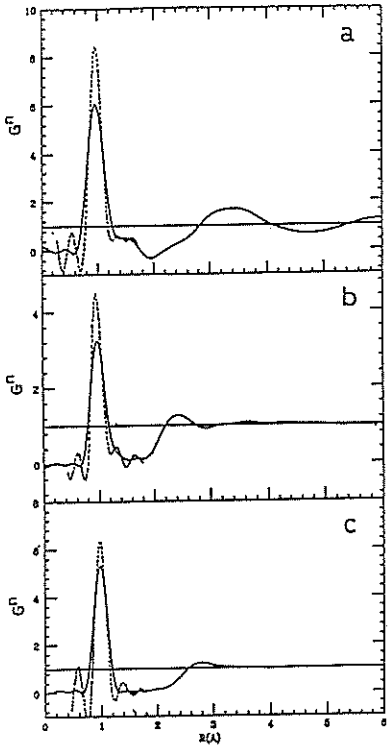

Fig. 2 Radial distribution functions $G^n(r)$ for molten alkali hydroxides at 773K. (a), (b), and (c) refer to ^{7}LiOD, NaOD, and KOD, respectively. ——— ; with a Riemann window, – – – –; without any window.

was observed for NaOD or KOD because of a much greater overlap with other atom-atom correlations. A negative "peak" at r = 250 pm for LiOD may reasonably correspond to Li-D correlation for neighobouring Li^+ and OD^- ions. However, it cannot be distinguished clearly from a Fourier truncation noise.

The $G^n(r)$ for ^{7}LiOD shows oscillatory behaviuor at r > 300 pm, while such behaviour is not observed for NaOD or KOD. This is traceable to the single and intense peak at Q = 0.023 pm^{-1} in reciprocal space for ^{7}LiOD. According to the result of MD calculation, the oscillatory behaviour in real space was also found and assigned to O-O correlation. For the present $G^n(r)$, there is a marked difference in the long range correlation between ^{7}LiOD and the others. There seems to exist a slight correlation around 150 pm in the $G^n(r)$ of ^{7}LiOD melt. This may represent D-D correlation, although large ghost peaks prevent from further analysis.

In order to examine each correlation in more detail, an isotope substitution method is required from an experimental point of view.

References

1) S. Okazaki and I. Okada, J. Chem. Phys. 90, 5595 (1989)
2) N. Ohtori, S. Okazaki, O. Odawara, I. Okada, T. Fukunaga, and M. Misawa, J. Phys. Condensed Matter, 2(1990), in press
3) S. Okazaki, N. Ohtori, and I. Okada, J. Chem. Phys. 92, 7505(1990)
4) R. D. Shannon, Acta. Cryst. A32, 751(1976)

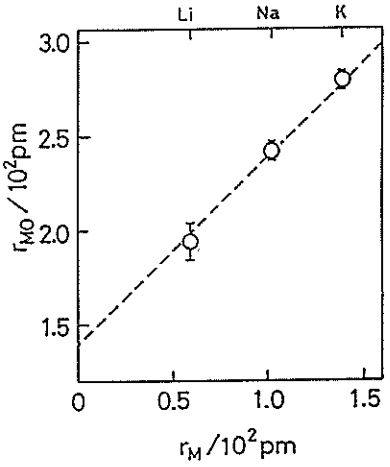

Fig. 3 Plot of the M-O distance r_{MO} vs. cation radius r_M. The dashed line is the best fit one to the plot with a slope of unity.

Structure of a Molten $0.80RbNO_3$-$0.29Sr(NO_3)_2$ Mixture

T. KAMIYAMA, K. SHIBATA, T. FUKUNAGA*, K. SUZUKI and M. MISAWA**

Institute for Materials Research, Tohoku University, Sendai 980, Japan
*Department of Crystalline Materials Science, Nagoya University, Nagoya 464, Japan
**National Laboratory for High Energy Physics, 1-1 Oho, Tsukuba 305

Many researches have been performed on the study of glass transition.[1] Some of alkali nitrate and alkaline earth nitrate mixtures are simple ionic-glass forming systems, and especially the Ca-K-NO_3 system has been studied by many methods.[2] But the neutron scattering length of a Ca atom and that of a K atom are different from each other, so the neutron scattering results are difficult to interpret.

In this study we used a mixture of $RbNO_3$ and $Sr(NO_3)_2$ as a melt sample (Figure 1). The $RbNO_3$-$Sr(NO_3)_2$ system is known to be vitrified in the range of 69 ~ 83 mol% $RbNO_3$ by melt-quenching.[4] In the neutron scattering experiment this system is regarded as a pseudo-binary system of metal cations and nitrate anions, because coherent neutron scattering lengths for Rb and Sr were almost equal and their ionic radii are close to each other (Table 1). The subject of this study was to obtain temperature dependence of the static structure factor S(Q) previous to neutron quasielastic scattering experiments.[5]

The mixed nitrate of $0.80RbNO_3$-$0.20Sr(NO_3)_2$ corresponding to an eutectic composition was prepared as a sample. The specimen in the shape of powders was dried in vacuum at 100°C to 150°C for one day before making it melt because of its extremely hygroscopic nature. DSC analysis shows that the glass transition and solidification temperature of the melt are about 70°C and 200°C, respectively.

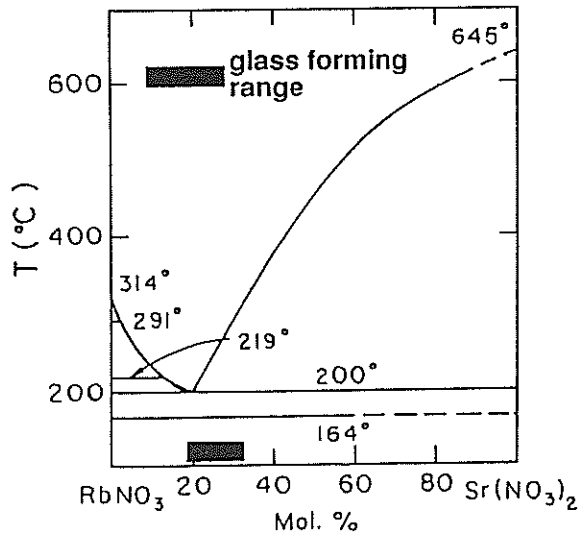

Figure 1. The phase diagram for $RbNO_3$-$Sr(NO_3)_2$.[3]

Table 1. Scattering cross sections and ionic radii for each atom in the sample.

	atomic weight	σ_{coh} ($10^{-24}cm^2$)	σ_{inc} ($10^{-24}cm^2$)	r ion (Å)
Rb	85.4678	6.299	0.001	1.49(1+)
Sr	87.62	6.19	0.03	1.27(2+)
N	14.0067	10.869	0.63	——
O	15.999	4.2346	0.0	——

The S(Q)'s measurements of the melt were directly observed as a function of temperature by

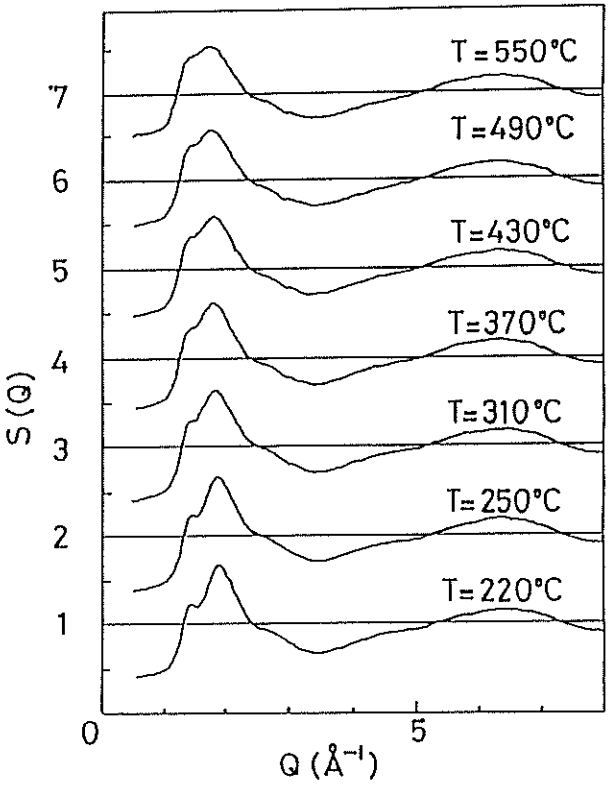

Figure 2. Measured structure factors for molten $0.80RbNO_3$-$0.20Sr(NO_3)_2$ mixture.

using HIT instrument. The measured temperature range was 220°C ~ 550°C on cooling. For these experiments the sample was sealed into a quartz glass cylindrical cell (8 mm in inner diameter, 40 mm in length) in a vacuum. The measurement times for each S(Q) were about 4.5 hours. Figure 2 shows the measured S(Q)'s. The width of the first peak and of the prepeak become broader with increasing temperature. We can write the expression of S(Q) as

$$S(Q)=F_1^{NO3}(Q)+S^{ion}(Q) \qquad (1)$$

where $F_1^{NO3}(Q)$ is a interionic structure factor from a nitrate ion and $S^{ion}(Q)$ is a intraionic structure factor from ion-ion interference terms. In the high-Q region, the interionic structural contribution is very small, so the oscillating S(Q) pattern comes from the contribution of intraionic structure. We determined the interionic parameters of the nitrate ion by using the high-Q region ($Q > 7Å^{-1}$) of S(Q). Figure 3 shows the temperature dependence of the parameters which determine the structure of a nitrate ion. These parameters are in good agreement with the reference 6 which determined for some alkali nitrate melts. At each temperature the nitrate ion is shaped almost a flat equilateral triangle and interatomic distance of N-N

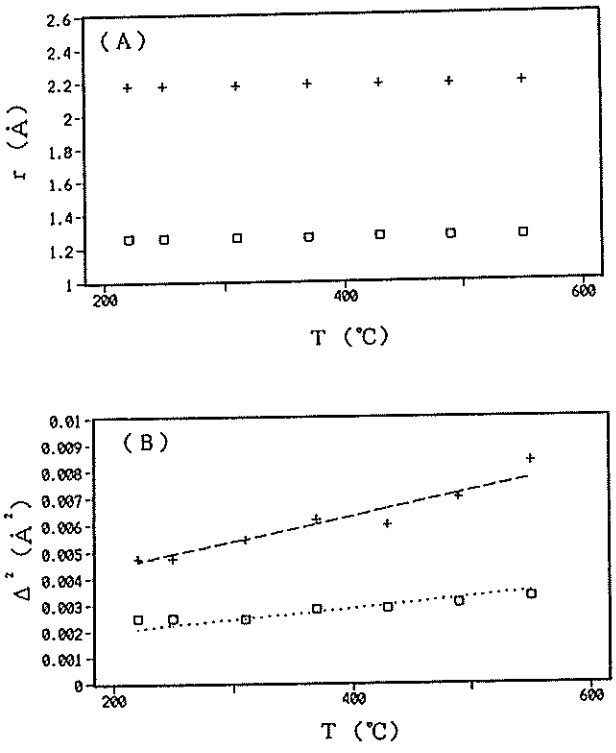

Figure 3. Temperature dependence of parameters that determine a nitrate ion structure.
(A) Atomic distance of O-O (+) and N-O (□)
(B) Mean square displacement for O-O (+) and N-O (□)

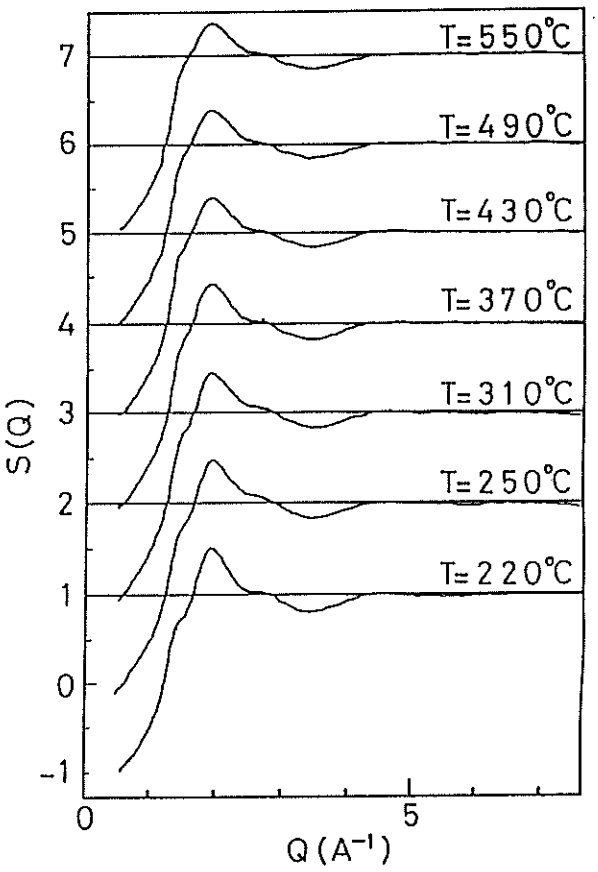

Figure 4. Interionic structure factors for molten $0.80RbNO_3$-$0.20Sr(NO_3)_2$ mixture.

and N-O are not changed. But mean square displacement for N-N and N-O are increased with increasing temperature. The interionic structure factors obtained by subtracting $F_1^{NO3}(Q)$ from S(Q) are showed in Figure 4. The interionic correlation appears in $Q<4.5$ Å^{-1} and the temperature dependence of this part is not so strong.

REFERENCES

1) J. Jäckle, Philos. Mag. B 56 (1987) 113.
2) F. Mezei, Springer Proceeding in Physics vol. 37 (Springer-Verlag Berlin, Heidelberg 1989).
3) V.E. Plyushcev, I.B. Markina and L.P. Shklover, Zhur. Neorg. Khim. 1 (1956) 1613.
4) E. Thilo, C. Wieker and W. Wieker, Silikattechn. 15 (1964) 109.
5) K. Shibata, T. Kamiyama, K. Suzuki and K. Inoue, J. Non-Cryst. Solids 117/118 (1990) 120.
6) T. Yamaguchi, I. Okada, H. Ohtaki, M. Mikami and K. Kawamura, Molec. Phys. 58 (1986) 349.

Temperature Effect on the Intramolecular Structure of a Water Molecule in Liquid Water at High Temperatures

K. ICHIKAWA, Y. KAMEDA,+ T. YAMAGUCHI,* H. WAKITA* and M. MISAWA**

Department of Chemistry, Faculty of Science, Hokkaido University, Sapporo 060
*Department of Chemistry, Fukuoka University, Nanakuma, Jonan-ku, Fukuoka 814-01
**National Laboratory for High Energy Physics, Oho, Tsukuba 305

Time-of-flight neutron diffraction measurements were carried out on liquid water at high temperatures. The data for the high-Q region observed at the high scattering angle ca. 90° have been analysed in terms of intramolecular interference, including an inelasticity correction,[1] to determine the temperature dependence of the intramolecular distances of a water molecule, r_{OD} and r_{DD} between 25 and 200 °C. In a region of sfficiently high Q ($40>Q>14$ Å^{-1}) the total interference cross section can be regarded as a contribution from the intramolecular interference function, which determines the structure of a molecule. The diffraction data for a large scattering angle have a great advantage because of their wide Q-range. A least-squares fit to the experimental total interference cross section gives two intramolecular distances r_{OD} and r_{DD}. Since the observed total scattering cross section includes uncertainties in the evaluation of the multiple-scattering correction and the overall normalisation factor, it is difficult to obtain the interference terms by subtracting the calculated self-term from the total scattering cross section.

The interference term was obtained by following the procedure described below.

(i) Calculated approximate values of $(d\sigma/d\Omega)_{int}^{intra}$ by using the initial approximate values of r_{OD}, r_{DD} and A. The normalisation constant A has been chosen to normalise the observed intramolecular interference function to give proper coordination values and proper values of the coherent scattering length b_i for the water molecule. The other parameters, such as the RMS amplitudes l_{OD} and l_{DD}, are taken from the spectroscopic data for pure D_2O.

(ii) Subtract $(d\sigma/d\Omega)_{int}^{intra}$ from the observed total scattering cross section to yield the difference $\Delta(Q)$.

(iii) Smooth the $\Delta(Q)$ obtained in (ii) to remove all the oscillation associated with high frequency, resulting form uncertainty in the parameters r_{OD}, r_{DD} and A. The smoothed $\Delta(Q)$ can be regarded as the self-term because of the very small contribution from $(d\sigma/d\Omega)_{int}^{inter}$ in the high-Q region.

(iv) Subtract $(d\sigma/d\Omega)_{self}$ obtained in (iii) from the total scattering cross section to obtain $(d\sigma/d\Omega)_{int}^{intra}$ for $40>Q>14$ Å^{-1}.

(v) Determine r_{OD}, r_{DD} and A from a

least-square fit of $(d\sigma/d\Omega)_{int}^{intra}$. Repeat the procedures from (i)to (v) until there is no change in the parameters and the square sum of the residue is minimised. The best-fit results for the intramolecular interference terms are shown as follows: the self-terms evaluated are sufficiently smooth for our purposes and do not show any oscillations. An excellent agreement between the experimental and calculated molecular interference terms at 25, 50, 75, 100, 150 and 200 ℃ proves the validity of our inelasticity correction evaluation.[1] The table 1 shows the temperature dependenc of the final structural papameters of D_2O molecules determined by a least- squares fit. The values r_{OD} and r_{DD} remain unchanged as termperature is varied in the range between 25 and 200 ℃, within experimental error: r_{OD}=0.970 ± 0.003 Å and r_{DD}=1.556 ± 0.007 Å. The limits of error are estimated to be 2.58 times the standard deviation (cited in table 1) in least-squares fitting.

References

1) K. Ichikawa and Y. Kameda, J.Phys. Condens. matter 1, 257(1989).

+ Present address: Department of Chemistry, Faculty of Science, Yamagata University, yamagata 990

Table 1. Temperature dependence of intramolecular distances of a D_2O molecule in liquid water. The values in parentheses stand for the limits of the standard deviation.

Temp/ ℃	25	50	75	100	150	200
r_{OD}/Å	0.970(1)	0.970(1)	0.970(1)	0.970(1)	0.970(1)	0969(1)
r_{DD}/Å	1.555(3)	1.563(3)	1.554(3)	1.556(3)	1.555(4)	1.558(3)
A/b sr^{-1}	1.002(8)	1.001(9)	0.990(9)	0.999(9)	0.990(10)	0.975(9)

Structure of Liquid Water in Porous Silica in the Undercooled State

T. Yamaguchi, Y. Kato, H. Wakita, and M. Misawa†

Department of Chemistry, Fukuoka University, Nanakuma, Jonan-ku, Fukuoka 814-01
†National Laboratory for High Energy Physics, Oho, Tsukuba 305

The structure and properties of liquid water in micropores are essential in understanding the function and mechanism of chemical reactions in porous materials and of biological reactions in a living cell. Previously, we reported the structure of liquid D_2O in porous silica with an inner diameter of 30 and 100 Å at room temperature.[1] When the temperature is lowered, liquid water in micropores is undercooled and thus may be a model of non-freezing water in a biological cell.

In the present study, we perform neutron diffraction measurements of liquid D_2O in porous silica at subzero temperatures to investigate the structural change in undercooled water. The dynamic properties of liquid water in the porous silica have also been studied by the incoherent quasi-elastic neutron scattering using LAM40 spectrometer (see this report).

Porous silica, Develosil 30, was purchased from Nomura Chemicals. Develosil 30 has an inner diameter of 30 Å. The silica was filled with deuterium oxide up to about 80% of the pore volume by a evaporation method. The filling percentage was checked by thermal analysis. The neutron scattering measurements were made at 2, -15, -30, -50, and -80 °C both for silica samples containing D_2O. Dry silica was also measured at room temperature.

The scatterings from liquid D_2O in the silica were obtained by subtracting the scattered intensities of the dry silica from those of the D_2O filled silica. In order to clarify the change in structure the difference structure factors were derived on the basis of that measured at 2 °C.

Figure 1 shows the difference radial distribution functions at -15, -30, -50, and -80 °C. Apparently the structure of liquid water, particularly the long-range ordering, is enhanced with decreasing temperature. The peak at 1.8 Å, assigned to the hydrogen bonded O...D interactions, increases when the temperature is lowered; this result clearly demonstrates an increase in the number of hydrogen-bonds in liquid water. DSC measurements of Develosil 30 filled with light water showed two exothermic peaks at -36.1 and -39.5 °C, indicating two different types of freezing of liquid water in the pores. However, no typical Bragg patterns owing to ice formation were observed in the difference structure factors at the temperatures measured. This fact may be interpreted in terms of either the formation of amorphous ice, or irregular three dimensional network of ice formed in the small pores.

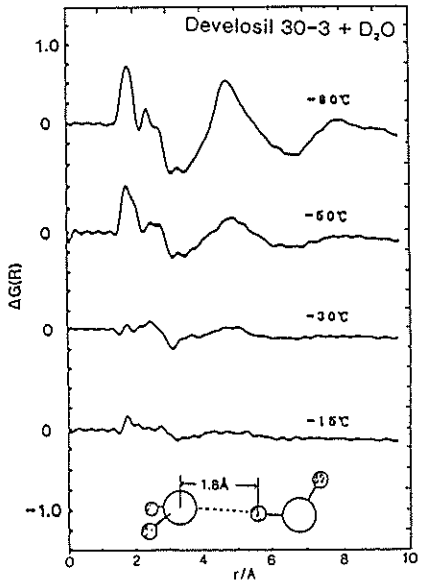

Fig. 1 The difference G(r) obtained for liquid D_2O in Develosil 30 for various temperatures.

References

1) T. Yamaguchi, N. Suehiro, H. Wakita, and M. Misawa, KENS Report, 7, 50 (1988).

Hydration of Lanthanide(III) Ions in Aqueous Perchlorate Solutions

T. Yamaguchi, S. Tanaka, H. Wakita, M. Misawa*, I. Okada†,
A. K. Soper‡, and W. S. Howells‡

Department of Chemistry, Fukuoka University, Nanakuma, Jonan-ku, Fukuoka 814-01
*National Laboratory for High Energy Physics, Oho, Tsukuba 305
†Department of Electronic Chemistry, Tokyo Institute of Technology,
Nagatsuta, Midori-ku, Yokohama 227
‡Rutherford Appleton Laboratory, Chilton, Didcot, Oxon, OX11 0QX, UK

Recently, the hydration number of a series of lanthanide(Ⅲ) ions has been a subject of controversy among coordination chemists, in particular, whether or not the hydration number of the lanthanide(Ⅲ) ions changes from the light to heavy ions. In a previous paper,[1] we reported the structure of hydrated Yb(Ⅲ) and Tm(Ⅲ) ions in perchlorate solutions. In the present study, we have further investigated the hydration of Tb(Ⅲ), Dy(Ⅲ), Pr(Ⅲ), and Nd(Ⅲ) ions in aqueous perchlorate solutions by the neutron diffraction method combined with isomorphous substitution.

Sample solutions were prepared by dissolving the corresponding metal oxides into aqueous perchloric acid, which had been deuterated by repeated substitution with heavy water. In order to prevent the hydrolysis of the metal ions a small amount of deuterated perchloric acid was added into the solutions. The sample solutions of each isomorphous pairs were prepared so that the concentrations of constituents are the same in the two solutions as given in Table 1. Neutron diffraction measurements were performed on HIT for solutions of Tb(Ⅲ) and Dy(Ⅲ) ions, but on LAD for solutions of Pr(Ⅲ) and Nd(Ⅲ) ions. The sample solution was contained in a Ti-Zr cell of an inner diameter of 8 mm. The data were corrected for absorption and multiple scattering and then normalized using the data of a vanadium rod.

A difference $\Delta_M(Q)$ between the structure factors of $M(ClO_4)_3$-D_2O and $M'(ClO_4)_3$-D_2O solutions can be written in the form

$$\Delta_M(Q)=A[S_{HD}(Q)-1]+B[S_{ND}(Q)-1]+C[S_{HCl}(Q)-1]+D[S_{HH'}(Q)-1$$

$A=2C_DC_Hb_D\Delta b_H$, $B=2C_DC_Nb_D\Delta b_N$,

$C=2C_{Cl}C_Hb_{Cl}\Delta b_H$, $D=2C_H^2(b_H^2-b_{H'}^2)$,

$Q=4\pi\sin\theta/\lambda$, $\Delta b_M=b_M-b_{M'}$

Table 1 The compositions and important parameters of aqueous lanthanide(Ⅲ) perchlorate solutions

Solutions	Pr	Nd	Tb	Dy	Tm	Yb
b(M) (10^{-12} cm)	0.445	0.769	0.738	1.69	0.705	1.24
Ionic radius (Å)	1.09	1.08	1.00	0.99	0.95	0.94
Concentration (mol dm^{-3})						
M^{3+}	2.56	2.51	1.98	1.98	2.56	2.54
D^+	0.0788	0.0753	3.03	3.04	0.0773	0.0776
ClO_4^-	7.76	7.61	8.97	8.98	7.76	7.70
D_2O	37.4	36.4	36.5	36.6	40.0	39.7
Density (atoms $Å^{-3}$)	0.0926	0.0903	0.0956	0.0962	0.0972	0.0964

where C_i is the atomic fraction of atom i and b_i its scattering length. The reduced correlation function is then given by

$$G_H(r)=(2\pi^2 r\rho)^{-1}\int Q\,\Delta_H(Q)\exp(-0.003Q^2)\sin(Qr)dQ$$

The data of aqueous solutions of Pr(Ⅲ) and Nd(Ⅲ) ions were analyzed by the maximum entropy method.

Figures 1, 2, and 3 show, respectively, the reduced correlation functions for aqueous perchlorate solutions of Pr(Ⅲ) and Nd(Ⅲ) ions, of Tb(Ⅲ) and Dy(Ⅲ) ions, and of Yb(Ⅲ) and Tm(Ⅲ) ions. In all reduced correlation functions, two distinct peaks are observed; the first one is assigned to the M-O bonds and the second one to the M-D interactions within the hydrated lanthanide(Ⅲ) ions. On the basis of the known structure of a D_2O molecule the tilt angle was calculated. The hydration number was calculated from the integration of the M-O and M-D peaks according to

$$N=C_a\rho\int 4\pi r^2 g_{Ma}(r)dr.$$

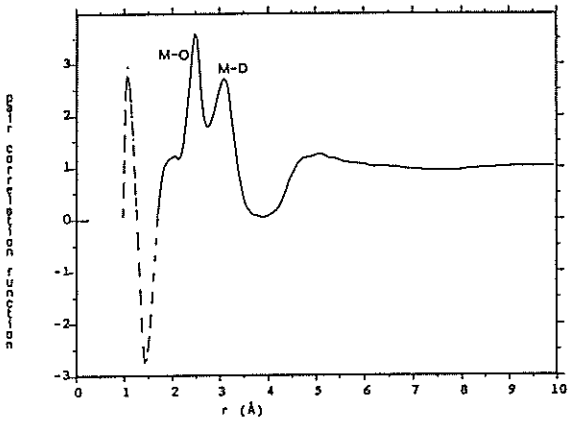

Fig. 1 The reduced correlation function for solutions of Pr(Ⅲ) and Nd(Ⅲ) ions.

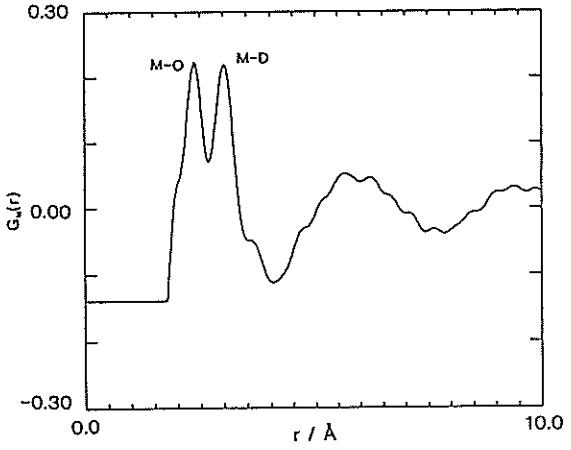

Fig. 2 The reduced correlation function for solutions of Tb(Ⅲ) and Dy(Ⅲ) ions.

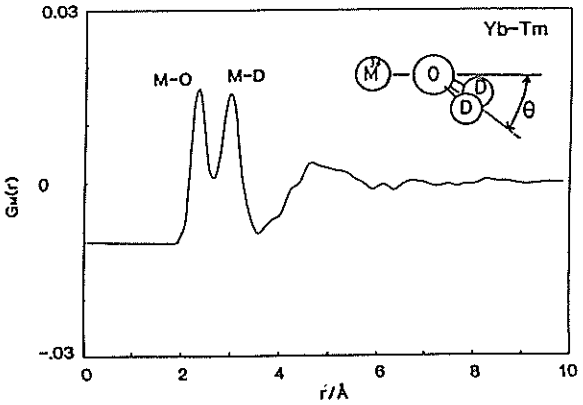

Fig. 3 The reduced correlation function for solutions of Tm(Ⅲ) and Yb(Ⅲ) ions.

The final results obtained in the present works are summarized in Table 2 with those reported by other techniques. The present results have confirmed that the change in the hydration number occurs from the light to heavy lanthanide(Ⅲ) ions in the aqueous solutions. As seen in Table 2, in the case of lanthanide(Ⅲ) ions the isomorphous substitution method works within the experimental uncertainties as well as the isotopic substitution technique.

References

1) S. Tanaka, T. Yamaguchi, H. Wakita, and M. Misawa, KENS Report, 7, 49 (1988).

2) B. K. Annis, R. L. Hahn, and A. H. Narten, J. Chem. Phys., 82, 2086 (1985).

3) A. H. Narten and R. L. Hahn, J. Phys. Chem., 87, 3193 (1983).

4) A. Habenschuss and F. H. Spedding, J. Chem. Phys., 70, 3758 (1979).

5) A. Habenschuss and F. H. Spedding, J. Chem. Phys., 70, 2797 (1979).

6) G. Johansson and H. Wakita, Inorg. Chem., 24, 3047 (1985).

7) T. Yamaguchi, M. Nomura, H. Wakita, and H. Ohtaki, J. Chem. Phys., 89, 5153 (1988).

8) C. Cossy, A. C. Barnes, J. Enderby, and A. Merbach, J. Chem. Phys., 90, 3254 (1989).

Table 2 The structure of hydrated lanthanide(Ⅲ) ions in aqueous solutions. r is the interatomic distance, N the hydration number, θ the tilt angle.

System	r(M-O) / Å	r(M-D) / Å	N	θ / °	Method	Reference
Pr^{3+}/Nd^{3+}	2.48	3.14	10	22	neurton	This work
Nd^{3+}	2.479	3.129	8.4	25	neutron	Ref.3
Nd^{3+}	2.513		8.90		X-ray	Ref.4
Nd^{3+}	2.51		9.5		EXAFS	Ref.7
Pr^{3+}	2.539		9.22		X-ray	Ref.4
Tb^{3+}/Dy^{3+}	2.39	3.08	9	10	neutron	This work
Dy^{3+}	2.370	3.042	7.4	18	neutron	Ref.2
Dy^{3+}	2.396		7.93		X-ray	Ref.5
Tb^{3+}	2.409		8.18		X-ray	Ref.5
Tb^{3+}	2.40		8.0		X-ray	Ref.6
Dy^{3+}	2.39	3.03	7.9	29	neutron	Ref.8
Tm^{3+}/Yb^{3+}	2.33	3.02	8	12	neutron	This work
Tm^{3+}	2.358		8.12		X-ray	Ref.5
Tm^{3+}	2.33		8.0		EXAFS	Ref.7
Yb^{3+}	2.32	2.98	7.8	24	neutron	Ref.8

The Intramolecular Structure of a Water Molecule in Hydrated and Incompletely Hydrated LiCl Solutions

K. ICHIKAWA and Y. KAMEDA

Department of Chemistry, Faculty of Science, Hokkaido University, Sapporo 060

Time-of-flight neutron diffraction measurements were carried out on the hydrated and incompletely hydrate solutions $(liCl)_x(D_2O)_{1-x}$ for x = 0.20, 0.27, 0.32 and 0.35. The data for the high-Q region observed at the high scattering angle ca. 91° have been analysed in terms of intramolecular interference, including an inelasticity correction, to determine the intramolecular distances of a water molecule, r_{OD} and r_{DD}. Here, the best-fit results for intramolecular interference terms are shown as follows: the self-terms evaluated are sufficiently smooth for our purposes and do not show any oscillations. An excellent agreement between the experimental and calculated intramolecular interference terms for 20, 27, 32 and 35 mol% LiCl proves the validity of our inelasticity correction evaluation. The table 1 shows the composition dependence of the final structural parameters of D_2O molecules determined by a least-squares fit. The distance r_{OD} shows no composition dependence within experimental error; the distance r_{OD}=0.970 ± 0.006 Å is equal to that in pure D_2O. On the other hand, the distance r_{DD}=1.59 ± 0.02 Å in the solutions with above 20 mol% LiCl is 0.04 Å longer than that of liquid D_2O because of the strong interaction between the D_2O molecule and the ions. The limits of error are estimated to be 2.58 times the standard deviation (cited in table 1) in least-squares fitting. The conclusion reached in this work suggests that the results of the moleculardynamics simulation are not reasonalbe.

*) This article has been appeared in J. Phys.: Condens. Matter 1 (1989) 257-266, in which the references should be cited.

Table 1. Intramolecular distances of a D_2O molecule in $(LiCl)_x(D_2O)_{1-x}$ solutions at 125 °C. The values in parentheses stand for the limits of the standard deviation.

X	0.20	0.27	0.32	0.35
r_{OD}(A)	0.970(2)	0.971(2)	0.970(2)	0.971(2)
r_{DD}(A)	1.59(1)	1.58(1)	1.59(1)	1.58(1)
A(b sr^{-1})	0.40(1)	0.41(1)	0.39(1)	0.40(1)

For pure liquid water (i.e., x=0) r_{OD}=0.970(1) Å and r_{DD}=1.55(1) Å

Structure of Concentrated Lithium Nitrate Solutions

T. Yamaguchi, S. Tanaka, H. Wakita, and M. Misawa†

Department of Chemistry, Fukuoka University, Nanakuma, Jonan-ku, Fukuoka 814-01
†National Laboratory for High Energy Physics, Oho, Tsukuba 305

Hydrate melts, which are classified between aqueous solutions and anhydrous molten salts, have recently attracted the attention of people in the fields of both fundamental and applied chemistry; interest includes the basic physico-chemical properties of the solutions, crystallization of the salts, supercooling of the solutions, and various technological applications in thermal energy storage. Since the ion-water and ion-ion interactions play an key role in the hydrate melts, it is very important to investigate the ionic hydration and ion-ion correlation in the hydrate melts at a molecular level for understanding the physico-chemical properties of the hydrate melts.

In the preset study the neutron first-order difference method using lithium and nitrogen isotopes is applied to an 8.6 mol dm^{-3} D_2O solution of lithium nitrate to elucidate the hydration structure of lithium and nitrate ions and the ion-ion correlation.

Aqueous lithium nitrate solutions with six different isotopic compositions were prepared from a reaction of lithium carbonate and nitric acid. Table 1 shows the compositions and important parameters of the solutions. Solutions (C) and (D) were prepared so that the scattering length of an atom of interest in the solutions becomes a half of the sum of the scattering lengths of two isotopic pairs. Neutron scattering measurements were performed at room temperature on the HIT instrument. The sample solutions were contained in a Ti-Zr null alloy cell with an inner diameter of 8 mm.

The first-order difference method was applied to solutions (B)-(A) for lithium ion hydration, and to solutions (B)-(F) for nitrate ion hydration. The second-order difference method was employed to derive the lithium ion - lithium ion and nitrate ion - nitrate ion interactions by taking the difference of (A)+(E)-2x(D) and of (A)+(B)-2x(C),

Table 1 The compositions and important parameters for the sample solutions investigated.

Solutions	A	B	C	D	E	F
b(Li) (10^{-12}cm)	-.2218	0.0000	-.1109	-.2218	-.2218	0.0000
b(N) (10^{-12}cm)	0.9359	0.9539	0.9359	0.7913	0.6466	0.6466
Concentration (mol dm^{-3})						
$LiNO_3$	8.644	8.615	8.635	8.657	8.704	8.675
D_2O	40.33	40.28	40.31	40.27	40.18	40.04
Density (atoms $Å^{-3}$)	0.09889	0.09869	0.09882	0.09882	0.09882	0.09845

(A)--- ^{7}Li $^{Nat}NO_3$ + D_2O (D)--- $^{7}Li^{Nat-15}NO_3$ + D_2O

(B)--- ^{6}Li $^{Nat}NO_3$ + D_2O (E)--- ^{7}Li $^{15}NO_3$ + D_2O

(C)--- ^{6-7}Li $^{Nat}NO_3$ + D_2O (F)--- ^{6}Li $^{15}NO_3$ + D_2O

respectively.

Figure 1 shows the $G_{Li}(r)$ obtained for solutions (B)-(A). The first and second peaks are ascribed to lithium-oxygen and lithium-hydrogen interactions within the hydrated lithium ions in the solutions. The sharp peak clearly demonstrates that water molecules are firmly bonded to a central lithium ion in the solutions. A broad peak appears at 4.0 - 6.0 Å probably arises from the second hydration shell of the lithium ion.

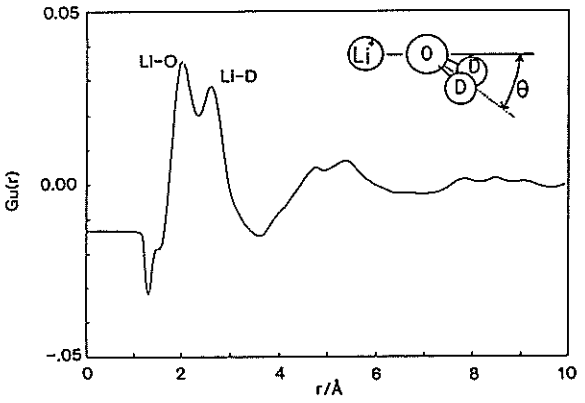

Fig. 1 The values of $G_{Li}(r)$ obtained for solutions (A) and (B).

Figure 2 shows the $G_N(r)$ for solutions (B)-(F). The first predominant peak at 1.25 Å is assigned to the nitrogen-oxygen bonds within a nitrate ion. The very symmetric peak indicates the regular triangular structure of nitrate ion in the solutions. Small, broad peaks around 2.8 and 3.8 Å originate from the interactions between a nitrate ion and the nearest neighbor water molecules; they are attributed to the N...O and N...D interactions, respectively. The very broad peak for nitrate ion is in marked contrast with that for lithium ion, showing a very weak hydration of the nitrate ion. However, the presence of the N...O and N...D peaks suggests some preferred orientation of bound water molecules around a nitrate ion.

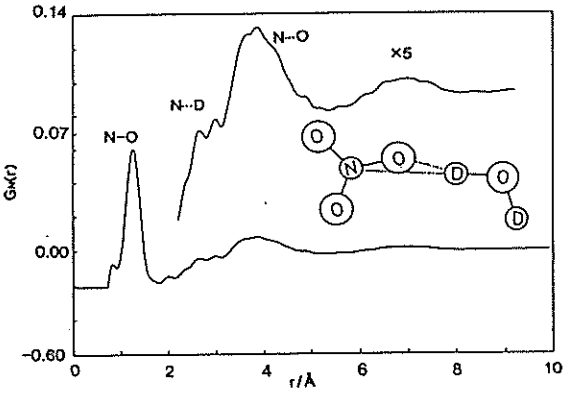

Fig. 2 The values of $G_N(r)$ obtained for solutions (B) and (F).

Figure 3 shows the $G_N(r)$ obtained from the second order difference for solutions (A), (E), and (D). The first peak centered at 3.8 Å appears, which should be assigned to $N(NO_3^-)...N(NO_3^-)$ interactions. However, since the values of $G_N(r)$ are very small (see the scale of ordinate), a more careful investigation of the peak will be necessary. For this purpose a computer simulation of the same system is now

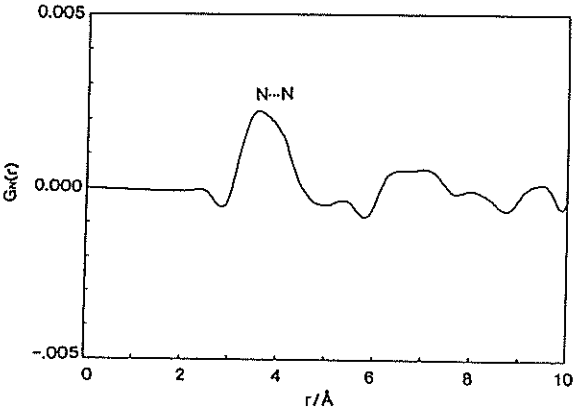

Fig. 3 The values of $G_N(r)$ obtained for solutions (A), (B), and (C).

in progress.

It was not successful to elucidate the lithium ion - lithium ion correlation from the present data because of a very small difference in the scattering lengths. Final results on structural parameters are summarized in Table 2.

Table 2 Structural parameters obtained for 8.6 mol dm^{-3} aqueous lithium nitrate solutions. r is the interatomic distance, N the hydration number, and θ the tilt angle.

	r/Å	N	θ
Li-O	1.98±0.01		
Li-D	2.61±0.03	5 ±1	37°±9°
N -O	1.26±0.01	3.1±0.1	
N…D	~2.8		
N…O	~3.8		
N…N	3.8 ±0.2		

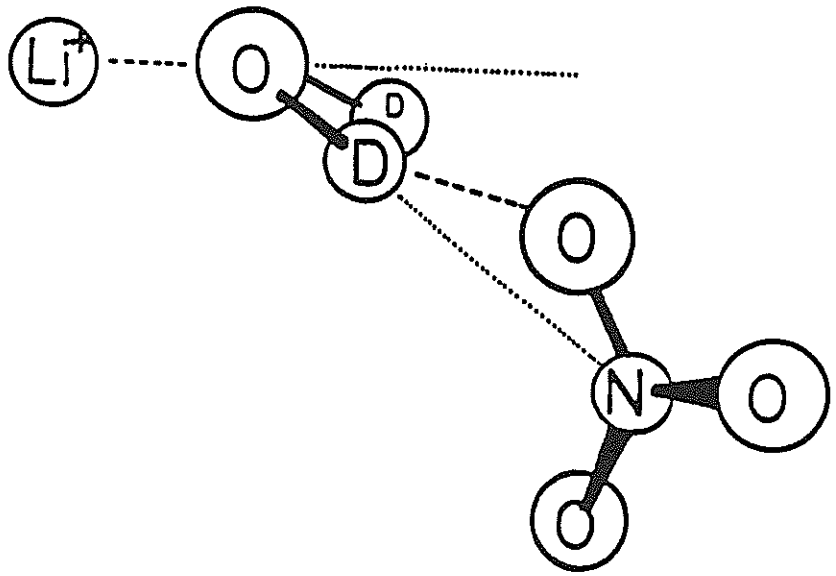

The Hydration Structure around the Nitrate Ion in Concentrated Aqueous Solution

Y.KAMEDA, K.HANGAI and O.UEMURA.

Department of Chemistry, Faculty of Science, Yamagata University, Yamagata 990 Japan.

The hydration structure of poly-atomic anion has long been a matter of interest. However, the definitive informations cannot be supplied from a single diffraction measurement according to the followings, a) the ion-water contribution in the total interference function is generally small, b) since the scattering power of atoms in anion (typically, O, N or Cl) are comparable to that in water molecule, it is difficult to discriminate the anion-water interaction, c) the distribution of water molecules around the poly-atomic anion tends to be broadened compared with the case of cation-water correlation. The neutron diffraction with isotopic substitution method can overcome these difficulties.

In this paper, we report the result of TOF neutron diffraction measurements on D_2O solutions including 10 mol% $NaNO_2$ with two kinds of nitrogen isotope. We have obtained direct experimental information on the hydration structure around NO_2^-.

Two 10 mol% $NaNO_2$ aqueous solutions with different isotopic composition of nitrogen were prepared by dissolving anhydrous $Na^{14}NO_2$ (99.6% ^{14}N, natural abundance) and $Na^{15}NO_2$ (99.0% ^{15}N) to D_2O (99.8% D). The solutions were sealed in vacuo in a quartz cell (8mm in inner diameter and 0.4mm in thickness). Neutron diffraction measurements were carried out at 25°C using HIT spectrometer installed at a pulsed spallation neutron source (the National Laboratory for High Energy Physics; Tsukuba, Japan). The exposure time was 8hrs for respective samples. The measurements were also made for a vanadium rod (8mm in diameter), empty cell and a background.

After corrections for background, absorption and multiple scattering, the observed count rate was converted to the absolute scale by using the scattering data from the vanadium rod. The first-order difference function[1] $\Delta_N(Q)$ was determined from the difference between two normalized scattering cross sections for 10 mol% solutions of $Na^{14}NO_2$ and $Na^{15}NO_2$ (Fig.1a),

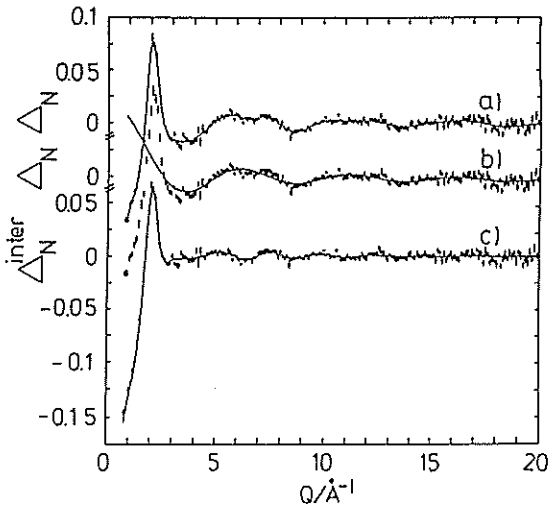

Fig.1 a)The observed difference function $\Delta_N(Q)$ for 10 mol% $NaNO_2$ solution in D_2O. b) The solid line shows the intramolecular N-O contribution, $i^{intra}(Q)$. c)The intermolecular contribution (dots). The solid curve represents the back Fourier transform of $\overline{G}_N^{inter}(r)$ shown in Fig.2b.

$\Delta_N(Q)$ is the weighted sum of four partial structure factors which include several contributions from nitrogen atom, i.e.,

$$\Delta_N(Q)=A[a_{NO}(Q)-1]+B[a_{ND}(Q)-1]$$
$$+C[a_{NNa}(Q)-1]+D[a_{NN}(Q)-1], \quad (1)$$

where

$$A=2c_Nc_Ob_O(b_{14N}-b_{15N})$$
$$B=2c_Nc_Db_D(b_{14N}-b_{15N})$$
$$C=2c_Nc_{Na}b_{Na}(b_{14N}-b_{15N})$$
$$D=c_N^2(b_{14N}^2-b_{15N}^2),$$

and c_i is the number of ith atom in the stoichiometric unit $(NaNO_2)_{0.1}(D_2O)_{0.9}$. The Fourier transform of $\Delta_N(Q)$ yields the distribution function $\bar{G}_N(r)$ around nitrogen atom (Fig.2a),

$$\bar{G}_N(r)=\{Ag_{NO}(r)+Bg_{ND}(r)$$
$$+Cg_{NNa}(r)+Dg_{NN}(r)\}/(A+B+C+D). \quad (2)$$

$\bar{G}_N(r)$ is mainly dominated by $g_{NO}(r)$ and $g_{ND}(r)$ because A and B are much larger than C and D.

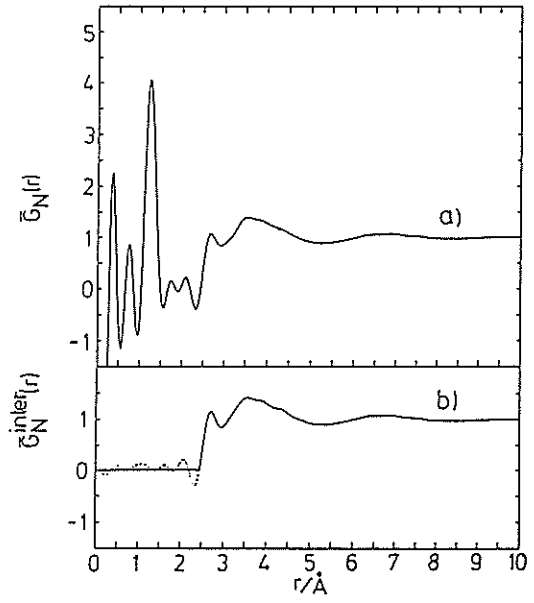

Fig.2 a)The total and b)intermolecular distribution functions, $\bar{G}_N(r)$, truncated at Q_{max}=15.4 Å^{-1}, for the nitrogen atom in 10 mol% $NaNO_2$ solution in D_2O.

The large first peak located at r=1.26 Å is assigned to the intramolecular N-O interaction in NO_2^-. The position of this peak is in good agreement with that obtained from the X-ray diffraction study of molten $NaNO_2$[2]. The intramolecular interference function, $i^{intra}(Q)$, defined below,

$$i^{intra}(Q)=2c_Nn_{NO}b_O(b_{14N}-b_{15N})$$
$$\times \exp(-l_{NO}^2Q^2/2)\frac{\sin Qr_{NO}}{Qr_{NO}}, \quad (3)$$

was calculated and subtracted from $\Delta_N(Q)$ (Fig.1b,1c) ,to remove termination ripples appeared around the first peak in $\bar{G}_N(r)$. The parameters, n_{NO}, l_{NO} and r_{NO}, in eq(3) were respectively determined to 2.03±0.03, 0.062±0.010 Å and 1.258±0.006 Å from calculations to minimize residual oscillations in $\bar{G}_N(r)$ at r<2 Å. The second peak located at r=2.71 Å in $\bar{G}_N(r)$ remains unchanged after removing the intramolecular N-O peak. From this we can judge that this peak arises from real structure. Since it is unlikely, on the electrostatic ground, that the oxygen atom of the nearest neighbour water molecule is facing toward the nitrogen atom in NO_2^- in the solution, the second peak is assigned to the nearest neighbour N···D interaction, and the coordination number n_{ND}=3.7±0.5 is obtained. The nearest neighbour N···D distance r(N···D)=2.71 Å is close to the sum of van der Waals radii of nitrogen and hydrogen atoms (1.6+1.2=2.8 Å). This result may be considered to reflect the weak hydration behaviour of NO_2^- in aqueous solutions.

The authors would like to acknowledge the members of HIT group during the course of diffraction measurements.

References

1) A.K.Soper, G.W.Neilson, J.E.Enderby and R.A.Howe, J.Phys.C, 10, 1793 (1977).
2) A.K.Adya, R.Takagi, K.Kawamura and M.Mikami, Mol.Phys., 62, 227 (1987).

Liquid Structure of GaSb at Different Temperatures

J. MIZUKI, K. KAKIMOTO, M. MISAWA*, T. FUKUNAGA** and N. WATANABE*

Fundamental Research Labs., NEC Corp., Tsukuba Ibaraki 305
*National Laboratory for High Energy Physics, 1-1 Oho, Tsukuba Ibaraki 305
**Institute for Materials Research, Tohoku Univ., 2-1-1 Katahira, Sendai 980

It is well-known that semiconductor compounds are important materials for electronic devices. The quality of their single crystals, however, is rather poor in comparison with that of Si, partly because the crystal consists of the two elements. In order to overcome this problem, we believe that the physical properties in the molten state, such as viscosity, thermal diffusivity, thermal expansion coefficient, and structures should be understood. Although most experimental and theoretical efforts so far have focused on the liquid phase of the elemental semiconductors, particularly Si and Ge, the structural studies of molten semiconductor compounds offer the possibility of investigating questions related to the crystal growth from the melt as well as chemical ordering and its influence on the electronic properties. Quite recently, the dynamical viscosity measurements for several molten semiconductor compounds by Kakimoto et al. [1]suggested the change in the molten structure with temperatures. Therefore, we have studied the atomic structure of molten GaSb by neutron diffraction at several temperatures.

The furnace used for the present experiment was home-made furnace, so called thermal-image furnace. High temperatures, maximum about 1100 °C, can be readiliy attained by focussing radiation from two halogen lamps on the sample with a gold-plated internal ellipsoidal reflector. The temperature fluctuation in the sample of 50 mm long and 10 mm in outer diameter is ±2 °C. GaSb was encapsulated in a quartz tube of 1 mm thick. The experiment was carried out at a HIT spectrometer.

The observed structure factors at 800 °C, and 1050 °C are shown in Fig. 1. As it can be seen, no change in structure factors was observed except that the structure factors at 1050 °C becomes a little bit broader than those at 800 °C. The common distinctive feature on the structure factors is that a small shoulder just after a first peak was observed.

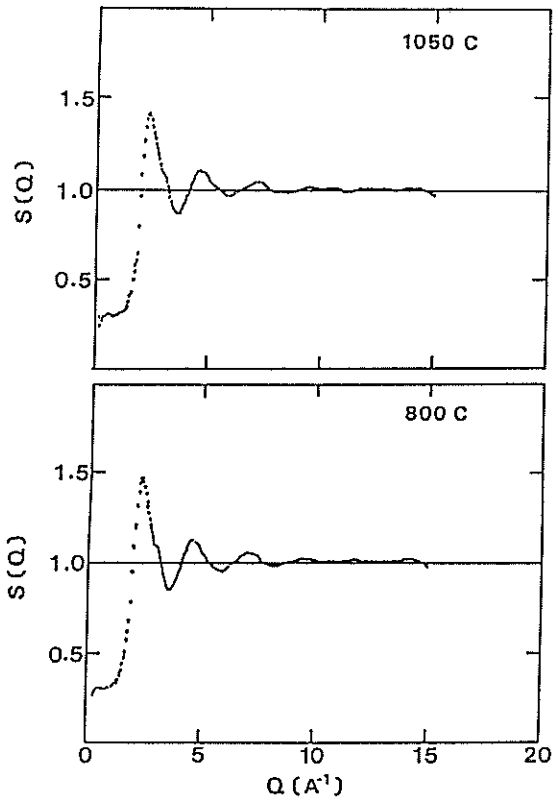

Fig. 1 Observed structure factors at 800 °C(below) and 1050 °C(above).

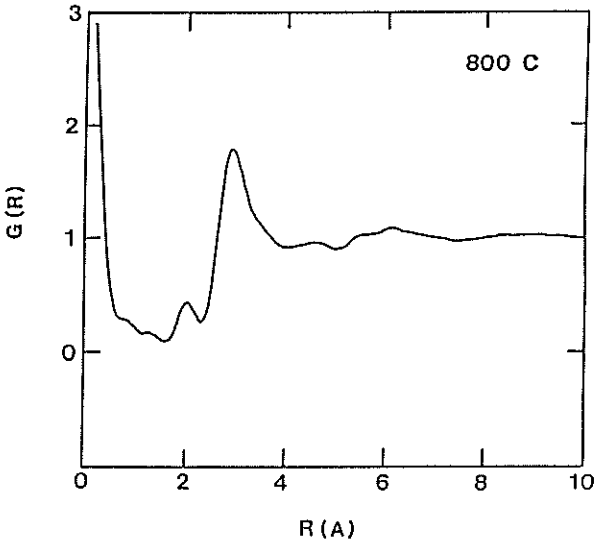

Fig. 2 Pair-correlation function at 800 °C.

This shoulder is not seen in the molten structure understood with a hard-sphere model, such as Al and Pb. Therefore, this shoulder suggests that there exists a short range ordering in the molten state. Figure 2 shows the pair-correlation function at 800 °C. An asymmetric shape of the first peak is emphasized when compairing the pair-correlation function to that of normal liquid metals mentioned above. This implies that the first peak could be analysed into two peaks which correspond to the two nearest neibour distances although it is difficult to say the position of the second peak. The radial distribution function at 800 °C is shown in Fig. 3. The area of the first maximum gives us the number of nearest neighbour atoms. We got 5.4 for that number with using averaged form factor.

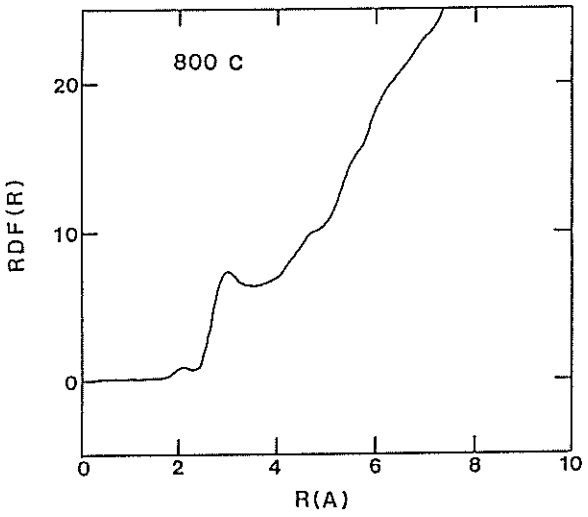

Fig. 3 Radial distribution function at 800 °C.

Now a brief discussion is given of the model for the molten structure of GaSb. The most promising model, we believe, is of β-Sn-type structure. The environment in this structure consists of four nearest neighbours in the corners of a flattened tetrahedron, with two others slightly farther away, which is shown in Fig. 4. This is supported by the fact that the first peak of the pair-correlation function could be analysed into two peaks with coordination number of four and two. Therefore, the number of nearest neighbour atoms turns out to be close to six experimentally because of the experimental resolution. Another point we should emphasize is that the electronic conductivity of GaSb becomes metalic on melting. This is consistent with the fact that the diamond structure of Si and Ge undergoes a β-Sn structure under pressure with a change in the electronic conductivity from semiconductor to metal[2),3)]. Recently, French group reported a β-Sn structure model for a molten structure of GaAs[4)].

In summary, although no drastic change in structure was observed in the temperature range from 800 °C to 1050 °C, a β-Sn type short range order exists in that temperature range.

Then, we have to explain the anomalous feature on the temperature dependence of the dynamical viscosity without introducing the structure change. One possible qualitative explanation is the following. If there are at least two diffusion paths which give different activation energies in the molten state, the dynamical viscosity plotted in logarithmic scale as a function of inverse temperature should show the different derivative at different temperatures. This feature was observed experimentally[1)].

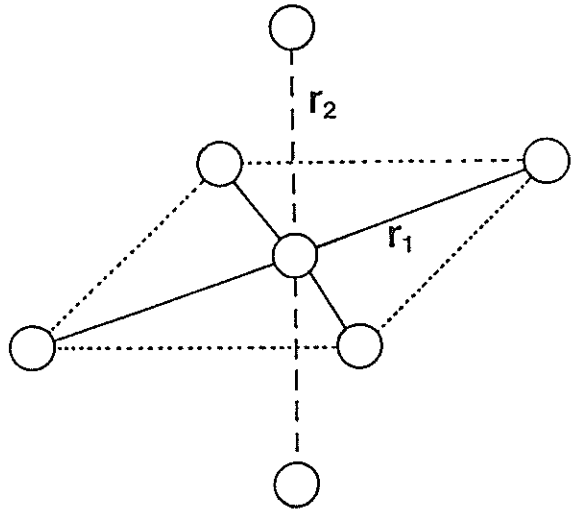

Fig. 4 β-Sn-type local environment. r_1 is a little larger than r_2.

References

**Present address; Nagoya University
1) K. Kaimoto and T. Hibiya, J. Apply. Phys. 66, 4181 (1989)
2) S. Minomura and H. G. Drickamer, J. Phys. Chem. Solids 23, 451 (1962)
3) J. C. Jamieson, Science 139, 762 (1963)
4) C. Bergman, C. Bichara, P. Chieux and J. P. Gaspard, Journal de Physique C8, 97 (1985)

Neutron Diffraction Study of Liquid Sb-Se Alloys

F.Kakinuma, T.Fukunaga*, M.Misawa** and K.Suzuki***

Niigata College of Pharmacy, 5-13-2 kamishin'ei-cho, Niigata 950-21
*Department of Crystalline Materials Science, Nagoya University, Furo-cho, Chikusa-ku, Nagoya 464
**National Laboratory for High-Energy Physics, 1-1 Oho, Tukuba-shi, Ibaraki 305
***Institute for Material Research,Tohoku University, 2-1-1 Katahira, Sendai 980

In the solid state, Sb-Se alloy system has a intermediate compound Sb_2Se_3 which has a layered structure.[1] Liquid Sb-Se system is characterized by a continuous transformation from a nonmetallic to a metallic state with a change of composition and/or temperature. The chemical short-range order due to covalent bonds in the solid state is retained after melting.[2] The structural changes associated with the formation of chemical bonds basically control the nonmetal-metal transition. It is interesting to study the structural modification due to the change of composition and temperature.

The structures of liquid $Sb_{1-x}Se_x$ alloys with x = 0.5, 0.6 and 0.7 were investigated in a temperature range of 600-800 °C. The sample was sealed in vacuum in a thin walled quartz glass cell(8 mm in inner diameter, 0.4 mm in wall thickness). The neutron diffraction measurements were carried out by using High Intensity Total scattering spectrometer (HIT) of BSF in the National Laboratory for High Energy Physics.

Figure 1 shows the structure factors S(Q) for liquid $Sb_{0.5}Se_{0.5}$, $Sb_{0.4}Se_{0.6}$ and $Sb_{0.3}Se_{0.7}$ alloys at 700°C. There exists prepeak at q = 1.2 A in S(Q) for these liquid alloys. It suggests that the layered structure of Sb_2Se_3 alloy in the solid state is partly retained after melting. The position of prepeak dose not change with composition. The prepeak for liquid Sb_2Se_3 alloy exhibits no change with the change of temperature. The prepeak for liquid $Sb_{0.5}Se_{0.5}$ alloy shows a trend to disappear with increasing temperature. The conductivity for liquid Sb_2Se_3 alloy is in a semiconducting region within a measured temperature range in this experiment. On the other hand, the conductivity for liquid $Sb_{0.5}Se_{0.5}$ alloy exhibits a nonmetal-metal transition around 700 °C. The temperature variation of prepeak may indicate that the nonmetal-metal transition for liquid Sb-Se system is closely related to the structural modification of intermediate range.

Atomic pair distribution functions g(r)'s were obtained by Fourier transform of the S(Q)'s. The first peak positions r_1 of g(r) for liquid $Sb_{1-x}Se_x$ alloys at 700 °C are 2.66, 2.66 and 2.60 A for x = 0.5, 0.6 and 0.7, respectively. The intensities of first peak in g(r) decrease as the composition deviates from the stoichiometric composition. This change is apparent for liquid $Sb_{0.3}Se_{0.7}$ alloy. The shift of r_1 to 2.60 A is due to the appearance of Se-Se bond. It means that selenium chains may be composed of excess Se atoms over the stoichimetric composition in liquid $Sb_{0.3}Se_{0.7}$ alloy.

References

1) M.Hansen and K.Anderko, Constitution of Binary Alloys(McGraw Hill, New York, 1958) 1173.
2) T.Maekawa, T.Yokoyama and K.Niwa, J. Chem. Thermodynamics 4 (1972) 873.

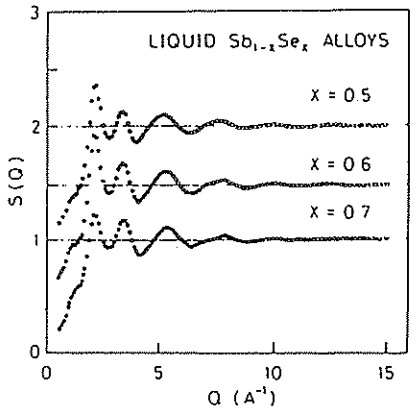

Fig.1 Structure factor S(Q) of liquid $Sb_{1-x}Se_x$ alloys at 700 °C.

Neutron Diffraction Studies of the Structure of Bulk Quenched and Evaporated Amorphous Seleniums

K. ICHIKAWA, S. KOTANI, N. SHIGA[+] and T. FUKUNAGA[*]

Department of Chemistry, Faculty of Science, Hokkaido University, Sapporo 060
*Department of Applied Physics, Faculty of Engineering, Nagoya University, Nagoya 464

Time-of-flight neutron diffraction measurements were carried out on bulk quenched amorphous selenium (abbreviated as g-Se) and evaporated amorphous selenium (abbreviated as a-Se). The data for the Q region (i.e., from 1 $\mathring{A}^{-1}$ to 20 $\mathring{A}^{-1}$) observed at the scattering angle ca. 48° have been analysed in terms of intermolecular interference to determine the structural nature and to show the difference in atomic configuration between g-Se and a-Se.

Results

Figure 1 shows the structure factor S(Q) which is given by the interference differential scattering cross sections $[d\sigma/d\Omega]_{int}$ of g-Se and a-Se measured by the ca. 48° detector. From the Fourier transform of S(Q) the radial distribution function RDF(r) is given by

$$RDF(r) = 4\pi\rho r^2 + D(r)$$

and

$$D(r) = \frac{2}{\pi} r \int [S(Q)-1]Q \sin(Qr)dQ$$

From D(r) and RDF(r) shown in figures 2 and 3 the nearest-neighbour distance r_1, the bond-angle θ, and the number of the nearest neighbours n have been obtained, as shown in table 1.

Pointed out in S(Q) and D(r) (or RDF(r)) can be the distinction between g-Se and a-Se as follows: (1) the S(Q) of a-Se shows the oscillation in the high-Q region from 12 to 20 $\mathring{A}^{-1}$, whereas the oscillation is almost washed out in g-Se. (2) The second peak (∿3.7 A) in D(r) as well as RDF(r) is dissymetric in g-Se, but symmetric in a-Se. (3) The third peak (∿6.7 A)in D(r) of a-Se is changed to the partially separated line-profile for g-se. It is concluded that the structure of amorphous Se depends on the method of sample preparation. However, there is no possible differences of the nearest neighbour distance and bond-angle within experimental uncertainty (see table 1).

+Present address: Kawasaki Co. LTD

Table 1. Structural parameters of a-Se and g-Se

	a-Se	g-Se
$r_1/\mathring{A}$	2.33 ± 0.01	2.32 ± 0.01
n	2.0 ± 0.1	2.2 ± 0.1
θ/°	105 ± 1	106 ± 1

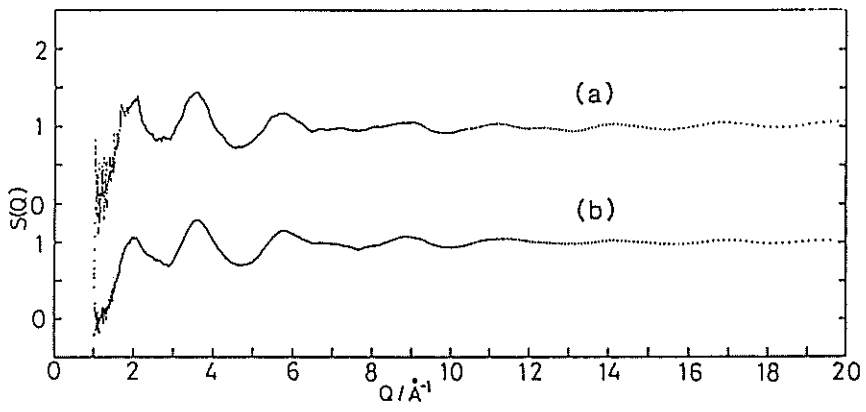

Figure 1. Structure factors S(Q) of a-Se(a) and g-Se(b), measured by the ca. 48° detector.

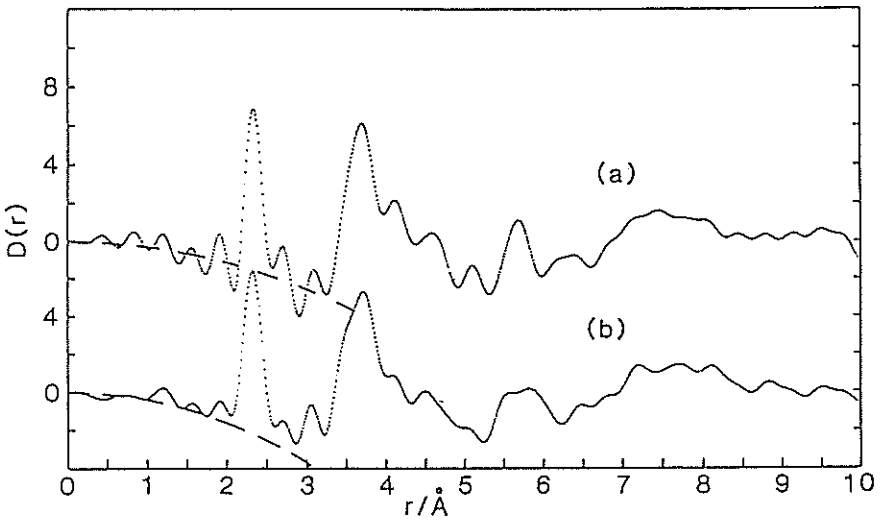

Figure 2. D(r) of a-Se(a) and g-Se(b). The broken lines mean $4\pi\rho r^2$, where ρ is the number density.

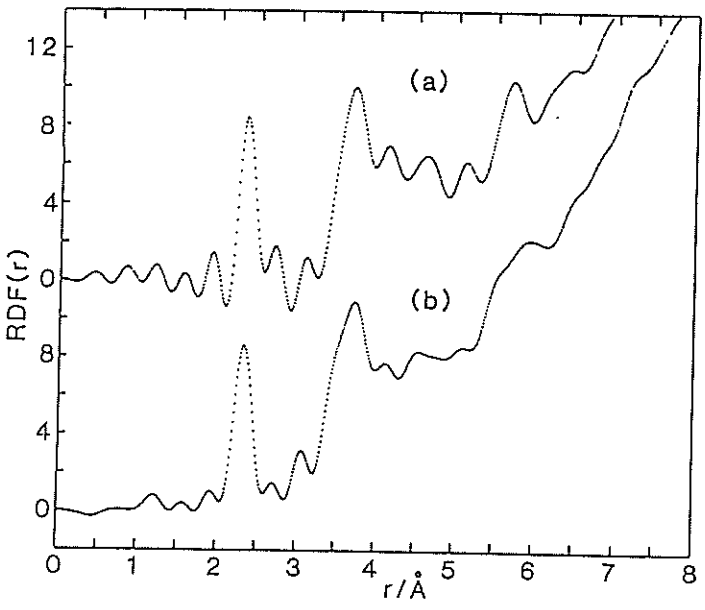

Figure 3. RDF(r) of a-Se(a) and g-Se(b).

Structure and Glass Transition of Boron Trioxide

M. MISAWA

National Laboratory for High Energy Physics, 1-1 Oho, Tsukuba 305

In a previous report[1] structure factors S(Q) of boron trioxide B_2O_3 measured in rather limited range of temperature, *i.e.* 298 to 673K have been reported. Despite of this limited range, it was found that the temperature dependence of Q_1, the position of the first peak of S(Q), was changed at the glass transition temperature T_g (540K). It seemed that the change corresponded to that of the observed density. However, no conclusion was given, because the measured temperature range was too narrow.

Since a low temperature refrigerator and a high temperature furnace are now available in the HIT instrument, we performed measurements of S(Q) extending to both the lower and the higher temperatures. Figure 1 shows the Q(S(Q)-1) curves measured at 121, 773 and 1073K together with the previous results at 298, 523 and 633K.

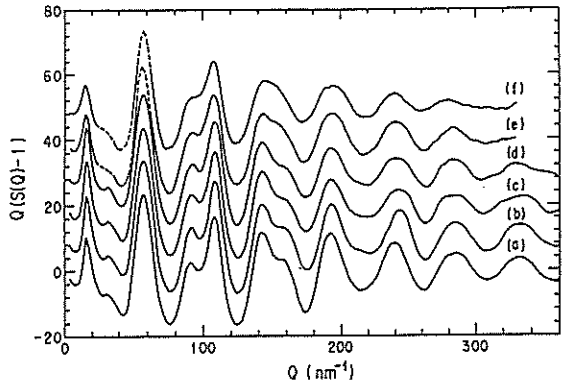

Fig. 1 Structure factors Q(S(Q)-1) measured at (a)121, (e)773 and (f)1073K, together with the previous results at (b)298, (c)523 and (d)633K.

Radial distribution function RDF(r) obtained by Fourier transform of the experimental Q(S(Q)-1) curves are compared in Fig. 2. The analysis of the temperature dependences of the position and width of the first and second peaks in the RDF(r) curves suggest that the BO_3 units are stable through the T_g, while the connectivity of the units begins to change at the T_g.

Figure 3 plots the position of Q_1 against temperature. Roughly speaking, the value of Q_1 is inversely proportional to a mean separation d of structural units, i.e., $Q_1 \propto 1/d$. Furthermore, $1/d$ is related to the density such that: $1/d \propto \rho^{1/3}$ if the structural units are isotropically packed; $1/d \propto \rho^{1/2}$ if the structural units are chainlike; and $1/d \propto \rho$ if the structural units are sheetlike. In Fig.3 the curves of $\rho^{1/3}$ and $\rho^{1/2}$ as well as ρ are also shown, each of which is scaled to the value of Q_1 at 523K. Below T_g the value of Q_1 is close to the curve for $\rho^{1/3}$, suggesting that the structural units are isotropically packed, while above T_g it tends to shift gradually toward the curve for $\rho^{1/2}$, suggesting that the units gradually change into chainlike ones. The increase of chainlike nature of the structural units with increasing temperature may be attributed to the opening of boroxol rings.

Details on the experimental results and data analysis have been reported elsewhere[2].

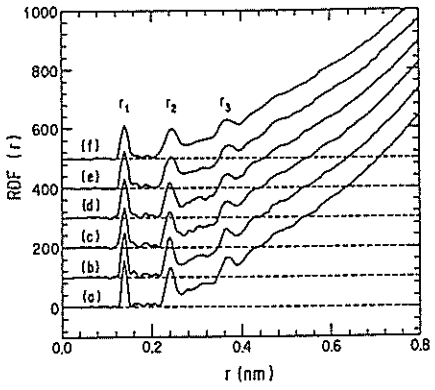

Fig. 2 Radial distribution function RDF(r)'s obtained for (a)121, (b)298, (c)523, (d)633, (e)773 and (f)1073K.

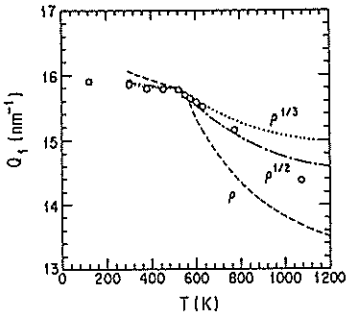

Fig. 3 Position of Q_1 of the first peak of S(Q) vs. temperature.

References

1)M. Misawa, KENS-report V (1984) 43.
2)M. Misawa, J. Non-cryst. Solids (in press).

The Structure of $SrO.2B_2O_3$ and $PbO.2B_2O_3$ Glass

Y.Akasaka, H.Hasegawa, T.Nanba, I.Yasui and M.Misawa(KEK)

Institute of Industrial Science, University of Tokyo
7-22-1, Roppongi, Minato-ku, Tokyo 106, Japan

1. Introduction

The structure of borate glasses have been studied spectroscopically. Bray et al. revealed from ^{11}B-NMR studies that the environments of boron atoms change as a function of composition in borate glasses.[1,2] Number of 4 coordinated boron increases till the content of SrO reaches 40mol% in $SrO.2B_2O_3$ glass and the content of PbO reaches 50mol% in $PbO.2B_2O_3$ glass. This results is some different from those of $Li_2O.2B_2O_3$, $Na_2O.2B_2O_3$ and $BaO.2B_2O_3$ glasses.[3] Krogh-Moe measured infrared spectra of alkali borate glasses and proposed that there are structure units specific to the ranges of alkali concentration.[4] He suggested from X-ray diffraction of $BaO.xB_2O_3$ (x=1.7, 3 and 4) glasses that the cations are not randomly distributed and structural groups characteristic of the crystalline tetraborates appear to be largely retained in the glass phase for a range of composition around 20mol% barium oxides.[5] Konijnendijk supported the conclusion of Krogh-Moe from the measurement of Raman spectra on alkali borate glasses and proposed that alkaline-earth borate glasses possess the same tendency with alkali borate glasses.[6] In our previous paper, we suggested from X-ray and neutron diffraction measurements that $BaO.2B_2O_3$ has some complex structure which seems unsuitable for glass structure.[7] Although it is reported from X-ray and neutron diffraction measurement that $SrO.2B_2O_3$ and $PbO.2B_2O_3$ crystal have 3 coordinated oxygen[8], we reported that $SrO.2B_2O_3$ and $PbO.2B_2O_3$ glasses could not have rigid structure with 3 coordination oxygen.[9] This composition correspond to a turning point of propertie's unlinierly change called " borate anomaly ". Hence it is interesting to clarify the structure of these glasses. We used two diffraction methods, X-ray and neutron, because X-ray scattering factor is in proportion to atomic number and strong signals from heavy metals clarify the structure concerning to heavy atoms but, at the same time, hide the information about the network structure consisting of light atoms. On the other hand neutron diffraction gives information about network structure of glasses which consists of lighter atoms owing to comparable scattering cross sections of all the constituent atoms. Thus the combined use of X-ray and neutron diffraction is effective for structure analysis of borate glasses containing heavy metal ions.

2. Results and Discussion

The structure of $RO.2B_2O_3$ crystals can be classified into three types. The crystals consist of diborate group in case of R=Mg, Zn or Cd, of only BO_4 unit with 3 coordinated oxygen in case of R=Sr or Pb and of ditriborate and dipentaborate in case of R=Ba. X-ray study of Krogh-Moe[5], Raman study of Konijnendijk[6] and our X-ray and neutron diffraction study[7] suggested $BaO.2B_2O_3$ glass consist of complex structure just like its crystal structure. In the case of $SrO.2B_2O_3$ glass and $PbO.2B_2O_3$ glass, many measurements such as Raman, X-ray, neutron and ESR indicate that glass structure is largely different from crystal structure with the same composition.[1,7,9]

2.1. $SrO.2B_2O_3$ glass

Konijnendijk measured Raman and infrared spectra of $SrO.2B_2O_3$ glass, which showed good agreement with the spectra of $Li_2O.2B_2O_3$ glass consisting of diborate group.[6] Among $RO.2B_2O_3$ crystals, $CdO.2B_2O_3$ consists of diborate group and ion radius of Cd^{2+}(0.97A) is near to that of Sr^{2+}(1.16A). The RDFs were calculated for $CdO.2B_2O_3$ crystal whose Cd ion was replaced with Sr ion and compared with observed ones. (Fig.1) It shows good agreement in peak position on RDF obtained from neutron diffraction except the second peak containing R-O pairs. This suggests the similarity of network structure. However, the model does not shows good agreement with the RDF obtained from X-ray diffraction, especially the second peak shifted 0.2A (which is the difference of ion radii), which indicates that the positions of alkaline earth ion are not proper. In this model a little bigger Sr ions than Cd ion are forcibly stuffed in a narrow space of Cd ions. Hence, we tried to improve the coordinate of Sr ion's by the relaxation using MD method without changing the network structure greatly, that is, at 300K. The parameters of Born-Mayer potential for MD are listed in Table 1. Fig.2 shows the RDF calculated from the model replaced with MD method and observed one and they show

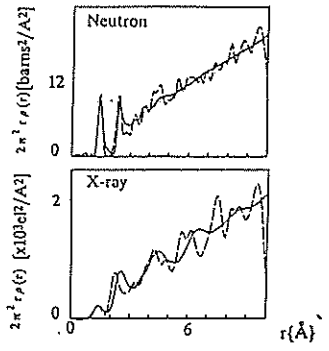

Fig.1 RDF of $SrO.2B_2O_3$ glass and that calculated from the structure of $CdO.2B_2O_3$ crystal.

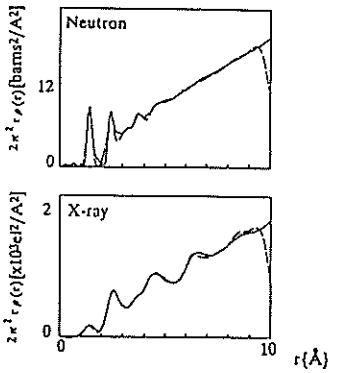

Fig.2 RDF of $SrO.2B_2O_3$ glass and that calculated from the structure of MD simulation model.

satisfactorily good agreement. The density of model agrees with observed one in ±0.1.(Table 2) The structure model is shown in Fig.3 which indicates that the structural unit in this model is diborate group

Table 1 Parameters of Born-Mayer potential

$SrO.2B_2O_3$

(x10^{-16} J)

	Sr	B	O
Sr	11.74	0.85	21.46
B		1.38	1.18
O			3.09

Table 2 Comparison of Density

$SrO.2B_2O_3$	g/cm^3
reported	3.117
observed	3.07
Model	3.186

Fig.3

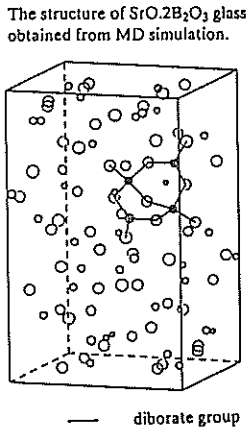

consisting of the same number of 3 coordinated boron and 4 coordinated boron. This structure unit is the one proposed by Krogh-Moe for $RO.2B_2O_3$ glass. This agree with the result of Bray's NMR study[1] and nonexistence of nonbridging oxygen in the model agrees with the results of Ohta's ESR study.[10] This model is different from the model suggested by Block et al. from X-ray diffraction data.[11] Their model consists of ditriborate and dipentaborate, but they did not carry any quantitative certification.

2.2.$PbO.2B_2O_3$ glass

$PbO.2B_2O_3$ crystal structure seems to be not suitable as a structure of glass because of its rigid densely packed structure and the RDF calculated from this crystal really shows poor agreement with observed one. A comparison of Raman spectra indicates $SrO.2B_2O_3$ and $PbO.2B_2O_3$ glass have different structure, which have the same structure in crystalline phase. As radius of Ba ion is near to that of Pb ion, we calculated RDF for the model based on $BaO.2B_2O_3$ crystal. The structural units of this crystal are not diborate groups but dipentaborate and ditriborate. The calculated RDF (Fig.4) from this model is fairly similar to the observed RDF deduced

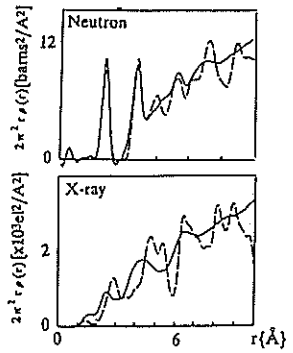

Fig.4 RDF of $PbO.2B_2O_3$ glass and that calculated from the structure of $BaO.2B_2O_3$ crystal.

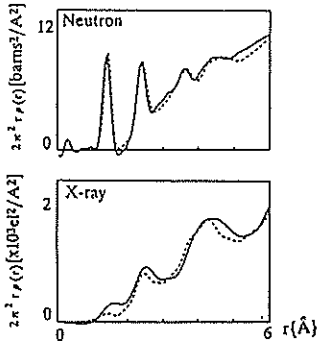

Fig.5 RDF of $PbO.2B_2O_3$ glass and that calculated from the structure of MD simulation model.

from neutron diffraction measurement but not so when compared with the RDF deduced from X-ray diffraction measurement. This disagreement may be caused from the difference of radii between Pb ion and Ba ion. Therefore we tried to relax the model with MD method. The parameters are listed in Table 3. RDF calculated with MD method (Fig.5) showed good agreement not only with RDF deduced from neutron but also with that deduced from X-ray measurement. The structure model is shown in Fig.6 which indicates that the structural unit in this model is dipentaborate and ditriborate. Table 4 shows the comparison of the densities of the model and glass. Model's density agrees with observed one in ±0.01. The proportion of non-bridging oxygen is 0.07 and B-O coordinated number is 3.53, which indicates that the number of non-bridging oxygen is very few and the number of 3-coordinated and 4-coordinated boron are almost equal. Network structure of this glass is similar to $BaO.2B_2O_3$ glass and its crystal.

Table 3 Parameters of Born-Mayer potential

$PbO.2B_2O_3$

	Pb	B	O
Pb	60.8	1.34	1.05
B		1.75	1.34
O			2.24

Table 4 Comparison of Density

$PbO.2B_2O_3$	g/cm^3
reported	4.409
observed	4.42
Model	4.426

Fig.6 The structure of $PbO.2B_2O_3$ glass obtained from MD simulation.

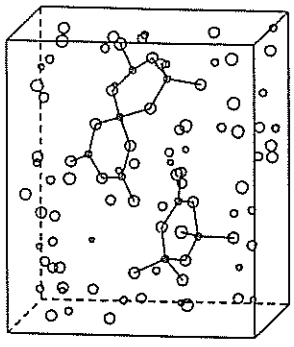

—— ditriborate and dipentaborate groups

3.Conclusion

The structure of $SrO.2B_2O_3$ and $PbO.2B_2O_3$ glass were analyzed using X-ray and neutron diffraction data. The structure models for $SrO.2B_2O_3$ and $PbO.2B_2O_3$ glass were constructed by relaxation from $CdO.2B_2O_3$ and $BaO.2B_2O_3$ crystal, respectively. As a result, it has been clarified that $SrO.2B_2O_3$ glass consists of diborate group which was thought by Krogh-Moe suitable for $RO.2B_2O_3$ glass structure, while $PbO.2B_2O_3$ glass consists of dipentaborate and ditriborate as $BaO.2B_2O_3$ glass does.

4.Reference

1) M.J.Park and P.J.Bray, Phys.Chem.Glass, Vol.13, No.2, (1972) 50
2) P.J.Bray, M.Leventhal and H.O.Hooper, Phys.Chem.Glass,Vol.4,No.2 (1963)47
3) P.J.Bray, J.Non-Cryst. Solids 95 and 96 (1987) 45
4) J.Krogh-Moe, Phys.Chem.Glass, 6 (1965) 46
5) J.Krogh-Moe, Phys.Chem.Glass, Vol.3, No.6 (1962) 208
6) W.L.Konijendijk and J.M.Stevels, 18 (1975) 307
7) I.Yasui, H.Hasegawa and Y.Saito, J.Non-Cryst. Solids, 106 (1988) 30
8) R.W.G.Wycoff,Crystal Structure,4,120(1968),Interscience Publishers,New York
9) I.Yasui,H.Hasegawa, Y.Saito and Y.Akasaka, J.Non-Cryst. Solids (in published)
10) Y.Ohta, M.Shimada and M.Koizumi, J.Non-Cryst.Solids, 51 (1982) 161
11) S.Block and G.J.Piermarini, Phys. Chem. glass, Vol.5, No.5 (1964) 142

The Partial Ni-Ni Correlation of $Ni_{40}V_{60}$ Powders Observed by Neutron Scattering During Mechanical Amorphization Process

T. FUKUNAGA, Y. HOMMA**, M. MISAWA* and K. SUZUKI**

Department of Crystalline Materials Science, Nagoya Univ. Furo-cho, Chikusa-ku, Nagoya 464
*National Laboratory for High Energy Physics, 1-1 Oho, Tsukuba-shi, Ibaraki 305
**Institute for Materials Research, Tohoku Univ., 2-1-1 Katahira, Aoba-ku, Sendai 980

Amorphous materials have been mainly prepared by rapid quenching methods such as metls spinning, sputtering, evaporation and so on. Recently it has been demonstrated that amorphous materials can be also synthesized through ball-milling techniques, which are mechanical alloying(MA) and mechanical grinding(MG). The amorphization by ball milling is achieved after longer solid-state reaction time in comparison with the amorphization time of rapid quenching methods. Therefore, a detailed structural investigation at an atomic level can be carried out during the amorphization process by ball-milling.

In this paper, we report the structural evolution of Ni-V powders as a function of the milling time. It is well known that the coherent scattering length of a V atom is close to zero in comparison with that of a Ni atom for neutron scattering. This means that only the information attributed to the Ni-Ni correlation can be directly observed by neutron diffarction during amorphization process by MA.

Pure elemental powders of nickel(99.9%, ~100μm) and vanadium(99.5%, ~50μm) were mixed to give the starting composition of $Ni_{40}V_{60}$ powders. The MA was carried out in a conventional ball-milling apparatus, where the rotating speed is 110rpm, under Ar atmosphere. The measurements of the neutron scattering intensities from the $Ni_{40}V_{60}$ samples were carried out at room temperature by using High Intensity Total scattering spectrometer (HIT).

Figure 1 shows the partial radial distribution functions $RDF_{NiNi}(r)$'s of the Ni-Ni correlation derived as the Fourier transform of $S_{NiNi}(Q)$'s truncated at Q_{max} =30 A^{-1}, together with atomic positions of fcc-Ni crystal. Most of the distribution peaks attributued to the atomic positions of fcc-Ni crystal become broadened and approach gradually the broad halo originating from amorphous structure. However, it is worth noting that the peaks of the 2nd and 5th Ni-Ni neighbor positions observed within 7 A distance drastically decrease and eventually disappear after 400h milling. It can be easily shown that the 2nd and 5th Ni-Ni neighbors contribute exclusively to the formation of the octahedral units in fcc structure. This means definitely that the amorphization of $Ni_{40}V_{60}$ sample takes place chemically by alloying V atoms with Ni atoms and topologically increasing the tetrahedral unit characteristic of an amorphous structure at the expense of the octahedral unit in fcc.

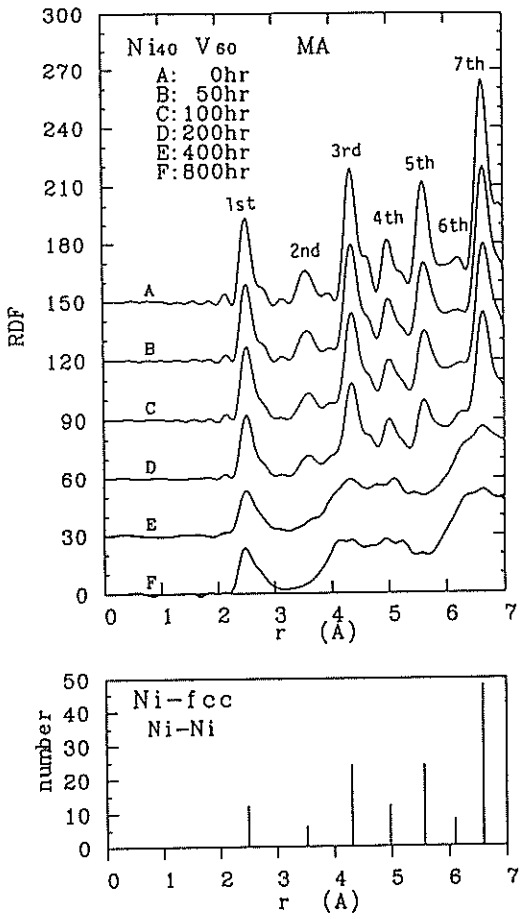

Fig. 1 Total radial distribution functions (RDF(r)'s ~$RDF_{NiNi}(r)$'s) of $Ni_{40}V_{60}$ samples after 0, 50, 100, 400 and 800 hours of MA, together with atomic distribution of fcc Ni crystal.

Structural Observation in Amorphization of $Cu_{50}V_{50}$ System During Mechanical Alloying Process

T. FUKUNAGA, M. MORI, K. INOU, M. MISAWA* and U. MIZUTANI

Department of Crystalline Materials Science, Nagoya Univ. Furo-cho, Chikusa-ku, Nagoya 464
*National Laboratory for High Energy Physics, 1-1 Oho, Tsukuba-shi, Ibaraki 305

Mechanical alloying(MA) is focused as a method for synthesizing amorphous materials by solid state reaction. This was first established by Koch *et al.* [1], who poduced amorphous $Ni_{60}Nb_{40}$ powders by MA of pure crystalline Ni and Nb powders. Subsequently, amorphous alloy powders have been formed by MA in a large number of alloy systems, particularly those in which a heat of mixing is negative. This is because a negative heat of mixing is assumed to provide a chemical driving force which favours interdiffusion for the formation of an amorphous phase by MA. However, recently the formation of the amorphous phase of Cu-Ta system with a positive heat of mixing by MA was reported[2]. In the system a chemical driving cannot be expected and, instead, the energizing process is required to allow the formation of the amorphous phase.

In this paper, we report the formation of an amorphous phase of mixed powders of pure Cu and V, in which the heat of mixing is positive. The mixing at an atomic level and amorphization process during MA were studied by neutron diffraction. For neutron total scattering the partial Cu-Cu structure factor $S_{CuCu}(Q)$ of Cu-V MA powders can be directly observed, because the coherent scattering length of V atom is negligibly small in comparison with that of Cu atom.

Pure elemental powders of copper(99.9%, ~150μm)and vanadium(99.5%, ~50μm) were mixed to give the starting composition of $Cu_{50}V_{50}$ powders. MA was carried out in a planetary ball mill(Fritsch, P-5, intensity 7) using a Cu-Be vial and balls under Ar gas atmosphere. DSC measurement was performed with a heating rate of 20 K/min. Measurements of neutron diffraction were carried out by using High Intensity Total scattering spectrometer(HIT).

DSC measurements were performed up to 700°C and repeated again after cooling down to room temperature. The area enclosed by the 1st snd 2nd runs, which ought to represent the release of energy accumulated by MA, increased with increasing MA time. The accumulated energy approaches a saturation value of 14.2 kJ/mol after 120 h of MA. But a sharp exothermic peak characteristic of a crystallization of an amorphous phase can not be observed in the DSC curve.

The partial $S_{CuCu}(Q)$ observed by neutron diffraction before MA clearly indicates the fcc pattern of Cu crystal as shown in fig. 1. Bragg peaks of fcc-Cu crystal quickly diminish and become broadened with increasing milling time. A halo pattern dominates after 60 h of MA, though the 1st peak remains rather sharp in comparison with that of a typical amorphous alloy. The partial radial distribution function $RDF_{CuCu}(r)$ of the Cu-Cu correlation was obtained by a Fourier transformation of $S_{CuCu}(Q)$. The distribution peaks of fcc-Cu crystal broaden and approach gradually to those characteristic of an amorphous state. Especially it is noteworthy that the peaks of the 2nd and 5th Cu-Cu neighbor positions observed within 7 A distance drastically decrease and eventually disappear. These results mean that the amorphization of Cu-V powders by MA gradually but definitely proceeds by mixing V and Cu atoms at an atomic level. Moreover, the disappearance of the 2nd and 5th peaks in RDF(r) indicates that the tetrahedral unit characteristic of an amorphous structure increases at the expense of the octahedral unit unique to fcc or bcc structure.

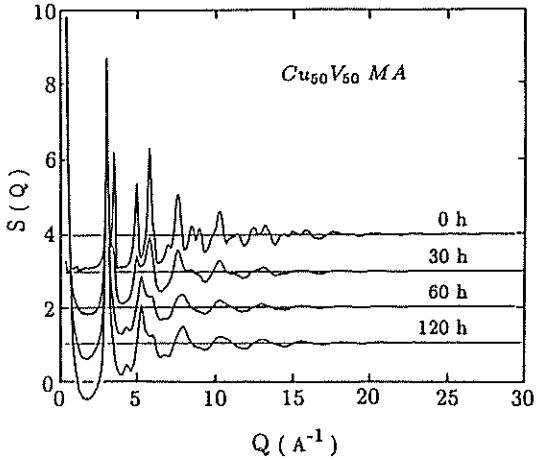

Fig. 1 Total structure factors S(Q)'s of $Cu_{50}V_{50}$ samples after 0, 30, 60 and 120 h of MA.

References

1) C.C. Koch, O.B. Cavin, C.G Mckamey and J.O. Scarbrough, Appl. Phys. Lett. 43 (1983) 1017
2) T. Fukunaga, K. Nakamura, K. Suzuki and U. Mizutani, J. Non-Cryst. Solids 117/118 (1990) 700

Amorphization in Immiscible Cu-Ta Sytem by Mechanical Alloying

T. FUKUNAGA, K. NAKAMURA, K. SUZUKI* and U. MIZUTANI

Department of Crystalline Materials Science, Nagoya Univ. Furo-cho, Chikusa-ku, Nagoya 464
*Institute for Materials Research, Tohoku Univ., 2-1-1 Katahira, Aoba-ku, Sendai 980

Recently mechanical alloying(MA) techniques have received strong attention in synthesizing the amorphous alloy powders[1]. MA is applied to a system where a heat of mixing is negative, because the chemical driving force plays an important role in lowering the free energy of starting materials in the amorphization process.

In the present study, we investigated the effect of MA on Cu-Ta powders, where Cu and Ta atoms are immiscible with each other even in the liquid state and the Cu-Ta system is characterized by a positive heat of mixing. Therfore, a chemical driving force cannot be expected in the system with a positive heat of mixing and , instead, the energizing process is required to allow the formation of an amorphous phase.

Pure elemental powders of copper (99.9%, <150μm) and tantalum (99.9%, ~45μm)were mixed to give starting compositions and put in a vial with balls made of Cu-Be(1.8-2.0%Be) under Ar gas atmosphere. MA was carried out in a planetary-type (Fritsch P-5). The formation of an amorphous phase in Cu-Ta alloy system by MA was confirmed by neutron and X-ray diffractions as tools for structural analyses and DTA, DSC and scanning electron microscopy as supplimentaly tools.

DTA curves measured for the Cu-Ta powders subjected to MA indicated exothermic peaks characterized of a crystallization of the amorphous state at 526, 490 and 500°C in $Cu_{30}Ta_{70}$, $Cu_{40}Ta_{60}$ and $Cu_{50}Ta_{50}$ samples, respectively. A total heat release associated with the exothermic peak for the $Cu_{30}Ta_{70}$ sample after 75 hours of MA was measured with a differential scanning calorimetry and turns out to be 2.8 kJ/mol. The vale is close to 3.2-3.6 kJ/mol obtained upon crystallization of the $Ni_{100-X}Zr_X$ (X=30-80) amorphos alloys prepared by MA[2].

Figure 1 shows the structure factors S(Q)'s of $Cu_{40}Ta_{60}$ and $Cu_{50}Ta_{50}$ samples prepared by 75 hours of milling in the Cu-Be vial and balls. The S(Q)'s for $Cu_{40}Ta_{60}$ and $Cu_{50}Ta_{50}$ samples possess features characteristic of an amorphous structure, though some Bragg peaks remain finite. These weak Bragg peaks are identified with the diffraction lines of pure Cu and Ta, as marked by arrows in fig. 1. This clearly demonstrates that the Cu-Ta samples still possess unreacted pure Cu and Ta, even though MA is done for 75 hours. However, as shown in the inset to fig. 1, a small peak or shoulder is unambiguously observable in between the Cu-Cu and Ta-Ta correlations. We attribute this to the Cu-Ta correlation, the presence of which can be taken as the mixing of the two immiscible elements Cu and Ta at the atomic level or the evidence that alloying proceeds by MA.

Radial ditribution functions RDF's were derived as the Fourier transform of S(Q)'s truncated at Qmax=30 A^{-1}. The RDF's for the $Cu_{40}Ta_{60}$ and $Cu_{50}Ta_{50}$ samples identify the formation of the amorphous phase in spite of the presence of remaining unreacted Cu and Ta crystals.

From the observed S(Q)'s and RDF's coupled with the DTA and DSC analyses we reach the conclusion that the amorphization in the Cu-Ta system, which possesses a positive heat of mixing , does proceed slowly but definitely by the mechanical alloying.

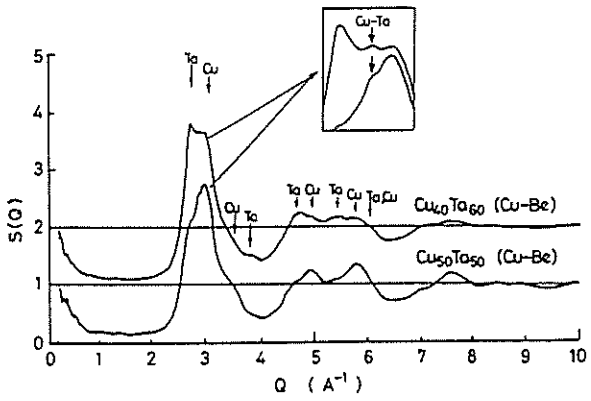

Fig. 1 Total structure factors S(Q)'s of $Cu_{40}Ta_{60}$ and $Cu_{50}Ta_{50}$ powders after 75 hours of milling. Arrows show the diffraction line due to Cu and Ta .

References

1) C.C. Koch, O.B. Calvin, C.G. Mckamey and J.O. Scarbrough, Allp. Phys. Lett., 43 (1983) 1017
2) M. Nastasi, F.W. Saris, L.S. Hung and J.W. Mayer, J. Appl. Phys., 58 (1985) 3052

Chemical Short Range Structures of $Ni_{100-X}V_X$ Amorphous Alloys Prepared by MA

T. FUKUNAGA, Y. HOMMA**, M. MISAWA* and K. SUZUKI**

Department of Crystalline Materials Science, Nagoya Univ. Furo-cho, Chikusa-ku, Nagoya 464
*National Laboratory for High Energy Physics, 1-1 Oho, Tsukuba-shi, Ibaraki 305
**Institute for Materials Research, Tohoku Univ., 2-1-1 Katahira, Aoba-ku, Sendai 980

Amorphous alloys have been synthesized by many types of rapid quenching techniques, whereby a cooling rate in the range of 10^4 to 10^{12} K/s is required to form an amorphous state[1]. Recently, several new methods of synthesis of amorphous alloys based on solid state reactions below a crystallization temperature have been advanced. One of them is mechanical alloying(MA)[2], by which the amorphization proceeds on the time scale of hours or days. However, the formation range of an amorphous phase by MA is usually much wider than that of splat quenching with the high cooling rate.

In this paper, we report the formation of an amorphous phase in the wide range of $Ni_{100-X}V_X$ system by MA, the amorhization of which by splat quenching has not been reported, and the chemical short range structure depended on the concentration. For neutron scattering the concentration dependence of the Ni-Ni partial structure is directly observed in $Ni_{100-X}V_X$(X=45, 50, 55, 60, 65 and 70) amorphous alloys produced by MA, because the coherent scattering length of V atom is negligibly small compared to that of Ni atom.

MA for the mixture of elemental Ni and V powders was carried out in a conventional ball-milling apparatus using SUS vial and balls under Ar gas atmosphere, where the rotating speed is 110 rpm. Measurements of neutron scattering were carried out by using High Intensity Total scattering spectrometer (HIT).

Bragg peaks of fcc-Ni crystal powders observed in the structure factor $S_{NiNi}(Q)$ reduce intensity and broaden width with increasing ball-milling time. After 400 h of MA all peaks of $Ni_{100-X}V_X$ powders transformed to broad halo patterns characteristic of an amorphous state. The most striking aspect of the $S_{NiNi}(Q)$'s is that overall features are independent on V concentration. This may mean that the topological and chemical arrangement of the Ni-Ni correlation does not drastically change in the formation range of the amorphous phase.

The partial radial distribution functions $RDF_{NiNi}(r)$'s were derived as the Fourier transform of $S_{NiNi}(Q)$'s of $Ni_{100-X}V_X$ amorphous alloys. The coordination number of Ni atom around a Ni atom calculated from the area under the 1st peak decreases with increasing V concentration as shown in fig. 1. The concentration dependence of the coordination number of the first nearest Ni-Ni correlation for the amorphous phase was compared with those for two types of σ-phases, one of which has an ordered atomic arrangement topologically and chemically, and the other has a topologically ordered but chemically disordered one. Figure 1 shows the analogy of the concentration dependence of the first nearest Ni-Ni coordination number for the amorphous phase with that for chemical ordered σ-phase. Therefore, we concluded that the chemical short range order in the Ni-V amorphous alloy obtained by MA is analogous to that of the σ-phase existing as a stable phase in the range 50-70at%V.

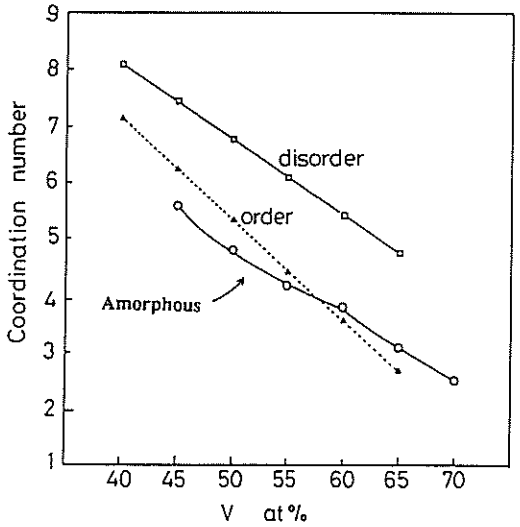

Fig. 1 Coordination numbers of Ni atom around a Ni atom in the first nearest neighbor for ordered, disordered σ phases and amorphous $Ni_{100-X}V_X$ powders.

References

1) D. Turnbull, Metall. Trans. 12B (1981)217
2) R.B. Schwarz and W.L. Johnson, Phys.Rev. Lett. 51 (1983) 415

Structure Characterization of NiZr Amorphous Alloys Prepared by MA, MG and MQ

T. FUKUNAGA, T. SEKIUCHI* and K. SUZUKI*

Department of Crystalline Materials Science, Nagoya Univ. Furo-cho, Chikusa-ku, Nagoya 464
*Institute for Materials Research, Tohoku Univ., 2-1-1 Katahira, Aoba-ku, Sendai 980

Amorphous alloys have been synthesized by rapid quenching techniques. In the last few years, some new methods have been developed to produce amorphous alloys based on solid state reactions below a crystallization temperature. Among them, the ball milling has been most frequently employed. A use of a mixture of elemental powders as starting materials is refered to as the mechanical alloying(MA), whereas that of an intermetalic compound as the mechanical grinding(MG).

In this paper, we report a comparison of atomic structures among NiZr amorphous alloys prepared by MA, MG and melt quenching(MQ).

MA for the mixture of elemental Ni(99.9%, ~100μm) and Zr(98%, ~40μm) powders and MG for NiZr crystalline compound powders(~150μm) were carried out in a conventional ball-milling apparatus using SUS vial and balls under Ar gas atmosphere, where the rotating speed is 110rpm. MQ was carried out by using a single roll spinning apparatus under Ar gas atmosphere. The measurements of neutron total scattering intensities were carried out by using High Intensity Total scattering spectrometer(HIT).

The overall profiles of structure factors S(Q)'s and pair distribution functions g(r)'s observed MA, MG and MQ NiZr amorphous alloys are apparently similar respectively. However, a carefull comparison of S(Q)'s and g(r)'s allows us to realize differences of the atomic structues. S(Q) observed for the MA NiZr amorphous alloy clearly has a significant intensity of small angle scattering in low scattering vector range of $Q<0.5$ A^{-1}, while MG NiZr amorphous alloy does not as shown in fig. 1. This result suggests that the MA NiZr amorphous alloy still contain some inhomogenieties and the MG NiZr amorphous alloy has a homogeneous structure similar to that of the MQ NiZr amorphous alloy.

Figure 2 shows g(r)'s for MG and MQ NiZr amorphous alloys. The main peaks located at r~2.8 A in the 1st peak of g(r) are entirely overlapped each other, but the shoulder at r~3.3 A, the 2nd and 3rd peaks of the MG NiZr amorphous alloy have broader shapes than that of the MQ NiZr amorphous alloy. The results may indicate that atomic structure units within the first nearest neighbor distance are same each other, but the excess defects and strain stored during MG process increase the topological and chemical disorder in a long range structure for the MG NiZr amorphous alloy, compared with the MQ amorphous alloy.

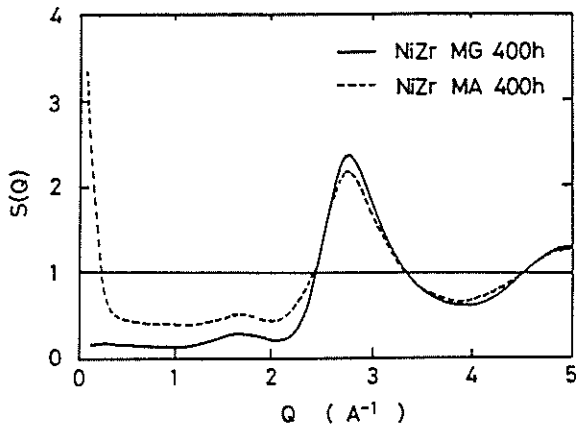

Fig. 1 Structure factors S(Q)'s for MA and MG NiZr amorphous alloys.

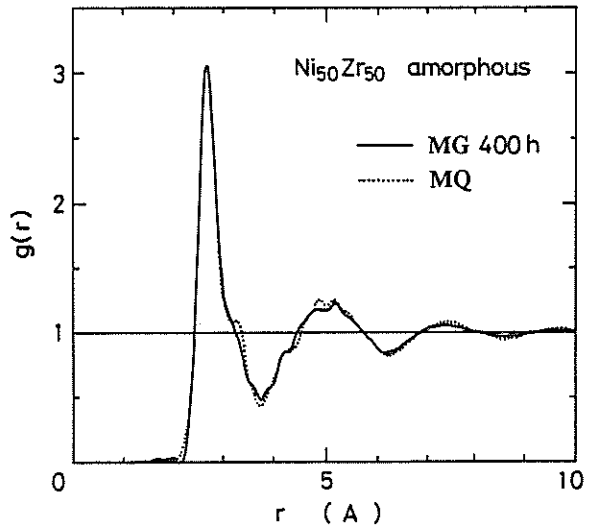

Fig. 2 Pair distribution functions g(r)'s for MG and MQ NiZr amorphous alloys.

Amorphization of σ-$Ni_{40}V_{60}$ Crystal by Mecahnical Grinding and its Structure

T. FUKUNAGA, Y. HOMMA**, M. MISAWA* and K. SUZUKI**

Department of Crystalline Materials Science, Nagoya Univ. Furo-cho, Chikusa-ku, Nagoya 464
*National Laboratory for High Energy Physics, 1-1 Oho, Tsukuba-shi, Ibaraki 305
**Institute for Materials Research, Tohoku Univ., 2-1-1 Katahira, Aoba-ku, Sendai 980

Mechanical grinding(MG) is one of new methods for synthesizing an amorphous alloy based on the solid state reaction. The MG process starts with powders of an intermetallic compound, which possesses the atomistically homogeneous distribution of elements in addition to the lowest free energy at a given composition. Nevetheless, some intermetallic compounds undergo the transformation to an amorphous phase by MG. This implies that the energizing process has to be involved in the MG. The energy is likely to be stored in the form of defects and the total amount of energy thus stored should exceed some critical value to allow the transformation into an amorphous phase.

In this paper we report the amorphization of σ-$Ni_{40}V_{60}$ crystal by MG. It is well known that the coherent scattering length of a V atom is close to zero compared with that of a Ni atom for neutron scattering. This means that only the structural evolution of the Ni-Ni correlation can be directly observed during the transformation process from σ-phase to amorphous phase.

The $Ni_{40}V_{60}$ alloy for the MG process was prepared by arc-melting and ground into powders of average size less than 150μm. The powders were annealed for 7 hours at 600°C to transform to single σ-phase. MG was carried out in a conventional ball-milling apparatus using SUS vial and balls under Ar gas atmosphere, where the rotating speed is 110rpm. Measurements of neutron scattering intensities from the σ-$Ni_{40}V_{60}$ crystal were carried out by using High Intensity Total scattering spectrometer(HIT).

Figure 1 shows the structure factors S(Q)'s of $Ni_{40}V_{60}$ powders during the amorphization process by MG. Bragg peaks of σ-phase gradually dimish and become broadened with increasing milling time. A halo pattern dominates after 400h of MG, though Bragg peak of (101) plane remains in the prepeak around the Q range of 1.5 to 2.5 A^{-1}. The prepeak was pointed out to be associated with the medium range ordering by Steeb and Lamparter[1]. Moreover, the peaks located around the Q range from 1 to 2 A^{-1} in S(Q)'s of net-work glasses are well known to be originated from the packing of structure units in medium range length scale. To realize this point it is interesting to know how atoms arrange in (101) and (220) planes, Bragg peaks of which are located in the prepeak. (101) and (220) planes have a large number of a pair of triangles composed of mainly Ni atoms. Since the structure of a metal-metal amorphous alloy is poit out to be largely built up by tetrahedral units experimentally2) and theoretically3), it can be imagine that the existence of a number of a pair of triangles composed of maily Ni atoms in (101) and (220) planes is associated with the packing of the tetrahedral units characteristic of the amorphous structure and the medium range order of the Ni-Ni correlation.

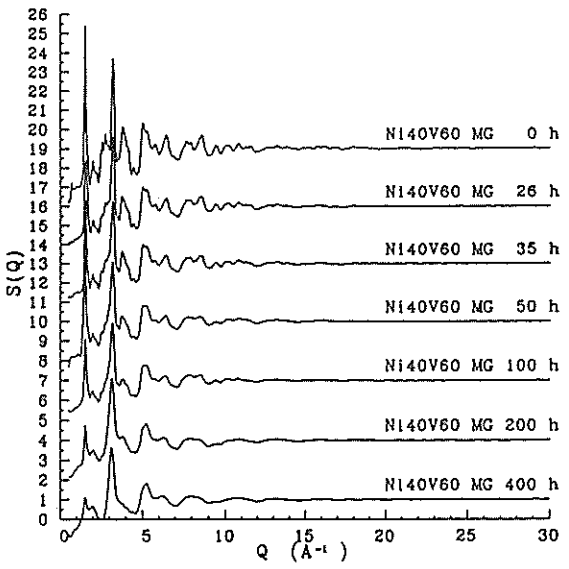

Fig. 1 Total structure factors S(Q)'s of $Ni_{40}V_{60}$ samples after 0, 26, 35, 50, 100, 200 and 400 h of MG.

References

1) S. Steeb and P. Lamparter, J. Non-Cryst. Solids 61/62 (1984) 237
2) T. Fukunaga, Y. Homma, M. Misawa and K. Suzuki, J. Non-Cryst. Solids 117/118 (1990) 721
3) J.L. Finney and J. Wallace, J. Non-Cryst. Solids 43 (1981) 165

Chemical Short Range Order of Amorphous $Ni_{24}Ti_{76}$ Neutron Zero Alloy Produced by Mechanical Alloying

T. FUKUNAGA

Department of Crystalline Materials Science, Nagoya Univ. Furo-cho, Chikusa-ku, Nagoya 464

Mechanical alloying(MA) has been used for production of oxide-dispersion strengthened superalloys. Recently, MA was applicable to the preparation of an amorphous alloy from a mixture of pure elemental crystal powders by Koch *et al.*[1]. MA is continued to the point where the starting elemental powders are mixed to dimensions of an atomic spacing, by which an amorphous alloy of elemental powders can be formed.

In this paper, I report a chemical structural rearrangement during the mixing process at an atomic level induced by MA. The interest point is whether the atomic structure for an amorphous alloy produced by MA is chemically order or not.

Pure elemental powders of nickel (99.9%, ~100μm) and titanium (99.9%, ~50μm) were mixed to give the statrting composition of $Ni_{24.3}Ti_{75.7}$ powders. MA was carried out in a conventional ball-milling apparatus, where the rotating speed is 110 rpm, under Ar gas atmosphere. Measurements of neutron scattering were carried out by using High Intensity Total scattering spectrometer(HIT). For neutron scattering of $Ni_{24.3}Ti_{75.7}$ alloy which is so-called neutron zero scattering alloy, the concentration-concentration structure factor $S_{CC}(Q)$ is directly observed, because the average coherent scattering length of the alloy powders is ajustited to zero i.e. $<b>=0$.

Bragg peaks of fcc-Ni and hcp-Ti crystal powders observed in the total structure factor S(Q) reduce intensity and broaden width with increasing MA time. After 400h of MA a halo pattern dominates, which indicates $S_{CC}(Q)$. The overall feature of $S_{CC}(Q)$ after 800h of MA is the almost same as that of the amorphous alloy obtained by splat quenching.

Figure 1 shows the reduced radial concentration correlation functions $G_{CC}(r)$'s ($=4\pi r\rho_{CC}(r)$'s) for $Ni_{24.3}Ti_{75.7}$ amorphous alloys prepared by MA and splat quenching, together with Ti-Ti, Ni-Ti and Ni-Ni atomic distributions of $NiTi_2$ crystalline compound. The negative peaks of r=2.54 A in $G_{CC}(r)$'s exactly corresponds to the Ni-Ti unlike atom pairs in the $NiTi_2$ crystalline compound, which is smaller than the distance of Ni-Ti correlation obtained from the diameters of Ni and Ti atoms ($(\sigma_{Ni}+\sigma_{Ti})/2$=2.71 A). The fact may indicate that there is a chemical affinity between Ni and Ti atoms even in the amorphous alloy similar to that of the $NiTi_2$ crystalline compound.

To examine further this point, the Warren chemical short-range order parameter α of the $Ni_{24.3}Ti_{75.7}$ amorphous alloy was evaluated. The values of α are -0.097 for the amorphous alloy by MA and -0.102 for one by splat quenching. The negative values of α certainly mean the preferential existence of Ni-Ti unlike atom pairs at the nearest neighbor coordination.

It can be concluded that the chemical short-range structure even in the $Ni_{24.3}Ti_{75.7}$ amorphous alloy by MA is quite analogous to that in $NiTi_2$ crystalline compound.

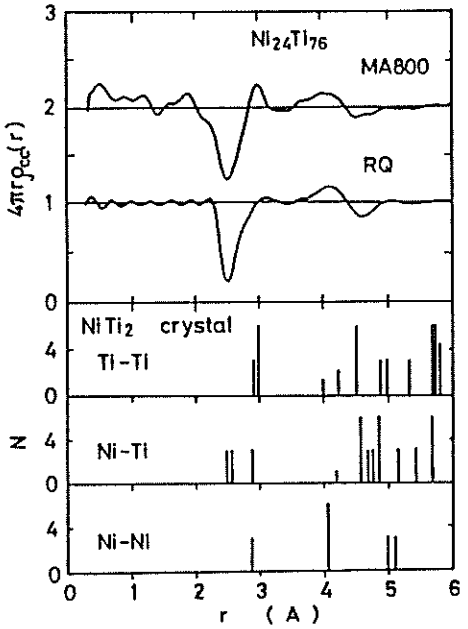

Fig. 1 Reduced concentration correlation functions GCC(r)'s for amorphous $Ni_{24.3}Ti_{75.7}$ neutron zero alloys produced by MA and splat quenching, and Ti-Ti, Ni-Ti and Ni-Ni correlations in crystalline $NiTi_2$ compound.

References

1) C.C. Koch, O.B. Cavin, C.G Mckamey and J.O. Scarbrough, Appl. Phys. Lett. 43 (1983) 1017

1-3. Magnetic Structures and Excitations

Spin Wave Excitations from Single-Crystal Quasi 1-D Antiferromagnet $CsVCl_3$

K. Kakurai, M. Arai[1)], M. Kohgi, K. Nakajima, T. Nakane[2)] and K. Ohyama

Department of Physics, Tohoku University, Aoba, Aramaki, Sendai 980
[1)] National Laboratory for High Energy Physics, 1-1 Oho, Tsukuba-shi, Ibaraki 305
[2)] Institute fot Materials Research, Tohoku University, Sendai 980

$CsVCl_3$, a S=3/2, quasi 1-D Heisenberg antiferromagnet (HAF) with a small easy plane anisotropy, is of graet interest as an half-integer spin system in connection with the "Haldane conjecture". 1983 Haldane conjectured that the spin dynamics of the half integer and integer spin value S are essentially different[1]. One of the consequence of this conjecture was the existance of the gap in an isotropic HAF with integer spin, in contrast to the gapless case of the half-integer spin. Experimentally clear evidences for the new type of quantum effect were found in the S=1 HAF chains. It then was discovered that even in the 3-D ordered phase the S=1 quasi 1-D HAF systems of ABX_3 type cannot be adequately described by the classical spin wave(SW) theory. If this is related to the specific Haldane ground state with the integer spin value, the half-integer system should behave differently. The comparison with the classical SW picture demands the knowledge of the whole SW dispersion relations in and perpendicular to the chain direction. Using the triple axis spectrometer(TAS) technique the dispersion perpendicular to the chain direction was measured. But the dispersion in the chain direction could be only followed up to an energy transfer of ~20 meV covering only 20% of the Brillouin zone[2]. Here we report the spin wave measurement up to 90 meV energy transfer at single crystal $CsVCl_3$ using the newly installed chopper spectrometer INC.

The sample consists of four, in c-direction (chain direction) oriented single crystals with the total volume of ~$3cm^3$. The scattering condition is choosen such that the chain direction is aligned parallel to the incident beam. Due to the 1-D magnetic property the k_f with the same scattering angle forming a cone around k_i probe at the equivalent q value, thus the integration over the detectors forming a ring in the forward direction is possible. Furthermore because of the large k_f, the intensities in all the small angle detectors can be summed up without causing too large an uncertainty in q. This effective use of the forward counter due to the 1-D property is the key to the successful measurement. In fig.1 the spectrum for ~38μAh with Ei=305meV is depicted. Here the intensities in all the detectors in the forward direction with 2θ=5.5-8.5° are added. The three peaks correspond to the cuts of the 1-D SW dispersion surface with the paraboloid of the accessible region of the (Q,ω) space for the group of the detectors. In fig.2 all peak positions observed with Ei=305 and 400 meV runs are displayed. The bars indicate the energy resolutions and the corresponding q-resolutions. The TAS results[2] are also indicated. Thus these INC results complete the dispersion relation in the chain direction. The analysis of the whole dispersion relation including the direction perpendicular to the chain is in progress to pursue the Haldane problem addressed in the introduction.

References : [1] F.D.M. Haldane, Phys.Rev. Lett., 50 (1983) 1153;[2]H. Kadowaki et al.,J. Phys. Soc. Japn ., 52 (1983) 1799

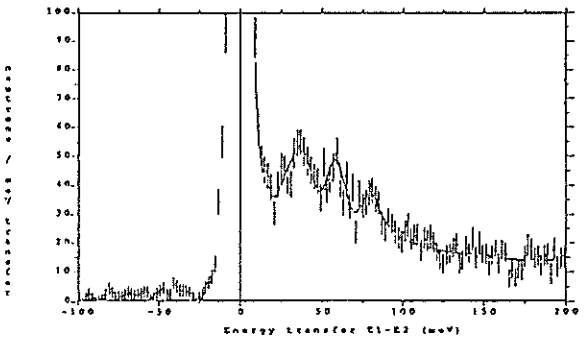

Fig.1

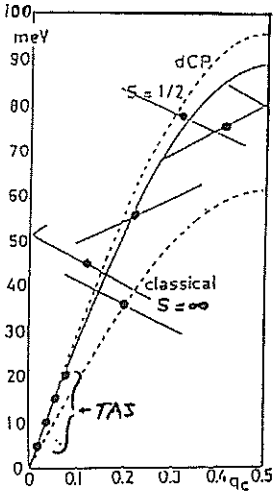

Fig.2

Neutron Inelastic Scattering from Isolated Clusters in Dilute Anisotropic Magnets $Rb_2Co_cMg_{1-c}F_4$

H. IKEDA, M. KOHGI*, K. OHOYAMA*, M. ARAI, T. NAKANE**

National Laboratory for High Energy Physics, 1-1 Oho, Tsukuba-shi, Ibaraki 305
*Department of Physics, Tohoku University, Sendai 980
**Institute for Materials Research, Tohoku University, Sendai 980

We have observed internal energy levels of two-spin clusters in the dilute magnetic systems $Rb_2Co_cMg_{1-c}F_4$ (c=0.2 and 0.3). Rb_2CoF_4 is a protoypical two-dimensional Ising-like antiferromagnet with Neel temperature of 103 K [1] and spin Hamiltonian is described by anisotropic exchange interactions between Co^{2+} spins (S=1/2) as follows, $H = \sum_{I,J} I S_I^z S_J^z + \sum_{I,J} J(S_I^x S_J^x + S_I^y S_J^y)$,where intralayer coupling constants I and J have already been determined from the spin-wave energy dispersion relation to be 7.73 and 4.27 meV respectively.[2]

The samples used in the present study are diluted systems with nonmagnetic Mg atoms and the concentration c of magnetic atoms (c=0.2 and 0.3) is far below the percolation concentration of the square lattice, c_p=0.593. We chose the Co concentration so as to realize the systems with the smallest cluster consisting of only two magnetic atoms. In the two-spin cluster with S=1/2, there are four eigenstates. By diagonalizing the above described anisotropic exchange Hamiltonian, we can easily obtain the lowest state (S_{12}=0, S_{12}^z=0), a first excited state E1 (S_{12}=1, S_{12}^z=0) with energy of 2J, and a doublet state E2 (S_{12}=1, S_{12}^z=±1) with higher energy of 1+J, where $S_{12}=S_1+S_2$.

In order to perform direct observation of transitions between different states, we have utilized a chopper-type neutron scattering instrument (INC) installed at KENS.[3] In Fig. 1, we show the intensity distribution at 20 K as a function of energy transfer in $Rb_2Co_{0.3}Mg_{0.7}F_4$. The total measuring time was about 7 hours. As is evident from the figure, four inelastic peaks are distinguished. The fourth peak at 13.6 meV arises from the local phonon excitations. When the pure crystal value of I and J are utilized, the transition energies between different three states in the two-spin cluters are calculated to be 3.46, 8.54 and 12.00 meV. In our experiments on Co 30% sample, first three peaks appear at 3.8, 7.7 and 11.4 meV. From these latter values, we can deduce the exchange constants in Co 30% sample as I=7.6 meV and J=3.8 meV. which are slightly smaller than the pure-crystal values.

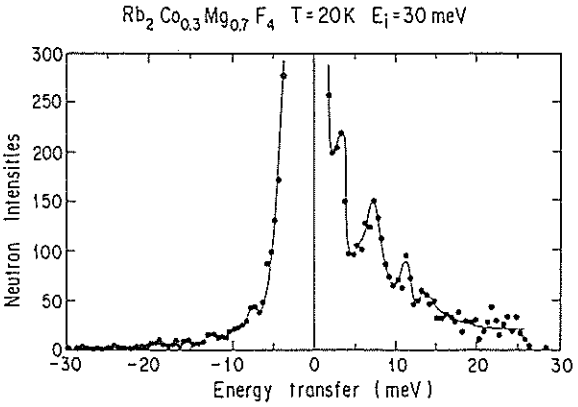

Fig.1 Scattering intensity distribution in $Rb_2Co_{0.3}Mg_{0.7}F_4$ as a function of energy transfer at T=20 K. The lines are guide to the eyes.

From the present experiments, we have successfully observed the intra-cluster magnetic excitations in the diluted antiferromagnets of both Co 30% and Co 20% samples and determined the anisotropic exchange constants directly from inelastic neutron scattering and hence neutron scattering can offer a useful information for the magnetic interactions even in the systems with "magnetic impurities" in the host nonmagnetic materials.

References

1) E. J. Samulesen, Phys. Rev. Lett. 31, 936 (1973)
2) H. Ikeda and M. T. Hutchings, J. Phys. C 11, L529 (1987)
3) M. Arai, M. Kohgi, M. Itoh, H. Iwasa, N. Watanabe, S. Ikeda and Y. Endoh, Proc. of the 10th Meeting of the Int. Collaboration on Adv. Neutron Source, Los Alamos, USA, 297 (1988)

Magnetic Excitations in Isolated Clusters of a Diluted Heisenberg Magnet $RbMn_{0.15}Mg_{0.85}F_3$

M. TAKAHASHI, S. IKEDA*, H. IKEDA*

Department of Physics, Ochanomizu University, Bunkyo-ku, Tokyo 112
*National Laboratory for High Energy Physics, 1-1 Oho, Tsukuba-shi, Ibaraki 305

We have performed neutron inelastic scattering measurements on a diluted Heisenberg magnet $RbMn_{0.15}Mg_{0.85}F_3$, in which the concentration of magnetic atoms is far below the percolation threshould (c_p=0.31). The aim of the present study is to observe directly the intracluster excitations inherent in the isolated clusters. The corresponding pure system of $RbMnF_3$ is a most ideal three-dimensional Heisenberg antiferromagnet with cubic perovskite structure. The exchange interaction is antiferromagnetic and dominant for only nearest-neighbors. The diluted system $RbMn_{0.15}Mg_{0.85}F_3$ predominantly consists of two- or three-spin clusters in which spins also interact only with nearest-neighbors. The ratio between the population rates of two-spin (p2) and three spin (p3), p2/p3, is about 5.1 for Mn concentration of 0.15. Therefore, we can expect to observe the inelastic neutron scattering predominantly from the two-spin clusters.

The experiments have been carried out on a polycrystalline sample, with volume of 12 cm^3, by using LAM40 spectrometer installed at KENS.[1] Figure 1 shows the result taken at 20 K, where we show the integrated intensities over 5 independent counters with different scattering angles. The time required to take the data was about 7 hours. We can see five peaks in the spectrum, which correspond to intracluster transition energies within two-spin cluters, 2J, 4J, 6J, 8J and 10J. The curves in the figure show the fitting of the data to the Lorentzian line-shape. From this, we can determine the exchange constant in this compound as J=0.36 meV. The exchange constant for pure crystal is J=0.29 meV.[2] The increse of J is mainly due to the decrease of the lattice constant by dilution. The measured value of diluted system by X-ray is 4.1338 A and is smaller than 4.2281 A in $RbMnF_3$. As for the scattering intensities, we compared the calculated scattering cross section with the observed ones and obtained the good agreement between them.

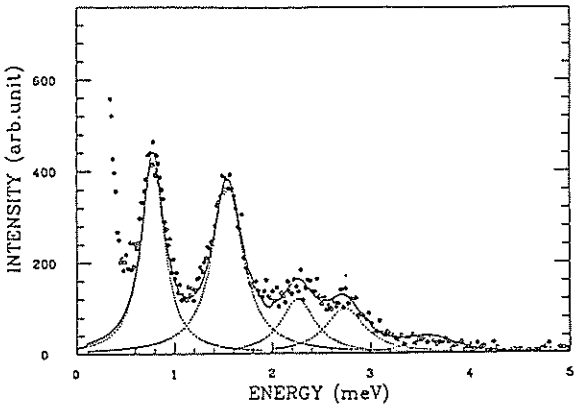

Fig. 1 Observed energy spectrum in a diluted magnet $RbMn_{0.15}Mg_{0.85}F_3$ at 20 K. The lines are fits to the Lorentzian shape.

Finally, it should be noted here that the feasibility of LAM40 for observation of the magnetic excitations even in such a non-condensed spin system is quite high. The detailes of the present study will be published elsewhere in the near future.

References

1) K. Inoue et al., Nucl. Inst. Meth. A238, 401 (1985)
2) C. G. Windsor and R. W. H. Stevenson, Proc. Phys. Soc. 87, 501 (1966)

Magnetic Excitations in Ni_3Mn Alloy with Various Atomic Ordering States.

K. TAJIMA, Y. KITADE, Y. TANAKA, Y. TODATE# and H. IKEDA#

Department of Physics, Keio University, Hiyoshi, Yokohama 223
#Department of Physics, Ochanomizu University, Ohtsuka, Tokyo115

Ni_3Mn alloy exhibits anomalous magnetic behaviours which depend strongly on atomic ordering states [1~3]. Neutron diffraction study [4] confirmed that the intensity and the width of the superlattice line which reflects the mean degree of atomic order and the size of the ordered region respectively are sensitively controlled by both temperature and time of the heat treatment. The aim of the present experiment is to study the magnetic excitation in various atomic ordered states, especially to find the effect of the size of the atomic ordered region on the magnetic excitations. The magnetic excitation in Ni_3Mn with nearly perfect atomic ordered state has been already measured[5~7] and the spin wave constant D which is defined as $\hbar\omega = D\,q^2$ has been obtained to be 300 ± 20 meVA^{-2} at room temperature. Measurements for the same sample with various heat treatment have been performed at room temperature, but no significant difference with the results of the nearly perfect ordered sample could be observed, although magnetic properties such as magnetic moment and the Curie temperature are drastically changed by heat treatment. In a disordered sample, however, magnetic excitations have been found to smear out in low energy region. Examples of the time of flight spectra of the disordered and the partially ordered samples at room temperature are shown in Figs.1 and 2. The magnetic excitations which are indicated by arrows smeared out in disordered sample at the energy of 10 meV while it still exist at 16 meV. In order to obtain the disordered state, the sample was quenched to the water from 800C, but

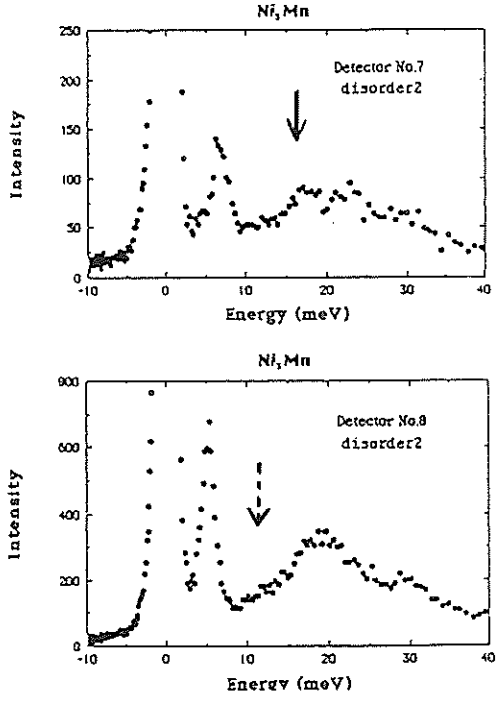

Fig.1 Energy spectra of the disordered Ni_3Mn at room temperature. Arrows indicate magnetic excitations. The magnetic peak around 10meV which was observed in the ordered or partially ordered sample has been smeared out.

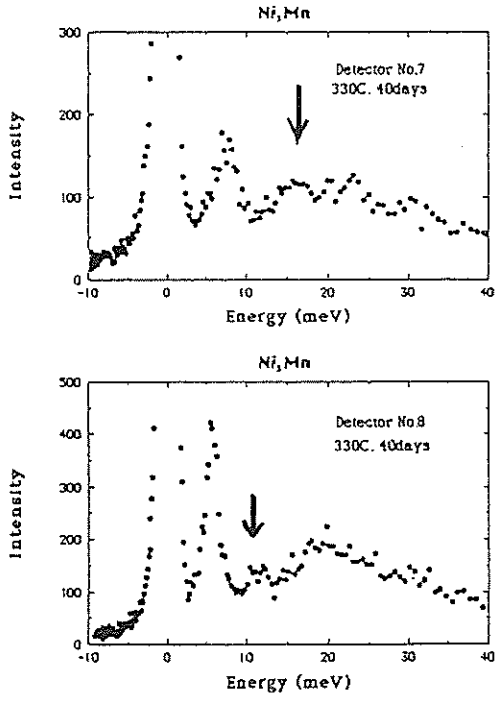

Fig.2 Energy spectra of the partially ordered Ni_3Mn at room temperature. Arrows indicate magnetic excitations.

because of the big size of the sample(11 cm^3) the quenching was not complete and relatively broad superlattice line still remains. These results may suggest that the magnetic excitation in Ni_3Mn is only from ordered clusters in the sample and that the smearing out of the low energy excitation spectrum reflects that the size of the ordered cluster which still exists in disordered sample is smaller than the wave length of the spin waves of the low energy range. Although the large incoherent scattering from Ni which has a broad maximum peak around 20 meV make it difficult to observe the magnetic excitation spectrum accurately, more detailed experiments and analysis should be required to confirm the results.

References

1)M.Marcinkovski and N.Brown;J.Appl.Phys. **32,** 375(1961)

2) A.Paoletti, F.Ricci and L.Passari: J.Appl.Phys. **37** 3236(1966)

3) N.Naono, K.Tajima, T.Suzuki and H.Asano: KENS Report-**VII**,85(1988)

4) N Wakabayashi; Phys. Rev. **B33**,6441(1986)

5) P.Blankenhagen and B.Scheerer: J. Mag .Mag. Mat. **13**,116(1979)

6)P.Blankenhagen, C.Lin, B.Hennion and M.Hennion: Phisica**120B,**170(1983)

7) K.Tajima,Y.Kitade, Y.Todate and H.Ikeda; KENS Report-**VII**, 92 (1988)

High Energy Magnetic Excitation in High Tc Superconductor LaSrCuO4.

M.Arai*, K.Yamada, M.Kohgi, Y.Endoh, K.Ohoyama and T.Nakane+

*National Lab. for High Energy Physics
Physics department of Tohoku Univ.
+Institute of Material Science of Tohoku Univ.

The magnetism in high Tc superconductor is one of the most important key for understanding the novel superconductivity. Extensive studies have been achieved on the magnetic properties of $La_{2-x}Sr_xCuO_4$ because of its simplest crystal structure among the relevant materials.

The neutron scattering from this system revealed a microscopic magnetic features and got remarkable properties[1] contrast with the spin dynamics in typical quasi-two dimensional (2D) antiferromagnet such as K_2NiF_4. At high temperature the system with low-hole concentration has a 2D magnetic correlations on the a-c plane (CuO_2-plane) of the orthorhombic crystal structure with spins in plane. The spins on Cu^{2+} atoms are interact through O^{2-} by superexchange interaction making the direction collinearly. The coupling constant J is estimated to be 0.05-0.1eV by several methods. This ordering is very sensitive to the oxygen and Sr concentration, i.e. hole concentration. The spin wave from the 2D magnetic correlation has recently been explained very well by a quantum nonlinear sigma model[2] suggesting that the system does not have RVB[3] state in normal state. On doping Sr or hole, incommensurate 2D correlation and weak 3D correlation appear and at the same time spin wave is destroyed. By increasing Sr and making system superconductor, inelastic scattering diminishes and quasi-elastic scattering increases. This is due to frustration by additional ferromagnetic interaction which is introduced between Cu^{2+} neighbouring hole doped O^-. The hole doping make the system metallic, thus the holes can move easily in the system. In this situation it is expected that spin singlet pair can be wonder in system associated with the hole moving. This state could be RVB state as expected in the early stage. Excitation from RVB is calculated and we expect to have scattering around hw=0 and hw=2J[4].

Here we show the neutron inelastic scattering results from La1.8Sr0.2CuO4 (powder, Tc=30K). The data at 200K was subtracted from that at 20K. Around 60meV , which is unexpected energy value though, a possible excitation was observed and the intensity decreases rapidly for higher momentum transfer. The statistics is extremely weak due to the spin 1/2 system, and we can not have confidence on this results. However the this is an encouraging preliminary step for a high statistics measurement in future.

References
1) Y. Endoh, et al. Phys. Rev. B37, 7443(1988)
2) K. Yamada et al. Phys. Rev. in press
3) P.W.Anderson, Science 235, 1196(1987)
4) T. Matsubara

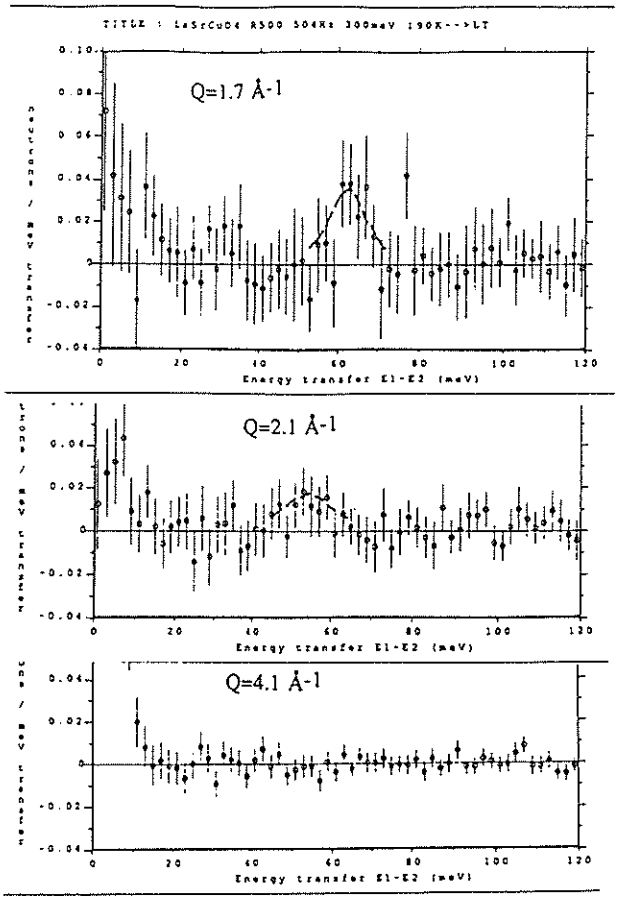

The intensity difference between that at 20K and at 200K. Intensity at 60meV is a possible magnetic scattering from RVB state, which diminishes rapidly with the momentum transfer.

Neutron Inelastic scattering from Yb monopnictides

K.OHOYAMA,M.KOHGI,T.NAKANE*,A.OYAMADA,T.SUZUKI,M.ARAI**

Department of Physics,Tohoku University ,Aramaki Aoba Sendai 980
*Institute for Materials Research, Tohoku University,Katahira Aoba Sendai 980
**National Laboratory for High Energy Physics,Oho Tsukuba Ibaraki 305

Yb monopnictides, YbX(X=N,P,and As), which have the cubic NaCl-type crystal structure, show strongly enhanced low temperature specific-heat. They undergo antiferromagnetic transition around 0.5K[1] with small moment. In YbP, total molar entropy of Rln2, which is expected for a doublet ground state[2], is only recovered if the temperature is raised to much above 20K. Therefore, Yb monopnictides are of particular interest as the systems which are characterized by competition between RKKY interaction and Kondo effect.

In order to study the mixing effect in this system through the observation of crystal field(CF) excitations, we performed inelastic neutron scattering experiment on powder samples of YbN,YbP, and YbAs using the Time-of-Flight chopper type spectrometer INC installed at the pulsed neutron source KENS in National Laboratory for High Energy Physics (KEK). In order to estimate the phonon contribution, the scattering from non-magnetic reference materials LaN and LuN was also measured with INC with the same condition. A part of the experimental results was reported in elsewhere[3]. Recently, Dönni et al. also reported the neutron scattering results on the same system[4][5]. Their results are in good agreement with ours for YbAs[5], but with some discrepancies for YbN and YbP. In order to make clear the origin of the discrepancy, we performed some additional experiments on INC and reanalized the data. We also performed the experiments on the crystal analyzer type spectrometer LAM-D at KENS, KEK. The spectrometer uses the final energy of 4.5meV and has rather high resolution at low energy transfer range.

The CF Hamiltonian for cubic symmetry can be written as:

$$Hcf=B_4(O_0^4+5O_4^4)+B_6(O_0^6-21O_4^6), \qquad (1)$$

where O_n^m are the Stevens operator and the B_n are the CF parameters, respectively. The effect of the CF Hamiltonian(1) is to split the Hund's rule ground state $^2F_{7/2}$ of Yb^{3+} into two doublets Γ_6, Γ_7 and a quartet Γ_8. The order of CF level scheme of this system has been determined as Γ_6(ground state)-Γ_8-Γ_7[2][3]. The Γ_8–Γ_7 excitation is forbidden because of symmetry reason. Therefore, the low temperature magnetic scattering should involve only Γ_6-Γ_8 excitation.

Fig.1 and Fig.3 show magnetic parts of energy spectra of YbP and YbN at 20K(open circles) and room temperature(solid circles) observed with INC with incident energy of 60meV at the scattering angles from 5.5 to 12degrees. All of these spectra were corrected for the back ground and absorption. The phonon scattering contribution estimated from the high scattering angle(about 130degrees) data are subtracted from the raw data[3], where we assumed that the scattering angle dependence of the phonon component in the YbX data is same as that of the reference material case. The solid and dashed curve in Fig.1 and Fig.3 show the results of of the least squares fit with resolution convolution to INC data. The details of the fitting procedure will be described latter. Fig.2 and Fig.4 show energy spectra of YbP and YbN on LAM-D at 15K and room temperature at the scattering angle of 35degrees, which were corrected for the back ground and the wavelength dependence of incident neutron flux. It is noticed that these spectra include both magnetic and phonon scattering.

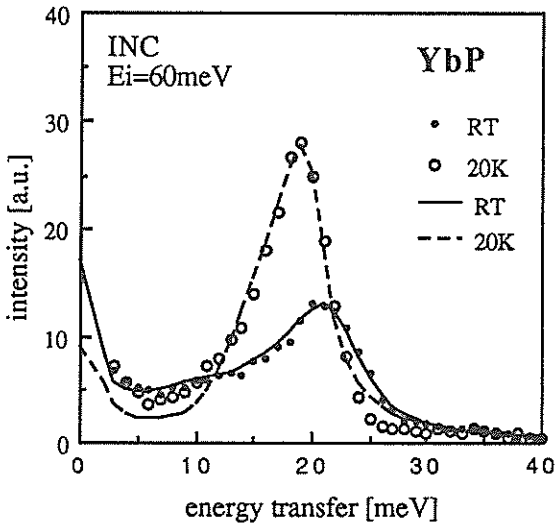

Fig.1 Energy spectrum of YbP at 20K (open circles) and room temperature (solid circles)

First, we discuss the results of YbP. In Fig.1(INC) and Fig.2(LAM-D), a single peak is seen at about 19meV at low temperature, so that we assign this peak as Γ_6-Γ_8 excitation. By means of the fitting procedure to the INC data at 20K where the cross section is assumed to be a Lorentzian, the best agreement was obtained with the following result:Γ_6-Γ_8(19.8meV). The dashed curve in Fig.1 shows the result of the best fit. In the fitting procedure, the linewidth of quesi-elastic scattering were held fixed using the values determined from the LAM-D data. At room temperature, it is noticed that the peak shifts to larger energy. Dönni et al. reported that this shift comes from growth of Γ_8-$\Gamma_7$scattering at 24meV[4]. However, we propose that the peak position of Γ_8-Γ_7 excitation is at 12meV rather than at 24meV as reported in [3] because of the following two reasons. (i)If it is assumed that Γ_8-Γ_7 excitation is at 24meV, its intensity is only about 40% of that of Γ_6-Γ_8 excitation at room temperature. It is too weak to cause the shift of the peak. (ii)LAM-D data(Fig.2) shows a phonon peak at around 10meV as seen in the spectrum at 15K. However, there seems to be that an additional intensity other than the phonon scattering grows at around 12meV at room temperature. Therefore, it is natural to think that the scattering is magnetic and is assigned as the Γ_8-Γ_7 excitation.

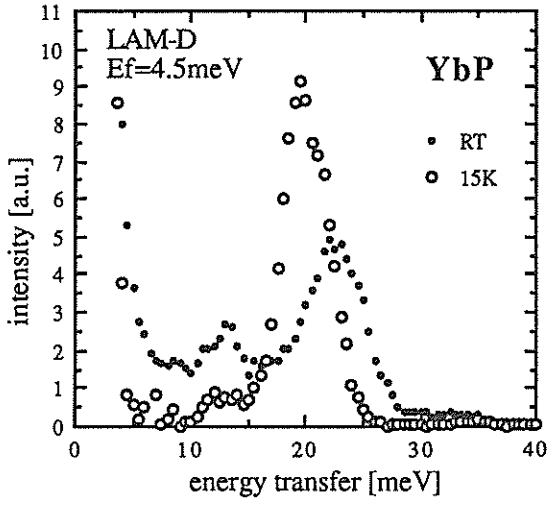

Fig.2 Energy spectrum of YbP at 15K (open circles) and room temperature (solid circles) observed with LAM-D

Hence, by means of the least squares fitting procedure to INC data where the cross section is assumed to be two Lorentzians, the CF level scheme of YbP at room temperature was established to be Γ_6-Γ_8(22.4meV)-Γ_7(34.3meV). This result is consistent with that of our previous work[3], and disagrees with the result of Dönni et al.[4]. The result of the best fit to the data at room temperature is shown by the solid curve in Fig.1.

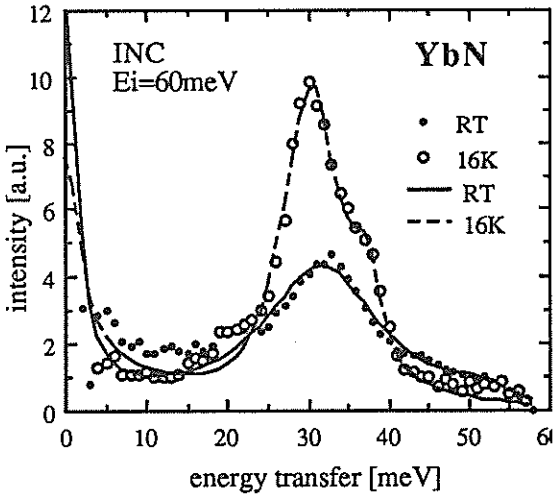

Fig.3 Energy spectrum of YbN at 16K (open circles) and room temperature(solid circles)

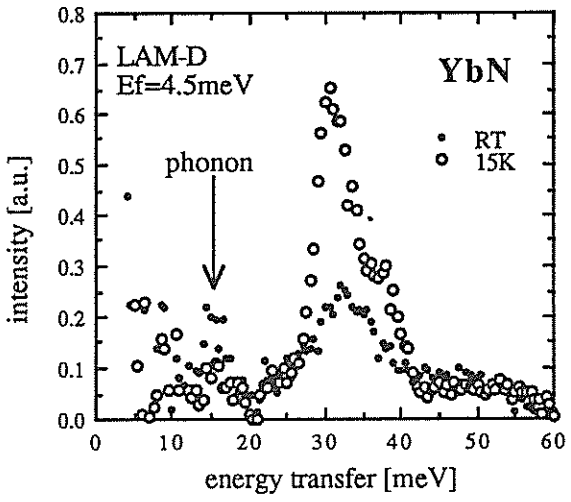

Fig.4 Energy spectrum of YbN at 15K (open circles) and room temperature (solid circles) observed with LAM-D

Next, we discuss the results of YbN. First of all, notice that the spectrum of at 16K shows not a simple single peak but with a shoulder as seen in Fig.3(INC)

and in Fig.4(LAM-D). This fact indicates that the Γ_8 quartet splits into two doublets at low temperature. However, neutron powder diffraction experiment performed on HRP at KENS proved that YbN still has the NaCl structure at 16K. The one possible mechanism of this phenomena may be the coupling between CF excitation and phonons[3]. A detailed study on this point is now under way. From the fitting procedure to the INC data at 16K where the cross section is assumed to be two Lorentzians, the best agreement was obtained with following level scheme:Γ_6-Γ_8(31.6meV,38.3meV). The result of the best fit is shown by the dashed curve in Fig.3.

At room temperature, there are two possible positions for the Γ_8-Γ_7 excitation in INC data(Fig.3), which are at about 15meV or at about 45meV. A same temperature dependent behavior occurs also in LAM-D(Fig.4). The LAM-D data(Fig.4) shows, however, that there is a peak at about 15meV even at 15K and that its temperature dependence can be explained as that of the Bose factor. Therefore, the peak at 15meV is assigned to the phonon scattering, and the intensity increase at about 45meV at high temperature should be regarded as growth of the Γ_8-Γ_7 excitation. Based on the above level assignment, from the least squares fitting to INC data at room temperature, where the cross section is assumed to be two Lorentzians, the best agreement was obtained with following level scheme:Γ_6-Γ_8(33.1meV)-Γ_7(85.0meV). The result of the best fit to the data at room temperature is shown by the solid curve in Fig.3. This result of the level scheme agrees with the result of Dönni et al.[4]. The reason of the discrepancy of the level scheme between the present work and our previous work[3] is the difference of estimation of phonon component at around 45meV. However, at present, the origin of the intensity at around 15meV at room temperature in INC data is not clear. In this fitting procedure, we assumed that Γ_8 quartet do not split at room temperature. However, best fit procedure gives the unusually wide linewidth of Γ_6-Γ_8 for 7.2meV. Therefore, Γ_8 quartet may also split at room temperature.

In the simple effective point charge model for cubic symmetry, CF parameter, B_4 is written by,

$$B_4=7/36\ (Ze^2\langle r^4\rangle\chi_4)\ /\ R^5, \qquad (2)$$

where R is the distance of the coordinating charge from magnetic ion, χ_4 is a reduced matrix element, and $\langle r^4\rangle$ is the 4th moment of the radial integral of the 4f electrons.

From eqs.(2), the obtained CF splitting of YbN,YbP and YbAs[3] correspond to the effective charge using the Dirac-Fock values for $\langle r^4\rangle$ of 3.6e(YbN), 2.9e(YbP), and 4.3e(YbAs). The results is shown in Fig.5. In the our previous work[3], we proposed the systematic change of the effective charge when going from YbN to YbAs. However, in the present work, there is no signs of systematic change.

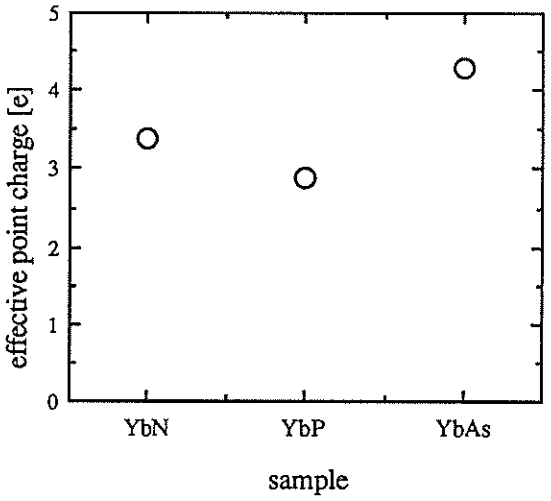

Fig.5 effective point charge of YbX (X=N,P,As)

references

[1]H.R.Ott,H.Rudigier,F.Hulliger.
:Solid State Commun.**55**(1985)113
[2]R.J.Birgeneau,E.Bucher,J.P.Maita,L.Passell,
K.C.Turberfield.:Phys.Rev.**B8**(1973)5345
[3]M.Kohgi,K.Ohoyama,A.Oyamada,T.Suzuki,
M.Arai:Phys. Rev. **B163**(1990)625
[4]A.Dönni,P.Fisher.A.Furrer:to be published
A.Dönni,P.Fisher,A.Furrer,F.Hulliger,H.R.Ott:to be published
[5]A.Dönni,P.Fisher,F.Hulliger:Solid State Commun.**71**(1989)365

Competition between the Kondo effect and RKKY Interactions in $CeSi_x$

M. KOHGI, T. SATOH, K. OHOYAMA, M. ARAI *

Department of Physics, Faculty of Science, Tohoku University, Sendai 980
* National Laboratory for High Energy Physics, 1-1 Oho, Tsukuba, Ibaraki 305

The intermetallic compound $CeSi_x$ is a typical system which shows a crossover transition from a Kondo-like state to a magnetically ordered state. The compound shows typical heavy Fermion anomalies with no magnetic ordering down to 0.1 K for $1.85 \leq x \leq 2.0$ and becomes ferromagnetic for $1.6 < x < 1.85$ with a Curie temperature less than about 13 K [1,2]. It crystallizes in the tetragonal α-$ThSi_2$ type structure in the concentration range $1.8 \leq x \leq 2$, and is distorted slightly to the orthorhombic α-$GdSi_2$ type structures for $1.6 < x < 1.8$ [1,3,4]. We consider that the crystal distortion has little correlation with the crossover phenomena, because the distortion is rather small (~1%) and the magnetization as well as the unit cell volume shows no distinct jump around the boundary concentration x=1.85 [3,4,5].

In order to investigate the crossover phenomena in this system, we performed the neutron inelastic scattering experiments on the polycrystalline samples of the compounds $CeSi_x$ with x=1.68, 1.80, 1.85 and 1.90 at the chopper type spectrometer INC at KENS, KEK. The first two compounds were found to be ferromagnetic with the Curie temperatures of 13 and 12 K, respectively. A part of the experimental results was reported elsewhere [6]. Fig. 1 shows the spectra of these compound at about 20 K with the incident neutron energy of 60 meV and with the scattering angles from 5.5 to 12 degrees. The phonon contribution estimated from the high angle (~130 degrees) scattering data are subtracted from the raw data [6]. The instrumental resolution is demonstrated by a curve with shade. Two inelastic peaks with large linewidths are seen for all spectra. They correspond to the excitations from the ground state to the two excited states of the Ce f-electron in the crystal field, the energies and linewidths of which increase with increasing x. The solid curves in the figure show the least squares fit of the calculated intensity with resolution convolution to the data, where the cross section is assumed to be the sum of two Lorentzian spectral functions. The obtained excitation energies Δ_1 and Δ_2 are listed in the Table I.

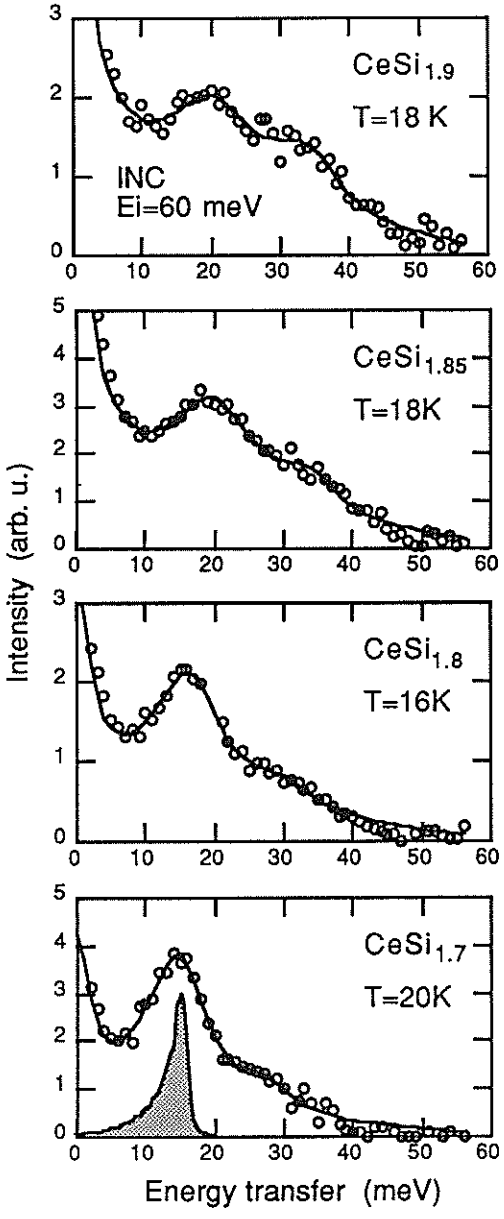

Fig. 1 The magnetic response in $CeSi_x$ at low temperatures measured on INC. Solid curves show the least squares fit to the data.

First, we discuss the origin of the crossover phenomena in this system by taking account of the present experimental results. The Kondo temperature T_K of a Ce impurity in the crystal field is expressed

Table I. Crystal field level splitting Δ_1 and Δ_2, electonic specific heat coefficient γ, estimated c-f coupling constant $|\rho J|$ and characteristic temperatures T_K, $T_K^{(6)}$ and T_{RKKY} of $CeSi_x$.

x	Δ_1(K)	Δ_2(K)	γ(J mol^{-1}K^{-2})	$\|\rho J\|$	T_K (K)	$T_K^{(6)}$ (K)	T_{RKKY} (K)
2.0	290#	557#	0.104*	0.043	42	204	22
1.9	245	411	0.151*	0.040	29	152	19
1.85	245	411	0.234*	0.038	19	123	17
1.8	202	366	–	0.036†	13	103	16
1.7	172	325	–	0.033†	5	66	13

#after reference [9]; *after reference [2]; †extrapolated value.

in the most divergent approximation of the Coqblin-Schrieffer model as [7]:

$$T_K = D\left(\frac{D}{T_K+\Delta_1}\right)\left(\frac{D}{T_K+\Delta_2}\right)\exp\left[-\frac{1}{2|\rho J|}\right], \quad (1)$$

where D is the half width of the conduction band, ρ is the density of states of the conduction electrons at the Fermi energy and J is the exchange integral between 4f electron and conduction electrons. For the doublet state impurity case, the Kondo temperature is also related with the electronic specific heat coefficient γ as [8]:

$$T_K = \frac{\pi R}{6\gamma}, \quad (2)$$

where R is the gas constant. Since the crystal field ground state of the $CeSi_x$ system is the doublet, we may use the equation (2) to estimate the Kondo temperature T_K of the system in the non-magnetic region (x≥1.85) from the observed γ values [2]. Then, assuming tentatively as D ~10000 K, we estimated the c-f coupling constant $|\rho J|$ in this region by applying the equations (1) using the estimated T_K's and the observed values of the crystal field splitting. For x=2 compound, we used the crystal field values reported by Galera et al. [9]. For the ferromagnetic compounds (x≤1.8), we did not use the equation (2) to estimate T_K, because, in this region, the Kondo screening must be strongly suppressed by the ferromagnetic ordering and the equation can not be used to estimate the real Kondo temperature. Instead, we calculated it from the equation (1) by using the linearly extrapolated values of $|\rho J|$ from the nonmagnetic region.

On the other hand, the characteristic temperature of the RKKY interactions, T_{RKKY}, is expressed as [7]:

$$T_{RKKY} \sim D|\rho J|^2. \quad (3)$$

In order to estimate T_{RKKY} in the $CeSi_x$ system, we assumed that its value at x=1.7 is equal to the observed Curie temperature of $CeSi_{1.7}$, say T_C=13 K. Then, we obtain the relation T_{RKKY} ($CeSi_x$) = 1.19 x10^4 $|\rho J|^2$. It is noted that this estimation gives the lower bound for the T_{RKKY} of this system, because there are strong evidences that the ferromagnetism in $CeSi_{1.7}$ is weakened by the Kondo effect [2]. Table I summarizes the estimeted T_K, T_{RKKY} and $|\rho J|$ values of $CeSi_x$ as well as the neutron scattering results. Fig. 2 shows the

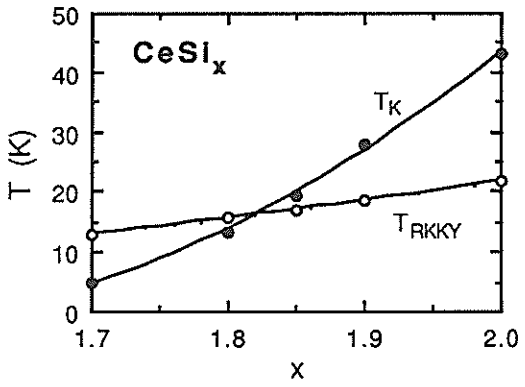

Fig. 2 Estimated Kondo temperature T_K and RKKY intteraction characteristic temperature T_{RKKY} of $CeSi_x$.

estimated T_K and T_{RKKY} of the $CeSi_x$ system. The solid lines are the guide to eye. Notice that there occurs the crossing of the T_K and T_{RKKY} curves at around x=1.82. This is in good agreement with the fact that the crossover from the ferromagnetic ordering to nonmagnetic Kondo state occurs at around x=1.85 in this system. Therefore, the present analysis strongly suggests that the crossover phenomena in the $CeSi_x$ system is caused by the increase of the c-f coupling constant $|\rho J|$ with increasing x over its critical value where the intra-site Kondo screening effect competes with the ferromagnetic ordering caused by the inter-site RKKY interactions.

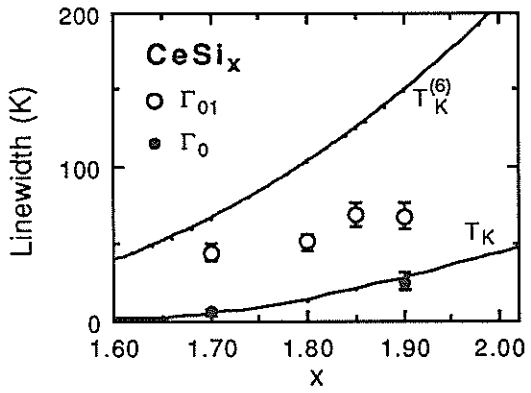

Fig. 3 Linewidths of neutron scattering of $CeSi_x$. Γ_{01}: crystal field excitations, Γ_0: spin wave (x=1.7) and quasi-elastic scattering (x=1.9).

Next, we discuss the linewidths of the crystal field excitations on the basis of the above analysis. Using the c-f coupling constant $|\rho J|$ estimated above, we can calculate another characteristic temperature $T_K^{(6)}$ which stands for the Kondo temperature in the six-fold degenerate state case and is expressed as:

$$T_K^{(6)} = D \exp\left[-\frac{1}{6|\rho J|}\right]. \qquad (4)$$

It is also regarded as the Kondo temperature defined in the temperature regime well above the crystal field splitting energy ($T >> \Delta_1, \Delta_2$). The estimated $T_K^{(6)}$ values of $CeSi_x$ are listed also in Table I. In Fig. 3, the observed linewidths of the crystal field excitation from the ground to first excited state at the low temperatures are compared with the estimated T_K and $T_K^{(6)}$. We also plotted the linewidths of the spin wave scattering for $CeSi_{1.7}$ [10] and the QES for $CeSi_{1.9}$ [11] at q=0 and at the low temperatures. The latters are in good agreement with the value of T_K as expected. Here, it is emphasized that the value of the observed linewidths of the crystal field excitations are rather the same order of $T_K^{(6)}$. From this result, it is suggested that the linewidth of the crystal field excitation is a measure of the high temperature regime Kondo temperature $T_K^{(6)}$. This is quite understandable since $T_K^{(6)}$ is the Kondo temperature associated with all the possible states of the f-electron while the crystal field excitation spectra contain the information on the Kondo effects not only in the ground state but also in the excited state.

References

[1] H. Yashima and T. Satoh, Solid state Commun. **41**(1982)723.

[2] H.Yashima, H. Mori, T. Satoh and K. Kohn, Solid State Commun.**43**(1982)193, H. Yashima, N. Sato, H. Mori and T. Satoh, ibid 595.

[3] S.A. Shaheen and J.S. Schilling, Phys. Rev. **B35**(1987)6880.

[4] W.H. Lee, R.N. Shelton, S.K. Dhar and K.A. Gschneider, Jr., Phys. Rev. **B35**(1987)8523.

[5] M. Kohgi, M. Ito, T. Satoh, H. Asano, T. Ishigaki and F. Izumi, J. Magn. Magn. Mat., to be published.

[6] M. Kohgi, T. Satoh, K. Ohoyama, M. Arai and R. Osborn: Physica B **163**(1990)137.

[7] K. Hanzawa, K. Yamada and K. Yoshida, J. Magn. Magn. Mat. **47&48**(1985)357.

[8] V.T. Rajan, Phys. Rev. Lett. **51**(1983)308.

[9] R. M. Galera, A. P. Murani and J. Pierre, Physica B **156 & 157**(1989) 801.

[10] M. Kohgi, F. Hippert, L.P.Regnault, J. Rossat-Mignod, B. Hennion, T. Satoh, F.L. Chui, T. Miura and H. Takei: Jpn J. Appl. Phys. **26**Suppl.(1987) 559.

[11] F. Hippert, B. Hennion, M . Kohgi and T. Satoh: unpublished.

Magnetic Excitations in $CoTiO_3$

Y.TODATE, H.IKEDA†, M.TAKAHASHI and Y.ENDOH††

Department of Physics, Faculty of Science, Ochanomizu Univ. Bunkyo-ku Otsuka 112
†National Laboratory for High Energy Physics, Oho, Tsukuba-shi 305
††Department Physics, Faculty of Science, Tohoku Univ. Aoba-ku Sendai 980

Cobalt titanate $CoTiO_3$ is isomorphous with ilmenite $FeTiO_3$ and antiferromagnetic below 38K [1]. Although the magnetic susceptibility of polycrystalline sample shows a typical behabiour of a three-dimensional antiferromagnet [2], that of single crystal shows significant anisotropy [3]. In the paramagnetic region above 38K, χ follows a Curie-Weiss law with p_{eff} = 5.3 Bohr magnetons [2]. Magnetic structure of $CoTiO_3$ is identical with that of $NiTiO_3$, i.e. the direction of moments is perpendicular to the hexagonal c-axis and, within the c-plane, the moments are ferromagnetically coupled but are antiparallel with respect to the c-direction [2].

Magnetic excitations in $CoTiO_3$ along the hexagonal [110] direction were measured at 15K. Thirteen detectors of MAX were used to cover the (1,1,4.5) Brillouin zone. The result is shown in fig.1. The lower two branches of excitation in the figure are an acoustic and an optical spin-wave modes . Note that the magnetic unit cell contains four Co^{2+} ions. These two branches are similar to those found in $FeTiO_3$, although $FeTiO_3$ has an oblique spin structure and exhibits complicated spin-wave spectrum [4]. Above these two modes, there exist another excitation at about $\hbar\omega$=26meV. This may be the excitation to the higher state (j=3/2, j_z=3/2) of $^4T_{1g}$ (^4F) split by the spin-orbit interaction and a trigonal component of the crystal field [5]. It should be noted that this excitation has a substantial dispersion. The dispersion may result in a small q-dependent mixing between j=1/2 and j=3/2 states.

In the ilmenite structure, there are five principal exchange interaction paths. The interaction between nearest neighbour Co^{2+} ions within the c-plane consists of two contributions: direct and 90° superexchange interaction. The latter seems to be dominant and, from the superexchange rules, is positive (ferromagnetic). If, however, the effective spin s '=1/2 is used to analyse the lower spin-wave mode, the exchange interactions may take an anisotropic form. Further experiment will be carried out .

References

1) Y.Ishikawa and S.Akimoto : J.Phis. Soc. Japan, 13(1958) 1110.
2) R.E.Newnham, J.H.Fang and R.P.Santoro: Acta Cryst. 17 (1964) 240.
3) H.Watanabe, H.Yamauchi and H.Takei: J.Magn.Magn.Mat. 15-18 (1980) 549.
4) H.Kato, Y.Yamaguchi, M.Yamada, S.Funahashi, Y.Nakagawa and H.Takei: J.Phys. C: Solid State Phys. 19 (1986) 6993.
5) J.B.Goodenough and J.J.Stickler: Phys. Rev. 164 (1067) 768.

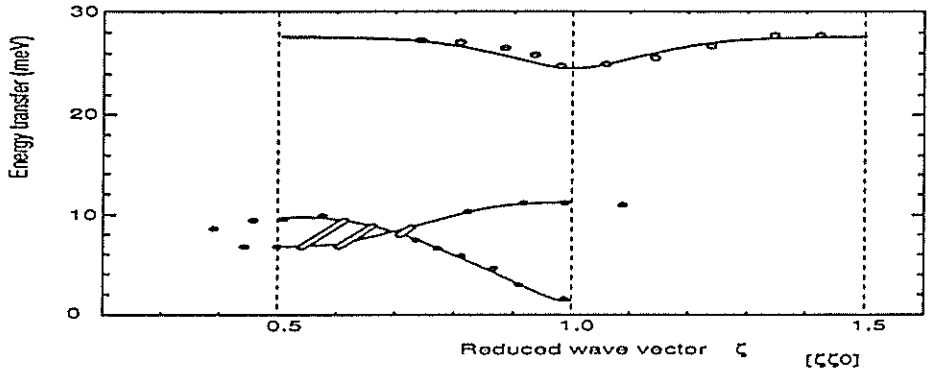

Fig. 1 Dispersion relation in CoTiO3 along the hexagonal [110] direction. The lines are guides to the eye.

Magnetic Excitations in Random Antiferromagnet $K(MnCoNi)_{1/3}F_3$

Y.TODATE, H.IKEDA†, M.TAKAHASHI, K.TAJIMA†† and Y.TANAKA††

Department of Physics, Faculty of Science,
Ochanomizu University, Otsuka,Bunkyo-ku,Tokyo 112
†National Laboratory for High Energy Physics, Oho, Tsukuba 305
††Department of Physics, Faculty of Science and Technology,
Keio University, Hiyoshi, Yokohama 223

Magnetic excitations in random antiferromagnet $K(MnCoNi)_{1/3}F_3$ have been investigated using MAX. In this crystal, three kind of magnetic ions are randomly distributed. The simplest model to describe the magnetic excitations in such random magnets may be a spin-wave theory with a mean crystal model [1]. The model regards the mixed crystal as a homogeneous system by averaging the random distribution of the magnetic ions. Together with the mean crystal model, an empirical relation on the magnetic exchange interaction [2] is also used: the magnitude of the interaction between different kind of magnetic ions can be estimated as $J_{\alpha\beta} = (J_{\alpha\alpha} J_{\beta\beta})^{1/2}$. As calculated for many other two-component random antiferromagnets, the dispersion relations of the magnetic excitations in this three-component system can be calculated using the exchange constants which have already been determined for pure materials. However, as we have noted in the previous study on $Rb_2Co_cNi_{1-c}F_4$, which is a two-dimensional random antiferromagnet, the complex behaviour of Co^{2+} ions in a crystal should be taken into consideration[3]. Since we use an effective spin $S' = 1/2$ model for the Co spin for brevity, an effective exchange constant J' between the fictitious spin pair should be determined first. In order to estimate J', energy levels and matrix elements for the Co^{2+} in $K(MnCoNi)_{1/3}F_3$ have been calculated using a single ion Hamiltonian

$$H_m = -\alpha\lambda\, l.S - H_a S_{zCo} - \frac{1}{3} 2z(J_{MnCo}\langle S_{zMn}\rangle + J_{NiCo}\langle S_{zNi}\rangle + J_{CoCo}\langle S_{zCo}\rangle) S_{zCo} .$$

We assume that the spin-orbit coupling constant, the exchange constant J between the real Co^{2+} spins and the anisotropy energy H_a have the same values as those in the pure $KCoF_3$[4]. In the molecular (exchange) field which can be determined self-consistently, splitting of the lowest Kramers doublet is 34.3meV and $\langle S_{zCo}\rangle$ is 1.22 in the ground state. (However, the state with $j = 3/2$ and $j_z = 3/2$ is only 2.5meV above the $j = 1/2, j_z = -1/2$ level.) The effective exchange constant J' which gives 34.3meV as the [111] zone boundary spin-wave energy is 3.66meV, which is 0.76 of pure crystal J'. Using $J'_{CoCo} = 3.66$meV, $J_{MnMn} = 0.31$meV and $J_{NiNi} = 4.39$meV, the dispersion relations have been calculated. The dispersion relation of spin-waves in the averaged crystal takes a form of spin-waves in a six-sublattice antiferromagnet. From the calculation, three bands of excitations seem to be observed as indicated by solid lines in Fig.2. It should be noted that there are no adjustable parameters in this calculation.

Experiments were carried out at 15K along three principal axes of the crystal: [100],[110] and [111] direction. Excitation spectrum were measured around the (0.5 0.5 0.5), (0.5 0.5 1.5) and (1.5 1.5 1.5) Brillioun zone. Energy region above 20meV was surveyed extensively. However, no clear evidence for the existence of the third branch has been obtained as shown in Fig.1 and Fig.2. The main reason of the discrepancy between the calculation and the observation is not clear at present. Further information such as relative intensities between modes and peak profiles of the excitations may become important.

References

1) R.J.Birgeneau, L.R.Walker, H.J.Guggenheim, J.Als-Nielsen and G.Shirane: J. Phys. C, 8(1975) L328.
2) R.A.Cowley and W.J.L.Buyers:1972, Rev. Mod. Phys., 44 (1972) 406.
3) Y.Todate, H.Ikeda, E.Sano, F.Shibata, K.Tajima and Y.Endoh: J. Phys.: Condens.Matter, 1(1989) 5895.
4) W.J.L.Buyers, T.M.Holden, E.C.Svensson, R.A.Cowley and M.T. Hutchings: J.Phys.C,4 (1987) 2139.

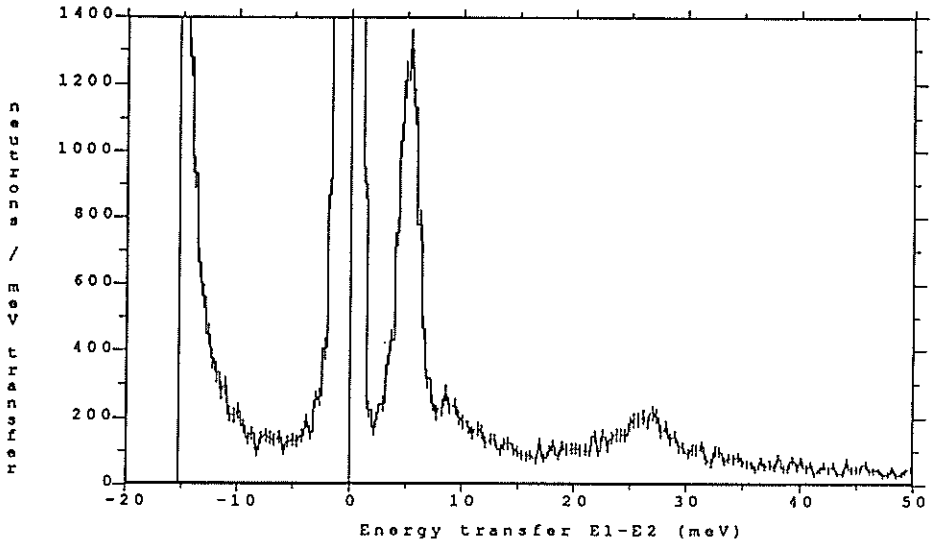

Fig. 1 Typical example of the observed inelastic scattering spectra.

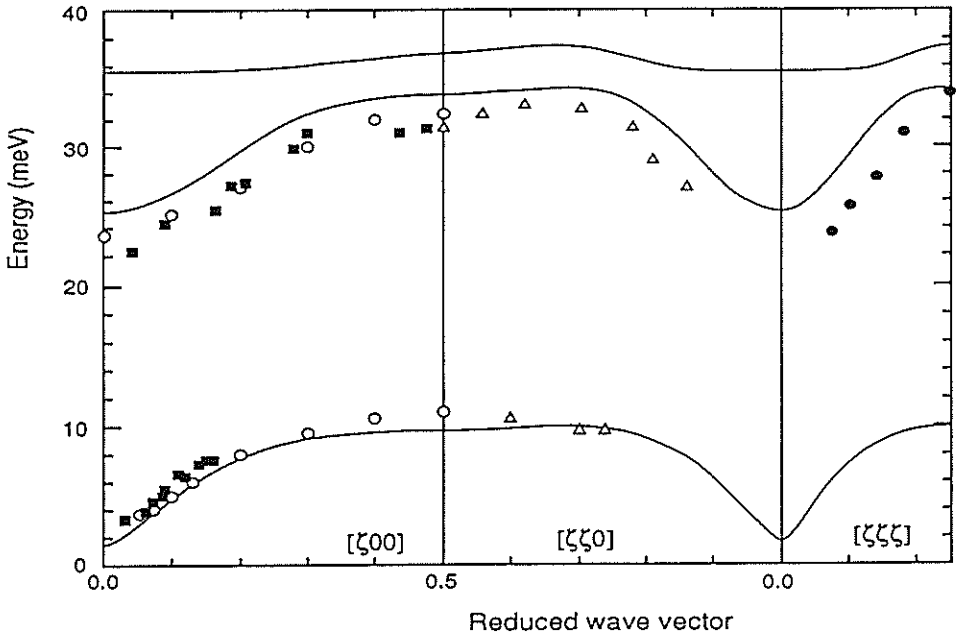

Fig. 2 Solid lines are the calculated spin-wave dispersion relations described in the text. Marks indicate the observed peak positons. Open circles are the date taken by triple-axis spectrometer TUNS at JRR-2.

Spin Waves in the Triangular Phase of Mn_3Pt

S. Tomiyoshi, H. Yasui, T. Kaneko, Y. Yamaguchi, H. Ikeda*, Y. Todate** and K. Tajima***

The Institute for Materials Research, Tohoku University, Sendai 980
*National Laboratory for High Energy Physics,1-1 Oho,Tsukuba 305
**Department of Physics, Faculty of Science, Ochanomizu University, 2-1-1, Otuka, Tokyo 112
***Department of Physics, Faculty of Science and Technology, Keio University, Hiyoshi, Yokohama 233

Intermetallic compound Mn_3Pt with the cubic Cu_3Au type structure shows very intersting first-order antiferromagnetic-antiferromagnetic phase transition. Kren et al. revealed that at low temperatures Mn_3Pt has a triangular spin arrangement with the spins lying on (111) plane and it transforms above about 400K to a collinear spin structure in which the crystallographically equivalent Mn site is devided into two magnetic sites; one with no Mn moment and the others with $3\mu_B$ per Mn atom [1,2]. This phase transition does not acccompany any change of the crystal symmetry except large volume change. Several models are proposed to explain this anomalous phenomenon, however, in order to understand the magnetic properties of this compound we need much more acccurate experimental data, especially the study of magnetic excitaions by neutron scattering is essential.

Recentry, Yasui [3] measured spin waves in both of the phases by using triple axis spectrometer, and found that a steepy slope dispersion is developing to higher energies. His measurements are confined to relatively lower energies, so in this work we tried to measure much higher energies by using the crystal analyzer spectrometr MAX which is advantageous for the measurement at higher energies compared with a triple axis spectrometer which uses usual reactors.

The sample used in the present experiments was a fairly good single crystal grown by the Bridgman technique, which has a volume of about 2.5cc. And the concentration of Mn atoms was found to be very near to the stoickiometry. In this work we measured the spin waves in the triangular phase at room temperature and 20K. And the scanning direction of q in the reciprocal lattice is along [100] through Bragg points (010), (110), (210).

Figure 1 shows some typical intensity data obtained at 20K (in the triangular phase) plotted as functions of energy and monentum transfer. The momentum q of the spin waves is measured from the reciprocal lattice point indicated in respective figure.

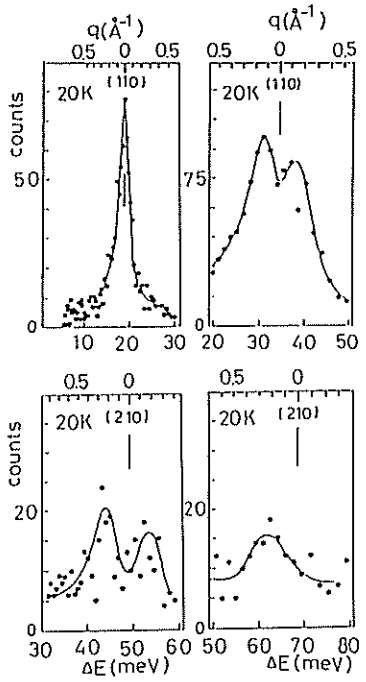

Fig. 1 Inelastic scattering peaks of Mn3Pt at 20K. As shown in the figure the inelastic peak is a single peak centered at the origin of the Brillouin zone below the energy of 20meV, but as the energy increases the singlet splits into doublet. Due to the resolution functions the intensity of the right hand side of the doublet is in general weak. The intensity of the inelastic peaks is fairly weak, especially for (210) zone. However, the spin wave peaks are well defined and the line width is not much wide. Similar patterns have been observed at room temperature.

Figure 2 shows dispersion relations obtained from the peak positions of time of flight specrtrum. The spin wave dispersion in the triangular phase is almost linear in q for q parallel to [100] direction. The dispersion begins to deviate from the q-linear line at about $q=0.3Å^{-1}$ at 20K and $q=0.4Å^{-1}$ at 295K, and

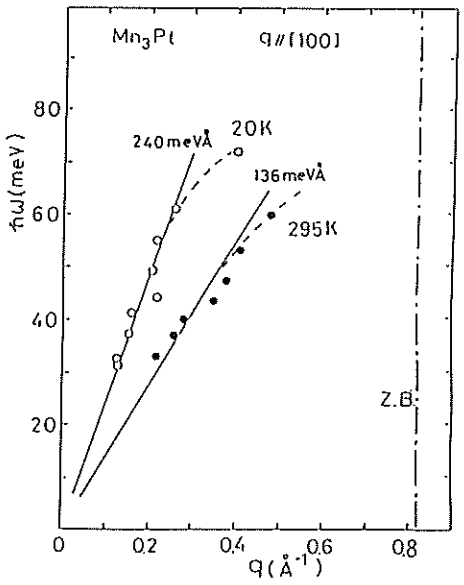

Fig. 2 Dispersion relation of the spin waves in Mn3Pt beyond that the dispersion curve begins to saturate. The intensity in higher energies is very weak, so in the present experiment the behavior of the spin waves in these regions is not clear.

In small q regions the dispersion relation of the triangular spin phase can be given by a quadratic relation $(\hbar\omega)^2=E_g^2+(cq)^2$, where c is the stiffness constant and E_g is the gap energy. Except very small q region this relation gives a q-linear dispersion. From the experimental data shown in Fig. 2 the slope c is determined to be 240meVÅ at 20K and 136meVÅ at room temperature, respectively. These values agree well with those determined by Yasui[3] from the lower energy part of the dispersion. Large value of the slope of the dispersion and large damping of the spin wave peaks are the most prominent features of the spin wave excitaions in itinerant electron antiferromagnets as found in Mn_3Ni [4]. In Mn_3Pt the damping is not small and the stiffness constnat is very large, so we can say that this compound is a system with considerable amount of itinerancy. The tempeature variation of the slope in triangular phase of Mn_3Pt is very large as shown in Fig. 2. This may be closely connected with the first-order phase transition above room temperature. Similar large reduction of the stiffness constant with the elevation of temperature has been observed in Fe_3Pt [5].

In the present experiment we measured spin waves only one q direction parallel to [100]. Measurements for q parallel to [110] and [111] are very important for the theoretical analysis. For further experiments we must do measurement for another direction and also measurements in the collinear phase is indispensable.

References.

1) E. Kren et al., Phys. Rev. 171 (1968) 574.
2) E. Kren et al., Solid State Commu. 9 (1971) 27.
3) H. Yasui, Doctor Thesis (1990), Tohoku Univ.
4) B. Hennion et al., Proc. Conf. on Neutron Scatt. (1976) 825.
5) M. Kohgi and Y. Ishikawa, J. Phys. Soc. Jpn. 49 (1980) 985.

Neutron Diffraction Study in Pulsed High Magnetic Field

H.NOJIRI, M.UCHI, M.WATAMURA, M.MOTOKAWA, H.KAWAI* and Y.ENDOH*

Department of Physics, Faculty of Science, Kobe University, Rokkodai Kobe 657
*Department of Physics, Faculty of Science, Tohoku University, Sendai 980

The purpose of this study is to perform neutron diffraction experiments using a pulsed high magnetic field and to determine magnetic structures in high field. As is well known, many magnetic materials show magnetic phase transitions in high magnetic field and it is important to investigate such high field phases by neutron diffraction. However, the magnetic field available in neutron diffraction experiments has been limited below 10 T so far even superconducting magnet is used. On the other hand, technique for producing pulsed high magnetic field and its application to physics have been well developed in this decade[1,2,3]. We consider pulsed fields synchronized with the neutron beam pulses will enable us to make high field neutron diffraction experiments. As the matter of fact, we have already tried to apply the similar way to muon experiment at KEK and have been developing a pulsed field instrument for it[4,5,6]. Our equipment is capable to produce fields up to 20 T every 2 sec and this technique is transferred to neutron diffraction experiments. The first trial has been done for determination of high field magnetic structure of metamagnetic $PrCo_2Si_2$ and succeeded to observe Bragg reflections at 16 T which is the highest field used so far for neutron diffraction experiments. In this report, we describe the outline of our first experiment.

$PrCo_2Si_2$ has Ising spin pointing to the c-axis only at Pr-site and shows[7] antiferromagnetic structure below T_1=9 K with ferromagnetic coupling in the c-plane and antiferromagnetic coupling along the c-axis. In this structure, the Bragg reflection occurs at (1,0,k') with k'=0. Between T_1 and T_2=17 K and between T_2 and T_3=30 K, it turns to complex structures with long periods along the c-axis whose reflection indices are k=0.926 and k=0.777, respectively, where k'=1-k. It is paramagnetic above 30 K. On the other hand, when an external field is applied to the c-axis at 4.2 K, it shows metamagnetic transitions[7,8] at around 1.2, 3.8 and 12.2 T. The structures at the fields between 1.2 and 3.5 T and between 3.5 and 12.5 T are expected[8] to be same as those observed between 9 and 17 K and between 17 and 30 K at zero field, respectively. The present purpose of our experiment is to confirm this model at high field. At low fields below 1.7 T, Osada *et al.* have observed decrease of T_1 and T_2 with increasing field[9].

The experiment was done using MRP diffractmeter at KEK. The magnet was the so-called Bitter type water cooling solenoid with 40 mm inner diameter, 240 mm outer diameter and 220 mm length. It was horizontally installed on the goniometer. The flow type cryostat made of FRP was set in the magnet and the temperature was down to almost 4.2 K but there was a heating problem for metal sample when a magnetic field was applied as will be mentioned later. Metal Dewar cannot be used because of integration of Joule heating due to repeating pulsed field. The sample size was 7mm in diameter and 10 mm thickness and the magnetic field was parallel to the c-axis. The beam size was about 15 X 10 mm^2. As is shown in Fig.1, the diffraction angle was kept at 2θ=10° and the horizontal rotation of the sample was limited within a few degrees because of small aperture of the magnet. the wave length of used neutron was about 1 A. The

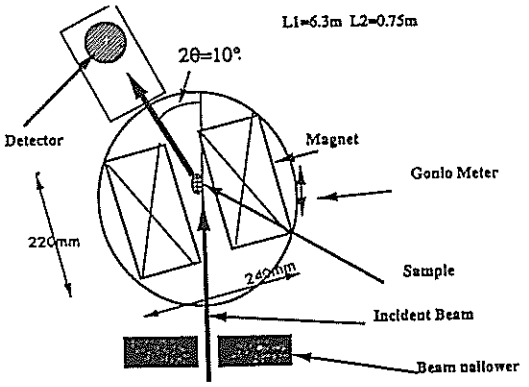

Fig.1 Experimental configuration of magnet, sample, detector and neutron beam.

expected magnetic Bragg reflections in this configuration were (1,0,k'). If the above mentioned model was right, k'=0 for antiferromagnetic state and K'=0.074 or 0.223 for two complex structures. What we had to do was observation of appearance and disappearance of these satellite reflections in magnetic fields. Our experiment takes 43 times longer time than usual experiment because of low repetition rate of field production. But the Bragg reflection inten-

sity was fairly strong and the time necessary to take one reflection signal was two hours or so.

First we observed diffraction changing temperature at zero field to adjust the configuration of equipment and to check the sensitivity and accuracy of the system. The results were consistent with previous report[7].

Next we applied external fields up to 16 T at 4.2 K. At 7.4 T, we observed a Bragg reflection at k'=0.232 which disappeared at 5 T and below it due to the change of magnetic structure as is shown in Fig.2. We consider that the magnetic structure at 7.4 T is similar to that observed between 17 and 30 K without field and the small difference between two k's seems to be due to the experimental error. At 11.5 T, similar diffraction was observed at k'=0.225 but not observed at 14 T due to a transition to paramagnetic state. These data up to 16 T are plotted in Fig.3.

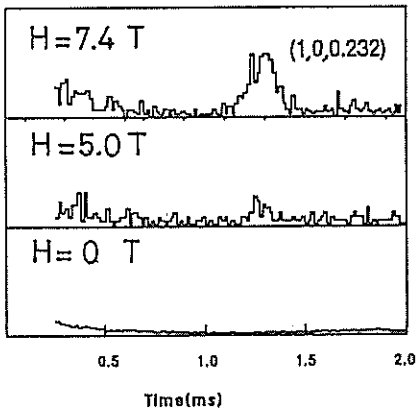

Fig.2 Field dependence of Bragg reflection at constant angle at 4.2 K.

Because the sample was metallic, we had a problem of Joule heating due to eddy current. We estimated the real temperature of the sample by the following method. External fields were applied to the sample just before the diffraction and we observed the diffractions at zero field just after heating up. Changing the field strength, we measured the intensities of magnetic Bragg reflections around (1,0,0), and compared them to the temperature dependence of diffraction intensity measured by Shigeoka *et al.*[7]. Then we could estimate the sample temperatures at the field peak. The relation between the intensity of applied field and the estimated temperature is shown in Fig.4. If an insulater material is used, this heating problem does not occur.

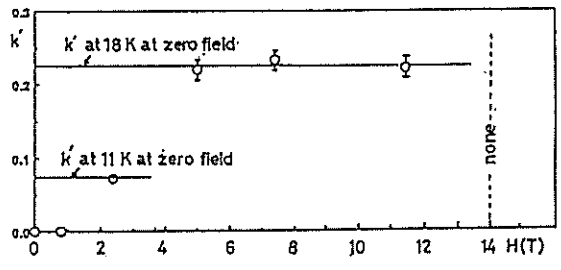

Fig.3 Field dependence of K'.

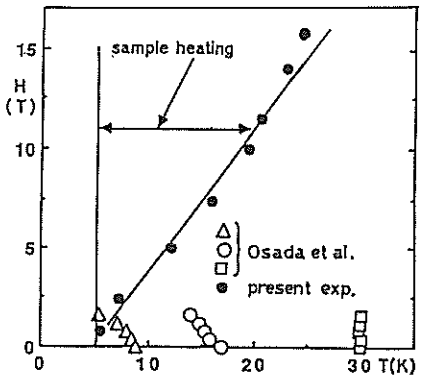

Fig.4 Observed points in phase diagram with Osada *et al.*'s result.

From these results, we conclude that our pulsed field system is usuful for high field nutron diffraction experiments.

We acknowledge Professor M.Date and Professor N.Watanabe for their encouragements and Dr. M.Arai and Dr. M.Furusaka for their helps. We also thank Dr. T.Shigeoka and N.Iwata for supplying single crystals.

References

1) Strong and Ultrastrong magnetic Fields and Their Applications, ed. F.Herlach(Springer-Verlag, 1985)
2) High Field Magnetism, ed.M.Date(North-Holland, 1983)
3) High Field Magnetism, eds. F.Herlach and J.J.M.Franse (North-Holland, 1989) or Physica B155
4) M.Motokawa, H.Nojiri, J.Ishihara and K.Ohnishi: Physica B155 (1989) 340
5) M.Motokawa, H.Nojiri, M.Uchi, S.Watamura, K.Nishiyama and K.Nagamine: to be published in Hyperfine Interactions
6) M.Motokawa, H.Nojiri, M.Uchi, K.Nishiyama and K.Nagamine: to be published in J.Mag. Mag.Mat.
7) T.Shigeoka, N.Iwata, H.Fujii, T,Okamoto and Y.Hashimoto: J.Mag.Mag.Mat. 70(1987)239
8) T.Shigeoka, H.Fujii, K.Yonenobu, K.Sugiyama and M.Date: J. Phys. Soc. Jpn 58 (1989) 394
9) M.Osada: Master Thesis, unpublished

Neutron Depolarization Study on the Magnetic Flux State in Superconductors

T.Watanabe, Y.Endoh, S.Itoh, H.Kojima*, I.Tanaka*, and N.Toyoda**

Department of Physics, Tohoku University, Aramaki Aoba-ku Sendai 980
* Institute of Inorganic Synthesis, Yamanashi University, Minamae Kofu 400
** Institute for Material Research, Tohoku University, Katahira Aoba-ku, Sendai 980

We have studied the magnetic flux state trapped in the superconductor by using neutron depolarization method. The principle of the neutron depolarization experiments is simple. A polarized neutron precesses about the field direction with the Larmor frequency. Therefore, the component of the neutron polarization perpendicular to the direction of the magnetic flux may oscillate sinusoidally with respect to neutron wavelength. In addition, on depolarization occurs in the parallel component. If the flux forms a regular lattice so that magnetic field inside the sample is uniform regardless the fine structure, the amplitude of the oscillation in polarization should also be constant with respect to the wavelength. The oscillation period corresponding to the Larmor frequency gives the magnitude of the local fiels integrated over the sample. On the other hand, if the local field is not the polarization shows exponential decay such that the polarization is eventually lost by the random local field at long wavelength limit.

We have measured two single crystalline plates of V_3Si (T_c=16.1K)[1], and $La_{1.85}Sr_{0.15}CuO_4$ (T_c=34K)[2]. The former is the typical typeII superconductor and the latter is the high temperature oxide superconductor. Typical wavelength dependent depolarization data from the latter crystal are shown in Fig.1. The sample was cooled under the magnetic field (FC) and after reaching the desired temperature to measure the polarization measurement, the applied field to induce the flux was removed. In the depolarization measurements the small external field (7Oe) was applied in such a was that the neutron polarization becomes perpendicular to the trapped flux direction, which should be along the FC magnetic field. In the zero field cooling (ZFC) process we observed no depolarization of neutrons, which impliers a perfect Meissner state with an external field of 7Oe.

On the other hand in the FC sample when the FC field becomes larger, the oscillation in polarization becomes visible with changeing the periodicity with increasing the FC field. The damping feature of the polarization with respect to the wavelength is also apprecaible in the large FC field. This result indicates that the flux distribution in the sample plate is not uniform in particular in the large field. This feature is essentially similar to the data form the V_3Si single crystal.

The lower critical field Hc1 was determined[3),4)] from the fit of the depolarization spectrum to the functional form of the damped sinusoidal oscillation in polarization, which is shown in Fig.2 as the function of the temerature. As is seen in the figure, the strong anisotropy is a characteristic feature in the oxide superconductor.

One remarkable aspect in the depolarization experiments studying the superconducting flux state is that the ploarization spectra for various FC procedures changing the field strength can be reduced a unique curve[5)] as the function of $H_{FC}\lambda$ as shown in Fig.3. It inclued by the applied field, because the induction in the sample is proportional to H_{FC}. Therefore the magnetic flux is trapped in the superconductors as expected even in the oxide superconducting crystal at lower temperatures. It is also important that neutrons are not depolarized at the infinit wavelength, which states that neutron polarization just follow in the superconducting flux state.

The quantitative analysis based on certain models for the typeII superconducting flux lattices are now processing.

The present studies are partly supported by the Grant-in-Aids for Scientific Reserch from the Ministry of Education, Science and Culture.

References

1) M.Ishino, T.Kobayashi, N.Toyota, T.Fukase and Y.Muto: Phys. Rev. 38 (1988) 4457
2) I.Tanaka and H.Kojima: Nature (London) 33 (1989) 21
3) C.P.Bean: Rev.Mod.Phys.36, (1964) 31.
4) M.Naito, A.Matsuda, K.Kitazawa and S.Kambe: Phys.Rew.B 41 (1990) 4823.
5) S.Itoh and Y.Endoh: KENS REPORT-VII (1987/88),KEK Progress Report 88-2,77.

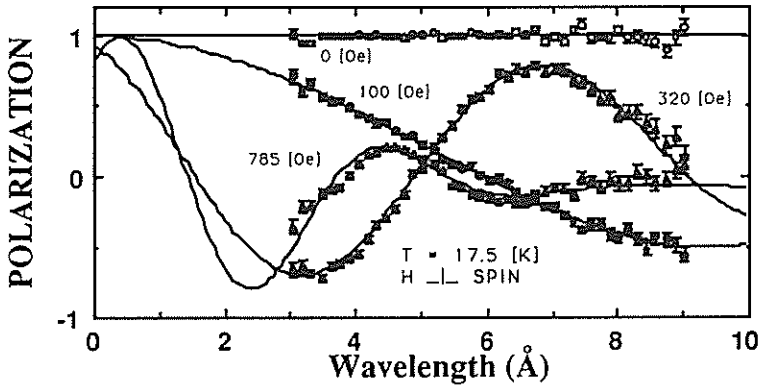

Fig.1 H_{FC}-dependentce of polarization spectra in $La_{1.85}Sr_{0.15}CuO_4$.

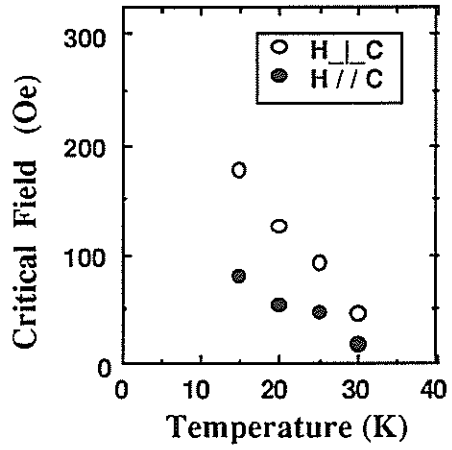

Fig.2 Temperature dependences of lower critical fields of $La_{1.85}Sr_{0.15}CuO_4$. The strong anisotropy concerning the C-axis was observed.

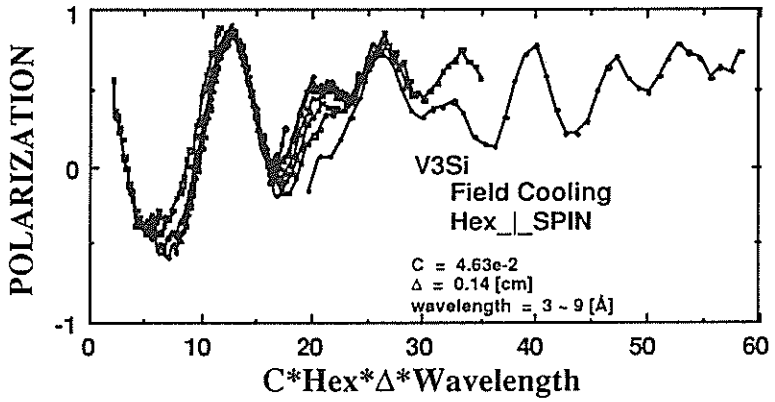

Fig.3 Polarization spectra scaled with the cooling field H_{FC}(G). Each spectra is on a uniqe curve. Δ is the sample thickness and C is a physical constant related to gyromagnetic ratio of neutron.

Magnetic Small Angle Neutron Scattering from $La_{2-2x}Sr_{2x}CuO_4$

*M.Arai, J.Suzuki and Y.Endoh

*National Lab. for High Energy Physics
Physics Dep. of Tohoku Univ.

Here we report on magnetic small angle neutron scattering from $La_{2-2x}Sr_{2x}CuO_4$ compound which has the simplest crystal structure among the relevant materials. The magnetism in high Tc superconductor is considered to be one of the keys for understanding the superconducting mechanism. The electron state of Cu^{2+} on CuO_2 sheet is $3d^9$, having spin 1/2 and an intrinsic hole, and the system has antiferromagnetic correlation expected by the Mott-Hubbard model in 1950's through the O^{2-} superexchange interaction. By adding additional charge, the system undergoes a metal-insulator transition. The crystal structure realizes a strong two-dimensional (2D) correlation with a strong quantum effec in the spin correlation as observed by neutron scattering works[1], giving an idea of resonating valence bond model as discussed on 2D triangular antiferromagnets.

The doped holes produced by the deficiency of O^{2-} or the substitution of La^{3+} by Sr^{2+} are believed to enter at the O^{2-} above the Cu^{2+} or O^{2-} in the sheet and make them O^-. The situation is very critical in the correlation between the spins on Cu^{2+} and O^- depending on where holes actually goes in. The Mott-Hubbard antiferromagnetic state or the charge transfer state is to be realised when the holes enter at the P orbit of the O^{2-} above Cu^{2+} or P_π or P_σ orbit of O^{2-} in the sheet. When the holes enter at the oxygen in the sheet, the correlation of the spins of Cu^{2+} becomes ferromagnetic because of the appearance of the direct correlation between the spins on Cu^{2-} and O^-.

A theory[2] suggests that if the system is a charge transfer state by having a hole at P_σ orbit, the system has lower energy state and the intrinsic hole on Cu^{2+} and the hole on P_σ orbit make a pair and wander around the system making the system superconducting. Another theory[3] says that a lower energy state is to be realized when the ferromagnetic clusters , which are produced centred at O^- in the sheet, make a pair due to the magnetic correlation between the clusters and system becomes superconducting. In both cases the ferromagnetic correlation (cluster) is essential, so this is the motivation of our measurement.

Here we show the scattering functions of the samples with different hole concentration, i.e. as-grown, Ar-anealed and O_2-anealed La_2CuO_4 and $La_{1.88}Sr_{0.12}CuO_4$. For every cases the scattering function obeys $I \approx Q^{-4}$ relation giving an image of an existence of a sharp surface of a ferromagnetic cluster imbedded in an antiferromagnetically correlated sea. The temperature dependence, though it is weak, gave us a confirmation that the intensity is magnetic scattering. For the pure La_2CuO_4 the intensity increases with the hole concentration, but the Sr-doped superconducting sample has lowest intensity. This seems to deny the relation of the superconductivity and the role of the ferromagnetic cluster, however we can explain this situation as follows.

Upon doping holes in pure system, the holes enter at P_π orbit in the sheet. In this case the spins on Cu^{2+} and O^- become parallel and this correlation gives a higher intensity leaving the system in semiconducting. On the other hand for Sr-doped system, the holes enter at P_σ orbit and the spins on Cu^{2+} and O^- couples anti-parallelly diminishing the scattering intensity and making the system metallic. However, this conclusion should be made more carefully after the measurement on the field dependence of the scattering function.

1) G.Shirane et at.:Phys, Rev. Lett. 59, 1613 (1988)
2) Shiba, Kanamori, Kotani:
3) A.Aharony: Phys. Rev. Lett. 60, 1330 (1988)

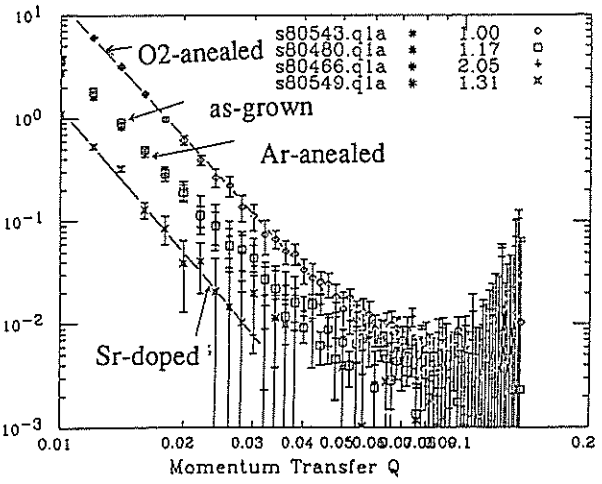

Polarized Neutron Study of Ferrofluid

S. ITOH and Y. ENDOH

Department of Physics, Tohoku University, Sendai 980

1.Introduction

Ferrofluids are colloidal suspensions of ferromagnetic particles stabilized by surfactants. Since the size of ferromagnetic particles in a ferrofluid is about 100Å(=d) in diameter and the distance between two particles is more than diameter, the range of structure scale is more than 100Å. Therefore the measurements in the momentum space of $Q<2\pi/d=0.1Å^{-1}$ are required. The polarized cold neutron spectrometer at KENS, the TOP spectrometer, can be operated in two modes; small angle scattering mode and depolarization mode. In the small angle scattering mode, since the Q-range of 0.01- $0.3Å^{-1}$ is covered, both intraparticle structure and interparticle correlations are studied. The so-called mesoscopic structure also can be studied in the depolarization mode. Overall the TOP spectrometer is suitable tool for studies of ferrofluids. We have studied the magnetism of Co ferrofluid[1),2)] by using the TOP spectrometer.

2 interparticle correlation

In order to investigate the interparticle correlations, we measured the small angle scattering intensities at room temperature. In the case that the magnetization is saturated under a strong external field ($m=\mu H/k_BT>>1$), the scattering intensities are approximately expressed as follows;

$$I_{\perp}^{\pm}(Q) = \alpha<[F_N(Q)\pm F_M(Q)]^2>S_{\perp}(Q) + I_{incoh},$$
$$I_{//}(Q) = \alpha<F_N(Q)^2> S_{//}(Q)+ I_{incoh}.$$

We denote the structure factors $S_{\perp}(Q)$ and $S_{//}(Q)$ for $Q\perp H$ and $Q//H$, respectively, which represent the interparticle correlations. I_{incoh} is the incoherent scattering intensity and α is a proportional constant. There are three scattering qualities and three unknown values $S_{\perp}(Q)$, $S_{//}(Q)$ and I_{incoh}, if the nuclear and the magnetic scattering amplitude, $F_N(Q)$ and $F_M(Q)$, are known. Thus unknown values can be determined. The structure factors can also be distinguished under a weak external field ($m<<1$), where the scattering intensities are approximately expressed as follows;

$$I_{\perp}^{\pm}(Q) = \alpha<[F_N(Q)\pm L(m)F_M(Q)]^2>S_{\perp}(Q) + I'(Q),$$
$$I_{//}(Q) = \alpha<F_N(Q)^2> S_{//}(Q) + I'(Q),$$

where I'(Q) consists of the magnetic fluctuation and incoherent scattering, and L(m) is Langevin function.

The structure factors were distinguished from the scattering intensities under the weak and strong external field using the scattering amplitudes determined previously[2)], and Fig.1 shows the structure factors. The interparticle correlation was almost isotropic under the weak field. In contrast, the interparticle correlations are anisotropic under the strong external field. Furthermore the peak position of the structure factor under the strong field is in higher Q than under the weak field.

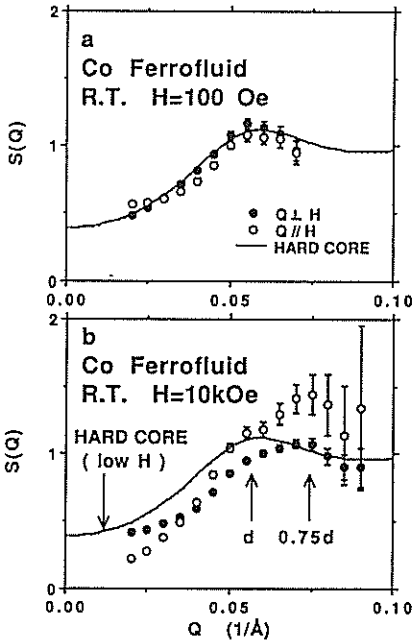

Fig.1 Anisotropy of the structure factors. The interparticle structure is isotropic under a weak external field (a) and anisotropic under 10 kOe (b).

First, the structure factors under the weak field are well approximated to that of rigid sphere approximation, so-called Percus-Yevick approximation[3]. The solid line in Fig.1 is the calculation for the parameters of η=0.11 and d=90Å, which fits to the experimental data. The diameter d and the volume fraction η are including surfactants and calculated with the magnetic volume fraction and the parameters of the intraparticle structure.

Next, we discuss the interparticle correlations under the strong field. Each structure factor under the strong field has a main peak in the position corresponding to the particle-particle distance 0.75d and a shoulder corresponding to d. This result indicates the aggregation of particles as follows. We consider that particles are configured on the lattice points of face-centered-cubic for the field direction as shown in Fig.2. and the distance between the nearest neighbors is d, the diameter of the particle. The spacing of lattice plane along the field direction is $d/\sqrt{2}$ and the main peak of $S_{//}(Q)$ corresponds to the distance. For the perpendicular direction to the external field, the angle between the direction of scattering vector Q and that of lattice is free. Since there exists the scattering for the spacing of lattice plane $d/\sqrt{2}$ in the Q-range of observation, the main peak of $S_{\perp}(Q)$ corresponds to the distance. The shoulder of $S_{//}(Q)$ corresponding to d suggests that there coexist chains of particles aligned along the field. The shoulder of $S_{\perp}(Q)$ appears at the scattering position corresponding to d when the configuration of particles in the next layer (black particles in Fig.2) is disordered. The broadening of the profile of $S_{//}(Q)$ or $S_{\perp}(Q)$ may be due to the particle size distribution and the randomness of the configuration of the particles.

Finally, we consider the anisotropy of the interparticle correlations. Since the direction of Q is fixed in our experiments, we observed one-dimensional interparticle correlations projected to the direction of Q. The pair distribution function g(r) is given by the one-dimensional Fourier transformation of S(Q). g(r) has a peak around $r=d/\sqrt{2}$, "first peak." The area under the first peak is the mean coordination number and equal to 2-2/N for a one-dimensional alignment of N particles. We obtained $N_{//} > N_{\perp}$ where $N_{//}$ and $N_{\perp}$ are the number along the parallel and perpendicular direction to the field in the aggregation of the particles. Therefore the difference between the structure factors shows the anisotropic aggregation stretching along the external field.

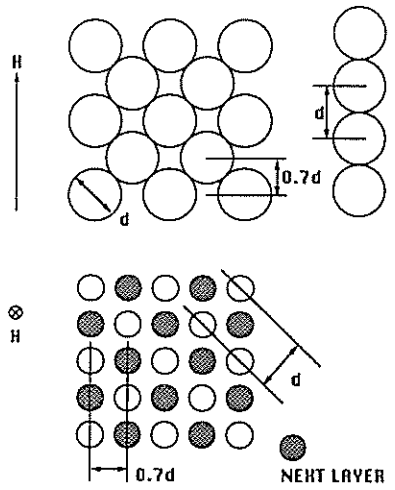

Fig.2 The model for the particle configuration in the aggregation. Each spacing of lattice plane corresponds to the position of the peak or the shoulder in the structure factor shown in Fig.1.

3. aggregation process

We investigated aggregation process of particles in the external field by neutron depolarization measurements. The polarization of transmitted neutron beams is related to the Larmor precession of neutron polarization vector around the magnetic induction in a sample. We define that z-axis is parallel to the incident beam polarization and y-axis is beam direction. We observed neutron wavelength dependence of z-component of the polarization of the transmitted beams, $P(\lambda)$. The field dependence of $P(\lambda)$ was measured by following way: An external field Hc is applied to x-direction of the sample at room temperature. We consider the spatial configuration of particles is determined by Hc. Next, the sample was cooled down to 30K where the solvent was frozen and the configuration of particles was fixed. After the application of 10kOe parallel to x, we measured $P(\lambda)$ without external field by using three-dimensional spin turner.[4]

We consider the model of ferromagnetic clusters in a nonmagnetic medium, where the direction of the magnetic moments of whole clusters are aligned to a certain direction. In this case, $P(\lambda)$ is given by the following form;

$$P(\lambda) = C_{//} + C_{\perp} \exp\left(-\frac{1}{2}\sigma^2\lambda^2\right) \cos I\lambda,$$

$$I = C.4\pi M.L$$

where $C_{//}$ and $C_{\perp}$ are square of the component of magnetization parallel and perpendicular to z, M is the magnetization of sample, L is sample thickness and C is a physical constant. I is the field integral

along the neutron passage averaged over the beam area. The field integral of each neutron passage is not uniform because of inhomogeneous spatial distribution of clusters. Assuming the distribution function of field integral to be Gaussian with the deviation σ, we obtained the above formula. In this picture, σ/I is dependent on the spatial configuration of clusters and independent of M. These features are realized in our experiments as follows: First, $P(\lambda)$ could be fitted to the above formula. Second, I was equal to $C.4\pi M.L$ in any measurement. Third, σ/I was independent of M when the spatial configuration was not changed. The experimental condition where M is changed without changing the spatial configuration was realized by the procedure where temperature dependence of $P(\lambda)$ was measured below melting point of the solvent under fixed Hc.

Hc-dependence of $P(\lambda)$ is shown in Fig.3(a). The solid lines are fitted curves to the above damped oscillation function. Fig.3(b) shows Hc-dependence of $(\sigma/I)^2$ given from the fitting. The maximum of $(\sigma/I)^2$ appears with increasing Hc. This result is consistent to the result from small angle scattering above mentioned; random distribution of particles in the weak field and aggregations in the strong field, and suggests that the two stages bound with aggregation process observed by depolarization measurements. When the particles are uniformly distributed in the weak field, σ has a small value because the field integral along each passage has the same values of each other. And σ is also small for the same reason when the particles are aggregated along the strong field. In contrast, σ is large in the medium field region. The large σ suggests more inhomogeneous distribution of clusters of particles, where the field integral along each passage is more distributed. We can draw the picture shown in Fig.4. The field dependence suggests that homogeneous dispersion stage at a weak field is transformed to aggregated stage at a strong field through inhomogeneous stage.

4. conclusion

We demonstrated polarized neutron experiments of ferrofluids indicating that polarized neutrons are powerful tool for these studies. We obtained excellent results for studies of ferrofluids.

The interparticle correlations under a weak field show the random distribution of rigid spheres. However under a strong field the magnetic particles were aggregated in the external field and the aggregation was densely packing but stretching along the field. Furthermore, the result from depolarization measurements suggests that homogeneous dispersion stage at a weak field is transformed to aggregation stage at a strong field through inhomogeneous stage.

References

1) R.Pynn, J.B.Hayter and S.W.Charles, Phys. Rev. Lett. 51(1983)710.
2) S.Itoh and Y.Endoh, in this report.
3) K.Percus and G.J.Yevick Phys. Rev. 110 (1958) 1.
4) S.Mitsuda, S.Itoh and Y.Endoh, KENS Report-VI (1987) 45.

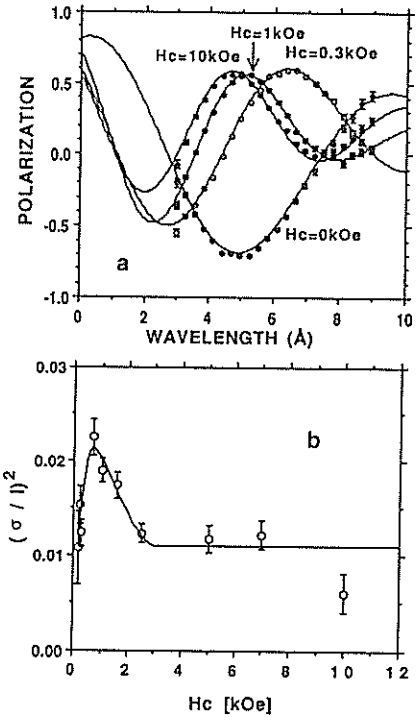

Fig.3 Hc-dependence of $P(\lambda)$ and $(\sigma/I)^2$. The solid lines in (a) are fitted curves and the parameter $(\sigma/I)^2$ in (b) were given by the fitting.

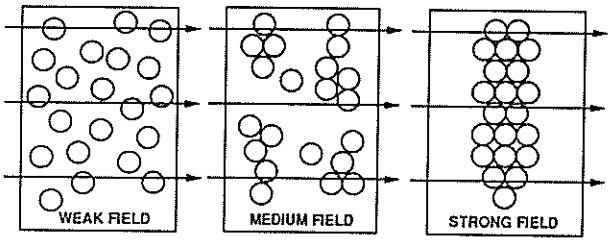

Fig.4 Schematic picture of aggregation process of particles against the external field.

Study of Intraparticle Structure of Ferrofluid

S. ITOH and Y. ENDOH

Department of Physics, Tohoku University, Sendai 980

Ferrofluids are stable colloidal suspensions of ferromagnetic particles coated with surfactants. The size of a particle is about 10^2Å and the nuclear and the magnetic scattering amplitudes are the same order, thus ferrofluids are suitable system to the small angle scattering experiments of polarized neutrons. The structure of a ferrofluid consists of the intraparticle structure and the interparticle correlation. We investigated the intraparticle structure of particles in a diluted ferrofluid by using the TOP spectrometer.

Co ferrofluid[1] used in the present experiments is composed of cobalt particles in a saturated hydrocarbon solvent of average carbon chain length of 13, and a Monoxol-OT and Imidrol-OC surfactant.

The electron micrographical studies revealed that each particle is approximately spherical and its size is distributed as shown in the histogram in Fig.1. The distribution is 30Å in mean radius and 10Å in its standard deviation.

The magnetization process M(H) at room temperature well obeys Langevin function averaged over the distribution of particle size. Assuming the particles to be of single domain, with a saturation magnetization equal to the bulk cobalt and the distribution function to be log normal distribution, we obtained the values of 25.7Å and 9.1Å for the mean value and its standard deviation of the magnetic radius, respectively. The solid line in Fig.1 is the distribution function for these parameters.

Comparing the particle size distribution from the magnetization measurement with that from the electron micrograph, the particle size determined from the magnetization measurements is definitely smaller. It suggests the existence of nonmagnetic surface layers.

In addition, the magnetic volume fraction of cobalt particles in the ferrofluid was determined to be 2% from the magnetization measurement.

In order to determine the intraparticle structure, we measured scattering intensities from a diluted ferrofluid at room temperature under 10 kOe of the external field. The magnetic volume fraction of cobalt particles in the ferrofluid used in the small angle scattering experiments is 0.3%. Neglecting the interparticle correlation, the scattering intensities under a higher external field exceeding the saturation field are expressed as follows;

$Q \perp H$

$$I_{\perp}^{\pm}(Q) = \alpha < [\, F_N(Q) \pm F_M(Q)\,]^2 > + I_{incoh},$$

$Q // H$

$$I_{//}(Q) = \alpha \langle F_N(Q)^2 \rangle + I_{incoh}$$

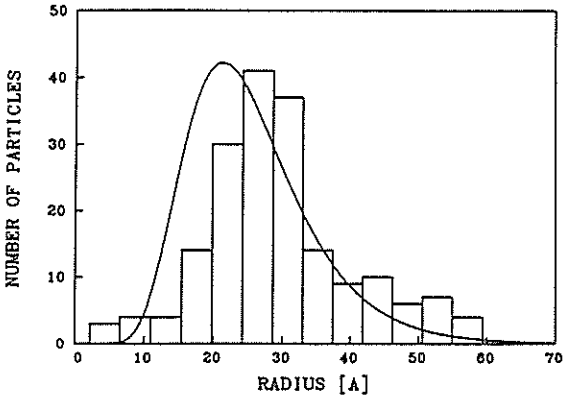

Fig.1 The size distribution determined by magnetization measurement (solid line) and electron micrograph (histogram).

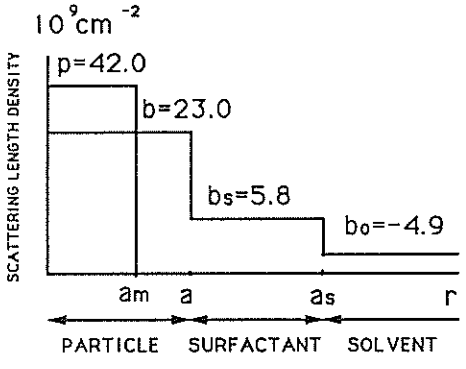

Fig.2 Coherent scattering length densities and geometrical parameters for the model of a magnetic spherical particle in a cobalt ferrofluid.

where $F_N(Q)$ and $F_M(Q)$ are the nuclear and magnetic scattering amplitude, I_{incoh} represents the incoherent scattering intensity, and α is a proportional constant related to the number density of particles as well as the instrumental coefficient. $F_N(Q)$ and $F_M(Q)$ represent the nuclear and magnetic intraparticle structure. It can be preseted the analytical forms[2] for a spherical particle shown in Fig.2. Since there are three independent scattering qualities and three unknown values $\alpha F_N(Q)$, $\alpha F_M(Q)$ and I_{incoh}. Thus unknown values can be determined unambiguously. The brackets <...> represent an average weighted by the particle size distribution. The width of surfactant layer was fixed to 15Å, which could be estimated on the assumption that all surfactant materials are sticked to the particles. Therefore parameters to be determined are mean nuclear radius a and mean magnetic radius a_m of a cobalt particle.

The intensities $\alpha<F_M(Q)^2>$ and $\alpha<F_N(Q)F_M(Q)>$ can be distinguished form these intensities. The solid lines in Fig. 3 are the fitted curve to the distinguished intensities by parameterizing a, a_m and α. We obtained a_m=25Å with ±3Å of the experimental errors and a=30Å±2Å. The magnetic radius determined by neutron scattering agrees well with that determined by magnetization measurement. As mentioned above, we assumed the saturation magnetization of the bulk for the moment of a particle in the analysis of the magnetization data. Thus we can conclude the validity of our assumption that a cobalt particle has the same magnetization as the bulk cobalt. The nuclear radius is also a perfect agreement with the radius determined by electron micrograph.

Eventually we can conclude that there exists nonmagnetic layer of 5Å on the surface of a cobalt particle. The width of 5Å corresponds to about two cobalt layers. We cannot however clarify the detailed magnetic structure of the nonmagnetic layer, which needs further investigations.

In conclusion, we determined the intraparticle structure. The magnetic and nuclear radius well agree the results from magnetization measurements and of electron micrographs, respectively. Combining the result of the neutron scattering and that of the magnetization measurements, we found that the magnetic moment of cobalt particle is the same as the saturation magnetization of the bulk cobalt within the statistical errors and that there exists nonmagnetic interface of about two atomic layers.

References

1) R.Pynn, J.B.Hayter and S.W.Charles, Phys. Rev. Lett. 51(1983)710.
2) S.Itoh and Y.Endoh, KENS Report VII (1988) 79.

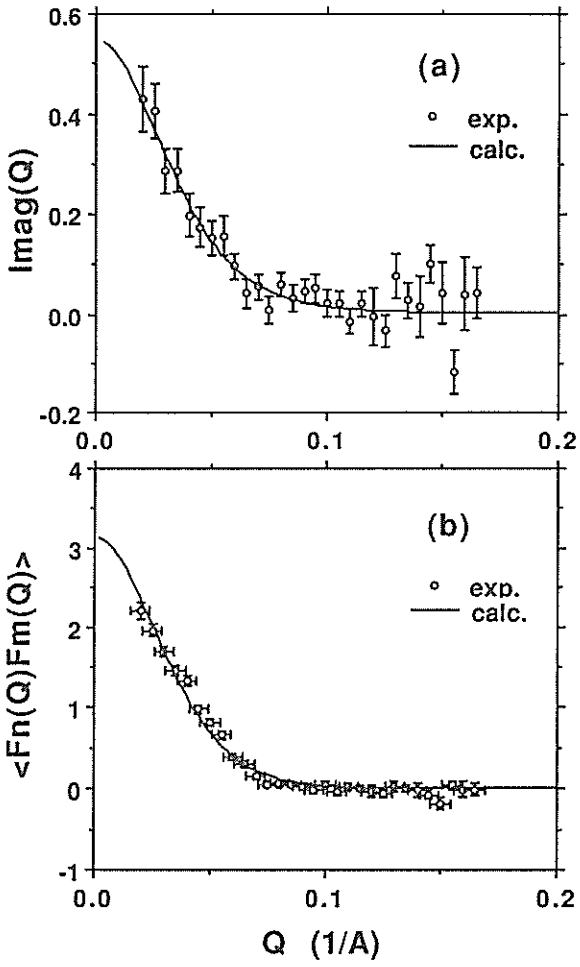

Fig.3 Determination of the intraparticle structure. The magnetic intensity $I_{mag}(Q)=<F_M(Q)^2>$ (a) and the cross term of nuclear and magnetic scattering amplitude $<F_N(Q)F_M(Q)>$ (b) are distinguished from the observed intensities The solid lines are the fitted curve by parameterizing the parameters of the intraparticle structure.

Detemination of Intraparticle Structure of Magnetite Particles in a Solvent by Contrast Variation Method using Polarized Neutrons

S. ITOH, S. TAKETOMI*, Y. ENDOH AND S. CHIKAZUMI*

Department of Physics, Tohoku University, Sendai 980
*Department of Physics, Keio University, Yokohama 223

We tried to determine the intraparticle structure of fine particles in a magnetite ferrofluid by combination of polarized neutrons and contrast variation method on the TOP spectrometer at KENS. The contrast variation method is known as the powerful method for studies of biological materials, however, few studies of industrial materials have been performed by this method. The studies on the intraparticle structure of ferrofluids were mainly of magnetic particles up to present, however, few knowledges of surfactants were given. We tried to determine the intraparticle structure including surfactants. Since the solvent of the ferrofluid we used is water, it is easy to control the "contrast"; the difference of the scattering length densities between the particle and the solvent. Figure 1 depicts a model in the scale of the scattering length densities of a spherical particle. In the case A, where the scattering length density of a surfactant is equal to that of a solvent, the small angle neutron scattering reflects the intraparticle structure excluding a surfactant. On the other hand, the intraparticle structure including a surfactant corresponds to the case B. Therefore, first, the intraparticle structure excluding a surfactant is determined in the case A, and next, the width of the surfactant layer is determined by analysis of the scattering intensity in the case B using the intraparticle structure from the case A.

We used D_2O-based magnetite ferrofluid[1] where the ferromagnetic particles are magnetite of about 100Å in diameter, surfactant consists of erucic acid, naphthenic acid and dodecylbenzenesulfonic acid, and the solvent is D_2O. The value of the scattering length density of each material can be calculated form the chemical formula and is shown in Fig.1. Assuming that the volume of a material itself is not changed in the mixture, the sample A ($b_O=b_S$) obtained by mixing the original ferrofluid with H_2O. Moreover we obtained the sample B ($b_O \neq b_S$) by mixing the original ferrofluid with D_2O so that the number density of particles in each sample might be equal. Both the sample A and B are diluted so that the interparticle correlation can be ignored. In fact we obtained reasonable results from analyses by neglecting the correlation.

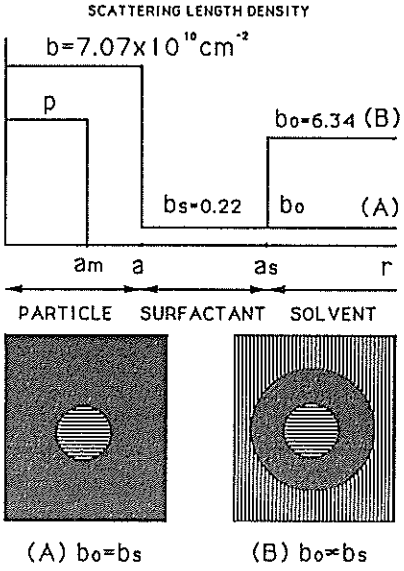

Fig.1 The model for the scattering length densities of a spherical particle in a ferrofluid and the concept of contrast variation method.

In order to characterize the ferrofluid, we performed electron micrograph and magnetization measurement. From the electron micrograph, we found that the shape of each particle was approximately sphere and its size was distributed. The histogram in Fig. 2 is the size distribution from the micrograph and the distribution is 46Å in the mean radius and 16Å in its standard deviation. The magnetization against the external field at room temperature obeys Langevin function averaged over the size distribution. Assuming that the distribution is the log normal distribution and that the particle is of single domain and its magnetic moment per unit volume is the bulk saturation magnetization, we could fit the magnetization curve to the parameterized curve of the distribution. The distribution function determined is the solid line in Fig. 2. The distribution was 44.4Å in the mean radius and 15.7Å in its deviation. The result from the micrograph and that from magnetization agree within the errors of the measurements. From the above results, we analyze the scattering intensities assuming particles to be of single

domain and of sphere shape and the size distribution to be log normal distribution.

In the condition where the scattering vector Q is perpendicular to the external field H, the scattering intensity where the neutron polarization P is parallel to H, $I^+(Q)$, differs from that where P is antiparallel to H, $I^-(Q)$. Neglecting the interparticle correlation, the difference of the above intensities $I^+(Q)$ and $I^-(Q)$ under the high external field where the magnetization is fully saturated is connected to the intraparticle structure as follows;

$$I^+(Q) - I^-(Q) = \alpha < F_N(Q)\, F_M(Q) > ,$$

where $F_N(Q)$ and $F_M(Q)$ are the nuclear and magnetic scattering amplitudes, respectively, and α is a proportional constant. And the bracket <...> represents the average over the distribution of the size of particles. The incoherent scattering and the background are automatically vanished by taking the difference of intensities. This is an important point of polarized neutron scattering. The scattering amplitudes are corresponding to the intraparticle structure, and have analytical expressions[2] for a spherical particle shown in Fig.1.

Figure 3 shows the difference intensity of both samples under 10kOe of the external field. First, analyzing the intensity of sample A, we determine the intraparticle structure excluding surfactant layer. We fixed the deviation of the size distribution and parameterized the proportional constant α and the mean values of radius a and magnetic radius a_m. We obtained a=45.1 Å (±2.5Å; statistical error) and nonmagnetic layer $a-a_m$=1.8Å (±3.5Å) by parameterizing the three parameters. Fixed a to a_m, we obtained $a=a_m$=45.8Å (±2.1Å). Therefore, the radius of magnetite particle is the almost same as the magnetic radius and the nonmagnetic layer on the magnetite surface is negligible. These results well agree with that of the electron micrograph and the magnetization measurement, and the magnetic moment of particles was equal to the bulk saturation magnetization. Next, Analyzing the intensity of sample B on the basis of the result from sample A, we tried to determine the width of the surfactant layer. We obtained 38.7Å (±2.7Å), the width of the surfactant layer by parameterizing the width and the proportional constant.

In conclusion, we tried to determine the intraparticle structure by contrast variation method of polarized neutrons and the results were consistent with that from electron micrograph and magnetization measurement. We analyzed the neutron intensities using calculation value of the scattering length densities based on the assumption that the volume of a material itself is not changed in the mixture. We are planning further experiments where the scattering length densities are determined experimentally.

References

1) S.Taketomi et al., J. Phys. Soc. Japan 56 (1987) 3362.

2) S.Itoh and Y.Endoh, KENS REPORT-VII (1988) 79.

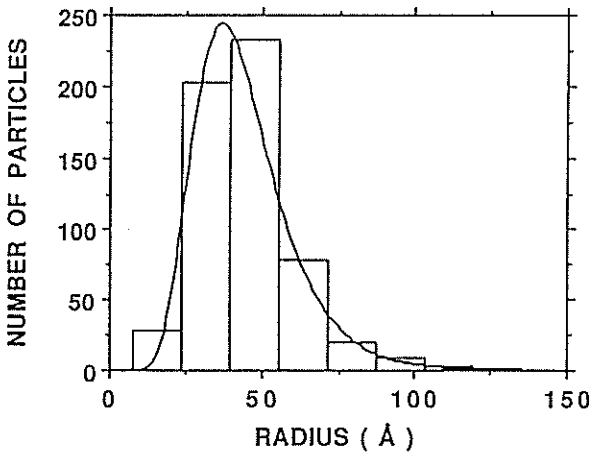

Fig.2 The size distribution determined from electron micrograph (histogram) and from magnetization measurement (solid line).

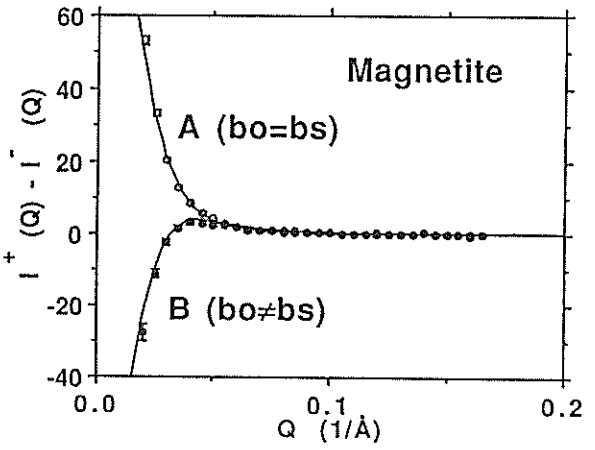

Fig.3 The difference intensities and determination of the intraparticle structure. A and B are corresponding to those in Fig. 1. The solid lines are the fitted curves.

Study of Nickel Ferrite Fine Particles

S.ITOH, K.HANEDA*,** and Y.ENDOH

Department Physics, Tohoku University, Sendai 980
*Research Institute for Scientific Measurements,
Tohoku University, Sendai 980

It is known that the anomalous magnetization appears on the fine particles.[1] On the surface of fine particles of nickel ferrite $NiFe_2O_4$, there exists an anomalous magnetism, the magnetization component which does not align to the external field even in a high field of several Teslas. We investigated the surface magnetism of nickel ferrite fine particles by using the TOP spectrometer.

The small angle scattering intensities of polarized neutrons from nickel ferrite fine particles under a high external field where the magnetization is technically saturated is expressed by the following simple form;

$$Q\perp H \quad I_{\perp}^{\pm}(Q) = \alpha < [\, F_N(Q) \pm F_M(Q)\,]^2 >,$$
$$Q//H \quad I_{//}(Q) = \alpha <F_N(Q)^2>,$$

because the incoherent scattering is negligible, where Q is the wavenumber, the brackets <...> represent the average over the size distribution and α is a proportional constant dependent on the number of particles. The nuclear and the magnetic scattering amplitudes $F_N(Q)$ and $F_M(Q)$ for a spherical particle are expressed as follows;

$$F_N(Q) = 4\pi\, b\, a^3\, g(Qa),$$
$$F_M(Q) = 4\pi\, p\, a_m^3\, g(Qa_m),$$
$$g(x) = (\sin x - x\cos x)/x^3,$$

where a is the radius of a particle itself and a_m is the magnetic radius of ferromagnetic region within a particle. b and p are nuclear and magnetic scattering length densities, b=7.27x10^{10}cm^{-2} for $NiFe_2O_4$ and p=0.78x10^{10}cm^{-2} at room temperature. p is proportional to the bulk saturation magnetization. The flipping ratio is defined as follows;

$$R(Q) = \frac{I_{\perp}^{+}(Q)}{I_{\perp}^{-}(Q)} = \frac{< [\, F_N(Q) + F_M(Q)\,]^2 >}{< [\, F_N(Q) - F_M(Q)\,]^2 >}.$$

R(Q) described as the function only of the structure of particles. If there exists a surface layer ($a \neq a_m$), R(Q) is dependent on Q because of the difference of the phase between $F_N(Q)$ and $F_M(Q)$. In contrast, R(Q) is independent of Q if there exists no surface layer ($a=a_m$).

According to an electron micrograph, we found that the particles were almost spherical and that their size were distributed from half a hundred angstroms to several hundred angstroms. Therefore we analyze the scattering intensities assuming particles to be sphere with the size distribution.

We performed the small angle scattering experiment at room temperature and low temperature(30K) under 10kOe of the external field H in both configurations Q⊥H and Q//H. The intensities in Q//H are shown in Fig. 1 and the flipping ratios in Q⊥H are in Fig. 2. Q-dependence of R(Q) suggests the existence of surface layers.

First, in order to determine the particle size, we analyze the intensities in Q//H. $I_{//}(Q)$ consists only of the nuclear scattering and can be fitted by parameterizing the size distribution. Assuming log normal distribution, we obtained 51Å in the mean radius and 34Å in its deviation. The solid lines are the fitted curves. This result is consistent to that from the electron micrograph and the size is independent of temperature.

Next, we estimate the thickness of surface layer, Δ. We calculated R(Q) by parameterizing Δ using the nuclear size determined above. We obtained Δ=18Å at room temperature. The solid lines in Fig. 2 are the calculation curves for several values of Δ and the calculation shows that R(Q) is sensitive to Δ. At low temperature, we calculated using p=0.9x10^{10}cm^{-2} which is corresponding to the magnetization at 30K, we obtained Δ=18Å. Therefore the temperature dependence of R(Q) is corresponding to that of the magnetization and the thickness of a surface layer is independent of temperature.

In conclusion, we observed surface layers of nickel ferrite fine particles, which corresponds to about two atomic layers. This result is consistent to that from Mössbauer spectroscopy and magnetization measurements.[1]

References
1) A.H.Morrish and K.Haneda, J. Magn. Magn. Mat. 35 (1983) 105.
2) M.Sato and K.Hirakawa, J. Phys. Soc. Jpn. 39 (1975) 1467.

** present address; Ishinomaki Senshu University, Ishinomaki.

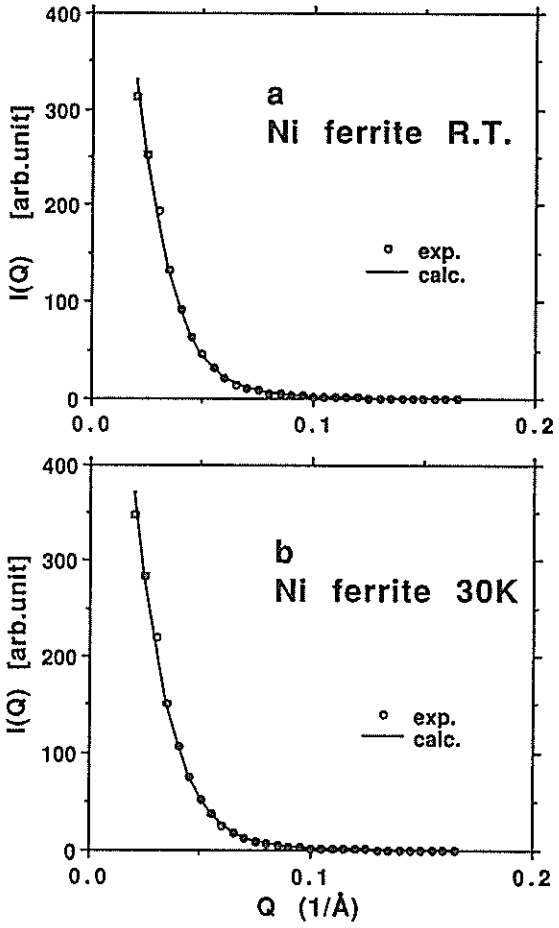

Fig.1 Scattering intensities in Q//H and determination of the particle size. The solid lines are fitted curves.

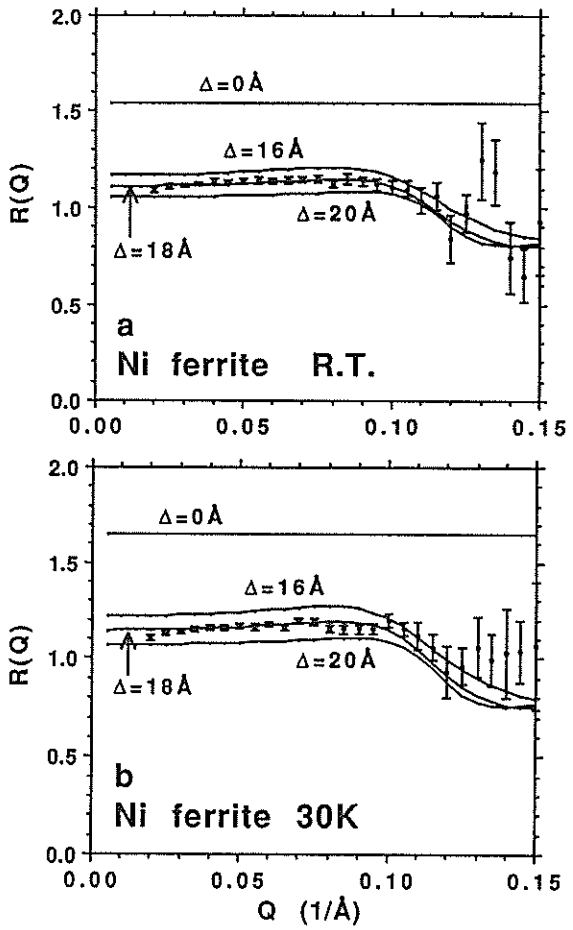

Fig.2 Flipping ratio R(Q) and thickness of a surface nonmagnetic layer, Δ. The solid lines are the calculation for Δ.

Spin Reorientation in Fe/Nd Multilayered Films with Artificial Periodic Structures

N. HOSOITO, K. MIBU and T. SHINJO

Institute for Chemical Research, Kyoto University, Uji, Kyoto-fu 611

Multilayered films consisting of ferromagnetic 3-d transition metals (TM) and rare-earth metals (RE) show various magnetic properties. Transition metals have relatively high Curie temperatures and weak magnetic anisotropies. On the other hand, rare-earth metals have low magnetic transition temperatures and strong anisotropies. In multilayered TM/RE films, two magnetic layers of dissimilar characteristics interact with each other at the interfaces through a magnetic exchange interaction and make various magnetic structures.

For example, it is found from ^{57}Fe Mössbauer spectroscopy that direction of Fe moments in some of multilayered Fe/Nd films changes with temperatures[1]. The spin reorientation phenomenon of the Fe moments are shown in Fig.1. The average angle between the Fe moments and the film normal is estimated from the intensity ratio of magnetically split six lines of an Fe Mössbauer spectrum.

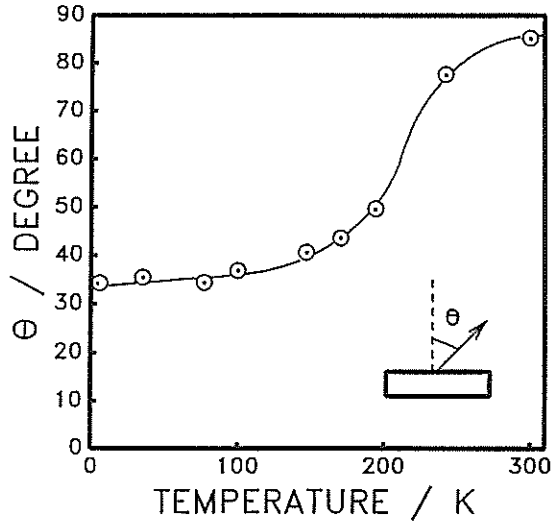

Fig.1 Direction of Fe moments determined from Fe Mössbauer spectra. The sample is [Fe(39Å)/ Nd(28Å)].

The Fe moments are in-plane direction at room temperature and begin to turn to the film normal direction at around 200K. At lower temperatures, the direction of the Fe moments is nearly perpendicular to the film plane. Such spin reorientation phenomena are also observed in multilayered Fe/Dy and Fe/Pr films, but are not observed in Fe/Y films. These facts suggest that magnetic moments of rare-earth metals, especially orbital angular moments, play an important role in Fe spin reorientation phenomena. We speculate the mechanism of the spin reorientation as follows. The rare-earth atoms near Fe/RE interfaces have a perpendicular magnetic anisotropy and the perpendicular anisotropy acts on Fe atoms at the interfaces through a magnetic exchange interaction. On the other hand, the Fe layer has a shape anisotropy which comes from demagnetization energy. These two anisotropies compete on the Fe layer. If we consider temperature dependence of Fe and RE moments, it is expected that the shape anisotropy is temperature independent and the perpendicular anisotropy becomes stronger at lower temperatures. Therefore the direction of Fe moments is in-plane at room temperature and film normal at lower temperatures.

To confirm the above speculation, it is important to investigate the change in the direction of RE moment as a function of temperature. Thus polarized neutron diffraction measurements were carried out with using the TOP spectrometer. The sample was prepared by ultra-high vacuum deposition. The Fe layer of 39Å thick and the Nd layer of 28Å thick are periodically stacked on a glass substrate. The number of the bilayer is 40. To observe diffraction peaks corresponding to the artificial period, the sample was located between pole pieces of an electromagnet and magnetic field was applied in-plane direction. The scattering vector is

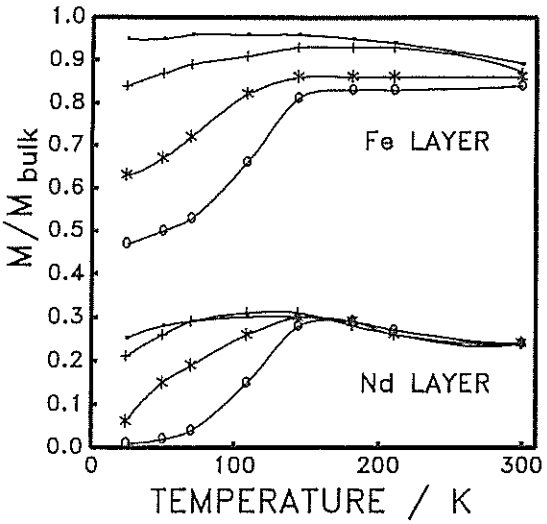

Fig.2 Normalized average magnetization of Fe and Nd layers estimated from polarized neutron diffraction and magnetization measurements. Applied fields are · 6.0kOe, + 4.0kOe, * 2.0kOe and o 1.0kOe.

perpendicular to the direction of applied field and parallel to the layer-stacking direction. Temperature was changed between 20K and 300K, and applied field between 1.0kOe and 9.4kOe. From TOF spectra, flipping ratios were determined as a function of temperature and applied field.

To elucidate the magnetic structure of multilayered Fe/Nd films, the same model which was applied in the analysis of Fe/Dy films[2] is used. Concerning a nuclear scattering, the Fe and Nd layers are regarded as uniform scatters with scattering amplitude densities of $b_i \cdot d_i$, respectively, where b_i is a nuclear scattering amplitude and d_i is a number density and i means Fe or Nd. As for a magnetic scattering, it is expected that magnetization vectors of the Fe and Nd layers lie in the plane generated by polarization and scattering vectors. Therefore the magnetic scattering density, which is not necessarily constant throughout Fe or Nd layers, is given as $p_i \cdot d_i \cdot g_i(x)z$, where p_i is a magnetic scattering amplitude of i atom with a full moment, $g_i(x)$ expresses a magnetic moment distribution in i layer and z is a unit vector parallel to the neutron polarization. Here we put magnetic form factors of atoms to be unity because the scattering vector is small. Suggested by calculations about Fe/Gd multilayers[3], we take g_i as

$$g_i(x)=A_i+B_i(\exp[-x/C_i]+\exp[-(T_i-x)/C_i]),$$

where A_i, B_i, and C_i are parameters which characterize the distribution, and T_i is a thickness of i layer. Based on this model, the flipping ratio and magnetization of the sample can be calculated in a standard way. Details of the analysis were given in Ref.2.

The estimated magnetizations of the Fe and Nd layers in various magnetic fields are plotted in Fig.2 as a function of temperature. The magnetization of each layer is normalized by a bulk value (1744 emu/cm^{-3} for Fe and 886 emu/cm^{-3} for Nd). It should be noticed that the magnetization is a component of magnetization vector parallel to the neutron polarization. The magnetization curves in the field of 8.0 and 9.4kOe are almost the same as that in 6.0kOe and are not shown in the figure. It is clear that the magnetizations of both Fe and Nd layers decrease below 150K when the applied field is lower than 4.0kOe. We interpret that the decrease is due to the turn of magnetization vectors of Fe and Nd layers from in-plane to normal to the film plane directions. In other words, the spin reorientation occurs not only in the Fe moments, as was confirmed by Mössbauer spectroscopy, but also in the Nd moments. This fact is consistent with our speculation that the RE layer induces a perpendicular anisotropy on the Fe layer. In the field of 6.0kOe, M vs. T curves show very little change, indicating that the spin reorientation is suppressed by applied field of 6.0kOe.

The authors would like to thank Prof. Y. Endoh for helpful discussion.

References

1) K. Mibu, N. Hosoito and T. Shinjo, J. Phys. Soc. Jpn. 58, 2916(1989)
2) N. Hosoito, K. Yoden, K. Mibu, T. Shinjo and Y. Endoh, J. Phys. Soc. Jpn. 58, 1775(1989)
3) R.E. Camley, Phys. Rev. B39, 12316(1989)

Microscopic Spin Fluctuations in FeAl Reentrant Spin Glass in an Applied Field

J. Suzuki, M. Arai,* M. Furusaka,* H. Yoshizawa** and Y. Endoh

Department of Physics, Tohoku University, Aramaki, Aoba-ku, Sendai 980
*Booster Synchrotron Facility, National Laboratory for High Energy Physics, Oho, Tsukuba 305
**Institute for Solid State Physics, University of Tokyo, Roppongi, Minato-ku, Tokyo 106

Coexistence of ferromagnetism and spin glass order in the mixed phases was predicted by the infinite-range model for classical vector spins. This reentrance is believed to occur by freezing of spin components transverse to the mean magnetization or replica symmetry breaking.[1] Experimentally it was shown by means of Mössbauer measurement and the strong irreversibility in the magnetization process from $Au_{.81}Fe_{.19}$.[2] We report here how long range order and spin glass one coexist spatially in a spin glass alloy Fe_xAl_{1-x} by using neutron scattering in more detail.

Small angle neutron scattering studies on a single crystal $Fe_{.715}Al_{.285}$ were performed in an applied field of $0 \leqq H \leqq 5$ kOe at various temperatures of $15 \leqq T \leqq 300$ K by using SAN spectrometer at KENS.[3] Although the magnetization cannot be saturated even in the applied field of 5 kOe, spins are well aligned parallel to the field judging from the magnetization measurement. Figure 1(a) and (b) show the field dependences of the scattering intensity of the spin correlations perpendicular and parallel to the field at 15 K, respectively. The intensities are suppressed drastically independent of the direction upon increasing the field and a peak appears at a shifted Q to the higher value. The situation is very similar for the both scattering direction, therefore we consider the former case. The transverse spin correlation function in the real space is obtained by the Fourier transform of the scattering data in Fig. 1(a), which is shown in Fig. 2. In order to understand the microscopic spin fluctuations we adopt a simple model for Nc spin clusters with a radius ξ. Each magnetic component of clusters which is perpendicular to an applied field is assumed to be randomly oriented each other at intervals of r_O. This situation projected on xz-plane is schematically presented in Fig. 3. The scattering intensity from the transverse spin component S_X is described as follows,

$$I(Q) = \gamma_0^2 \cdot N_C \cdot |F(Q)|^2 \cdot \langle S_X^2 \rangle \cdot \{1 - \sin(Q \cdot r_O)/(Q \cdot r_O)\},$$

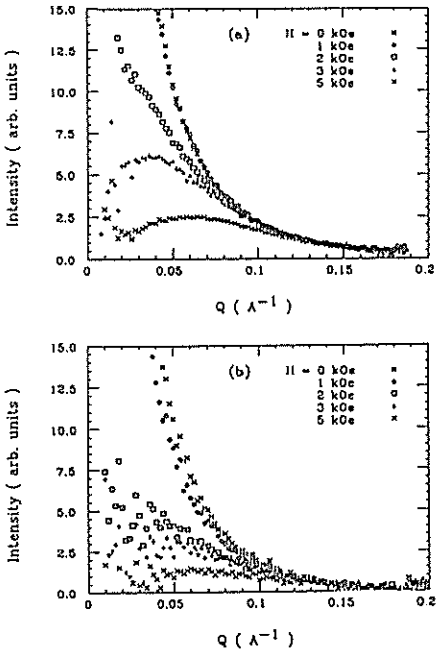

Fig. 1. Field dependences of the SANS intensity for (a) spin transverse correlations and (b) spin longitudinal ones.

where $\langle \cdots \rangle$ denotes the thermal average over all spins in a cluster.
Here,

$$F(Q) = (4\pi) \cdot (2c)/(a \cdot Q)^3 \cdot \{\sin(Q \cdot \xi) - Q \cdot \xi \cdot \cos(Q \cdot \xi)\}$$

is a form factor of a cluster, where c is a concentration of an iron atom and a is a lattice constant. In this formula there exist three unknown parameters ξ, ro and $\langle S_X^2 \rangle^{1/2}$. These parameters can be evaluated by the result of model fitting for the scattering data. For instance, in the case of $H = 5$ kOe and $T = 15$ K, these values are fitted to be $\xi = 17.$ Å, $r_O = 66.$ Å and $\langle S_X^2 \rangle^{1/2} = 0.62\ \mu_B$. Figure 4 shows the scattering

raw data with the fitting curve. The comparison between these parameters and the spin radial distribution is also shown in Fig. 5. On the other hand, the scattering shown in Fig. 1(b) can be explained similarly by replacing the transverse spin fluctuations with the longitudinal fluctuations from the mean magnetization in the above formula. These results suggest that a randomly oriented cluster model represents the microscopic fluctuation in $Fe_{.715}Al_{.285}$ in an applied field very well.

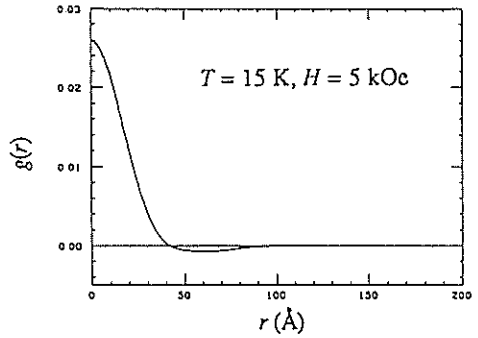

Fig. 2. Spin transverse correlation function in H = 5kOe at T =15 K.

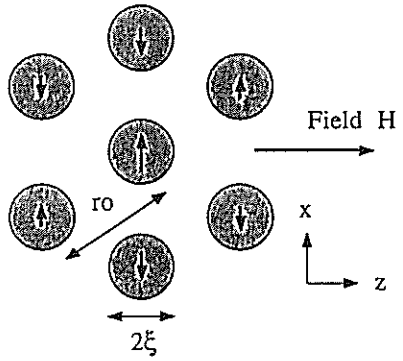

Fig. 3. Schematic diagram of a randomly oriented spin cluster model projected on xz-plane.

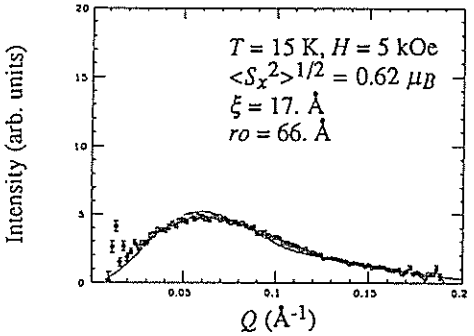

Fig. 4. SANS intensity in H = 5kOe at T =15 K and a result of a model calculation.

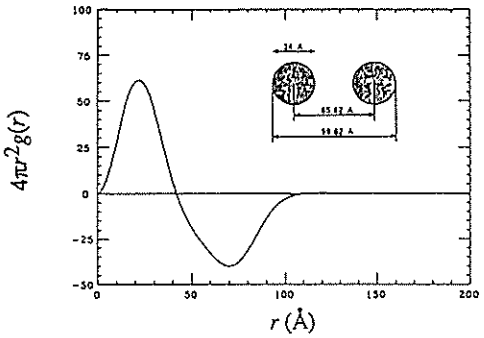

Fig. 5. Spin radial distribution and configuration of spin clusters in H = 5kOe at T =15 K.

The spin correlations in zero magnetic field on the same material were already reported.[4] In that paper we argued that the microscopic fluctuations of the correlation length about 15 Å may have an important role to trigger the break of the ferromagnetic long range order into the spin glass state. This length scale of the microscopic fluctuation is consistent with that in an applied field in the present study. The spin state in zero field may be interpreted as the state in which randomly oriented microscopic clusters aggregate upon decreasing the field and coexist with the remains of ferromagnetic order.

In conclusion, we presented the evidence of the existence of the microscopic fluctuations which are hard in applying a field. These fluctuations could be explained by a randomly oriented cluster spin model. The present results indicate that the mixed phases in FeAl RSG are different from a prospect by the mean field theory that local fluctuations are enhanced.

References

1) M. Gabay and G. Toulouse: Phys. Rev. Lett. 47 (1981) 201.
2) I. A. Campbell, S. Senoussi, F. Varret, J. Teillet and A. Hamzic: Phys. Rev. Lett. 50 (1983) 1615.
3) J. Suzuki, M. Arai, M. Furusaka, H. Yoshizawa and Y. Endoh: KENS. Rpt. 7 (1988) 69.
4) J. Suzuki, Y. Endoh, M. Arai, M. Furusaka and H. Yoshizawa: J. Phys. Soc. Jpn. 59 (1990) 718.

Magnetization Process in Reentrant Spin Glass $Ni_{77}Mn_{23}$

T. SATO, T. ANDO, Y. IRIE, S. ITOH*, T. WATANABE* and Y. ENDO*

Department of Instrumentation Engineering, Keio University, Yokohama 223

*Department of Physics, Tohoku University, Sendai 980

The magnetization process in reentrant Ni-Mn alloys has been characterized by remarkable stability of induced unidirectional anisotropy and ferromagnetic domain structure existing even in the reentrant spin glass (RSG) state.[1-4] Such reentrant nature should be investigated by means of techniques which probe the magnetic structure on a scale of medium range (few micrometers to several hundred micrometers). Then, we made the neutron depolarization measurements of reentrant $Ni_{77}Mn_{23}$ at temperatures below and above the reentrant transition temperature as a function of the wavelength at traveling of polarized neutron through the sample. The resultant data were analyzed on the basis of the previous work.[5,6]

Neutron depolarization measurements of a plate $Ni_{77}Mn_{23}$ sample of 1.04mm thick were performed using the TOP spectrometer at KENS. All the incident neutron spins are polarized along the z direction. The polarization $P(\lambda)$ along the z direction is measured as a function of the wavelength (3-9 A) using the polarization analyzer just after the neutron passes through the sample along x direction.

Figure 1 shows the polarization $P(\lambda)$ as a function of the wavelength in the three magnetic states, i.e., spin glass (SG) (a), ferromagnetic (FM) (b) and paramagnetic (PM) (c) states. Depolarization is observed in SG and FM states. Remarkable depolarization is observed for the sample cooled in zero field in the SG region, while the field cooling condition (H_c = 1020 Oe) results in the oscillating behavior with decay in $P(\lambda)$. The damped oscillation in FM state, independent of the cooling condition, has a period longer than that in SG state.

Mitsuda et al.[5,6] gave the expressions of $P(\lambda)$ corresponding to the different scales of inhomogeneity. First, no depolarization is expected for the inhomogeneity of the atomic scale (SG state) or first spin fluctuation (PM state). On the other hand, the depolarization in FM state should depend on the domain structure. For large domain limit in ferromagnet or spin glass containing large ferromagnetic clusters, $P(\lambda)$ results in the following form:

$$P(\lambda) = C_1 + C_2\exp(C_3\lambda^2)\cos(C_4\lambda), \quad (1)$$

where

$$C_1 = \langle B_z^2/B^2\rangle_B, \quad (2)$$

$$C_2 = \langle (B_x^2 + B_y^2)/B^2\rangle_B, \quad (3)$$

$$C_3 = (1/2)\sigma^2, \quad (4)$$

$$C_4 = cB\langle(\delta_1 + \delta_2 + \cdots)\rangle_{path}. \quad (5)$$

The bracket $\langle\ \rangle_B$ represents the ensemble average over the local induction B in each domain and the average $\langle\ \rangle_{path}$ for the field integral must be taken over the beam area due to the distribution of the field integral, centered at C_4 with half width σ. The symbol c is constant and δ_i is the domain size of each domain. We note that C_4 must be replaced by cBd and C_3 should become 0 for large domain limit of ferromagnet, where d is the sample thickness. On the other hand, $P(\lambda)$ becomes the following expression for the multi-domain configuration in ferromagnet:

$$P(\lambda) = \exp(-C_2'(1-\exp(-C_3\lambda^2)\cos(C_4'\lambda)), \quad (6)$$

where

$$C_2' = (d/\delta)\langle(B_x^2 + B_y^2)/B^2\rangle_B, \quad (7)$$

$$C_4' = cB\delta, \quad (8)$$

δ is the mean domain size.

As shown in Fig.1(a), zero field cooled (ZFC) data can be fitted by Eq.(6). The ZFC data in SG state is consistent with the multi-domain configuration. The FC data in SG state show the damped oscillation with a period longer than in FM state. This feature suggests larger field integral in SG state on the basis of Eq.(1). To analyze the magnetization process in $Ni_{77}Mn_{23}$, the thermal evolution of the parameters C_1, C_4 and $(-C_3)^{1/2}/C_4$, obtained by fitting to Eq.(1), are shown in Fig.2. Here, C_1 is replaced by the average polarization when no oscillatory polarization is observed. The value of C1 depends on the cooling process at temperatures below about 80 K. Scarce polarization is observed at low temperatures in the ZFC process, while the FC data show finite polarization. This behavior is consistent with the idea of the ferromagnetic domains which hardly change with applying weak field in RSG state.[7]

The value of C_4 shows the thermal evolution with noticeable feature, i.e., the outstanding variation at temperatures lower than the characteristic temperature T_D which depends on the applied field. Since T_D is suggestive of the spin freezing temperature T_f, the low temperature variation should correlate with RSG nature, although lower value of field integral may be expected for the spin frustrated state. This behavior of the field integral seems to be inherent in reentrant Ni-Mn alloy. Then, we claim that the rapid change in C_4 is mainly attributed to the temperature dependent anisotropy field. Our evaluated unidirectional and uniaxial anisotropy fields H_d = 290 Oe and H_e = 40 Oe at 4.2 K[4] roughly correspond to the half of the decrement of C_4 from 15 K to 80 K. We must also examine the exchange field of coupling between adjacent domains to obtain more sufficient explanation about whole thermal evolution of the field integral. Furthermore, we note that C_4 is smaller than that estimated from $4\pi M_D$ over whole temperature below 150 K, where M_D is the spontaneous magnetization evaluated from the magnetic measurements. This comparison indicates frustrated spins in each domain at temperatures even above Tf, which is suggestive of the Gabey-Toulouse temperature T_{GT}[8] much higher than T_f.

For H_{ex} = 90 Oe, the value of $(-C_3)^{1/2}/C_4$ is essentially identical in FM and RSG states, which suggests that the ferromagnetic domains remain in RSG state. We note detectable difference between ZFC and FC data at 35 K. The larger distribution of the field integral in ZFC process is consistent with more disarranged domain configuration which is hardly affected by applying weak field. The idea of ferromagnetic domain structure in RSG state is strongly supported by the thermal evolution of $(-C_3)^{1/2}/C_4$ accompanied by that of C_1.

In conclusion, the depolarization analysis of reentrant $Ni_{77}Mn_{23}$ gives some evidence which supports the previous interpretation of the reentrant nature, i.e., the idea of domain-anisotropy model.

References

1) J. Kouvel, W. Abdul-Razzaq, and Kh. Zip, Phys. Rev. B35, 1768 (1987)
2) S. Senoussi, Phys. Rev. Lett. 56, 2314 (1986)
3) S. Senoussi, and Y. Oner, J. Phys. (Paris) 46, 1435 (1985)
4) T. Sato, Phys. Rev. B41, 2550 (1990)
5) S. Mitsuda, and Y. Endoh, J. Phys. Soc. Jpn. 54, 1570 (1985)
6) S. Mitsuda, H. Yoshizawa, and Y. Endoh, Technical Report of ISSP, Ser. A, No.2195 (1989)
7) I. Mirebeau, S. Itoh, S. Mitsuda, T. Watanabe, Y. Endoh, M. Hennion, and P. Calmettes, J. Appl. Phys. 67, 5232 (1990)
8) M. Gabay, and G. Toulouse, Phys. Rev. Lett. 47, 201 (1981)

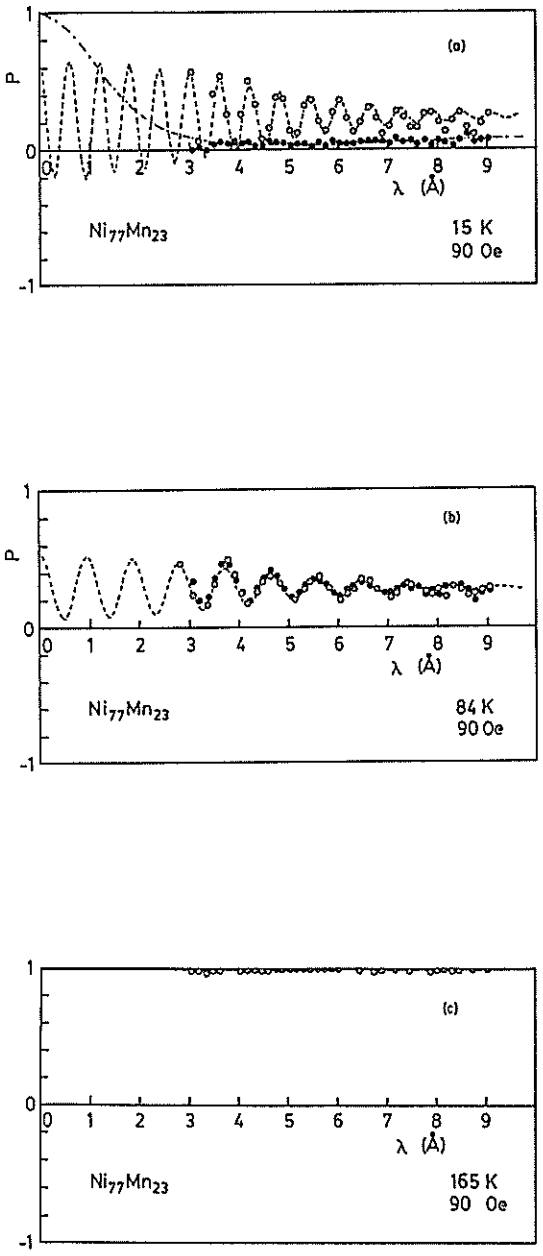

Fig.1 Wavelength dependence of polarization P(λ) for $Ni_{77}Mn_{23}$ on spin glass (a), ferromagnetic (b), and paramagnetic state (c). Filled and open circles correspond to ZFC and FC process respectively.

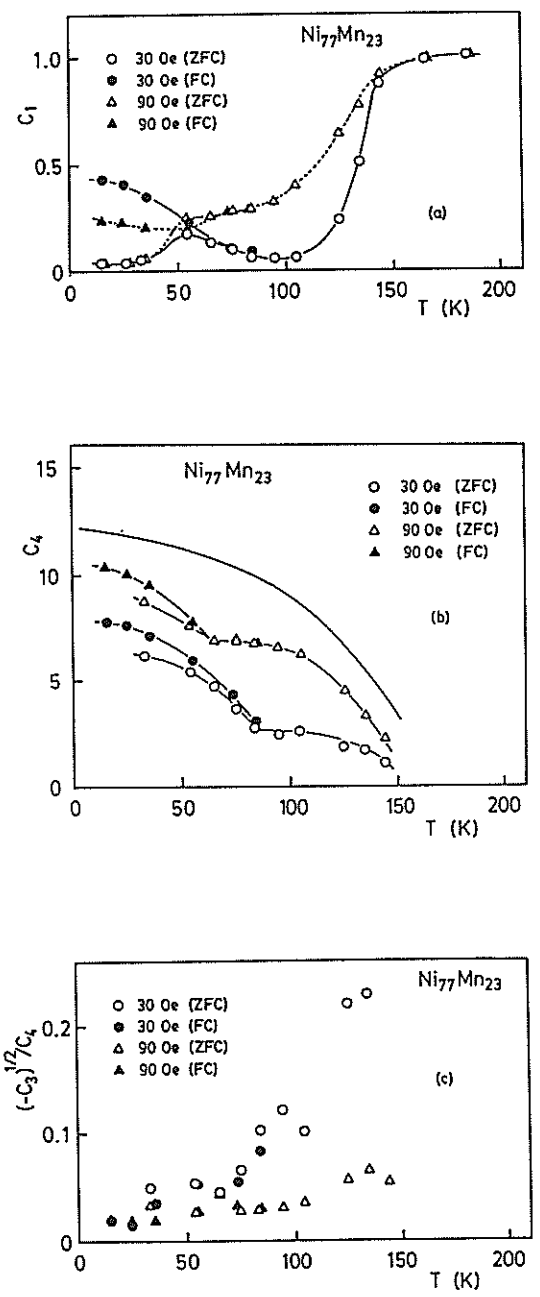

Fig.2 Temperature dependence of C_1 (a), C_4(b), and $(-C_3)^{1/2}/C_4$ (c) for $Ni_{77}Mn_{23}$. Filled and open marks correspond to ZFC and FC process respectively.

Neutron Depolarization Studies on Reentrant Spin Glass AuFe Alloy

S. Mitsuda, I. Mirebeau*, T. Watanabe**, S. Itoh**, H. Yoshizawa and Y. Endoh**

Institute for Solid State Physics, University of Tokyo, Roppongi, Tokyo, 106 Japan
*Laboratoire Leon Brillouin, CEN-Saclay, 91191 Gif-sur-Yvette Cedex, France
**Department of Physics, Tohoku University, Aramaki Aoba, Sendai, 980 Japan

Recently we have studied Reentrant Spin Glass(RSG) problem in view of magnetic inhomogeneities on mesoscopic scale by neutron depolarization technique where the wavelength dependence of polarization P(λ) transmitted through the thin plate of sample is analyzed. As demonstrated in recent depolarization experiments on FeAl[1], amorphous FeMn[2], AuFe[3] and NiMn[4], the wavelength dependent neutron depolarization technique has been used successively to reveal the nature of RSG phase on mesoscopic scale. In this short report, we present the depolarization data from polycrystalline $Au_{1-x}Fe_x$ thin disk plate specimens[3] and will discuss mainly following two points. [1] the origin of nearly universal behavior of low field bulk magnetization below RSG temperature Tg. [2] anomalous decreasing of local magnetization found in this experiments on the basis of the spin canting model suggested by Mössbauer experiment[5] as well as with the spin rotation model of Saslow and Parker[6].

Neutron depolarization measurements have been carried out on the TOP spectrometer. The wavelength dependent depolarization was measured with the thermal scans for both zero field cooling (ZFC) and field cooling (FC) scans under weak magnetic field(~30 Oe) in which magnetizations show characteristic RSG temperature dependences with T_C~100K,T_g~30K and T_C~175K,T_g~25K for x=0.16 and x=0.19 specimens respectively as shown in Fig.2(a). The profile P(λ) in Fig.1(a) and (d) shows that no depolarization occurs in the paramagnetic phase, which reflects the fast spin fluctuations above T_C. In the ferromagnetic phase below T_C, the profile shows oscillation feature with respect to the wavelength λ (i.e. P(λ)~cos(Iλ)) as seen in Fig.1(b) and (e), which indicates the existence of the "ferromagnetic mono-domain state" where each ferromagnetic domain extends over the entire sample along the beam direction. In this situation we can obtain the local magnetization B within mono-domain through the field integral value I of the oscillation, being independent of orientation of domains[1,3].

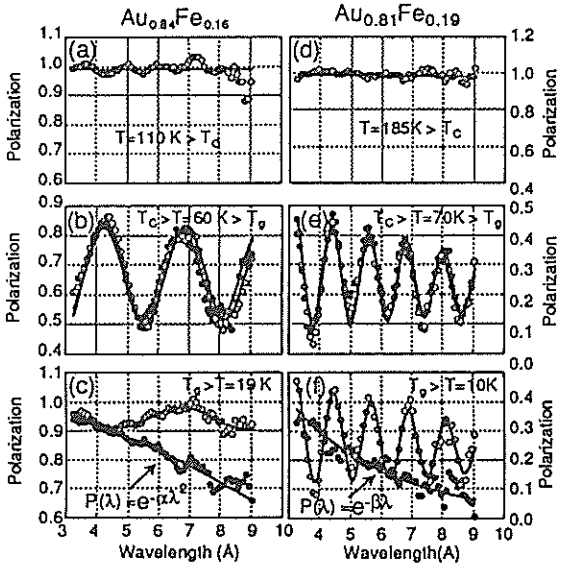

Fig.1 Typical wavelength dependence of polarization P(λ) in typical phase of paramagnetic (a) & (d), ferromagnetic (b) & (e), and RSG (c) & (f) for x=0.16 (Left panel) and x=0.19 (Right panel), respectively. Filled and open circles correspond to ZFC and FC scans respectively. Solid line is a result of fitting.

Contrast to that no appreciable field cooling effect was observed in ferromagnetic phase, in RSG phase, the pronounced differences in the profile for ZFC and FC scans are visible as seen in Fig.1(c) and (f), which reflects the hysteresis below Tg seen in the low field magnetization data. As for the FC scan, the oscillatory feature still remains, although the oscillation periodicity is different from in the ferromagnetic phase. For the ZFC scan, on the other hand, P(λ) shows the monotonic wavelength dependence instead of oscillation feature, which reflects the existence of "ferromagnetic multi-domain state" consisting of many small ferromagnetic domains in which ferromagnetic long range order remains. The estimated average domain size δ from those profiles is about 6 μ for x=0.16 sample and 20 μ for x=0.19 sample

respectively, which seems to be reasonable as typical ferromagnetic domain size. This fact strongly suggests that ferromagnetic long range order still remains even in RSG phase. By contrast, the pure spin glass specimen with x=0.15 (≥ critical concentration x_c) which exhibits only the spin glass transition shows no depolarization over whole temperature range, which means no existence of ferromagnetic long range order. This different behavior of depolarization around critical concentration x_c shows that RSG phase($x>x_c$) is indeed qualitatively different from the pure spin glass phase($x<x_c$), which is consistent with new phase boundary found in Ising Antiferromagnetic RSG $Fe_xMn_{1-x}TiO_3$[7]. Similar conclusion has been obtained by recent depolarization experiments on amorphous FeMn[2] and NiMn[4].

Next we discuss the temperature dependence of local magnetization B on mesoscopic scale determined from the field integral I=cBL, where c and L are the physical constant related to neutron gyromagnetic ratio and sample thickness respectively. As shown in Fig.2(b), we plot the normalized field integral I* with respect to the unit thickness of 1 [mm] instead of I to allow a direct comparison between samples with different sample thickness L.

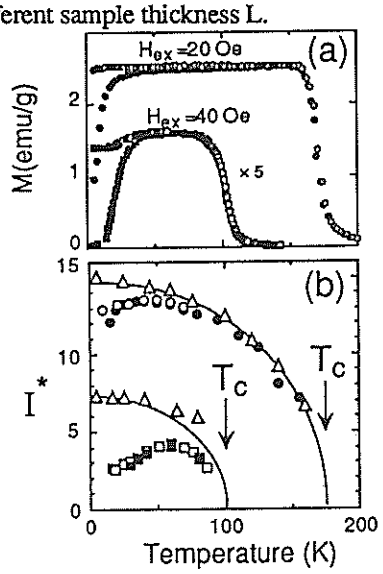

Fig.2 Temperature dependence of (a) low field magnetization and (b) normalized field integral I* for both x=0.16 (circle) and x=0.19 (rectangle). Filled and open marks correspond to ZFC and FC scans respectively. I* is normalized with respect to unit thickness of L=1 [mm], and calculated field integral (triangular) from spontaneous magnetization is also plotted in (b). Solid line is guide to eyes.

In a normal ferromagnet, I* should increase monotonically with decreasing temperature below T_c and saturate at low temperature reflecting the usual thermal evolution of the local induction $B(=4\pi M_S)$. However in both samples an anomalous decreasing of I* is seen at low temperature.

For the better understanding, we also plot the calculated I*(T) defined by $c4\pi M_S(T)L$ with L=1 [mm] in Fig.2(b) (denoted by triangle Δ), where spontaneous magnetization $M_S(T)$ was determined by linearly extrapolating back from high magnetic field(~10K Oe) to zero field in magnetization curves. For x=0.19 sample, the observed field integral I*(T) is well approached by the calculated I*(T) in the high temperature region, which also supports the realization of "ferromagnetic mono domain state" stated above. Namely, the averaged local magnetic field B within a "mono-domain"(δ=L) can be well represented by the spontaneous magnetization. However, I*(T) start to deviate from calculated I*(T) below the temperature ~60K. Interestingly this temperature is well above Tg ~25K and is close to Gabay and Toulouse(GT)[8] transition temperature determined by Mössbauer experiment [5]. For x=0.16 sample, close to critical concentration x_c ~0.15, it is clear that the deviation of observed I*(T) occurs at higher temperature as well as that relative amount of deviation is bigger than in x=0.19 sample, although the spontaneous magnetization of x=0.16 sample near Tc is hard to be determined due to lack of a well defined knee in the magnetization curve. Those behaviors of the field integral I*(T) are consistent with the results from Ising Antiferromagnetic RSG $Fe_xMn_{1-x}TiO_3$[7], where the anomalous decreasing of magnetic Bragg scattering intensity depends on the distance of each sample from the multi-critical point in the RSG phase diagram.

For x=0.19 we observed at low temperature only a small reduction in the local magnetization, which is not inconsistent with GT picture where additional increasing of total spin length due to the freezing of local transverse spin component was observed in Mössbauer experiment by Cambell et. al[5], since the effect of the longitudinal component essentially determines the neutron depolarization and randomly oriented transverse components in an atomic scale have no influence to the neutron depolarization as are the spins in the pure spin glass. On the other hand, in GT picture one can not explain the anomalous reduction of local magnetization clearly seen in x=0.16 sample. The picture presented by Saslow and Parker[6] is more suitable to our results.Their numerical calculation showed that the freezing of the frustrated spins at low temperature leads to a spin rearrangement in order to minimized the total free energy of the system. This

effect results in a rotation of the spins with respect to their direction at high temperature, and thus in a decrease of the longitudinal component(local magnetization on mesoscopic scale). Note that in this second approach we could also understand the Mössbauer data, as suggested by B. Huck et. al [9].

Finally we discussed the origin of the nearly universal behavior of low field bulk magnetization below RSG temperature Tg. As described above, we found that the anomalous decreasing of local magnetization associated with reentrance into the spin glass state, occurs well above Tg below which low field bulk magnetization exhibits hysteretic behavior. This suggests the following question. What is the relation between the irreversibilities in the low field bulk magnetization and the irreversibilities in the depolarization evidenced by the dramatic difference in ZFC and FC scans(Fig.1(c) and Fig.1(f)). To clarify this point, we have measured the magnetic field dependence of the profile $P(\lambda)$ at several temperature below and above Tg specially for x=0.16 sample.

At T=16K(below Tg~30K) the profile $P(\lambda)=\exp(-\alpha\lambda^2)$ which corresponds to "multi-domain state" consisting of many small ferromagnetic domains hardly changes at all, when external magnetic field increases up to 100 Oe starting from ZFC state and decreased down to 7 Oe. It means that a technical magnetization process (growth of domain size as well as reorientation of local magnetization in each domain) dose not set up at this temperature. However, at T=25K(still below Tg~30K) the profile $P(\lambda)$ exhibits a dramatic change for identical magnetic field scan as shown in Fig.3. With increasing magnetic field, the functional form of $\exp(-\alpha\lambda^2)$ is still obeyed even in medium range of magnetic field, nevertheless, the oscillation in polarization appears and remains even in the lowest field of 7 Oe when the field is further decreased, which indicates that technical magnetization process occurs with delay. Moreover, hysteretic behavior was not observed within experimental accuracy both at T=40 K(above Tg) and at T=65 K(well above Tg). Those experimental facts suggest that the ferromagnetic domain wall motion which determines the technical magnetization process gradually becomes mobile up to Tg with increasing temperature. In other words, those facts suggest that the nearly universal behavior of ZFC and FC bulk magnetization below Tg mainly results not from break down of ferromagnetic long range order but from low mobility of domain wall motion due to the spin freezing below Tg, although anomalous decreasing of local magnetization on mesoscopic scale associated with reentrance into RSG state occurs at low temperature. Namely, the temperature dependence of ZFC low field bulk magnetization up to Tg can be explained as follows. When the sample is cooled in zero field down to the lowest temperature, demagnetizing state may be realized. Then, even after the finite external magnetic field 30~40 Oe is applied, the "ferromagnetic multi-domain state" still remains due to the magnetic viscosity or low mobility of domain wall motion, which results in that ZFC magnetization is lower than FC magnetization under the same amount of magnetic field. As temperature is raised in ZFC scan, technical magnetization process gradually progresses and ZFC magnetization gradually recovers up to Tg, since the domain walls gradually become mobile due to the melting of frozen spins by thermal fluctuations. Similar conclusion has been obtained by recent depolarization experiments on amorphous FeMn[2] and NiMn[4].

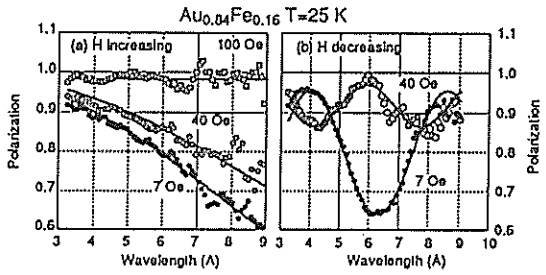

Fig.3 Magnetic field dependence of $P(\lambda)$ for x=0.16 sample at T=25 K below Tg. (a) Sample was cooled down to 25K under zero field, and measured with increasing external field up to H=100 Oe. (b) then, measured with decreasing field down to H=7 Oe. Solid line is a result of fitting.

References

1) S. Mitsuda, H. Yoshizawa, and Y. Endoh submitted to Phys. Rev. B
2) I. Mirebeau, S. Itoh, S. Mitsuda, T. Watanabe,Y. Endoh, M. Hennion and R.Papoular to be published in Phys. Rev. B(1990)
3) S. Mitsuda, H. Yoshizawa, T. Watanabe, S. Itoh, Y. Endoh, I. Mirebeau, in preparation
4) I. Mirebeau, S. Itoh, S. Mitsuda, T. Watanabe,Y. Endoh, M. Hennion and P.Calmettes, to be published in J. App. Phys.(1990)
5) I. A. Campbell, S. Senoussi, F. Varret, J. Teillet and A. Hamzic, Phys. Rev. Lett. 48, 1490, (1982).
6) W. M. Saslow and G. N. Parker, Phys. Rev. Lett. 56, 1074, (1986).
7) H. Yoshizawa, S. Mitsuda, H. Aruga and A. Itoh, Phys. Rev. Lett. 59, 2636, (1987).
8) M. Gabay and G. Toulouse, Phys. Rev. Lett. 47, 201, (1981).
9) B. Huck and J. Hesse; J. M. M. M. 78, 247, (1989)

1-4. Dynamics of Solids and Liquids

Phonon Dispersion Law Measurement on g-SiO2

MASATOSHI ARAI and JENS-ERIK JØRGENSEN*

National Laboratory for High Energy Physics (KEK), Japan
*Aarhus Univ., Denmark

It is well known that non-crystalline materials have universal properties as exhibited in their thermal conductivities and their specific heats. By using conventional kinetic theory, we infer that the phonon mean free path exhibits a decrease by resonant relaxation of two-level tunneling states [1] less than the frequency corresponding to 1K and a precipitous drop by Rayleigh scattering by local density inhomogeneity, and becomes less than an atomic spacing above the frequency corresponding to 10K explained by Ioffe-Regel criteria. Thus the normal phonon theory does not give a satisfactory description for the dynamical properties of non-crystalline systems. Recent theories[2] suggest that the vibrations of non-crystalline materials on a sufficiently short length scale should be described by "*fractons*" instead of the more conventional phonons . The theory predicts the existence of a cross-over frequency at which the vibrations change from a phonon to a fracton character. Furthermore, a quantum diffusion process in the fracton regime is expected[3].

We performed inelastic neutron scattering at KENS to measure a vibrational density of state of Epoxy Resin[4]. We could successfully understand the vibrational density of states at low energy region with a model containing an acoustic phonon and a phonon-assisted migration, and the measurement revealed a cross-over from an phonon to a fracton regime at 1.8meV, giving 1.9±0.1 for fracton dimension. The propagation characteristics of the two vibration of phonon and fracton is very different. This is explicitly seen only in the vibrational dispersion law. So it is indispensable to measure a vibrational dispersion law to clarify a detailed description of the dynamics of non-crystalline materials. The dispersion is expected to be a Roton-like curve and the width rapidly increases at fracton regime[5].

We show below a phonon dispersion curve on SiO2 (Typical Glass System) done by LAM-40 in KENS . The measurement on SiO2 was also done by Buchenoux[6] in ILL, but on density of state, not dispersion itself, because of the weak scattering intensity. They also saw an additional density of states which is described by phonon-assisted migration in our description. A theoretical expectation on phonon and fracton dispartion is also displayed. The preliminary results shows encoureging feature to understand the dynamics of non-crystarine materials.The detailed analysis is under way.

1) W. A. Phillips, J. Low Temp. Phys. 7, 351 (1972)
P. W. Anderson, B. I. Halperin and C. M. Varma, Phil. Mag. **25**, 1 (1972)
2) S. Alexander and R. Orbach, J. de Phys. (Paris) Lett. **43**, L-625 (1982),
S. Alexander, C. Laermans, R. Orbach and H. M. Rosenberg, Phys. Rev. **B 28**, 4615 (1983)
P. H. Tua, S. J. Putterman and R. Orbach, Phys. Lett. **98A**, 357 (1983)
3) A. Aharony, S. Alexander, O. Entin-Wohlman and R. Orback, Phys. Rev. Lett **58**, 132 (1987)
4) M. Arai and J.E. Jorgensen, Phys. Lett. **A133**, 70 (1988)
5) O. Entin-Wohlman, S. Alexander, R. Orbach and K.W. Yu Phys. Rev. B29 4588 (1984)
6) U. Buchenoux, N.Nücker and A. J. Dianoux, Phys. Rev. Lett. **53**, 2316 (1984)

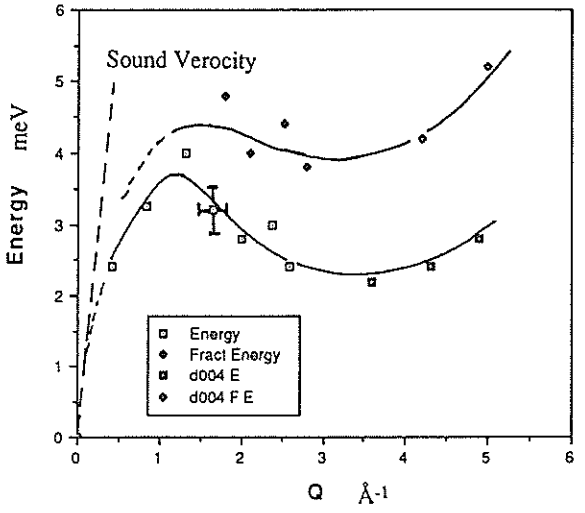

Observed Dispartion law of Accourstic Phonons of SiO_2. The lines are just for guide to eye.

Measurement on Dynamic Structure of Cu-Zr amorphous alloy by INC

T.NAKANE, M.ARAI*, K.SHIBATA, K.SUZUKI, K.OHOYAMA** and M.KOHGI**

Institute for Materials Research, Tohoku Univ.,Sendai 980
*National Laboratory for High Energy Physics, 1-1 Oho, Tsukuba-shi, Ibaraki 305
**Department of Physics, Faculty of Science, Tohoku Univ., Sendai 980

Dynamical structure factor S(Q,ω) of glass and liquids provides very important informations about their atomic dynamics. Neutron inelastic scattering is the most powerful technique for investigating S(Q,ω). INC is a direct geometry chopper inelastic neutron spectrometer which is installed at the pulsed neutron source KENS. Its measurable S(Q,ω) is covered over a wide momentum and energy transfer region. So, INC is suitable for studying glass and liquid dynamics[1].

We choose $Cu_{57}Zr_{43}$ amorphous alloy (a-CuZr) as a first amorphous alloy sample to study S(Q,ω) on INC. Because dynamical structure factor of a-CuZr has been reported by Sück[2]. It is possible to compare present result with it and check the machine performance of INC.

Amorphous CuZr tape was prepared by rapid quenching from molten state. We need 40g sample for this inelastic scattering measurement on INC. A cylindrical aluminium sample cell was used to reduce background (20mm in diameter , 0.5mm in wall thickness and 50mm in length). Sample was packed in He gas atmosphere for the homogeneity of the sample temperature. The incident neutron energy was chosen at 60meV($0.5Å^{-1} < Q < 12Å^{-1}$), and in this condition energy resolutions(ΔE/Ei) at are about 5% and 8%, at the low angle and high angle counter banks, respectively. Energy resolution was derived from Vanadium standard measurement. The sample was cooled down to 16K to reduce multiple phonon scattering. It took 2 days for this measurement.

Figure 1, 2 show experimental results. Absorption, background and counter efficiency correction have been done but multiple scattering correction has not been done yet. Figure 1 shows I(Q,ω) of a-CuZr, where I(Q,ω) is an unnormalized S(Q,ω). Figure 2 shows the comparison of I(Q) of a-CuZr with S(Q) of a-CuZr measured on HIT, where

$$I(Q) = \int_{-50meV}^{50meV} I(Q,\hbar\omega)\, d\hbar\omega$$

I(Q) is in good agreement with S(Q) data on HIT. To coincide I(Q) with S(Q), constant value was subtracted from I(Q).

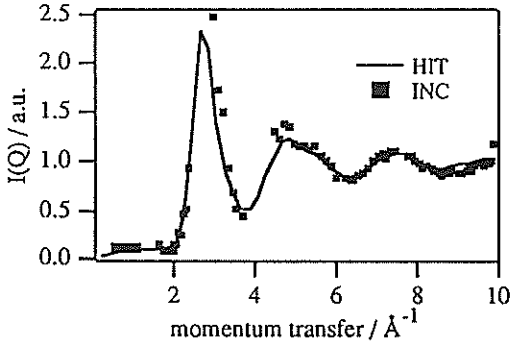

Fig. 2 I(Q) of a-$Cu_{53}Zr_{47}$ and S(Q) measured on HIT

Further data analysis is now in progress.

References

1) M. Arai et.al : KENS report-VII p.9
2) J-.B. Sück et.al : J.Phys.C: Solid State Phys 13 (1980) L167

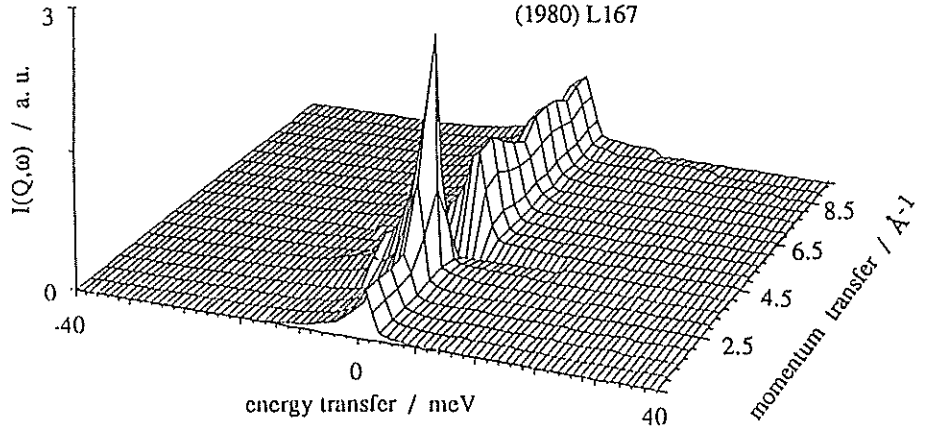

Fig. 1 Wide range I(Q,ω) of a-$Cu_{53}Zr_{47}$ measured on INC

Dynamic Properties of Molten $0.80RbNO_3$-$0.20Sr(NO_3)_2$ Mixture near the Glass Transition

K. Shibata, T. Kamiyama and K. Suzuki

Institute for Materials Research, Tohoku University, 2-1-1 Katahira, Aoba-ku, Sendai 980, Japan

1. INTRODUCTION

Many studies have been performed on the dynamic behavior of melts in the range of glass transition.[1,2,3] There are some difficulties in choosing an appropriate melt specimen, which must be easily brought into the supercooled state in spite of having a relatively simple structure.

In this study we use a mixture of simple metal nitrates of $0.80RbNO_3$-$0.20Sr(NO_3)_2$ as a melt specimen for neutron scattering measurements, because coherent neutron scattering lengths for Rb and Sr are almost equal each other and the static structure of $RbNO_3$ melt has been well established.[4]

A scientifically interesting point for using the melt of nitrates is to find whether intra-ionic fast motions in a NO_3^- anion are dynamically correlated with the glass transition as well as inter-ionic slow motions do.

2. EXPERIMENTAL

$RbNO_3$-$Sr(NO_3)_2$ system is known to be vitrified in the range of 69 to 83 mol%$RbNO_3$ by melt-quenching.[5] The mixed nitrate of $0.80RbNO_3$-$0.20Sr(NO_3)_2$ corresponding to an eutectic composition was prepared as a specimen for quasielastic neutron scattering measurement. This specimen was always handled in vacuum or dry Ar gas atmosphere because of its extremely hygroscopic nature. DSC analysis shows that the glass transition and solidification temperature of the melt are about 70°C and 200°C, respectively.

The dynamic structure factors S(Q,w) of the melt were measured in the temperature range from 210°C to 490°C by using the quasielastic neutron scattering spectrometer LAM-40[6] installed at KENS. This spectrometer provides the energy resolution of about 200 μeV at elastic scattering and the momentum transfer range from 0.2 to 2.6 $Å^{-1}$. The specimen was sealed in vacuum into an aluminium metal double-walled cylinder (14.0 mm in outer diameter, 8.0 mm in inner diameter and 80 mm in length). At the present stage of data analysis, we corrected only background and ignored multiple scattering effect, because the thickness of specimen is thin enough to reduce the multiple scattering below 10%.[7]

3. THEORETICAL

It is very difficult to distinguish the nuclear scattering contributed from Rb and Sr in the melt of $0.80RbNO_3$-$0.20Sr(NO_3)_2$, because both the nuclei have almost equal neutron scattering cross sections of σ_S=6.30 barns for Rb and 6.22 barns for Sr. Therefore, the melt can be regarded as a two-component system consisting of $M^{1.2+}$ cations and NO_3^- anions during the process of data analysis.

In the melt of nitrates, the intra-ionic motions like as rotation of a NO_3^- anion (its relaxation time ≈ 10^{-12} sec) are much faster than the inter-ionic motions like as structure relaxation among ionic centers of gravity (its relaxation time ≈ 10^{-11} sec). Therefore, the intra-ionic motions in a NO_3^- anion are thermally averaged out in the time scale of inter-ionic motions in the melt. This approximation is often assumed in the data analysis of incoherent quasielastic neutron scattering for molecular liquids.[8]

Figure 1 shows the time-of-flight spectrum observed at the temperature of 408°C for the melt, which contains obviously the both of narrow and broad components. The narrow component in the spectrum is contributed from the inter-ionic interactions, while the broad component in the spectrum is assigned to the intra-ionic motions.

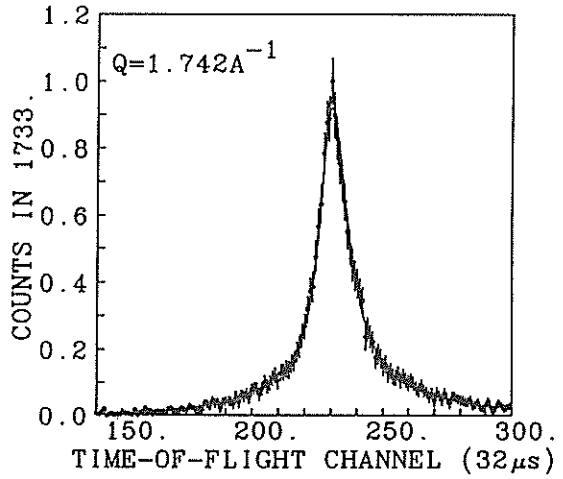

FIGURE 1. Time-of-flight spectrum of neutron scattering observed for $0.80RbNO_3$-$0.20Sr(NO_3)_2$ melt near a Q value of peak maximum in S(Q) at 408°C.

According to the assumption described above, the dynamical structure factor $S(Q,\omega)$ is derived as follows: $S(Q,\omega)=S_{inter}(Q,\omega)+S_{intra}(Q,\omega)$, (1)
where

$S_{inter}(Q,\omega)=S^{tr}_{ion\text{-}ion}(Q,\omega)$, (2)

$S_{intra}(Q,\omega)=S^{tr}_{NO3}{}^{S}(Q,\omega)\otimes S_{NO3\text{-}intra}(Q,\omega)$ (3)

$S^{tr}_{ion\text{-}ion}(Q,\omega)$ is the coherent dynamic structure factor contributed from the inter-ionic interactions of three different kinds of pairs, i.e. cation-cation, cation-anion and anion-anion. The intra-ionic motions in a NO3- anion is thermally averaged out.

$S^{tr}_{NO3}{}^{S}(Q,\omega)$ is the incoherent dynamic structure factor for self diffusion of center of gravity of a NO_3^- anion.

$S_{NO3\text{-}intra}(Q,\omega)$ is the dynamic structure factor for intra-ionic motions in a NO_3^- anion. $\otimes$ means convolution.

The integrated intensity of $S^{tr}_{NO3}{}^{S}(Q,\omega)$ is unity. The width of $S^{tr}_{NO3}{}^{S}(Q,\omega)$ is much narrower than that of $S_{NO3\text{-}intra}(Q,\omega)$. Therefore, eq.(1) is simplified to:

$S(Q,\omega)=S^{tr}_{ion\text{-}ion}(Q,\omega)+S_{NO3\text{-}intra}(Q,\omega)$. (4)

Based on the theoretical consideration described above, eq.(4) is empirically fitted to a model of Lorentz functions:

$$s(Q,\omega)=\frac{S(Q)}{\pi}\left\{(1-A)\frac{\Gamma_1}{\omega^2+\Gamma_1^2}+A\frac{\Gamma_2}{\omega^2+\Gamma_2^2}\right\} \quad (5)$$

$\Gamma_1=D_2\times Q^2$

$\Gamma_2=D_2\times Q^2$, $\Gamma_1 \ll \Gamma_2$,

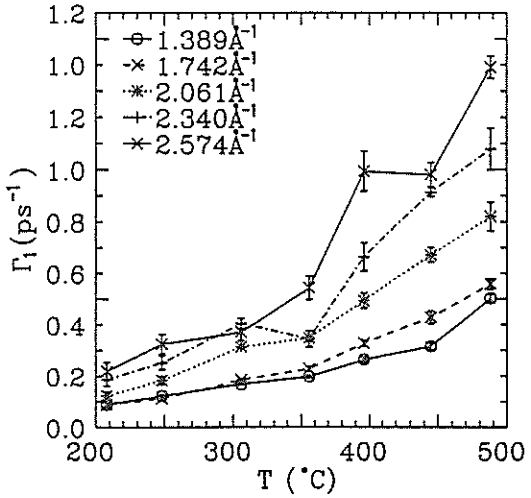

FIGURE 2. Temperature dependence of the half width at half maximum Γ_1 of narrow quasielastic component at several momentum values.

where A, D_1, and D_2 are the parameters decided by a least-squared fitting.The first term (Γ_1 term) in eq.(5) corresponds to the narrow component in the spectrum as shown in figure 1. The broad component is represented by the second term (Γ_2 term) in eq.(5). The resolution function of the LAM-40 spectrometer used for the fitting is experimentally determined from the elastic scattering profile observed for a standard specimen of metallic vanadium. A solid line in figure 1 is the result of the least-squared fitting.

4. RESULTS AND DISCUSSION

4.1. Narrow component

Figure 2 shows the temperature dependences of the half width at half maximum Γ_1 for the narrow component at several different momentum transfer values. All Γ_1 values become nonlinear narrow with decreasing temperature. If scale factors are properly selected depending on Q values, we can make the temperature dependences of Γ_1 coincide with each other to obtain a common curve. This means that all the modes of inter-ionic motions in the melt may be frozen in similar Q dependence around the glass transition temperature.

Correlations between the width Γ_1 and viscosity η are examined in figure 3. Experimental values are shown by points with error bars. Calculations of eq.(6) derived from the Stokes-Einstein[1,2] relation are drawn by solid and dotted lines in figure 3.

$$\tau^{-1}=D_1\times Q^2=\frac{k_B T Q^2}{6\pi\eta R} \quad ,(6)$$

where R is an adjustable parameter and the other symbols are the conventional. The solid and dotted

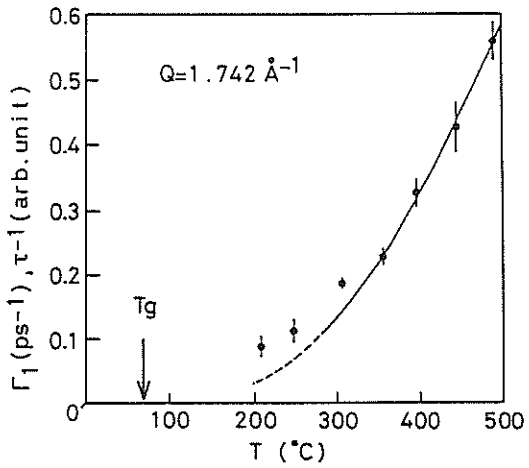

FIGURE 3. Comparison between temperature dependence of Γ_1 and that of viscosity. Solid and dotted lines are calculated using the Stokes-Einstein relation. Tg is the glass transition temperature.

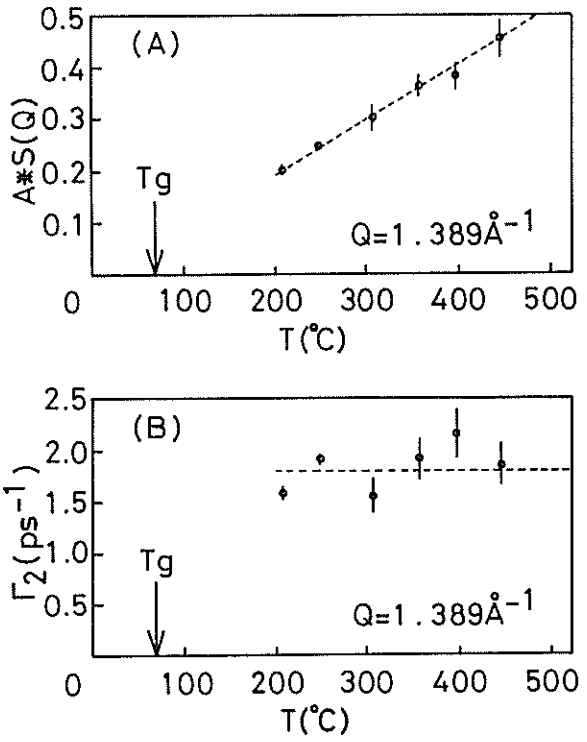

FIGURE 4. Temperature dependences of integrated intensity A*S(Q) and the half width at half maximum Γ_2 for broad quasielastic component.

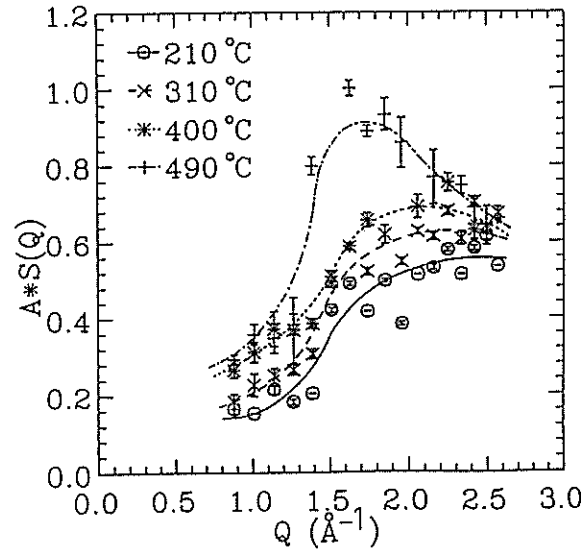

FIGURE 5. Relations of integrated intensity A*S(Q) versus momentum transfer Q. Lines are a guide for reader's eyes.

lines are calculated by using experimental data and the Vogel-Fulcher relation for viscosity, respectively.

Figure 3 shows that the relation between the width Γ_1 and viscosity η are not satisfactorily described in the temperature range examined in this study by eq.(6) based on the Stokes-Einstein relation, but present the significant discrepancy from eq.(6) below about 300°C. This conclusion is obviously against the results obtained by Mezei et al.[1)]

4.2. Broad component

The temperature dependences of the integrated intensity A*S(Q) and the width Γ_2 are plotted as a function of temperature in figure 4. The integrated intensity A*S(Q) decreases linearly with decreasing temperature and is extrapolated toward zero near the glass transition temperature. Figure 5 shows the plot of the integrated intensity versus momentum transfer at each temperature. Lines in the figure are illustrated for the guide of reader's eyes. Maximum peaks shift toward high momentum side with decreasing temperature. This means that the spatial amplitude of the motion is suppressed with decreasing temperature.[9)]

Based on the results obtained in figures 4 and 5, we conclude that the relaxation time of the intra-ionic motion does not show any trends of diverging, but the amplitude of the motion is rather confined within more restricted space decreasing as the temperature approaches the glass transition point.

REFERENCES

1) F. Mezei, W. Knaak and B. Farago, Phys. Rev. Lett. 58 (1987) 571.
2) J. B. Suck, J. H. Perepezko, I. E. Anderson and C. A. Angell, Phys. Rev. Lett. 47 (1981) 424.
3) J. Jäckle, Rep. Prog. Phys. 49 (1986) 171.
4) K. Suzuki and Y. Fukushima, Z. Naturforsch 32A (1977) 1438.
5) E. Thilo, C. Wieker and W. Wieker, Silikattechn. 15 (1964) 109.
6) K. Inoue, Y. Ishikawa, N. Watanabe, K. Kaji, Y. Kiyanagi, H. Iwasa and M. Kohgi, Nucl. Instr. and Meth. A238 (1985) 401.
7) V. F. Sears, Adv. in Phys. 24 (1975) 1.
8) G. Allen and J. S. Higgins, Rep. Prog. Phys. 36 (1973) 1073.
9) T. Springer, Springer Tracts in Modern Physics vol.64 (Splinger, Berlin, 1972).

A Preliminary Report on Neutron Inelastic Scattering of KDP Under a Uniaxial Stress

T.YAGI, S.KINOSHITA, S.IKEDA* and K.SHIBATA*
Research Institute of Applied Electricity, Hokkaido University,
Sapporo 060
*National Laboratory of High Energy Physics, Tsukuba 305

Since the discovery of the low frequency Raman scattering spectra of KDP (KH_2PO_4) crystal,[1] the phase transition mechanism has been controversial until now on its dynamical aspects,[2] in particular on the role of the motion of protons in the hydrogen bond. An amazing increase of Tc by the substitution of deuterium, "isotope shift of Tc", suggests an important role of the hydrogen motion in the transition mechanism.[3] The hydrogen bonds in KDP direct nearly perpendicular to the c axis of the tetragonal system. On the other hand, the spontaneous polarization, which is an order parameter of the ferroelctric phase transition, occurs in parallel to the c axis, that is, perpendicular to the hydrogen bonds. Therefore some coupling mechanism between the fluctuating polarization and the motion of protons in the bond should be introduced to explain consistently the large isotope effect and the occurrence of the spontaneous polarization below Tc. However there has been no direct evidence for the coupling mechanism.

In order to elucidate the coupling mechanism, we tried to observe the spectra of the proton motion under a uniaxial compressive stress along the ferroelectric c axis. If the coupling mechanism exists, the spectra of the proton motion will be affected considerably under an appropriate value of stresses along the ferroelctric axis, which restricts the motions of P, O and K atoms along the c axis.

Neutron inelastic scattering is quite adequate method for the observation of the proton spectra due to the large incoherent cross section of proton. The pulse neutron source of KEK, KENS is able to supply a high intensity beam in a wide range of the incident energy. In the present study, the spectra of the neutron scattering were detected under several values of the uniaxial stresses using the lattice-crystal analyser-mirror spectrometer of D type, LAM-D. The energy resolution is 300μeV for the elastic peak. The inelastic spectra were detected in the energy range 5-200 meV at two scattering angles 35 and 85 degree. The size of the sample crystal is 2.8 x 25.0 x 60.0 mm^3 along the a, a and c axes of the tetragonal system.

Figures 1 illustrates the uniaxial stress

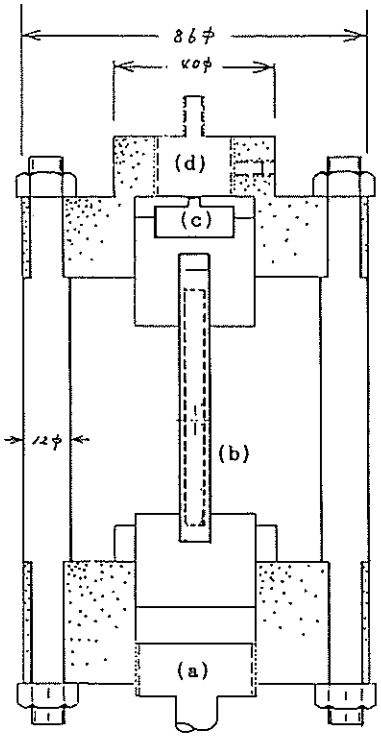

Fig.1 Uniaxial-stress cell. By rotation of the screw (a) on the bottom plate, we can apply a compressive stress to the sample plate of KDP (b) with the thickness of 2.8 mm. The value of the stress is monitored by the bridge of the strain-gauges (c) placed in the top plate (d).

cell employed in the present study to apply the compressive stress along the c axis of KDP crystal.

A preliminary result of the present study is shown in Fig. 2 and also in a magnified scale of energy in Fig.3. The spectrum shown by a dashed line was observed under a uniaxial stress 16 bar at room temperature. The data shown by a solid line are observed under atmospheric pressure at room temperature. According to the assignment of the peaks in the spectra reported by the previous neutron inelastic scattering by using another spectrometer CAT of KENS,[4] several peaks at 28, 125 and 160 meV in Fig.2 have been confirmed to be the low frequency stretching mode, the bending mode and the degenerated bending-stretching mode, respectively. In the present case the direction of the scattering vector Q lies on the (001) plane (A-scan). The peak positions in the spectra seem to be affected by applying stress; both of the peaks at 28 meV and 125 meV shift to higher energy side. Figure 3 shows the shift of the peak position of the lowest 28 meV peak in a magnified scale. The bending/stretching mode at 160 meV does not alter both of its position and width with the stress.

The value of stress 16 bar employed here induces a compressive strain along the c axis. Using the value of the elastic stiffness constant c_{33}= 5.68 x 10^{10} Nm^{-2}, we can estimate the amount of the deformation of the unit cell along the c axis, 1.9 x 10^{-4} A. This is nearly one tenth of the value of the discontinuous jump of the lattice constant c at Tc due to the occurrence of the spontaneous polarization. Thus the strain induced by the stress 16 bar is expected to affect the motion of protons even at room temperature. Though the shift of the peak is apparently seen in Figs.2 and 3, the reproducibility of the present result is not sufficient for the qualitative analysis in the further discussion. More precise experiment on the present study are now in progress in KENS.

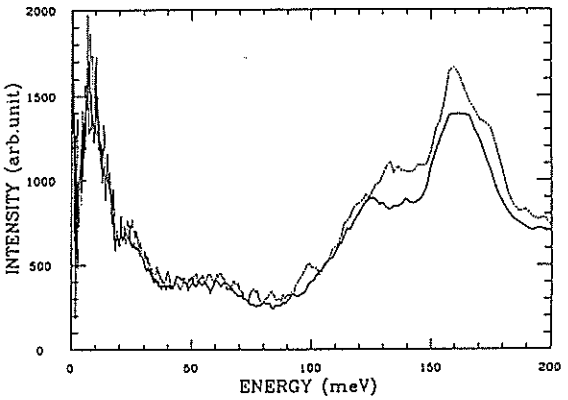

Fig.2 Spectra of the neutron inelastic scattering of KDP observed by LAM-D in the A scan at atmospheric pressure (solid lines) and at 16 bar (dashed lines).

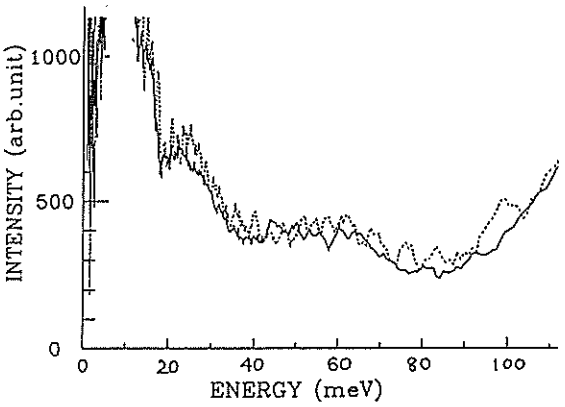

Fig.3 The low frequency part of the same spectra as shown in Fig.2. The horizontal scale is expanded twice the scale of Fig.2. Dashed and solid lines correspond to the data at 16 bar and at atmospheric pressure, respectively.

The authors express their sincere thanks to Prof.Kiyanagi of Hokkaido University for his kind guidance in the early stage of the present study.

References

1)I.P.Kaminow and T.C.Damen: Phys.Rev.Lett. 20(1968)1105.

2)T.Yagi, M.Arima and A.Sakai: J.Phys.Soc.Jpn. 59,1430 (1990).

3)R.Blinc:J.Phys.Chem.Solids 13(1960)204.

4)S.Ikeda and K.Shibata: Tech. Report of Res. Reactor Inst., Kyoto Univ., KURRI-TR-311, p.38 (1989) [in Japanese].

Neutron Scattering Study of Pd-H and Pd-D with RAC

Y. NAKAI, E. AKIBA*, H. ASANO and S. IKEDA**

Institute of Materials Science, University of Tsukuba, Tsukuba 305
*National Chemical Laboratory for Industry, Tsukuba 305
**National Laboratory for High Energy Physics, Tsukuba 305

Pd-H and Pd-D are well-known as having the inverse isotope effect in superconductivity. The superconducting critical temperature T_C of Pd-D (T_C=10K) is higher than that of Pd-H (T_C=8K), contrary to the expectation from the simple BCS theory. Several mechanisms have been proposed to explain this inverse isotope effect. There are two major theories; one is based on anharmonicity of the Pd-H potential and the other on electronic effect resulting from the large zero-point motion of hydrogen. They both affect the electron-phonon coupling parameter λ in McMillan's formula given by

$$T_c=\frac{\theta_D}{1.45}\exp\frac{-1.04(1+\lambda)}{\lambda-\mu^*(1+0.62\lambda)} \quad ,$$

where θ_D is the Debye temperature and μ^* the Coulomb pseudo-potential. In order to explain the mechanism or give some information to the above theories, we measured energy spectrum and momentum distribution of H and D in these materials. As reported in "Present Status of eV Neutron Scattering Spectrometer (RAC)" in this Proc., one can observe the ground state's wave function by the neutron compton scattering (NCS). This technique may be a powerful tool especially for the present case.

Figures 1 and 2 show the energy spectra of Pd-H and Pd-D at 50K (measured by CAT). It is found that the 1st excitation energies for Pd-H and Pd-D are 56meV and 36meV, respectively, and that the isotope shift (ω_H/ω_D) is 1.55. The present results are consistent with the previous ones[1].

We can estimate the mean value of the momentum distribution <p> from the results of CAT, assuming that the hydrogen atom is bound in the harmonic potential well. $\langle p\rangle_H$ and $\langle p\rangle_D$ are estimated to be 3.67Å^{-1} and 2.95Å^{-1}, respectively.

The NCS experiments on Pd-H and Pd-D were performed with the scattering angle 30° and E_f=4.28eV (Ta-foil). Figures 3 shows the momentum distribution of H in Pd-H. Squares and crosses represent the measured values, the dotted line the calculated momentum distribution with <p>=3.80Å^{-1}. The solid line represents the calculated one including Q-resolution of the spectrometer. From this NCS measuremet, <p> of H in Pd-H was determined to be 3.80Å^{-1}. This is consistent with the result obtained by CAT ($\langle p\rangle_H$= 3.67Å^{-1}). Figure 4 shows the momentum distribution of D in Pd-D. Squares and crosses are measured values and the solid line represents the calculated ones with <p>=4.39Å^{-1} including the spectrometer resolution. From this comparison, <p> of D in Pd-D was determined to be <p>=4.39Å^{-1}. It is about 1.5 times larger than estimated value from CAT result ($\langle p\rangle_D$=2.95Å^{-1}). This means that the potential in Pd-D is very anharmonic and D is localized in very narrow position.

References

1) A. Rahman et al., Phys. Rev. B14, 3630 (1976)

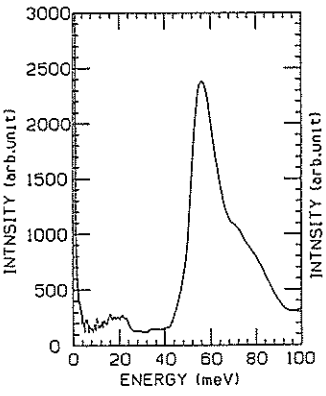

Fig.1 Energy spectra of Pd-H

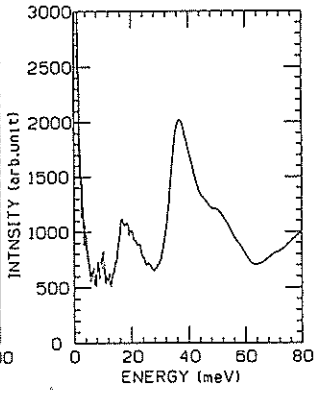

Fig.2 Energy spectra of Pd-D

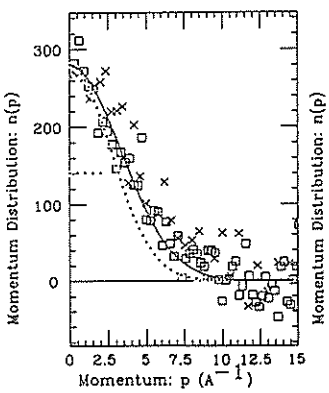

Fig.3 Momentum distribution of Pd-H

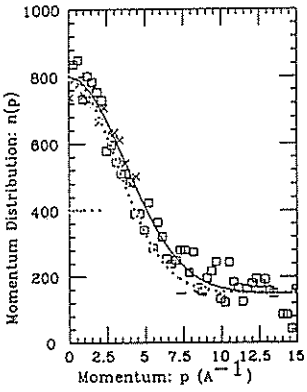

Fig.4 Momentum distribution of Pd-D

Low-Energy Excitation in Copper Ion Conductors

T.SAKUMA, K.SHIBATA* and S.HOSHINO**

Department of Physics, Faculty of Science, Ibaraki Univ. , Mito 310
*Institute for Materials Research, Tohoku Univ., Sendai 980
**Institute of Applied Physics, Univ. of Tsukuba, Tsukuba 305

Inelastic neutron scattering measurements were performed at room temperature with LAM-40. Powdered samples of $Cu_{1.8}S$, $Cu_{1.8}Se$, CuI and Cu_2Se were contained in an aluminum cylindrical tube of 13 mm diameter and 80 mm length with a thin wall. The Q range covered by this spectrometer is 0.2~2.6 $Å^{-1}$. Data collection time for each specimen was about 5 h.

A low-lying, dispersionless excitation near 3.0 - 4.5 meV was observed in inelastic scattering spectra of powder samples over the measured range of Q.

The generalized density of states was derived from the observed data and was displayed in figure 2. The density of states at the lower-energy side is approximated by those due to the low-lying local vibrational mode. The density of states at the higher-energy side is approximated by the phonon modes mainly due to the acoustic branch.

The low-energy dispersionless excitation in Cu_2Se, $Cu_{1.8}Se$ and $Cu_{1.8}S$ was about 3.4 meV. This excitation seems to be common to copper ion conductors.

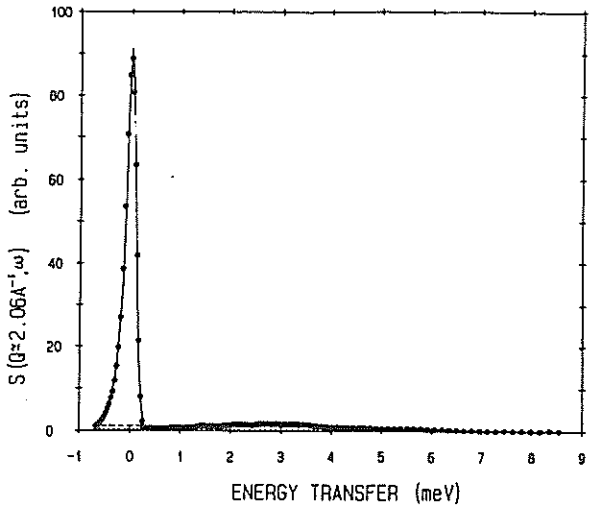

Fig. 1 The dynamic scattering function of β-Cu_2Se at room temperature.

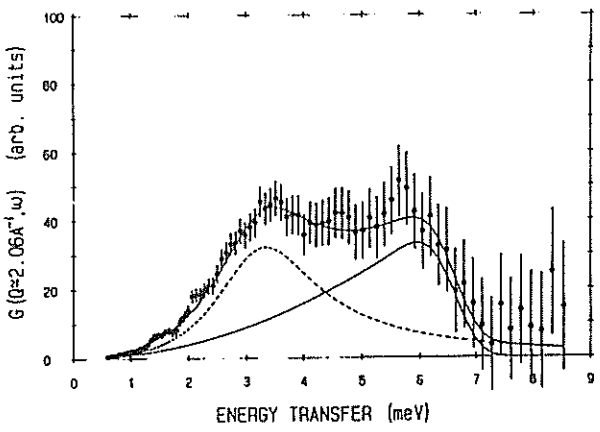

Fig. 2 The generalized density of states of β-Cu_2Se at room temperature.

The value of the low excitation energy increases as the atomic number of the cation decreases. The excitation energy is proportional to the square root of 1/M, where M is the atomic weight of the cation. Using this relation, the values of the excitation energy of Ag and Na are calculated as 2.6 and 5.7 meV,respectively. These values agree with measurement values[1-3]. The result that the excitation energy depends not on the Lattice type but on the mass of the cation suggests that the local potential is similar for each group.

The results have been published in J.Phys.Soc.Jpn 58(1989)3061 and Solid State Ionics 40/41(1990).

References

1) K.Shibata and S.Hoshino, J. Phys. Soc. Jpn. 54(1985)3671.
2) S.Hoshino, S.M.Shapiro and K.Shibata, J. Phys. Soc. Jpn. 55(1986)429.
3) Edited by M. B. Salamon: *Physics of Superionic Conductors* (Springer-Verlag, 1979).

Dynamics of Liquid Water in Porous Silica in the Undercooled State

T. Yamaguchi, Y. Kato, H. Wakita, and K. Inoue†

Department of Chemistry, Fukuoka University, Nanakuma, Jonan-ku, Fukuoka 814-01
†Department of Nuclear Engineering, Hokkaido University, Sapporo 060

The dynamic properties of liquid water at interfaces have been the subject of considerable interest among various application fields like separation columns, catalytic reactions in zeolites, etc. Moreover, liquid water in micropores is undercooled and thus liquid water in the pores may be a model of the non-freezing water in biological cells.

In the present study, we measure incoherent quasi-elastic neutron scattering from liquid water in porous silica of two different pore sizes (30 and 100 Å) at various subzero temperatures. Our aim is to study the behaviour of the translational and rotational motions of water molecules in porous silica in the undercooled state.

Porous silica, Develosil 30 and 100, was purchased from Nomura Chemicals. Develosil 30 and 100 have an inner diameter of 30 and 100 Å, respectively. Silica pores were filled up to about 80% of the volume with light water by a evaporation method. The silica samples were kept in a double wall aluminum container with a sample thickness of 1 mm. Neutron scattering measurements were carried out by using LAM40 spectrometer at 2, -15, -30, and -60°C for Develosil 30 and at 2, -15, -25°C for Develosil 100. Dry silica samples were also measured.

Figures 1 and 2 show spectra obtained at various temperatures for water in Develosil 30 and 100, respectively. From a comparison of two spectra for the different sizes of pores measured at the same temperature the peak width of the spectra for Develosil 30 is smaller than that for Develosil 100. This indicates the motion of water molecules is more suppressed in smaller pores. Since more water molecules at silica interfaces are present for Develosil 30,

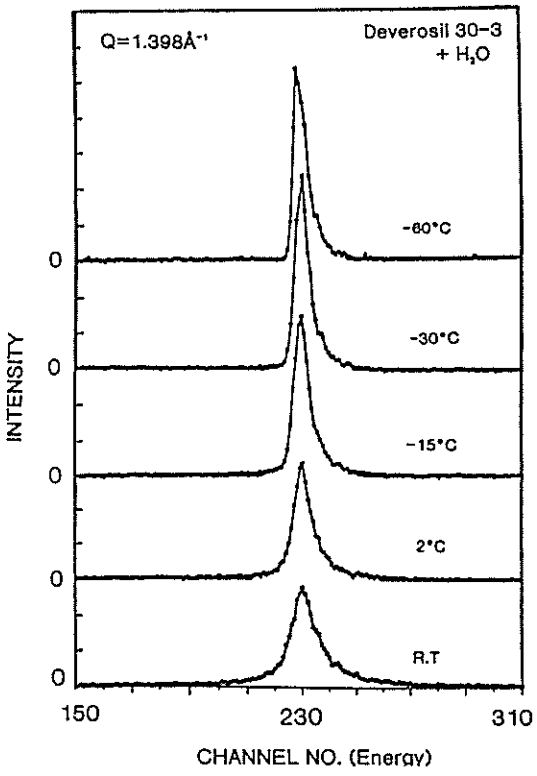

Fig. 1 The LAM40 spectra obtained for light water in Develosil 30 at the momentum transfer Q = 1.398 $Å^{-1}$ for various temperatures.

this fact reflects the hindered motion of water molecules near the surface of silica.

For both silica samples the peak width of the spectra decreases with decreasing temperature, indicating slowing down of the motions of water molecules in the pores. In the case of Develosil 30 the peak does not change further at temperatures below -30°C; this indicates water molecules in the pores are frozen below this temperature. A value of -30°C is consistent with the temperature where the T_1 and T_2 values of ^{1}H-NMR spectra for water in Develosil 30 show an inflection point.[1)]

We are now analyzing the spectra in detail to obtain information on the translational and rotational motions of water molecules in the pores.

References

1) T. Yamaguchi, R. Shirouse, H. Wakita, and S. Masuda, unpublished data.

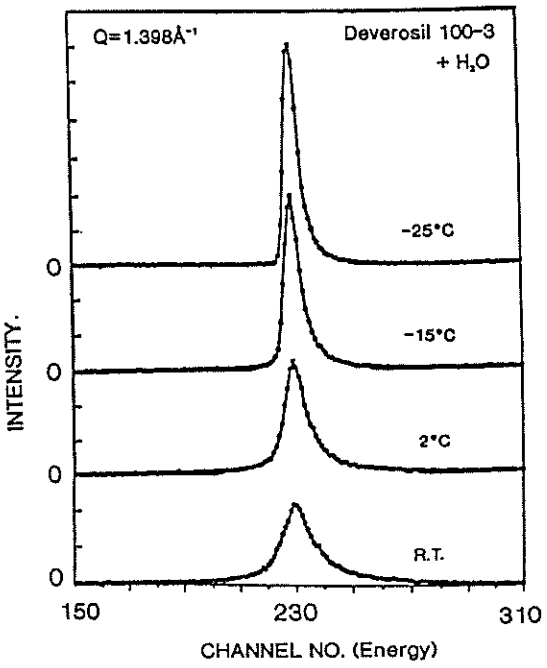

Fig. 2 The LAM40 spectra obtained for light water in Develosil 100 at the momentum transfer Q = 1.398 $Å^{-1}$ for various temperatures.

Molecular Motion of Water Molecules in Hydrate Melts

Y.NAKAMURA, Y.IZUMI AND K.INOUE[+]

Faculty of Science, and Faculty of Engineering[+], Hokkaido University, Kita 8 Nishi 10, Kita-ku, Sapporo 060, Japan.

The motion of H_2O molecules in hydrate melts of highly concentrated electrolyte solutions are strongly impeded by dissolved ions. Neutron scattering experiments may provide useful information on the diffusional dynamics of H_2O molecules in such solutions. In the present study we chose concentrated aqueous $ZnCl_2$ solutions as hydrate melts. The mole ratio of H_2O to $ZnCl_2$(R) is 1.8 in the most concentrated solution at room temperature.

In previous reports[1,2], we have presented the results of quasi-elastic neutron scattering from concentrated aqueous zinc chloride ($ZnCl_2$) solutions. We have first studied the concentration dependence of the motion of water molecules in solutions, using the LAM 40 and 80 spectrometers. Here we report the results of the temperature dependence of the quasi-elastic neutron scattering spectra for the $ZnCl_2$-H_2O system, obtained by the LAM 40 spectrometer.

Sample solutions were contained in a vessel of tantalum, which consists of inner and outer tubes sealed with caps of teflon. The thickness of the tube walls was 0.25 mm. Sample solutions were introduced into the annular region between the two tubes. The sample thickness was 0.15 mm.

Fig.1 shows the observed spectra for the solution with R=4 at three different temperatures, i.e., 313, 293 and 273 K for three scattering angles. The half-width of the spectra change considerably with relatively small temperature change. More quantitative analysis for the motion of water molecules will be made after appropriate corrections for the observed spectra and the results will be compared with NMR results[3] and others[4,5].

References

1) Y.Nakamura, Y.Izumi and K.Inoue, KENS REPORT VI, 252 (1986).
2) Y.Nakamura, Y.Izumi and K.Inoue, KENS REPORT VII, 100 (1988).
3) Y.Nakamura et al. J. Chem. Phys. 77, 3258 (1982).
4) M.P.Fontana et al. Physica 136B, 179 (1986).
5) P.S.Salmon et al. J. Phys.: Condens. Matter 2, 4297 (1990).

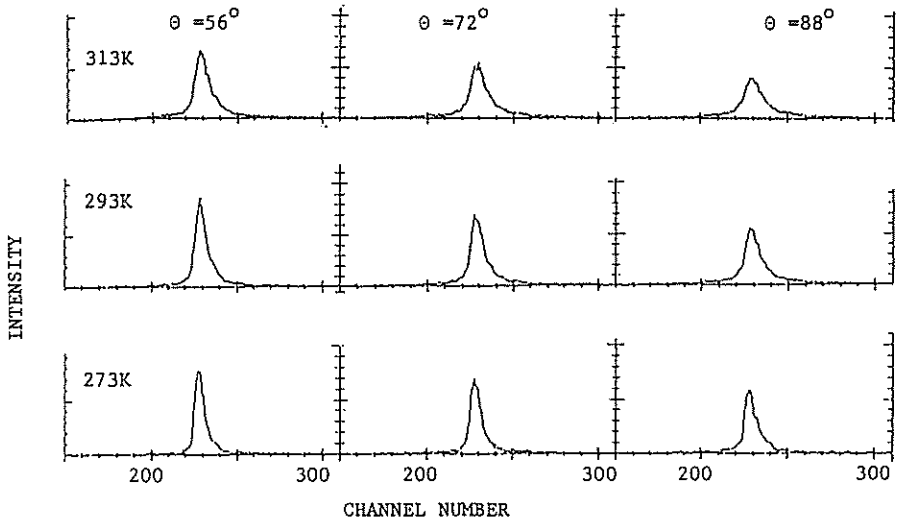

Fig. 1 Experimental results with the LAM 40 spectrometer for the $ZnCl_2$-H_2O system (R=4).

Preliminary Study on Inelastic Scattering by HRP

T. KAMIYAMA, M. OSAWA, T. ISHIGAKI, H. ASANO and K. SHIBATA*

Institute of Materials Science, University of Tsukuba, Tsukuba 305
*Research Institute for Materials Science, Tohoku University, Sendai 980

HRP has been contributing to the crystal structure determination of various types of high-Tc superconductors and has gained a status as one of the major powder diffractometers in the world. The advantages of HRP, the high resolution and the fairly low background, also enable us to study on the subjects of high-resolution single-crystal diffraction, phonon or magnon excitations, internal stress in bulk materials, etc.

Here we report on the preliminary result of neutron inelastic scattering from PG and derive the sound velocity for the out-of-plane mode. The method is known as the diffraction method[1-3], in which the energy dispersion relations can be derived from the momentum distribution of the scattered neutrons alone, without the energy analysis. Because of experimental limitations, the diffraction method was never fully developed. However, Willis et al.[4] combined this method with high-resolution pulsed neutron diffraction, and this combination enabled the the method to be developed further.

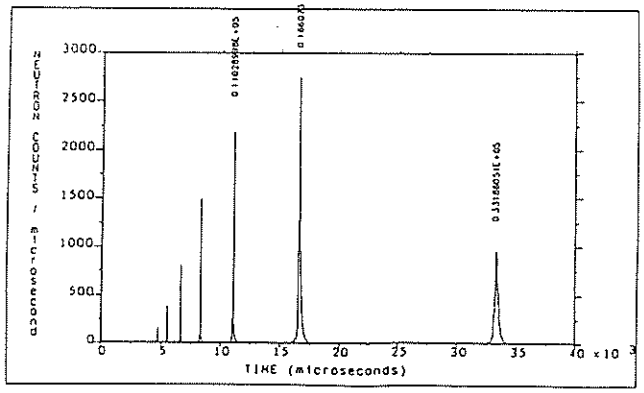

Fig. 1 Bragg peaks from the (00l) planes of PG in the first experiment (see text). The scattering angle is 170 °.

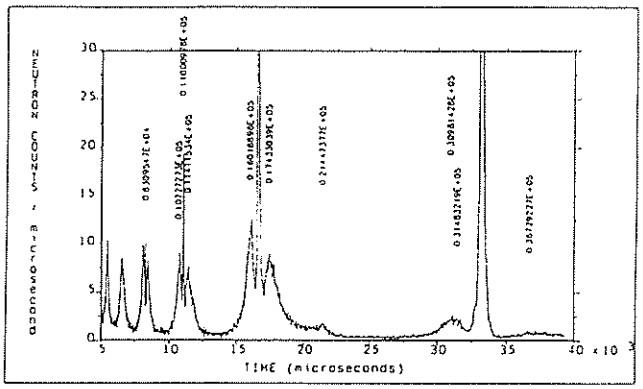

Fig.2 Thermal diffuse scattering intensity observed in the first experiment (see text). The scattering angle is 166.4 °.

The present experimental setup is as follows. The detectors cover a range of scattering angles from 160° to 172° in increment of 1.8°. Each detector has vertical divergence of 11.5°. The [001] axis of the PG crystal is set at 5° to the incoming neutron beam in the first experiment, 7° in the second and 11° in the third. Figure 1 shows the Bragg reflections in the first experiment at a 170° detector, which almost satisfies the Bragg condition The other detectors measure the thermal diffuse scattering at -1.8°,1.8°, 3.6°, 5.4° and 7.2° from the Bragg condition. An example of diffuse scattering is shown in Fig.2. A multiplot of data near (002) is shown in Fig.3. Figure 4 shows the multiplot of diffuse scattering observed in the second experiment. In these figures, thermal diffuse scattering intensity rises to a maximum on each side of the Bragg position: one peak corresponds to neutron energy gain(e=-1) and the other to neutron energy loss (e=+1). This position can be used to determine the sound velocity. Figure 5 shows the phase velocity of out-of-plane modes as a function of the angle between [001] and the phonon propagation direction. The sound velocity along [001] determined by neutron inelastic scattering[4] and ultrasound measurements[5] is also indicated. The data collection time is only 1.5 hours and the analysis is preliminary. Nevertheless,

the agreement is satisfactory. More detailed analysis is in progress to clarify the possibility and limitation of this method.

We wish to thank Dr. C. Carlile for giving us the information of the diffraction method.

References

1) R.J.Elliott and R.D.Lowde, Proc. Roy. Soc. London, Ser. A,**230**(1955)46.
2) E.J.Samuelson, Phys.Lett.A,**26**(1968)160.
3) D.Hohlwein, Proc. IAEA Symp. Neutron Inelastic Scattering (Vienna, 1977)p.197.
4) B.T.M.Willis, C.J.Carlile, R.C.Ward, W.I.F.David and M.W.Johnson, Europhys. Lett. 2(1986)767.
5) R.Nicklow, N.Wakabayashi and H.G.Smith, Phys.Rev.B, 5(1972)4951.

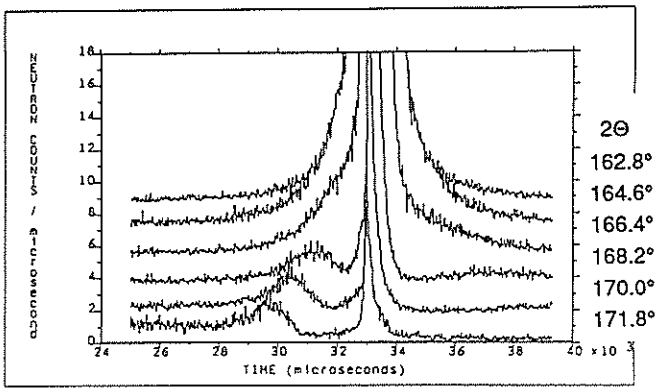

Fig.3 Typical diffuse scattering pattern around the (002) reflection as a function of time-of-flight and scattering angle.

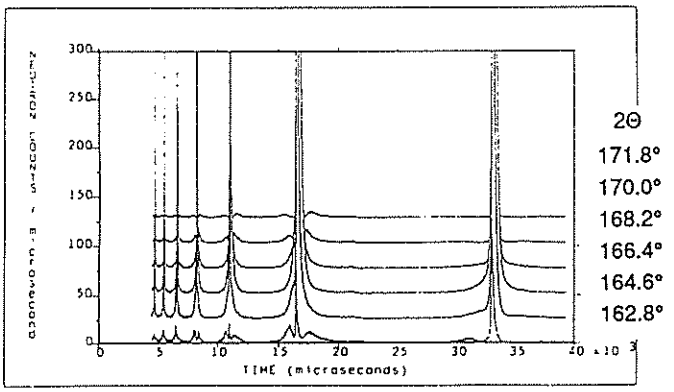

Fig.4 Multiplot of diffuse scattering observed in the second experiment.

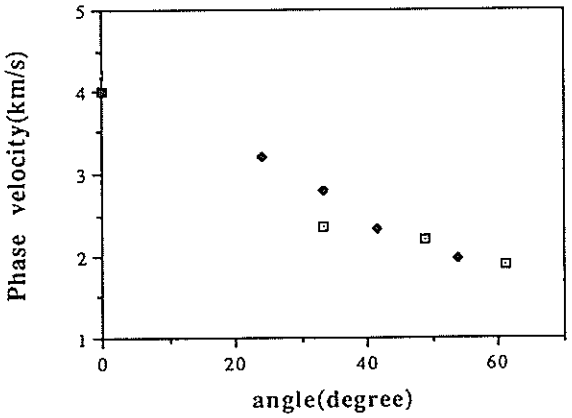

Fig.5 The phase velocity of the out-of-plane modes in PG as a function of the angle between [001] and the propagation direction. ⊡: present study, ◆ : Willis et al., ■ : ultrasound measurements.

1-5. Non-Equilibrium Systems

Phase separation in Al-Li alloys during 373 K ageing studied by small angle neutron scattering

Shin-itiro Fujikawa * and Michihiro Furusaka**

* Department of Materials Science, Tohoku University, Aoba-ku, Sendai 980, Japan
** National Laboratory for High Energy Physics, Tsukuba-shi, Ibaraki 305, Japan

Phase decomposition of Al-Li alloys has now attracted many workers because of the occurrence of the phase separation with ordering in these alloys. Al-Li alloys decompose at lower temperature by the formation of the metastable δ' phase. This phase has an ordered structure of the Cu_3Au-type (Al_3Li). We have already published the results of the phase separation process at 423 K ageing in Al-Li alloys.[1)-4)] Recently, Khachaturyan et al.[5)] have made a theoretical study of the precipitation of δ' phase in Al-Li alloys and concluded that the uniformly ordered solid solution then decomposes on ageing by a spinodal mechanism into ordered regions that differ in Li content, and the low Li regions then disorder on reaching the limit of stability for the ordered phase so that the final mixture is α+δ'. According to their computed subregions with the metastable α+δ' field, the spinodal decomposition of the ordered solid solution possibly occurs for 373 K ageing in Al-Li alloys with Li content more than about 10 at.%. Therefore, it is very interesting to study the phase separation process during 373 K ageing in such an alloy using a small angle neutron scattering SANS.

In the present work, the change of sturucture during 373 K ageing in Al-9.50 and 11.4 at.% Li alloys was investigated using the SAN with respect to the time evolution of representative stuructural parameters. The structural and kinetic features were simply discussed.

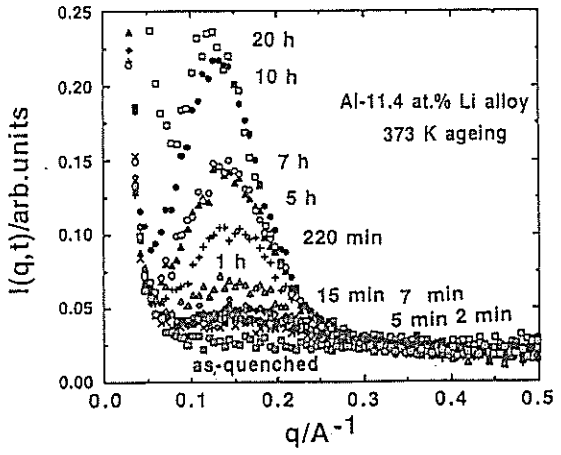

Fig.1 Time evolution of scattering intensity I(q,t) at early stage in Al-11.4 at.% Li alloy aged at 373 K.

The cast ingots of high purity Al-Li alloys containing 9.50 and 11.4 at.% Li were cold-rolled into 2 mm in the thickness. These were cut into small specimens with the size of 2 mm x 10 mm x 30 mm for the SANS experiment.
Solution treatmentss were carried out at 773 K for Al-9.50 at.% Li alloy and 823 K for Al-11.4 at.% Li alloy. The specimens were water-quenched and aged in an oil bath at 373 K in the range of ageing time between 2 minutes and 811 hours. The SANS measurement was carried out using the SAN of KEK. The sample-to-detector distance was selected to be 1 m to cover the q range of $0.02<q<0.6$ A^{-1}. The scattering data were corrected for background and trasmission, and normalized by scattering from water.

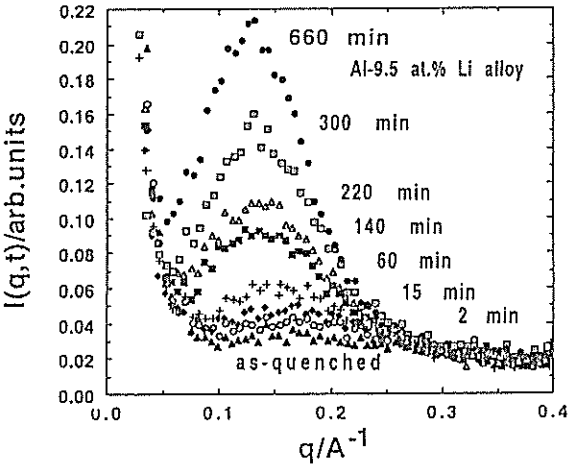

Fig.2 Time evolution fo scattering intensity I(q,t) at early stage in Al-9.50 at.% Li alloy aged at 373 K.

All scattering measurements were carried out at room temperature.

Fig. 1 and Fig. 2 show the time evolution of the scattering intensity in Al-11.4 and 9.50 at.% Li alloys aged for short time at 373 K, respectively. The scattering is characterized by the presence of an inteference peak. Here, the strong scattering at smaller q (<0.04 A-1) than the peak position is attributed to a small amount of large precipitates on grain boundaries. A broad but week peak is also observed in the as-quenched specimens of both alloys. The peak position q_{max} is nearly constant during ageing for short time. Fig. 3 shows the typical results of the time evolution of scattering intensity for longer time, indicating that the

q_{max} shiftes towards lower values of q as time elapsesand the peak intensityI_{max} is about one orders of magnitude larger than the earlier one. Fig.4 and Fig.5 show the time evolution of q_{max} and I_{max} in Al-11.4 and 9.50 at.% Li alloys, respectively, indicating that two regions are observed. Here, we define these regions as the early stage and the late stage,respectively. At the early stage, q_{max} does not change in Al-11.4 at.% Li alloy and the time dependence of q_{max} in Al-

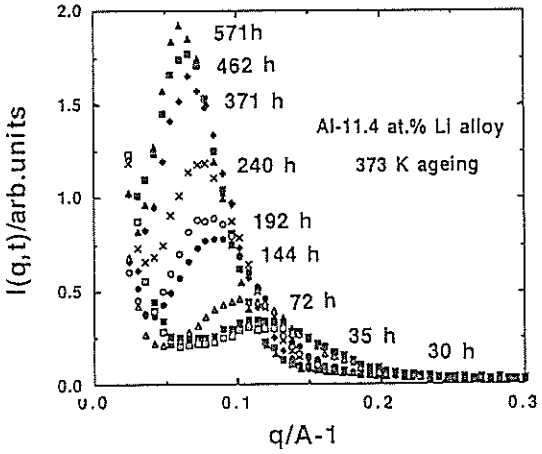

Fig.3 Time evolution of scattering intensity I(q,t) at late stage in Al-11.4 at.% Li alloy aged at 373 K.

9.50 at.% Li alloy is negligibly small. According to the so-called Porod's law, if the sharp interface is established between the precipitates and matrix, for the larger value of q than the q range where Guinier approximation holds., the product $q^4 \cdot I(q,t)$ approaches constant. As shown in Fig. 6, Porod's law is not satisfied at the early stage and the

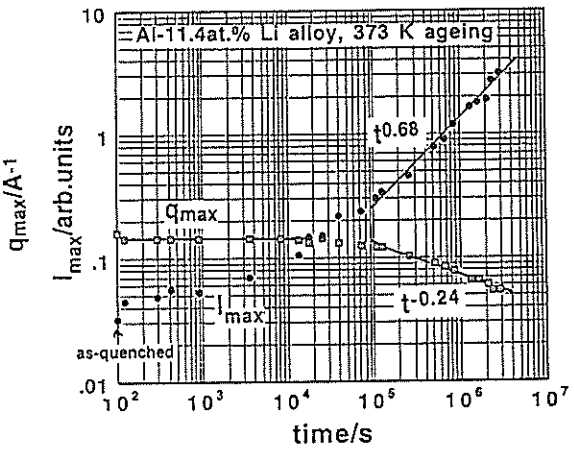

Fig.4 Time dependence of peak intensity I_{max} and peak position q_{max} of scattering intensity in Al-11.4 at.% Li alloy.

late stage in Al-11.4 at.% Li alloy. The result indicates that the interface between δ'phases and matrix is diffuse during ageing at 373 K. The result is one of evidences for the spinodal decomposition for the phase separation during 373 K ageing in

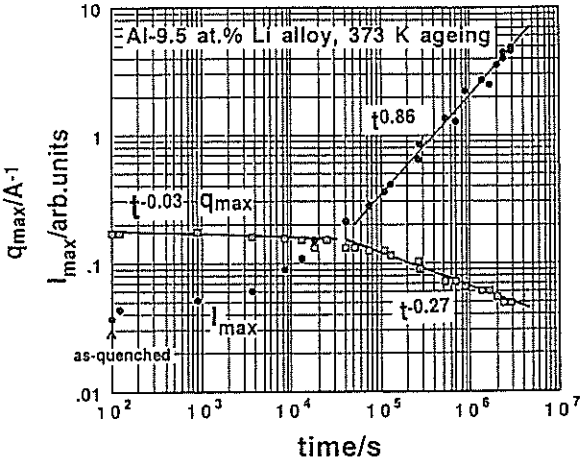

Fig.5 Time dependence of peak intensity I_{max} and peak position q_{max} of scattering intensity in Al-9.50at.% Li alloy.

Al-11.4 at.% Li alloy. We have obtained the other evidence of the spinodal decomposition from the detailed analysis using the Cahn-Hilliard-Cook theory. After ageing for longer time than about 5×10^4 s, the following power laws hold: $q_{max} \propto t^{-0.24}$ and $I_{max} \propto t^{0.68}$ in Al-11.4 at.% Li alloy and $q_{max} \propto t^{-0.27}$ and $I_{max} \propto t^{0.86}$ in Al-9.50 at.% Li alloy.

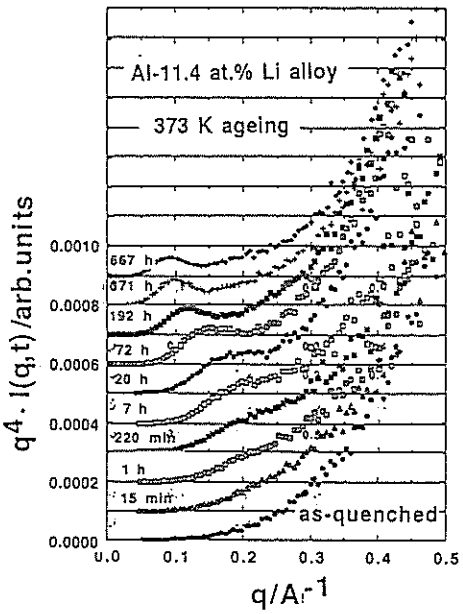

Fig.6 Porod plot in Al-11.4 at.% Li alloy aged at 373 K.

But these power laws are different from those for 423 K ageing[1)-4)] and can not well explained by the usual coarsening theory. Fig. 7 shows the Log-Log plot of the time evolution of the Guinier radius R_G in Al-11.4 at.% Li alloy determined from the Guinier plot. It is interesting that the the dependence is divided into two portions and at the late stage,the so-called $t^{1/3}$ power law does not hold, in agreemet with the results shown in Fig. 4 and Fig. 5. The power law coefficient 0.25 is found in general in percolated coarsening patterns. Fig. 8 shows the typical Log-Log plots of the q dependence of scattering intensity at the early stage and the late stage in Al-11.4 at.% Li alloys. The straight line is drawn to the intermediate q range between the peak position and the tail part. The most significant features of the resuts are as follows; the scattering intensity,I(q) in the intermediate q range is not proportional to q^{-2} nor q^{-4}, but it obeys $q^{-a(t)}$ where a(t) is not necessarily integer. The value of a(t) varies from 0.7 to 6.

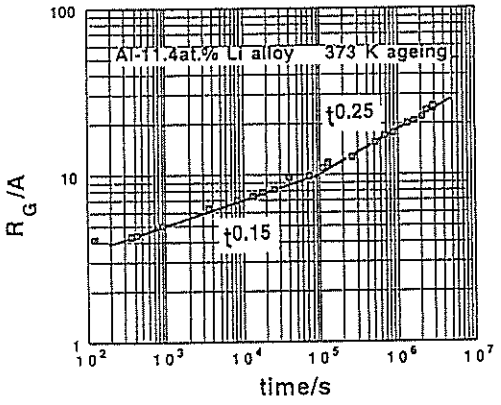

Fig.7 Logarithmic time evolution of Guinier radius in Al-11.4 at.% Li alloy aged at 373 K.

The time variations of a(t) is shown in Fig. 9. The similar change has been already reported in the early stage of Al-Li alloys aged at 423 K.[1)-4)]. Then, it takes only less than 60 minutes to attain to a(t)=6, but at 373 K it takes very longer time than one month to attain to a(t) = 6. The peculiar variation of a(t) observed in Al-Li alloys has not been observed in other alloys.
In conclusion, at the early stage of phase separation at 373 K the spinodal decomposition possibly occurs in Al-9.50 and 11.4 at. % Li alloys. On the other hand, the results of various power laws at the late stage can not be explained using the usual Ostwald ripening theory.

The authors acknowledge the financial support from Grant-in Aid for General Reserch C (No. 62550458) from Ministry of Education. Science and Culture and Light Metal Foundation Inc..

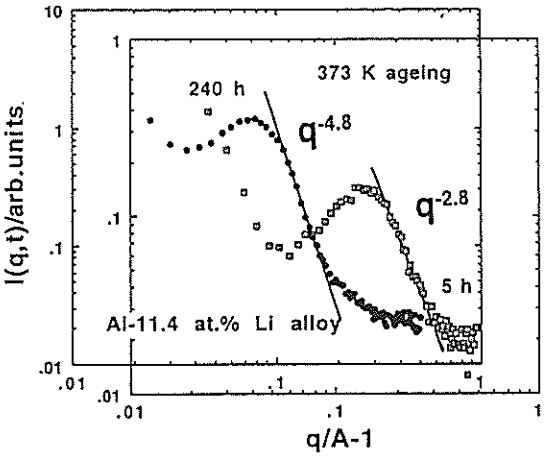

Fig.8 Logarithmic plot of time evolution of scattering intensity I(q,t) at early and late stages in Al-11.4 at.% Li alloy aged at 373 K.

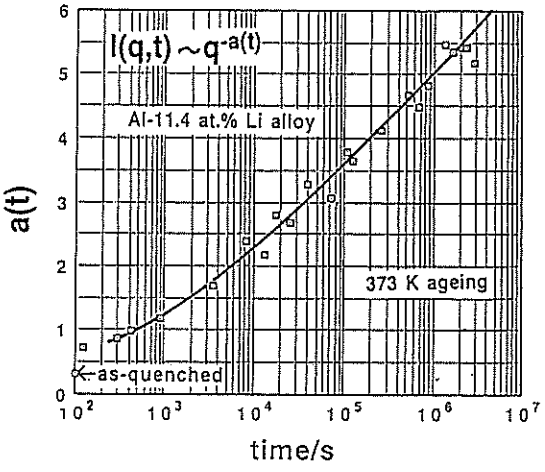

Fig.9 Time dependence of power law coefficient in equation $I(q,t)\ q^{-a(t)}$ in intermediate q range between peak position and tail part in Al-11.4 at.% Li alloy aged at 373 K.

References

1) S. I. Fujikawa and M. Furusaka et at., J. de Physique, C3, 48 (1987),365.
2) M. Furusaka and S. I. Fujikawa et al., Dynamics of Ordering Process in Condensed Matter, Plenum Press, New York, 1988, p. 281.
3) S. I. Fujikawa, M. Sakauchi and M. Furusaka, KENS REPORT-VII, 1987/88, p.101.
4) S. I. Fujikawa, Special Report, No.21 on Al-Li alloys, Japan Inst Light Metals, 1989, p.22 and 32.
5) A. G. Khachaturyan, T. F. Lindsey and J. W. Morrii,Jr.,Met. Trans. A. 19A(1988), 249.

Precipitation Process in Fe-Cu Binary Alloys

H.Okuda, K.Osamura, M.Takashima, and M.Furusaka*
Department of Metallurgy, Faculty of Engineering, Kyoto Univ. Kyoto 606.
*National Laboratory for High Energy Physics, Tsukuba 305.

Phase decomposition in Fe-Cu binary alloys has been investigated by small angle neutron scattering at SAN. Phase decomposition in Fe-Cu alloys has two aspects of interest, i.e., a fundamental interst as an alloy system where precipitates change their crystal structure during aging, and a practical interest that the alloy can be used as a low temperature age-harden -able materials. The sample was solution treated at 1173K for 10.8ks, and aged at 773K. SANS measurements were performed under the magnetic field of about 1 T.

Change of Guinier radius and the integrated intensity of Fe-1.2at%Cu is shown in Fig.1. It is seen that the integrated intensity increased rapidly till about 5×10^3s in the first stage, and then gradually saturated. Little change in Guinier radius is observed in the first stage, and it increased with the power of 1/3 in the later stage. The later stage corresponds to the coarsening period. The radii obtained from the nuclear scattering agreed with those obtained from the magnetic scattering in this period.

Figure 2 shows the two dimensional contour of scattering intensity obtained for the sample aged for 360ks. The scattering intensity along q_x axis is due to the nuclear scattering, whereas the intensity along q_y axis contains both nuclear and magnetic scattering. The ratio of the magnetic scattering to the nuclear scattering, A, is indep -endent of the scattering vector, q, and sensitive to the number density of atoms in the precipitates.

Figure 3 shows the change of A as a function of time. The ratio increased in the early stage, and then saturated at $t=10^4$s. It suggests the change in the number density inside the Cu precipitates, i.e., transition from coherent bcc structure to semicoherent fcc structure. There still exisits someproblems on the structure and kinetics in the early stage. Further investigation is now under way.

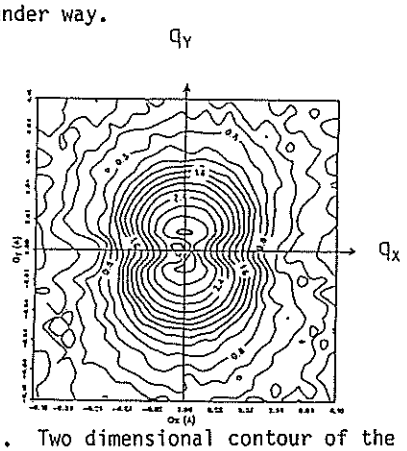

Fig. 2. Two dimensional contour of the scatter -ing intensity for Fe-1.2Cu alloy.

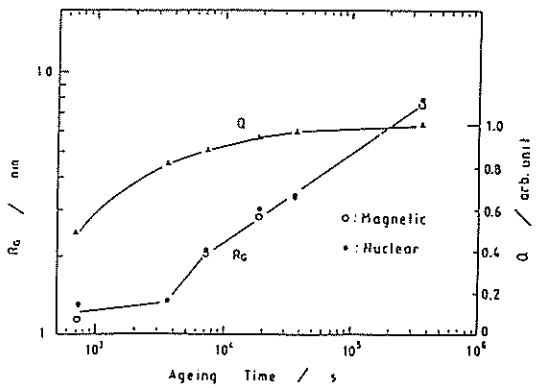

Fig.1. Change of Guinier radius and the integrated intensity

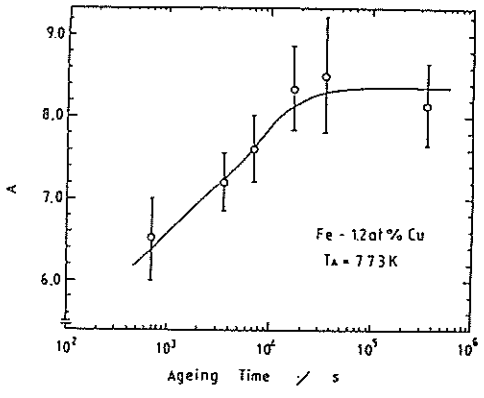

Fig. 3. Change of the ratio A as a function of time

Domain Growth under Shear Flow

TAKAO OHTA, HANAE NOZAKI and MASAO DOI*

Department of Physics, Ochanomizu University, Otsuka, Bunkyo-ku, Tokyo, 112
*Department of Applied Physics, Nagoya University, Nagoya, 464

Computer simulations of domain growth under a simple steady shear flow in a phase separating binary fluid have been performed in two dimensions to investigate domain deformation and the effect to macroscopic quantities such as the shear viscosity and the normal stress effect. The model equation is given in terms of the local concentration difference $C(\mathbf{r},t)$ by

$$\partial_t C(\mathbf{r}, t) + v\nabla C = L\nabla\{(1 - aC^2)\nabla(-D\nabla^2 C + F(C))\} \qquad (1)$$

where $F(C) = -A\tanh C + C$. We have chosen the constants as L=1, D=0.5 and A=1.3 as in the study of spinodal decomposition[1] without the second term in the left hand side of (1). The external flow v is given in two dimensions by $v(\mathbf{r})=(Sy, 0)$ with S the shear rate. We ignore the hydrodynamic interaction in the present simulations.

We have used the cell dynamic version[1] of (1) in simulations. The system size is 111 x 111 with a suitable boundary condition. We have evaluated the anisotropic factor $Q_{xy} = -\langle(\partial_x C)(\partial_y C)\rangle$ which is proportional to the X-Y component of the stress tensor and is related to the effective viscosity as $\Delta\eta = Q_{xy} / S$. We have found that $\Delta\eta$ obeys approximately the scaling law.

$$\Delta\eta = S^{-\omega} f(\gamma) \qquad (2)$$

where $\omega \approx 0.86$ and $\gamma = St$ is the shear strain. This value is slightly larger than our theoretical estimate $\omega = 2/3$ for $a = 0$[2].

The pattern evolution of domains for the volume fraction 0.5 and $S = 1.2 \times 10^{-3}$ with $a = 0$ in (1) is displayed in Fig. 2 where the black (white) regions indicate $C > (<) 0$. Stretching, shear coagulation and recombination of domains can be clearly seen in Fig. 1.

We have made a video movie[3] of the simulations of burst of a single domain and the time-evolution of interconnected domains as in Fig. 1.

The results obtained have been (will be) published in Refs. 2) and 4).

A similar study for block copolymer melts subject to an oscillatory shear flow has now been carried out where the system undergoes, if the flow is absent, a micro-phase separation with regular mesophase structures.

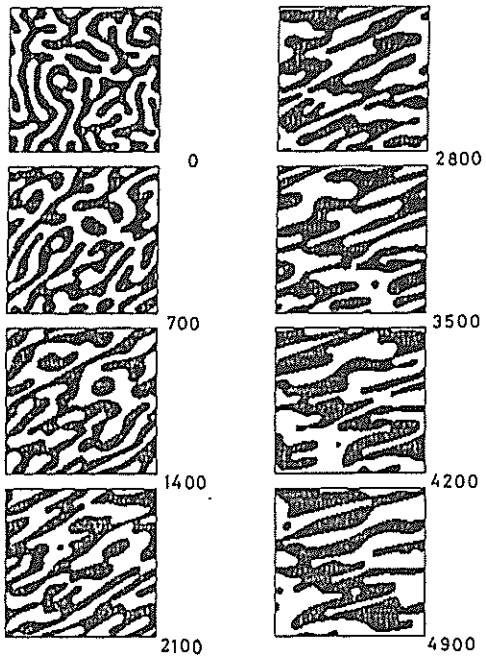

Fig. 1 Time-evolution of interconnected domains. The time is indicated below each figure.

References

1) Y. Oono amd S. Puri, Phys. Rev. A38, 434 (1988).
2) T. Ohta, H. Nozaki and M. Doi, Phys. Letters A145, 304 (1990) and M. Doi and T. Ohta, J. Chem. Phys. (submitted).
3) H. Nozaki, T. Ohta and R. Kobayashi. movie on "Domain Growth under Shear Flow".
4) T. Ohta, H. Nozaki and M. Doi, J. Chem. Phys. (in press).

1-6. Materials Science

Small Angle Neutron Scattering from Isotropic Graphite

K.Aizawa, S.Yamaguchi and N.Niimura*

Institute for Material Research, Tohoku University, Sendai 980
*Laboratory of Nuclear Science, Tohoku University, Sendai 982

Small angle neutron scattering(SANS) measurements from isotropic graphite have been performed on WIT spectrometer. Samples are isotropic graphite of reactor grade T-6P, ETP-10 and T-4MP (Ibiden Corporation) with dimensions of 20mm*20mm*1mm.

Figure 1 shows SANS intensity on arbitrary units. All the data points lie nearly -3 exponent curves in the Porod's region.

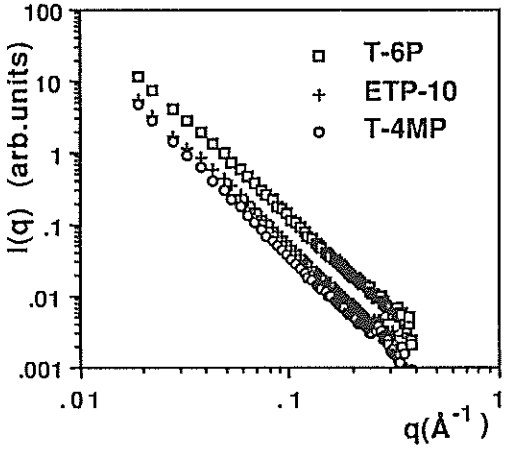

Fig. 1 SANS intensity for T-6P, ETP-10 and T-4MP. The intensity for T-6P is displayed as multipliyed by 2.

In the two-phase systems, systematic positive deviations from the Porod's law can occur when there are density fluctuations within the phases. In the case of isotropic graphite, density fluctuations can exist only in the matrix, and one-dimensional fluctuations have an appreciable value in the direction to the c-axe. Then, in the Porod's region, SANS intensity is given by

$$I(q)=b_0/q^4+b_1/q^2, \qquad (1)$$

where b_0 is a limiting value of $q^4I(q)$ and b_1 is a parameter associated with one dimensional fluctuations. The scattering curve of eq.(1) is proportional to q^{-3} in the Porod's region.[1)]

Structure parameters l_p,'range of inhomogeneity' and l_c,'length of coherence' were estimated from the scattering curve. l_p [2)] is a parameter related to the average size of regions occupied by phase1 and phase2 and given by

$$l_p = \frac{4\pi\int_0^\infty q^2I(q)dq}{\lim_{n\to\infty} 2\pi^3q^4I(q)} = C_1*C_2*4V/S$$
$$= C_2\langle l_1\rangle = C_1\langle l_2\rangle, \qquad (2)$$

where S/V is the area of the interface per unit volume, C_1 and C_2 are volume fraction of the phase1 and phase2, respectively.

$\langle l_1\rangle$ and $\langle l_2\rangle$ are the average lengths of segments of straight lines in the domains of phase1 and phase2, respectively, intercepted by the interface between the domains. A denominator of the 2nd term of eq.(2) is called the limiting value of $q^4I(q)$ and means an intercept of y-ordinate obtained by plots of $q^4I(q)$ versus q^2. For example, Fig.2 shows q^2-$q^4I(q)$ plots of T-6P. A slope of the plot is related to a density fluctuation, Fl_1. A numerator of the 2nd term of eq.(2) is called 'invariant'. For a region of q less than measured minimum value ,we have used the integral of I(q) by extrapolation of q.

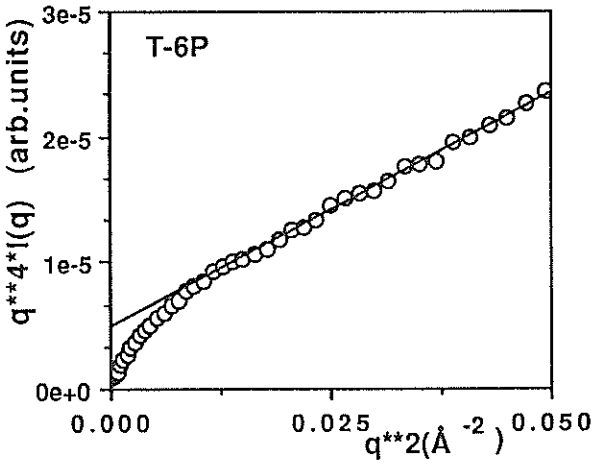

Fig. 2 q2-q4I(q) plot for T-6P.

l_c [2)] is given by

$$l_c = \frac{2\pi\int_0^\infty qI(q)dq}{4\pi\int_0^\infty q^2I(q)dq} = \frac{1}{C_2} * \frac{\langle(\Sigma l_1)^2\rangle-\langle\Sigma l_1\rangle^2}{\langle\Sigma l_1\rangle}$$

$$= \frac{1}{C_1} * \frac{<(\Sigma l_2)^2> - <\Sigma l_2>^2}{<\Sigma l_2>} , \qquad (3)$$

where Σl_1 and Σl_2 are the sums of lengths of all segments along a straight line in phase1 and phase2, respectively and < > denotes average of the space. When the 2nd term of eq.(3) was calculated, a region of q less than measured minimum value was treated as same as above.

Further, if volume fraction of one phase is known, $<l_1>$, $<l_2>$ and Ssp (S/V) can be estimated. We use values of a pore volume fraction (porosity) of ref(3) to obtain these parameters. The numerical results are shown in Table1 and Table2.

Table1. Structure parameters.

Sample	Porosity	lp	lc	<l pore>	<l matrix>
T-6P	0.09	23.59Å	236Å	25.92Å	262.1Å
ETP-10	0.13	27.58	260	31.70	212.1
T-4MP	0.15	52.48	320	617.4	349.9

Table2. Structure parameters.

Sample	Ssp	Fl_1
T-6P	138.87 m^2cm^{-3}	0.00619
ETP-10	142.71	0.00917
T-4MP	97.18	0.00635

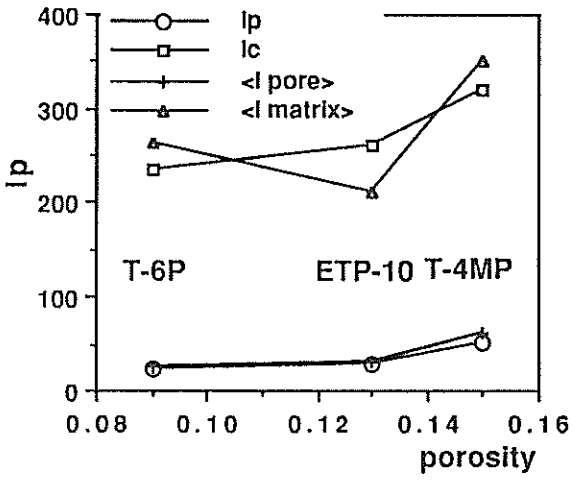

Fig. 3 lp, <l pore>, <l matrix> and lc plotted against porosity.

Figure 3 shows l_p,<l pore>, <l matrix>, l_c plotted against porosity. These values have an inclination to increase when porosity increases. Figure 4 Ssp plotted against porosity. On the contrary, these values have an inclination to decrease when porosity increases. Figure 5 shows Fl_1 plotted against porosity. The variation of Fl_1 might not related to porosity.

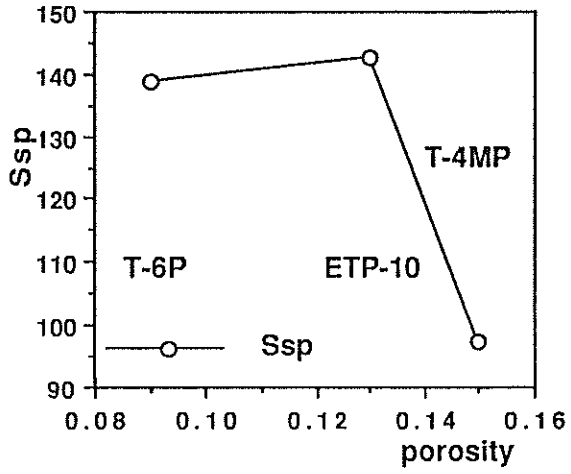

Fig. 4 Ssp plotted against porosity.

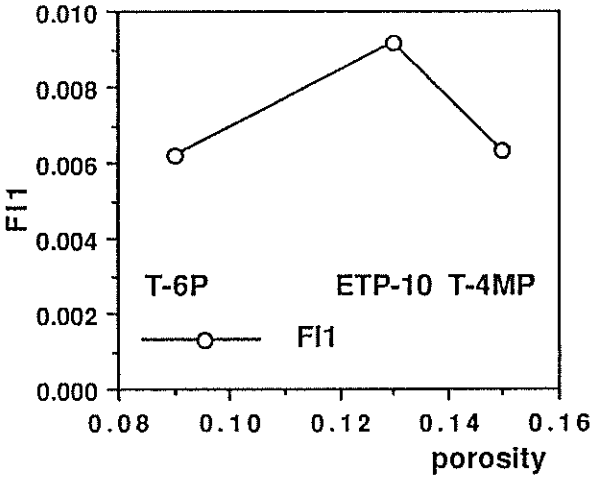

Fig. 5 Fl1 plotted against porosity .

References

(1) W. Ruland, J.Appl.Cryst. 4, 70 (1971)
(2) R. Perret and W. Ruland, J.Appl.Cryst. 1,308 (1968)
(3) T. Yamashina and T.Hino, J.Nucl.Mater. **162-164**, 841-850 (1989)

Small Angle Neutron Scattering from Glass-like Carbon

K.Aizawa, S.Yamaguchi and N.Niimura*

Institute for Material Research, Tohoku University, Sendai 980
*Laboratory of Nuclear Science, Tohoku University, Sendai 982

Carbon materials are considered to be candidates of materials of first walls for magnetic confinement fusion reactors. Therefore, carbon materials are characterized in the nature of defects produced by the irradiation of fast neutrons. Small angle neutron scattering (SANS) measurement can give many informations on defects of these materials.

Before we investigate defects produced by neutron-irradiation and their annealing behaviour of glass-like carbon,the nature of the unirradiated specimen should be well known. First of all, SANS measurements of the unirradiated ones have been performed on WIT spectrometer.

Glass-like carbon is produced by pyrolysis of an organic resin, which consists of graphite crystallites. The density of glass-like carbon is about 1.5g/cm^3 while that of ideal graphite is 2.25g/cm^3, so large amount of micro voids exist in it.

Samples are glassy carbon GC-10,GC-20 and GC-30 , final heat-treatment temperature of which are 1300 ^{0}C, 2000 ^{0}C and 3000 ^{0}C, respectively (Tokai Carbon corporation). The sample dimensions of each specimen are 25mm*25mm*3mm. The measured q-range is between 0.01 and 1.0Å^{-1}.

Figure 1 shows SANS intensity derived from micro voids of glassy carbons on arbitrary intensity units.

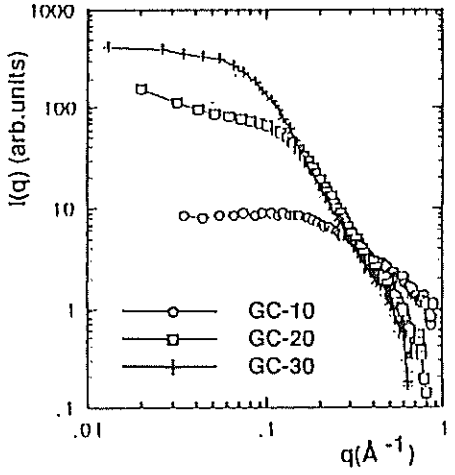

Fig. 1 SANS intensity for GC-10, GC-20 and GC-30.

These Guinier plots are shown in Fig.2.

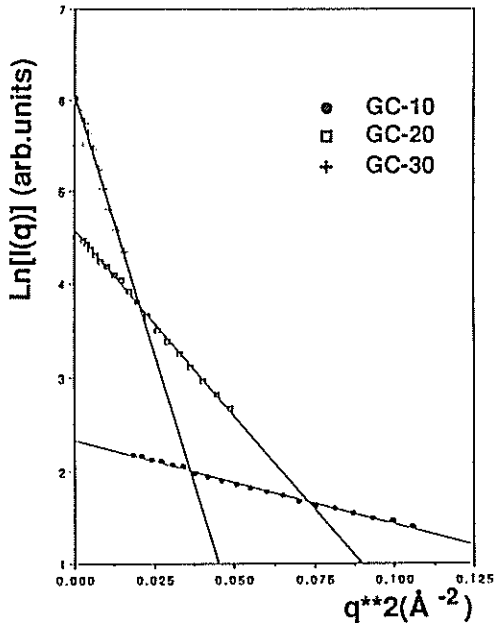

Fig. 2 Guinier plots for GC-10, GC-20 and GC-30.

The radii of gyration of GC-10,GC-20 and GC-30 are obtained to be 5.2Å, 10.9Å and 18.5Å, respectively.

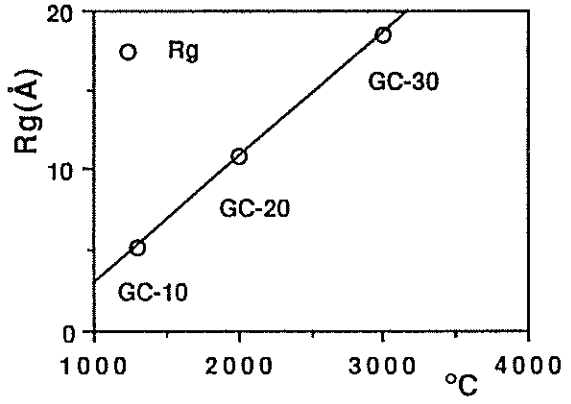

Fig. 3 Rg plotted against final heat-treatment temperature. Line is fitted curve.

Figure 3 shows the radii of gyration plotted against final heat treatment temperature. It is found that the radii of gyration are linearly proportional to the final heat-treatment temperature.

Small Angle Neutron Scattering from Neutron-irradiated Glass-like Carbon

K.Aizawa, S.Yamaguchi and N.Niimura*

Institute for Material Research, Tohoku University, Sendai 980
*Laboratory of Nuclear Science, Tohoku University, Sendai 982

In order to investigate defects produced by neutron-irradiation and their annealing behaviour of glass-like carbon, small angle neutron scattering(SANS) have been performed on WIT spectrometer. In the present work, samples are glassy carbon GC-30(Tokai Carbon corporation).

Their dimensions are 6.2mm*6.0mm*1mm. Irradiation were performed on JMTR to a dose of $1.2*10^{20}$ fast neutron (>1MeV), at temperature between 135 ^{0}C and 140 ^{0}C. SANS measurements of unirradiated sample, as irradiated one and isochronal annealed one have been performed. Isochronal annealing were carried out for one hour at 300 ^{0}C and 600 ^{0}C in vacuum under less than $2.0*10^{-5}$ Torr. Figure 1 shows SANS intensity on arbitrary units. SANS intensity of unirradiated sample decreases when irradiated, that of 300 ^{0}C annealed one increases and that of 600 ^{0}C annealed one slightly increases.

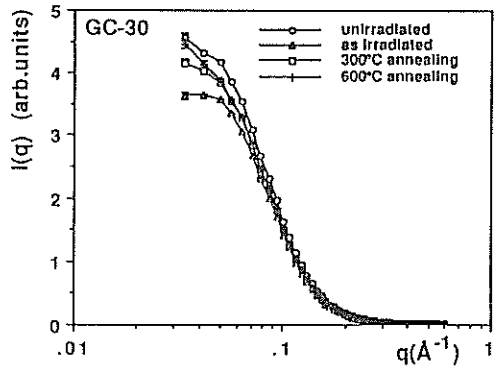

Fig.1 SANS intensity for unirradiated,irradiated,300^{0}C annealing and 600^{0}C annealing of GC-30.

Figure 2 shows ratios of intensity as irradiated sample to unirradiated one and annealed ones to unirradiated one. The ratios are nearly constant between 0.03Å^{-1} and 0.3Å^{-1} in all cases. Guinier plots are shown in Fig.3. The radii of gyration are not changed in all cases as shown in Fig.3. Those above facts might mean that shapes of micro voids in glassy carbon are not changed by neutron-irradiation under our condition and defects produced by the irradiation are not very large.

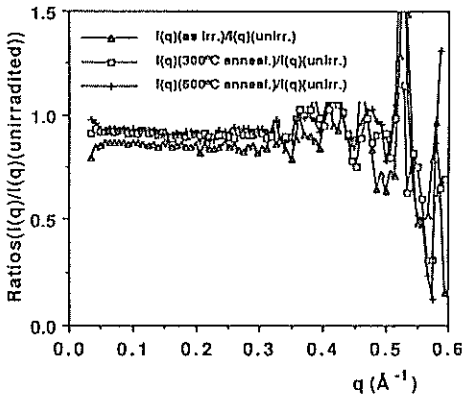

Fig. 2 Ratios of intensity as irradiated GC-30 to unirradiated one, 300^{0}C annealing one to unirradiated one, 600^{0}C annealing one to unirradiated one.

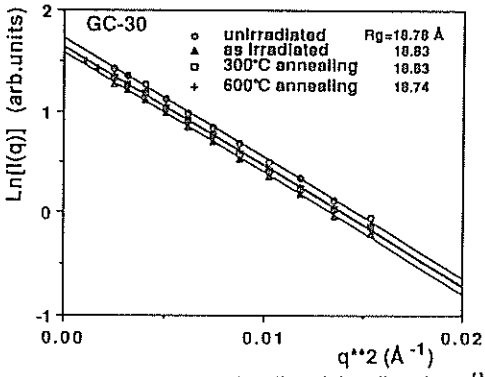

Fig. 3 Guinier plots for unirradiated, irradiated 300^{0}C annealing and 600^{0}C annealing of GC-30.

In the two-phase systems, decrease of intensity without changing a scattering profile could be explained by either decrease of contrast of the scattering length density or that of total amount of particles. In the case of glassy carbon, scattering length density of micro voids is equal to zero, since micro voids are assumed to be vacuum. As a result, the contrast is equal to scattering length density of matrix phase(graphite crystallites). Therefore, decrease of intensity may be due to decrease of scattering length density of matrix phase grown to c-axis by neutron-irradiation. In order to know the detail of annealing behaviour of glass-like carbon, annealing above 600 ^{0}C will be planned.

Small Angle Neutron Scattering from Neutron-irradiated Highly Oriented Pyrolytic Graphite

K.Aizawa, S.Yamaguchi, T.Iwata* and M.Furusaka**
Institute for Materials Research, Tohoku University, Sendai 980
*Japan Atomic Research Institute, Tokai 319-11
**National Laboratory for High Energy Physics,1-1 Oho,Tsukuba-shi Ibaraki 305

Carbon material is a potential plasma facing material for magnetic confinement fusion reactors. It is, therefore, essential that its response to fast particles irradiation is well characterized. In the present work, small angle neutron scattering (SANS) measurements from a neutron-irradiated highly oriented pyrolytic graphite have been performed on SAN spectrometer.

Irradiation were performed on JRR-2 at JAERI to a dose of $1.4*10^{20}$ fast neutron (>1MeV), at temperature less than 60 ^{0}C.

The samples, which had been cut from larger blocks such that their axes either parallel or perpendicular to the fiber axis (c-axis) and were rectangular in shape (9.5mm*9.5mm*8.5mm).

SANS measurements were carried out at specimen-to-detector distance of 1m, which covers a q-range of 0.03 to 0.6 Å^{-1}.

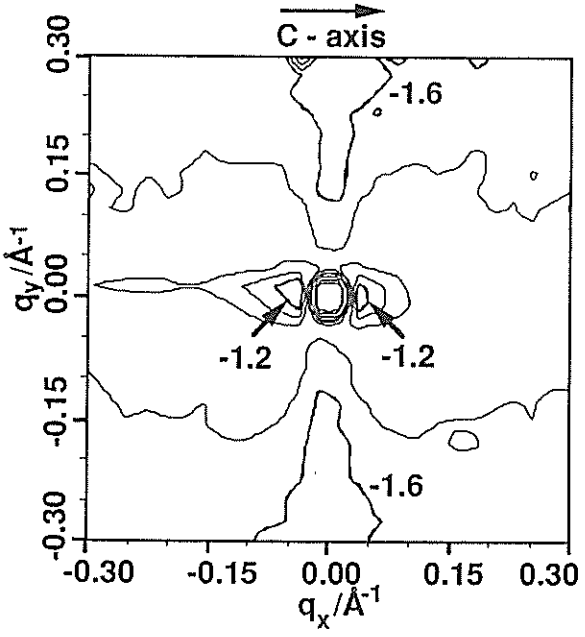

Fig. 1 Two-dimensional isointensity contour map for as irradiated sample. The map is drawn to a scale of common logarithms.

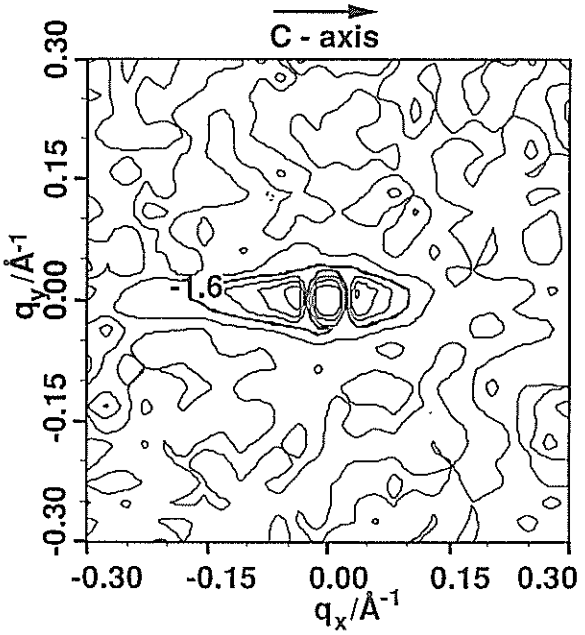

Fig. 2 Two-dimensional isointensity contour map for unirradiated sample. The map is drawn to a scale of common logarithms.

Figure 1 shows a two-dimensional isointensity contour map for as irradiated sample, the c-axis of which was perpendicular to the incident wave vector, $\mathbf{k_0}$. The one for the unirradiated sample is also shown in Fig. 2. The contour lines indicated by number -1.6 in both figures mean the same intensity. It is clearly seen that the scattering intensity increases considerably and an anisotropy appears for the irradiated sample. It suggests that some defects are aggregated into clusters which grow parallel to the c-planes.

Analysis of the data is now in progress for determining the concentration and state of agglomeration of the defects produced by irradiation .

1-7. Polymers

Phase Structure Study of the Barium Ethyl(octyl)phosphate-Water System by Small Angle Neutron Scattering

H. OKABAYASHI, K. TAGA, K. MIYAGAI, S. AOKI, A. SHIZUNO,* J. SUZUKI** and M. FURUSAKA***

Department of Applied Chemistry, Nagoya Institute of Technology, Gokiso-cho, Showa-ku, Nagoya 466
*College of Science and Technology, Nihon University, Tokyo 101
**Faculty of Science, Tohoku University, Sendai 980
***National Laboratory for High Energy Physics, 1-1 Oho, Tsukuba-shi, Ibaraki 305

Studies on dialkylphosphates with different alkyl chains are very few. We treat barium ethyl(octyl)phosphate (EOP) as a new surfactant molecule and report the phase structure study of the EOP-water system by small angle neutron scattering (SANS).

The phase diagram of the EOP-water system consists of four regions (Ⅰ, Ⅱ, Ⅲ and Ⅳ)[1]. In region Ⅰ, a critical micelle concentration (1.2 wt%) was found, indicating the presence of a monomer ⇄ micelle equilibrium. Region Ⅱ is a two-phase area in which region Ⅰ and Ⅲ coexist. For region Ⅲ, the structure of the aggregate system depends upon the concentration. In region Ⅳ, solid EOP and its solution coexist.

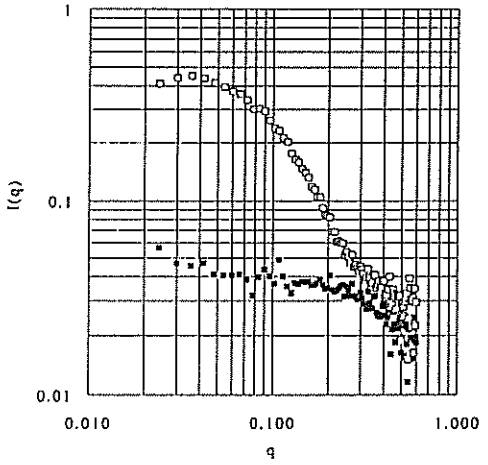

Fig. 1 SANS spectra of SⅠ (■) and SⅡ (□) at 50 °C.

Figure 1 shows the SANS spectra of the EOP-D_2O solutions (SⅠ: 1 wt% and SⅡ: 2 wt%) in region Ⅰ at 50 °C. The neutron scattering intensity (I(q)) for the sample SⅡ differs markedly from that of the monomer solution (SⅠ). For the observed I(q) values, a Guinier plot of $\ln[I(q)]$ *vs.* q^2 is a straight line in the small q region in the range of room temperature - 50 °C. This shows that the EOP micelles are monodispersed in region Ⅰ. A Guinier plot gives the amplitude (I_0) and the radius of gyration (R_g) of the micelle. The I_0 term depends upon the aggregation number of a micelle and R_g contains information on the micellar shape[2].

Table 1. R_g and I_0 of SⅡ at different temperature.

	r.t.	40°C	50°C
R_g(Å)	8.89	10.99	11.30
$I_0(m^{-1})$	0.14	0.34	0.40

Table 1 lists the R_g values of samples SⅠ and SⅡ at different temperatures. The R_g value tends to increase with an increase in temperature, indicating the temperature dependence of a micellar size.

With an increase in temperature, the I_0 value increases. This observation may imply an increase in aggregation number (N), since I_0 depends on N. At the present time, it is difficult to discuss the aggregate structure in detail if one only uses the present data for SⅠ and SⅡ. Further SANS measurements by the external and internal contrast variation are required.

For region Ⅲ, SANS measurements of three samples (60, 65 and 70 wt%) were made at 50 °C and the Bragg reflections were obtained (not shown here), indicating the existence of periodic structure in the aggregate. The SANS measurements for the samples of lower water-content are desirable.

For region Ⅱ, SANS measurements for the upper and lower phases were also made. The results show the coexistence of region Ⅰ and Ⅲ in this region.

References

1) T. Yoshida, K. Miyagai, S. Aoki, K. Taga and H. Okabayashi, Colliod & Polymer Sci. (1990) in press.
2) T.-L. Lin, S.-H. Chen, N. E. Gabriel and M. F. Roberts, J. Am. Chem. Soc. 108, 3499 (1986)

Thermoreversible Gelation of the System of Polystyrene-Carbon Disulfide

Y. IZUMI, M. FURUSAKA*, and M. ARAI*

Macromolecular Research Laboratory, Faculty of Engineering, Yamagata University, Yonezawa, Yamagata 992.
*National Laboratory for High Energy Physics, 1-1 Oho, Tsukuba-shi, Ibaraki 305

The physical gelation of atactic polystyrene (aPS) solutions has received much attention over the past several years. Although the occurrence has been supported by several experimental works[1-4], the physical gelation of aPS solution is still puzzling. In order to settle this conflicting problem and to obtain a more direct evidence of the appearance of order in the physical gels of this polymer, we have studied the static behavior on the physical gelation of aPS-carbon disulfide (CS_2) by means of neutron scattering[5].

In this report, the neutron scattering data are analyzed on the basis of a classical branching theory[6,7]. The mechanism of the physical gelation and the structure of the branching point are discussed on the sol-gel transition of aPS (normal or deuterated) in CS_2.

In the classical experimental conditions, i.e., for solutions of identical polymers, the Kratky plots are characterized by the appearance and growth of a maximum, as the temperature is lowered. The appearance of the maximum is the most striking feature of the scattering curves of branched polymers[8-9]. The appearance and growth of a maximum are related to the appearance of the branching point and the increase of the number of the branching points. This is shown by comparing the Kratky plots obtained experimentaly with the prediction of a branching theory.

The particle scattering factor for a star molecule with monodisperse rays[6] is given by
$P(u,f)=(2/fV^2)[V-\{1-\exp(-V)\}+(f-1)\{1-\exp(-V)\}^2/2]$,
where f is the functionality of the star center unit, $V=fu^2/(3f-2)$ and $u^2=q^2\langle s^2\rangle$.
The particle scattering factor for a star molecule with polydisperse rays (most probable distribution)[7] is given by $P(u,f)=(1+u^2/3f)/[1+u^2(f+1)/6f]^2$, where $u^2=q^2\langle s^2\rangle_z$.

The scattering data was analyzed in the Kratky plot, because the effect of branching is displayed even more marked in the scattering behavior of the intermediate q range.

Fig. 1 shows a comparison between these scattering factors and the scattering data of $c_D=c_T=0.068g/cm^3$. The Kratky plots obtained experimentally can be described by the model of stars with abput 7 to 140 monodisperse rays or with about 10 to 460 polydisperse rays. A better agreement was observed in the plot for monodisperse stars. From a wide angle scattering experiment, the clustering occurs as a result of the formation of branching point which would be formed by a specific interaction between aPS and CS_2[9,10]. The Bragg spacing observed in the wide angle diffraction would correspond to the distance between two phenyl rings via CS_2. The deuteration effect enhances the strength of this interaction and shifts the sol-gel transition curve at higher temperatures and lower concentrations.

References

1)H.M.Tan et al., Macromolecules 16,28(1983).
2)R.F.Boyer, et al., Macromolecules 18,427(1985).
3)J.Francois,et al., Macromolecules 19,2755(1986).
4)J.Francois et al, Polymer 29,898(1988).
5)Y.Izumi et al., Rept.Prog.Polym.Phys.Jpn. 31,5(1988).
6)W.Burchard, Macromolecules, 7,835,841(1974).
7)W.Burchard, Macromolecules,10,919(1977).
8)K.Kajiwara & C.A.M.Ribeiro, Macromolecules,7,121(1974)
9)J.M.Guenet, et al., Macromolecules, 22,494(1989).
10)Y.Izumi,International Conference on Polymer Research by Neutron Scattering, Kyoto, Nov. 7-9(1989), The Taniguchi Conference, Division of Polym. Chemi.

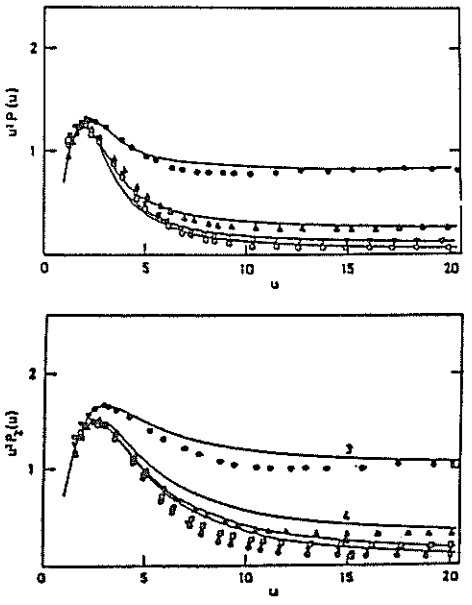

Fig. 1. Comparison between experiments and calculations.
(a) monodisperse regular stars (up),
(b) polydisperse stars (down).

Small Angle Neutron Scattering from Poly(vinyl alcohol) Gels

T. Kanaya, M. Ohkura, K. Kaji and M. Furusaka+

Institute for Chemical Research, Kyoto University, Uji,
Kyoto-fu 611, Japan
+) National Laboratory for High Energy Physics, Tsukuba,
Ibaraki-ken 305, Japan

Structures of poly(vinyl alcohol) (PVA) gels formed in a mixture of deuterated dimethylsulfoxide and deuterium oxide (v/v=60/40) have been investigated using small angle neutron scattering.

The measurements were carried out with the spectrometer SAN installed at KENS. The length of the scattering vector Q ranges from 0.008 to 0.2 A^{-1}. The degrees of polymerization (DP) of PVA are 200, 600 and 1700 and the concentration range of PVA is 0.2 to 15 g/dl. The temperature range for the measurements were -50C to 23C, but in this report we will focus on the results at 23C. The gel samples were prepared by quenching the PVA solutions homogenized at 130C to a given temperature and allowed to stand for 24 hours. We have also performed time-resolved measurements to investigate the gelation process from the homogeneous solution. In such measurements, we began the measurements immediately after quenching the solution from 130C to a given temperature.

The observed scattering intensity I(Q) of the PVA (DP=1700) gel for the concentration 5 g/dl is shown in Fig.1(a) where it is plotted in double-logarithmic form. It is found that the scattering intensity I(Q) in the lower Q range can be represented by the function $I(Q) \sim \xi/(1+\xi^2Q^2)$ where ξ is a correlation length. On the other hand, I(Q) in the higher Q range obeys so-called Porod's law, i.e., I(Q) decreases with Q^{-4}. The critical concentration of the gelation of the PVA (DP=1700) solution at 23C is 1.35 g/dl which has been determinded from macroscopic observation. The scattering intensity of the PVA sol (Cp=1.0 g/dl) is shown in Fig.1(b). The Q-dependence of the scattering intensity I(Q) is very similar to that of

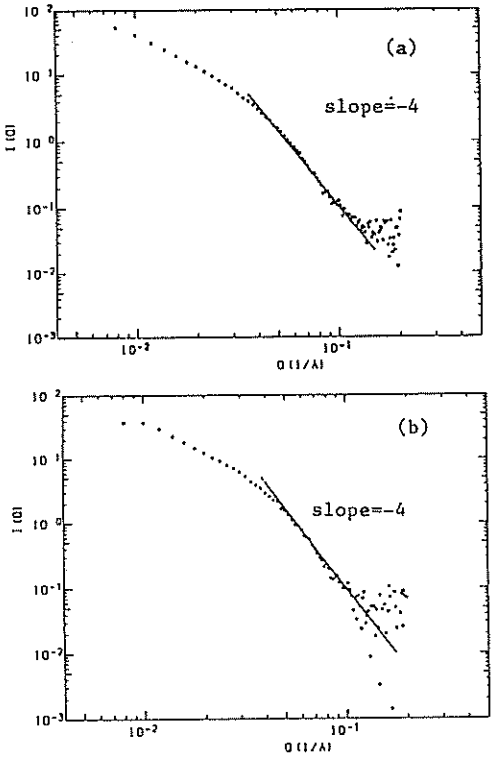

Fig.1. Observed scattering intensity I(Q) of PVA (a):gel and (b):sol in a mixture of deuterated dimethylsulfoxide and deuterium oxide (v/v=60/40). The degree of the polymerization of PVA is 1700. The concentrations of PVA are (a): 5 g/dl and (b): 1 g/dl. The critical gelation concentration of the PVA solution (DP=1700) at 23C is 1.35 g/dl.

the PVA gel (Cp=5.0 g/dl) in Fig.1(a). In fact, I(Q) of the PVA sol can be described by the functions $\xi/(1+\xi^2Q^2)$ and Q^{-4} for the lower and higher Q ranges, respectively. The PVA sol has probably a "micro-gel" structure which is very similar to that of the gel from microscopic viewpoints.

In order to see another aspects of the gel, we convert the scattering intensity I(Q) to the distance distribution function P(r) by inverse Fourier transformation. The distance distribution function P(r) for the PVA (DP=1700) gel with the concentration Cp=5 g/dl is shown in Fig.2(a). In the distance distribution function P(r), two peaks or shoulders are observed at ca. 70 A and ca. 200 A. What are the origins of the peaks or shoulders? We have already confirmed that the cross-linking points of PVA gels are crystallites from the diffraction measurements.[1] The peak at ca. 80 A in P(r) has been assigned to the size of the crystallites and the peak at ca. 200 A to the distance between the crystallites. The Porod's law in the higher Q range should reflect the smooth surface of the crystallite. The distance distribution function of the PVA sol (Cp=1 g/dl) is shown in Fig.2(b). The ratio of the intra-crystallite correlation to the inter-crystallite one P(r=80)/P(r=200) is very large compared with that of the PVA gel (Cp=5 g/dl) in Fig.2(a). This may indicate that the size of the cluster of the "micro-gel" in the PVA sol is not very large.

Time-resolved measurements are very powerful to investigate the gelation process. The observed scattering intensities I(Q) at 23°C for the PVA (DP=1700) solution with the concentration 5 g/dl are shown in Fig.3 as a function of time. The scattering intensity gradually becomes stronger with time t, especially in the lower Q range, suggesting that the PVA solution becomes more heterogeneous as the gel structure grows. In the whole time range observed,

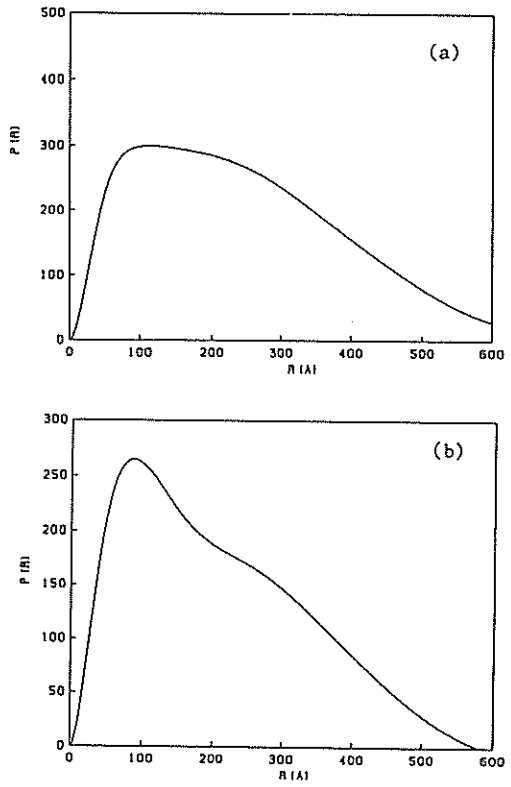

Fig.2. Distance distribution function P(r) of PVA (a):gel and (b):sol obtained from inverse Fourier transformation of I(Q) in Fig.1(a) and (b), respectively.

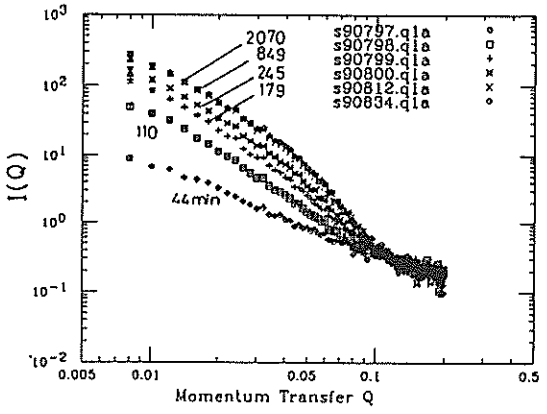

Fig.3. Observed scattering intensities I(Q) at 23°C as a function of time. Concentration of PVA is 5 g/dl and the degree of the polymerization is 1700.

the scattering curves I(Q) can be described by $\xi/(1+\xi^2Q^2)$ and Q^n for the higher and lower Q ranges, respectively. Then, we fitted the scattering curves I(Q) in with these two functions in the corresponding Q ranges to evaluate the correlation length ξ and the exponent n. Time dependence of ξ and n are shown in Fig.4 where the gelation time and the clouding time determined from macroscopic observations are also indicated. The exponent n decreases with time from 0 to -4 (Porod's law). According to the discussion based on the fractal concepts[2], the time at which the exponent n becomes -3 corresponds to the development of the crystallites. This idea is supported by the fact that this time of n=-3 is very close to the gelation time. The correlation length ξ has a maximum at about 170 min. which is almost the same as the clouding time (see Fig.4). It is considered that the maximum can be related to the phase separation of the PVA solution. The distance distribution functions P(r) are also calculated from the scattering curves I(Q) in Fig.3. The results are shown in Fig.5. Corresponding to the maximum of ξ, values of P(r) at t=179 min. are very large in the r range larger than 300 Å.

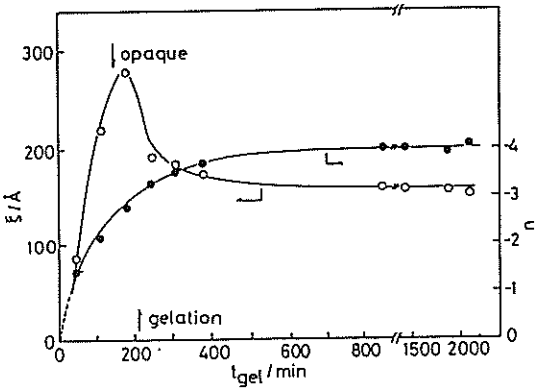

Fig.4. Time dependence of the correlation length ξ and the exponent n. These values are evaluated from the scattering curves I(Q) in Fig.3.

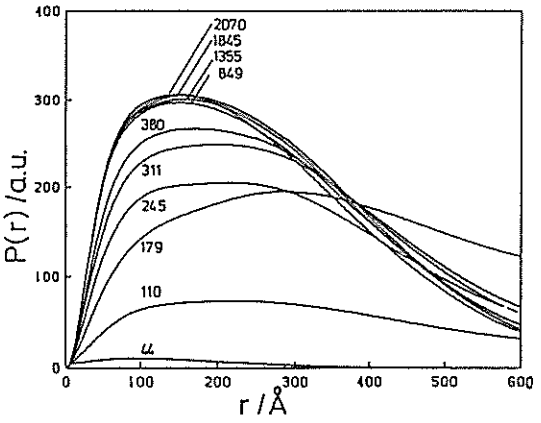

Fig.5. Distance distribution function as a function of time. These functions are calculated from inverse Fourier transformation of the scattering curves I(Q) in Fig.3.

References

1) M. Ohkura, T.Kanaya, K.Kaji and M.Misawa, unpublished data.

2) C. Janot, Annual Report 88, Institut Laue Langevin, 1988, p.63.

Quasielastic Neutron Scattering from Polysterene-Carbon Disulfide System near the Geration Point

Yoshinobu Izumi and Kazuhiko Inoue*

Macromolecular Research Laboratory, Department of Engineering,
Yamagata University, Yonezawa, Yamagata 992
*Department of Nuclear Engineering, Hokkaido University, Sapporo 060

The physical gelation in atactic polystyrene (aPS) solutions is of great interest from microscopic dynamical viewpoints[1,2]. APS is one of typical amorphous materials and therefore the physical gelation of aPS solution is still puzzling. In order to reveal the gelation mechanism from microscopic dynamical view points, we measured incoherent neutron scattering spectra from aPS-carbon disulfide (CS_2) with both the conventional (LAM-40) and high resolution spectrometer (LAM-80). APS (Pressure Chemicals Company) characterized by MW=9000 and Mn/Mw<1.06 was used and the polymer concentration was 25wt%.

Figure 1(a)-1(f) show the scattering spectra from aPS-CS_2 at six temperatures obtained with LAM-80. Figure 2(a)-2(h) show the corresponding scattering spectra from LAM-40. A drastic narowing of the central peak is observed in Figs. 1 and 2, as the gelation proceeds. The narrowing of the central peak is completed at the glass transition temperature of this solution. In the present experimental condition, i.e., qa>1, where q is a scattering vector and a is the statistical segment length, one observe a local segmental motion in a PS chain. This is suggested by the fact that the observed width drastically changes in the measured q range. Furthermore, the results indicate that two types of local segmental motions (Ω_n', Ω_n'') exist at least in the present system. According to the theory[3], the local segmental motion is described by $\Omega_n(q) = D_n q^2$, where D_n is the diffusion coefficient of a single monomer and equals to $kT/\eta_0 a$,

The present results are qualitatively described by this theory. More quantitative analysis for the local segmental motion during the gelation process will be made after appropriate corrections for the present data. And more work will be made to assign the local segmental motions using the deuterated samples.

References
1)Y.Izumi, Y.Miyake, & K.Inoue, KENS Report V,135(1984).
2)Y.Izumi, et al., KENS Report VI,IV-148(1985/86).
3)A.Z.Ackcasu, M.Benmouna, C.C.Han, Polymer 21, 866(1980).

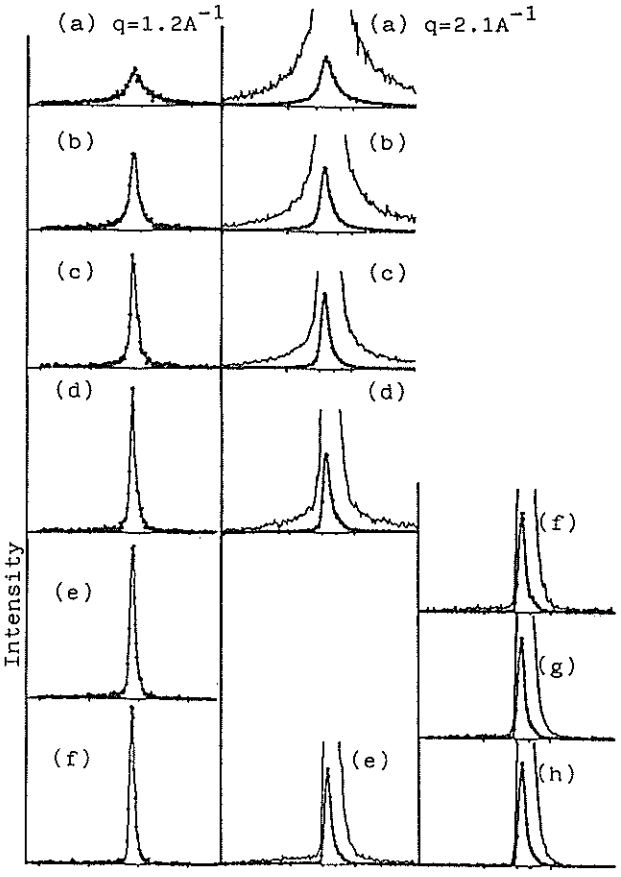

Fig. 1 Fig. 2

Fig. 1 Neutron scattering spectra from aPS (Mw=9000,Mw/Mn< 1.06)-carbon disulfide system near the gelation point obtained from LAM-80 at six temperatures 298, 248, 223, 203, 183, and 163 K, respectively (q=1.2Å^{-1}).

Fig. 2 Neutron scattering spectra from LAM-40 at eight temperatures, 300, 243, 223, 203, 148, 123, 98, and 73 K, respectively (q=2.1Å^{-1}).

Local Motions of cis-1,4-Polybutadiene in the Melts

Toshiji KANAYA, Keisuke KAJI and Kazuhiko INOUE+

Institute for Chemical Research, Kyoto University, Uji,
Kyoto-fu 611, Japan
+) Department of Nuclear Engineering, Hokkaido University,
Sapporo 060, Japan

Introduction

In polymer chains, conformational transitions between rotational isomeric states are fundamental to understand many of the rapid relaxation processes. Crankshaft-like motions were considered to be the most reasonable explanation of the local motions. Recent important progress in this field is the computer simulation by Helfand and coworkers[1] and has given an argument against the crankshaft-like motions. The computer simulation has indicated that isolated transitions as well as cooperative transitions occur in a polymer chain. The isolated transitions occur by distorting the neighboring degrees of freedom and the softest mode or bond rotations are the most favorable to use for the distortion.

Our attention is forcused on the mechanism of the local conformational transitions in polymer chains. The conformational transitions are assisted by distortions in a polymer chain through vibrational motions, especially bond rotations or torsional vibrations. We are also interested in the vibrational motions which are probably damped in the melts due to thermal agitations or high friction. In order to investigate these motions, we carry out neutron quasielastic scattering measurements on cis-1,4-polybutadienes (PB) in the melts.

Experimental

Neutron quasielastic scattering measurements were performed with the inverted geometry time-of-flight (TOF) spectrometers LAM-40 and LAM-80 installed at the pulsed spallation cold neutron source in KENS. The measurements were carried out at 23, 45, 60, 80, 100, 120 and 140°C enough above the melting temperature of PB (about 2°C). Analysis of the observed dynamic scattering laws was carried out by curve-fitting with model functions using the computer codes QUESA40 and QUESA80.

Results and Discussion

Damped Vibrational Motions from LAM-40 Data. The observed neutron quasielastic scattering spectra $S_{inc}(Q,w)$ at Q=1.76 A^{-1} of molten PB with molecular weight 8.1 x 10^5 are shown in Fig.1 as a function of temperature from 23 to 100°C. Each spectrum consists of elastic scattering and broad quasielastic

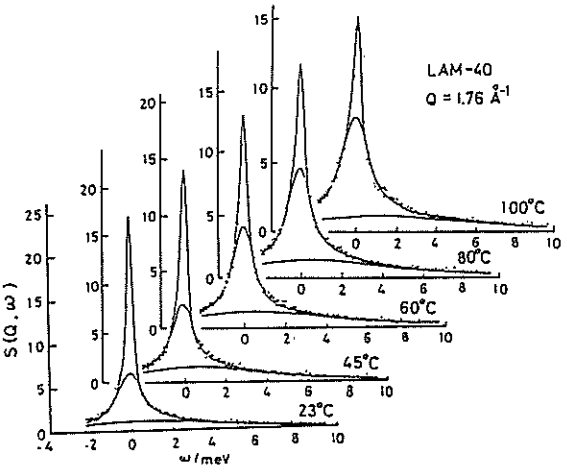

Fig.1. Neutron quasielastic scattering spectra at Q=1.76 A^{-1} of molten cis-1,4-polybutadiene measured by LAM-40 as a function of temperature from 23 to 100°C. Solid lines represent the fitting results including elastic and two quasielastic components.

scattering. We have fitted the spectra in with a model function given by the sum of a δ-function and two Lorentzians. This function gives an excellent agreement with the experimental spectra. The solid lines in Figure 1 show the results of the fit.

The very weak temperature dependences of the HWHM of the broad and narrow components give an activation energies $E_a \simeq 0.5$kcal/mol. Furthermore, the HWHMs are almost independent of Q. Then, the broad (faster) and narrow (slower) components have been assigned to a damped vibrational motion. The spatial scale of the motion is evaluated assuming that the Q dependence of the elastic scattering intensity can be described by the Debye-Waller manner, i.e., $I_{el} \sim \exp(-\langle U^2 \rangle Q^2)$ where $\langle U^2 \rangle$ is the mean square amplitude of the damped vibrational motion. The results are summarized in Table I.

Local Conformational Transition from LAM-80 Data. The observed quasielastic scattering spectra at Q=1.23 A^{-1} of PB are shown in Fig.2 as a function of temperature from 23 to 100°C. The Arrhenius plots of HWHM of the new narrow component Γ_{2c} gives an activation energies to be 2.5 kcal/mol. This value corresponds nearly to the height of one energy barrier separating RIS. It means that the new quasielastic component can be related to the local conformational transitions.

For the local conformational transition, we adopt a jump diffusion model with the damped vibrational motions by taking into accounts the retults of the computer simulation by Helfand.[1] The schematic sketch of the jump diffusion model with the damped vibrational motions is shown in Fig.3. This type of model has been generally formulated by Singwi and Sjolander[2]. In Figure 4, the observed HWHM Γ_{2c} is plotted against Q^2 for 23, 60, 80, 100, 120 and 140°C. In order to evaluate the parameters τ_0 and $\langle l^2 \rangle$ in the jump diffusion model, the Q dependence of

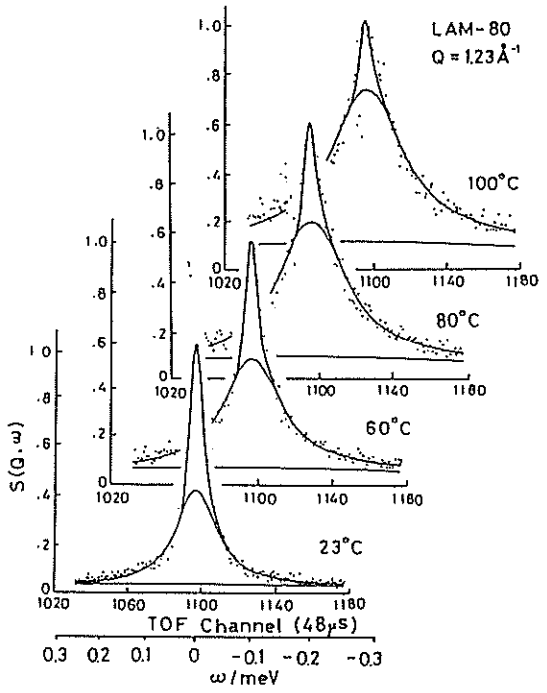

Fig.2. Neutron quasielastic scattering spectra at Q=1.23A^{-1} of molten cis-1,4-polybutadiene measured by LAM-80 as a function of temperature from 23 to 100°C.

Table I. Parameters of the jump diffusion model for the local conformational transitions determined from LAM-40 and LAM-80 data.

T/°C	$\langle U^2 \rangle^{1/2}$/A	$\langle l^2 \rangle^{1/2}$/A(a)	τ_0/ps(b)	D/$10^2 A^2 ps^{-1}$(c)	$\langle \Delta\phi \rangle$/deg	τ_K/ps(d)
23	0.44	(3.71)	81.0	(4.5)	33	102
45	0.49	-	-	-	35	72.6
60	0.51	2.31	48.6	1.8	36	59.1
80	0.55	2.12	35.6	2.1	38	46.0
100	0.58	1.76	28.9	1.8	39	36.8
120	0.62	1.43	22.4	1.5	41	30.2
140	0.66	1.85	21.2	2.7	42	25.3

(a) Value of $\langle l^2 \rangle^{1/2}$ calculated from molecular structure is 2.03 A.
(b) Activation energy of τ_0 (E^*) is 2.9 kcal/mol.
(c) Calculated from $D = \langle l^2 \rangle / 6\tau_0$.
(d) Calculated from the Kramers' rate theory.

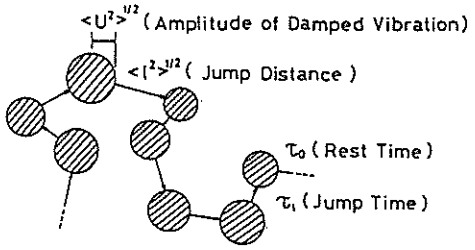

Fig.3. Schematic sketch of the jump diffusion model with damped vibrational motions.

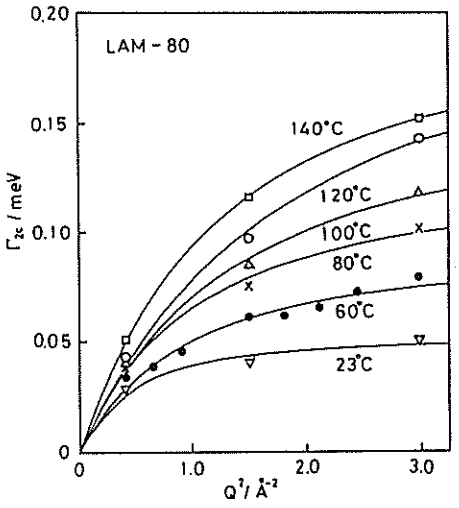

Fig.4. Q^2 dependence of half-width at half-maximum (HWHM) of the quasielastic component Γ_{2c} revealed by LAM-80. Solid lines represent the best fits with theoretical curve.

Γ_{2c} is fitted in with the theoretical curves.[2] The mean square amplitude $\langle U^2 \rangle$ evaluated from LAM-40 data was used as a fixed parameter. Solid lines in Figure 4 show the results of the fit. The agreement is good and it is confirmed that the jump diffusion model is appropriate to describe the local conformational transitions. The values of τ_0 and $\langle l^2 \rangle$ are summarized in Table I where the diffusion coefficient D ($= \langle l^2 \rangle / 6\tau_0$) are also listed.

Comparison with the rate theory. In this section, we will compare the rest time with the Kramers' rate theory.[3] Based on teh structure of PB, we calculated the rate of the local conformational transition k_K and the corresponding rest time τ_K ($=k_K^{-1}$), which are summarized in Table I. The agreement between τ_0 and τ_K is very good. The agreement may offer an evidence that the Kramers' theory is appropriate for description of the local conformational transitions of the molten PB.

Geometrical Consideration. The mean square amplitude of the damped vibration $\langle U^2 \rangle$ and the jump distance $\langle l^2 \rangle$ have been evaluated based on the jump diffusion model. These observed quantities are calculated from the molecular structure of PB.

The amplitude $\langle U^2 \rangle$ should be originated from vibrational motions near the potential minima. The softest mode or bond rotation mainly contributes to the amplitude $\langle U^2 \rangle$, so that it can be roughly given by

$$\langle U^2 \rangle \simeq \langle x^2 \sin^2 \Delta\varphi \rangle \simeq \langle x^2 \rangle \sin^2 \langle \Delta\varphi \rangle \qquad (1)$$

where x is the distance from the rotational bond to hydrogen atom and $\Delta\varphi$ the angular displacement from the potential minimum. In the calculation, we found that the average value $\langle x^2 \rangle$ is 1.20 A. The corresponding angular displacements $\langle \Delta\varphi \rangle$ calculated from eq.(1) are in the range from 33 to 42 deg for the temperature range from 23 to 140°C. The results are summarized in Table I.

Half of the jump distance $\langle l^2 \rangle$ can be also given from eq.(1) by putting $\langle \Delta\varphi \rangle$ = 60 deg. In the calculation, we get $\langle l^2 \rangle_{cal}^{1/2}$ = 2.03 A. The agreement between the calculated and observed values is fairly good, suggesting the conformational transitions are mainly caused through a single bond rotation.

References

1) Helfand, E.; Wasserman, Z. R.; Weber, T. A. *J. Chem. Phys.* 1979, *70*, 2016. Helfand, E.; Wasserman, Z. R.; Weber, T. A. *Macromolecules*, 1980, *13*, 526.
2) Singwi, K. S.; Sjolander, A. *J. Chem. Phys.*, 1960, *119*, 863.
3) Kramers, H. A. *Physica*, 1940, *7*, 284.

1-8. Biologies

Penetration of Water into Hydrophobic Interior Regions of Phosphatidylinositol Diphosphate Bilayers

S. Yabuki, T. Takizawa, K. Hayashi*, N. Niimura**,
K. Mikami**, U. Sangawa** and M. Furusaka***

Department of Physics, Faculty of General Studies, Gunma University Maebashi, Gunma 371
* Department of Physiology, Faculty of Education, Ibaraki University Mito, Ibaraki 310
** Laboratory of Nuclear Science, Faculty of Science, Tohoku University Sendai, Miyagi 982
*** National Laboratory for High Energy Physics 1 - 1 Oho, Tsukuba, Ibaraki 305

Phosphatidylinositol diphosphate (PIP_2) is a highly hydrophilic phospholipid rich in nervous tissues, and has been considered to play an important role in the nerve excitation through the regulation by Ca^{2+} ions[1]. Recent physicochemical studies have suggested for PIP_2 multibilayers that water molecules may penetrate even into the interior regions consisting of hydrocarbon chains, which are usually supposed to be very hydrophobic[2]. To get direct evidences for it, the interaction of water with PIP_2 multibilayers was studied by small angle neutron scattering method.

PIP_2 was extracted from bovine brain and purified by conventional methods[3, 4]. The preparations of ammonium salts of PIP_2 were free of divalent cations. Samples for scattering measurements were prepared by changing the water content from 0 to 100 wt% (relative to the lipid weight) and the isotopic composition of water (100% and 50% D_2O) in the absence or presence of Ca^{2+} ions. Water content was controlled by using the time dependence of water adsorption to PIP_2 powder kept closed in a vessel containing the saturated amount of water vapors.

Each PIP_2 sample was sandwitched between two glass plates and sealed with thin teflon films tight enough to avoid any evaporation of adsorbed water. Scattering measurements were made using the small angle scattering spectrometer SAN in National Laboratory for High Energy Physics. Three experimental tempertures were chosen (10, 25 and 40 ^{0} C), which corresponds to the temperature before the beginning of the endothermal transition of PIP_2 hydrated membranes, the temperature during the pre-transition and the temperature after its completion, respectively.

Scattering profiles with two or three reflections were obtained for all cases (for example, see Fig. 1).

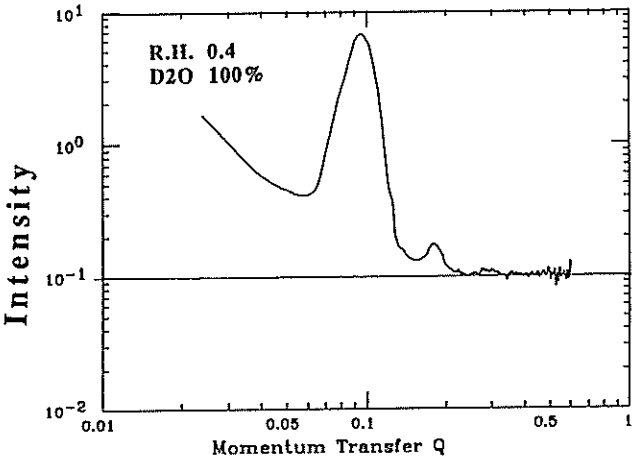

Fig. 1 Scattering profile for multibilayers of PIP_2 containing 40% water (100% D_2O)

Model fitting in terms of intensity of reflection was carried out with a simplified multibilayer model represented by a series of three strips, each strip corresponding to the layer of water, that of head groups and that of tail groups (hydrocarbon chains). A specified width and scattering length density were assigned for each of the strips as functions of the number of water molecules involved. The numbers of water molecules per lipid molecule in the head group regions and the tail group regions of the model bilayer were determined to make the calculated intensities of reflections fit best to the observed ones are shown in Fig. 2. A typical example of the changes of neutron scattering density profiles for multibilayers of PIP_2 with the change of water content calculated using the observed reflection intensities are presented in Fig 3. These results lead to the following conclusions concerning the penetration of water into hydrophobic interior region of PIP_2 multibilayers:

(1) with the water content below 20%, water molecules are found only in interbilayer regions and in the head group regions;

(2) the quantity of water in the head group region appears to monotonously increase with the increase of water content of the whole membrane;

(3) within the temperature range measured, the quantity of water in the heads group region appears independent of the surrounding temperature;

(4) at the lowest temperature measured (10 ^{0} C), water begins to penetrate into the hydrophobic interior regions as soon as the water content of the whole membrane goes beyond 20%;

(5) as the surrounding temperature increases, the water content threshold of the whole membrane beyond which water penetration into the hydrophobic interior region is allowed, shifts to a higher value;

(6) within the water content range measured (0 ~ 100%), the quantity of water to penetrate into the interior region increases monotonously according to the increase in the water content of the whole membrane;

(7) at the highest temperature measured (40 ^{0} C), water molecules seem unable to stay in the interior region any longer.

Further study to detect higher order reflection peaks is in progress with another spectrometer WIT.

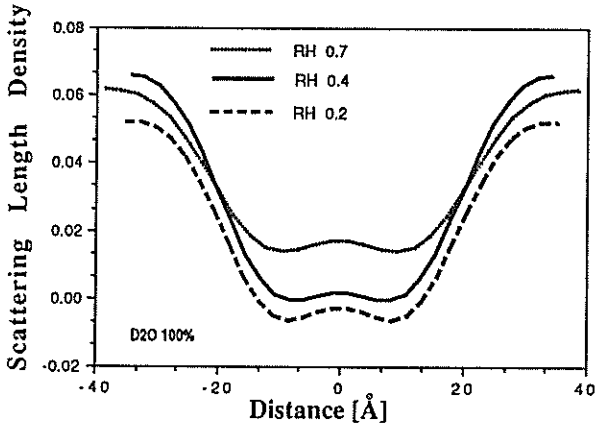

Fig. 3 The change of neutron scattering dsensity profiles for multibilayers of PIP_2 with the change of water content (10 ^{0}C).

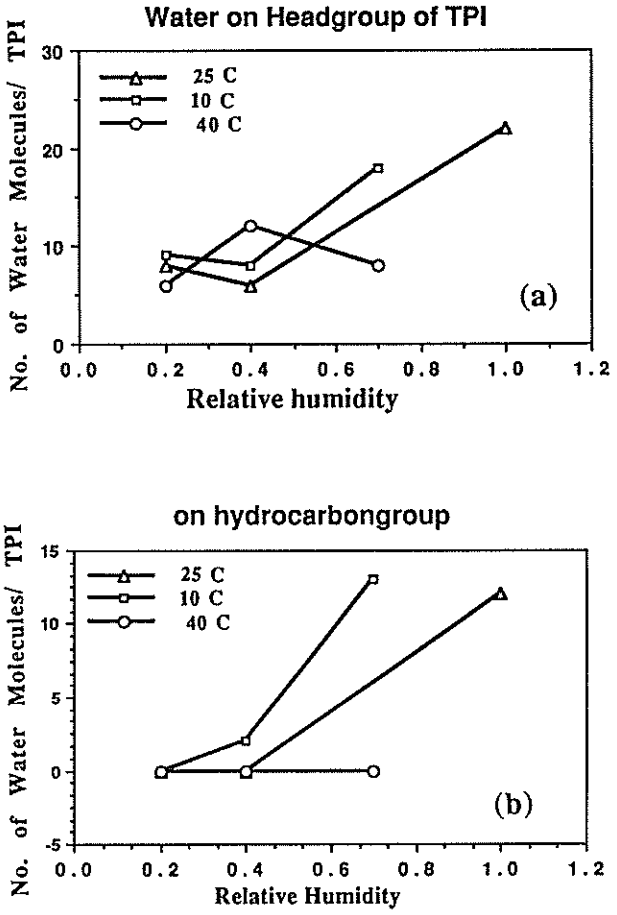

Fig2. The number of water molecules per lipid molecule contained in (a) the head group region and (b) the tail group region of multibilayers of PIP_2

References

1) K. Hayashi, Maku (Membrane) 2, 86(1977) (Japanese)
2) T. Takizawa, K . Hayashi, S. Yabuki and Y. Nakata, Thermochim. Acta 123, 247(1988)
3) J. Folch, J. Biol. Chem. 177, 97(1949)
4) J. S. Hendrickson and C. E. Ballou, J. Biol. Chem. 239, 1369 (1964)

Small Angle Neutron Scattering of TMV Particle

Y.SANO[1], N.NIIMURA[2], Y.HIRAGI[3], Y.HIRAI[4] and H.INOUE[5],

1) National Food Research Institute, Tsukuba City, Ibaraki 305, Japan
2) Laboratry of Nuclear Science, Tohoku University, Sendai,Miyagi 982, Japan
3) Institute for Chemical Research, Kyoto University, Uji-shi, Kyoto 611, Japan
4) Kanagawa Institute of Technology, Atsugi-shi, Kanagawa 243-02, Japan
5) Shimadzu Corporation, Nishinokyo Nakagyo-ku Kyoto 604, Japan

Tobacco mosaic virus (TMV) is reconstituted in vitro into an infective virion from its constituents RNA and coat protein (TMVP). This assembly process has been mainly investigated by electron microscopy and turbidity, and the reaction is thought to complete approximately 20-40 min under physiological conditions. TMV particle reconstituted was observed in a dried state by the former method, while the latter method gave little information about the size and shape of the particle in solution. A small-angle neutron scattering (SANS) method is exceedingly useful for this case, in particular, with the contrast variation method. When the TMV assembly process is traced by the SANS method, we can observe,in principle,growth of reconstituted particles,i.e. ,growth of rod of the coat protein and of helix of TMV-RNA, separately. Prior to monitoring the TMV assembly process kinetically by SANS technique, the preliminary neutron scattering experiments of TMV particle itself were done with the constrast variation method in three kinds of solvents, i.e., 100%H_2O, 70%D_2O and 100%D_2O.

Neutron scattering measurements were carried out with the instrument SANS where a sample to detector distrance is 3 m. A cell was specially designed to keep the cell temperature constant by circulating temperature-controlled liquid round a cell chamber.

An example of the results obtained is shown in Fig.1 where logarithms of neutron intensities were plotted against logarithm of momentum trans fer q.The Guinier plot was almost linear in each cases and the radii of gyration was 36.1-37.1.

The detailed structure of TMVP and RNA in TMV particle is now proceeding with the data shown in Fig.1.

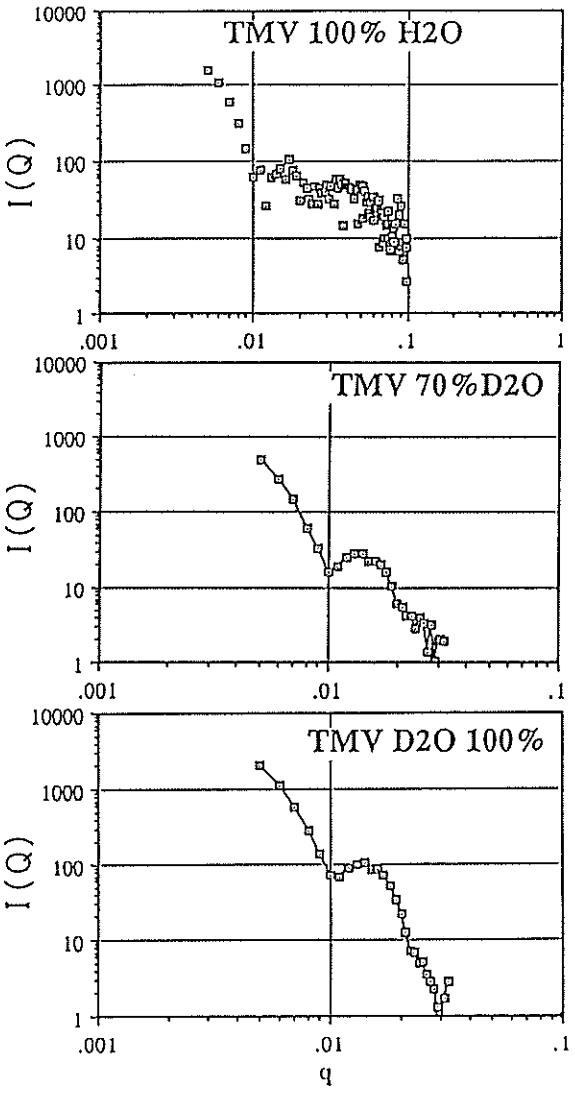

Fig.1 Scattering intensity I(Q) versus q for TMV particle (25mg/ml) in 0%, 70% and 100%D_2O in the presence of 10mM phosphate buffer (pH7.2).

Small-Angle Neutron Scattering of Hen Egg-White Lysozyme in aqueous solution

U.SANGAWA, N.NIIMURA and K.AIZAWA*

Laboratory of nuclear science, Tohoku University, Mikamine 1-2,Sendai 982
*Institue of material resrarch, Tohoku University, Katahira,Sendai 982

We have constructed small-angle neuton scattering (SANS) spectrometer which is named as WIT[1]. Normally SANS spectrometer is installed and connected to cold neutron source. However, WIT is installed at a thermal neutron source site. Since we have much less experience of SANS using thermal neutron than the one using cold neutron, it is very important to carry out feasibility test of WIT carefully.

Lysozyme is one of the most typical biological materials as a sample to test a qualification of a SANS spectrometer. Lysozyme consists of 129 amino acid residuals and the molecular weight is about 14.3 kD. The three dimensional molecular structure has been determined by X-ray crystallography and the size of the molecule is 45* 30*30 A^3. Pure lysozyme is commercially available as a powder.

Small-angle neutron scattering measurement was made using WIT for a lysozyme sample in aqueous solution of different D_2O/H_2O ratio i.e. 100%, 90%, 66%, 12% and 0%, where a unit of the ratio is mol%. Sample thickness was selected in accordance with D_2O/H_2O ratio by taking transmission into account, and was 5mm or 2mm in the case of or 100%, 90% and 66% or 12% and 0%, respectively. Lysozyme concentration is 120 mg/ml and pH of the solution is kept about 7.0 using 100mM HEPES as the particles do not aggregate each other.

The obtained scattering functions I(Q) for the lysozyme of different D_2O/H_2O ratio are shown in Fig. 1, where the base line of the each function is shifted arbitrarily to see easily. Decrease of I(Q) at very low Q region is due to an interpaticle interaction.

The Guinier plots derived from the above I(Q) are shown in Fig.2. A radius of gyration R_g of lysozyme is calculated using the least square fitting of Q range 0.089-0.187 A^{-1} at the different D_2O/H_2O ratio.

A contrast matching point of lysozyme in aqueous solution was estimated to be 46.0% using $\sqrt{I(0)}$ vs D_2O/H_2O ratio as shown in Fig.3, where I(0) was an extrapolated intercept of the ordinate of Guinier plot. The mean excess scattering density $\overline{\rho}$ was determined as 2.647×10^{-10} cm^{-2}.

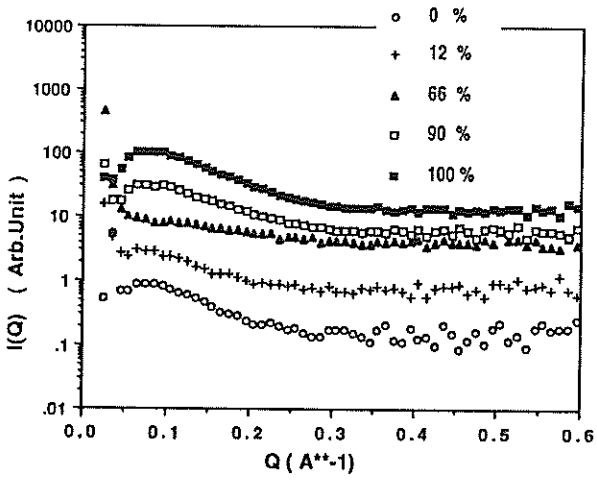

Fig.1. Scattering functions of lysozyme in aqueous solution at different D_2O/H_2O ratio.

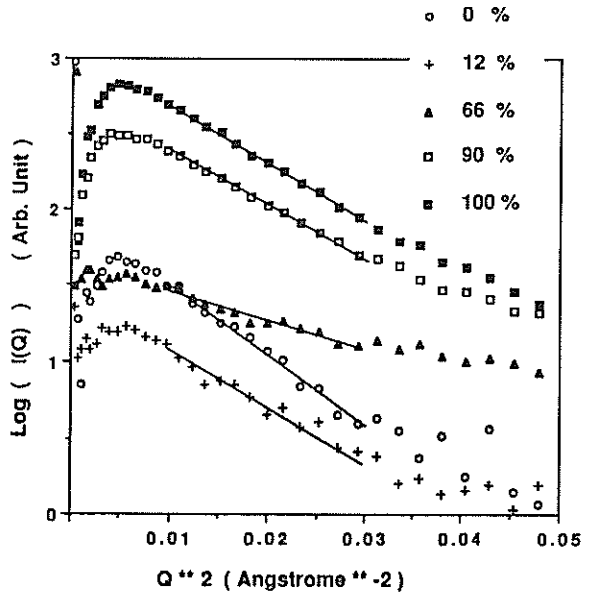

Fig.2. Guinier plot of Lysozyme in aqueous solution at different D_2O/H_2O ratio.

The plots of R_g^2 versus $1/\overline{\rho}$ (Stuhrmann plots) for lysozyme are shown in Fig. 4. R_g^2 is given by

$$R_g^2 = R_{gc}^2 + \alpha^*(1/\bar{\rho}) - \beta^*(1/\bar{\rho})^2,$$

where R_{gc}, α and β are the radius of gyration of the particle at infinite contast ($\bar{\rho}$=0), a radial second moment of the scattering density distribution and a displacement of the center of the scattering density distribution with respect to the center of the geometrical shape,respectively. The obtained values are tabulated in Table as well as the already reported ones[2].

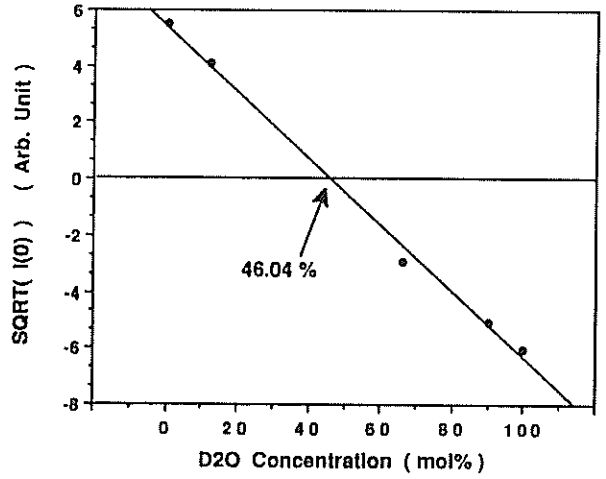

Fig.3. $\sqrt{I(0)}$ vs D_2O/H_2O ratio of Lysozyme in aqueous solution.

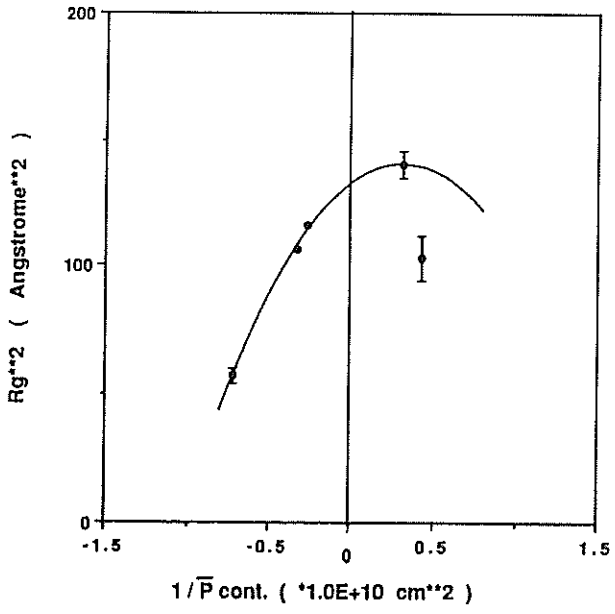

Fig.4.Stuhrmann plot of Lysozyme in aqueous solution .

Table R_{gc}, α and β of lysozyme

	R_{gc} (A)	α (A^{-1})	$\beta(A^{-2})$
Present Results	11.5	4.9×10^{-5}	8×10^{-12}
Stuhrmann *et al*[2]	13.8	3.5×10^{-5}	4×10^{-12}

Since the errors of the values α and β are about 50% in both measurements, we may say that the differences between two data are within the statistical errors. However, the reason why R_{gc} of the present results is about 2A smaller than the one of Stuhrmann *et al* 's result should be examined. In order to check the dependence of the interparticle interaction on R_g, the SANS measurement of more dilute lysozyme solution (10mg/ml) of 100% D_2O/H_2O ratio was made and R_g was calculated. R_g of lysozyme in 120 mg/ml and 10 mg/ml concentration are 10.78 $\pm$0.02 A and 11.06$\pm$0.18 A, respectively. The difference is not so large that the difference of 2A cannot be explained. At present, corrections of instrumental spatial resolution and incident neutron spectrum are taken into consideration.

The scattering function of the small-angle neutron scattering (SANS) of particles in solutions is given by

$$I(Q)=\bar{\rho}^2 I_c(Q) + \bar{\rho} I_{cs}(Q) + I_s(Q) \qquad (1)$$

where $\bar{\rho}$ is the mean excess scattering density, i.e. the difference $\langle\rho_{solute}\rangle - \rho_{solvent}$ between the mean scattering density $\langle\rho_{solute}\rangle$ of the protein and the scattering density $\rho_{solvent}$ of the solvent, and is called as **contrast**, and $I_c(Q)$, $I_s(Q)$ and $I_{cs}(Q)$ are the scattering functions of the shape, the internal structure and the both cross term, respectively. Three scattering functions can be calculated when SANS intensity I(Q)s are measured at more than three different constants $\bar{\rho}$.

One of the distinctive features of WIT is that the coverage range of Q is from 0.02 A^{-1} to 1.0 A^{-1} and it is proper to obtain informations of the internal structure of proteins. Since five equations of (1) corresponding to five different $\bar{\rho}$ values were obtained, $I_c(Q)$, $I_s(Q)$ and $I_{cs}(Q)$ can be resolved using least squares method, and now this is in progress.

References

1) N.Niimura *et a*; KENS REPORT VIII, (1989/90)
2) H.B.Stuhrmann and H.Fuess; Acta Cryst., A32(1976),67

1-9. Nuclear Physics

Parity-nonconserving Effect in the Neutron Radiative Capture Reaction III

H.M.Shimizu, Y.Masuda*, T.Adachi*, A.Masaike, and K.Morimoto*

Department of Physics, Kyoto Univ. Kyoto 606
*National Laboratory for High Energy Physics, 1-1 Oho, Tsukuba-shi, Ibaraki 305

In the previous papers[1),2)], we reported the large longitudinal asymmetry A_L with respect to the helicity of incident neutron, which violates parity conservation, in ^{139}La p-wave resonance at E_n=0.734eV. A_L is defined by

$$A_L = (\sigma_+ - \sigma_-) / (\sigma_+ + \sigma_-)$$

where σ_+ and σ_- are neutron cross sections for positive helicity neutron and negative helicity neutron, respectively. We measured A_L using two different methods. One is neutron transmission measurement and the other is capture gamma ray measurement. We denote A_L in transmission measurement as $A_{L,n}$, capture gamma measurement as $A_{L,\gamma}$. In this paper, we will report the measurements of $a_{L,\gamma}(\vartheta_\gamma)$ for ^{139}La , a_γ for ^{139}La, $A_{L,\gamma}$ for other targets.

(1) $a_{L,\gamma}(\vartheta_\gamma)$ in ^{139}La

$a_{L,\gamma}(\vartheta_\gamma)$ is a logitudinal asymmetry in capture gamma ray counts for opposite neutron helicity at certain ϑ_γ defined by

$$p_n a_{L,\gamma}(\vartheta_\gamma) = (N_+(\vartheta_\gamma) - N_-(\vartheta_\gamma)) / (N_+(\vartheta_\gamma) + N_-(\vartheta_\gamma)),$$

where ϑ_γ denotes the angle between incident neutron momentum and emitted gamma ray momentum. We have built a new gamma ray detector (named 4π-counter) for this measurement. The schematic view of experimental setup is shown in Figure 1. This gamma ray counter consists of three BaF_2 scintillators placed at ϑ_γ=45°, 90°,and 135°. The result of $a_{L,\gamma}(\vartheta_\gamma)$ for ^{139}La(E_n=0.734eV) is shown in Figure 2. The value of $a_{L,\gamma}(\vartheta_\gamma) / A_{L,\gamma}$ is plotted in this figure. $A_{L,\gamma}$ was determined by the sum counts of 4π-counter. The present 4π-counter covers about 90% of 4π steradians. As shown in Figure 2, no significant angular dependence of $a_{L,\gamma}(\vartheta_\gamma)$ was observed. Thus, the contribution of a_2 (2nd order Legendre) term argued by Vanhoy et al. [3)] is small.

(2) a_γ in ^{139}La

In the same experiment, we also measured another interesting observable a_γ, which is defined by

$$W(\vartheta_\gamma) = \text{const.} (1 + a_\gamma p_n \cos \vartheta_\gamma) .$$

Here $W(\vartheta_\gamma)$ is capture gamma ray angular distribution and p_n is the logitudinal polarization of incident neutron. The parameter a_γ comes from parity violation in the exit channel of the compound nucleus state[4)]. The results for ^{139}La(0.734eV) are $(-1.5\pm4.8)\times10^{-3}$ and $(-5.6\pm2.5)\times10^{-3}$ for the target of 3mm and 10mm thickness, respectively. In this experiment, the threshold of E_γ is approximately 1MeV. The measurement of a_γ with higher and better E_γ discrimination will be performed in near future.

(3) $A_{L,\gamma}$ in other target nuclei

We have measured $A_{L,\gamma}$'s for Br, Cd, Sn, Pd, and Ho. The significant parity violation effect was found only in radiative capture process not in potential scattering process. Therefore, in the measurement of p-wave resonance, the $A_{L,\gamma}$ takes advatage to $A_{L,n}$ since $A_{L,\gamma}$ is sensitive to small p-wave resonance, and not sensitive to large potential scattering contribution. And we can achieve a good statistics for small resonances. The preliminary results are shown in Table 1. In this table, only $A_{L,\gamma}^{raw}$ beyond 4 sigma effect is listed. $A_{L,\gamma}^{raw}$ is the raw value of $A_{L,\gamma}$. We need to correct $A_{L,\gamma}^{raw}$ to get the value of $A_{L,\gamma}$ from the following reason. We use the Time-Of-Flight method to determine the incident neutron energy. Incoming neutrons are scattered by target nucleus. And some of them are captured inside the target after scattered. Such scattered nuetrons have different energy and helicity state from that of direct capture process. However, we cannot distinguish these two kinds of gamma rays emitted through direct capture and indirect capture processes. Indirect capture gamma rays contribute to smear the helicity dependence. We will use a Monte Carlo simulation to correct this effect.

We used natural target for each measurement, and CBr_4 with natural bromine. The TOF spectrum of CBr_4 is shown in Figure 3. In our measurement, the contribution of carbon nuclei around ^{81}Br(0.88eV) resonance is negligible .

A large enhancement of parity violating amplitude was argued by Stodolsky.[5)] for ^{108}Pd theoretically. However, we observed no significant helicity

dependence for ^{108}Pd(2.96eV) p-wave resonance. The value was $(0.6\pm1.3)\times10^{-3}$. It can be said that the nearest s-wave resonance at E_n=33.10eV does not interfere because it has different channel spin.

For ^{124}Sn(62eV), large enhancement of parity violation was estimated by Forte[6] for spin rotation experiment. However, we observed no sizable helicity dependence. The result was $(-0.3\pm1.9)\times10^{-3}$.

References

1) Masuda, Y. et al.: Nucl. Phys. A478 (1988) 737C
2) Masuda, Y. et al.: Nucl. Phys. A504 (1989) 269
3) Vanhoy, J.R. et al.: Z.Phys. A331 (1988) 1
4) Krupchitsky,P.A.: Nucl.Inst.Meth. A284 (1989) 71
5) Stodolsky, L.: Phys. Lett. 96B (1980) 127
6) Forte, M.: Fundamental Physics with Reactor Neutrons and Neutrinos, 1977. Institute of Physics Conference Series N°42. von Edigy. T. (ed.). Chap. 2, p.86. Bristol and London: Institute of Physics 1978
7) Mughabghab, S.F. et al.: Neutron Cross Sections (Academic Press, New York, 1981)

Table 1. List of $A_{L,\gamma}^{RAW}$ beyond 4.0 sigma effect.

Target Nucleus	Thickness ($\times10^{22}$cm^{-2})	E_n (eV) (Ref.7,4)	$A_{L,\gamma}^{RAW}$ (x10-3)
^{81}Br	29.3	0.88	17.2±1.3
^{111}Cd	0.68	4.53	-8.4±2.0
^{139}La	10mm	0.734	77.2±1.7
	3mm		84.7±2.9

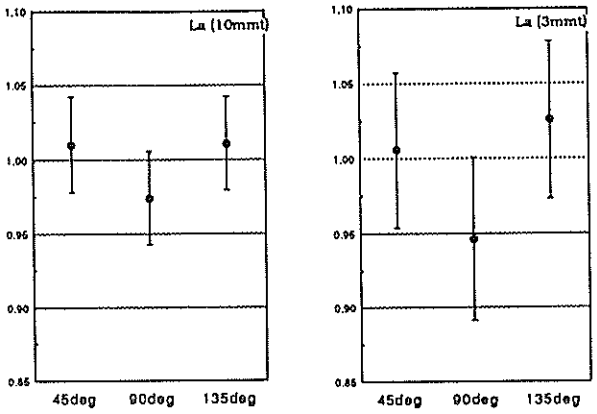

Fig. 2 Plotting of $a_{L,\gamma}(\vartheta_\gamma)$ /$A_{L,\gamma}$ for ^{139}La(E_n=0.734eV) p-wave resonance. Target thickness 3mm and 10mm.

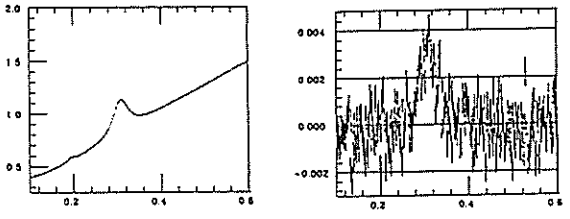

Fig. 3 TOF spectrum of CBr_4 counts in arbitrary unit (left) and TOF spectrum of $(N_+-N_-)/(N_++N_-)$ (right). Here N_+ and N_- are gamma ray raw counts for positive and negative helicity incident neutrons, respectively. The x-axis is shown in wave length of incident neutrons (Angstrom).

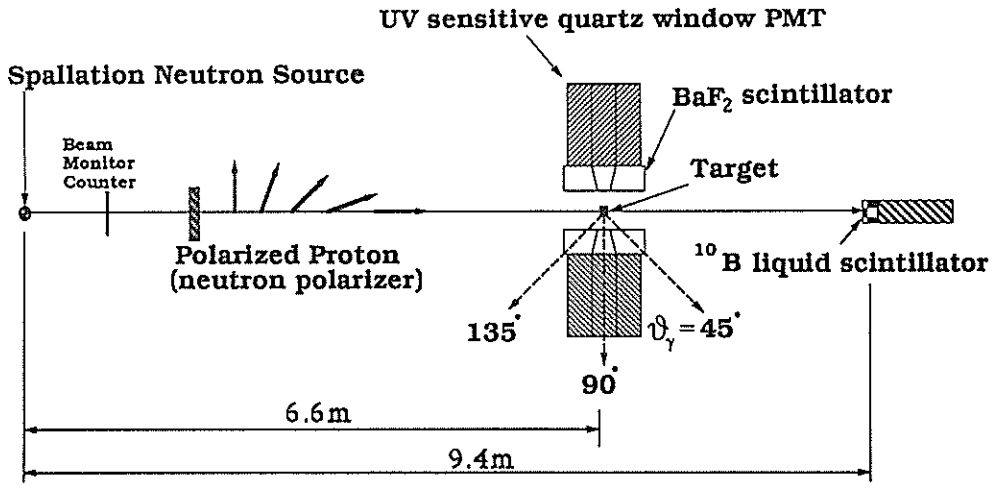

Fig. 1 Schematic view of experimental setup.

2. Instrumentations

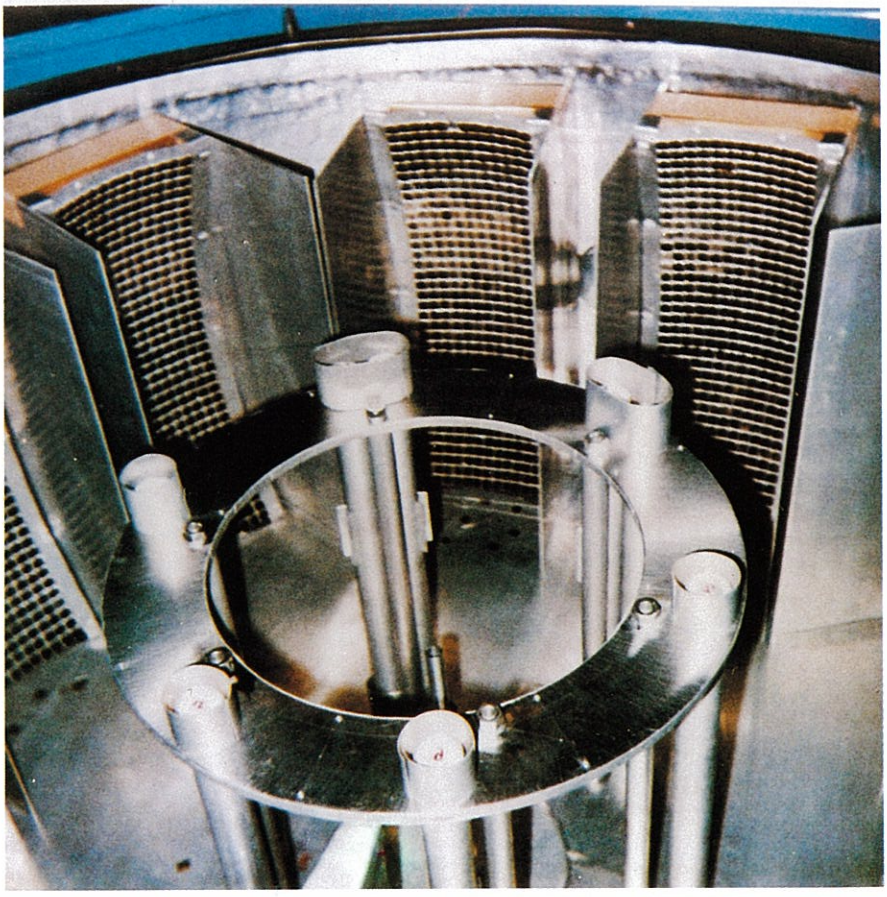

Photograph of LAM-80ET

Resolution Function of MAX

Y.TODATE, K.TAJIMA†, H.IKEDA†† and S.TOMIYOSHI*

Department of Physics, Faculty of Science,
Ochanomizu University, Otsuka,Bunkyo-ku,Tokyo 112
†Department of Physics, Faculty of Science and Technology,
Keio University, Hiyoshi, Yokohama 223
††National Laboratory for High Energy Physics, Oho, Tsukuba 305
*Institute for Materials Research ,Tohoku University, Sendai 980

Analytical resolution function of MAX was derived and examined experimentally. The derivation is based on the formalism of Cooper and Nathans [1], Komura and Cooper [2] and Windsor and Heenan [3]. Since, as is usual, Gaussian distributions were assumed for all the broadenings which occur due to the finite angular collimations, the mosaic of the analyser crystal, the time distribution of the neutron pulse and the time broadenings due to the finite sample size or gate width, the resolution function can be expressed analytically in terms of a Gaussian form in the 4-dimensional (Q , ω) space. Derivation of the resolution function and the resolution matrix of MAX is shown in reference 4. Here we only give a useful expression for the energy width which can be derived from the resolution function:

$$(\Delta \hbar\omega)^2 = 4E_I^2\left[\left(\frac{\tau}{T_I}\right)^2 + \left(\frac{E_F}{E_I} + \frac{L_F}{L_I}\sqrt{\frac{E_I}{E_F}}\right)^2 \cot^2\theta_A \left(\Delta\Theta_A\right)^2\right]. \quad (1)$$

τ in the time part is $\tau^2=\tau_m^2+\tau_s^2+\tau_c^2$ and $\Delta\Theta_A$ in the analyser (angular) part is

$$\left(\Delta\Theta_A\right)^2 = \frac{\alpha_2^2\alpha_3^2 + \alpha_3^2\eta_A^2 + \eta_A^2\alpha_2^2}{\alpha_2^2 + \alpha_3^2 + 4\eta_A^2}.$$

α_2 (α_3) corresponds to the divergence angle of the collimator placed between sample to analyser (analyser to detector) and η_A is the mosaicness of the analyser crystal. The time distribution of incident neutron pulse is a function of wavelength. At a shorter wavelength region (< 0.8 Å), for example, its width τ_m is proportional to the wavelength: $\tau_m(\mu\text{sec}) \approx 60/k_i$ (Å^{-1}). τ_s gives the finite sample size time broadening and is order of several micro seconds. τ_c is chosen to be 0.29 × (channel width) so that the Gaussian has the same standard deviation as the actual distribution caused by the finite time channel width. Usually τ_m is the largest compared with the others: τ_s and τ_c. Parameters α_2, α_3 and η_A in the analyser part were determined so as to reproduce the observed energy width. We have plotted in Fig. 1 the observed energy width of incoherent elastic scattering from Vanadium for various collimations. The calculated widths using eq.(1) are indicated by solid lines in the figure. Note that, by putting $E_F = E_I$, the elastic width for the analyser part of eq.(1) depends on E_F as $E_F^{3/2}$. It is apparent that this analyser part mainly contributes to the resolution of the instrument because the observed E_F dependence of the width is very close to $E_F^{3/2}$ as indicated by a dotted line in Fig. 1. Figure 2 is a graph of calculated energy width as a function of E_F and $\hbar\omega = E_I - E_F$. In the figures the nominal aperture angles of the Sollar collimators are denoted as 20', 30', ... ("B" : without the Sollar collimator).

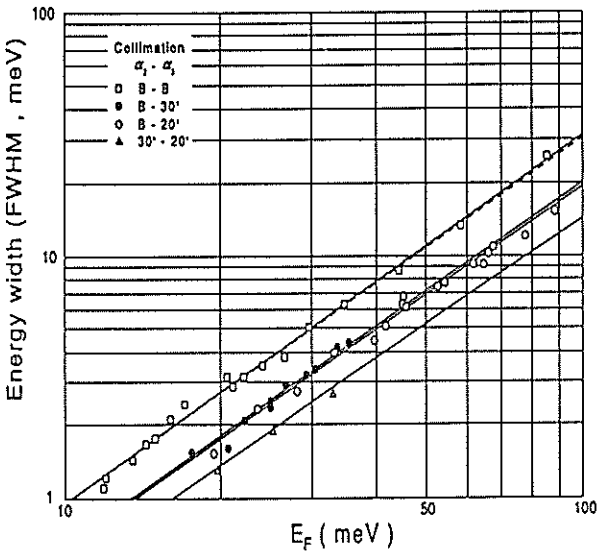

Fig.1 Observed and calculated (solid lines) energy resolution of MAX for various collimations as functions of E_F at $\hbar\omega$ =0. The dotted line shows $E_F^{3/2}$ dependence of the width.

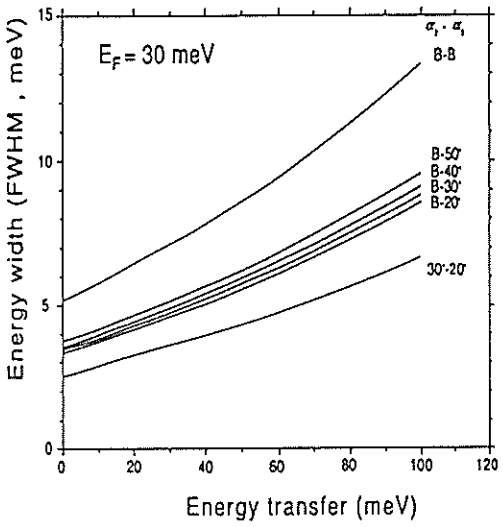

Fig.2 Calculated energy width as a function of $\hbar\omega$ in the case of E_F =30meV.

We have also measured the spatial shape of the resolution at the elastic position by using Bragg scattering from a small perfect Ge single crystal. A spatial map of the intensity was drawn by rocking the sample and the analyser. Good agreement was obtained in both volume and spatial orientation of the resolution ellipsoid. By using the resolution function derived here the effect of the spectrometer configuration on the resolution was estimated. The volume of the ellipsoid for the present configuration (with the detector arms rotated clockwise) is larger than the previous one (counterclockwise rotation or "W-configuration"). However, present configuration has more flexibility. In cases of coarse collimations these differences are small and may not be important. When, however, a good resolution is required, we must take into account the effect of focusing in order to minimize the peak broadening.

Occasionally, observed peak shapes do not have the symmetric Gaussian form because the incident neutron pulse has the asymmetric time distribution. The resolution function derived above cannot reproduce this asymmetry. With the detailed information on the time structure of the neutron pulse,[5] full numerical calculation of the resolution function is now in progress for crucial quantitative estimation of the resolution effect. The resolution function derived analytically may be useful for qualitative discussion of the instrumental resolution characteristics.

References

1) M.J. Cooper and R. Nathans: Acta. Crystallogr. 23 (1967) 357.
2) S. Komura and M.J. Cooper: Jpn. J. Appl. Phys. 9 (1970) 866.
3) C.G. Windsor and R.K. Heenan: Nucl. Instrum. & Methods **171** (1980) 115.
4) Y.Todate, K.Tajima, H.Ikeda and S.Tomiyoshi: Jpn. J. Appl. Phys. (in press).
5) S. Ikeda, J.M. Carpenter: Nucle. Instrum. & Methods A239(1985)536.

Improvement of LAM-80ET

K.Inoue, T.Kanaya*, S.Ikeda**, Y.Kiyanagi, K.Shibata***, T.Kamiyama***, H.Iwasa, and Y.Izumi****

Department of Nuclear Enineering, Hokkaido University, Sapporo 060
*Institute for Chemical Research, Kyoto University, Uji, Kyoto 611
**National Laboratory for High Energy Physics, Tsukuba, Ibaraki 305
***Institute for Material Research, Tohoku University, Sendai, Miyagi 980
****Macromolecular Research Laboratory, Yamagata University, Yonezawa, Yamagata 992

The down-scattering crystal spectrometer LAM-80 using mica analyzers[1] was improved in order to gain high intensity without changing the resolution. The improved LAM-80 (LAM-80ET) gave a desirable performance of energy resolution accompanying by a surprisingly sharp rise shape of resolution function on the energy loss scattering side and gained 8 times intensity.

Figure 1 shows the configuration of the LAM-80ET. The structural frames supporting the crystal pieces were fabricated according to the same design method reported previously[2]. The spectrometer is installed at the C-2 neutron guide hole, of which the distance from the cold source is about 26 m. As seen in the figure, there are eight identical mirrors, each containing 400 mica crystal pieces of 12mmx12mmx3mm in size. Each analyzer mirrors are mounted at four fixed angles: ±15°, ±51.7°, ±78°, and ±118°.

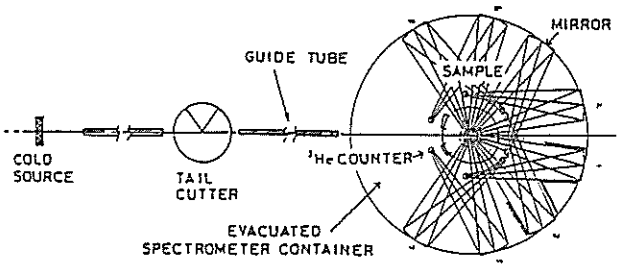

Fig. 1 The configuration of the high resolution quasielastic spectrometer (LAM-80ET)

The LAM-80ET adopts the mirror of 4 times large size compared with that of the LAM-80. This generally means that the intensity gain is 4 times and the resolution is much worse. However, there is a solution in which the intensity gain is held without changing the resolution. Figure 2 shows the typical results of the resolution function for two reflections from mica. The solid lines are the vanadium runs by the LAM-80 and the filled circles are those by LAM-80ET. From this figure, one can see that the resolution for the LAM-80ET is almost the same as that for the LAM-80.

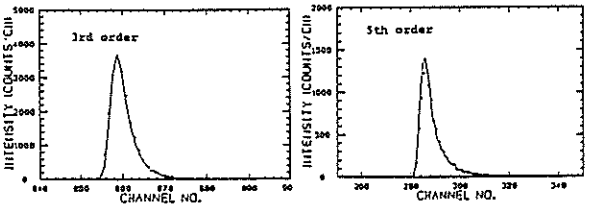

Fig. 2 The typical results of the resolution functions for the reflections (006) and (0010).

Figure 3 shows a comparison between the intensities obtained by using the LAM-80 and the LAM-80ET. The scattering sample was vanadium at ambient temperature. The intensity was normalized by monitor counts. One can see that the total intensity for the LAM-80ET is now 8 times compared with LAM-80 for each reflection from mica.

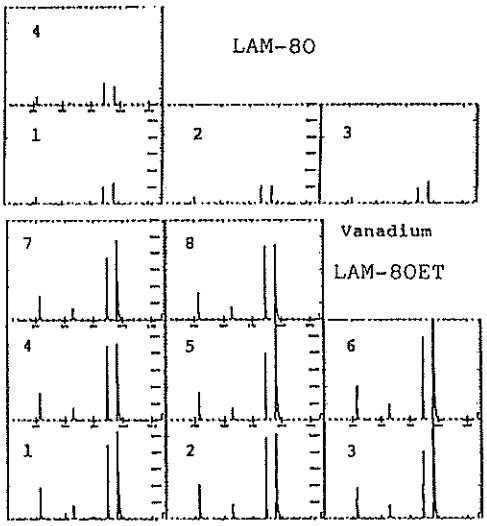

Fig. 3 A comparison between the intensities obtained by using the LAM-80 (up) and LAM-80ET (down).

These results indicate the usefulness of the LAM-80ET in the quasielastic neutron scattering studies of fluctuational and low energy motions in condensed matters.

1)K.Inoue et al., KENS Report-VII, 17(1987/88).
2)K.Inoue et al., Nucl.Instr. & Meth. A238,401(1985).

Development of Thermal Neutron Small Angle Scattering Spectrometer (WIT)

N. NIIMURA, K. AIZAWA*, U. SANGAWA and M. HIRAI**

Laboratory of Nuclear Science, Tohoku University, 1-2 Mikamine, Sendai 982
* Institute for Materials Research, Tohoku University,Sendai 980
**Kanagawa Institute of Technology, 1030 Shimo-ogino, Atsugi-shi 243-02

1. Introduction

We have developed a thermal neutron small-angle scattering spectrometer installed at the pulsed thermal neutron source. The first report on general survey of the spectrometer has been already given in this report.[1] Afterwards several modifications of some parts have been carried out on WIT.

A new optical system of an annular detector,that is, eight photomultipliers (PMTs) are coupled to the rear side of annular acrylic resin,on the front surface of which pieces of Li glass scintillators (2 mm in thickness) were stuck has been tested and reported preliminarily. [2]

A converging Soller slit system has been replaced by a converging pin hole slit in order to increase transmission of incident neutrons.

A special beam stopper which provides both scattering and transmission measurements of a sample simultaniously has been designed and installed.

In this report the modified principal parts above mentioned are explained with several experimental results.

2. Layout of WIT

The current layout of WIT is given in Fig. 1.

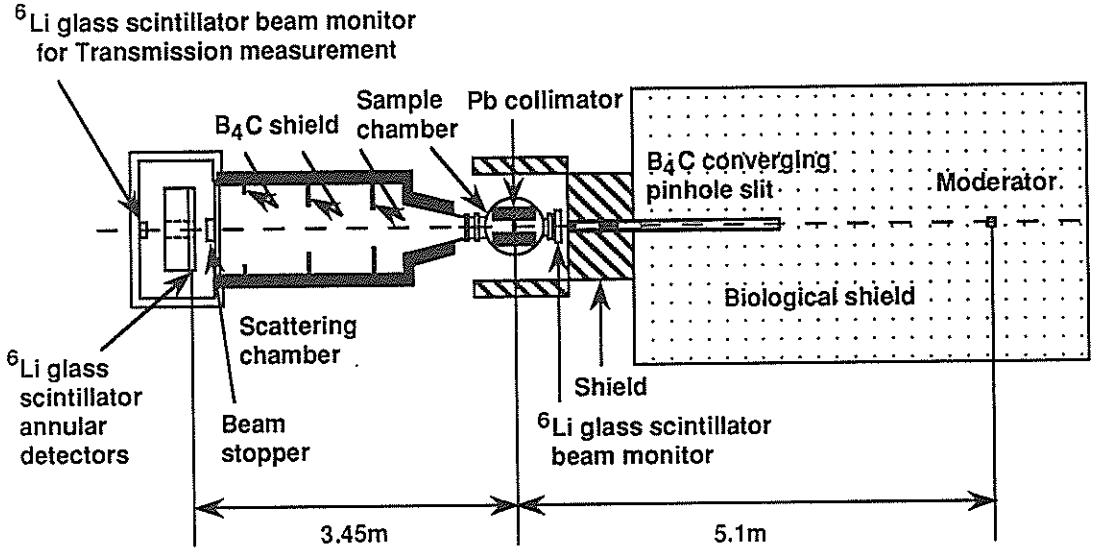

Fig. 1. The current layout of WIT.

3. Annular detectors equipped with glass scintillator

Pieces of Li glass scintillators (2 mm in thickness) were stuck on the surface of the annular transparent acrylic resin with optical cement. The ring was wrapped with aluminium foil to reflect scintillation photons escaping out of the acrylic resin. As shown in Fig. 2., eight PMTs were coupled to the rear side of the annular acrylic resin. Thickness of the acrylic resin has been determined to be 5 cm so that any position where a scintillation event occurs can be subtended directly by more than two PMTs, to allow detection of scintillation photons in coincidence.

The whole assembly of the annular detectors is given in Fig. 3, where #1 and #2 are not used for measurement any more because the foot of the incident beam profile touches them, and #11 is neither used because PMTs are not yet installed there.

The Q-range covered by the detector assembly is from 0.027 A^{-1} to 0.967 A^{-1} when neutron wavelengths from 0.5 A to 6 A are used.

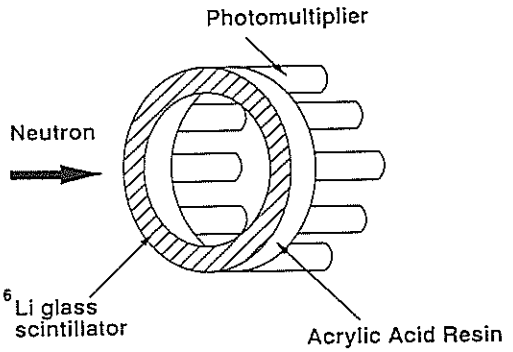

Fig. 2. The schematic layout of the annular detector.

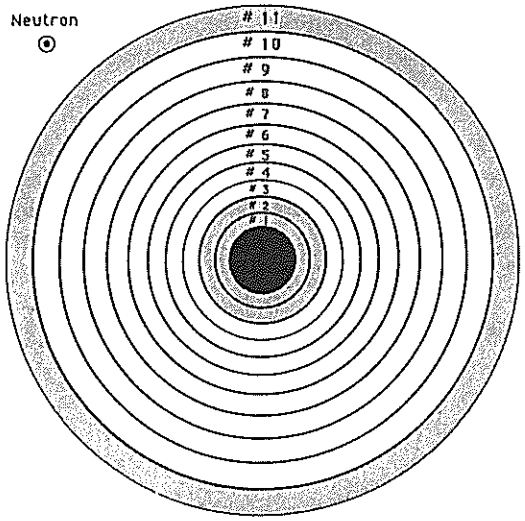

Fig. 3. The assembly of the annular detectors.

4. Slit system

An initial slit system was a two-dimensional converging Soller collimator. Transmission of incident neutrons through the collimator was found to be less than 2 % without considering a spatial resolution. In order to identify WIT as a spectrometer which covers Q-range from 0.02 to 0.1 A $^{-1}$, we have chosen higher intensity one even though spatial resolution might be sacrificed.

Two-dimensional converging Soller collimator was replaced by a converging pin-hole collimator which was developed in INC spectrometer.[3] The rectangular holes made by sintered B_4C plates and steels were alternatively placed at about 15cm interval to realize converging condition of focusing on the center of the detector position. The sizes of inlet and exit are 47 mm * 47 mm and 32 mm * 32 mm respectively. The distance between them is 2870 mm.

The beam profiles through the slit system were measured at the sample and detector position and are shown in Fig. 4. The full width at half maxima is the one expected from the geometrical conditions of the slit system. The calculated Q resolution assuming the above results is shown in Fig. 5.

The intensity at the sample position is increased about 40 times more than before.

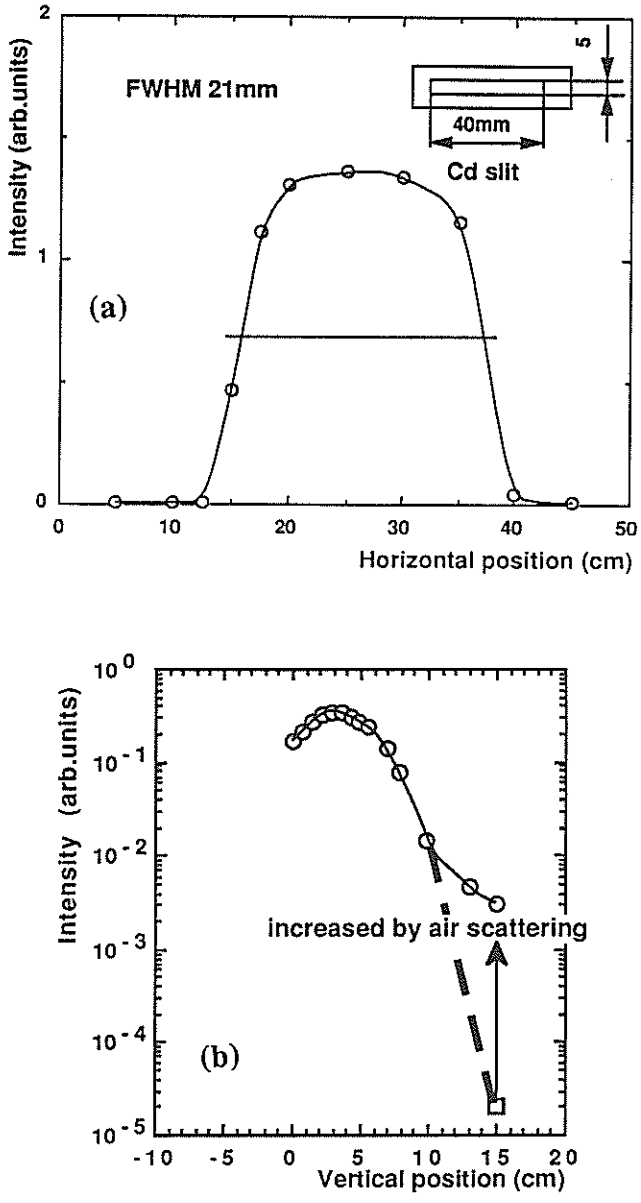

Fig. 4. The beam profile (a) at the sample position and (b) at the detector position, respectively through the slit system.

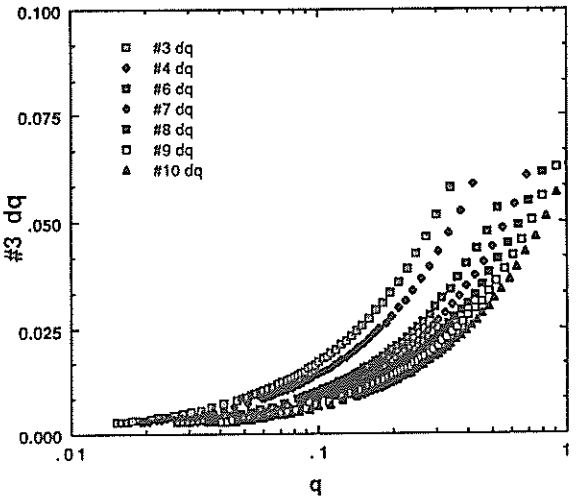

Fig. 5. The calculated Q resolution obtained by the new collimator system.

5. Beam stopper

In small-angle neutron scattering experiment, it is very important to measure neutron transmission of a sample, which is used as an absorption correction. In general, scattering and transmission measurement cannot be carried out simultaneously, because the detector system of each measurement is different. In the case of scattering measurement a beam stopper should be placed in front of the center of an area detector to prevent the detector from the damage of direct intense irradiation. On the contrary, in the case of transmission measurement the beam stopper must be removed and an attenuated neutron beam is used not to kill the detector.

We have specially designed and settled a new beam stopper which enables us to measure both scattering and transmission simultaneously. The schematic layout of the beam stopper is shown in Fig. 6. In the center of a cylinder (155 mm in diameter and 150 mm in length) which is made of B_4C powder solidified by epoxy resin, a hole of 5 mm in diameter is drilled as transmitted neutrons pass through. Moreover in our case it is not necessary to attenuate incident beams, because the transmitted neutrons are detected with another Li glass scintillator and the dead time of the glass scintillator is estimated to be less than 500 nsec.

The wavelength dependences of trnsmission have been measured both with and without the new beam stopper and both results have coinside within statistical errors.

The realization of the simultanious measurements of scattering and transmission provides several benefits, those are,

1) to save the maschine time,

2) to remove the nuisance to mount and then dismount the beam stopper, and

3) to avoid the unexpected change of sample which might occur between scattering and transmission measurements.

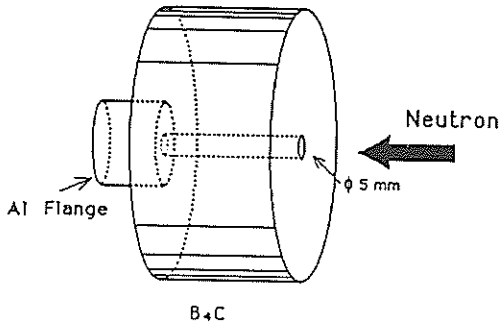

Fig. 6. The schematic layout of the beam stopper.

6. Several examples

Measurements of several samples have been made using WIT under the above mentioned conditions. Most of the results are given in this report.[4,5] As an typical result, obtained I(q) of SiC (623SIC) is shown in Fig. 7. The detailed method how to process raw data will be report separately elsewhere.

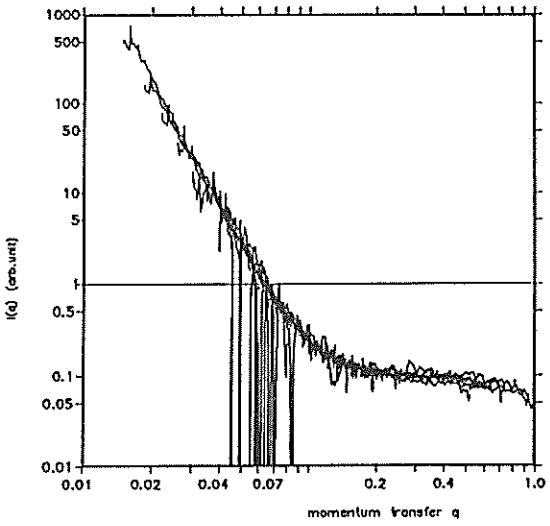

Fig. 7. The obtained I(Q) of SiC(623SIC).

references

1) N.Niimura *et al*; KENS REPORT VI (1985/86) 18-25

2) N.Niimura *et al.*;KENS REPORT VII (1987/88) 20

3) M.Arai *et al.*; KENS REPORT VII (1987/88) 9-15

4) U.Sangawa *et al;* KENS REPORT VIII (1989/90)

5) K.AIZAWA *et al;* KENS REPORT VIII (1989/90)

APPLICATION OF CROSSCORRELATION METHOD ON A PULSED POLARIZED WHITE NEUTRON BEAM

*H. Fujimoto, K. Ohoyama and M. Kohgi
Physics Department, Tohoku University, Sendai 980, Japan

1. Introduction

Polarized neutron technique is a powerful tool for studying magnetism in condensed matter. It has been mainly developed for the monochromatic polarized neutron beams in steady state reactors. In pulsed neutron sources, the technique has not yet been well established, because the conventional techniques in steady state neutron sources can not be directly applied to pulsed neutron spectroscopy. In implementing the polarized neutron technique at a pulsed neutron beam, it is especially important to utilize as many neutrons as possible, that is, to polarize incident neutrons in a broad energy band and to utilize all of them. The combination of the filter type polarizer and the crosscorrelation method at pulsed neutron sources is expected to be a good approximation to it. The aim of the present work is to show the feasibility of this technique.

2. Method

Crosscorrelation methods were first applied to unpolarized neutrons as the combination of statistical chopper and neutron time-of-flight (TOF) spectroscopy.[1] In this case, the monochromatic incident neutron beam is modulated in time according to a pseudorandom binary sequence (PRBS) by using a disk type chopper. The conventional TOF spectrum is recovered by the crosscorrelation of the count rate at the detector with the modulating sequence. This method can be expanded to polarized white neutron beam in pulsed source, where the polarization of the pulsed incident neutron beam is modulated by using a spin flipper coil whose driving current is modulated according to a PRBS.[2] The polarization modulation is controlled so that the PRBS pattern shifts cyclically at each sequential counting frame triggered by the neutron burst. The procedure continues until one cycle shift of the PRBS is finished, and then it repeats a new sequence of the counting of scattered neutrons. In this way, the scattered neutron events are counted in a two-dimensional time analyzer, one time label of which is the total TOF, and the other corresponding to the counting frame number which represents the shift number of the PRBS. The crosscorrelation of the count rate along the frame number axis at each total TOF channel with the PRBS patterns recovers the two dimensional TOF spectrum which is characterized by the incident time at the sample and the total TOF. Since only the polarization of the incident neutrons is modulated, the recovered TOF spectrum consists of a spectrum which is proportional to the difference between the spin flipper-on and -off spectra and an otherwise flat background.

A neutron spin flipper system and a two dimensional time analyzer were constructed for the present work. The flipper coil is made of aluminum wire (diameter 0.6 mm) and its size is $7 \times 4 \times 1$ cm^3. The direction of the field (along the longest side of the coil) is perpendicular to both the neutron beam and the guide field in which the coil is placed. The guide field inside the coil is canceled by using another coil which is wound on the flipper coil along its second longer side. The driving current intensity for the flipper coil is controlled to be proportional to the 1/t relation, where t is the time from each neutron burst, so that a 180 degree flip of the neutron spin is ensured for any incident neutron energy. The current is then switched on and off according to the PRBS. The timing of the switching is given by a module which generates the PRBS pattern which shifts by one step at each frame of the neutron burst. The scattered neutron events are counted in the appropriate memories in the two dimensional time analyzer according to their total flight time and frame number.

3. Experimental results

The polarized neutron scattering experiments were carried out on the PEN spectrometer at the spallation neutron source KENS at KEK. The spectrometer produces polarized white neutrons by passing the neutrons through a dynamically polarized proton filter. Typical neutron polarizations obtained by the spectrometer are 90 % at 100 meV and 70 % at 1 eV. Details of the spectrometer are described elsewhere.[3]

As an example of an application of the present technique, the observation of spin wave scattering will be described here. The experimental setup is shown schematically in Fig.1. Since the cross section for spin wave scattering in ferromagnets has a term which is proportional to the incident neutron polarization if the magnetization is parallel to the scattering vector, it can be observed by using the present technique with no

*Present address:National Research Laboratory of Metrology, Umezono 1-1-4, Tsukuba, Ibaraki 305, Japan

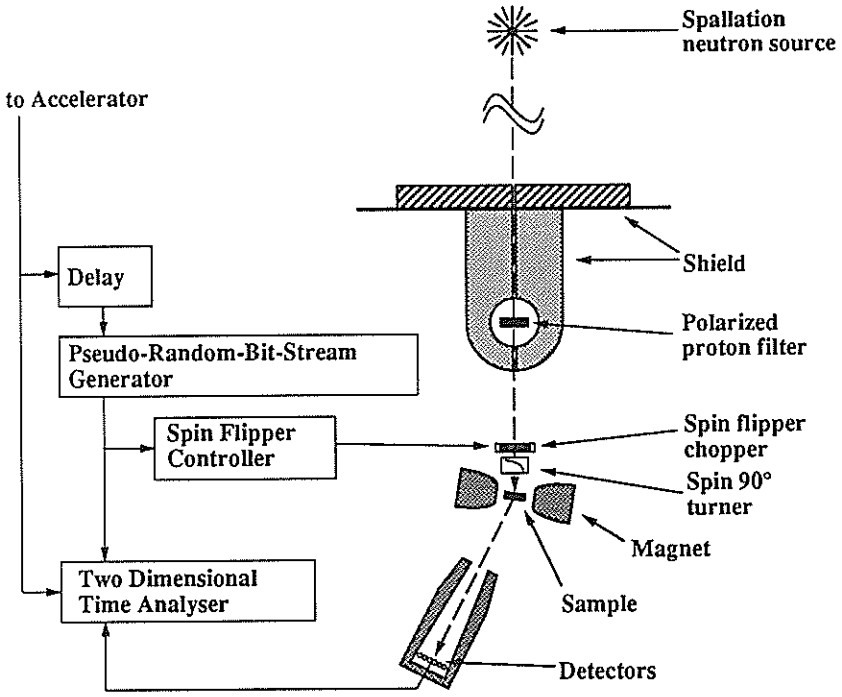

Fig.1. Experimental setup of the crosscorrelation method at the KENS pulsed neutron source.

spin analyzing device in the scattered neutron beam. The sample was a single crystal of ferromagnetic Heusler alloy Cu_2MnAl, the size of which is 3 x 2 x 0.8 cm^3. The sample position from the neutron source was 7 m. The crystal was oriented so that the [111] reciprocal lattice vector coincided with the scattering vector of neutrons with initial and final energies of 50 and 42 meV, respectively. A magnetic field of 1 T was applied to the sample along the reciprocal lattice vector. Therefore scattering with an energy loss of around 10 meV is expected to be observed for the case where the energy and momentum conservation law is fulfilled on the dispersion surface of the spin wave excitation, that is, $D(k-\tau)^2$, where D is the spin wave stiffness constant (175 $meVA^2$ for Cu_2MnAl), k is the scattering vector and τ is the (111) reciprocal lattice vector. Since the magnetization of the sample is almost parallel to the scattering vector, only those incident neutrons whose polarization is parallel to the magnetization are scattered. Therefore, the difference spectrum between the spin flipper-on and -off spectra corresponds to the spin wave scattering cross section. The flipper coil was placed 50 cm upstream from the sample. The polarization of the neutrons with energy from 30 to 80 meV was modulated by the spin flipper according to a PRBS of 31 steps. The time unit of the sequence was 30 μs. The scattered neutrons were detected by ^3He detectors placed at a distance of 1.5 m from the sample.

Fig.2 shows the spectrum recovered from the crosscorrelation of the count rate with the PRBS patterns at a detector with scattering angle of 21.8 degrees (detector 3). The data at contiguous total TOF channels from 170 to 174 (the channel width was 16 μs), whose loca of scans pass through the middle of the dispersion surface, are plotted together in the figure as a function of energy transfer. Since their loca of the inelastic scans in the scattering plane are close to each other and cross the dispersion surface twice, the scattering is expected to occur at two energy transfers, that is, around 5 and 14 meV. Although the energy resolution is not high and the counting statistics are rather low, a clear peak at around 5 meV and a hump at around 14 meV are visible in the figure. The reason that only the peak at 5 meV is distinct is due to the difference of the temperature factors between the two peaks. The solid line shows the result of a simulation of the spin wave scattering in the present configuration. In the simulation, the neutron pulse shape at the moderator and the time uncertainty at the spin flipper

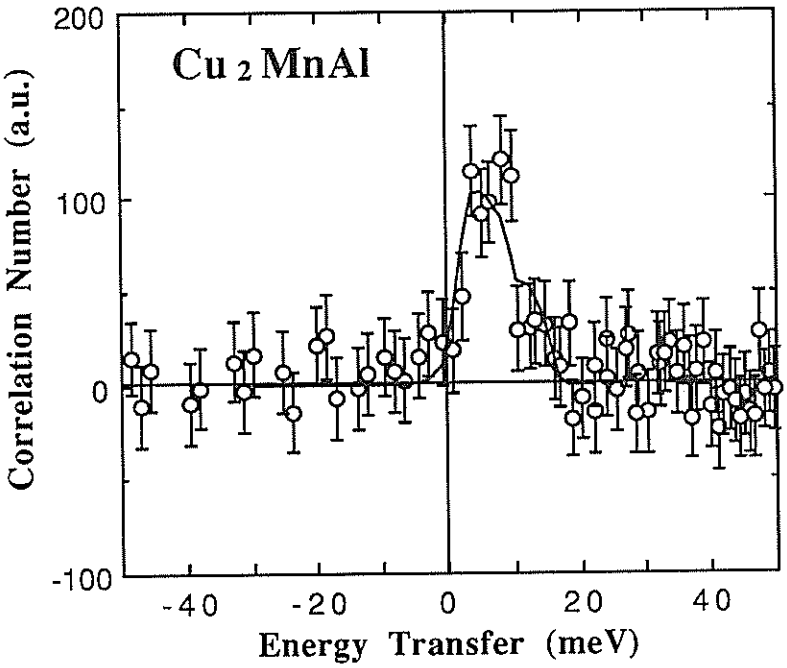

Fig.2. Observed spin wave scattering from Cu 2 MnAl

were taken into account. It can be seen that the observed spectrum is in good agreement with that of the simulation. Nearly the same results were obtained for the other data with total TOF from about 140 to 200 channels. This means that the spin wave scattering was observed with incident neutrons whose energies ranged from about 40 to 70 meV. It is in good agreement with our expectations under these scattering conditions.

4. Summary

The results of the present experiment show that the combination of the pulsed polarized white neutron beam with the crosscorrelation method with polarization modulation is quite promising for the study of magnetic excitations or fluctuations in various magnetic materials. In the present experiment, the energy resolution dE/Ei was about 12 % at the incident and final energies of 50 and 40 meV respectively. However, there is no difficulty in improving the resolution to the order of a few % if the neutron source intensity permits it; for example, if the time unit of the modulation sequence and the incident and final flight lengths were chosen to be the moderate values of 10 μs, 11 m and 4 m, respectively, the resolution is expected to be about 2 %.

Although in the present experimental configuration no spin analyzer was used in the scattered beam, this configuration used with a spin analyzer will provide the full power of the technique. By using a broad energy band spin analyzer in the scattered beam, the crosscorrelation technique should allow a dense mapping in momentum and energy space of the magnetic dynamical response of all kinds of magnetic materials in a single measurement. In order to obtain results with good resolution an intense pulsed neutron source is required of course.

References

1) F. Gompf,W. Reichardt, W. Gläser and K. H. Beckurts,Neutron Inelastic Scattering (Proc. Symp. Copenhagen, 1968)2, IAEA, Vienna (1968) 417.

2) R. Cywinski and W. G. Williams, Nucl. Instr. and Meth. 228(1985)406.

For the principles of the crosscorrelation method, see also the references herein.

3) M. Ishida, Y. Ishikawa, S. Ishimoto, M. Kohgi, A. Masaike, Y. Masuda, K. Morimoto and T. Nakajima, Proceedings of the Eighth Meeting of the International Collaboration on Advanced Neutron Sources, RAL-85-110(1985)612.

Neutron Compton Scattering with RAT

Y. NAKAI, H. ASANO, P. STEPHENS** and S. IKEDA*

Institute of Materials Science, University of Tsukuba, Tsukuba, Ibaraki 305
*National Laboratory for High Energy Physics, Tsukuba, Ibaraki 305
**Department of Physics, State University of New York, Stony Brook, New York

This report presents the results of a feasibility experiment of the neutron compton scattering (NCS) with RAT.

The set-up of the NCS experiment is shown in Fig.1. The collimator was specially designed for NCS and constructed with lead blocks and B_4C-regined plates in order to realize low-background and high S/N mesurements. Scattered neutrons were detected by the U-foil (12.5 x 50 mm, E_f=6.67eV), which was set at a scattering angle of 30°.

We chose TiH_2 as a standard sample, in which the hydrogen atom is bound in the almost harmonic potential well. The sample was contained in the aluminum cell (25 x 90 x 2mm) and cooled down to 20K in order to reduce the effect of thermal fluctuation.

To certify that the technique of NCS is available, it is required that the observed spectrum must be fitted with the calculated one. We calculated the TOF spectrum I(t) given by eq.(1) with the geometry function $G(x_D,x_S)$, probability function $P(t_0)$, detector energy resolution $P(E_f)$ and multiple scattering processes. Here, x_S is the position of the moderator, x_D the position of the detector, $S^H(Q,\omega)$ the scattering function for hydrogen, $S^{Ti}(Q,\omega)$ the scattering function for Ti. (l_i, l_f) and (v_i,v_f) are the neutron flight paths and velocities before and after the scattering, respectively. In this calculation we adopted the mean value of the momentum distribution, $\langle p\rangle$=5.97Å^{-1}, which was estimated from the result of CAT with the harmonic aproximation. As shown in Fig.2, the results of the calculation agree much more with the experimental data. In this figure, calculated single scattering from hydrogen and titanium, and multiple scattering are drawn as the broken lines. Sum of those are drawn as the solid line, and squares are the experimental data.

We also checked the spectra measured with higher-order resonance energies (20.90, 36.80, 66.15 eV) of the U-foil, and compared those with the calculated TOF profiles in the same manner. These fittings were also very well.

In conclusion, the NCS technique with RAT is available for studying the ground state wave function of hydrogen.

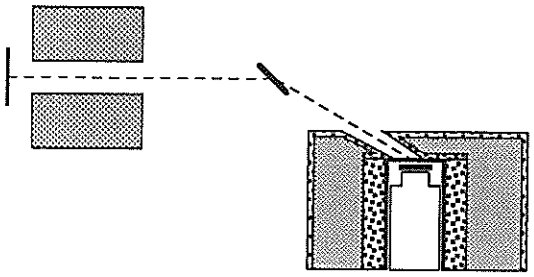

Fig. 1 The set-up of the NCS experiment

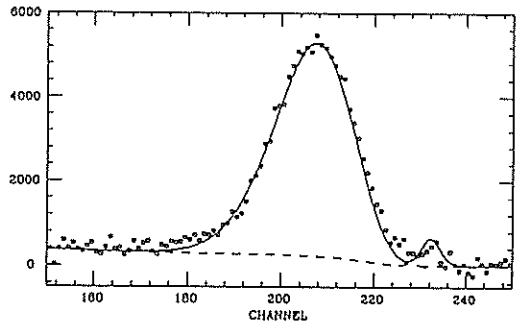

Fig. 2 Calculated line profile and observed one

$$I(t)=\int dx_S dx_D dt_0 dE_i G(x_D,x_S) I(E_i) P(t_0) P(E_f) [S^H(Q,\omega)+S^{Ti}(Q,\omega)] \delta\left(t - t_0 - \frac{l_f}{v_f} - \frac{l_i}{v_i}\right) \quad (1)$$

Position Sensitive Detector in MRP

H.Kawai , K.Yamada , and Y.Endoh

Physics Department, Faculty of Science,Tohoku University, Sendai, Japan

A position sensitive detector(PSD) is able to scan a wide reciprocal space simultaneously when it is combined with Time-Of-Flight (TOF) method. Here we present the characteristics of the PSD recently installed in MRP and a single crystal measurement by using the PSD. The ^{3}He gas-type proportional detector is utilized as the one dimensional PSD (Reuter-Stokes, 1' in diameter; 24' in sensitive length ; 10 atom. gas pressure). The bias voltage of 1.85kV is provided to the detector. Out put neutron pulses from both ends of the detector are amplified through a charge sensitive pre-amplifier (ORTEC Model 142PC) and a delay line amplifier (ORTEC Model 460). The output pulses from the amplifiers are peak-holded to determine both position and TOF of each event by the multi-dimensional time analyzer. The PSD has 128 channels in position and 1024 channels in time. The position resolution and linearity are measured by using a cadmium plate with 5mm wide slits in 50mm intervals, placed in front of the detector and the incoherent scattering from vanadium powder. As shown in Fig.1 the observed pattern of the neutrons passed through the slits has Full-Width-Half-Maximum in 2 or 3 position channels that corresponds to 10 ~15 mm. The uniformity of the detective efficiency has been measured by using vanadium powder. The uniformity is constant within 15% in the position channels between 15 and 110. Final adjustment and the computer control of the goniometer will be finished by the end of this year.

The magnetic successive phase transitions from the single crystal $PrCo_2Si_2$ (~ 0.4cc) have been measured by using the PSD. The Fig.2 shows the TOF spectra measured at 15K for 1.5 hours. The magnetic peaks from the incommensurate magnetic structure of the Pr spins ($3.2\mu_B$) with the k vectors of 0.074 and 0.223 in c* unit ($0.63Å^{-1}$) are clearly observed.. The background is very clean in this Q region. This PSD will be utilized effectively for the measurements under extreme sample conditions such as high magnetic field or high pressure.

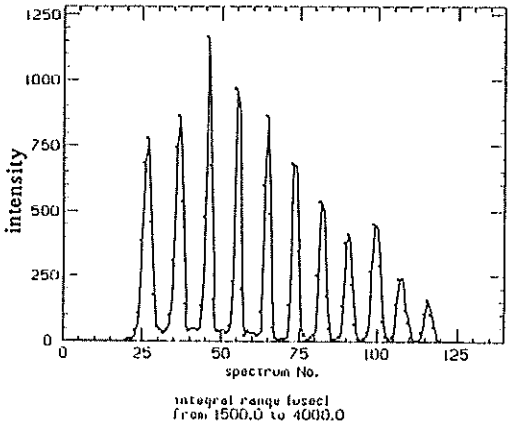

Fig. 1 Slit pattern in PSD; spectrum number (=position channel) vs. TOF integrated intensity.

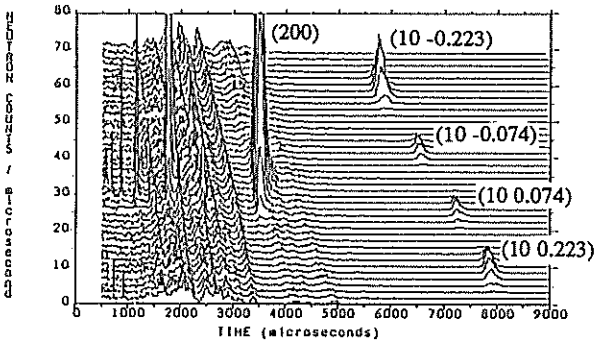

Fig. 2 TOF spectra of $PrCo_2Si_2$ single crystal at 15K.

More on Cooling Mark-3000 and a Test Measurement

H. YOSHIKI and S. ISHIMOTO KEK
S. TANAKA, A. YAMAGUCHI, K. SAKAI and M. OGURA University of Tohoku
T. KAWAI KUR, University of Kyoto

In the previous volume[1] we reported on the 3 meter horizontal cryostat designed to produce ultracold neutrons (UCN) by means of superthermal liquid helium and 9A cold neutrons[2]. We report what has been achieved since then. The assembly of roots pumps ($2000m^3/hr$ + $350m^3/hr$) and a rotary pump ($60m^3/hr$) of Alcatel Co. for He^3 refrigeration has been raised by 1.4m to increase the conductance of the circulating He^3 gas. A similar measure was taken for the 1K pumps to increase the precooling power for the liquid He^3 in 1K helium pot. These resulted in the improvement of the final temperature of the 15 litre liquid helium of the UCN bottle from 0.75K as reported[1] previously to 0.65K.

Fig.1 shows the temperature change with time. The precooling started on March 22 and the liquid pouring began on March 31 and on April 3 the UCN bottle was filled with the liquid whose temperature was below 4.2K. The circulation of He^3 followed immediately and in the dawn of April 6 the temperature reached 0.65K. We expected the cold neutron beam at this moment but it delayed until April 12 with 1/3 of the usual beam intensity. On April 14 we rose the temperature for the planned transmission experiment. We could create very stable temperatures by means of a heater in the vessel while the He^3 circulation remained intact. We can see this by stepwise temperature variation in Fig.1 from April 15 to 20. The apparent peak on the 20th has in fact a flat top since the measuremnt time is shorter for a high temperature. The beam was swithced over to the meson group on April 21. We kept the liquid in the UCN bottle and tried to keep it cold during this idle period while turning off the He^3 circulation and only keeping 1K pot pumped down. The transfer of about 60 litres of liquid helium each time was carried out twice a day. However because the thermal coupling between the 1K pot and the UCN bottle is weak, the temperature of the bottle liquid inevitably rose up to 4.2K (1 atm) on April 30. From May 6 we experienced first time cooling the bottle liquid of 4.2K solely depending on the He^3 circulation. The He^3 circulation had been started at 2.5-3K till then, since the precooled liquid had been supplied by the 1K pot. Datafrom May 6 to 11 show the result.

In spite of several minus factors such as BS performance, cold source instabilities, we show raw (no correction) of transmission cross section of cold neutrons (10-17.5A) through the superthermal liquid at different tmeperatures. The overall fitting (broken line) looks less steep than what is expected from theory, but the data from 1.5 to 2K is fitted to $\exp(-(10.9\pm0.3)/T)$ (solid line). -11K is expected for the one phonon annihilation[3].

Remarks to follow are: 1) The thermal conductivity of the liquid He^4 below 1K has been measured on the sample of about 1mm in diameter[4]. No report has been made on such a large diameter (80 mm) and length (3000mm) as Mark-3000. We will look into this problem. 2) A better thermal contact between He^3 and He^4 must be devised (He^3 final temperature is 0.47K). We are designing a new refrigerator (fin type) to reduce the temperature difference. The planned high-power operation should be studied in this connection as well.

In conclusion, Mark-3000 has well showed its durability and stability as a future UCN generator.

1) KENS Report-VII (1987/88), KEK Progress Report 88-2, KEK, p.21
2) R.P.Feynman and M.Cohen, Phys.Rev.102(1956)21. R.Golub and J.M.Pendlebury, Phys.Lett.53A(1975) 133.
3) A.Griffin, KEK Report88-3(1988)p.8.
4) H.A.Fairbank and J.Wilks, Proc.Roy.Soc.Ser.A231 (1955)545.

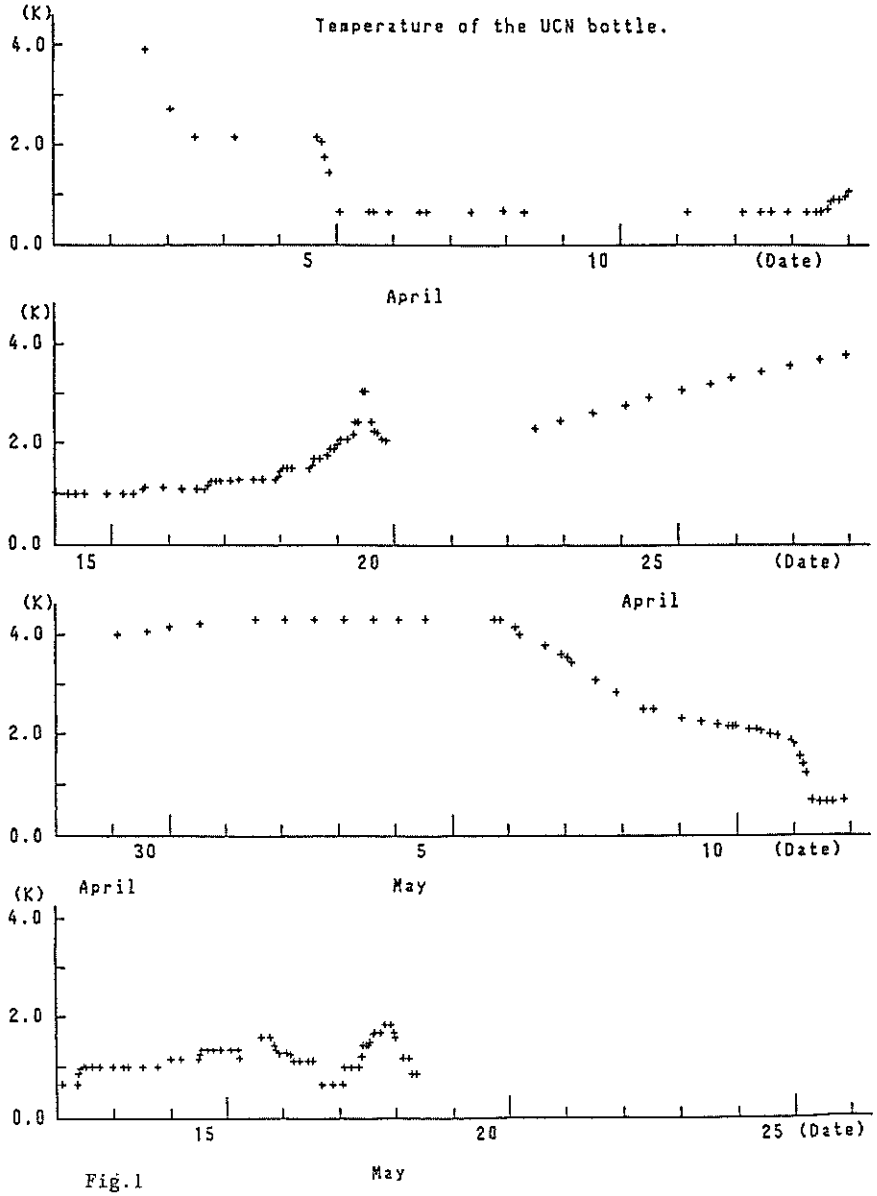
Temperature of the UCN bottle.
(K)
4.0
2.0
0.0
5
10
(Date)
April
15
20
25
30
May

Fig.1

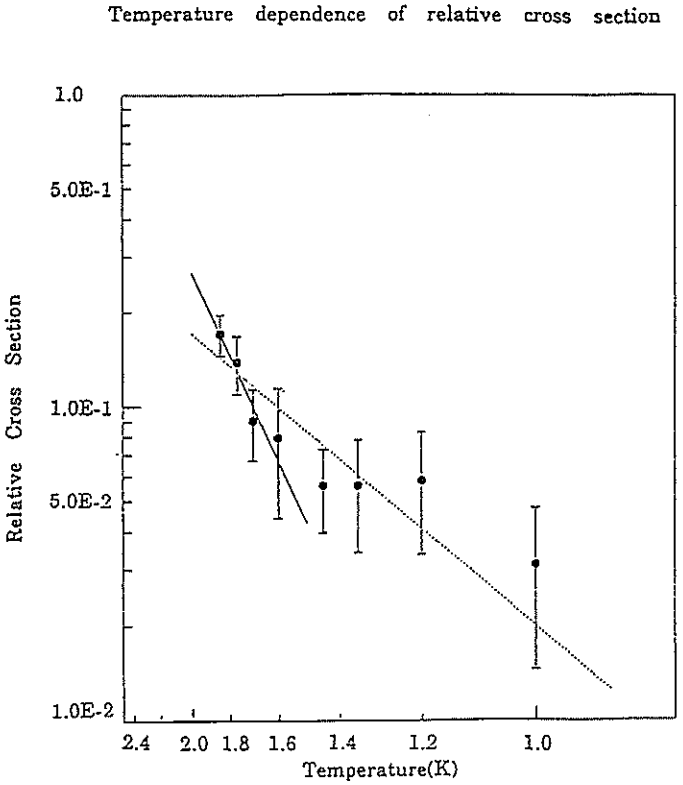
Temperature dependence of relative cross section
Relative Cross Section
1.0
5.0E-1
1.0E-1
5.0E-2
1.0E-2
2.4
2.0
1.8
1.6
1.4
1.2
1.0
Temperature(K)

Fig.2

Development of 8-Input Amplifier Module

S. SATOH, K. HASEGAWA* and M. FURUSAKA

National Laboratory for High Energy Physics, 1-1 Oho, Tsukuba-shi, Ibaraki 305
*Faculty of Engineering, Hosei University, 3-7-2 Kajio-cho, Koganei-shi, Tokyo 184

In recent years, there have been increasing opportunities to construct pulsed-neutron spectrometers which are equiped with a huge number of ^{3}He detectors ranging to 10^3.

Due to the limit of the space dimension of the detector bank, it is inevitable to develop a compact detector system. In addition to it, a development of diagnosing system for a detector system with a large number of detectors, amplifiers, discriminators etc. has been required for reliable operation of these.

We report here the development of new amplifier module which has the following characteristis: (1) one amplifier module with volume of 260 (width) × 70 (height) × 240 (depth) mm^3 contains 8 amplifieres and discriminators. (2) we can automatically make certain of the corect operation of all amplifiers and descriminators by using microcomputer. (3) as a power supply to the amplifier module, only AC100V in supplied to it, in which a high-voltage power supply for detectors is stored.

In Feg. 1, a block diagram of the amplifier module, which consists of 8 sets of amplifier units, high-voltage suppliy and digital controler, is depicted. In Feg. 2, is shown an electrical diagram of the amplifier unit, which consisits of integrator, differential circuit, filter, restorer and discriminator. A charge sensitive amplifier for detector is connected to Input and TTL level is to Output.

We show in Fig. 3 the whole amplifier system which is connected to the microcomputer through amplifier checker. Each amplifier module is connected to the others through daisy-chained line. During neutron experiment, amplifier checker's TestIn and TestOut are completely cut off by lead relay. This system has three functions for checking up each amplifier module by using microcomputer, which we call digital-check, analog-check and PHA-check respectively.

Digital-check is for confirmation of the total number of connected amplifier module and the high-voltage value. Analog-check is for the level of discriminators whithin 0.1 second. PHA-check is for each amplifier unit and we can analyze the output of it by PHA.

In this report we briefly explained the presert status of newly developed amplifier module which is quite compact enough and highly reliable. The system is now under operation at WINK instrument at KENS and maintains high performance. This system can be used by VAX through CAMAC.

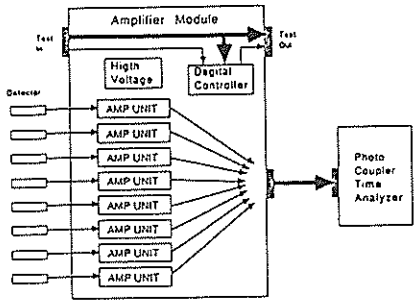

Fig. 1 Block diagram of amplifier module.

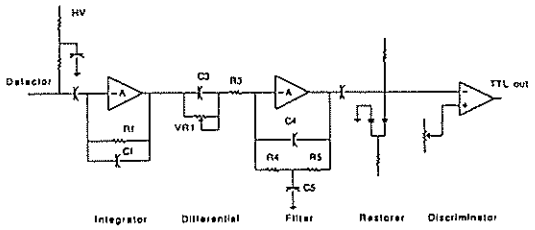

Fig. 2 Electrical diagram of the amplifier unit.

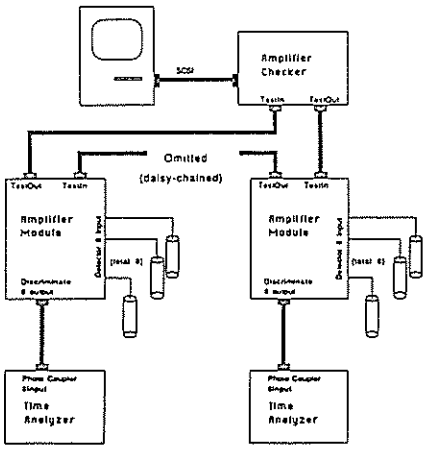

Fig. 3 The whole amplifier system.

3. Developments for Future Program

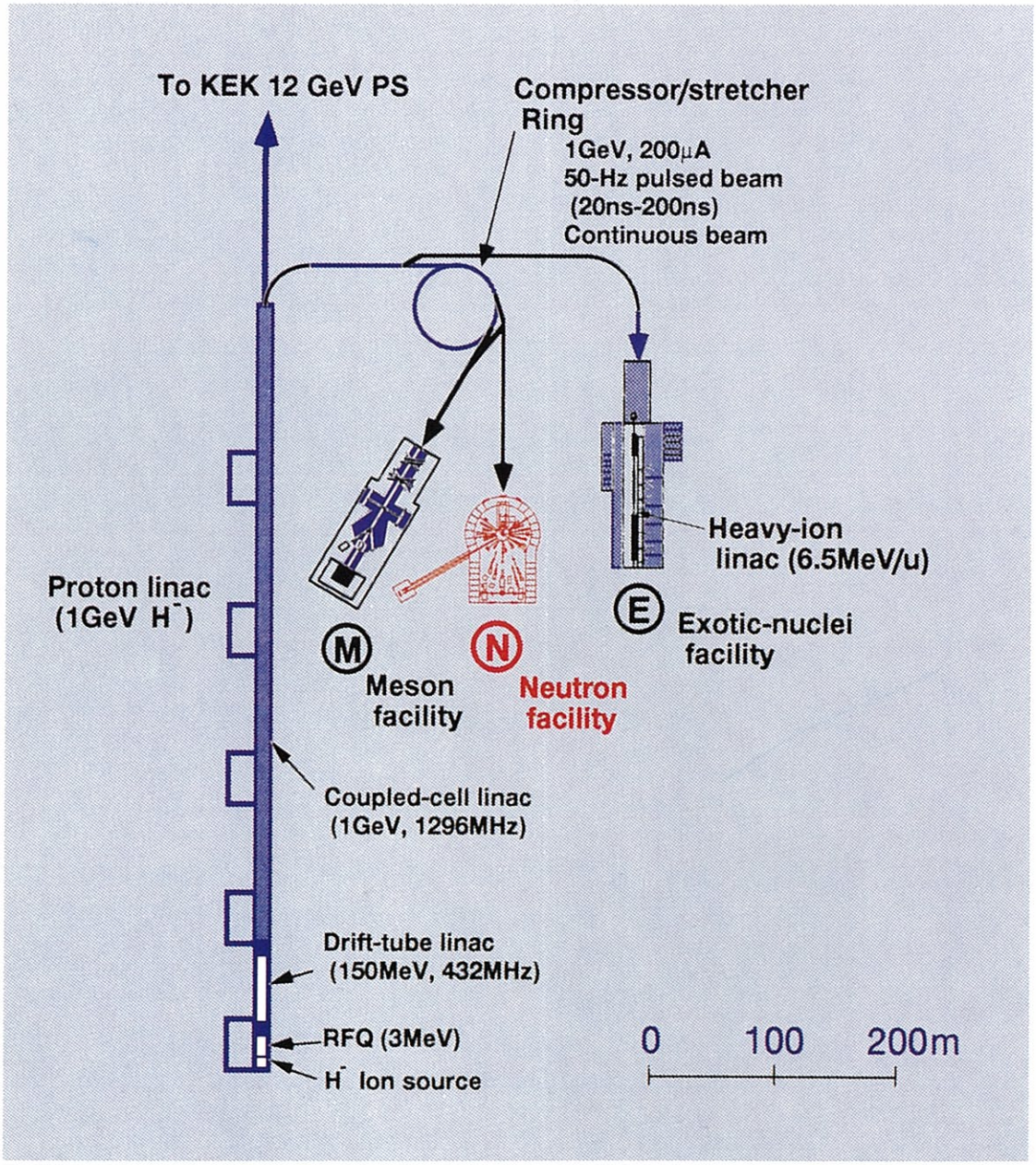

Layout of JHP

Premoderator Optimization Studies of Coupled Liquid Hydrogen Moderator

Y. KIYANAGI, N. WATANABE*, M. FURUSAKA*, H. IWASA and I. FUJIKAWA*

Department of Nuclear Engineering, Faculty of Engineering, Hokkaido University, Sapporo, 060 Japan
*National Laboratory for High Energy Physics, 1-1 Oho, Tsukuba-shi, Ibaraki, 305 Japan

One of the most important objectives for KENS-II is to realize an intense cold neutron source. A coupled liquid-hydrogen-moderator is one of the most promising candidates for this. It was revealed by our preliminary experiments[1] that the cold neutron intensity from a coupled hydrogen moderator in a wing geometry is very much higher than that from a decoupled one and also the pulse width is not broadened so much by coupling. These results encouraged us to perform further experiments using a dedicated cryostat to this moderator system.

The cryostat used in the preliminary experiments had a large void space above the moderator chamber, resulting in a large reflector missing. We prepared a new cryostat which has a slim neck above the moderator chamber. We studied the neutronic performance of coupled liquid-hydrogen-moderators in more detail. Here, we report the results of premoderator optimization.

Figure 1 shows a coupled liquid-hydrogen-moderator system used in the present experiments. The size of the liquid hydrogen moderator is fixed to 12×12×5 cm^3. Polyethylene plates are attached to a cryostat to compose a premoderator. The front part of the premoderator has a window of 12×12 cm^2 for extracting the neutron beam. A neutron generating target is placed just below the premoderator to form a wing geometry. The target and the moderator are surrounded by a graphite reflector of about $1m^3$. There is no decoupler between moderator and reflector; that means the system is a coupled one.

The electron linac at Hokkaido university was used as a fast neutron generator. Figure 2 shows the experimental arrangement for measurements of the time-of-flight spectra. The flight path length between moderator and He-3 neutron detector is 5.6 m. A set of Cd collimators is placed at both ends of an evacuated flight tube to define a viewed surface of the moderator 10×10 cm^2.

As a first step, we studied the effects of the premoderator thickness on the cold-neutron-beam intensity. Figure 3 shows the premoderator gain factor. We defined the premoderator gain factor as the ratio of the cold-neutron-beam intensity from a liquid-hydrogen-moderator with a premoderator to that from one without. The gain factor increases rapidly with increasing bottom-premoderator thickness and then saturates to a value of about 1.75. Side-premoderator brings about an additional gain of about 20 %, resulting in a premoderator gain factor of about 2 in total. The maximum appears at about 2 cm thick. We found that the bottom-premoderator is most effective for the intensity enhancement, while the effect of the side-premoderator is rather small. In

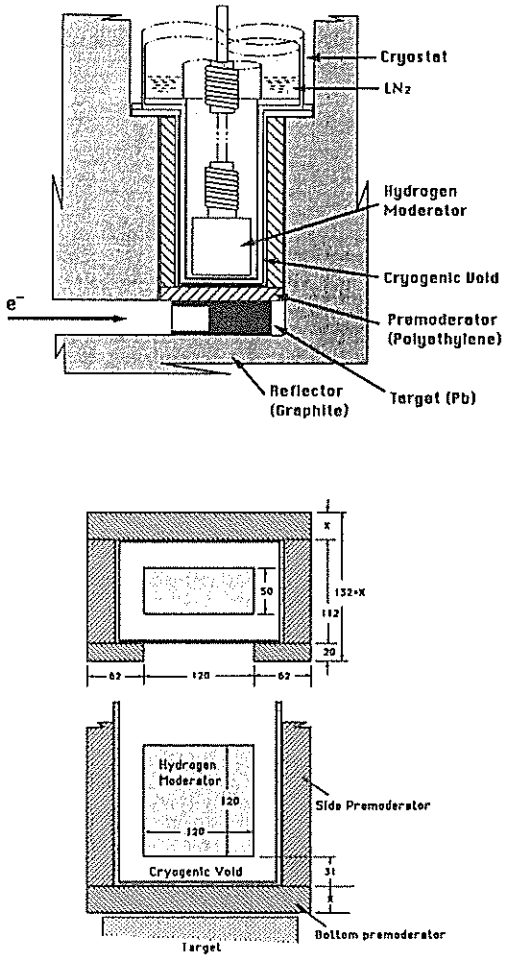

Fig. 1 Schematic representation of the target-moderator-reflector assembly. The lower figure shows the layout of the premoderator.

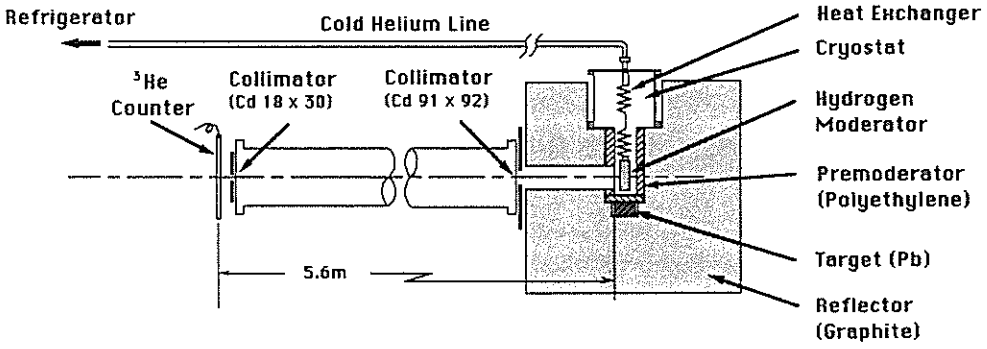

Fig. 2 Experimental arrangement for time-of-flight measurements.

the previous preliminary experiment we obtained the optimal premoderator thickness of about 3 cm. The smaller value in the present experiment is due to a better upper reflector and a higher height of the side-premoderator than before.

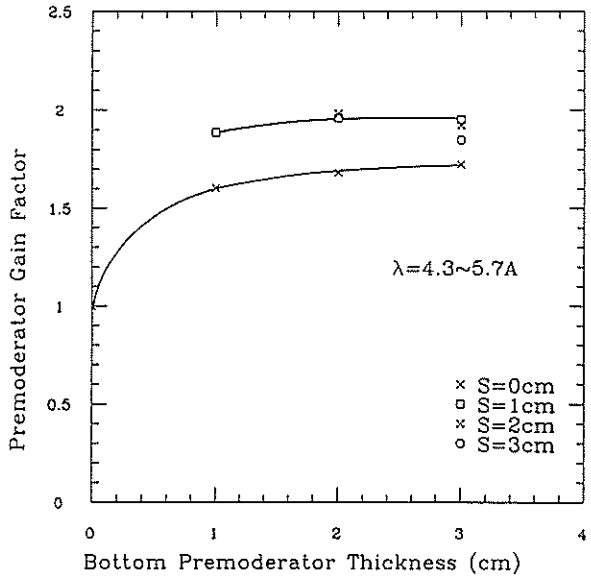

Fig. 3 Premoderator gain factor at wavelength 4.3~5.7A as a function of bottom- and side-premoderator thickness. S means side-premoderator thickness.

Figure 4 shows the energy spectra of neutrons from coupled and decoupled liquid-hydrogen-moderators. The energy spectra at the cold neutron region are not so different, except that the spectrum peak of the coupled moderator shifts slightly to a lower energy.

Figure 5 shows the wavelength dependence of the premoderator gain factor of the liquid-hydrogen-moderator with a 2 cm thick premoderator. There is a maximum around 2.5 A and above this wavelength the gain factor approaches 2.

Figure 6 shows the total gain factor of the coupled liquid-hydrogen-moderator with a 2 cm premoderator. The total gain factor is defined here as the ratio of the cold-neutron-beam intensity of this moderator to that of a reference decoupled 5 cm thick liquid-hydrogen-moderator. The total gain factor increases rapidly with increasing wavelength until about 3 A and approaches 6 in the long wavelength region. Very large values of the total gain factor were attained. The values are almost the same as previous ones in the preliminary experiments. However, the absolute

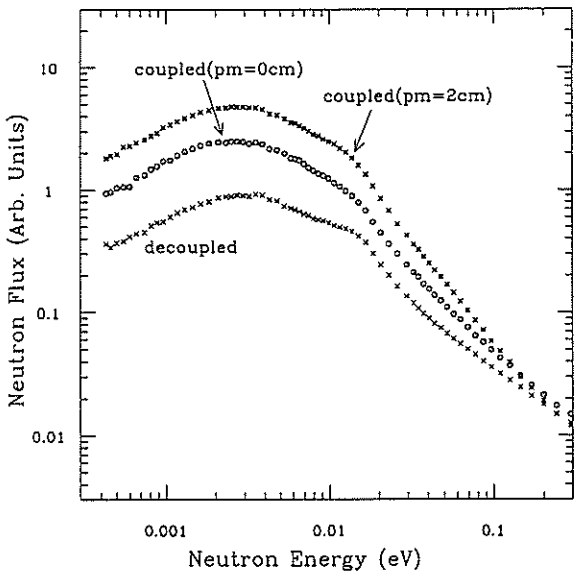

Fig. 4 Energy spectra of coupled and decoupled liquid-hydrogen-moderators. pm means premoderator thickness.

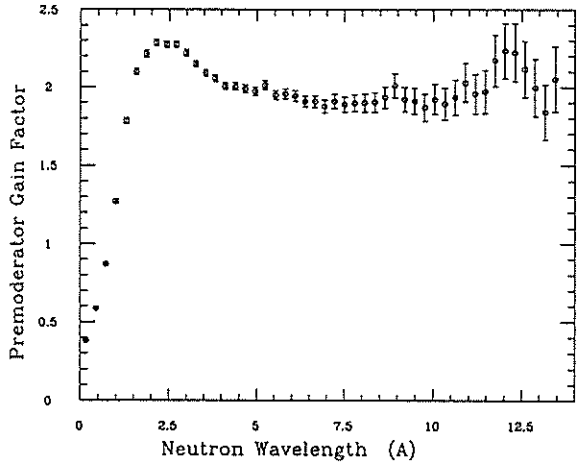

Fig. 5 Wavelength dependence of premoderator gain factor; the ratio of the neutron-beam intensity from the coupled moderator with 2 cm thick premoderator to that from one without premoderator.

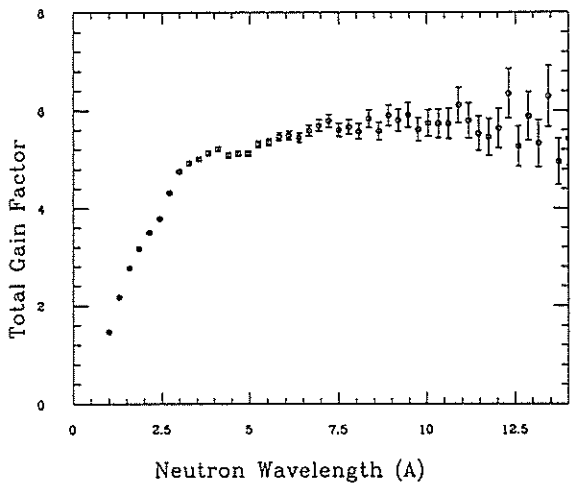

Fig. 6 Total gain factor as a function of neutron wavelength; the ratio of neutron-beam intensity from the coupled moderator with 2 cm thick premoderator to that from the decoupled one.

intensity obtained in this experiment is about 1.5 times higher than the previous. This is due to the better reflector saving in the present system.

Grooved surface moderators were extensively studied so far and a finite gain has already been recognized. We examined a grooved-surface bottom-premoderator. The bottom-premoderator had grooves of 2 cm deep and 2 cm wide with 2 cm spacing (total thickness being 4 cm). A gain factor obtained by this was only 3 % which was unexpectedly small.

The authors are indebted to Prof. K. Inoue for his encouragement and interest shown through the course of this work.

Reference

1) N. Watanabe, Y. Kiyanagi, K. Inoue, M. Furusaka, S. Ikeda, M. Arai and H. Iwasa, Advanced Neutron Sources 1988 (Proc. ICANS-X (1988)), Institute of Physics Conference Series Number 97, Institute of Physics, Bristol and New York, p-787.

Reflector Studies of Coupled Liquid Hydrogen Moderator

Y. KIYANAGI, N. WATANABE*, M. FURUSAKA* and H. IWASA

Department of Nuclear Engineering, Faculty of Engineering, Hokkaido University, Sapporo, 060 Japan
*National Laboratory for High Energy Physics, 1-1 Oho, Tsukuba-shi, Ibaraki, 305 Japan

We studied experimentally the reflector effect on the cold-neutron-beam intensity in a coupled liquid-hydrogen-moderator system, because the effect is not well understood in this system. We measured the neutron-beam intensities from the coupled liquid-hydrogen-moderator proposed in the preceding report[1] with various reflector configurations. The premoderator thickness was fixed to 2 cm (optimal thickness).

Firstly, we examined the effect of the rear-upper-reflector. Figure 1 shows the neutron-beam intensity at three different energies as a function of reflector thickness of the part indicated in the inset. The intensities are saturated at a thickness of about 40 cm, independent of neutron energy. The required thickness is rather large compared to a decoupled moderator system.

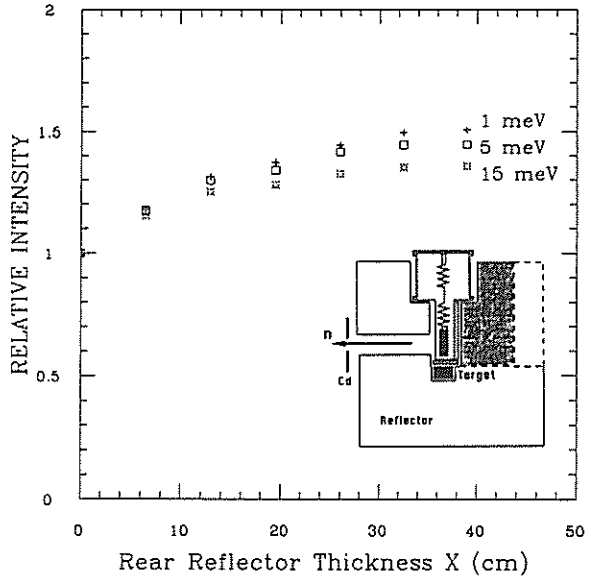

Fig. 1 Effect of the rear-upper-reflector thickness on the neutron-beam intensity. The part of reflector changed is shown in the inset.

Secondly, we examined the effect of the upper reflector. Figure 2 shows the measured neutron-beam intensities as a function of the upper reflector height (see the inset). For longer wavelength neutrons the intensity is still increasing with the reflector height. This is probably due to the reflector missing caused by the cryogenic void. In a real system the void space produced by liquid hydrogen piping above the moderator chamber would be smaller than that of the present cryostat. However, a thicker upper reflector is important for a coupled liquid-hydrogen-moderator system.

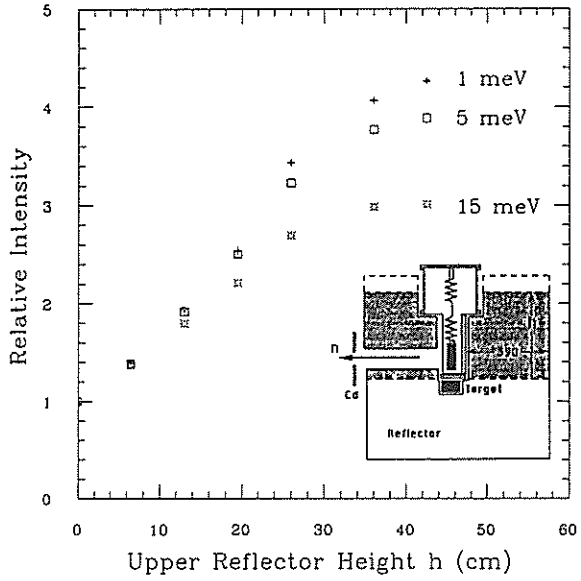

Fig. 2 Effect of upper reflector height on the neutron-beam intensity. The part of reflector changed is shown in the inset.

Next, we examined the effect of the opening angle of beam extraction hole in the reflector. Figure 3 shows the neutron-beam intensities as a function of the opening angle (see the inset). The reduction in the neutron-beam intensity is rather small (only 3-5 % even at 30°) and independent of neutron energy.

Then, we examined the effects of the cadmium liner around beam extraction hole in the reflector, another beam extraction hole, front-premoderator, etc. on the cold-neutron-beam intensity. Figure 4 shows the moderator-reflector configurations studied. The observed cold-neutron-beam intensities are summarized in Table I. We chose the configuration (a) as a reference since it gave the highest intensity. The values in the table are the relative ones to the

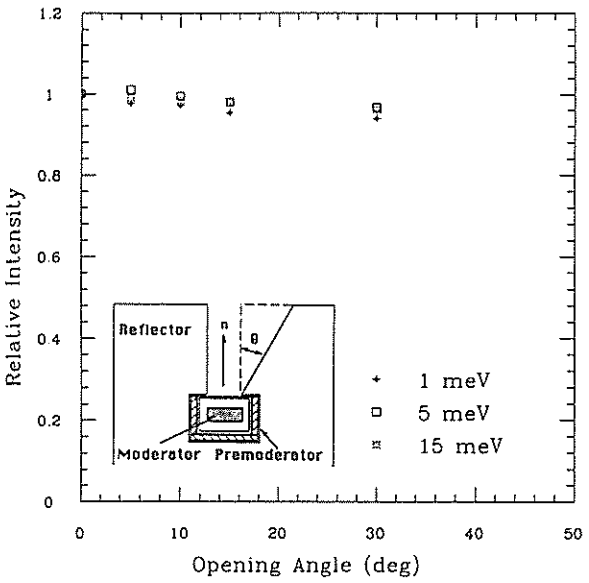

Fig. 3 Effect of the opening angle of the beam extraction hole on the neutron-beam intensity.

configuration (a).

By removing the front-premoderator (configuration (b)) we have about 12 % reduction in the beam intensity. By inserting a cadmium liner around the beam extraction hole (configuration (c)), about 40 % reduction comes out in total. The insertion of another cadmium mask in place of the front-premoderator (configuration (d)) results in the beam intensity reduction of about 50% in total. An additional beam extraction hole to the configuration (b) (configuration (e)) brings about 7 % loss in the beam intensity. The insertion of a cadmium liner in this hole (configuration (f)) gives almost no effect. The existence of another decoupled polyethylene moderator 15×15×5 cm^3 (at ambient temperature) in this hole (configuration (g)) does not give an appreciable reduction. As an extra we examined the configuration (h) where a 1.5 cm-thick polyethylene liner is attached to the extraction hole. This configuration gives the highest beam intensity, but it is necessary to check if the pulse shape deterioration is acceptable for scattering experiment.

We measured time-distribution of the cold neutrons from the moderator in configuration (d). In Fig. 5 plotted is the measured pulse width in FWHM as a function of neutron wavelength. Two solid curves are the results of a coupled moderator (configuration (c)) and a decoupled one for comparison. The pulse widths in configuration (d) lie between both.

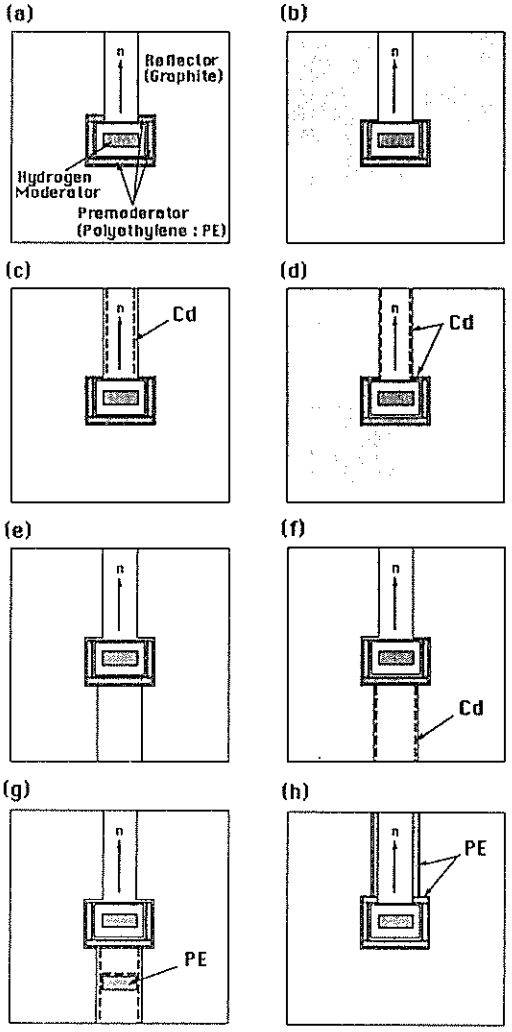

Fig. 4 Various moderator-reflector assemblies studied.

Configuration	Relative intensity to configuration (a)
(a)	1.00
(b)	0.88
(c)	0.62
(d)	0.52
(e)	0.81
(f)	0.78
(g)	0.74
(h)	1.05

Table 1 Relative intensities from the moderator-reflector assemblies shown in Fig. 4.

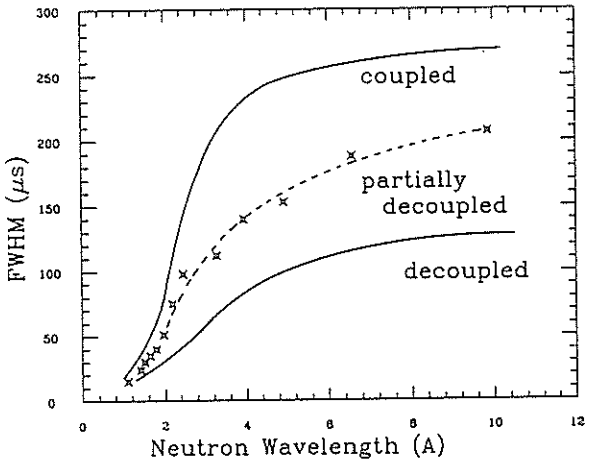

Fig 5 Pulse widths (FWHM) of neutrons from the partially decoupled moderator (configuration (d)).

The authors are indebted to Prof. K. Inoue for his encouragement and interest shown through the course of this work.

References

1) Y. Kiyanagi, N. Watanabe, M. Furusaka, H. Iwasa and I. Fujikawa : KENS Report-VIII (1990) p-

Time-Distribution of Pulsed Cold Neutrons from a Coupled Liquid Hydrogen Moderator

Y. KIYANAGI, N. WATANABE*, M. FURUSAKA*, H. IWASA and I. FUJIKAWA*

Department of Nuclear Engineering, Faculty of Engineering, Hokkaido University, Sapporo, 060 Japan
*National Laboratory for High Energy Physics, 1-1 Oho, Tsukuba-shi, Ibaraki, 305 Japan

Time-distributions of cold neutrons from a proposed coupled liquid-hydrogen-moderator system[1] were studied as a part of a developing program for KENS-II cold neutron sources.

The experimental arrangement for time-distribution measurements is shown in Fig. 1. A mica crystal is used as an energy analyzer with Bragg angle of 85°. The flight path length is 6.61 m. Measurements were performed on a coupled liquid-hydrogen-moderator with 2 cm thick premoderator (optimal thickness) and on a decoupled one without premoderator. Size of the hydrogen moderator was 12×12×5 cm^3.

Figure 2 compares time-distributions of cold

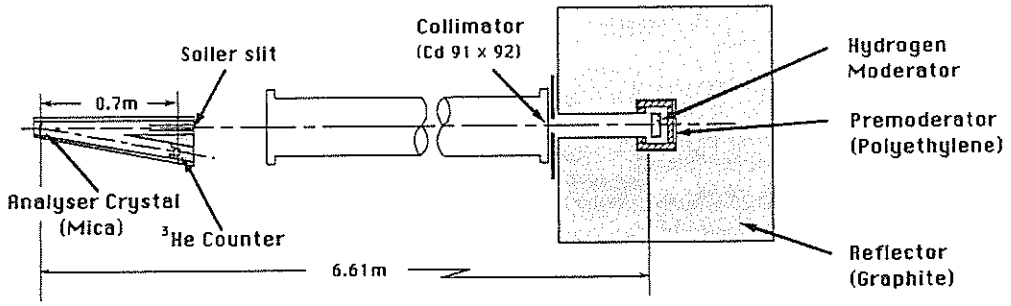

Fig. 1 Experimental set-up for measurements of time-distributions.

neutrons from both moderators at three typical wavelengths . Solid curve shows an enlarged profile from the decoupled moderator normalized at the pulse peak of the coupled moderator for direct comparison. The coupled moderator gives broader pulses than the decoupled one as expected, but the broadening is rather modest and the increase in the peak intensity is unexpectedly high. This means that the larger gain of the coupled moderator is not only due to the increase in the pulse width but also due to the increase in the peak intensity.

Pulse widths in full width at half maximum

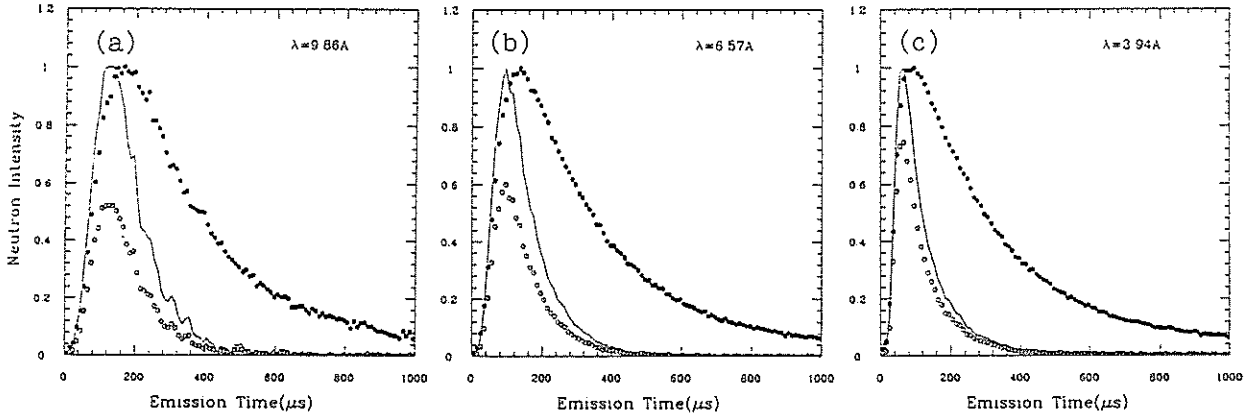

Fig. 2 Time-distributions of neutrons from the coupled liquid-hydrogen-moderator with 2 cm thick premoderator (solid circle) and the decoupled one (open circle) at three wavelengths, (a) 9.86A, (b) 6.57 A and (c) 3.94 A. Solid curve shows the pulse shape of the decoupled moderator normalized at pulse peak for direct comparison.

(FWHM) are plotted in Fig. 3 as a function of neutron wavelength. The pulse widths of neutrons from the coupled moderator is about 2 times larger than that from the decoupled one in the cold neutron region.

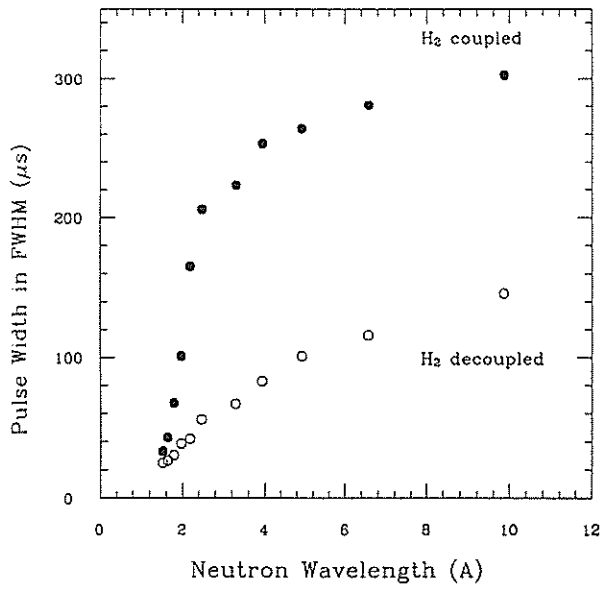

Fig. 3 Pulse widths (FWHM) of neutrons from the coupled (solid circle) and decoupled (open circle) moderator as a function of neutron wavelength.

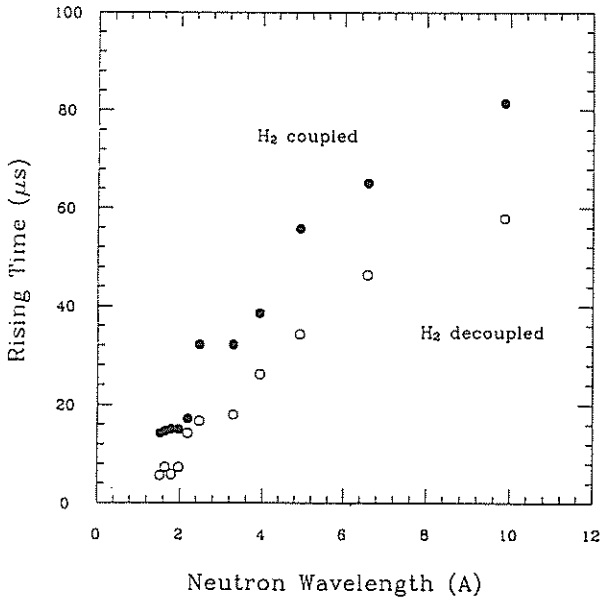

Fig. 4 Rising time of neutron pulses as a function neutron wavelength : the coupled (solid circle), the decoupled (open circle).

Rising times of the neutron pulses are also plotted in Fig. 4. Here, the rising time is defined as the duration between 10 and 90 percent pulse height of the rising edge. The difference between the coupled and the decoupled moderators is not so large as in the pulse widths.

Figure 5 shows the decay time of the neutron pulses as a function of neutron wavelength. The decay time of the coupled moderator is about 2.5 times as long as the decoupled one.

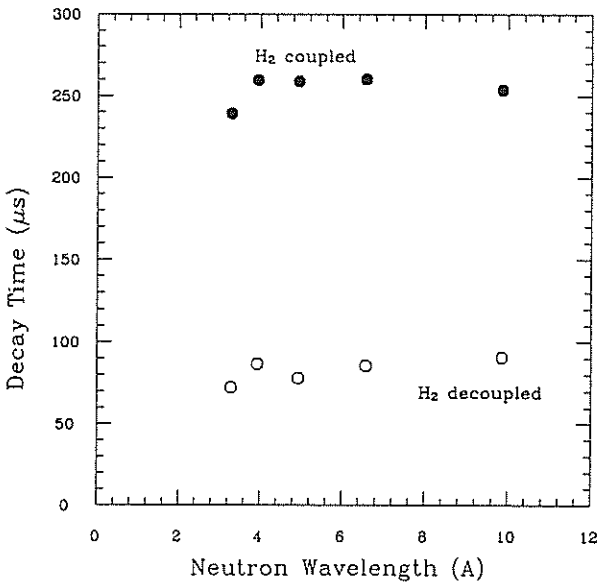

Fig. 5 Decay time of neutron pulses as a function of neutron wavelength : the coupled (solid circle), the decoupled (open circle).

It was so far believed by computer simulation that the pulse broadening in a coupled moderator is significant: about 5 times as broad as a typical decoupled one[2]. It is revealed in the present experiment that the broadening is not as significant as expected by computer simulation.

The authors are indebted to Prof. K. Inoue for his encouragement and interest shown through the course of this work.

References

1) Y. Kiyanagi, N. Watanabe, M. Furusaka, H. Iwasa and I. Fujikawa : KENS Report-VIII (1990) p-
2) G. J. Russell, H. Robinson, G. L. Legate, R. Woods, E. R. Whitaker, A. Bridge and K. J. Hughes : Proc. ICANS-IX (Villigen, Sept. 22-26, 1986) p-177

Direct Comparison of Neutronic Performance between Coupled Liquid Hydrogen Moderator and Solid Methane Moderator

Y. KIYANAGI, N. WATANABE*, M. FURUSAKA* and H. IWASA

Department of Nuclear Engineering, Faculty of Engineering, Hokkaido University, Sapporo, 060 Japan
*National Laboratory for High Energy Physics, 1-1 Oho, Tsukuba-shi, Ibaraki, 305 Japan

We proposed a coupled liquid-hydrogen-moderator system and found that the system can provide a much higher beam intensity of cold neutrons than a decoupled one[1]. Those results however were of the relative values to a reference decoupled moderator. It is necessary to know either the beam intensity in the absolute scale or the cold-neutron conversion-efficiency. We, then, performed a measurement on a reference decoupled moderator of solid methane (20 K) as used at the present KENS facility and compared the results with those on the proposed coupled moderator.

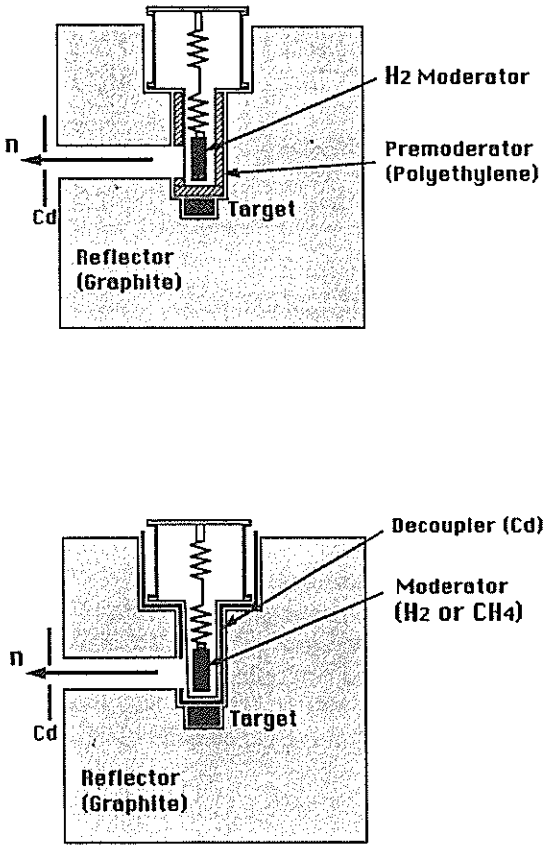

Fig. 1 Target-moderator reflector assemblies of the coupled (a) and the decoupled (b) moderator systems.

Figure 1 shows the coupled and decoupled moderator systems used in this experiment. The coupled moderator is composed of a liquid-hydrogen-moderator $12\times12\times5$ cm^3 and a polyethylene premoderator of 2 cm-thick coupled to a graphite reflector. The system is the same as discussed in the preceding reports [1), 2)]. On the other hand, the reference solid methane moderator is of the same size, decoupled from the reflector by 0.5 mm-thick cadmium as shown in the lower figure.

Measuring set-up of TOF spectrum and time-distribution is the same as described in the preceding report [1) 2)].

Figure 2 shows the energy spectra from both moderators in direct comparison. It should be stressed that the cold-neutron-beam intensity from the proposed coupled moderator is superior to that from the reference decoupled moderator of solid methane. Figure 3 shows the ratio of the intensity of coupled liquid-hydrogen-moderator to that of the reference. A

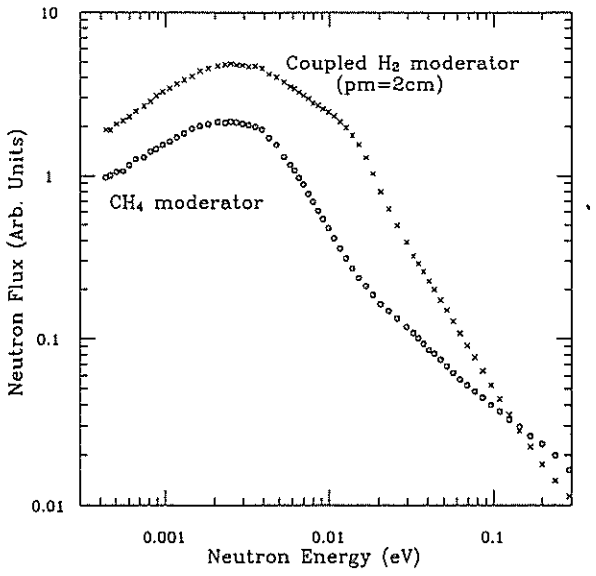

Fig. 2 Energy spectra from the coupled liquid-hydrogen-moderator with 2 cm thick premoderator and the decoupled solid methane moderator.

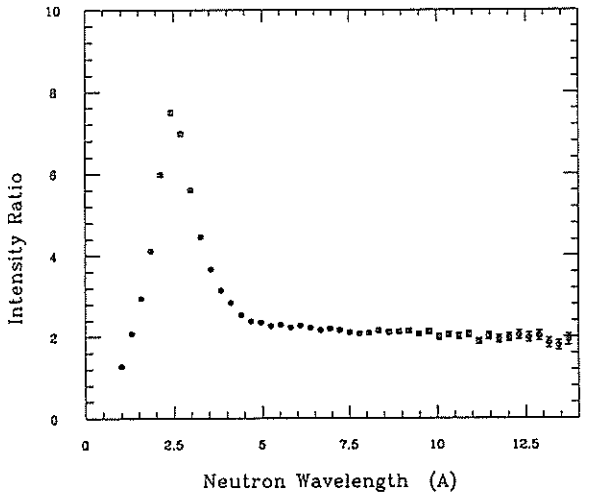

Fig. 3 Intensity ratio of the coupled liquid hydrogen moderator with 2 cm thick premoderator to the decoupled solid methane moderator.

gain of about 2 has been attained. There is a peak at about 2.5 A which is caused by the neutron trap at this wavelength in connection with ortho-para transion of hydrogen.

Next, we measured a spatial distribution of cold-neutron-beam intensity along the vertical direction of the viewed surface of the moderator, by scanning a cadmium slit of 1 cm-high at the entrance of the beam extraction hole (see Fig. 1). The results are shown in Fig. 4. The superiority of the proposed coupled moderator is clearly demonstrated. The peak in intensity appears close to bottom of the moderator.

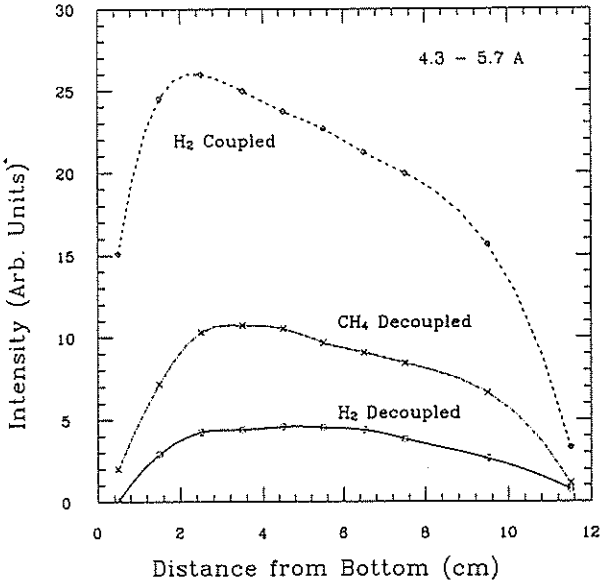

Fig. 4 Spatial distributions of the cold-neutron-beam intensity along the vertical direction of the viewed surface.

Such feature is enhanced more in the proposed coupled moderator. This is due to the fact that the bottom-premoderator feeds source neutrons of a more soft-spectrum to the liquid-hydrogen-moderator.

The target-moderator distance allowed for the target engineering design is one of the most important parameters, so, we measured the cold-neutron-beam intensity by changing the distance between the target and the moderator. Figure 5 shows the results. Intensities from each moderator are normalized to unity at zero distance by extrapolation. It is revealed that the intensity reduction with distance is rather modest and dose not depend on moderator.

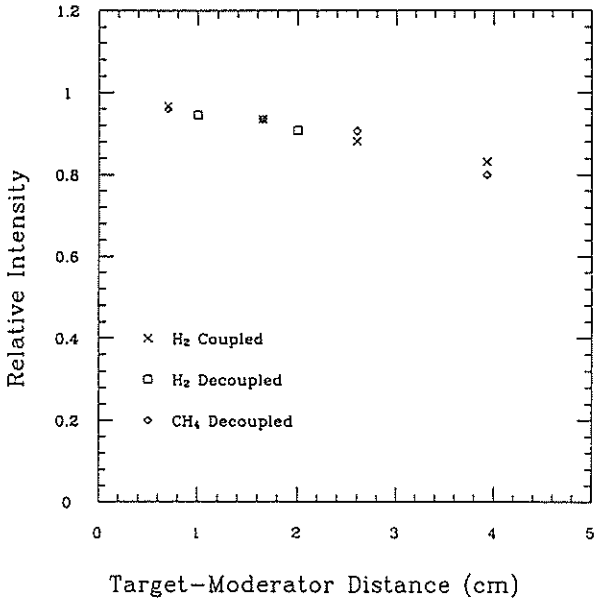

Fig. 5 Cold-neutron-beam intensity as a function of moderator-target distance.

We performed a pulse shape measurement from the reference moderator of solid methane. Figure 6 shows the results at three neutron-wavelngths. Two solid curves are the results from the proposed coupled and the reference decoupled moderators for comparison. The pulse width in FWHM and the rising time are plotted in Fig's 7 and 8 compared with those from other two moderators.

The authors are indebted to Prof. K. Inoue for his encouragement and interest shown through the course of this work.

References

1) Y. Kiyanagi, N. Watanabe, M. Furusaka, H. Iwasa and I. Fujikawa : KENS Report-VIII (1990) p-
2) Y. Kiyanagi, N. Watanabe, M. Furusaka, H. Iwasa and I. Fujikawa : ibid, p-

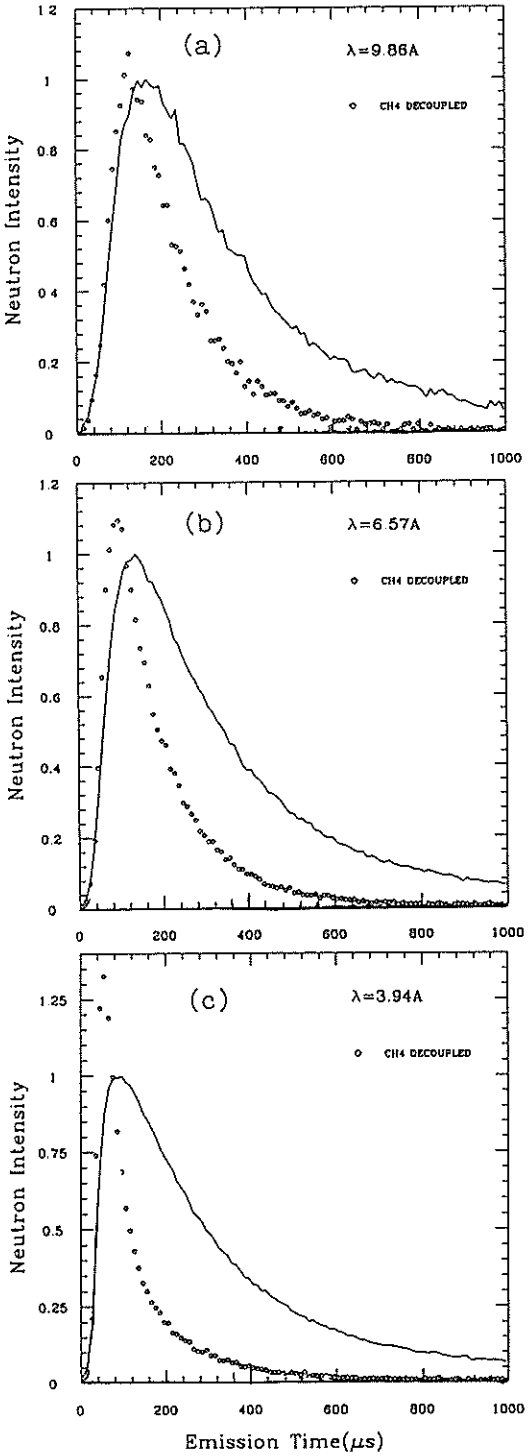

Fig. 6 Time-distributions of neutron from the coupled liquid-hydrogen-moderator with 2 cm thick premoderator and decoupled methane moderators at three neutron wavelengths (a) 9.86 A, (b) 6.57 A and (c) 3.94 A.

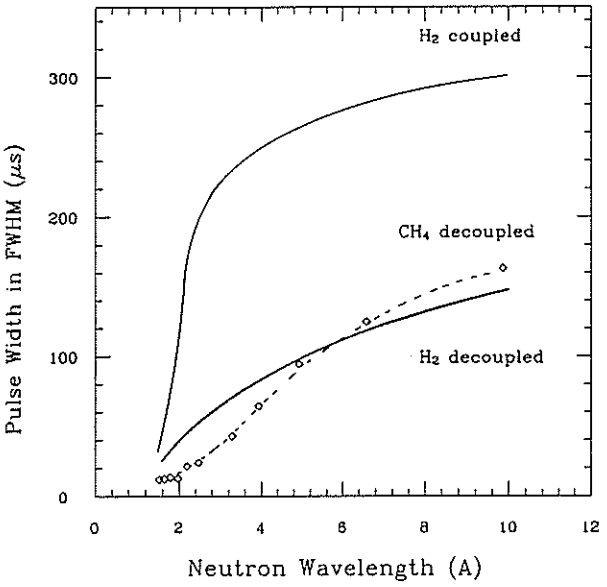

Fig. 7 Pulse width (FWHM) of neutrons from the liquid hydrogen moderators and the decoupled solid methane moderator.

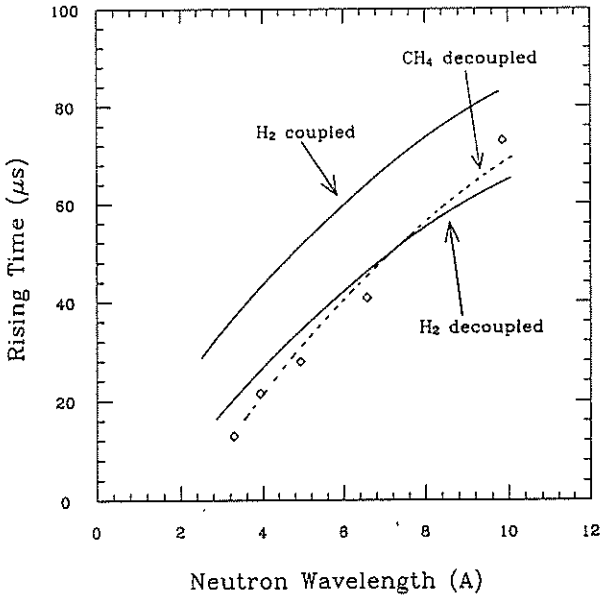

Fig. 8 Rising time of the liquid hydrogen moderators and solid methane moderator.

Some Optimization Studies on Flux-Trap Type Moderator

Y. KIYANAGI and N. WATANABE*
Department of Nuclear Engineering, Faculty of Engineering, Hokkaido University, Sapporo, 060 Japan
*National Laboratory for High Energy Physics, 1-1 Oho, Tsukuba-shi, Ibaraki, 305 Japan

A flux-trap type moderator was first proposed by the Los Alamos group with a better neutronic performance[1]. We performed some optimization studies on this moderator system by computer simulation in order to examine whether this can be a promising candidate for the target-moderator system in KENS-II.

The calculational model of the target-moderator system is shown in Fig. 1. The system is surrounded by a beryllium reflector of 30 cm thick. The moderator is light water with a size of 10×10×5 cm^3 and the target is made from tungsten. For calculation a Monte Carlo code for low energy neutron transport, MORSE-DD, was used combined with a high energy transport code, NMTC/JAERI.

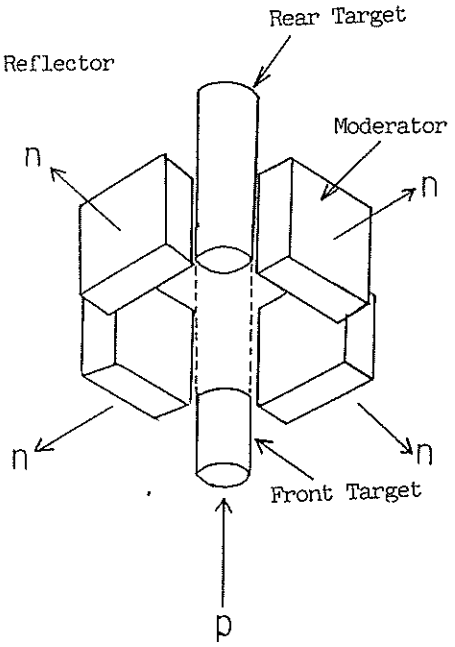

Fig. 1 Calculational model of the flux-trap type target-moderator system.

Firstly, we examined the optimal length of the front target keeping the length of the void space between front and rear targets at 14 cm, the target radius at 5 cm, and the gap between moderator and target void at 2 cm. Figure 2 shows the slow-neutron intensities for various front-target lengths. The length dependence of the slow neutron intensity is rather modest : the optimal length is about 7-8 cm.

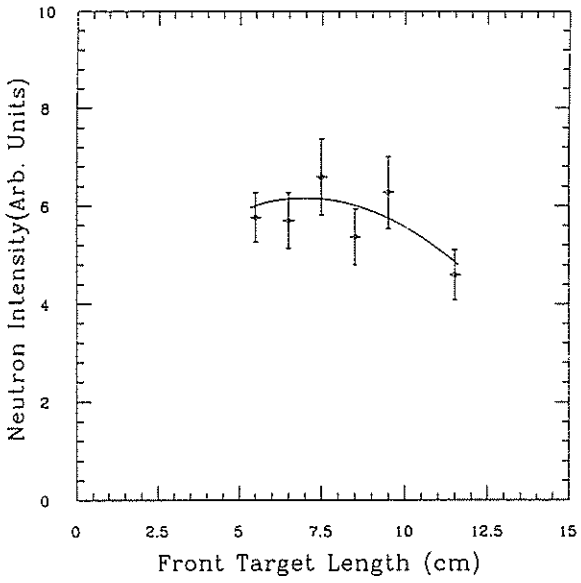

Fig. 2 Slow neutron intensity vs. front-target length.

Secondly, we examined the optimal length of the void space between the two targets. The moderator was located at the center height of the target void keeping the gap between target void and moderator at 2 cm. The front-target length was kept at 7.5 cm. Figure 3 shows the result. The slow-neutron intensity is almost unchanged within the statistical accuracy. This suggests the possibility to adopt a longer void space which makes it easy to suppress the hard component of neutrons leaking to beam holes.

Thirdly, we examined the optimal target radius keeping the front-target length at 7.5 cm, the length of the target void at 14 cm and the distance between the target center-line and the moderator at 7 cm. Figure 4 shows the slow-neutron intensities for different target radii. The intensity is again unchanged up to a radius of about 8 cm. There is no gain with increasing target radius. This may be due to the tungsten target. We

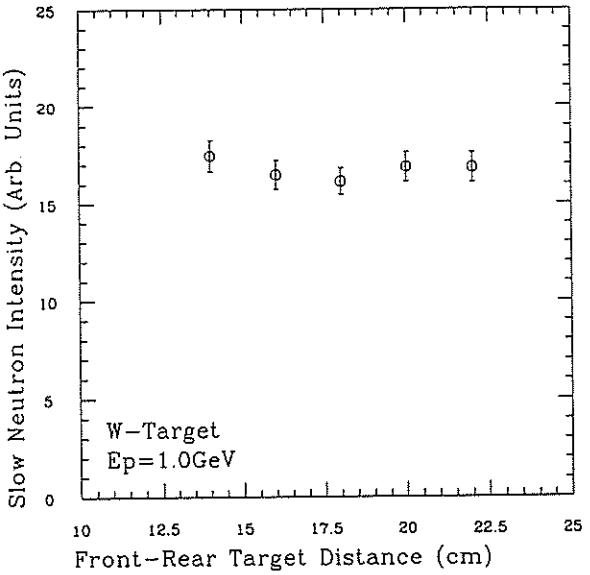

Fig. 3 Slow-neutron intensity vs. void length between front and rear targets.

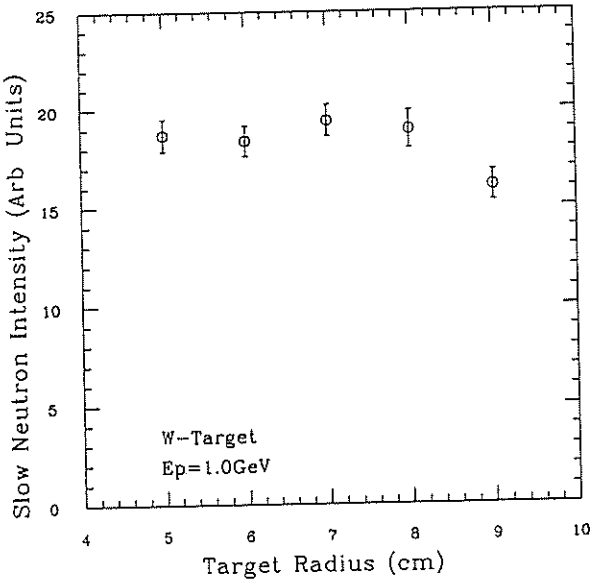

Fig. 4 Slow-neutron intensity vs. target radius.

intend to look into a uranium target system later.

Next, we examined the slow-neutron intensity as a function of target-moderator distance. All other parameters were fixed constant as before. Figure 5 shows the slow-neutron intensities from the front surface and the rear surface of the moderator. The intensity gain from the rear compared to the front is unexpectedly small; only 10 %. The slope is rather modest; approximately 10 % per 2 cm. This will make the engineering design of the target-moderator system easier.

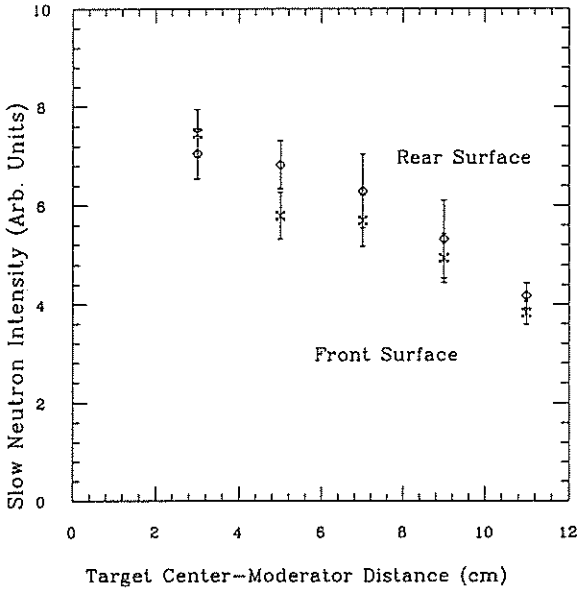

Fig. 5 Slow-neutron intensity vs. target-moderator distance.

Then, we examined the slow-neutron intensity as a function of moderator thickness, keeping the other parameters constant as before. Figure 6 shows slow-neutron intensity vs. moderator thickness. The maximum appears at about 7 cm. The feature is similar to the result of the slab-geometry moderator. The result suggests that a flux-trap type moderator is closer to a slab-geometry moderator rather than a wing-geometry moderator in neutronic performance.

Finally, we compared the slow-neutron intensity from a flux-trap type moderator system with that from a reference moderator system in a wing geometry. In all cases the gap between the cylindrical target surface and the moderator is kept at 2 cm. Figure 7 show the configurations of both systems. The relative values of the slow-neutron intensity per moderator surface, I, are indicated in the figure. In the configurations of 4 beam holes, the reflector is not depicted for reason of simplicity. The results show that the flux-trap type moderator can provide 1.3-1.4 times higher intensity than the wing-geometry moderator.

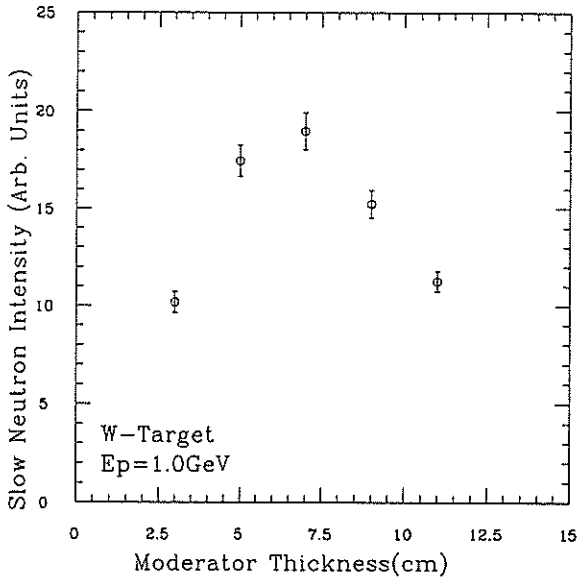

Fig. 6 Slow-neutron intensity vs. moderator thickness.

These results suggest it is a promising candidate for the target-moderator system in KENS-II. We are now investigating similar optimization studies on a coupled liquid-hydrogen-moderator system.

Reference

1) G. J. Russell, H. Robinson, G. L. Legate, R. Woods, E. R. Whitaker, A. Bridge and K. J. Hughes : Proc. ICANS-IX (Villigen, Sept. 22-26, 1986) p-177

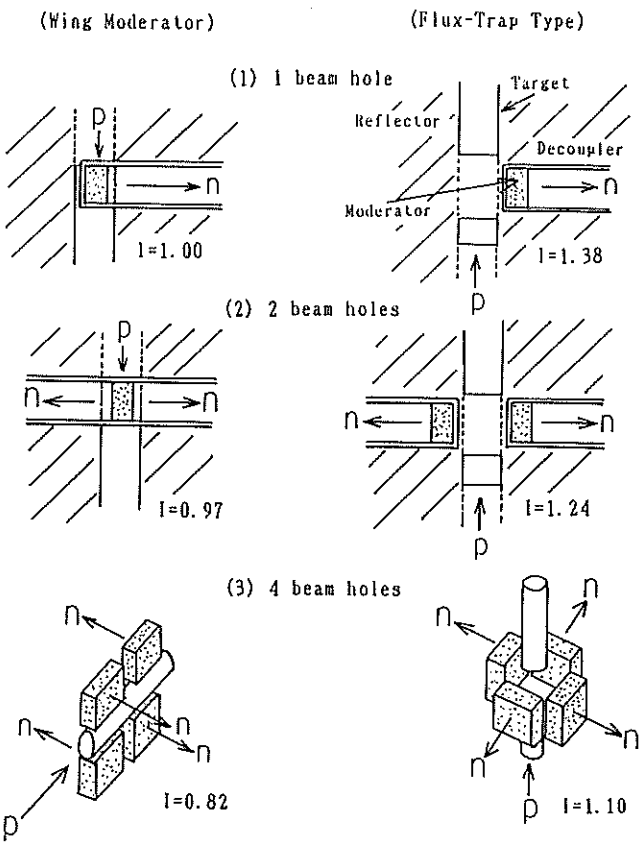

Fig. 7 Comparison of slow-neutron intensity between flux trap type moderator and wing-geometry moderator.

V. JAPAN-UK COLLABORATION ON NEUTRON SCATTERING

MARI Commissioning

*M.Arai, A.D.Taylor, S.M.Bennington and Z.A.Bowden

Rutherford Appleton Lab.
(*National Lab. for High Energy Physics)

MARI is a spectrometer developed at the ISIS facility of the Rutherford Appleton Laboratory under an international collaboration between Science and Engineering Research Committee of UK and Japanese Ministry of Education, Science and Culture. Figure 1 shows MARI spectrometer. The spectrometer was designed to have high resolution, high incident energy and wide accessible energy-momentum space based on the technology of the highly successful HET[1] spectrometer in ISIS. The burst suppression chopper eliminates the fast neutron background. A fermi chopper with a magnetic suspension bearing spins at 600Hz phased to the accelerator within ± 0.3μs and monochromates the incident neutrons from 20 to 2000meV with high energy resolution of 2%[2] of the incident energy. The detector banks are at 4m from the sample position and spread from 3° to 135°. The small angle bank has 8-fold windows and covers the angle from 3° to 12°. The medium angle and high angle windows have three strips cover from 12° to 135°. At this stage a half of the 128 ^{3}He detectors at the small angle bank and the 320 ^{3}He detector in the middle strip of the higher detector windows are available. Further detectors will be installed after funding is available. The collimator system makes a 50x50mm^2 image at the sample position. The vacuum chamber of 25m^3 is evacuated and its two parts are separated by a thin aluminium membrane so as to have a cryogenic vacuum for sample environment volume.

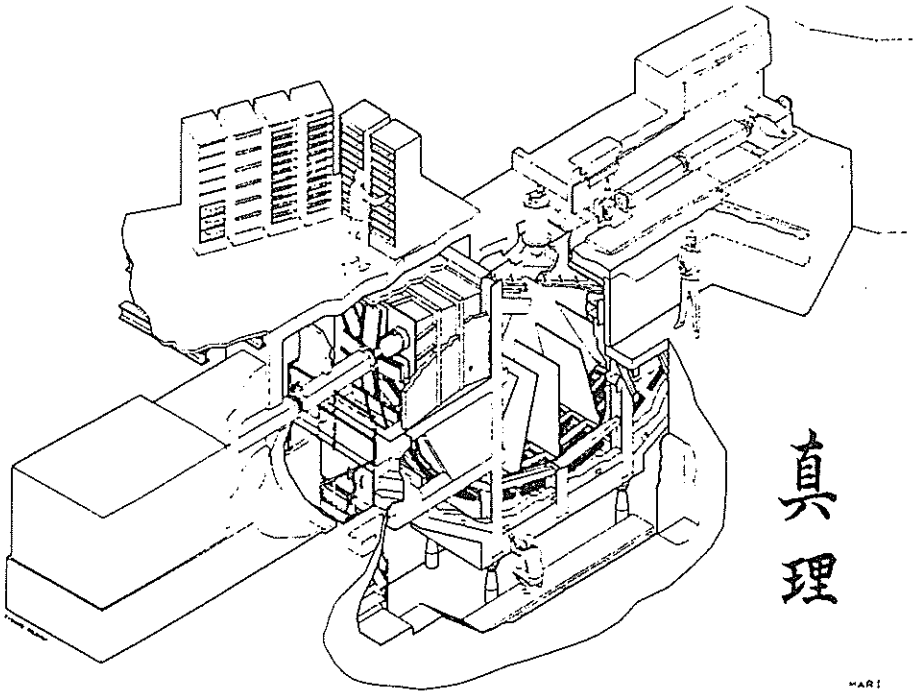

Fig. 1 Schematic layout of the MARI spectrometer

The spectrometer was installed at the S3 beam hole late in 1989 and views the 100K CH_3 moderator. This situation gives us a great advantage in the energy resolution even down to 50meV and give us a good opportunity to use less than 20meV incident energies. Since then the spectrometer was in commissioning stage. In the early stage of the commissioning, the background level was reduced practically reasonable level, 0.1c/min/detector for shutter-close run. The sample born background mechanism are fully

understood by measuring several runs at different configuration in incident energy and sample geometry. This phase has been highly successful due to the dedication of the ISIS support staff and hard work of MARI "team" !. Several examples have been measured to gauge the actual performance of the spectrometer, which are represented in the following paragraphs, and the results gave us an encouraging prospect of the spectrometer. The spectrometer will be scheduled for outside users from the latter half of 1990. The spectrometer has a wide scientific appeal, so that the proposals are considered by three Experimental Selection Panels: Liquids and Amorphous, Excitations and Momentum Distribution and Molecular Science.

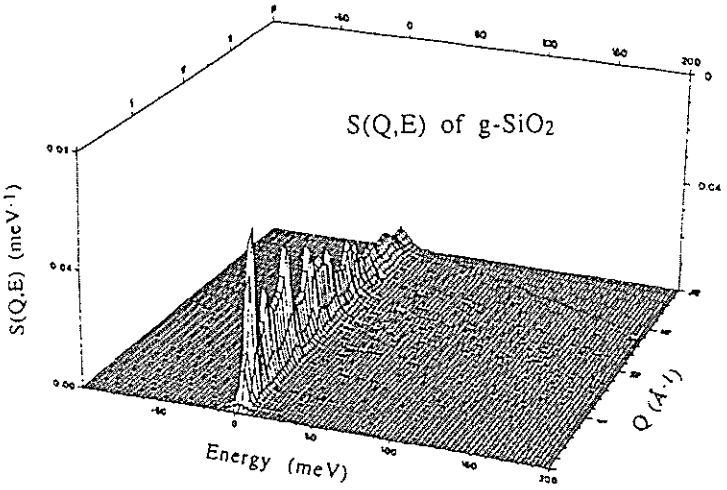

Fig. 2 The S(Q,E) for SiO2

Many attempts have been made to determine the structure of glasses on a microscopic scale, but in the absence of periodic structure, the results gave often proved discouraging, in spite of the accuracy and completeness of much of the experimental data. This was mainly due to the fact that not only diffraction but also spectral data are essentially one dimensional and are ill suited to the task to differentiating three-dimensional fragments of the complex structures. MARI gives us essentially 2-dimensional information on the microscopic structure from its wide coverage of Q-E space ,which gives us additional information for understanding the microscopic structure. Here in Fig. 2 the S(Q,E) of the commissioning experiment on tetrahedral oxide glass SiO2 are shown. The data was taken in a day. The integration over the energy transfer at a constant momentum transfer gives structure factor S(Q) as shown in Fig. 3, and confirms us the accuracy of the measurement and the data analysis with absolute value basis. The averaged vibrational density of states obtained by averaging between Q=5~15Å^{-1} is shown in Fig. 4. The fine structure at around 50meV and 150meV may prompt new extension of the theory and better understanding of the structure. Higher statistics measurements are scheduled for August 1990 in order to confirm the details.

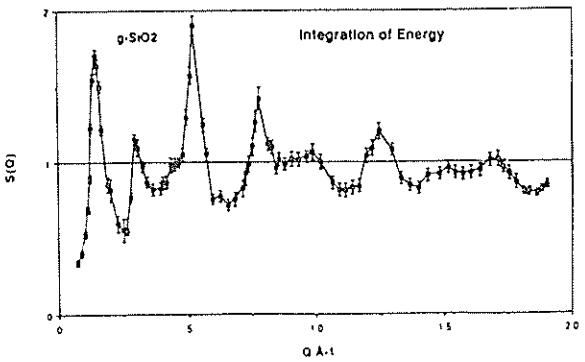

Fig. 3 S(Q) for SiO2 obtained by integration over energy on constant momentum transfer.

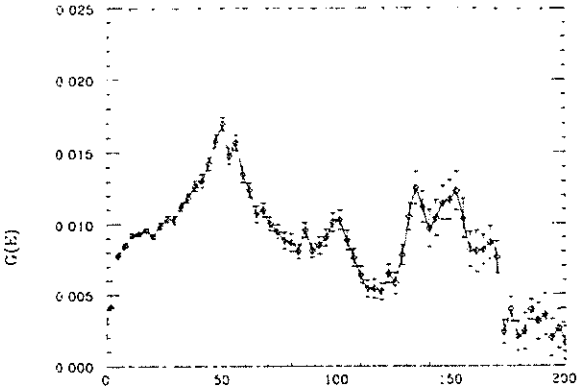

Fig. 4. The density of states G(E) for SiO2.

The wide coverage in Q-E space on MARI is again well illustrated by a commissioning experiment on super-fluid 4He as shown in Fig. 5. The experiment was done in two days. Neutrons are recoiled by ^{4}He atoms then the structure factor shift into the inelastic region according to the scattered momentum transfer. This full set of the behaviour in the inelasticity gives us a better understanding on the interaction between the Bose condensed fluid. Previously this kind of measurement was done with a triple-axis spectrometer with much worse resolution in these energy-momentum transfer, or HET spectrometer with very limited angular coverage by changing the incident energy. MARI measured this feature with the supreme condition among the existing spectrometers. A single measurement with incident energy of 250meV provide the full S(Q,E) ranging Q=0.5~15Å^{-1}.

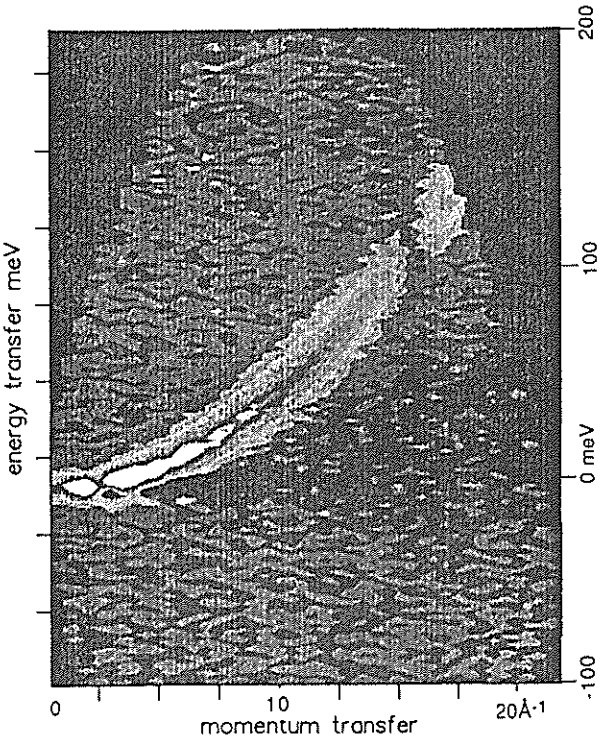

Fig. 5 The S(Q,E) for 4He at 1.2K with 250meV neutrons.

MARI also have a significant impact on vibrational spectroscopy including the study of the local modes in metal hydrides. With the wide coverage and the high resolution in Q-E space, the behaviour of the scattering cross section on vibration with Q^2 dependent rise and fall by Debye-waller factor can be clearly followed by a single measurement by MARI, and gives sophisticated assignment on the observed vibrational modes. Figure 6 shows the results on rare-earth hydride LuH on which the effect of the hexagonal lattice on short range order and the vibrational spectrum of hydrogen is studied.

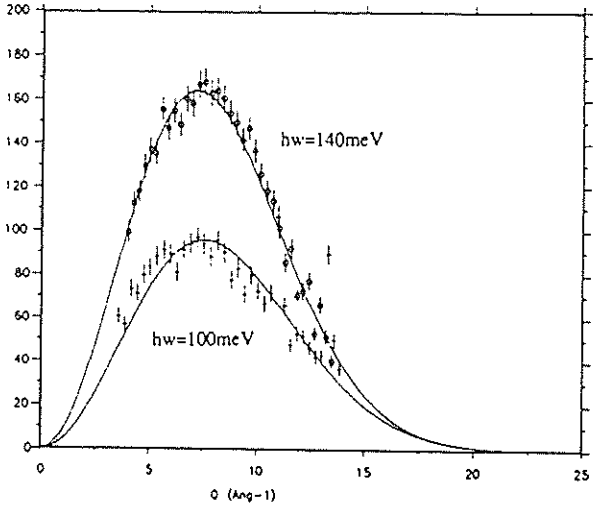

Fig. 6 The Variation of the intensity with Q in LuH.

The concentration of detectors in the small angle bank of MARI gives a very good opportunity to measure a low dimensional magnetic ordered system of a single crystal at high energy transfer. The covalent chains of iron-centered, edge-sharing sulphur tetrahedra in KFeS2 order antiferromagnetically in one dimension. When the one-dimensional axis is parallel to the incident neutron the integration of the small angle bank data provide the proper observation on the excitation. Figure 7 shows the results. The locus for different incident energy measures in its entirity the steep spinwave dispersion relation up to 220meV. The measurement was done in two days.

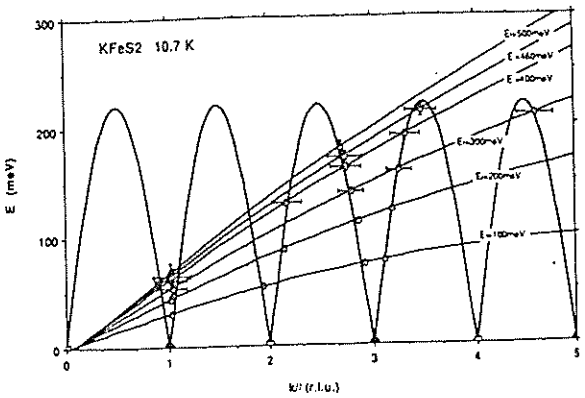

Fig. 7 The dispersion of the One-dimensional antiferromagnet KFeS2.

Reffernce

1) A.D.Taylor et al.:RAL-87-012
2) C.J.Carlile et al.:RAL-85-052

VI. PUBLICATIONS

Publications of all work carried out at KENS together with work performed elsewhere by KENS staff are listed.

1. General

KEK Neutron Source and Neutron Scattering Research Facility,
Ishikawa Y and Watanabe N;
Presented at 2nd Meeting Int. Collaboration on advanced Neutron Sources, (Rutherford Lab., July 10-15, 1978), and KEK Report KEK-78-19.

Neutron Scattering Experiments at Pulsed Spallation Neutron Source (KENS),
Ishikawa Y, Endoh Y, Watanabe N and Inoue K;
Proc. Symp. Neutron Scattering (Argonne, Aug. 12-14, 1981) 57.

Present Status of the KENS Facility,
Ishikawa Y;
Proc. 4 th Meeting Int. Collaboration on Advanced Neutron Sources (KEK, Tsukuba, Oct. 20-24, 1980), KENS Report -II (1981) 89.

Present Status and Future Program of KENS,
Watanabe N, Sasaki H, Ishikawa Y, Endoh Y and Inoue K;
Proc 5th Meeting Int. Collaboration on Advanced Neutron Sources (Jülich, June 22-26, 1981) 21.

Status and Neutron Scattering Experiments at KENS,
Watanabe N, Sasaki H, Ishikawa Y, Endoh Y and Inoue K;
Proc. 6th Meeting Int. Collaboration Advanced Neutron Sources (Argonne, June 28-July 2), ANL-82-80 (1982) 15.

Studies of Condensed Matter with Pulsed Neutron Source (KENS),
Ishikawa Y;
Physica 120B (1983) 3.

Present Status of Booster Synchrotron Utilization Facility at KEK,
Sasaki H;
Proc. 7th Meeting Int. Collaboration on Advanced Neutron Sources (Chalk River, Sept. 13-16, 1983), AECL-8488 (1984) 15.

Neutron Scattering and Muon Spin Rotation,
Ishikawa Y;
Proc. Yamada Conf. VII, Muon Spin Rotation (Shimoda, 1984), Hyperfine Interactions 17-19 (1984) 17.

Pulsed Polarized Neutron Studies,
Endoh Y and Ishikawa Y;
Physica 136B (1985) 64.

Neutron Scattering Spectrometers at KENS Cold Spallation Neutron Source,
Ishikawa Y, Endoh Y and Inoue K;
Proc. International Conf. on Neutron Scattering in '90s, (Jülich, 14-18 Jan. 1985), IAEA-VIENNA, IAEA-CN46/027 (1985) 285.

Present Status and Future Project of KENS Facility,
Ishikawa Y and the KENS Group;
Proc. Proc. 8th Meeting Int. Collaboration on Advanced Neutron Sources (Rutherford Appleton Lab., July 8-12, 1985), RAL-85-110 (1985) 17.

Physics of Spallation Neutrons,
Endoh Y;
Phys. Chem. Research 80 (1986) 38.

Status Report on the KENS Facility,
Watanabe N, Endoh Y, Inoue K and Misawa M;
Proc. 9th Meeting Int. Collaboration on Advanced Neutron Sources (SIN, Villigen, Switzerland, Sept. 22-26, 1986) 65.

KENS Program —Present and Future—,
Watanabe N, Misawa M and Sasaki H;
Proc. Int. Workshop on Hadron Facility Technology (Santa Fe, Feb. 2-5, 1987) 169.

Progress at the Pulsed-Spallation Neutron Facility KENS,
N. Watanabe N;
Advanced Neutron Sources 1988 (Proc. ICANS X) (Los Alamos, Oct. 3-7, 1988) Institute of Physics Conference Series No. 97, Institute of Physics, Bristol and New York, P.53.

Status of KENS-I' and KENS-II
Watanabe N;
Proc. 11th Meeting Int. Collaboration on Advanced Neutron Sources (KEK, Oct. 22-26, 1990), 61

2. Accelerator and Beam Line

Injection System of H^- Beam in KEK Booster Synchrotron,
Kawakubo T, Sasaki H, Sakai I and Suetake M;
Proc.3rd.Symp.on Accelerator Science and Technology (Osaka Univ. Aug. 27-29, 1980) 31.

500 MeV Proton Beam Line for KEK Booster Synchrotron Utilization Facility,
Sakai I, Someya H, Adachi T, Irie Y and Sasaki H;
Proc.3rd.Symp.on Accelerator Science and Technology (Osaka Univ. Aug. 27-29, 1980) 33.

BSF Beam Control System,
Irie Y;
Proc.Proc. 4th Meeting Int. Collaboration on Advanced Neutron Sources (KEK, Tsukuba, Oct. 20-24, 1980), KENS Report-II (1981) 406.

The Booster Synchrotron Utilization Facility at KEK,
Sasaki H;
Proc. 4th Meeting Int. Collaboration on Advanced Neutron Sources (KEK, Tsukuba, Oct. 20-24, 1980), KENS Report-II (1981) 77.

Proton Synchrotron for Intense Neutron and Meson Beam,
Adachi T, Inagaki S, Irie Y, Kaneko N, Kawakubo T, Kumada N, Sakai I, Someya Y, Baba H, Matsumoto S, Miki M and Yano Y;
Proc.4th Symp.on Accelerator Science and Technology (RIKEN, Nov. 24-26, 1982) 281.

80MeV Injector Linac for BSF Future Project,
Inagaki S, Baba H, Miki M and Sasaki H;
Proc. 7th Meeting on Linear Accelerators (KEK, Aug. 24-26, 1982) 110.

Evaluation of the Field Homogeneity of the Magnet by Phase Space Mapping,
Kumada K;
Proc. 4th Symp. on Accelerator Science and Technology (RIKEN, Nov. 24-26, 1982) 87.

Present Status of Booster Synchrotron Utilization Facility at KEK,
Sasaki H;
Proc. 4th Symp. on Accelerator Science and Technology (RIKEN, Nov. 24-26, 1982) 21.

Bi-resonant Circuit for Excitation of Synchrotron Magnet,
Someya H, Adachi T, Kumada M, Baba H, Matsumoto S, Sasaki H and Sakai I;
Proc.4th Symp.on Accelerator Science and Technology (RIKEN, Nov. 24-26, 1982) 317.

Optimization on the End-Shaping of Quadrupole Magnet,
Kumada M, Sasaki H, Someya H and Sakai I;
Nucl. Instrum. Methods 211 (1983) 283.

Accelerator Project GEMINI for Intense Pulsed Neutron and Meson Source at KEK,
Sasaki H and GEMINI Study Group;
Proc.7th Meeting Int. Collaboration on Advanced Neutron Sources (Chalk River, Sept. 13-16, 1983), AECL-8488 (1984) and Proc. 5th Symp. on Accelerator Science and Technology (KEK, Sept. 26-28, 1984) 394.

The first acceleration test of H^- charge exchange injection in the KEK Booster,
Kawakubo T, Sakai I, Suetake M and Sasaki H;
KEK Report 84-6 (1984) 274.

The First Experiment of Test H^- Charge Exchange Injection in the KEK Booster,
Kawakubo T, Sakai I, Suetake and Sasaki H;
Proc. 5th Symp.on Accelerator Science & Technology (KEK, Sept. 26-28, 1984) 274.

Magnetic field measurement of high gradient $SmCo_5$ permanent quadrupole magnets,
Kumada M, Kaneko N, Inagaki S, Baba H and Sasaki H;
Proc.5th Symp.on Accelerator Science & Technology (KEK, Sept. 26-28, 1984) 203.

Application of GTO Thyristor to a Dual Resonant Frequency Circuit for Excitation of Synchrotron Magnet,
Someya H, Adachi T, Irie Y, Yano Y and Sasaki H;
Proc.5th Symp.on Accelerator Science & Technology (KEK, Sept. 26-28, 1984) 221.

Beam Chopper for GEMINI,
Yano Y, Kawakubo T, Kumada M and Sasaki H;
Proc. 5th Symp. on Accelerator Science and Technology (KEK, Sept. 26-28, 1984) 166.

250T/m Rare Earth Permanent Quadrupole Magnet,
Kumada M, Kaneko N, Baba H, Inagaki S and Sasaki H;
Proc. 9th Int. Conf. on Magnet Technology (Zürich Sept. 9-13, 1985) 142.

Application of Rare Earth Permanent Magnet to a High Energy Accelerator,
Kumada M, Kaneko N and Sasaki H;
Proc. Symp on Rare Earths (Tokyo, March 3, 1985) 38.

Application of a GTO thyristor to a dual resonant frequency circuit for the magnet of a rapid-cycling synchrotron,
Someya H, Adachi T, Baba H, Irie Y, Matsumoto S, Sasaki H and Yano Y;
Proc. The 1985 Particle Accelerator Conf. (Vancouver, May 13-16, 1985) IEEE NS-32 (1985) 3775.

Construction and Calculation of High Gradient Rare Earth Permanent Magnet,
Kumada M, Inagaki S, Kaneko N, Baba H and Sasaki H;
Proc. 11th Meeting on Linear Accelerators (KEK Sept. 1-3, 1986) 42.

Drive Stage for Cathode Follower RF System,,
Irie Y;
Proc. Int. Workshop on Hadron Facility Technology (Santa Fe, Feb. 2-5, 1987) 349.

Performance of Prototype Rapid Cycling Magnet and Power Supply for KEK GEMINI Project,
Sasaki H, Someya H, Adachi I, Sakai I and Nakanishi M;
Proc Int. Workshop on Hadron Facility Technology (Santa Fe, Feb. 2-5, 1987) 408.

Magnet Exciting System with Dual Resonant Frequency Circuit,
Adachi T, Someya H and Sasaki H;
European Particle Accelerator Conf. (Rome, June 7-11, 1988).

3. Neutron Source

Shielding Design for KENS,
Watanabe N, Katoh K and Thomas R.H;
KEK Report, KEK-78-7 (1978) 29.

Target-Moderator Mock-up Experiment for KENS,
Watanabe N, Misawa M and Yamaguchi S;
Presented at 2nd Meeting Int. Collaboration on advanced Neutron Sources (Rutherford Lab., July 10-15, 1978).

Experimental Studies of the Induced Radioactivities in a Uranium Target,
Katoh K, Ban S, Hirayama H, Ikeda S, Irie K, Kondoh K, Miyajima M, Sato S, Watanabe N and Yamaguchi S;
Proc. 4th Meeting Int. Collaboration on Advanced Neutron Sources (KEK, Tsukuba, Oct. 20-24, 1980), KENS Report-II (1980) 381.

KENS Radiation Shield,
Ban S and Hirayama H;
Proc. 4th Meeting Int. Collaboration on Advanced Neutron Sources (KEK, Tsukuba, Oct. 20-24, 1980) KENS Report-II (1981) 355.

KENS Radiation Activity: Structural Materials,
Hirayama H and Ban S;
Proc. 4th Meeting Int. Collaboration on Advanced Neutron Sources (KEK, Tsukuba, Oct. 20-24, 1980), KENS Report-II (1981) 376.

KENS Cold Neutron Source,
Ikeda S, Ishikawa Y and Inoue K;
Proc. 4th Meeting Int. Collaboration on Advanced Neutron Sources (KEK, Tsukuba, Oct. 20-24, 1980), KENS Report-II (1981) 200.

Some Neutronic Aspects of Solid Methane Moderator System,
Inoue K, Kiyanagi Y, Iwasa H, Jinguji K, Watanabe N, Ikeda S and Ishikawa Y;
Proc. 5th Meeting Int. Collaboration on Advanced Neutron Sources (Jülich, June 22-26, 1981), Jul-Conf-45 (1981) 519.

Radioactivity and Radiolysis of the Solid Methane Used as a Cold Neutron Moderator in the KENS Target Assembly,
Kondoh K and Hozumi K;
Proc. 4th Meeting Int. Collaboration on Advanced Neutron Sources (KEK, Tsukuba, Oct. 20-24, 1980), KENS Report-II (1981) 381.

Characteristics of KENS Cold Neutron Guide Tube,
Mizuki J, Endoh Y, Ishikawa Y and Ikeda S;
Proc. 4th Meeting Int. Collaboration on Advanced Neutron Sources (KEK, Tsukuba, Oct. 20-24, 1980), KENS Report-II (1981) 521.

KENS Target Station,
Watanabe N, Ikeda S and Ishikawa Y;
Proc.Proc. 4th Meeting Int. Collaboration on Advanced Neutron Sources (KEK, Tsukuba, Oct. 20-24, 1980), KENS Report-II (1981) 181.

Grooved Cold Moderator Tests,
Inoue K, Kiyanagi Y, Iwasa H, Watanabe N, Ikeda S, Carpenter J.M and Ishikawa Y;
Proc. 6th Meeting Int. Collaboration on Advanced Neutron Sources (Argonne, June 28 -July 2, 1982), ANL-82-80 (1982) 391.

Grooved Cold Moderator at KENS,
Ishikawa Y, Ikeda S, Watanabe N, Kondoh K, Inoue K, Kiyanagi Y, Iwasa H and Tsuchihashi K;
Proc. 7th Meeting Int. Collaboration on Advanced Neutron Sources (Chalk River, Sept. 13-16, 1983), AECL-8488 AECL-8488 (1982) 230.

On the 20K Methane Moderator and its Application to the Intense Pulsed Cold Neutron Source,
Inoue K;
Nucl. Instrum. Methods 216 (1983) 537.

Mock-up Experiments for KENS-I' Cold Moderator,
Ishikawa Y, Furusaka M, Itoh S, Ikeda S, Watanabe N, Inoue K and Iwasa H;
Proc. 8th Meeting Int. Collaboration on Advanced Neutron Sources (Rutherford Appleton Lab., July 8-12, 1985) RAL-85-110 (1985) 329.

Some Neutronic Calculations for KENS-II,
Kiyanagi Y, Arai M, and Watanabe N;
Advanced Neutron Sources 1988 (Proc. ICANS X) (Los Alamos, Oct. 3-7, 1988) Institute of Physics Conference Series No. 97, Institute of Physics, Bristol and New York, P. 753.

A Consideration of Cold Neutron Source for KENS-II,
Watanabe N;
Advanced Neutron Sources 1988 (Proc. ICANS X) (Los Alamos, Oct. 3-7, 1988) Institute of Physics Conference Series No. 97, Institute of Physics, Bristol and New York, P. 763.

Preliminary Optimization Experiments of Coupled Liquid Hydrogen Moderator for KENS-II,
Watanabe N, Kiyanagi Y, Inoue K, Furusaka M, Ikeda S, Arai M, and Iwasa H;
Advanced Neutron Sources 1988 (Proc. ICANS X) (Los Alamos, Oct. 3-7, 1988) Institute of Physics Conference Series No. 97, Institute of Physics, Bristol and New York, P. 787.

Optimization Studies on Coupled Liquid Hydrogen Moderator,
Kiyanagi Y, Watanabe N, Furusaka M, Iwasa H and Fujikawa I;
Proc. 11th Meeting Int. Collaboration on Advanced Neutron Sources (KEK, Tsukuba, Oct. 22-26, 1990), 388.

Reflector Optimization for Coupled Liquid Hydrogen Moderator,
Kiyanagi Y, Watanabe N, Furusaka M and Iwasa H;
Proc. 11th Meeting Int. Collaboration on Advanced Neutron Sources (KEK, Tsukuba, Oct. 22-26, 1990), 401.

Some Neutronic Studies on Flux-Trap Type Moderator,
Kiyanagi Y and Watanabe N;
Proc. 11th Meeting Int. Collaboration on Advanced Neutron Sources (KEK, Tsukuba, Oct. 22-26, 1990), 408.

A Design Concept of Target-Moderator-Reflector Assemblies for KENS-II,
Watanabe N;
Proc. 11th Meeting Int. Collaboration on Advanced Neutron Sources (KEK, Tsukuba, Oct. 22-26, 1990), 471.

4. Instrumentations

Time of Flight Spectrometer with Optical Polarizer,
Endoh Y, Mizuki J and Ono H;
Proc. 4th Meeting Int. Collaboration on Advanced Neutron Sources (KEK, Tsukuba, Oct. 20-24, 1980), KENS Report-II (1981) 609.

Large Analyzer Mirror Low Energy Spectrometer LAM(KEK) and LANDAM(HU), and Electron Linac Cold Source,
Inoue K, Kiyanagi Y, Kohgi M, Ishikawa Y, Watanabe N, Iwasa H, Sakamoto Y and Jinguji K;
Proc. 4th Meeting Int. Collaboration on Advanced Neutron Sources (KEK, Tsukuba, Oct. 20-24, 1980), KENS Report-II (1981) 592.

Small Angle Scattering Spectrometer (KENS-SAN),
Ishikawa Y, Furusaka M, Arai M, Niimura N, Ikeda S and Hasegawa K;
Proc. 4th Meeting Int. Collaboration on Advanced Neutron Sources (KEK, Tsukuba, Oct. 20-24, 1980), KENS Report-II (1981) 563.

Neutron Polarization by Polarized Proton Filter,
Ishimoto S;
Proc. 4th Meeting Int. Collaboration on Advanced Neutron Sources (KEK, Tsukuba, Oct. 20-24, 1980), KENS Report-II (1981) 630.

Application of Position Sensitive Detectors to Structure Analysis Using Pulsed Neutron Source,
Niimura N, Ishikawa Y, Arai M and Furusaka M;
Proc. Symp. Neutron Scattering (Argonne, Aug. 12-13, 1981).

KENS Data Acquisition System,
Niimura N, Kohgi M, Arai M, Tomiyoshi S, Tajima K, Isobe M, Furusaka M and Fujino Y;
Proc. 4th Meeting Int. Collaboration on Advanced Neutron Sources (KEK, Tsukuba, Oct. 20-24, 1980), KENS Report-II (1981) 663.

Multi Analyzer Crystals Spectrometer at KENS,
Tajima K, Kanai K, Ishikawa Y, Tomiyoshi S and Windsor C.G;
Proc. 4th Meeting Int. Collaboration on Advanced Neutron Sources (KEK, Tsukuba, Oct. 20-24, 1980), KENS Report-II (1981) 600.

The High Intensity Total Scattering Spectrometer (HIT),
Watanabe N, Fukunaga T, Shinohe T, Yamada K and Mizoguchi T;
Proc. 4th Meeting Int. Collaboration on Advanced Neutron Sources (KEK, Tsukuba, Oct. 20-24, 1980), KENS Report-II (1981) 539.

The Ultra Cold Neutron Production at KENS,
Yoshiki H;
Proc. 4th Meeting Int. Collaboration on Advanced Neutron Sources (KEK, Tsukuba, Oct. 20-24, 1980), KENS Report-II (1981) 715.

Test of a Resonance Detector Spectrometer for Electron-Volt Spectroscopy,
Carpenter J.M, Watanabe N, Ikeda S, Masuda Y and Satoh S;
Proc. 6th Meeting Int. Collaboration on Advanced Neutron Sources (Argonne, June 28-July 2, 1982), ANL-82-80 (1982) 265.

Polarized Epithermal Neutron Spectrometer at KENS,
Kohgi M;
Proc. 6th Meeting Int. Collaboration on Advanced Neutron Sources (Argonne, June 28-July 2, 1982), ANL-82-80 (1982) 171.

A Multi Analyzer Crystal Spectrometer (MAX) for Pulsed Neutron Source,
Tajima K, Ishikawa Y, Kanai K, Windsor C.G and Tomiyoshi S;
Nucl. Instrum. Methods 201 (1982) 491.

Crystal Analyzer TOF Spectrometer (CAT) for High Energy Incoherent Neutron Scattering,
Watanabe N, Ikeda S and Kai K;
Proc. 6th Meeting Int. Collaboration on Advanced Neutron Sources (Argonne, June 28-July 2, 1982), ANL-82-80 (1982) 279.

A Resonance Detector Spectrometer at KENS,
Carpenter J.M, Watanabe N, Ikeda S, Masuda Y and Satoh S;
Physica 120B (1983) 126.

Time Focussing and Resolution in Resonance Detector Neutron Spectrometer,
Carpenter J.M and Watanabe N;
Nucl. Instrum. Methods 213 (1983) 311.

Polarized Neutron Scattering using Pulsed Spallation Neutron Source at KEK,
Endoh Y, Sasaki H, Ono H, Mitsuda S and Ikeda S;
Physica 120B (1983) 45.

Crystal Analyzer TOF Spectrometer (CAT),
Ikeda S. Watanabe N and Kai K;
Physica 120B (1983) 131.

Neutron Quasi-elastic Scattering Studies of Molecular liquids and Polymers by Pulsed Cold Neutron Source,
Inoue K, Kiyanagi Y, Kohgi M and Kaji K;
Physica 120B (1983) 422.

Position Sensitive Neutron Detectors using Li-6 Glass Scintillators and Fibre Optic Encoding,
Niimura , Yamada K, Kubota T, Matsumoto A and Hoshino S;
Nucl. Instrum. Methods 211 (1983) 203.

Position Sensitive Neutron Detectors using Li-6 Glass Scintillators,
Niimura N, Yamada K, Kubota T, Matsumoto A and Hoshino S;
Physica 120B (1983) 104.

Multi-Analyzer Crystal Spectrometer (MAX) for Pulsed Neutron Source and Its Application to Various Problem,
Tajima K, Ishikawa Y, Kanai K, Tomiyoshi S and Todate Y;
Physica 120B (1983) 136.

High Resolution TOF Crystal Analyzer Spectrometer for Large Energy Transfer Incoherent Neutron Scattering,
Ikeda S and Watanabe N;
Nucl. Instrum. Methods 221 (1984) 571.

Experimental Study of the Time-Focussing Effect in Resonance Detector Neutron Spectrometer,
Rauh H, Ikeda S and Watanabe N;
Nucl. Instrum. Methods 224 (1984) 469.

Detector Resolution of a Resonance Detector Neutron Spectrometer,
Rauh H and Watanabe N;
Nucl. Instrum. Methods 222 (1984) 507.

Resonance Detector Instruments,
Watanabe N;
Proc. Workshop on High-Energy Excitation in Condensed Matter (Los Alamos, Feb. 13-15, 1984) 56.

Simple thermo-level meter for He I and He II by a dynamic method,
Yoshiki H;
Cryogenics (1984) 704.

TOF Spectrometer with Optical Polarizer for Cold Neutrons,
Endoh Y, Ikeda S, Mitsuda S and Fujimoto H;
Nucl. Instrum. Methods A240 (1985) 115.

Pulsed Polarized Neutron Studies at KENS,
Endoh Y and Ishikawa Y;
Proc. Int Conf. on Neutron Scattering (Santa Fe, Aug. 19-23, 1985).

Crystal Analyzer Type Quasielastic Spectrometers using the Pulsed Cold Neutron Source,
Inoue K, Ishikawa Y, Watanabe N, Kaji K, Kiyanagi Y, Iwasa H and Kohgi M;
Nucl. Instrum. Methods A238 (1985) 401.

Development of Polarized Epithermal Neutron Spectrometer PEN at KENS,
Ishida M, Ishikawa Y, Ishimoto S, Kohgi M, Masaike A, Masuda Y, Morimoto K and Nakajima T;
Proc. 8th Meeting Int. Collaboration on Advanced Neutron Sources (Rutherford Appleton Lab., July 8-12, 1985), RAL-85-110 (1985) 612.

TOF Type Small Angle Scattering Spectrometer SAN at KENS Pulsed Cold Neutron Source,
Ishikawa Y, Furusaka M, Niimura N, Arai M and Hasegawa K;
Proc. 8th Meeting Int. Collaboration on Advanced Neutron Sources (Rutherford Appleton Lab., July 8-12, 1985), RAL-85-110 (1985) 454.

Resonance Detector Methods in Spectrometers,
Watanabe N;
Neutron Scattering in the 'Nineties, IAEA Vienna (1985) 279.

TOF Type Small Angle Scattering Spectrometer SAN at KENS Pulsed Cold Neutron Source,
Ishikawa Y, Furusaka M, Niimura N, Arai M, Hasegawa K;
J. Appl. Cryst. 19 (1986) 229.

Slow Neutron Polarization by Longitudinally Polarized Proton Filter,
Ishimoto S, Isagawa S, Masaike A, Masuda Y, Morimoto K, Nakajima T, Ishida M, Ishikawa Y, Kohgi M and Newsam J.M;
Jpn. J. Appl. Phys. 25 (1986) L246.

Dynamically Polarized Proton Filter for a Low Energy Neutron Polarizer,
Masuda Y, Hiramatsu S, Isagawa S, Ishida M, Ishikawa Y, Ishimoto S, Kohgi M, Masaike A, Morimoto K and Nakajima T;
Proc. 6th Int. Symp. on Polarization Phenomena in Nucl. Phys., (Osaka, 26-30 Aug. 1985) Supplement to Phys. Soc. Jpn. 55 (1986) Suppl.1070.

Evaluation of Data from 1D-PSD used in TOF Methods,
Niimura N;
J. Phys. Colloq. (France) 47 (1986) C5-129.

A Multi-Angle Rotor Spectrometer at the Pulsed Neutron Source ISIS,
Taylor A.D, Ward R.G, Williams W.G, Endoh Y and Watanabe N;
Proc. 9th Meeting Int. Collaboration on Advanced Neutron Sources (SIN, Villigen, Switzerland, Sept. 22-26, 1986) 535.

Liquid and Amorphous Total Scattering Instrument at KENS —HIT—,
Misawa M, Fukunaga T, Yamaguchi T and Watanabe N;
Proc. 9th Meeting Int. Collaboration on Advanced Neutron Sources (SIN. Villigen, Switzerland, Sept. 22-26, 1986) 539.

Epithermal and Thermal Neutron Beam Monitor using ^{6}Li Glass Scintillator,
Hirai M, Niimura N and Ishida A;
Nucl. Instrum. Methods A259 (1987) 497.

High Resolution Neutron Powder Diffractometer with a Solid Methane Moderator at Pulsed Spallation Neutron Source,
Watanabe N, Asano H, Iwasa H, Satoh S, Murata H, Karahashi K, Tomiyoshi S, Izumi F and Inoue K;
Jpn. J. Appl. Phys. 26 (1987) 1164.

New KENS Data Acquisition System,
Arai M, Furusaka M, and Satoh S;
Advanced Neutron Sources 1988 (Proc. ICANS X) (Los Alamos, Oct. 3-7, 1988) Institute of Physics Conference Series No. 97, Institute of Physics, Bristol and New York, P. 529.

Development of a Chopper Spectrometer at KENS,
Arai M, Kohgi M, Itoh M, Iwasa H, Watanabe N, Ikeda S, and Endoh Y;
Advanced Neutron Sources 1988 (Proc. ICANS X) (Los Alamos, Oct. 3-7, 1988) Institute of Physics Conference Series No. 97, Institute of Physics, Bristol and New York, P.297.

Application of eV Neutron Scattering and eV Neutron Absorption Techniques,
Ikeda S;
Advanced Neutron Sources 1988 (Proc. ICANS X) (Los Alamos, Oct. 3-7, 1988) Institute of Physics Conference Series No. 97, Institute of Physics, Bristol and New York, P.341.

Production of Highly Polarized White Epithermal Neutron Beams by Dynamically Polarized Proton Filter,
Ishida M, Hiramatsu S, Isagawa S, Ishikawa Y, Ishimoto S, Kanno K, Kohgi M, Masaike A, Morimoto K, Nakajima T and Newsam J.M;
Nucl. Instrum. Methods (1988).

Dynamically Polarized Proton Filter as a Neutron Spin Polarizer by the Use of a ^{3}He-^{4}He Heat Exchanger,
Masuda Y, Ishimoto S, Masaike A, Ishida M, Ishikawa Y and Kohgi M;
Nucl. Instrum. Methods A264 (1988) 169.

Development of a Chopper Spectrometer at KENS,
Arai M, Kohgi M, Itoh M, Iwasa H, Watanabe N, Ikeda S and Endoh Y;
Proc. 10th Meeting of the Int. Collaboration on Advanced Neutron Sources (Los Alamos, Oct. 3-7, 1988) 297.

Thermal Neutron Small-Angle Scattering Spectrometer (WIT) Using a 2D Converging slit and Annular Glass Scintillator Detectors at KENS,
Niimura N, Hirai M, Ishida A, Aizawa K, Yamada K and Ueno M;
Physica B 156&157 (1989) 611.

Total Performance of LAM-80ET,
Inoue K, Kanaya T, Kiyanagi Y, Shibata K, Kaji K, Iwasa H and Izumi Y;
Proc. 11th Meeting Int. Collaboration on Advanced Neutron Sources (KEK, Tsukuba, Oct. 22-26, 1990) 684.

Crystal Analyzer Type Spectrometer LAM-D at KENS Spallation Thermal Neutron Source,
Inoue K, Kanaya T, Kiyanagi Y, Shibata K, Kaji K, Ikeda S, Iwasa H and Izumi Y;
Proc. 11th Meeting Int. Collaboration on Advanced Neutron Sources (KEK, Tsukuba, Oct. 22-26, 1990) 1082.

Thermal Neutron Small-Angle Scattering Spectrometer (WIT),
Niimura N, Aizawa K, Hirai M, Sangawa U and Yamada K;
Proc. 11th Meeting Int. Collaboration on Advanced Neutron Sources (KEK, Oct. 22-26, 1990) 1095.

Several Experiences of Using Li-Glass Scintillators,
Niimura N, Hirai H, Aizawa K, Yamada K and Okamura F;
Proc. 11th Meeting Int. Collaboration on Advanced Neutron Sources (KEK, Oct. 22-26, 1990) 971.

Resolution Function and Recent Developments of the Multi Analyzer Crystal Spectrometer MAX,
Todate Y, Tajima K, Ikeda H and Tomiyoshi S;
Jpn. J. Appl. Phys. 29 (1990) 1220.

Why Total Performance,
Watanabe N;
Proc. 11th Meeting Int. Collaboration on Advanced Neutron Sources (KEK, Tsukuba, Oct. 22-26, 1990), 637.

Performance of Chopper Spectrometers,
Arai M, Taylor A. D, Bennington S. M, Bowden Z. A, Osborn R, Kohgi M, Ohoyama K and Nakane T;
Proc. 11th Meeting Int. Collaboration on Advanced Neutron Sources (KEK, Tsukuba, Oct. 22-26, 1990), 644.

Total Performance of KENS Small Angle Machines,
Furusaka M, Suzuya K, Watanabe N, Suzuki J and Fujikawa I;
Proc. 11th Meeting Int. Collaboration on Advanced Neutron Sources (KEK, Tsukuba, Oct. 22-26, 1990), 677.

First Results from the UK-Japanese Spectrometer MARI,
Taylor A. D, Arai M, Bennington S. M, Bowden Z. A, Osborn R, Andersen K, Stirling W. G, Nakane T, Yamada K and Welz D;
Proc. 11th Meeting Int. Collaboration on Advanced Neutron Sources (KEK, Tsukuba, Oct. 22-26, 1990), 705.

Crosscorrelation Method Using a Pulsed White Polarized Neutron Beam,
Kohgi M, Fujimoto H, Ohoyama K, Yamada K and Motoya M;
Proc. 11th Meeting Int. Collaboration on Advanced Neutron Sources (KEK, Tsukuba, Oct. 22-26, 1990), 733.

Recent Progress on MAX,
Todate Y, Ikeda H, Tajima K and Tomiyoshi S;
Proc. 11th Meeting Int. Collaboration on Advanced Neutron Sources (KEK, Tsukuba, Oct. 22-26, 1990), 739.

Recent Progress in TOP Spectrometer,
Itoh S, Watanabe T and Endoh Y;
Proc. 11th Meeting Int. Collaboration on Advanced Neutron Sources (KEK, Tsukuba, Oct. 22-26, 1990), 792.

5. Crystal Structures

Refinement of the Structure of Ta_2D by High-Resolution Powder Neutron Diffraction,
Murata H, Asano H, Izumi F, Tomiyoshi S, Iwasa H, Satoh S and Watanabe N;
Trans. Jpn. Inst. Met. 26 (1985) 795.

Neutron diffraction study on the low-temperature monoclinic form of $CeCu_6$,
Asano H, Umino M, Onuki Y, Komatsubara T, Izumi F and Watanabe N;
J. Phys. Soc. Jpn. 55 (1986) 454.

Time-of-flight neutron diffraction study of Li_3N at high temperature,
Kawada I, Isobe M, Okamura F, Watanabe H, Ohsumi K, Horiuchi H, Sata T and Ishii T;
Mineral. J 13 (1986) 28.

Crystal Structure of $Ba_2HoCu_3O_{7-x}$ Determined by Neutron Powder Diffraction,
Asano H, Takita K, Ishigaki T, Akinaga H, Katoh H, Masuda K, Izumi F and Watanabe N;
Jpn. J. Appl. Phys. 26 (1987) 1341.

Neutron and X-ray Diffraction Studies of $RBa_2Cu_3O_{7-x}$,
Asano H, Takita K, Ishigaki T, Izumi F, Takayama -Muromachi E, Uchida Y and Watanabe N;
Physica 148B (1987) 302.

Neutron Diffraction Study on the Low-Temperature Monoclinic Form of $PrCu_6$,
Asano H, Umino M, Onuki Y, Komatsubara T, Izumi F and Watanabe N;
J. Phys. Soc. Jpn. 56 (1987) 2245.

Cation Distribution in (M', M)$_3Se_4$:II.$(V,Ti)_3Se_4$ and $(Cr,V)_3Se_4$,
Hayashi A, Ueda Y, Kosuge K, Murata H, Asano H, Watanabe N and Izumi F;
J. Solid State Chem. 71 (1987) 237.

Crystal Structure of $Ba_2ErCu_3O_{7-x}$ Determined by Neutron Powder Diffraction,
Ishigaki T, Asano H, Takita K, Katoh H, Akinaga H, Izumi F and Watanabe N;
Jpn. J. Appl. Phys. 26 (1987) 1681.

Rietveld Refinement of the Structure of $Ba_2YCu_3O_{7-x}$ with Neutron Powder Diffraction Data,
Izumi F, Asano H, Ishigaki T, Takayama -Muromachi E, Uchida Y, Watanabe N and Nishikawa T;
Jpn. J. Appl. Phys. 26 (1987) L649.

Crystal Structure of Orthorhombic Form of $Ba_2YCu_3O_{7-x}$ at 42K,
Izumi F, Asano H, Ishigaki T. Takayama-Muromachi E, Uchida Y and Watanabe N;
Jpn. J. Appl. Phys. 26 (1987) L1193.

Crystal Structure of the Tetragonal Form of $Ba_2YCu_3O_{7-x}$,
Izumi F, Asano H, Ishigaki T, Takayama -Muromachi E, Uchida Y and Watanabe N;
Jpn. J. Appl. Phys. 26 (1987) L1214.

Rietveld Analysis of Powder Patterns Obtained by TOF Neutron Diffraction using Cold Neutron Source,
Izumi F, Asano H, Murata H and Watanabe N;
J. Appl. Cryst. 20 (1987) 411.

Crystal Structure of the Superconductor $Ba_{1.8}Nd_{1.2}Cu_3O_{7-y}$,
Izumi F, Takekawa S, Matsui Y, Iyi N, Asano H, Ishigaki T and Watanabe N;
Jpn. J. Appl. Phys. 26 (1987) 1616.

Time-of-flight Neutron Diffraction Study on the Deformed Heusler Alloy,
Kamiyama T, Tomiyoshi S, Shinohara T, Asano H, Yamamoto H, Watanabe N;
Proc. Int. Symp. on Physics of Magnetic Materials (Sendai, Apr. 1987), World Scientific, Singapore (1987) 579.

Neutron Powder Diffraction from Polymorphs of $BaPb_{0.75}Bi_{0.25}O_3$,
Asano H, Oda M. Endoh Y, Hidaka Y, Izumi F, Ishigaki T, Karahashi K, Murakami T and Watanabe N;
Jpn. J. Appl. Phys. 27 (1988) 1638.

Crystal Structure of Oxide Superconductors,
Asano H;
Proc. Int. Conf. Electronic Materials (Tokyo, 1988) 15.

Time-of-flight Powder Neutron Diffraction Study of $LaNi_5D_3$,
Hayakawa H, Nomura K, Ishido Y, Akiba E, Shin S, Asano H, Izumi F and Watanabe N;
J. Less-Common. Met. (1988).

Neutron Diffraction Study of Nonstoichiometry in $Ba_{1.5}La_{1.5}Cu_3O_y$,
Izumi F, Takayama-Muromachi E, Kobayashi M, Uchida Y, Asano H, Ishigaki T and Watanabe N;
Jpn. J. Appl. Phys. 27 (1988) L824.

Structural Study of $La_{1+x}Ba_{2-x}Cu_3O_y$,
Izumi M and Uchinokura;
Proc. Int. Conf. High Temperature Superconductors Materials and Mechanisms of Superconductivity (Interlaken, Feb. 29-Mar. 4, 1988), Physica B.

Formation of the Metastable γ Hydride in Titanium,
Numakura H, Koiwa M, Asano H and Izumi F;
Trans. JIM suppl. 29 (1988) 439.

Determination of Space Group and Refinement of Structure Parameters for $La_2CuO_{4-\delta}$,
Yamada K, Kudo E, Endoh Y, Tsuda K, Tanaka M, Kokusho K, Asano H, Izumi F, Oda M, Hidaka Y, Suzuki M and Murakami T;
Jpn. J. Appl. Phys. 27 (1988) 1132.

Neutron Diffraction Study of the Metastable g Titanium Deuteride
Numakura H, Koiwa M, Asano H and Izumi F;
Acta metall. 36 (1988) 2267

Rietveld Structure Refinement of Superconducting $YBaSrCu_3O_{7-z}$ Using X-Ray and Neutron Powder Diffraction Data,
Akiba E, Hayakawa H, Mizuno M, Izumi F and Asano H;
Proc. Int. Symp. Superconductivity (Tsukuba, 1989) 95.

Oxygen Deficiency and Atomic Displacement in Superconducting $(Ba_{1-x}Nd_x)_2(Nd_{1-y}Ce_y)_2Cu_3O_{8+z}$,
Izumi F, Kito H, Sawa H, Akimitsu J and Asano H;
Physica C160 (1989) 235.

Neutron and Electron Diffraction Study of the Electron-Doped Superconductor $Nd_{1.845}Ce_{0.155}CuO_{4-y}$,
Izumi F, Matsui Y, Takagi H, Uchida S, Tokura Y and Asano H;
Physica C158 (1989) 433.

Structure Refinement of $La_{1.9}Ca_{1.1}Cu_2O_6$ with neutron Powder Diffraction Data,
Izumi F, Takayama-Muromachi E, Nakai Y and Asano H;
Physica C157 (1989) 89.

Metal Ordering and Oxygen Displacement in (Nd, Sr, Ce)$_2CuO_{4-y}$,
Izumi F, Takayama-Muromachi E, Fujimori A, Kamiyama T, Asano H, Akimitsu J and Sawa H;
Physica C158 (1989) 440.

Structural Properties of the Superconductor $LaBa_2Cu_{3-y}O_{7-z}$ in the Solid Solution System $La_{1+x}Ba_{2-x}Cu_{3-y}O_{7-z}$,
Izumi M, Yabe T, Wada T, Maeda A, Uchinokura K, Tanaka S and Asano H;
Phys. Rev. B40 (1989) 6771.

EXAFS and Neutron Diffraction Studies of Local and Average Structures for $YB_2C_{2.8}Z_{0.2}O_{7-\delta}$,
Maeda H, Koizumi A, Bamba N, Takayama-Muromachi E, Izumi F, Asano H, Shimizu K, Moriwaki H, Maruyama H, Kuroda Y and Yamazaki H;
Physica C157 (1989) 483.

Unusually Simple Crystal Structure of an Nd-Ce-Sr-Cu-O Superconductor,
Sawa h, Suzuki S, Watanabe M, Akimitsu J, Matsubara H, Watabe H, Uchida S, Kokusho K, Asano H, Izumi F and Takayama-Muromachi E;
Nature 337 (1989) 347.

Oxygen Deficiency in the Electron-Doped Superconductor $Nd_{2-x}Ce_xCuO_{4-y}$,
Takayama-Muromachi E, Izumi F, Uchida Y, Kato K and Asano H;
Physica C159 (1989) 634.

Neutron Diffraction Studies of High-Tc Superconductors at KENS,
Asano H;
Proc. Int. Symp. Advanced Nuclear Energy Research (Mito, 1990) 633.

Neutron X-Ray Diffraction Study of a Valence Fluctuating Compound $YbInCu_4$,
Kojima K, Nakai Y, Suzuki T, Asano H, Izumi F, Fujita T and Hihara T;
J. Phys. Soc. Jpn. 59 (1990) 792.

Effect of Annealing under High Oxygen Pressure on the Structure and Superconductivity of $(Ba_{0.85}Nd_{0.15})_2NdCu_3O_{6+z}$,
Mochiku T, Asano H, Akinaga H, Ohshima T, Takika K, Izumi F, Takeda Y, Takano M and Mizoguchi K;
Physica C167 (1990) 560.

Effect of Deformation on Pd_2MnSn Heusler Alloy Studied with Transmission Electron Microscopy, Profile Analysis of Neutron Powder Diffraction Pattern, and Magnetization Measurement
Kamiyama T, Shinohara T, Tomiyoshi S, Minonishi Y, Yamamoto H, Asano H and Watanabe N;
J. Appl. Phys. 68 (1990) 4741

6. Structure of Liquids and Glasses

High Resolution Short-range Structure of Ni-Ti and Cu-Ti Alloy Glasses by Pulsed Neutron Total Scattering,
Fukunaga T, Kai K, Naka M, Watanabe N and Suzuki K;
Proc. 4th Int. Conf. Rapidly Quenched Metals (Sendai, Aug. 24-28, 1981) 347.

Structure Modification of Pd-Zr Alloy Glasses due to Hydrogen Absorption,
Kai K, Fukunaga T, Nomoto T, Watanabe N and Suzuki K;
Proc. 4th Int. Conf. Rapidly Quenched Metals (Sendai, 1981) 1609.

Atomic and Electronic Structure of Amorphous CuTi Alloys,
Mizoguchi T, Gubler U, Oelhafen P, Guntherodt H.J, Akutsu N and Watanabe N;
Proc. 4th Conf. on Rapidly Quenched Metals (Sendai, 1981) 1307.

Structure and Physical Properties of Amorphous (Fe, Co, Ni, Pd)-Zr Alloys,
Mizouguchi T, Yamada S, Suemasa T, Nishioka J, Akutsu N, Watanabe N and Takayama S;
Proc. 4th Conf. on Rapidly Quenched Metals (Sendai, 1981) 89.

Structure Characterization of Amorphous Alloys by T-O-F Pulsed Neutron Scattering using Accelerator Neutron Source,
Suzuki K;
Proc. 4th Conf. on Rapidly Quenched Metals (Sendai, 1981) 89.

Neutron Diffraction Study of Amorphous Binary Alloys,
Mizoguchi T, Nishioka J, Yamada S, Suemasa T, Yoda S, Akutsu A, Narumi H, Kudoh T, Aimitsu M, Watanabe N, Nishi M and Motoya K;
J. Phys. Colloq. (France) 43 (1982) C9-659.

Local Structures of Amorphous As-Chalcogenide Systems by Means of High-Q Neutron Scattering and Infrared Reflection,
Arai T, Onari S, Katoh M, Mori T, Saegusa H, Yasuoka H, Hatori M, Ohkawa K, Fukunaga T and Watanabe N;
Physica 117B & 118B (1983) 965.

Chemical Short-Range Structure of Ni_xTi_{1-x} (x=0.26-0.40) Alloy Glasses,
Fukunaga T, Hayashi N, Kai K, Watanabe N and Suzuki K;
Physica 120B (1983) 352.

Layer Correlation in a-As $(Se_x\ S_{1-x})_3$ System,
Mori T, Yasuoka H, Saegusa H, Okawa K, Kato M, Arai T, Fukunaga T and Watanabe N;
Jpn. J. Appl. Phys. 22 (1983) 1784.

Structure and Properties of Amorphous Metal Hydrides,
Suzuki K;
J. Less-Common. Met. 89 (1983).

Experimental Determination of Partial Structures in $Ni_{40}Ti_{60}$ Glass,
Fukunaga T, Watanabe N and Suzuki K;
J. Non-Cryst. Solids 61 & 62 (1984) 343.

Indirect and Direct Correlations between Unlike Ions in Incompletely Hydrated Solution,
Ichikawa K, Kameda Y, Matsumoto T and Misawa M;
J. Phys. C. Solid State 17 (1984) L725.

Hydrogen Atom Environment in a Hydrogenated ZrNi Glass,
Suzuki K, Hayashi N, Tomizuka Y, Fukunaga T, Kai K and Watanabe N;
J. Non-cryst. Solids 61 & 62 (1984) 637.

Partial Structure Functions of NiZi Alloy Glass Determined by an Isotope-Substitution Neutron Diffraction Methods,-
Fukunaga T, Hayashi N, Watanabe N and Suzuki K;
Proc. 5th Int. Conf. Rapidly Quenched Metals, Elsevier Science Publishers B.V. (1985) 475.

Structure and Local Anisotropy of Amorphous Tb-Fe Alloys,
Hatta S, Mizoguchi T and Watanabe N;
Proc. 5th Int. Conf. Rapidly Quenched Metals, Elsevier Science Publishers B.V. (1985) 589.

Structural Analysis of Sodium Silicate Glassed Containing TiO_2 by Pulsed Neutron Scattering Measurement,
Hidaka H, Iwamoto N, Umesaki N, Fukunaga T and Suzuki K;
J. Mat. Sci. 20 (1985) 2497.

Structural Study of an Amorphous $Ni_{36}Zr_{64}$ Alloy,
Mizoguchi T, Yoda S, Akutsu N, Yamada S, Nishioka J, Suemasa T and Watanabe N;
Proc. 5th Int. Conf. Rapidly Quenched Metals, Elsevier Science, Publisher B.V. (1985) 483.

Compositional Variations in the Short-range Structure of $Ni_{1-x}B_x$ (x=0.18-0.40) Alloy Glasses,
Suzuki K, Fukunaga T, Itoh F and Watanabe N;
Proc. 5th Int. Conf. Rapidly Quenched Metals, Elsevier Science Publishers B.V. (1985) 479.

What Difference Exists in the Structure of SiO_2 and GeO_2 between Melt-quenched Bulk Glass and Sputter-Deposited Amorphous Film,
Suzuki K, Misawa M and Kobayashi Y;
J. Phys. Colloq. (France) 46 (1985) C8-617.

Local Atomic and Magnetic Structures of Amorphous $Fe_{1-x}B_x$ Alloys Studied by Neutron Scattering,
Xianyu Ze, Ishikawa Y, Fukunaga T and Watanabe N;
J. Phys. F : Met. Phys. 15 (1985) 1799.

The Structure of Same Univalent Metal Nitrate Melts Studied by Means of Pulsed Neutron Diffraction,
Yamaguchi T, Tamura Y, Okada I, Ohtaki H, Misawa M and Watanabe N;
Z. Naturforsch. 40a (1985) 490.

Short Range Structural Analysis of Lead Silicate Glasses by Pulsed Neutron Total Scattering,
Yamada K, Matsumoto A, Niimura N, Fukunaga T, Hayashi N and Watanabe N;
J. Phys. Soc. Jpn. 55 (1986) 831.

X-ray and Neutron Diffraction and Molecular Dynamics Simulation on Molten Lithium and Rubidium Nitrate,
Yamaguchi T, Okada I, Ohtaki H, Mikami N and Kawamura K;
Mol. Phys. 58 (1986) 349.

A Neutron Diffraction Study of Liquid D_2O in the Temperature Range of 25°-200°C,
Yamaguchi T, Tamura Y, Ohtaki H and Misawa M;
Abstract of Int. Okazaki Conf. (1986).

Chemical Fluctuation of Ti-Zr Isomorphous Alloy obtained by Rapid Quenching,
Fukunaga T, Shibuya S, Suzuki K and Misawa M;
J. Material Sci. Lett. 6 (1987) 1435.

A Structure Analysis of (Ti, Zr)-X Ternary Alloy Glasses by Neutron Scattering,
Fukunaga T, Shibuya S, Misawa M and Suzuki K;
J. Non-cryst. Solids 95 & 96 (1987) 263.

X-ray and Neutron Diffraction Analysis of Barium Silicate Glass,
Hasegawa H and Yasui I;
J. Non-cryst. Solids 95 & 96 (1987) 201.

Cation Distribution in $(M', M)_3Se_4$:I. $(Cr,Ti)_3Se_4$,
Hayashi A, Ueda Y, Kosuge K, Murata H, Asano H, Watanabe N and Izumi F;
J. Solid State Chem. 67 (1987) 346.

Neutron Diffraction of As-Quenched Ge_{20} Te_{80} Glass near the Glass-Undercooled Liquid Transition,
Ichikawa K, Kameda Y, Xu Q and Misawa M;
J. non-cryst. Solids 95/96 (Part I) (1987) 185.

Intermolecular Structure around Lithium Monovalent Cation in the Molten $LiAlCl_4$,
Kameda Y and Ichikawa K;
J. Chem. Soc., Faraday Trans. 2 (1987) 2925.

Partial Structure of Ni-Ni Correlation in Ni-42at%V Amorphous Alloy by Neutron Diffraction,
Fukunaga T, Urai S, Watanabe N and Suzuki K;
J. Phys. F: Metal Phys. 18 (1988) 99.

The Intra-Molecular Structure of a Water Molecule in Hydrated and Incompletely Hydrated LiCl solutions,
Ichikawa K and Kameda Y;
J. Phys.: Condense. Matter 1 (1989) 257.

Temperature Dependence of Structure of Liquid Carbon Tetrachloride Measured by Pulsed Neutron Total Scattering,
Misawa M;
J. Chem. Phys. 91 (1989) 5648.

Molecular Orientational Correlation in Liquid Halogens,
Misawa M;
J. Chem. Phys. 91 (1989) 2575.

Experimental Estimation of Orientational Correlation in Liquid Bromine,
Misawa M;
J. Chem. Phys. 91 (1989) 6563.

Structural Characterization of Ni-V Amorphous Alloys Prepared by Mechanical Alloying,
Fukunaga T, Homma Y, Misawa M and Sizili K;
Mat. Sci. Eng. A (1990) in press.

The Ni-Ni Partial Structure in Ni-V Alloy System Observed by Neutron Scattering during Mechanical Alloying Amorphization Process,
Fukunaga T Homma Y, Misawa M and Suzuki K;
J. Non-Cryst. Solids (1990) 721.

Amorphization in Immiscible Cu-V System by Mechanical Alloying and its Structure Observation by Neutron Diffraction,
Fukunaga T, Mori M, Inou K and Mizutani U;
Mat. Sci. Eng. A (1990) in press.

Amorphization of Immiscible Cu-Ta System by Mechanical Alloying and its Structure Observation,
Fukunaga T, Nakamura K, Suzuki K and Mizutani U;
J. Non-Cryst. Solids 117/118 (1990) 700.

Orientational Correlation in Liquid Phosphorous Tribramide Studied by Pulsed Neutron Total Scattering,
Misawa M, Fukunaga T and Suzuki K;
J. Chem. Phys. 92 (1990) 5486.

Effective Diameter of Molecules and Liquid-Gas Critical Point,
Misawa M;
J. Chem. Phys. 93 (1990) 8401.

Structure Factor of X_4 Tetrahedral molecular Liquid : Competition between Intramolecular and Intermolecular Atomic Spacing,
Misawa M;
J. Chem. Phys. 93 (1990) 6774.

Structure of Vitreous and Molten B_2O_3 Measured by Pulsed Neutron Total Scattering,
Misawa M;
J. Non-Cryst. Solids 122 (1990) 33.

Structure of Liquid Benzene and Naphthalene Studied by Pulsed Neutron Total Scattering,
Misawa M and Fukunaga T;
J. Chem. Phys. 92 (1990) 3495.

Pulsed Neutron Diffraction Study on a Molten NaOD Structure using a Nickel Metal Cell,
Ohtori N, Okazaki S, Odawara O, Okada I, Misawa M and Fukunaga T;
J. Phys.: Condense. Matter 2 (1990) 5825.

Structural Study on Molten MOD (M=^{7}Ki, Na and K) by Pulsed Neutron Diffraction,
Ohtori N, Okazaki S, Odawara O, Okada I, Misawa M and Fukunaga T;
J. Phys.: Condense. Matter 2 (1990) 8439.

Pulsed Neutron Diffraction Studies on Lanthanide (III) Hydrogen in Aqueous Perchlorate Solutions,
Yamaguchi T, Tanaka S, Wakita H, Misawa M, Okada I, Soper A. K. and Howells S. W;
Z. Naturforsch. 45a (1990) (in press)

Diffraction and X-ray Absorption Studies of Electrolyte Solutions,
Yamaguchi T;
Pure & Appl. Chem. 59 (1990) 2251.

7. Magnetic Structures and Excitations

Application of Neutron Diffraction to the Study of Interface Magnetization on Thin Film with Artificial Superlattices,
Endoh Y, Hosoito N and Shinjo T;
J. Magn. & Magn. Mater. 35 (1982) 93.

Magnetism of Fe Interface Studied by Neutron Diffraction,
Endoh Y, Ono H, Hosoito N and Shinjo T;
J. Magn. & Mang. Mater. 31-34 (1982) 881.

Studies on the Magnetism at the Surface and Interface Using Polarized Neutrons,
Endoh Y;
J. Phys. Colloq. (France) 43 (1982) C7-159.

Spin Glass Properties and Magnetic Correlation in $FeTiO_3$-Fe_2O_3System,
Ishikawa Y, Arai M, Saitoh N, Kohgi M and Takei H;
J. Magn. & Magn. Mater. 31-34 (1983) 1381.

Magnetic Properties of $Cr_{1/3}$ NbS_2,
Miyadai M, Kikuchi K, Kondoh H, Sakka S, Arai M and Ishikawa Y;
J. Phys. Soc. Jpn. 52 (1983) 1394.

Interface Magnetism of Fe-Sb Multilayer Films with Artificial Superstructure from ^{57}Fe and ^{121}Sb Mössbauer Spectroscopy, Neutron Diffraction and NMR Experiments,
Shinjo T, Hosoito N, Kawaguchi K, Tabata T, Endoh Y, Ajiro Y and Friedt J.M;
J. Phys. Soc. Jpn. 52 (1983) 3154.

Magnetic Phase Diagram of MnSi near Critical Temperature Studied by Neutron Small Angle Scattering,
Ishikawa Y and Arai M;
J. Phys. Soc. Jpn. 53 (1984) 2726.

Re-Entrant Spin-Glass Behavior of the Randomly Mixed Insulating Ferromagnet and Antiferromagnet, Rb_2 $Mn_{(1-x)}$ Cr_x Cl_4,
Katsumata K, Tanimoto M, Mitsuda S and Endoh Y;
J. Phys. Soc. Jpn. 53 (1984) 3315.

Magnetism of Iron Interface in Contact with Vanadium,
Shinjo T, Hosoito N, Kawaguchi K, Takada T and Endoh Y;
J. Phys. Colloq. (France) 45 (1984) C5-361.

A New Oxide Spin Glass System of (1-x) $FeTiO_3$-xFe_2O_3 II. Neutron Scattering Studies of a Cluster type Spin Glass 90$FeTiO_3$-10Fe_2O_3,
Arai M, Ishikawa Y, Saito N and Takei H;
J. Phys. Soc. Jpn. 54 (1985) 781.

A New Oxide Spin Glass System of (1-x) $FeTiO_3$-xFe_2O_3 IV. Neutron Scattering Studies on a Re-entrant Spin Glass of 79 $FeTiO_3$-21FeO_3 Single Crystal,
Arai M , Ishikawa Y and Takei H;
J. Phys. Soc. Jpn. 54 (1985) 2279.

A New Oxide Spin Glass System of (1-x) $FeTiO_3$-xFe_2O_3 III. Neutron Scattering Studies of Magnetization Processes in a Cluster type Spin Glass 90 $FeTiO_3$-10Fe_2O_3,
Arai M and Ishikawa Y;
J. Phys. Soc. Jpn. 54 (1985) 795.

Time of Flight Spectrometer with Optical Polarizer for Cold pulsed Neutrons,
Endoh Y, Mitsuda S, Ikeda S and Fujimoto H;
Nucl. Instrum. Methods A240 (1985) 115.

Magnetic Properties of Fe-V Multi Layered Films with Artificial Superstructures,
Hosoito N, Kawaguchi K, Shinjo T, Takada T and Endoh Y;
J. Phys. Soc. Jpn. 53 (1985) 2659.

Helicity of the Helical Spin Density Wave in MnSi - II polarized Neutron Diffraction,
Ishida M, Endoh Y, Mitsuda S, Ishikawa Y, Tanaka M and Takayashi H;
J. Phys. Soc. Jpn. 54 (1985) 2975.

Crystal Chirality and Helicity of the Helical Spin Density Wave in MnSi, II Polarized Neutron Diffraction,
Ishida M, Endoh Y, Mitsuda S, Ishikawa Y and Tanaka M;
J. Phys. Soc. Jpn. 54 (1985) 2975.

A New Oxide Spin Glass System of (1-x) $FeTiO_3$-xFe_2O_3 I. Magnetic Properties,
Ishikawa Y, Saito N, Arai M, Watanabe Y and Takei H;
J. Phys. Soc. Jpn. 54 (1985) 312.

Stability and Winding of the Long Period Helical Spin Structure in $Fe_{1-x}Co_xSi$,
Ishimoto K, Yamaguchi Y, Mitsuda S, Ishida M and Endoh Y;
J. Main. & Magn. Mater. 54-57 (1985) 1003.

Evidence for the correlation of the magnetic inhomogeneous structure with the fluctuation of chemical composition in Fe-Ni invar alloys,
Komura S, Takeda T and Endoh Y;
J. Magn. & Magn. Mater. 50 (1985) 1570.

Neutron Depolarization Studies on Magnetization Process Using Pulsed Polarizing Neutrons,
Mitsuda S and Endoh Y;
J. Phys. Soc. Jpn. 45 (1985) 1570.

Magnetic Properties of Artificial Metallic Superlattices,
Shinjo T, Hosoito N, Kawaguchi K, Nakayama N, Takada T and Endoh Y;
J. Magn. & Magn. Mater. 54-57 (1985) 737.

Neutron Scattering Study on Artificial Metallic Superlattices,
Endoh Y;
Applied Magnetism Seminar. (1986) 37-43.

Spin Dynamics in a Quasi 2-Dimensional Antiferromagnet $MnTiO_3$,
Todate Y, Ishikawa Y, Tajima K, Tomiyoshi S and Takei F;
J. Phys. Soc. Jpn. 55 (1986) 4464.

Magnetic and Transport Properties of Ce_2Sb and Ce_2Bi,
Isobe A, Ochiai A, Onodera S, Yamada K, Kohgi M, Endoh Y, Suzuki T and Kasuya T;
J. Magn. & Magn. Mater. 70 (1987) 391.

Small-Angle Neutron Scattering from Dynamically Polarized Hydrogenous Materials,
Kohgi M, Ishida M, Ishikawa Y, Ishimoto S, Kanno K, Masaike A, Masuda Y and Morimoto K;
J. Phys. Soc. Jpn. 56 (1987) 2681.

Monolayer of Ferromagnetic MnSb,
Shinjo T, Nakayama N, Moritani I and Endoh Y;
J. Phys. Soc. Jpn. 55 (1987) 2512.

Small-Angle Scattering of Polarized Neutrons from an $Fe_{65}{}^{60}Ni_{35}$ Inver Alloy,
Takeda T, Komura S, Miyazaki T, Endoh Y and Itoh S;
J. Magn. & Magn. Mater. 70 (1987) 431.

Study of ferrofluids by Neutron Depolarization,
Itoh S, Endoh Y and Pynn R;
J. Magn. Magn. Mat. 73 (1988) L1.

Neutron Diffraction Studies on Magnetic Properties of Fe/Dy artificial Superstructural Films,
Hosoito N, Yoden K, Mibu K, Shinjo T and Endoh Y;
J. Phys. Soc Japan 58 (1989) 1775.

Long-Period Magnetic Structures along the Axial Direction in the Layered Antiferromagnetic Compound,
Ikeda H and Tamura T;
Physica B 156&157 (1989) 318.

Magnetic Excitations in Low-Dimensional Antiferromagnets Measured with the MAX Spectrometer,
Tajima K, Todate Y and Ikeda H;
Physica B 156&157 (1989) 301.

Magnetic Excitations in the Two-Dimensional Random Antiferromagnets $Rb_2Co_cNi_{1-c}F_4$,
Todate Y, Ikeda H, Sano E, Shibata F, Tajima K and Endoh Y;
J. Phys.: Condens. Matter 1 (1989) 5895.

Evidence for Antiferromagnetic Coupling between Fe Layers through Cr from Neutron Diffraction,
Hosoito N, Araki S and Mibu K;
J. Phys. Soc. Jpn 59 (1990) 1925.

Ordering Kinetics in a Two-Dimensional Percolation Magnet,
Ikeda H, Endoh Y and Itoh S;
Physical Review Letters 64 (1990) 1266.

Magnetic Phase Transition in $CsVF_4$,
Ikeda H, Hidaka M and Wanklyn B. M;
Physica B 160 (1990) 287.

Crystal Field Excitations in Yb Monopnictides,
Kohgi M, Ohoyama K, Oyamada A, Suzuki T and Arai M;
Physica B 163 (1990) 625.

Competition between the Kondo Effect and RKKY Interactions in $CeSi_x$,
Kohgi M, Satoh T, Ohoyama K and Arai M;
Physica B (1990) in press.

Crystal Field Excitations in $CeSi_x$,
Kohgi M, Satoh T, Ohoyama K, Arai M and Osborn R;
Physica B 163 (1990) 137.

Neutron Depolarization in Reentrant Spin Glasses $Ni_{1-x}Mn_x$,
Mirebeau I, Itoh S, Mitsuda S, Watanabe T, Endoh Y, Hennion M and Calmettes R;
J. Appl. Phys. 67 (1990) 5232.

Neutron Depolarization in a Reentrant Spin-Glass System: Amorphous Fe-Mn,
Mirebeau I, Itoh S, Mitsuda S, Watanabe T, Endoh Y, Hennion M and Papoular R;
Phys. Rev. B 41 (1990) 11405.

Small Angle Neutron Scattering Studies on $Fe_{0.715}Al_{0.285}$ Reentrant Spin Glass,
Suzuki J, Endoh Y, Arai M, Furusaka M and Yoshizawa H;
J. Phys. Soc. Jpn. 59 (1990) 718.

Measurements of Two-Dimensional Antimagnetic Spin Wave by Using Chopper Spectrometer Installed in Pulsed Neutron Source
Yamada K, Arai M, Taylor A. D, Hosoya S, Sano A, Nakajima K, Ohoyama K, Kohgi M, Nakane T, Perring T and Endoh Y;
Proc. 11th Meeting Int. Collaboration on Advanced Neutron Sources (KEK, Tsukuba, Oct. 22-26, 1990), 1078

8. Dynamics in Solids and Liquids

The Local Environment around Hydrogen Atoms in Hydrogenated $NiTi_2$ Alloy Glass,
Kai K, Ikeda S, Fukunaga T, Watanabe N and Suzuki K;
Physica 120B (1983) 342.

Neutron Compton Spectroscopy of Pyrolitic Graphite,
Rauh H and Watanabe N;
Phys. Lett. 100A (1984) 244.

High-Q Neutron Scattering with the Resonance Detector Neutron Spectrometer RAT at the Pulsed Spallation Neutron Source KENS,
Rauh H and Watanabe N;
Presented at Symp. Neutron Scattering (Berlin, Aug. 6-8, 1984).

Determination of the Momentum Distribution of Scattering Particles from High Q Scattering Spectra of a Resonance Detector Neutron Spectrometer,
Rauh H and Watanabe N;
Nucl. Instrum. Methods 228 (1984) 147.

Low energy excitations in Ag_3SI,
Shibata K and Hoshino S;
J. Phys. Soc. Jpn. 54 (1985) 3671.

Local Modes and Hydrogen Potential in Metal Hydrides,
Ikeda S and Watanabe N;
J. Phys. Soc. Jpn. 56 (1987) 565.

Neutron Scattering from Superfluid ^4He at Very Large Momentum Transfer,
Ikeda S and Watanabe N;
Phys. Lett. A126 (1987) 34.

Phonons in $(La_{1-x}\ Sr_x)_2\ CuO_4$ and $BaPb_{1-x}BixO_3$,
Masaki A, Satoh H, Uchida S, Katsuzawa K, Tanaka S and Inoue K;
Jpn. J. Appl. Phys. 26 (1987) L405.

Copper and Oxygen Vibrations in La_2CuO_4 and $YBa_2Cu_3O_7$,
Ikeda S, Misawa M, Tomiyoshi S, Suzuki T and Omori M;
Phys. Lett. A 134 (1989) 191.

Low-Energy Excitation in β-Cu_2Se,
Sakuma T and Shibata K;
J. Phys. Soc. Jpn. 58 (1989) 3061.

Low-Energy Excitation in Copper Ion Conductors,
Sakuma T, Shibata K and Hoshino S;
Solid State Ionics 40/41 (1990) 337.

Dynamic Structure of Molten $0.80RbNO_3$-$0.20Sr(NO_3)_2$ Mixture by Neutron Quasielastic Scattering,
Shibata K, kamiyama T, Suzuki K and Inoue K;
J. Non-Cryst. Solids 117/118 (1990) 120.

9. Materials Science

Influence of Microstructure on the Flux Pining in Nb-Ti Multifilamentary Superconducting Wires,
Gotoda H, Osamura K, Furusaka M, Arai M and Suzuki J;
Phil. Mag. B 60 (1989) 819.

10. Polymers

Folding-Unfolding of alpha-Lactalbumin,
Izumi Y, Miyake Y, Kuwajima K, Sugai S, Inoue K, Iizumi M and Katano S;
Physica 120B (1983) 444.

Compensation Point in Semi-Dilute Polymer Solutions as Observed by SANS,
Okano K, Kurita K, Nakajima S, Wada E, Furusaka M and Ishikawa Y;
Physica 120B (1983) 413.

Molecular Spectroscopy of Polymers by Neutron Inelastic Scattering,
Kaji K, Kanaya T and Inoue K;
Proc. 1st SPSJ Int. Polymer Conf. (Kyoto, Aug. 20-24, 1984) 288.

Local Motion of Polymers in the Rubbery State Studied by Neutron Quasielastic Scattering,
Kanaya T, Kaji K, Kitamaru R and Inoue K;
Proc. 1st SPSJ Int. Polymer Conf. (Kyoto, Aug. 20-24, 1984) 237.

Neutron Inelastic Seattering Spectra of Native and Regenerated Celluloses,
Kaji K, Kanaya T, Inoue K, Kitamaru R and Sakurada I;
Cellulose Chem. Tehnol. 19 (1985) 321.

Coexistence Curve of Semidilute Polymer Solutions,
Okano K, Ichimura T, Kurita K, and Wada E;
Polymer 28 (1987) 693.

Low Energy Excitations in Polyethylene: Comparison between Amorphous and Crystalline Phases,
Kanaya T, Kaji K, Ikeda S and Inoue K;
Chem, Phys. Lett. 150 (1988) 334.

Monoclinic to Orthorhombic Transformation in Polyethylene,
Takahashi Y, Ishida T and Furusaka M;
J. Polym Sci. Poly. Phys. (1988).

Sol-Gel Transition of Atactic Polystyrene Solutions,
Izumi Y;
Int. Conf. on Polymer Research by Neutron Scattering. The Taniguchi Conference (Kyoto, Nov. 7-9, 1989) 155.

Low Energy Excitations in Amorphous Polymers,
Kanaya T, Kaji K and Inoue K;
Int. Conf. Polymer Research by Neutron Scattering (The Taniguchi Conference, Kyoto, 1989) 119.

Vibrational Modes of trans-1, 4-Polychloroprene by Neutron Incoherent Inelastic Scattering,
Kanaya T, Ohkura M and Kaji K;
Bull. Inst. Chem. Res. Kyoto Univ. 60 (1989) 68.

Thermoreversible Gelation of the System of Atactic Polystyrene-Carbon Disulfide. VIII,
Izumi Y, Katano S, Funahashi S, Furusaka M and Arai M;
Repts. Prog. Polym. Phys. Jpn. 33 (1990) 15.

11. Biology

Small Angle Neutron Scattering Studies of the Structure of Nucleosome Cores at Low Ionic Strength,
Mita K, Zama M, Ichimura S, Niimura N, Kaji K, Hirai M and Ishikawa Y;
Physica 120B (1983) 436.

Studies of Constrained Dynamics of the Phase Transition in the Artificial Bilayer Membrane of Dialkyl Ammonium Amphiphile by Quasielastic Neutron Scattering,
Ito Y, Shigekawa N, Harada M, Inoue K, Boni P;
J. Phys. Soc. Jpn. 52 (1987) 2060.

Interparticle Interactions and Structural Change of Nucleosome Core Particles in Low Salt Solution,
Hirai M, Niimura N, Zama M, Mita K, Ishimura S, Tokunaga F and Ishikawa Y;
Biochemistry 27 (1988) 7924.

12. Non-Equilibrium Systems

Spinodal Decomposition in Fe-Cr Alloys Studied by Small Angle Neutron Scattering,
Furusaka M, Ishikawa Y, Yamaguchi Y and Fujino Y;
Physica 120B (1983) 383.

Early Stage of Phase Separation Processes in FeCr and AlZn Alloys,
Furusaka M, Ishikawa Y and Mera M;
Phys. Rev. Lett. 54 (1985) 2611.

Studies on Early and Late Stage of Formation of δ' phase in Al-Li Alloys by Neutron Small Angle Scattering,
Fujikawa S, Furusaka M. Sakauchi M and Hirano K;
Proc. 4th Int. Conf. on Aluminium-Lithium Alloys (Paris, June 10-12, 1987) Soc. Fancaise Metallurgie (1987).

Studies on Early and Late Stages of Formation of δ' Phase in Al-Li Alloys by Neutron Small Angle Scattering,
Fujikawa S, Furusaka M, Sakauchi M and Hirano K;
J. Phys. C3 (1987) 365.

The Very Early Stage of Phase Separation Process in Al-Li Alloys Studies by Small-Angle Neutron Scattering,
Furusaka M, Fujikawa S, Sakauchi M and Hirano K;
Proc. Int. Symp. on Dynamics of Ordering Process in Condensed Matter (Kyoto, Aug. 27-30, 1987), Plenum Press (1987) 281.

Computer Simulations of Domain Growth under Shear Flow,
Ohta T, Nozaki H and Doi M;
Phys. Lett. A 145 (1990) 304.

13. Nuclear Physics

Present and Future of Spin Physics at KEK,
Masaike A;
Proc. 7th Int. Symp on High Energy Spin Physics (Serpukhov, USSR, Sept. 1986).

Helicity Dependence of Neutron Radiative Capture Reactions,
Masuda Y, Adachi T, Ishimoto S, Masaike A and Morimoto K;
Proc. Test of Time Reversal Invariance in Neutron Physics (Chapel Hill, Apr. 17-19, 1987).

Parity Non-Conserving Effect in the Neutron Radiative Capture Reaction,
Masuda Y, Adachi T, Ishimoto S, Kikutani E, Koiso H, Morimoto K and Masaike A;
Hyperfine Interactions 34 (1987) 143.

Neutron Scattering by Inhomogeneous Distribution of Proton Polarization Produced by the Dynamic Nuclear Polarization,
Masuda Y;
Hyperfine Interactions 35 (1987) 1071.

Feasibility Study of a Strong Ultra Cold Neutron Source,
Yoshiki H and Ishimoto S;
Z. Phys. B-Condensed Matter 67 (1987) 161.

Measurement of Longitudinal Asymmetry in Neutron Radiative Capture Reactions,
Masuda Y, Adachi T, Ishimoto S, Kikutani E, Kohgi M, Koiso H, Masaike A and Morimoto K;
Proc. PANIC '87 (Kyoto, Apr. 20-24, 1987), Nucl. Phys. A478 (1988) 737C.

From Ultracold Antineutrons to neutron Spin Echo- the Bootstrap offers Significant gains in Sensitivity,
Golub R, Yoshiki H and Gaehler R;
Nucl. Inst. and Methods in Phys. Research A284 (1989) 16.

Ultra-Cold-Anti-Neutron (UCN) (I),
Golub R and Yoshiki H;
Nucl. Physics A501 (1989) 869.

Longitudinal Asymmetry in Neutron Radiative Capture Reaction of ^{139}La,
Masuda Y, Adachi T, Masaike A and Morimoto K;
Nuclear Physics A504 (1989) 269.

P- and T-violation in Slow- Neutron Scattering,
Masuda Y;
Proc. The XXIII Yamada Conf. on Nuclear Weak Process and nuclear Structure (June 12-15, 1989, Osaka, World Scientific) 151.

Parity Violation in Neutron Capture Reaction,
Masuda Y;
A.I.P. Conf. Proc. the 8th Int. Symp. on High Energy Spin Physics (Univ. of Minnesota, Minneapolis, Sep. 12-17, 1988) 482.

Enhancement of Parity-Violating Effect in Neutron-Nucleus Interaction,
Masuda Y;
Proc. 17th INS Int. Symp. on Nuclear Physics at Intermediate Energy (Nov. 15-17, 1988 Tokyo, World Scientific) 424.

Present Status of P Violation and Future T Violation Experiments on Neutron-Nucleus Interaction at KEK,
Masuda Y, Adachi t, Ishimoto S, Masaike A, Morimoto K and Shimizu H.M;
Proc. The 18th INS Int. Symp. on Physics with High-Intensity Hadron Accelerators (Tokyo, Mar. 14-16, 1990).

P-Violation and T-Violation Experiments on Neutron-Nucleus Interaction at KEK,
Masuda Y;
Proc. the VI Int. School on Neutron Physics (Alushta, USSR, Oct. 8-18, 1990).

T Violation in Neutron-Nucleus Interaction,
Masuda Y;
Proc. Int. Workshop on Polarized Ion Sources and Polarized Gas Jets KEK Report 90-15 (Feb. 12-17, 1990, KEK) 249.

14. Publications in Japanese

Pulsed Neutron Source and KENS Project,
Watanabe N;
J. Cryst. Soc. Jpn. 21 (1979) 151.

Pulsed Spallation Neutron Source and Neutron Scattering at KEK,
Watanabe N, Sasaki H and Ishikawa Y;
J. At. Energy Soc. Jpn. 23 (1981) 389.

Sealing with Gasket and Flanges of Superfluid Helium II,
Ishimaru H and Yoshiki H;
Cryogenic Eng. 17 (1982) 222.

Neutron Position Sensitive Detector using ^{6}Li-glass Scintillator,
Niimura N;
J. Cryst. Soc. Jpn. (1982) 396.

Neutron Scattering Studies on Biological materials (I), (II), (III), (IV),
Niimura N and Kaji H;
Chemistry and Biology 21 (1983) 250,328,405,466.

Chemical Short-range Structure of Amorphous Metals,
Fukunaga T and Suzuki K;
Gekkan Physics (1984) 209.

Structural Studies of Materials by Neutron Diffraction,
Horiuchi H and Kawada I;
Ceramics 19 (1984) 658.

Construction of High Gradient Permanent Quadrupole Magnets for 400MHz Linac,
Kumada M, Baba H, Inagaki S, Kaneko N and Sasaki H;
Proc. 9th Meeting on Linear Accelerator (Kyoto, July 20-22, 1984) 42.

Neutrons in Biology,
Niimura N;
Gekkan Physics 5 (1984) 96.

Generation and Utilization of Ultra-Cold Neutrons, Application in Condensed Matter Research and Elementary Particle Physics,
Utsuro M and Yoshiki H;
Gekkan Physics 5 (1984) 135.

Neutron Scattering Instruments at National Laboratory for High Energy Physics,
Watanabe N;
J. Cryst. Soc. Jpn. 26 (1984) 294.

Pulsed Neutron Source and its Utilization in Condensed Matter Research,
Watanabe N;
Gekkan Physics 5 (1984) 127.

Neutron Scattering Instruments at National Laboratory for High Energy Physics,
Watanabe N;
J. Cryst. Soc. Jpn. 26 (1984) 294.

Neutron Scattering Facility at National Laboratory for High Energy Physics,
Watanabe N and Ishikawa Y;
Butsuri 39 (1984) 826.

Operation of a Superfluid Ultra-cold Neutron Converter,
Yoshiki H;
KEK Report 84-2 (1984).

High Intensity Proton Synchrotron GEMINI and Intense Pulsed Neutron Source KENS-II,
Sasaki H and Watanabe N;
Spallation Neutron Engineering, Atomic Energy Society Japan (1984) 173.

Accelerator Based Cold Neutron Source and Cryogenic System,
Inoue K, Yanai M and Ishikawa Y;
Cryogenic Eng. 20 (1985) 63.

Spin Glasses in Dense Random System,
Ishikawa Y;
Solid State Phys. 20 (1985) 229.

Direct Observation of Bose Condensation in ^{4}He-II by Neutron Scattering with Very Large Momentum Transfer,
Watanabe N and Ikeda S;
Butsuri 40 (1985) 283.

Determination of Water Structure and Inelastic Scattering Effect by Time-of-flight Neutron Diffraction,
Kameda Y and Ishikawa K;
J. Chem Soc. Jpn. 11 (1986) 1509.

Neutron Sources Using Proton Accelerators and Their Utilization,
Watanabe N;
Nuclear Engineering 32,3 (1986) 20.

High Tc Superconductor $YBa_2Cu_3O_{7-\delta}$ Observed by Pulsed Neutrons,
Asano H, Izumi F and Watanabe N;
Butsuri 42 (1987) 901.

Neutron Scattering (Topics:New Progress in High Tc Superconductor III),
Endoh Y;
Parity 2 (1987) 48.

Partial Structure of Amorphous Metal,
Fukunaga T;
J. Jpn. Inst. Met. 26 (1987) 481.

Crystal Structure of High Tc Superconductor,
Izumi F and Asano H;
Chemistry Today Nov. (1987) 16.

Crystal Chemistry of Compounds with the Oxygen-Deficient Triperovskite Structure,
Izumi F and Asano H;
Kagaku to Kogyo 40 (1987) 1000.

Rietveld Analysis of the High-T_c Superconductor $Ba_2YCu_3O_{7-x}$,
Izumi F and Asano H;
Oyo-Butsuri 56 (1987) 1053.

Crystal Structure of High Tc Superconductors and Related Compounds,
Izumi F and Nakai I;
J. Cryst. Soc. Jpn. 29 (1987) 365.

Gelation of Polymer Chains — Solid-Gel Transition —,
Izumi Y and Miyake Y;
Butsuri 42 (1987) 327.

Oxygen Distribution in High Tc Superconductors Observed by Neutrons,
Watanabe N;
Parity 3 (1988) 42.

Neutron Scattering for Industrial Application,
Watanabe N;
Mirai-Sangyo Gijutsu IV, Kagaku-gijutsu Koho Zaidan (1988) 1092.

Recent Status of Neutron Scattering Facility at National Laboratory for High Energy Physics,
Watanabe N;
J. Cryst. Soc. Jpn. 30 (1988) 223.

New Data Acquisition System at KENS Pulsed Neutron Source,
Arai M and Furusaka M;
BUTSURI 44 (1989) 664.

Amorphization by Milling and its Atomic Structure,
Fukunaga T;
J. Adv. Sci. 1 (1989) 46.

Particle Physics by Ultra Low Energy Neutrons,
Masaike A and Masuda Y;
Butsuri 44 (1989) 649.

Polarizer for Epithermal Neutrons : Development in New Field of Nuclear Physics, Particle Physics, Condensed Matter Physics and Bio-Physics,
Masuda Y;
Butsuri 44 (1989) 755.

Structure and Dynamic Properties of Liquid Water in Micropores,
Yamaguchi T;
Denki Kagaku 57 (1989) 632.

Atomic Structure of Ni-V Amorphous Alloy Prepared by Mechanical Alloying,
Fukunaga T, Homma Y and Suzuki K;
J. S. P. M. 5 (1990) 52.

Chemical Structure of Ni-Ti Neutron Zero Scattering Amorphous Powders Prepared by MA,
Fukunaga T, Misawa M, Suzuki K and Mizutani U;
J. S. P. M. (1990) in press.

Compulsory Mixing Down to an Atomic level Immiscible Systems by Ball Milling,
Fukunaga T;
J. Adv. Sci. (1990) in press.

Amorphization of Immiscible Cu-Ta Powders Subjected to Mechanical Alloying,
Lee C. H, Sakurai K, Fukunaga T and Mizutani U;
J.S.P.M. (1990) in press.

Structural Changes in V-M(Fe, Cu) Systems Induced by Mechanical Alloying,
Mori M, Fukunaga T, Mizutani U and Misawa M;
J.S.P.M. (1990) in press.

Amorphous in Immiscible Cu-V System by Mechanical Alloying and its Atomic Structure,
Mori M, Inou K, Fukunaga T and Mizutani U;
J. S. P. M. 5 (1990) 56.

15. Proceedings of Workshops

The First KEK Symposium on Ultra Cold Neutrons (UCN) (KEK, Tsukuba, March 10, 1988),
Ed Yoshiki H;
KEK Report 88-3.

The Workshop on Neutron Scattering Research with Intense Spallation Neutron Source "Today and Tomorrow", (Tsukuba, October 6-7, 1987),
Ed. Watanabe N, Arai M et. al;
KEK Internal 88-9.

Proc. of the Workshop on Spin Glass Systems (KEK, Tuskuba, February 21, 1989),
Ed. Arai M;
KEK Internal 88-22.

The Workshop of the High Resolution Neutron Powder Diffraction Method, (KEK, Tuskuba, March 6, 1989),
Ed. Watanabe N and Asano H;
KEK Internal 89-3.

JHP/KENS-II Workshop (KEK, Tuskuba, March 29, 1989),
Ed. Ikeda S and Misawa M;
KEK Internal 89-13.

The 2nd KEK Symposium on Ultra Cold Neutrons (UCN) (KEK, Tsukuba, March 11, 1989),
Ed Yoshiki H;
KEK Report 89-13.

Proc. of the Second Workshop of Japan-UK Collaboration on Neutron Scattering Research (KEK, Tsukuba, November 1, 1989),
Ed. Watanabe N, Arai M and Ikeda S;
KEK Report 89-19.

Proc. of the Workshop on Polymer Science Studied by Neutron Scattering (KEK, Tuskuba, Mar. 15, 1989),
Ed. Kaji K., Kurita K, Izumi Y and Furusaka M;
KEK Internal 90-3.

Proc. of the Workshop on Materials Science Studied by Neutron Scattering (KEK, Tuskuba, Apr. 14-15, 1989),
Ed. Furusaka M;
KEK Internal 90-4.

Proc. of the Workshop on Structure Study of Biology by X-Ray and Neutron Scattering (KEK, Tsukuba, Mar. 6-7, 1989),
Ed. Niimura N and Furusaka M;
KEK Internal 90-5.

Proc. of the Workshop on Small Angle Neutron Scattering (KEK, Tuskuba, Feb. 23, 1989),
Ed. Furusaka M;
KEK Internal 90-6.

TUNNEL 901 (KEK, Tuskuba, March 8, 1990),
Ed. Ikeda S;
KEK Internal 90-7.

TUNNEL 902, Japan-UK collaboration on Neutron Scattering Research (KEK, Tuskuba, April 24, 1990),
Ed. Ikeda S;
KEK Internal 90-17.

Proc. of The Workshop on Statistical Physics on Magnetic Materials and Neutron Scattering (KEK, Tuskuba, February 23, 1990),
Ed. Yoshizawa H, Arai M and Endoh Y;
KEK Internal 90-18.

Proc. of the Workshop on Polymer Science Studied by Neutron Scattering (KEK, Tsukuba, Mar. 20, 1990),
Ed. Kanaya T and Furusaka M;
KEK Internal 90-26.

Current Status and Future Prospects of Powder Diffraction, Proc. of the Japan-UK Joint Meeting on Neutron Powder Diffraction (KEK, Tuskuba, April 23, 1990),
Ed. Kamiyama T, Asano H and Furusaka M;
KEK Internal 90-30.